SAPIENZA
UNIVERSITÀ DI ROMA

Dottorato di Ricerca in Fisica degli Acceleratori

Ciclo XXVIII

Space Charge Compensation and Electron Cloud Effects in Modern High Intensity Proton Accelerators

Thesis advisor
Prof. Luigi Palumbo

Candidate
Roberto Salemme

Supervisors
Dr. Dirk Vandeplassche (SCK•CEN)
Dr. Vincent Baglin (CERN)

October 2016

Preface

The present work deals with two of the numerous challenges of modern and future particle accelerators targeting high intensity proton beams: the beam dynamics of low energy intense beams in linear accelerators, which is influenced by space charge, and the beam induced multipacting causing the so called electron cloud in high energy circular accelerators. These themes have been the subject of my privileged involvement with two projects at the forefront of accelerator science and technology in the years 2013-2016. Space charge and its compensation was at the basis of the design of the Low Energy front-end of the Multi-purpose hYbrid Research Reactor for High-tech Applications (MYRRHA) accelerator project, which I joined in the period 2013-2014 in quality of Accelerator System Engineer at the Studiecentrum voor Kernenergie - Centre d'Étude de l'énergie Nuclaire (SCK•CEN), based in Mol and Louvain-la-Neuve, Belgium. The study of electron cloud effects and their mitigation comes from the involvement (since 2014) in the High Luminosity upgrade project of the Large Hadron Collider (LHC), in quality of Research Fellow of the European Organization for Nuclear Research (CERN) and in charge of the COLD bore EXperiment (COLDEX), in Meyrin, Switzerland.

The realization of this work is essentially based in the trust, encouragement and support of the people surrounding the professional and personal course of my doctoral undertaking, which was equally important, if not superior, to my dedication.

I acknowledge the faithful guidance of Prof. Luigi Palumbo, an extraordinary person who combines the passion for his work with the generous aperture and altruism toward his students. I particularly owe him the proposal and successful completion of this work. I thank Prof. P. Bagnaia and Prof. R. Faccini, coordinators of the PhD programme in Accelerator Physics at Sapienza University of Rome during the cycle XXVIII, for their guidance and patience in dealing with the assignments and deadlines of this PhD.

I warmly acknowledge the supervision of Dr. Dirk Vandeplassche, Head of the Accelerator Design and Tests (ADT) Unit at SCK•CEN, with whom I had the privilege to work with, not only for his professional leadership and for sharing his profound knowledge in an incredible extent of fields of accelerator science and technology, but also for his constructive and friendly approach in everyday life. I equally thank Dr. Luis Medeiros Romão, MYRRHA Linear Accelerator R&D manager, who constantly and trustfully provided support and motivation to my work at SCK•CEN, in combination with an exceptional human relationship. I would like to thank Dr. H. A. Abderrahim, head of the MYRRHA project and Deputy Director General of SCK•CEN, who welcomed me in the MYRRHA project under his direction. I am grate to Dr. M. Loiselet and the whole Centre de Ressources du Cyclotron of the Université Catholique de Louvain, for hosting and providing assistance to the RFQ@UCL programme, of which I have been technically responsible. I acknowledge the fruitful collaboration and friendly support of many of the collaborators to the MYRRHA project with whom I was delighted to work, in particular J.-L. Biarrotte (CNRS-IN2P3/IPNO), F. Bouly, M. Baylac, D. Bondoux (LPSC - Universitĕ Grenoble-Alpes, CNRS/IN2P3), D. Uriot (CEA-DSM/IRFU/SACM), D. Mader, H. Podlech (IAP Frankfurt), J.-P. Carneiro (FNAL), R. Modic (Cosylab), X. Donzel, G. Gaubert (Pantechnik), F. Davin (UCL/CRC). A warm thank you to F. Belloni, A. Ottonello, D. Bisogni (SCK•CEN) for the nice time spent in Mol.

I express sincere gratitude to Dr. Vincent Baglin, former leader of the LHC Beam Vacuum (LBV) section and now at the head of the Vacuum Studies and Measurements (VSM) section, while coordinator of the Work Package (WP) 12 - Vacuum & Beam Screen - in the HL-LHC project, for his guidance as supervisor at CERN. From him I inherited the COLD bore EXperiment, which he led in the 1997-2005 period. I owe most of the knowledge in the field of electron cloud and

cryogenic vacuum systems to his guide and experience, which boasts participation to the design, construction, commissioning and operation of the LHC vacuum system. I equally thank him for sharing with me his scientific and diligent approach to the field of the experimentation, in which he has shown me the talent of mixing rigorousness and never-ending curiosity. I am particularly indebted to Dr. Giuseppe Bregliozzi, now leader of the Beam Vacuum Operation (BVO) section, who has been in charge for the recommissioning of the COLD bore EXperiment in 2013-2014. I received the COLD bore EXperiment from his hands in great shape, and it is mostly thanks to his commitment and expertise that the experiment is so successful and fruitful since 2014. I am grateful and honoured of the encouragement of Dr. Paolo Chiggiato, head of the Vacuum, Surfaces and Coatings group at CERN. His keen passion in sharing his unique and profound knowledge in the field of vacuum science and technology is truly exemplar. I am grateful for the constant, friendly, support of Dr. R. Kersevan and Dr. M. Taborelli, from whom I often profited of expert advice and genuine interest. I am indebted to Dr. R. Cimino (INFN/LNF) for sharing with me his infinite knowledge in surface science and electron cloud. A special thank you to A. Marraffa, with whom I really had a great time once arrived at CERN. I would like to acknowledge the competent and professional support of a incredible number of colleagues at CERN, especially from the groups TE/VSC, TE/CRG, BE/OP, BE/ABP, TE/EPC, EN/ICE, EN/MME and from the consortium AL40-30, who, thanks for their true commitment, have allowed me to get out most of the results presented in this Thesis. I would like to specifically acknowledge the help of B. Jenninger and A. Gutierrez, who have put their best experience and competence in assisting me in the endless hours on the field of the Super Proton Synchrotron accelerator. I am indebted to G. Iadarola for his assistance with the pyECLOUD code. A special thanks to the guys of BE/OP/SPS with whom I spent several nights in the CERN Control Centre (CCC) during the beam runtime.

This work is the resume of an authentic success which was possible thanks to all these people. On a equal footing, I wish to express my sincere and respectful gratitude to my family and friends, which have upheld my soul ensuring a strong sustain to my growth. A particular dedication goes to my beloved father and mother, Antonio and Manuela, who have made me the person I am today.

Besides this dissertation, I had the honour of producing the following scientific production (in chronological order):

1. R. Salemme, L. Medeiros Romão, D. Vandeplassche, J.-P. Carneiro, J.-L. Biarrotte, M. Baylac, D. Uriot, H. Podlech, "The R&D@UCL program in support of the MYRRHA linear accelerator", Proceedings of Technology and Components of Accelerator-Driven Systems (TCADS-2), OECD Nuclear Energy Agency, Second International Workshop - Nantes, France, May 2013

2. J.-P. Carneiro, L. Medeiros Romão, R. Salemme, D. Vandeplassche, J.-L. Biarrotte, F. Bouly, D. Uriot, "Approach of a failure analysis for the MYRRHA linac", Proceedings of Technology and Components of Accelerator-Driven Systems (TCADS-2), OECD Nuclear Energy Agency, Second International Workshop - Nantes, France, May 2013

3. R. Salemme, L. Medeiros Romão, D. Vandeplassche, "The MYRRHA linear accelerator R&D program", Proceedings of AccApp 2013, Eleventh International Topical Meeting on Nuclear Applications of Accelerators - Bruges, Belgium, August 2013

4. D. Vandeplassche, L. Medeiros Romão, R. Salemme, J.-L. Biarrotte, F. Bouly, J.-P. Carneiro, "Toward a virtual accelerator control system for the MYRRHA LINAC", 5th International Particle Accelerator Conference (IPAC'14) - Dresden, Germany, June 2014

5. R. Modic, G. Pajor, K. Zagar, L. Medeiros Romão, R. Salemme, D. Vandeplassche "Control system design considerations for MYRRHA ADS", 5th International Particle Accelerator Conference (IPAC'14) - Dresden, Germany, June 2014

6. R. Salemme, L. Medeiros Romão, D. Vandeplassche, D. Uriot, J.-L. Biarrotte, M. Baylac, D. Bondoux, F. Bouly, J.-M. De Conto, E. Froidefond, "Design progress of the MYRRHA low energy beam line", 27th Linear Accelerator Conference (LINAC14) - Geneva, Switzerland, September 2014

7. R. Salemme, V. Baglin, F. Bellorini, G. Bregliozzi, K. Brodzinski, P. Chiggiato, P. Costa Pinto, P. Gomes, A. Gutierrez, V. Inglese, B. Jenninger, R. Kersevan, E. Michel, M. Pezzetti, B. Rio, A. Sapountzis, "Recommissioning of the COLDEX experiment at CERN", 6th International Particle Accelerator Conference (IPAC'15) - Richmond, Virginia, USA, May 2015
8. R. Salemme, V. Baglin, G. Bregliozzi, P. Chiggiato, R. Kersevan, "Amorphous carbon coatings at cryogenic temperatures with LHC type beams: first results with the COLDEX experiment", 6th International Particle Accelerator Conference (IPAC'15) - Richmond, Virginia, USA, May 2015
9. R. Salemme, V. Baglin, G. Bregliozzi, P. Chiggiato, R. Kersevan, "Vacuum performance of amorphous carbon coating at cryogenic temperature with presence of proton beams", 7th International Particle Accelerator Conference (IPAC'16) - Busan, South Korea, May 2016

participate to the following conference, workshops, Design Reviews, and schools:

- Technologies and Applications of Particle Accelerators - Joint Universities Accelerator School (JUAS) - Archamps, France, February-March 2013
- MYRRHA Accelerator eXperiment (MAX) 5th general meeting & 3rd PCC meeting - Louvain-la-Neuve, Belgium, April 2013
- SLHiPP-3: 3rd Open Collaboration Meeting on Superconducting Linacs for High Power Proton Beams - Louvain-la-Neuve, Belgium, April 2013
- Technology and Components of Accelerator-Driven Systems (TCADS2), Second International Workshop - Nantes, Francia, May2013
- Factory Acceptance Test (FAT) and Site Acceptance Test (SAT) of the MYRRHA ECR Ion Source - Pantechnik, Bayeux, France, June 2013 and UCL/CRC, Louvain-la-Neuve, October 2013
- MYRRHA Low Energy Beam Transport (LEBT) 1st Design Review - LPSC Grenoble, France, June 2013
- AccApp 2013 - Eleventh International Topical Meeting on Nuclear Applications of Accelerators - Bruges, Belgium, August 2013
- MAX (MYRRHA Accelerator eXperiment) School - Institut für Angewandte Physik, Goethe-Universität - Frankfurt, Germany, October 2013
- MYRRHA Low Energy Beam Transport (LEBT) 2nd Design Review, Mechanical Design - LPSC Grenoble, France, October 2013
- MYRRHA Low Energy Beam Transport (LEBT) Control System Kick-off Meeting with Cosylab and LPSC - Grenoble, France, October 2013
- MYRRHA Accelerator eXperiment (MAX) 6th general meeting & 4rd PCC meeting - Capri, Italy, November 2013
- Workshop on "Accelerators for Future Spallation Sources: ESS, MYRRHA and the ISIS Upgrade", Institute of Physics, Cockcroft Institute, Warrington, United Kingdom, December 2013
- EUCARD2/MAX workshop on "Accelerators for Accelerator Driven Systems (ADS)" - CERN, Meyrin, Switzerland, March 2014
- SLHiPP-4: 4th Open Collaboration Meeting on Superconducting Linacs for High Power Proton Beams - CERN, Meyrin, Switzerland, May 2014
- 1st EuCARD-2 Annual Meeting - DESY, Hamburg, Germany, May 2014

- Electron Cloud meeting #16, #18 and #120 - CERN, Meyrin, Switzerland, October, December 2014, March 2015
- 13th IUVSTA School on Vacuum Gas Dynamics: Theory, Experiments and Applications - Thessaloniki, Greece, May 2015
- 5th Joint HiLumi LHC-LARP Annual Meeting - CERN, Meyrin, Switzerland, October 2015
- 7th International Particle Accelerator Conference (IPAC'16) - Busan, South Korea, May 2016

and technical Committees:

- LHC Injectors and Experimental Facilities Committee (IEFC), 117th, 119th and 141th meetings - CERN, Meyrin, Switzerland, October, November 2014, April 2015
- LHC Machine Committee (LMC), 202nd and 263rd meetings - CERN, Meyrin, Switzerland, January 2015, May 2016
- SPS and LHC Machine Protection Panel Meeting (MPP), 104th meeting - CERN, Meyrin, Switzerland, April 2015
- High Luminosity LHC Technical Coordination Committee (HL-LHC TCC), 2nd meeting - CERN, Meyrin, Switzerland, February 2016

be organiser and speaker of the following seminars:

- R. Salemme, F. Belloni, "MYRRHA: a polyvalent research project around an ADS nuclear reactor" - INFN Rome, February 2014
- R. Salemme, "The MYRRHA project and its accelerator front end test stand" - INFN Milan, April 2014
- R. Salemme, V. Baglin, G. Bregliozzi, "Main experimental outcomes obtained with the COLDEX experiment during 2014/15", TE/VSC/VSM Section Meeting - CERN, Meyrin, Switzerland, October 2015

be author of the following monographs:

- R. Salemme, "Space Charge in Linear Accelerators", May 2014
- R. Salemme, "Recommissioning of the COLDEX experiment to qualify the performances of a-C coatings at cryogenic temperature with LHC type beams", SPS Engineering Specification, CERN, Meyrin, Switzerland, 2015

and be supervisor of one Summer Student at CERN, on

- C. Grech, C. Barreto, R. Salemme, "COLDEX New Data Acquisition Framework", CERN-STUDENTS-Note-2015-106 - CERN, Meyrin, Switzerland, August 2015.

Contents

Preface **3**

1 Introduction **11**
1.1 Context . . . 11
1.2 Research aim and objectives . . . 12
1.3 Structure of the report . . . 12

I Space charge effects **15**

2 Space charge **17**
2.1 Beam self-generated fields and forces . . . 17
2.2 Space charge forces for different beam distributions . . . 18
2.2.1 Circular and uniform beam density . . . 18
2.2.2 Gaussian beam density . . . 19
2.2.3 Comparison . . . 20
2.3 Space charge expansion in a drift . . . 20
2.3.1 Example . . . 22

3 The RMS envelope equation with space charge **23**
3.1 RMS quantities . . . 23
3.2 RMS envelope equation in presence of space charge . . . 24
3.2.1 RMS envelope equation of an elliptical continuous beam . . . 25

4 Transport of high intensity beams at low energy **27**
4.1 Introduction . . . 27
4.2 The space charge compensation (SCC) principle . . . 27
4.3 RMS envelope equation with space charge in presence of SCC . . . 30
4.4 Choices for transport in Low Energy Beam Transport (LEBT) lines . . . 32
4.4.1 Electrostatic LEBTs . . . 32
4.4.2 Magnetic LEBTs . . . 33

5 The MYRRHA project and its high power proton accelerator **35**
5.1 Accelerator Driven Systems (ADS) . . . 35
5.1.1 Partitioning and Transmutation . . . 37
5.2 Accelerator requirements for ADS . . . 40
5.3 Accelerator choices for ADS . . . 43
5.4 The MYRRHA project . . . 43
5.5 The MYRRHA high power proton accelerator . . . 44
Fault tolerance . . . 45
Design choices . . . 45
5.5.1 The superconducting LINAC . . . 46
5.5.2 The injectors . . . 48

6 The MYRRHA low energy front-end design **51**
6.1 The RFQ@UCL R&D programme . . . 51
6.2 The Ion Source . . . 52
6.3 The Low Energy Beam Transport (LEBT) line . . . 56
6.3.1 LEBT solenoid sets . . . 60
6.3.2 Collimator slits . . . 63
6.3.3 Vacuum . . . 63
6.3.4 Cooling . . . 65
6.4 Beam diagnostics . . . 65
6.4.1 Faraday cup . . . 65
6.4.2 Emittancemeters . . . 66
6.5 The RFQ interface . . . 68
6.5.1 Beam chopper . . . 68
Back-up position . . . 74
Chopper driver . . . 75
6.5.2 RFQ collimator . . . 76
Sputtering . . . 80
6.5.3 RFQ electron repeller . . . 83
6.5.4 Current Transformer . . . 86
6.6 Characterization of the Ion Source . . . 88
6.7 LEBT beam transport and space charge compensation . . . 93

II Electron cloud effects **101**

7 Electron cloud build-up **103**
7.1 Introduction . . . 103
7.2 Primary electrons production mechanisms . . . 104
7.2.1 Residual gas ionization . . . 104
7.2.2 Photoemission by synchrotron radiation . . . 105
7.2.3 Losses . . . 108
7.3 Secondary electron emission . . . 109
7.4 Energy gain . . . 112
7.5 Build-up and beam induced multipacting . . . 117
7.6 Effect of external magnetic fields . . . 120
7.7 Electron cloud implications . . . 121
7.7.1 Implications on the beam . . . 121
7.7.2 Implications on the machine . . . 124

8 Electron cloud mitigation in cryogenic vacuum systems **131**
8.1 The Large Hadron Collider (LHC) beam vacuum . . . 131
8.1.1 Electron cloud mitigation in the LHC cryogenic vacuum . . . 137
8.2 The High Luminosity upgrade of the Large Hadron Collider: HL-LHC . . . 139
8.2.1 From LHC to HL-LHC . . . 140
8.2.2 Present limitations and hardware upgrade . . . 141
8.2.3 HL-LHC parameter list . . . 142
8.3 Electron cloud in the HL-LHC . . . 144

9 The COLD bore EXperiment (COLDEX) **149**
9.1 Motivation and amorphous carbon coating . . . 149
9.2 Experimental layout . . . 149
9.3 COLDEX measurements . . . 156
9.4 Beam measurements . . . 158
9.5 Vacuum characterization of a-C coating at cryogenic temperature . . . 158

10 Electron cloud modeling and build-up simulations for COLDEX **161**
10.1 Introduction: the pyECLOUD code . . . 161
10.2 Build-up simulations . . . 162
10.2.1 LHC type beams at SPS injection energy . . . 164
10.2.2 LHC type beams at SPS flat-top energy . . . 168
10.2.3 Warm case . . . 173
10.2.4 Residual gas type influence . . . 174
10.3 Build-up simulations with a-C coatings . . . 174
10.3.1 Updated model of SEY . . . 174
10.3.2 Simulation results . . . 175
10.3.3 Effect of electron reflectivity . . . 180

11 Experimental results with a-C coating in COLDEX **181**
11.1 Introduction . . . 181
11.2 Results during Run 1 . . . 183
11.3 Results during Run 2 . . . 186
11.4 Results during Run 3 . . . 188
11.5 Results of dedicated experiments . . . 193
11.5.1 MD1: H_2 coverage . . . 193
11.5.2 MD2: CO coverage . . . 196
11.6 Discussion . . . 198

III Summary, conclusions and future perspectives **207**

12 Summary, conclusions and future perspectives **209**

Appendices **215**

A Vacuum at cryogenic temperatures **217**
A.1 Basic quantities . . . 217
A.2 Monolayer . . . 220
A.3 Cryopumping regimes . . . 221
A.4 Cryogenic pumping . . . 221
A.5 Adsorption isotherms . . . 223
A.6 Saturated vapour pressure . . . 224
A.7 Thermal Desorption Spectroscopy . . . 225

List of Figures **247**

List of Tables **250**

Chapter 1

Introduction

1.1 Context

Over the last two decades, the international scientific community has been increasingly interested in availability of high power light ion accelerators in the multi-Megawatt range for several physics and engineering experiments. The application fields of such accelerators are essentially different.

Moderate (up to few GeV) energy and high intensity (several mA) beams are required for spallation neutron sources dedicated to study condensed matter physics (like SNS [1], J-PARC [2], ISIS [3], ESS [4] and CSNS [5]), the muons factories (SPL [6], ISIS, J-PARC), for radioactive ion beam production (SPIRAL-2 [7], FAIR [8]), accelerator driven sub-critical systems (MYRRHA [9], C-ADS [10]) or irradiation facilities (IFMIF [11]). A notable number of such projects have been launched all over the world, and currently (2016) several machines have already seen realization and are in commissioning or operational phase (SNS, J-PARC, ISIS, SPIRAL-2), while others are in R&D, design or construction phases (ESS, MYRRHA, C-ADS, CSNS, FAIR, IFMIF). One of the current challenges of high intensity accelerators is the beam dynamics of low energy beams, which is dominated by their space charge (electromagnetic self-induced) field. The resulting force, acting on the intense beams, is generally non linear. Intense beams may evolve in formation of halo, emittance growth and beam losses along their transport while still at low energy. These phenomena may heavily influence the machine performance or in some cases dramatically reduce the machine operability and availability.

Extremely high (thousands of GeV) energy and relatively high intensity beams are employed to answer the most basic inquiries into the dynamics and structure of matter, space and time in modern high energy colliders. The Large Hadron Collider [12] is the most powerful machine in this field currently existing (2016). The build-up of low energy electrons have shown to be a serious concern in high energy positively charged (e.g. proton, positron, ion) particle accelerators since 50 years [13]. Beam induced multipacting, leading to the formation of an electron cloud, is of major concern for most of the storage rings operating with large bunch currents and low bunch spacing and its effects are among the major limitations of present high energy colliders, such the CERN Large Hadron Collider (LHC) [14], and electron-positron colliders, like Relativistic Heavy Ion Collider (RHIC) [15], KEKB [16] and DAΦNE [17]. Mitigation and eventually suppression of electron cloud multipacting is one of the targets of future high intensity colliders and was specifically addressed in the High Luminosity upgrade of the LHC (HL-LHC) [18] and in Super-KEKB upgrade [19].

In Part I of this Thesis, the problem of space charge at low energy is discussed and its possible compensation is studied and analysed. A beam propagating in a low energy beam line induces ionization of the residual gas present in the vacuum chamber. The secondary particles produced by ionization (i.e. electrons or ions), which have an opposite polarity to the particles of the beam, are trapped in the beam potential; the particles with the same polarity are repelled. If the density of the neutralizing particles is sufficiently high, the low energy beam can be considered as a "plasma" experiencing a focusing effect that counteracts the space charge electric field. This phenomena is called Space Charge Compensation (SCC) or neutralization. Space Charge Compensation is often not fully completed and not homogeneous in space; besides, it is time dependent (in pulsed beams, transitory regimes are required before a steady state is reached). In order to describe correctly

the dynamics of a beam propagating in a Low Energy Beam Transport line, it is necessary to know the degree of space charge compensation, its longitudinal, transverse and time dependency. These values can be qualitatively estimated by using simple analytical models but it is becoming more and more necessary to obtain predictive and quantitatively accurate results, which currently (2016) can be partially obtained only by experimental characterization.

In Part II of this Thesis, the electron cloud formation, build-up and multipacting is discussed. In particle accelerators, beam particles produce low energy negatively charged particles, so-called primary electrons, via different mechanisms. Beam induced multipacting is driven by the electric field generated by the successive passage of charged particle bunches associated to the secondary emission of the new electrons from the bombarded beam pipe surface. The process rises in a resonance motion of secondary electrons leading to a formation of a so-called electron cloud. Electron cloud can have a charge density so high to influence the beam quality at each passage, inducing instabilities and losses. On the machine side, detrimental effects impact negatively on the machine performance and operability. The electron cloud mitigation measures for the HL-LHC upgrade are presented, alongside with the outcomes of the validation of the mitigation strategy in a real machine environment, purpose of the COLD bore EXperiment (COLDEX) [20].

1.2 Research aim and objectives

The first objective of the Thesis is to present the space charge problem in high intensity, low energy beams, showing its effects on the beam dynamics. After introducing the RMS envelope equation in presence of space charge, we discuss how space charge compensation can be achieved with intense ion beams at low energy and present its effects on the transport describing the RMS envelope equation with compensated space charge. The problem of space charge and the application of compensation techniques are analysed in the applied case of the MYRRHA accelerator for ADS applications. We present the characteristic of an Accelerator Driven System and its accelerator requirements; then, we review the design principles and choices made for the MYRRHA accelerator. We then move to the MYRRHA Low Energy front-end, which is specifically designed basing on space charge compensation. After a review of the rationale and design of the components and systems of low energy beam line, we show the results of the first beam tests on the Ion Source. Finally, we analyse the beam design of the Low Energy Beam Transport (LEBT) line, with a specific address on the space charge compensation principles adopted both for steady state and transient regimes.

The second goal of the Thesis is to present the electron cloud formation and build-up in high intensity, high energy beams circulating in modern colliders, and investigate its mitigation strategy in the specific case of the HL-LHC upgrade. After an analysis of the main mechanisms behind the beam induced multipacting, leading to the formation of an electron cloud, we present its implications both on the beam and the machine performance and operability. We discuss the mitigation strategy adopted in the LHC and the choice made future HL-LHC, basing on a-C coating. Its validation at cryogenic temperatures in a real machine environment is discussed and analysed in the specific case of the COLDEX experiment. After a description of the experiment layout and measurements, we show the results of the simulation studies, introducing lately a model of secondary emission specific for the a-C coating. We then present the experimental results of five beam runs where the performance of a-C were qualified with LHC type beams at cryogenic temperature. A discussion is held on the outcomes of experimental campaign.

1.3 Structure of the report

The Thesis is divided in three main parts. Part I deals with the space charge effects, while Part II with the electron cloud effects. Each of these parts is characterized by a similar structure. The first Chapters are usually dedicated to the theory elements and applied applications required to understand and describe each phenomenon. The following Chapters describe the application in the case of interest. The phenomena are studied and analysed first with a simulation approach with available or new tools; the simulation results are combined and compared, where applicable,

to experimental measurements. For the electron cloud effects, a full experimental campaign of validation and performance qualification is presented and discussed.

After this Introduction, in Chapter 2 and Chapter 3 we investigate the beam self-generated field and forces, calculating analytical expressions of the forces due to space charge for difference beam distributions. A focus on a simple exercise of space charge acting onto a beam drifting in empty space is presented. We examine one of the most important properties of the distributions behind a beam of particles, the RMS emittance, which is defined from the second moments of the particle distribution. RMS emittance is an important measure of the beam quality; it determines the inherent capability of producing, by means of a suitable focusing system, small sizes for the waists, angular divergences, micropulse width, and energy spread. The presence of the space-charge fields not only reduces the effective focusing strength of a transport system, but also produces nonlinear terms, and causes growth of the RMS emittances, which in turn degrades the intrinsic beam quality. One consequence of space-charge induced emittance growth is formation of a low-density beam halo surrounding the core of the beam, which can be the cause of beam losses, resulting in radioactivation of the accelerating structure, or, in the case of high energy beams lost in uncontrolled manner, serious damages. In Chapter 3, we write the RMS envelope equation in presence of space charge, and then suddenly apply the obtained formalism to an elliptical continuous beam. The systematic and scientific approach in the analytical definition of the concepts presented in Chapters 2 and 3 is inspired by comprehensive and distinguished dissertations, to which we owe reference [21] [22] [23] [24].

In the Chapter 4, we briefly review the transport of high intensity proton beams in low energy sections of LINACs, with particular interest on the propagation of intense beams from their production to the first RF acceleration structures. We will introduce one of the most interesting phenomena currently under study as "design tool" of many low energy beam transport lines, the Space Charge Compensation principle, and we will estimate the impact that it has on the RMS envelope in presence of compensated space charge. We will finally overview some of the engineering choices adopted to practically transport intense ion beams in modern LINACs.

Chapter 5 describes the Accelerator Driven System (ADS) concept and its impact on the nuclear fuel cycle. ADS may play a unique role in the future nuclear energy production scenarios including GEN-IV nuclear reactors, as it is a potential and promising candidate for transmutation purposes. The introduction of the Partitioning&Transmutation technique in the nuclear waste reprocessing cycle has the potential to solve the one of the major weakness of fuel cycle of energy production schemes including nuclear fission. We introduce the accelerator requirements for ADS systems, which require moderate energy but high intensity beams, in the multi-MW class, and unprecedented reliability. The span of possible choices for candidate ADS accelerators is presented: the superconducting LINAC, thanks to its modularity and fault tolerance, has the highest potential. We present the MYRRHA project and the rationale behind the MYRRHA Linear Accelerator design principles and choices, which foresee a superconducting LINAC consisting in distinct sections providing the highest degree of fault tolerance via redundancy.

In Chapter 6, we make a full and detailed description of the MYRRHA low energy front-end design, which makes use of the Space Charge Compensation as design principle. We analyse and discuss each element from the Ion Source up to the RFQ: emphasis is given to the design aspects which target the design goals of a safe and efficient production of a proton beam with high quality and low losses, in compliance with the ADS reliability targets. In the last part of this Chapter we review the beam tests characterizing the performance of the commissioned Ion Source and present the LEBT beam transport dynamics taking into account the Space Charge Compensation both in steady state and transient regimes.

Chapter 7 marks the beginning of Part II with the electron cloud effects. We start from the foundations of the electron cloud build-up, reviewing one by one the primary electrons production mechanisms, the secondary electron emission process from material surfaces, the most up-to-date Secondary Electron Yield model, the energy gain in the beam field and finally the build-up and beam induced multipacting conditions. The effects of externally applied magnetic fields is presented. The negative implications of the electron cloud build-up is analysed presenting the beam coherent tune shift, transverse instabilities and incoherent beam effects arising from the interaction of the beam with the electron cloud. The implications on the machine and the detrimental effects of vacuum degradation, dissipated heat load and distorted beam diagnostic performance

are discussed.

In Chapter 8 we present the LHC vacuum system and its beam vacuum requirements. The functionalities of a cryogenic vacuum beam vacuum characterized by a Cold Bore, held at 1.9 K, protected by a perforated Beam Screen, held in the 5 to 20 K temperature range, are described. We describe the electron cloud mitigation measures applied to the LHC design. After an introduction of the High Luminosity upgrade of the Large Hadron Collider, HL-LHC, we describe its goals and hardware upgrade, required to overcome the present LHC limitations. An up-to-date (2016) HL-LHC parameter list is included. We describe the predictions of the LHC observations to the HL-LHC upgrade and the possible measures to mitigate the electron cloud, in particular the a-C coating under validation.

Chapter 9 is devoted to the presentation and description of the COLD bore EXperiment, COLDEX, which mimics a LHC-type cryogenic vacuum system and is installed in the Super Proton Synchrotron. The experimental setup is conceived to study the beam induced multipacting in a LHC type cryogenic vacuum system as a function of the BS temperature and the circulating beam parameters. The motivations of its recommissioning with an amorphous carbon coated beam screen are analysed and the goal of experimental validation at cryogenic temperatures in a real machine environment is enunciated. We present the full experimental layout and the measurements span possible in COLDEX. The vacuum characterization - without beams - of a-C coating at cryogenic temperature currently (2016) ongoing in the experiment is shortly presented, as it is a necessary basis for the understanding of the vacuum related results presented in Chapter 11.

With Chapter 10, we present the electron cloud modeling and build-up simulations for the COLDEX experiment, a necessary tool to master the influence of the different parameters on the experimental observations. The electron cloud build-up is in fact extremely sensitive to the beam and surface emission features and a full characterization by complete build-up simulation sets is required to predict the real effects, as no comprehensive scaling laws exist. We show the influence of the SEY, bunch intensity, beam energy, beam screen temperature and primary ionization on the electron cloud build-up in COLDEX expected by simulation. At the end of the Chapter, a novel and updated model of SEY specific for a-C coatings, developed on phenomenological modeling on real measurement datasets, is presented. This new input is inserted in a new simulation set where its influence, combined with the sensitivity to SEY, bunch intensity, beam energy, and electron reflectivity, is shown.

In the last chapter of Part II, Chapter 11, we include all the experimental results with a-C coating in COLDEX collected in the time period 2014-2015. After an introduction on the experimental protocols, we describe in details five beam runs with an a-C coated beam screen, analysing the experimental data arising from the measurement of dynamic pressure rise, gas composition, dissipated heat load and electron activity observed as a function of the beam parameters and the cold bore and beam screen surface conditions (temperature and gas coverage). The last Section is devoted to a joint and critic discussion of all the observation, with particular emphasis on a comparison with what was observed in past and what was expected by a-C coatings.

In the last Part III, a summary of the research objectives and results is made and the main conclusions are drawn. The future perspectives, in particular for the MYRRHA project and the COLDEX experiment, are presented.

The Appendix A presents the foundations of cryogenic vacuum science and is joint to this Thesis as supplementary expertise required to the reader for the full understanding of cryogenic vacuum systems discussed in Part II.

Part I

Space charge effects

Chapter 2

Space charge

2.1 Beam self-generated fields and forces

Let us consider two identical particles characterized by the same charge q (Fig. 2.1). The Coulomb force exerts repulsion between the two charges at rest. On the other hand, if the particles travel with a velocity $v = \beta c$, they represent two parallel currents $I = qv$. In such conditions, the particles attracts each other under effect of their magnetic field.

In particle accelerators, a high number of charged particles is focused and accelerated. We take for simplicity an unbunched beam of particles (charge q), with circular cross section. If we take an arbitrary test particle within the beam, the Coulomb repulsion pushes it outward. The induced overall force is zero in the beam center and increases toward the edge of the beam. At the same time, being the beam flowing as a continuous current ($I = \Sigma_i q_i v$), a radial and attractive magnetic force acts on the test particle in a traveling beam (parallel currents).

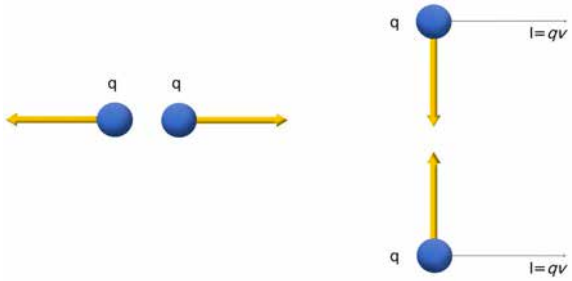

Figure 2.1: Repulsing Coulomb force exerted by two charges at rest and magnetic attractive force derived by Ampere's law for moving charges.

In order to compute the actual force exerted on the test particle, consider a continuous beam of cylindrical symmetry distribution that moves with a constant velocity $v = \beta c$. Its charge density depends only of the radius $r = \sqrt{x^2 + y^2}$:

$$\rho(x, y, z) = \rho(r). \tag{2.1}$$

For symmetry reason, the electric field has only a radial component E_r. Using the integral form of the Gauss law over a cylinder centered on the beam axis, we have the expression of the beam electric radial field:

$$E_r(r) = \frac{1}{\epsilon_0 r} \int_0^r \rho(r) r \; dr. \tag{2.2}$$

The beam current density is:

$$\mathbf{J}(x, y, z) = J(r)\mathbf{u}_z \tag{2.3}$$

where $\mathbf{u}_z$ is the unitary vector of the beam propagation. If the beam particles have the same longitudinal speed $\mathbf{v}_z = \beta_z c \mathbf{u}_z$, we have:

$$\mathbf{J}(r) = \rho(r)\beta_z c \mathbf{u}_z \tag{2.4}$$

Again for symmetry reasons, the magnetic field has only an azimuthal component B_θ. Using the integral form of the Ampere's law over a cylinder centered on the beam axis, it comes:

$$B_\theta(r) = \frac{\mu_0 \beta_z c}{r} \int_0^r \rho(r) r dr \tag{2.5}$$

From Eq. 2.2 and 2.5, being $c = \frac{1}{\sqrt{\epsilon_0 \mu_0}}$, we finally get to a relation between the electric radial field and the azimuthal magnetic field:

$$B_\theta(r) = \frac{\beta_z}{c} E_r(r) \tag{2.6}$$

From the previous equations we see that both the electric and magnetic fields vanish at the center of the beam distribution ($r = 0$), while both linearly increase with r up to the cylindrical envelope ($r = r_0$).

The space charge fields exert a force $\mathbf{F}$ on a test particle at radius r:

$$\mathbf{F} = q(\mathbf{E} + \mathbf{v} \times \mathbf{B}) \tag{2.7}$$

that in our geometry simplifies in:

$$F_r = q(E_r + \beta_z c B_\theta) \tag{2.8}$$

with F_r taking into account only the purely radial component of $\mathbf{F}$.

Assuming for the particle trajectories the paraxial approximation:

$$\beta^2 = \beta_x^2 + \beta_y^2 + \beta_z^2 \simeq \beta_z^2 \tag{2.9}$$

from Eq. 2.6 and 2.8, it finally follows:

$$F_r = qE_r(1 - \beta^2) = \frac{qE_r}{\gamma^2}. \tag{2.10}$$

From this initial result, few observations can be already done:

- in the above equation, the first term in the parenthesis (1) represents the electric force while the second ($-\beta^2$) refers to the magnetic force;
- the electric force is defocusing for the beam, the magnetic force is focusing;
- the ratio of magnetic to electric force, $-\beta^2$, is independent from the beam density distribution;
- for relativistic particles ($\beta \to 1$) the beam magnetic force almost balances the electric force;
- for non-relativistic particles (like low energy ion beams) the space magnetic force is negligible: the space charge has a net defocusing effect.

2.2 Space charge forces for different beam distributions

2.2.1 Circular and uniform beam density

Let us calculate the electric and magnetic field expressions due to space charge, in the case of a uniform beam density, of radius r_0 and total intensity I:

$$\rho(r) = \begin{cases} \rho_0 & \text{if } r \leq r_0 \\ 0 & \text{if } r > r_0 \end{cases} \tag{2.11}$$

with the charge per unit length being:

$$\lambda = \rho_0 \pi r_0^2 \tag{2.12}$$

and the beam density:

$$\rho = \frac{I}{\beta c \pi r_0^2}. \tag{2.13}$$

The total beam current can be expressed as:

$$I = \beta c \int_0^{r_0} 2\pi \rho(r') r' dr'. \tag{2.14}$$

From Eq. 2.2 and Eq. 2.13, the radial electric field is:

$$\begin{cases} E_r(r) = \frac{I}{2\pi\epsilon_0 \beta c r_0^2} r & \text{if } r \leq r_0 \\ E_r(r) = \frac{I}{2\pi\epsilon_0 \beta c r} & \text{if } r > r_0 \end{cases} \tag{2.15}$$

This example shows, for a uniform beam density, that the electric field is linear inside the beam, while outside of it, it varies according to $1/r$.

Similarly, for the magnetic field (recalling Eq. 2.5 and 2.14), we have:

$$\begin{cases} B_\theta(r) = \mu_0 \frac{I}{2\pi r_0^2} r & \text{if } r \leq r_0 \\ B_\theta(r) = \mu_0 \frac{I}{2\pi r} & \text{if } r > r_0 \end{cases} \tag{2.16}$$

Inserting the results obtained for the electric and magnetic field expressions inside the cylinder ($r < r_0$) in Eq. 2.8, we get to the radial force applied to a test particle at an arbitrary radius r:

$$F_r(r < r_0) = \frac{qI}{2\pi\epsilon_0 \beta c}(1 - \beta^2)\frac{r}{r_0^2} = \frac{qI}{2\pi\epsilon_0 \beta c}\frac{1}{\gamma^2}\frac{r}{r_0^2} \tag{2.17}$$

It is also interesting to replace r by using transverse coordinates x, y, resulting in the horizontal (F_x) and vertical (F_y) forces, that are linear with x and y, respectively:

$$F_x = \frac{qI}{2\pi\epsilon_0 \beta c \gamma^2 r_0^2} x \tag{2.18}$$

$$F_y = \frac{qI}{2\pi\epsilon_0 \beta c \gamma^2 r_0^2} y \tag{2.19}$$

2.2.2 Gaussian beam density

Let us now consider the case of a Gaussian beam density, of standard deviation σ_r, and charge distribution

$$\rho(r) = \rho_{0g} e^{\frac{-r^2}{2\sigma_r^2}} \tag{2.20}$$

having charge per unit length

$$\lambda = 2\rho_{0g} \pi \sigma_r^2. \tag{2.21}$$

The space charge electric field is:

$$E_r(r) = \frac{\rho_{0g}}{\epsilon_0}\frac{\sigma_r^2}{r}\left(1 - e^{\frac{-r^2}{2\sigma_r^2}}\right) \tag{2.22}$$

From this expression, and remembering the expression of the force due to space charge previously calculated in Eq. 2.10, we can now compute the force applied to an arbitrary test particle by space charge:

$$F_r(r) = \frac{\rho_{0g} q}{\epsilon_0 \gamma^2}\frac{\sigma_r^2}{r}(1 - e^{\frac{-r^2}{2\sigma_r^2}}) \tag{2.23}$$

From the above two equations, few following remarks can be suddenly done:

- the field, therefore the force, is heavily not linear inside the beam;
- far from the beam (so several σ_r away), the force varies according to $1/r$.

2.2.3 Comparison

Finally, we compare the focusing effects of a quadrupole magnet with the forces due to space charge in high-intensity beams of uniform circular and Gaussian beam distribution.

Fig. 2.2 shows the horizontal force versus the arbitrary transverse x direction exerted by a horizontally focusing quadrupole, for a space-charge dominated uniform beam and for a Gaussian beam density. While the quadrupole magnet is focusing in one and defocusing in the other plane, direct space charge leads to defocusing in both planes. The difference between uniform and Gaussian beam distributions can be seen in the defocusing term: in the first case it is linear, and, in principle, it can be compensated with a quadrupole-like or solenoidal magnetic force, while in the second case, the Gaussian shape of the beam leads to a defocusing non-linear behaviour.

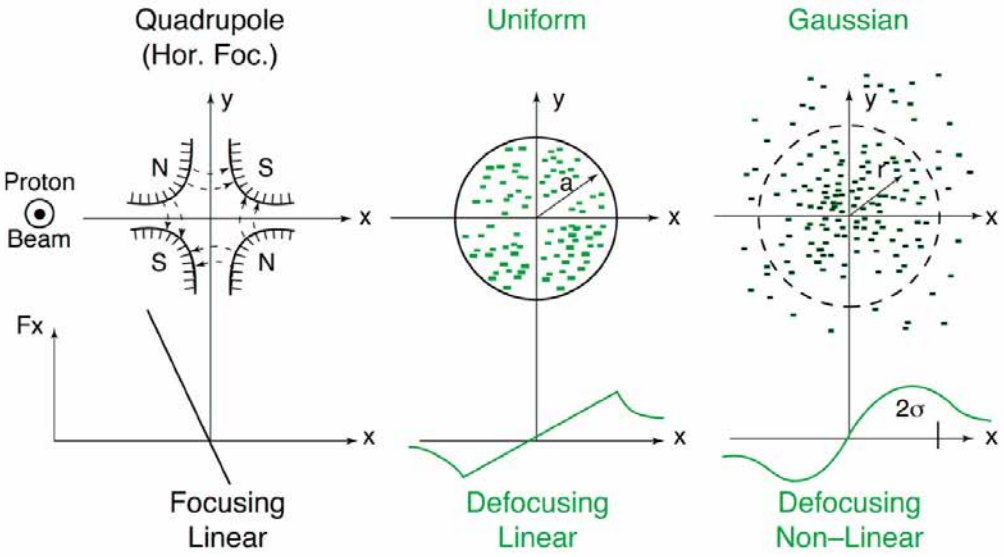

Figure 2.2: Focusing/defocusing force F_x vs. x of a quadrupole magnet (left), and of two space-charge dominated beams: uniform (center) and Gaussian (right) density distributions. From [25].

2.3 Space charge expansion in a drift

We consider a particle (charge q, mass m_0) beam of current I, propagating at speed $v = \beta c$ in a drift region, and with the following hypotheses:

- the beam has cylindrical symmetry and a radius r_0;
- the beam is paraxial ($\beta_r \ll \beta_z$);
- the beam has an no geometric emittance;
- the beam density is uniform.

From the second Newton's law, the equation of motion describing the transverse motion of this particle beam is:

$$\frac{d(m_0\gamma\beta_r c)}{dt} = m_0\gamma\frac{d^2r}{dt^2} = qE_r(r) - q\beta cB_\theta(r) \tag{2.24}$$

Adopting known expressions for the electric and magnetic fields in uniform beam density beams (Eq. 2.15 and 2.16), we find:

$$m_0\gamma\frac{d^2r}{dt^2} = \frac{qIr}{2\pi\epsilon_0 r_0^2\beta c}(1-\beta^2) \tag{2.25}$$

Remembering that:

$$\frac{d^2r}{dt^2} = \beta^2c^2\frac{d^2r}{dz^2} \tag{2.26}$$

Eq. 2.25 becomes

$$\frac{d^2r}{dz^2} = \frac{qIr}{2\pi\epsilon_0 r_0^2 m_0 c^3\beta^3\gamma^3} \tag{2.27}$$

It is now interesting to introduce a space charge important parameter, called *generalized perveance* (K), a dimensionless parameter referring to the magnitude of space charge effect in a beam, and defined by:

$$K = \frac{qI}{2\pi\epsilon_0 m_0 c^3\beta^3\gamma^3} \tag{2.28}$$

In Fig. 2.3 we observe the generalized perveance K values at different energies in various LINAC designs. We observe a rapid decrease during beam acceleration.

In this way the dynamics equation for particle trajectories can be reduced to

$$\frac{d^2r}{dz^2} = \frac{K}{r_0^2}r \tag{2.29}$$

In the case of a laminar beam, the trajectories of all particles are similar and, particularly, the particle at $r = r_0$ will always remain at the beam boundary. Considering $r = r_0 = r_{env}$, we now found the equation of the beam radius (or envelope) in a drift space:

$$\frac{d^2r_{env}}{dz^2} = \frac{K}{r_{env}} \tag{2.30}$$

The above equation shows the evolution of r_{env} over the z coordinate. The beam-generated forces cause, generally, a beam expansion: a converging beam, drifting in absence of focusing terms, reaches a minimum value of its envelope radius and then expands.

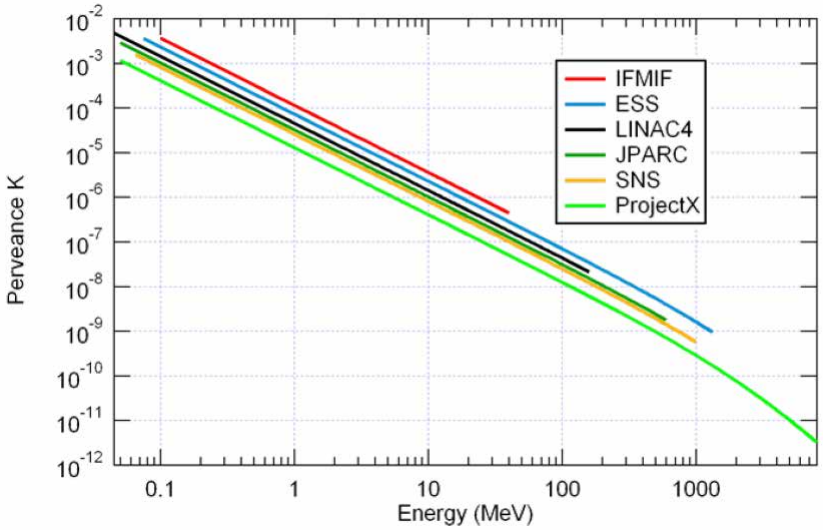

Figure 2.3: Examples of generalized perveance K values at different energies in various LINAC designs. Courtesy of N. Chauvin.

2.3.1 Example

Let us define the envelope radius at the beam *neck* as r_n. We now choose, for convenience, to have the neck axial position at $z = 0$. A first integral of Eq. 2.30 is found:

$$\frac{dr_{env}}{dz} = \sqrt{2K}\sqrt{ln\left(\frac{r_{env}(z)}{r_n}\right)} = \sqrt{2K}\sqrt{ln(\chi)} \tag{2.31}$$

having defined as χ the ratio of the beam envelope radius to the radius at the neck

$$\chi = \frac{r_{env}(z)}{r_n} \tag{2.32}$$

Thus, the variation of the envelope radius with distance from the neck is given by

$$z = \frac{r_n}{\sqrt{2K}}F(\chi) \tag{2.33}$$

where

$$F(\chi) = \int_1^{\chi} \frac{dy}{\sqrt{ln(y)}} \tag{2.34}$$

Given these equations, we can easily compute the expansion of an un-neutralized ion beam through a drift. For instance, take the example of a 200mA, 300 keV C^+ beam drifting into a vacuum region. Its generalized perveance is $K = 2.8 \times 10^{-3}$. The envelope angle is null at injection, meaning that the injection point is the beam neck. We suppose an initial radius of the beam of r_n=0.01 m=10 mm.

We can now find the beam radius at a position of 0.3 m downstream. Inserting our r_n, z and K into Eq. 2.34 we find $F(\chi) = 2.24$. In order to compute the integral in Eq. 2.34, which is not solvable analytically, we can either use tables or adopt numerical integration, employing a trapezoidal method.

The integral $F(\chi)$ versus χ, solved in Matlab®, is plotted in Fig. 2.4.

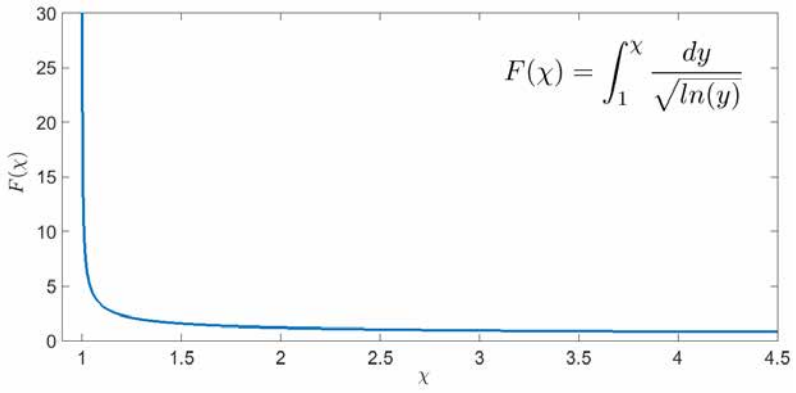

Figure 2.4: $F(\chi) = \int_1^{\chi} \frac{dy}{\sqrt{ln(y)}}$ between χ=1 and χ=4.5

For $F(\chi) = 2.24$, we get a $\chi = 2.1$. The final beam envelope radius, at z=0.3 m, is then $r_{env}(z = 0.3m)$=0.021 m = 21 mm, i.e. twice the initial value after a drift of only 0.3 m! By using Eq. 2.32, we can also compute the expansion angle of the envelope, in this case of 65 mrad (3.7°).

Chapter 3

The RMS envelope equation with space charge

3.1 RMS quantities

Generally, the notion of emittance, indicating the phase space surface occupied by a beam, is used to express the *quality* of a particle beam. This quantity is represented by an ellipse containing the particle distribution in a phase space (x, x')[1] such as $A = \pi\epsilon_x$.

The presence of only linear forces applied to a beam leads to have generally elliptical shapes of the beam emittance: this result comes from the trajectory of each particles, that, in this particular case, lies on an ellipse. In presence of non-linear fields, the particle beam can lose its laminar behaviour, therefore the particle distribution can be distorted and the phase space surface can become well different from an ellipse.

For this reason, we generally introduce the notion of *RMS emittance*, that is a statistical definition of emittance based on the RMS quantities[2] on the phase space:

$$\text{RMS size} : \tilde{x} = \sqrt{\langle x^2 \rangle - \langle x \rangle^2} \tag{3.1}$$

$$\text{RMS divergence} : \tilde{x'} = \sqrt{\langle x'^2 \rangle - \langle x' \rangle^2} \tag{3.2}$$

The ellipse projections on the phase space axes are equal to the RMS values of the distribution. The RMS emittance is therefore:

$$\text{RMS emittance} : \tilde{\epsilon_x} = \sqrt{\tilde{x}^2 \tilde{x'}^2 - \langle (x - \langle x \rangle)(x' - \langle x' \rangle) \rangle^2} \tag{3.3}$$

Obviously, beam Twiss parameters can be expressed from the RMS emittance definition as follows:

$$\beta_x = \frac{\tilde{x}^2}{\tilde{\epsilon_x}} \tag{3.4}$$

$$\gamma_x = \frac{\tilde{x'}^2}{\tilde{\epsilon_x}} \tag{3.5}$$

$$\alpha_x = -\frac{\langle (x - \langle x \rangle)(x' - \langle x' \rangle) \rangle}{\tilde{\epsilon_x}} \tag{3.6}$$

The RMS emittance gives important information about the phase space distribution under the effect of linear and non-linear forces acting on the beam. Let us consider an hypothetical particle beam whose divergence is given by the relation

$$x' = Cx^n \tag{3.7}$$

[1] the same applies to (y, y') and (z, z') 2D phase spaces

[2] the symbolism $\langle x \rangle$ represents the mean of a quantity x over the beam particle distribution

where C is a constant and n is positive. This distribution in the phase space lies on some curve that passes through the origin, as shown in Fig. 3.1 for $n = 1$ and $n = 3$.

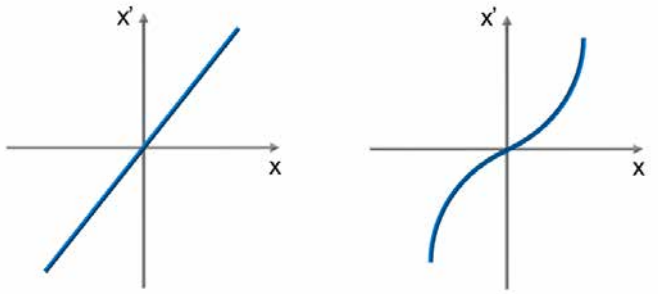

Figure 3.1: Examples of (x-x') phase spaces for two beam divergence relationships of zero geometric emittance: $n = 1$ (left), $n = 3$ (right).

If we now consider the RMS emittance, as expressed in Eq. 3.3, we have

$$\tilde{\epsilon_x} = C\sqrt{\langle x^2\rangle\langle x^{2n}\rangle - \langle x^{n+1}\rangle^2} \tag{3.8}$$

Let us study the cases for $n = 1$ and $n > 1$. This leads to

$$\begin{cases} n = 1 : x' = Cx \rightarrow \epsilon_{rms} = 0 \\ n > 1 : x' = Cx^n \rightarrow \epsilon_{rms} \neq 0 \end{cases} \tag{3.9}$$

When $n = 1$, the particle distribution lies on a line, that is straight, and the RMS emittance is null. When $n > 1$, the divergence relationship is not linear: although the distribution line still passes through the origin, the phase space line is distorted, and, more importantly, the RMS emittance is non-zero. In fact, both distributions have zero phase space area (emittance is null), but the presence of non-linear forces, producing a distorted particle distribution in the phase space, is well accounted by the RMS emittance.

3.2 RMS envelope equation in presence of space charge

We consider a beam moving in the s direction, where individual particles satisfy the general equation of motion

$$x'' + \kappa(s)x - F_s = 0, \tag{3.10}$$

where $\kappa(s)x$ represents a linear external focusing force (e.g. for quadrupole, $\kappa = qB/\gamma ma\beta c$), or focusing strength, and F_s is a space charge force term, including both self-electric and self-magnetic forces (and in general *not linear*).

In order to simplify, we here assume that the beam is centered on the axis, and has no divergence, thus $\langle x\rangle = 0$ and $\langle x'\rangle = 0$ (i.e. $\tilde{x}^2 = \langle x^2\rangle \equiv \overline{x^2}$). Let us write the equations of motion for the second moments of the particle distribution:

$$\frac{d\overline{x^2}}{ds} = 2\overline{xx'} \tag{3.11}$$

$$\frac{d\overline{xx'}}{ds} = \overline{x'^2} + \overline{xx''} = \overline{x'^2} - \kappa(s)\overline{x^2} + \overline{xF_s} \tag{3.12}$$

Differentiating two times Eq. 3.1 (using Eq. 3.11), we have:

$$\tilde{x}'' = \frac{\overline{x''} + \overline{x^2}}{\tilde{x}} - \frac{\overline{xx'}}{\tilde{x^3}} \tag{3.13}$$

Using Eq. 3.12 and Eq. 3.3, we finally get to the RMS envelope equation

$$\tilde{x}'' + \kappa(s)\tilde{x} - \frac{\tilde{\epsilon_x}^2}{\tilde{x}^3} - \frac{\overline{xF_s}}{\tilde{x}} = 0 \tag{3.14}$$

that is the equation of motion of the RMS beam size.

In this equation, the second term is the focusing term, while the third is the emittance term. The emittance term is negative and is analogous to a repulsive pressure force acting on the RMS beam size. The last term in Eq. 3.14 is the repulsive space-charge term.

3.2.1 RMS envelope equation of an elliptical continuous beam

The envelope equations for continuous beams with arbitrary density profiles, characterized by elliptical symmetry in the xy space, have been successfully analytically derived. Although a LINAC beam is bunched, the continuous beam results are still useful for an approximate description of the transverse fields of a long bunch, or of DC beams propagating after their production in low energy beam transport lines. Let us take the example of an elliptical continuous beam of uniform density, such as

$$\rho(r) = \begin{cases} \rho_0 & \text{if } \frac{x^2}{r_x^2} + \frac{y^2}{r_y^2} < 1 \\ 0 & \text{otherwise} \end{cases} \tag{3.15}$$

As the distribution is uniform, the semi-axes of the ellipse, r_x and r_y, are related to the RMS beam sizes, i.e. $r_x = 2\tilde{x}$ and $r_y = 2\tilde{y}$.

Like previously calculated for circular and uniform density beams (see Eq. 2.15), the electric field components for a uniform density *elliptic* distribution are

$$E_x = \frac{I}{\pi\epsilon_0\beta c(r_x + r_y)}\frac{x}{r_x} \tag{3.16}$$

$$E_y = \frac{I}{\pi\epsilon_0\beta c(r_x + r_y)}\frac{y}{r_x} \tag{3.17}$$

Substituting Eq. 3.16 and 3.17 in Eq. 3.14, we have the RMS envelope equations for a uniform density beam

$$\tilde{x}'' + \kappa_x(s)\tilde{x} - \frac{\tilde{\epsilon_x}^2}{\tilde{x}^3} - \frac{K}{2(\tilde{x} + \tilde{y})} = 0 \tag{3.18}$$

$$\tilde{y}'' + \kappa_y(s)\tilde{y} - \frac{\tilde{\epsilon_x}^2}{\tilde{y}^3} - \frac{K}{2(\tilde{x} + \tilde{y})} = 0 \tag{3.19}$$

These equations were first derived by Kapchinskiy and Vladimirskiy [26] for a stationary uniform beam in a quadrupole-focusing channel and are known as the *K-V envelope equations*. The second term of Eq. 3.18 and 3.19 is the focusing effect due to external forces, while the third is the defocusing effect due to beam emittance. The fourth term is the defocusing space charge term of the RMS envelope equation: it can be seen that the two planes are coupled.

We have seen in Eq. 2.18 and 2.19 that the space charge force is linear only if the beam density is uniform. This case is very unlikely in practical beams. The space charge force is fundamentally a non-linear term. However the remarkable result discovered by Lapostolle and Sacherer [27] [28], is that the RMS envelope equations with space charge are valid not only for uniform density beams, but for all density distributions with elliptical symmetry. The form of the envelope equations is independent of the density profile of the beam. For instance, for ellipsoidal form bunches, where the RMS emittance is either constant or specified in advance, the evolution of the RMS beam projection is nearly independent of the beam density.

Thus, in order to calculate the RMS beam dynamics, even in the presence of space-charge forces, it is possible to replace the beam distribution (not known a priori) by an equivalent uniform beam with the same intensity and second moments. It is convenient to work with an equivalent uniform

beam because the space-charge field of a uniform beam, with elliptical or ellipsoidal symmetry, is easily calculated and is linear.

Finally, it is worth to point out that the ratio of the space charge term over the emittance term in Eq. 3.18 and 3.19 can be used to determine when space charge is important, compared with the emittance, in determining the RMS beam size. If the emittance term is much larger than the space-charge term, then the beam transport is said to be *emittance dominated* (internal disorder effects are dominant). If the space-charge term is much larger than the emittance term, then the beam transport is said to be *space-charge dominated* (collective effects are dominant).

Chapter 4

Transport of high intensity beams at low energy

4.1 Introduction

The increasing interest of the international scientific community in the availability of high power (MW range) accelerators poses the problem of transport of intense beams, particularly at very low energy. For such machines, designed ion sources should deliver beam intensities ranging from several tens up to a hundred of mA, with typical initial energies very modest due to electrostatic multi-stage initial acceleration (tens of keV). One of the major challenges in these accelerators is to extract and transport the beam in the injectors, while minimizing the emittance growth and halo formation. The possible sources of beam halo and emittance growth in a high intensity injector are:

- aberrations due to the ion source extraction optics;
- optical aberrations of the focusing elements of the LEBT;
- beam fluctuations due to ion source instability or power regulation;
- beam scattering on gas;
- non-linearity of the electric field created by the beam space charge.

The first three points pose attention on the design and realization of ion sources and transport lines, while the last two point are related to the physics of intense beam transport.

Once a line is designed and built, a process of optimization is commonly performed to correctly inject beam into the first accelerating structures, generally the Radio Frequency Quadrupole (RFQ). Consequently, it is crucial to understand and predict the beam behaviour when designing low energy beam transport (LEBT) lines. Nowadays, in particular, during the study of beam dynamics is possible to take into account not only the space charge effects but also the potential space charge neutralization of the beam, induced by ionization of the residual gas. The physical phenomena occurring in a high intensity LEBT and their possible effects on the beam are presented in this Chapter, with a particular emphasis on space charge compensation.

4.2 The space charge compensation (SCC) principle

The space charge compensation (or neutralization) occurs on a beam propagating through the residual gas of the beam line and, subsequently, inducing ionization of the gas molecules. Secondary particles produced by ionization (i.e. electrons or ions), which have opposite polarity of the particle of the beam, are trapped within the beam potential until a steady state is reached. In principle, a low energy beam can be therefore considered as a *plasma* creating a focusing effect that counteracts the space charge effect.

For instance, let us consider a proton beam propagating through a H_2 residual gas. Generally, it can induce a production of pairs e^-/H_2^+ by ionization of the hydrogen molecule following the reaction

$$p \ + \ H_2 \ \rightarrow \ p + \ e^- + \ H_2^+ \tag{4.1}$$

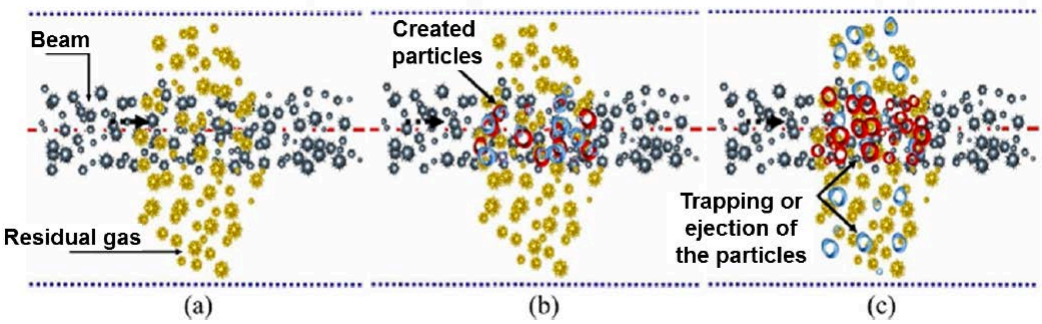

Figure 4.1: Pictorial depiction of ionization, production and trapping of neutralizing particles leading to Space Charge Compensation. From [29].

The created electron has negative polarity and is trapped within the beam potential, while the created H_2^+ ion has positive polarity and is expelled by the proton beam. The accumulation of negative charge creates a negative potential which superimposes to the beam potential with the net effect of reducing its strength. We now assume that $n_{gas}/n_{beam} \ll 1$, being η_{gas} and η_{beam} the gas and beam densities.

Consider a uniform, cylindrical beam of intensity I_B and radius r_B propagating into a cylindrical surrounding grounded beam pipe of radius r_P at $v = \beta_B c$ (see Fig. 4.2). Recalling Eq. 2.15, we can again express the electric field of such uniform cylindrical beam, i.e. the space charge electric fields inside and outside the beam envelope, as follows [30]:

$$\begin{cases} E_r(r) = \frac{I}{2\pi\epsilon_0\beta c r_0^2} r & \text{if } r \leq r_0 \\ E_r(r) = \frac{I}{2\pi\epsilon_0\beta c r} & \text{if } r > r_0 \end{cases} \tag{4.2}$$

If we now integrate these equations with the boundary condition for the electric scalar potential $\phi(r_p) = 0$ (grounded beam pipe), we find:

$$\begin{cases} \phi_r(r) = \frac{I_B}{4\pi\epsilon_0\beta_B c}(1 + 2ln\frac{r_p}{r_B} - \frac{r^2}{r_B^2}) & \text{if } r \leq r_B \\ \phi_r(r) = \frac{I_B}{2\pi\epsilon_0\beta_B c} ln\frac{r_p}{r} & \text{if } r_B \leq r \leq r_p \end{cases} \tag{4.3}$$

We have thus derived the potential generated by the beam space charge along r. The potential well scalar value corresponds to the potential on the beam axis, $r = 0$, that for a uniform beam without space charge compensation is:

$$\phi_0 = \frac{I_B}{4\pi\epsilon_0\beta_B c}(1 + 2ln\frac{r_p}{r_B}). \tag{4.4}$$

A more elaborated expression of the potential on axis taking into account the collisional effects in the beam as well as the space charge compensation can be found in [31]. Let us analyse the expression found in Eq. 4.4. The potential well (and with that, the space charge force) is deeper increasing with the beam intensity but more interestingly in a beam waist, where the radius of the beam is minimum.

During the SCC process, the neutralizing particles created by gas ionization are trapped by the described potential. We now take into account an arbitrary compensated beam in steady state. If we define by ϕ_c the potential well of the compensated beam, a SCC degree can be defined as

$$\eta = 1 - \frac{\phi_c}{\phi_0}. \tag{4.5}$$

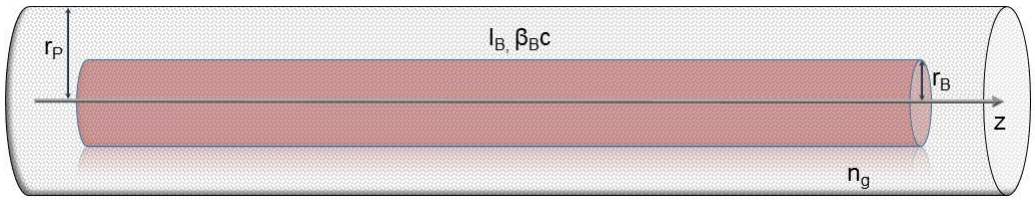

Figure 4.2: Scheme of an uniform cylindrical beam propagating through a beam pipe.

Figure 4.3 shows the dramatic evolution of the space charge potential in presence of space charge compensation in a section of the MYRRHA LEBT (H^+, 30 keV, 5mA). The beam space charge potential for a uniform beam density is calculated as found in Eqs. 4.3 and 4.5 inside and outside the beam envelope (r_b=20mm,r_p=80mm,).

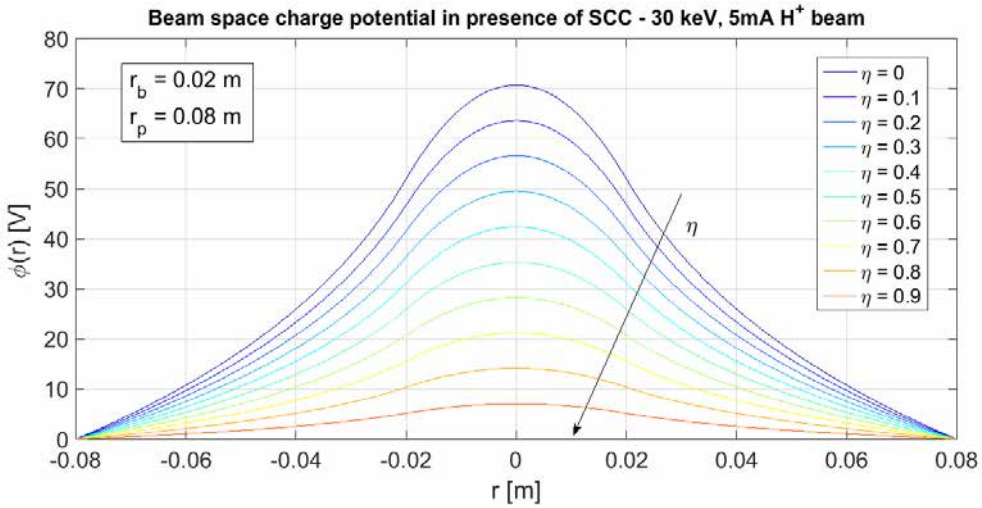

Figure 4.3: Space charge potential in the MYRRHA LEBT in presence of a degree of SCC ranging from 0 to 90%.

Experimental measurements of beam potential well in compensated regimes are available. In the Low-Energy Demonstration Accelerator (LEDA), the SCC degree values found for a 75 keV, 130 mA proton beam were ranging within the impressive value of 95% to 99% [32]. Along the Low Energy Beam Transport (LEBT) lines, the SCC degree is generally not constant due to the presence of external fields (like focusing elements, electric fields, etc.) so that the neutralizing particles trajectories can be modified. In such cases, neutralizing particle are not captured in the beam potential well and the SCC degree dramatically decreases.

We have, up to now, considered a compensated beam in steady state. Generally, this is not applicable for pulsed beams, or for beams which come from a SCC degree equal to zero. The characteristic space charge compensation transient time, τ , can be determined by considering the time it takes for a particle of the beam to produce a neutralizing particle on the residual gas. It results

$$\tau = \frac{1}{\sigma_{ioniz} n_g \beta_B c} \tag{4.6}$$

where σ_{ioniz} is the ionization cross section of the incoming particles on the residual gas and n_g the gas density in the beam line. We observe that such characteristic time depends from the dominant residual gas specie and is inversely proportional to its density and the time spent by the beam for ionization.

The characteristic space charge compensation transient time can be used to normalize the time evolution and compare different cases even when, for instance, the vacuum gas pressure changes.

The τ time constant gives the average time needed for one particle to produce one compensating particle. The higher the pressure, the faster will be the compensation process. It is generally admitted that in a beam line, the space charge compensation reaches a steady-state after 2-3 τ. For a practical application, in the case of the MYRRHA LEBT, the space charge compensation transient time transient time for a 30 keV proton beam propagating in H_2 gas with a pressure of $5 \cdot 10^5$ mbar is $\tau = 17\mu s$.

The positive impact of SCC regimes in low energy beam lines has been demonstrated in high current injectors. One of the first experiences of successful establishment of SCC was in the beam line of SILHI high intensity ECR Ion Source, tested a CEA, Saclay, delivering a 75 mA, 95 keV H^+ beam [33].

Fig. 4.4 show the qualitative impact of SCC on the measured beam emittance. We observe that the non-linear emittance behavior is far more mitigated with presence of SCC. The transverse beam emittance is measured without ^{84}Kr injection. The dominant residual as is H_2 coming from the ion source. With a pressure of p$p2.4 \cdot 10^{-5}$ hPa, the RMS emittance $\epsilon_{RMS} = 0.335\pi$·mm·mrad RMS norm. was achieved. On the right, we observe the same transverse phase space with ^{84}Kr injection, at $p = 4.6 \cdot 10^{-5} hPa$. The measured RMS emittance was $\epsilon_{RMS} = 0.116\pi$·mm·mrad RMS norm. The beneficial results are evident: a decrease of the RMS beam emittance has been observed along with an increase of the beam line pressure. Using ^{84}Kr, a decrease of a factor three in the RMS beam emittance value has been achieved.

In Fig. 4.5, the evolution of measured SILHI 75mA, 95 keV DC beam RMS emittance is plotted with different gas species injection and at different vacuum pressure. The presence of a rather high residual gas pressure, and preferably with a large number of electrons in low energetic atomic shells, helps the production of free electrons and the formation of a space charge neutralization steady state.

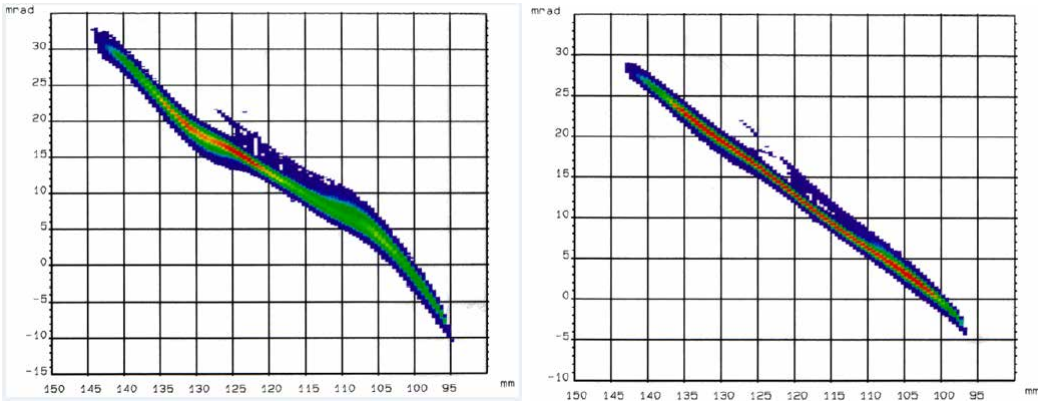

Figure 4.4: Measured SILHI 75mA, 95 keV DC beam emittance without (left) and with ^{84}Kr injection [33].

4.3 RMS envelope equation with space charge in presence of SCC

The evolution of the RMS beam size $\tilde{x}$ has been given in Section 3.2 by the envelope equation. We will now on refer to a circular uniform beam distribution (r coordinate) having a linear external focusing force term and space charge force term:

$$\frac{d^2\tilde{r}}{ds^2} + \kappa(s)\tilde{r} - \frac{\tilde{\epsilon_r}^2}{\tilde{r^3}} - \frac{\overline{rF_{s,r}}}{\tilde{r}} = 0 \tag{4.7}$$

As we said, for every particle distribution in the beam, the behavior of the RMS size can be modeled by this equation with a very good approximation using the linear space charge force of a uniform beam with the same RMS size.

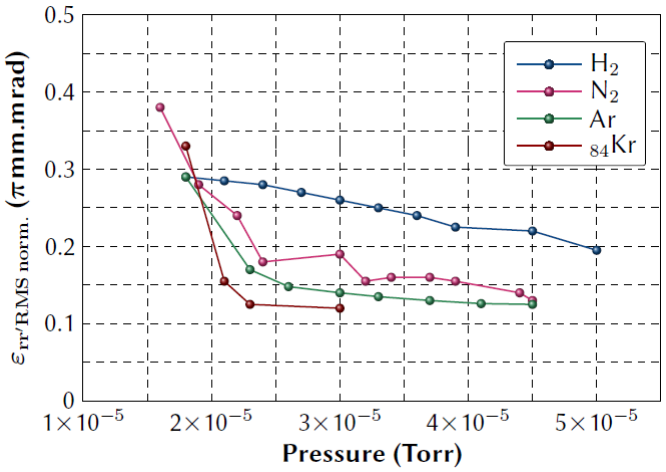

Figure 4.5: Evolution of measured SILHI 75mA, 95 keV DC beam emittance with different gas species injection and at different pressure [33].

When the beam is neutralized, the space charge force is reduced or even *canceled* by the charges trapped in the beam potential well. Many definitions of space charge neutralization have been used to quantify this compensation degree. In [34], [35], the ratio between the beam potential well depths with and without compensation is used. In [30], [36], the SCC degree is quantified with the ratio of the number of trapped particles over the number of beam particles. A drawback of these definitions is that they cannot be used directly in Eq. 4.7 to predict the beam transport in a SCC regime. In order to get to that, it has been proposed [37] to adopt the following ratio:

$$\eta = \frac{\langle r \cdot F_{comp}, r \rangle}{\langle r \cdot F_{sc}, r \rangle} \tag{4.8}$$

where $\langle r \cdot F_{comp}, r \rangle$ is the linearised compensated space charge force (induced by all ionized particles) and $\langle r \cdot F_{sc}, r \rangle$ the linearised beam space charge force at the beginning of the process. Employing this definition, we still have for $\eta = 0$ no compensation, and for $\eta = 1$ full compensation.

To express the effect of a SCC, we can indicate the SCC degree as a fictitious decrease of the beam current (or charge) by a factor $(1 - \eta)$, like

$$I_{SCC} = (1 - \eta) I_0 \tag{4.9}$$

The RMS envelope equation, in presence of focusing and space charge force, and with space charge compensation, therefore can be written as

$$\frac{d^2\tilde{r}}{ds^2} + \kappa(s)\tilde{r} - \frac{\tilde{\epsilon_r}^2}{\tilde{r^3}} - (1 - \tau) \cdot \frac{\overline{rF_{s0,r}}}{\tilde{r}} = 0 \tag{4.10}$$

The SSC degree of a cylindrical beam at a given time t is then defined as

$$\eta(t) = \frac{\int_0^\infty rF_{comp,r}(r,t)\rho(r,t)dr}{\int_0^\infty rF_{sc0,r}(r,t)\rho(r,t)dr} \tag{4.11}$$

Since the beam space charge force has an electric and a magnetic component, in the paraxial approximation, the radial space charge magnetic force $F_{sc0,r,B}$ partially compensates the radial space charge electric force $F_{sc0,r,E}$ as

$$F_{sc0,r,B} = -\beta^2 F_{sc0,r,E} \tag{4.12}$$

Considering the always low energy of particles trapped within the beam, the induced field is essentially electric, therefore this leads to

$$\eta(t) = \gamma^2 \frac{\int_0^\infty rE_{comp,r}(r,t)\rho(r,t)dr}{\int_0^\infty rE_{sc0,r}(r,t)\rho(r,t)dr} \tag{4.13}$$

where $E_{comp,r}$ is the electric field induced by the ionized particles and $E_{sc0,r}$ is the one induced by the beam.

This equation leads to an important result: at low energy, the SCC compensation is mainly due to compensation of the electric force. As at high energy, the magnetic force reduces partially the electric force, so a lower compensating electric field is needed to reach a complete neutralization.

4.4 Choices for transport in Low Energy Beam Transport (LEBT) lines

Once an intense beam of particle charges is created, the ion source extraction system is first in charge to accelerate and transports the beam into the low energy beam line (LEBT). In this line, beam is transported, focused and matched for final injection in the first accelerating structure, such as a RFQ. The beam transport can be achieved with electrostatic or magnetic focusing elements. After the ion source, because of the geometry of the extraction system[1], the beam usually presents a cylindrical symmetry. In order to preserve this symmetry and to simplify the beam tuning, magnetic solenoids[2] at low energies lenses or electrostatic Einzel lenses are more commonly used than quadrupoles.

4.4.1 Electrostatic LEBTs

In electrostatic LEBTs, the beam cannot experience any space charge compensation because of the absence of neutralizing particles. The electric field induced by the focusing elements attracts (or repels) the neutralizing particles out of the beam area. This kind of beam line is designed for transporting space charge dominated beams. Polarized electrodes are used as electric lenses for beam steering and focusing, as well as choppers for beam deflection. The design of electrostatic LEBTs is simplified by the fact that the beam line is very compact. Their short length and possibly combination with the source extraction minimizes the beam losses by charge exchange. Therefore, electrostatic LEBTs are suitable and compatible with beam fast tuning and chopping as there is no transient time limit for achieving SCC regimes.

As an example, we show in Fig. 4.6 the $H-$ ion source and 120mm long LEBT, equipped with two Einzel lenses, of the ORNL Spallation Neutron Source injector [38].

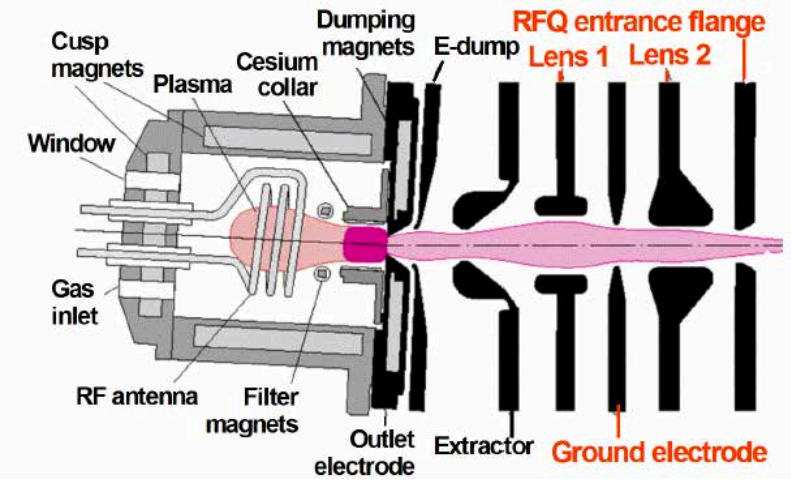

Figure 4.6: Spallation Neutron Source (SNS) electrostatic H^- LEBT.

Conversely, electrostatic LEBTs are particularly vulnerable to beam losses: high voltage breakdowns are unavoidable and beam trips can occur. Due to the presence of only electrostatic lenses

[1] in ECR ion sources, the plasma is extracted from a source electrode, and then accelerated via a multi-stage cascade of electrodes.

[2] magnetic solenoids have a cylindrical focusing effect and are suitable for low energy beams.

(working on the *charge* of the particles, instead of their *mass*), there is no mean for mass (beam species) separation. Their compact geometry allows no or tiny space for insertion of beam diagnostics. Besides, the Einzel lenses intrinsically (because of their design, and not only due to geometrical imperfections) induce optical aberrations that creates beam halo and emittance growth. To limit this effect, the beam radius should not exceed 2/3 of the lens aperture radius.

Finally, one should note that the design of the electrostatic LEBTs is somewhat intensity limited. The beam is not compensated, and its divergence and size increase rapidly with its intensity, particularly with beam intensity exceeding tens of mA. An electrostatic LEBT has a little margin in terms of handleable beam current: higher beam current than the design current induce beam losses or dramatic emittance growth.

4.4.2 Magnetic LEBTs

In magnetic LEBTs, magnetic fields produced by solenoid magnets are used to guide and focus beam into the next accelerating structure. Magnetic LEBTs are *spark-free* and exhibit low sensibility to beam losses. Separation and purification from different beam species can be easily achieved (different particle species have different magnetic rigidity). More space can be left for insertion of beam diagnostic.

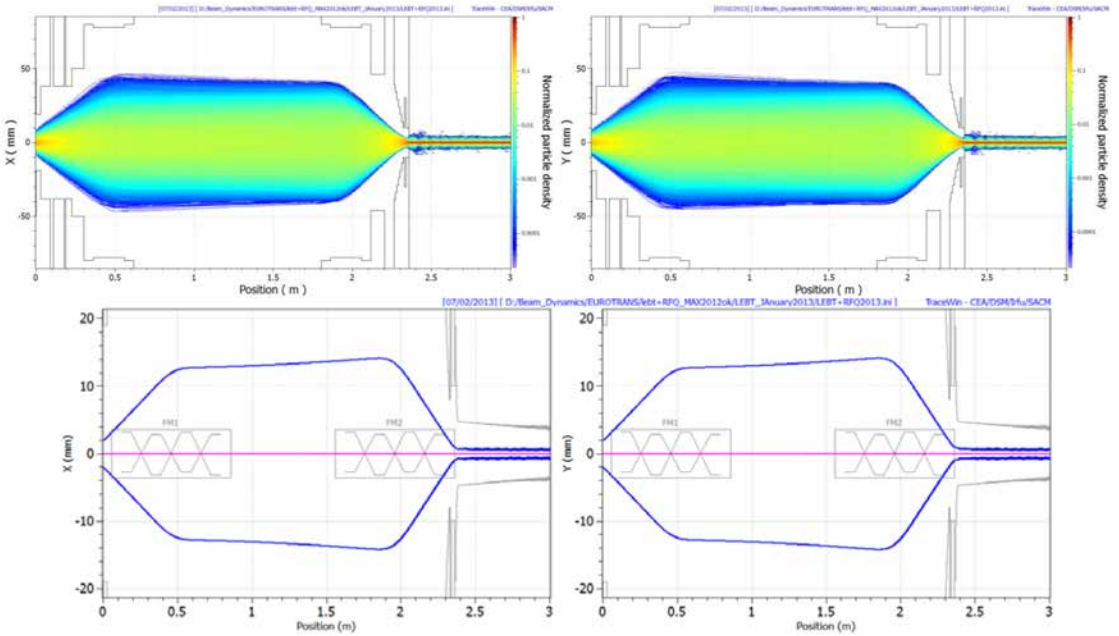

Figure 4.7: Multiparticle tracking simulation of the MYRRHA magnetic LEBT line from the ECR Ion Source to the first RFQ cells & corresponding RMS envelopes [39].

The beam is almost completely neutralized by the ionization on the residual gas, as previously explained. The gas in the LEBT comes mainly from the ion source; injecting specific elements' gaseous molecules, a higher pressure of a particular gas specie and a desired longitudinal profile can be achieved in the beam line. As previously mentioned, the nature of the injected gas has an influence on this emittance improvement. An arbitrary high pressure should however not be established in the beam line: the gas injection has to be done carefully to keep under control the beam losses due by charge exchange (see Section 6.7). For positive ion beam, an additional source of neutralizing particles can be mentioned: secondary electrons are produced when some particles of the beam hits the beam pipes (see Section 6.5.2).

At the end of the LEBT, the electric field of the RFQ tends to penetrate through the injection hole and have a significant effect on the SCC by attracting the neutralizing particles. Moreover, this region is critical from the space charge point of view, because a beam waist is performed to match the beam for its injection into the RFQ. So, like in the ion source extraction system, a

polarized electrode is placed as close as possible to the RFQ entrance to repel the neutralizing particles in the LEBT and to minimize the uncompensated zone.

In a magnetic LEBT transporting pulsed beams, the rise time is dominated by the SCC transient time (i.e, several tens of μs). A fast chopping system has to be inserted downstream to reach a beam rise time in the order of the hundreds of ns. In the case of the H^- ion beams, a phenomena of overcompensation occurs during the SCC transient time. When the beam is fully compensated, neutralizing particles (in that case H^+) are still created but, as they are significantly slower than the electrons, the SCC degree can be superior to 1 during the time it takes for the exceeding H^+ to be expelled from the beam. During that time, the beam is overfocused and instabilities can be observed.

One of the advantages of the magnetic LEBT is the possibility to purify the beams that contain different species, that are commonly produced and extracted from the ion source. Since these species have different magnetic rigidity, they have different trajectories in the focusing magnetic lenses, therefore different focal point: they are commonly stopped before the RFQ injection on a beam collimator. Like in the Einzel lenses, the magnetic solenoids lenses present geometrical aberrations that may lead to emittance growth. To limit this effect, the beam diameter should stay under half of the solenoid aperture (*good field region*).

Chapter 5

The MYRRHA project and its high power proton accelerator

5.1 Accelerator Driven Systems (ADS)

As of the beginnings of pacific adoption of nuclear energy, the possibility to employ sub-critical nuclear reactors, of neutron flux and power density comparable to critical assemblies adopted in nuclear power plants, has been explored. The solution of driving a non-critical assembly by an external powerful neutron source allows, in fact, for a more tolerant geometrical design of the reactor core and more freedom in the choice of materials, in particular the fuel composition. On top of that, less engineering burden is set on the requirements behind the reliability and efficacy of chain reaction control system.

Two concepts of sub-critical reactors have been proposed to address the need of production of fissile material from fertile elements (in competition with the breeder reactors), and the capability to "destroy" high level and long lived nuclear waste (transmutation) [40]:

- sub-critical assemblies coupled to an external neutron source realized by means of particle accelerators (Accelerator Driven Systems),
- sub-critical assemblies coupled to fusion reactors, the latter in charge of supplying the required neutron flux (hybrid fission/fusion reactors).

The advantage in the adoption of an external neutron source resides in the intrinsic safety inherited by the nuclear system: a removal of the external source turns into a sudden shut-down of the neutron chain reaction, with a time constant of milliseconds, as opposed to seconds in common critical reactors requiring insertion of neutron absorbers (safety rods). Reactivity excursions are made non-possible by design, being the criticality coefficient a sub-critical assembly K_{eff} less than the unity (for neutron economy and safety reasons, often $0.95 < K_{eff} < 0.97$).

The peculiarities of accelerator-driven sub-critical system as opposed to critical reactors can be resumed like so:

- ADS reactors allow to use fuels that would degrade the global reactor neutron economy, or considerable amounts of fertile fuels (e.g. Th);
- the gap from criticality in ADS reactors is equivalent to a supplementary amount of delayed neutrons. This property is essential for burning minor actinides, as a tiny fraction of delayed neutrons are available when fissioning those elements;
- the use of control rods can be, in principle, avoided for control and operation of the reactor power and follow-up of the reactivity margin during fissile burn-up. Reactivity insertions leading to prompt criticality would be avoided by design. Reactor power control in ADS can be achieved through modulation of the spallation beam current, which can provide margin for burn-up compensation;

- given the external neutron contribution, ADS reactors can run with an unfavourable neutron economy, i.e. a considerable amount of the neutron flux can be allocated to enhance the transmutation process of heavy nuclides or long-lived fission products;
- the distortion on the neutron flux close to the external source alters the power distribution along the core. This distortion is restrained only for values of K_{eff} close to the unity. It can be mitigated by a well-fit strategy in the fuel distribution and/or the adoption of burnable neutron poisons;
- ADS suffer reduction of reactivity feedback reactions linked to temperature coefficients (negative, due to density and Doppler effects). The absence of those feedback mechanisms can lead to coolant flow crisis;
- a dynamic follow-up of the impinging spallation beam intensity should be provided, as the reactor power is a multiple of it.

As of today, the availability of intense neutron sources is limited to nuclear spallation and fusion sources. Given the requirement of a constant, high intensity, durable and high-duty neutron flux, the first source is currently preferred on the second. Protons or deuteron, accelerated to relatively high energy ($\sim$ 1 GeV), have a wavelength similar to characteristic dimensions of the atomic nucleons:

$$\lambda = \frac{hc}{\sqrt{E(E + 2m_0c^2)}} \cong 10^{-14}\text{cm} \tag{5.1}$$

Selected target nuclei (usually of a high A/Z ratio, like Pb, Bi, W, U) undergo a spallation process when bombarded by such high energy particles (Fig. 5.1), and release 20 to 50 neutrons from the outer levels of the nucleus shells, depending on the impinging beam energy and the target A/Z ratio (Fig. 5.2).

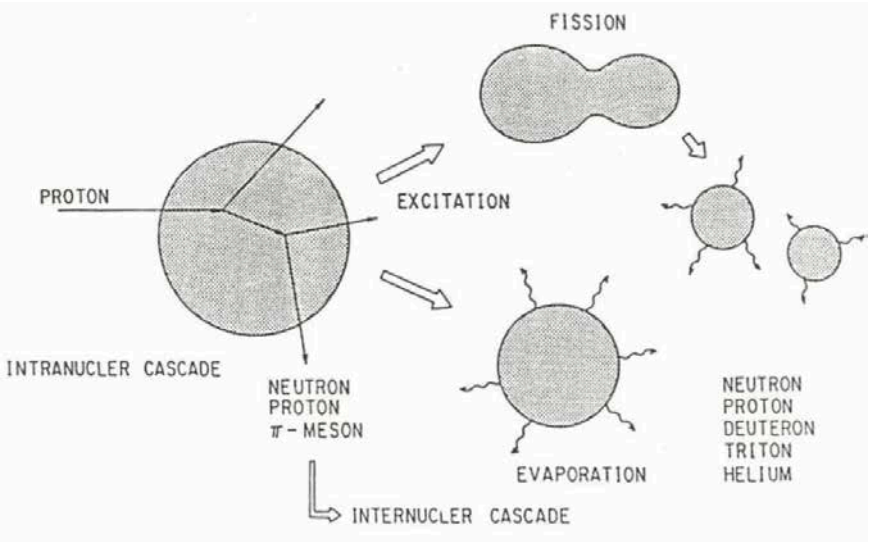

Figure 5.1: Schematic overview of the cascade and the products of a nuclear spallation reaction.

As visible in Fig. 5.2, the optimum energy cost per neutron lies in the proton energy range 0.6÷2 GeV, where roughly 10 to 40 neutrons per incoming proton are obtainable. Neutron flux effective for nuclear transmutation is in order of 10^{15} to $10^{16}\frac{1}{cm^2 s}$. Because of that, intense proton sources are required for ADS applications.

Sub-critical reactors have been also proposed in support of Th-U^{233}, in which small quantities of actinides and plutonium are produced as well. The conceptual design of a Pb cooled ADS with solid Th fuel has been produced under the name "Energy Amplifier" by C. Rubbia [41], the system being called amplifier thanks to the neutron population amplification operated by the fission reaction, sustained by the spallation beam.

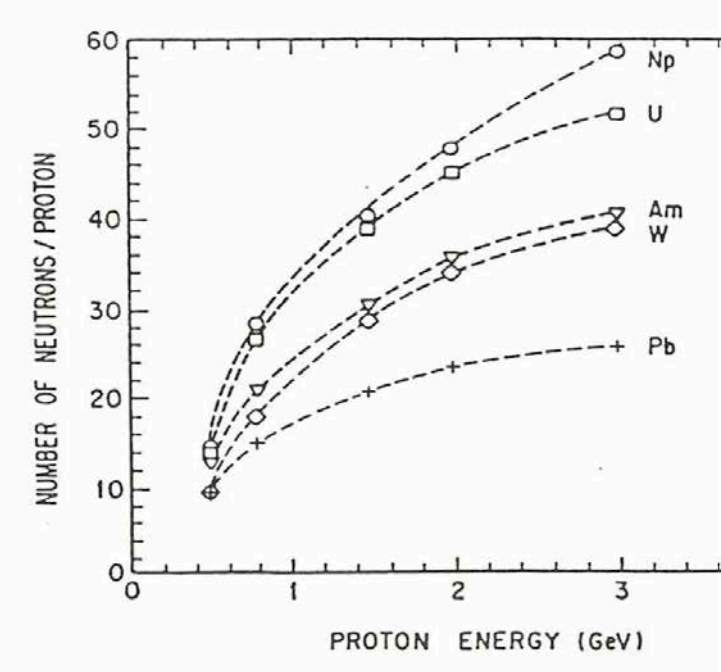

Figure 5.2: Spallation neutron yield per different incident proton energies and targets.

5.1.1 Partitioning and Transmutation

Accelerator Driven Systems are presently playing an important role in the future energy production scenarios including GEN-IV nuclear reactors, as they are potential and promising candidates for transmutation purposes [42]. Partitioning and Transmutation (P&T) is a high-level waste management strategy, currently under R&D worldwide, aimed to process the nuclear waste by partitioning specific hazardous elements or nuclides and then transmuting them into less hazardous forms. The introduction of the P&T technique in the nuclear waste reprocessing cycle allows isolation of long living radioisotopes and their subsequent transformation in much shorter lifetime isotopes via neutron irradiation. P&T aims to reduce the radiotoxicity[1] of disposed waste and the duration for which the waste represents a threat to the environment. The current European strategy for spent nuclear fuel consists in on-site in-pool cooling (up to 10 years) in the same operating nuclear power plants. Fuel reprocessing in (few) centralized and dedicated plants (1 year) is operated to extract U&Pu from the spent fuel (which is recycled as mixed oxide MOX fuel). Currently, disposal of nuclear waste is assured only in superficial or sub-superficial storage for Low Level and Intermediate Level waste (half lives $\sim 10^3$ years). Geological disposal is instead under study for safely storing High Level waste (half lives $\sim 10^6$ years), however a definitive technical solution is yet to be demonstrated. P&T would significantly alleviate the burden upon geological disposal of High Level nuclear waste.

The composition of the spent nuclear fuel can be roughly divide in two categories. Fission products are the atomic fragments left after physical fission of the fissile elements during neutron irradiation in the reactor core. Of those critical for the nuclear waste radiotoxicity, there are Se^{79}, Zr^{93},Tc^{99},Pd^{100}, I^{129} and Cs^{135}, i.e. the Long-Lived Fission Products (LLFP). Actinides (elements with atomic number larger than 89) other than the fuel itself (U, or Pu) - the so-called Minor Actinides (MA) - are instead produced by multiple neutron capture reactions (n,γ). Some of those are dangerous alpha-emitter, with half-lives of some millions of years. As an example, Fig. 5.3 summarizes and classifies the radioactive elements present in a typical U.S. Pressurized Water Reactor (PWR) spent nuclear fuel before any nuclear waste reprocessing.

In ADS, radionuclides belonging the to category of nuclear waste could transmute and decay in much lower half-life times. Efficient transmutation of MA is achieved with a a fast neutron

[1] A measure of radiotoxicity can be expressed as Sv/ton of reprocessed fuel.

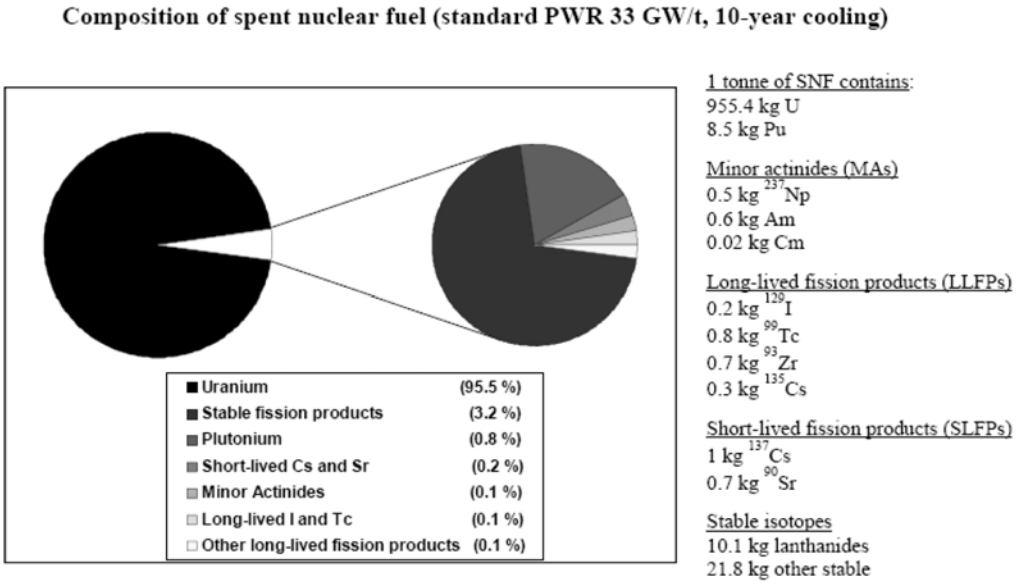

Figure 5.3: Composition of a typical PWR spent nuclear fuel after an average in-pile burn-up and in-pool radiation waiting-time decay

spectrum (E>0.75 MeV). The fission mechanism is preferred: the ratio between the nuclear cross section fission reaction and the radiative capture reaction is more favourable with fast neutrons. Transmutation of certain LLFPs (e.g. Tc^{99} and I^{129}) is in principle achievable in ADS, undergoing several neutron captures.

A global picture of the impact of P&T in the reduction of radiotoxicity of nuclear waster is available in Fig. 5.4. Radiotoxicity of nuclear waste is compared to the one naturally coming from Uranium extracted from ore. The impact of waste reprocessing and separation of U and Pu actinides (which in turn translates in a more efficient use of the energy content of the initial fuel) brings the radiotoxicity of spent fuel down already of a factor of few tens in a time scale, while chemical separation of minor actinides and transmutation in ADS facilities allows to cut down the duration of concern of a factor of thousand, i.e. to a time period which is comparable to human scale. Moreover, spent fuel undergoes a sizeable reduction in volume, which relaxes the need of storage capacity. From this picture, it is clear that the demonstration of the feasibility of transmutation of a relevant quantity of high-level nuclear waste to be sent to final storage, accompanied by a reduction of the period of radiotoxicity, is of manifest importance for the success of ADS industrial application.

Transmutation technologies under investigation belong to not only to fast sub-critical reactor coupled to a particle accelerators, but also high neutron flux in a fast or thermal critical reactor. Critical reactors can be used as MAs transmuters: nevertheless, if heavily loaded with MAs, critical assemblies can experience severe safety issue due to reactivity effect induced by the smaller fraction of delayed neutrons. ADS can instead operate in a more flexible and safer manner even if heavily loaded with MAs. A comparative study as been done by the Nuclear Energy Agency [43], of which the main outcomes are resumed in Table 5.1.

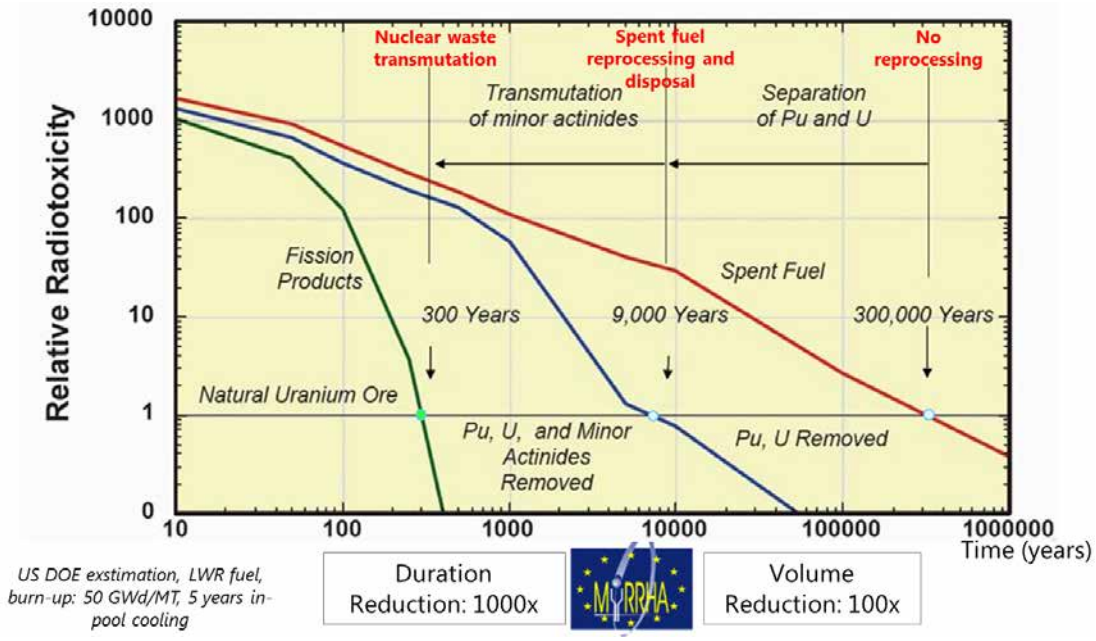

Figure 5.4: Nuclear waste problem: the impact of Partitioning & Transmutation

	Advantages of accelerator-driven systems	**Disadvantages of accelerator-driven systems**
Design and operation	♦ The possibility to operate a reactor core at a *neutron multiplication factor below 1* opens opportunities for new reactor concepts, including concepts which are otherwise ruled out by an insufficient neutron economy ♦ In particular, this allows transmuters to be designed as pure TRU or MA burners and hence the fraction of specialised transmuters in the reactor park to be minimised ♦ The proportionality of the reactor power to the accelerator current simplifies the reactor control	♦ *Accelerator:* Very high reliability required to protect structures from thermal shocks ♦ *Beam window and target* subjected to unusual stress, corrosion and irradiation conditions ♦ *Sub-critical core:* Increased power peaking effects due to external neutron source ♦ Compromises between neutron multiplication factor and accelerator power required ♦ Increased overall complexity of the plant ♦ Reduction in net plant electrical efficiency due to power consumption of accelerator
Safety	♦ The reactivity margin to prompt criticality can be increased by an extra margin which does *not depend on the delayed neutrons* ♦ This enables the safe operation of cores with degraded characteristics as they are typical e.g. for pure MA burners ♦ *Excess reactivity can be eliminated*, allowing the design of cores with a reduced potential for reactivity-induced accidents	♦ New types of reactivity and source transients have to be dealt with (external neutron source can vary rapidly and reactivity feedbacks in TRU- and MA-dominated cores are weak)

Note: Issues of particular relevance for the transmutation of TRU and minor actinides (MA) are underlined.

Table 5.1: Comparison of accelerator-driven sub-critical and critical reactor systems: issues particularly relevant to MA and transuranic (TRU) are underlined [43].

5.2 Accelerator requirements for ADS

A neutron population is multiplied through the fission mechanism in nuclear reactors. In critical assemblies, an equilibrium balance in the neutron population is reached between the increase due to multiplication and the losses (parasitic absorption, leakage) such that the reaction is self-sustained.

In sub-critical reactors, steady state can be reached in presence of an external source, which is multiplied by a factor $1/(1-k_{eff})$ by the assembly, being $1-k_{eff}$ the sub-criticality margin of the assembly. The total neutron population, to which corresponds the reactor thermal power, is controlled by the intensity of the external source. This is of paramount importance in ADS for safety and regulation considerations.

Given a certain sub-criticality margin and chosen the spallation mechanism as the reference external neutron source method, a beam power of $P_{source} = (1-k_{eff})P_{th}$ is required to close up the sub-criticality margin and lead a steady state neutron reaction. The corresponding beam intensity is given by

$$I_b \frac{N_n}{N_p} f E_f = (1-k_{eff})P_{th} \quad \Rightarrow \quad I_b = \frac{(1-k_{eff})P_{th}}{\frac{N_n}{N_p} f E_f} \tag{5.2}$$

where the E_f is the average energy release per fission ($\simeq$ 200 MeV), f is the fission factor (fraction of neutrons causing fission). The ratio $\frac{N_n}{N_p}$ is determined as a result of the spallation beam energy chosen and follows the spallation yield curve, available in Fig. 5.2. The proton energy must be high enough to maximize the efficiency of the spallation reaction, to limit the handling of high beam current and, at the same time, to contain the energy deposited in the target and its window. A compact reactor core neutronic design and cost considerations tend, instead, to lower the choice of the proton energy. For Pb or Pb-Bi ADS reactors driven by a proton beam, a good compromise is often found in the 0.6 to 1 GeV range, where the a typical yield of 25 to 30 neutrons per incident proton and per GeV is achievable. Inserting typical numbers in Eq. 5.2, a beam intensity of $\approx \frac{(1-k_{eff})P_{th}}{2E_{beam}}$ is required for ADS, depending on the reactor type (i.e. its power) and the corresponding sub-criticality margin. Table 5.2 resumes the typical figures for beam power and beam energy for different ADS stages. The beam power required for experimental demonstrators falls in the MW range, whereas industrial transmutation facilities will require an order of magnitude larger beam power.

	ADS transmutation demonstrator	ADS industrial scale trasmutator	ADS industrial scale transmutation power plant
Beam power	1 - 2 MW	10 - 20 MW	20 - 50 MW
Beam energy	0.5 - 3.0 GeV	1 - 2 GeV	1 - 2 GeV
Beam intensity	0.3 - 4 mA	5 - 20 mA	10 - 50 mA

Table 5.2: Accelerator beam requirements for different ADS stages.

The accelerator operational mode must be suited to the steady state character of the reactor operation. Continuous Wave (CW) mode must be adopted for ADS applications and this sets an additional accelerator requirement. In order to safely operate the reactor, a quasi-constant monitoring of its absolute reactivity is required in order to computed its power level. Therefore, besides beam intensity monitoring, the steady state operation has to be perturbed at regular intervals by beam delivery interruptions. For this purpose, the decay of the prompt neutron population is monitored inducing recurrent beam interruptions, giving access to the prompt multiplication factor [44]. Interruptions should last 4 to 5 times the prompt decay pediod, i.e. for typically 200 μs. The repetition rate, which has to be contained not to stress the reactor critic elements, can span from 1 to few hundreds of Hz.

The above requirements clearly set the ADS driver accelerators in the High Power Proton Accelerators domain. A particular and still debated argument concerns the acceptable fault rate for this particular machines. Although high reliability and availability are key in modern accelerators operation (see the efforts done for operating of Spallation Neutron Source, SNS, [45] or for the High

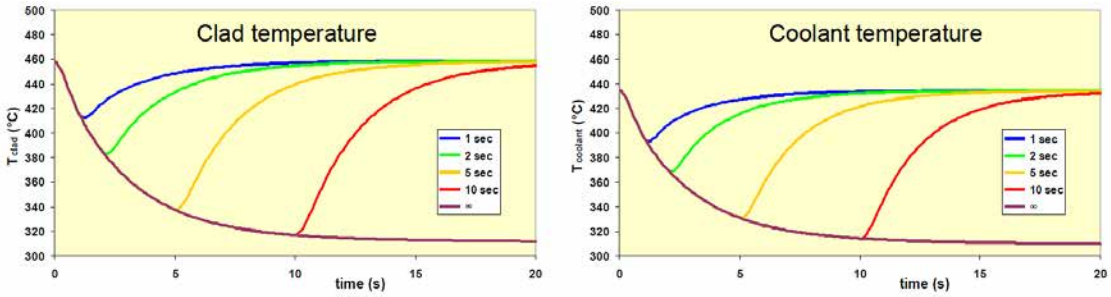

Figure 5.5: Simulation of fuel cladding (left) and reactor primary coolant (right) temperature evolution in the XT-ADS reactor caused by beam interruptions of different length [48].

Luminosity upgrade of the Large Hadron Collider, HL-LHC [46]), accelerators for ADS are required by design to deliver their mission with an acceptable spectrum of undesired beam interruptions, such are the beam trips. This comes from the nature of the target, a nuclear reactor, on which an intolerable beam trip rate could pose severe safety issues. The underlying motivation sits in the thermo-mechanical impact of repeated, long enough, beam interruptions, which could cause high thermal stress and fatigue on the highly irradiated materials of the target window, the fuel claddings and, in general, of the reactor internals (e.g. inner barrel) or vessel. On top of that, such beam interruptions could be systematically associated to a reactor scram (safe shutdown of the neutron reaction by insertion of safety absorber rods) for safety considerations, which would affect negatively the reactor availability to a significant extent, given the time-consuming common restarting procedures required after a reactor shutdown (typically lasting 20 hours) [47]. Fig. 5.5 shows the simulated evolution of the temperature of the fuel cladding and the XT-ADS reactor coolant following beam trip interruption of different durations [48]. During an interruption of delivery of the accelerator beam on the spallation target, the neutrons produced by external source are lost and the neutron population, as the number of nuclear reactions, decrease exponentially in the sub-critical reactor. The exponential relationship between the time duration of an abrupt failure in beam delivery and the resulting temperature difference allows for momentary interruptions only in the range of very few seconds. Repetitive beam trips lasting several seconds lead the reactor material experience significant temperature excursions, which accumulate stress and fatigue on the reactor structures, shorten the maintenance intervals and reduces the availability of ADS. Therefore, the beam trip spectrum is a paramount specification within the ADS requirements and restricts the number of tolerable failures in beam delivery.

Because of that, in ADS, the reliability requirements are expressed in the maximum number of allowed beam trips of a given duration, and depend on the design details, such as the coolant type and parameters, its system design and the materials employed in the reactor design. Of particular interest is the irradiance level and the deposited average power densities in the different ADS components. Usually, the performance and the target lifetime of the components where high neutron irradiation or high power is deposited (such as the target window - replaceable - or the reactor inner barrel - not replaceable by design) set the most stringent accelerator trip requirements.

In the last decade, detailed beam trip requirement analyses have been performed based on transient analyses of ADS reactor system components. Two analyses are of particular interest, as they set the beam trip requirements for two specific ADS projects, the JAEA reference ADS design [49] and the MYRRHA design [50] [51] [52]. The JAEA study considers a 800 MW_{th} subcritical reactor driven by a 30 MW proton beam. The MYRRHA design considers a 85 to 100 MW_{th} reactor, driven by a 1.5 to 2.4 MW proton beam. Results of the studies are resumed in Fig. 5.6 [53] and compared to the Spallation Neutron Source (SNS) accelerator performances (year 2008, [54]).

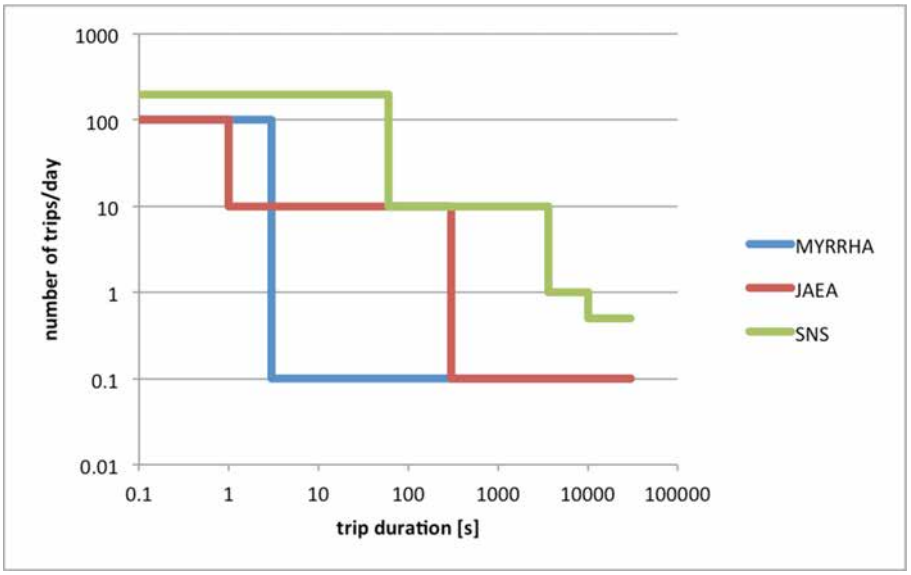

Figure 5.6: Beam trip frequency spectrum: recorded by SNS operation (2008), design basis for the Japanese ADS (JAEA), accepted for the MYRRHA accelerator project. From [53].

Beam trips lasting fractions of seconds are in general well-tolerated by both JAEA and MYRRHA design, as they induce little perturbation in the reactor operation, whereas a general agreement is to limit the beam trip lasting unities of seconds, as structural material integrity is concerned. In this respect, the JAEA analysis sets less severe reliability specifications with respect to the MYRRHA design (see Section 5.4).

As measure of comparison, the SNS operation fault statistics shows that the reliability target for the ADS accelerators is significantly higher than the current recorded performance of similar accelerators, that is a Mean Time Between Failures (MTBF) of a few hours. Being this said, it turns clear that the beam trip spectrum of ADS accelerator must be controlled and sized to the requirements by design, therefore permanent focus should be fixed on this issue by specific R&D.

For power generation applications, the ADS beam trip rate requirement could be somewhat more stringent, as the demands of continuous commercial power production limit to only a few long unscheduled interruptions per year the reliability requirements.

Given the continuous (CW) beam delivery of MW beams, ADS accelerators should exhibit very low and controlled beam losses. This allows, in turn, hands-on maintenance of the accelerator beamline components, which helps in reducing the accelerator down-time in case of breakdowns and decreases the Mean Time To Repair (MTTR). The uncontrolled beam loss specification is therefore suggested by typical values required in the High Power Proton Accelerators (HPPA) domain, and is less than 1 W/m, which translates into fractional beam loss requirements (at full energy) ranging from ~ 1 part-per-million per meter (ppm/m) for a demonstration facility to less than 0.1 ppm/m for an industrial scale facility. The SNS operation confirms that those figures are achievable [55], and a goal of 0.1 W/m seems to be realistic in the future.

Beam current swing is required in ADS systems in order to compensate for changes in reactivity during burn-up of solid fuel. As an example, in the MYRRHA design, a beam current swing from 2.4 mA to 4.0 mA is requested by design, as given a target beam energy (600 MeV), an increasing beam power (from 1.5 MW to 2.4 MW) is required to sustain a steady-state neutron reaction in the subcritical core and compensate the fuel burn-up. Beam power stability of $\pm 1\%$ is required and needs constant on-line monitoring, which can be provided by state-of-the-art beam current transformers for beam intensity measurement (however before the target), and time-of-flight diagnostic for beam energy measurement. In addition, beam size and position stability on the target of less than 10% and 0.1 RMS beam size, respectively, are required.

5.3 Accelerator choices for ADS

As discussed in the previous section, the accelerator candidates for ADS should be capable to deliver a high power (multi-MW class), Continuous Wave beam, characterized by modest energy but high current. Two accelerator designs have demonstrated this characteristics:

- the isochronous, separated sector, cyclotron, of which the highest power example operates at the Paul Scherrer Institute (PSI, Switzerland), delivering a 1.3 MW (2008) continuous wave proton beam (590 GeV, 2.2 mA) for a variety of research programmes, with availability which has reached a level of 90% [56];
- the superconducting LINAC, operable in continuous wave. The highest power example is the SNS superconducting LINAC (Oak Ridge National Laboratory, TN, USA), a - pulsed - machine delivering $>$ 1 MW (2009) proton beam (1 GeV) for neutron experiments, with availability $>$ 90% (2014) [55].

In principle, both accelerator types could deliver the required proton beam for ADS applications. However, there are many aspects which point to choose superconducting LINAC designs.

Given the recirculation principle adopted to guide and accelerate particle beam, the isochronous cyclotron design provides a compact and cost effective unit as ADS driver. For instance, isochronous cyclotrons were identified for the Energy Amplifier project [41]. This advantage translates into disadvantages if seen from a reliability point of view. The lack of any form of redundancy applicable to this design hinders fault tolerance. Hence, a cyclotron is penalised in terms of availability. The extraction of the beam is a rather complex task when the beam current increases over 1 mA, so, in terms of beam power, the scalability of such machines is potentially harder. Schemes for combining beams from multiple cyclotrons have been proposed to extend the use of such machines to beam power levels up to 10 MW [57], i.e. for deployment in industrial ADS facilities, but never applied. Cyclotron technology is commonly limited to a maximum energy of 0.8 to 1 GeV due to vertical focusing in isochronous machines and room temperature structures, which is however suited to ADS applications. An upgrade of its final beam energy instead implies complicated and expensive changes in its design, and cannot be considered as realistic optional feature as desirable for demonstration ADS machines.

The superconducting LINAC is, on the other hand, by definition a modular structured device. In a LINAC, a series of fixed fields at fixed frequencies follows the frozen particle velocity profile along the accelerator, therefore it is built as a sequence of many independent accelerating structures (RF cavities) and magnetic focusing elements. This provides inherently a highly modular structure, which is particularly well-suited to enhance fault tolerance and increase availability. Handling of intense beam currents is achievable in nowadays superconducting LINACs. The final accelerator beam energy can be chosen and adapted as a result of accelerating scheme and the number of modules chosen. Finally, superconducting linear acceleration technology has the biggest beam power potential, as it will be required for industrial scale application of ADS.

An interesting alternative accelerator design candidate, in principle capable to deliver beam power in excess of 1 MW, is the Fixed-Field Alternating Gradient (FFAG) accelerator concept. The repetition rate of FFAGs could span very high, and R&D is ongoing for conception of true CW machines [58].

5.4 The MYRRHA project

The Multi-purpose hYbrid Research Reactor for High-tech Applications (MYRRHA) project [9] [59] is a polyvalent research facility currently being developed at SCK•CEN. MYRRHA is based on the ADS concept and principally aims to demonstrate the feasibility and operability of a safe and efficient transmuter, comprising a subcritical core fed by an external neutron source, in turn obtained by a proton accelerator.

The reactor power level is in the tents of MWth, and so MYRRHA is considered a demonstrator for the ADS concept. As a flexible irradiation facility, the MYRRHA will be able to work in both critical as subcritical modes. In such way, MYRRHA will deliver a fast, flexible spectrum of

Table 5.3: MYRRHA beam characteristics

Particles		protons
Beam energy		600 MeV
Beam current		0.1 to 4 mA
Time structure	*beam delivery*	CW
	repetition rate	1 to 250 Hz
	duty cycle	10^{-4} to 1
Beam delivery to reactor	*position*	Vertically, from above
	design	LBE cooled beam window
Beam power stability	*energy*	±1%
	current	±2% (time scale: 100 ms)
Beam footprint on window	*geometry*	Circular, diameter 85 mm
	stability	<±10% (time scale: 1 s)
Allowed beam interruptions	*t <0.1* s	unlimited
	0.1 s < t <3 s	max 100 per day
	t >3 s	max 10 per 3 month operation cycle
MTBF		>250 h

neutron flux allowing for fuel developments for innovative reactor systems, material developments for GEN IV and fusion reactors and radioisotope production for medical and industrial applications. Besides, MYRRHA will employ lead-bismuth eutectic as coolant and spallation target and such feature will play an important role in the development of the Pb alloys technology under study for the LFR (Lead Fast Reactor) GEN IV concept.

The MYRRHA design has progressed through various Framework Programmes (FP) of the European Commission in the context of the EURATOM research on Partitioning and Transmutation. The XT-ADS version was a short-term, small-scale (57 MWth) experimental facility, and has been developed within the EUROTRANS project in the FP6 (2005-2010). The most recent version, called FASTEF, is a further upgrade of XT-ADS, still conceived as a flexible irradiation facility, now able to work in both subcritical and critical modes. FASTEF has been developed within the CDT project in FP7 (2009-2012). The MYRRHA design has entered into the Front End Engineering Design (FEED) Phase in 2014 and a safety file was prepared for the authority pre-licensing.

5.5 The MYRRHA high power proton accelerator

The MYRRHA reactor rates a thermal power of approximately 85 MWth in ADS sub-critical configuration and is cooled by liquid Pb-Bi eutectic (LBE). The core is a loaded with Mixed Oxides (MOX) fuel, resulting in a design $k_{eff} = 0.955$. Given these parameters, the subcritical core of such an ADS requires an intense external neutron source to deliver a continuous fission power, of beam power falling in the MW class. The spallation mechanism is considered for obtaining a source of fast neutrons through an external high energy and high intensity proton beam. The subcritical core geometry of MYRRHA is optimized for an impinging proton beam energy of 600 MeV, where the Pb-Bi coolant is also used as the heavy target for the spallation reaction. At this energy the neutron yield obtained by spallation on lead is around 15 per incoming proton. From Eq. 5.2, for a design $k_{eff} = 0.955$, a beam power of 1.9 MW is required to sustain the reactor chain reaction. The requested beam intensity has been more precisely calculated by Monte-Carlo simulations, and varies between 2.5 and 4 mA, depending on the operation cycle and the burn-up of the nuclear fuel and the fuel elements reshuffling scheme. This up to 2.4 MW beam is delivered above the core in Continuous Wave mode, through a beam window.

While the specificity and difficulty of the Continuous Wave (CW) nature of the beam delivery of MYRRHA is acknowledged, the really outstanding challenge is the design requirement set on the Mean Time Between Failures (MTBF). In the MYRRHA operational context, the beam is considered to fail if its delivery to the subcritical core is interrupted during a time period that lasts longer than 3 s. Since the MYRRHA cycle will span 3 months and during such a cycle it is requested to have not more than 10 beam failures, the quoted MTBF is then set on 250 hours [47]. This demanding reliability requirements package is strongly related to the thermal shocks which a beam interruption causes in an ADS, adversely affecting structural materials of the reactor and possibly causing safety issues. A high available proton beam is required for long operability of the plant. Beam delivery interruption between 0.1 s and 3 s, typical in the accelerator domain, are tolerated with a maximum of 100 per day. Short (t <0.1 s) beam trips are accepted at a virtually unlimited occurrence frequency. The allowed beam trip spectrum of the whole accelerator is thus significantly lower than observed on today's reported achievements of comparable accelerators [54], therefore the issue of reliability is considered the main challenge and concerns all the R&D activities around the MYRRHA accelerator.

Table 5.3 resumes the MYRRHA project beam characteristics, and are the current baseline set for the MYRRHA accelerator design, discussed in the following.

Fault tolerance

The general philosophy to reach a high natural MTBF on the MYRRHA accelerator is identified in the fault tolerance capability, achieved only if a single failed element does not automatically imply a global failure [60]. Such a fault tolerance can only be effective if it is accompanied by a realistic switching time (fault detection time plus reconfiguration time: in MYRRHA this time is necessarily 3 s) and a Mean Time To Repair (MTTR) shorter than the MTBF of the failing element or chain. The fault tolerance concept is addressed by design, following three general design principles to accomplish the reliability goal:

- the adoption of redundancy, with a maximum of the serial version;
- use of components far from their limits;
- repairability.

The parallel redundancy scenario provides a back-up functionality upon an accelerator element failure, although requires more than one component per only one mission, therefore for economic reasons should be avoided if not mandatory. The serial redundancy scheme replaces a missing element's functionality by retuning adjacent elements with equivalent functionalities, and may be accomplished if applicable and foreseen as of the design phase. However, this strategy implies an high degree of modularity of the accelerating and focusing structures. From the beam dynamics point of view, robust but flexible optics is key for achieving fault tolerance.

The adoption of solid and established technologies as from the accelerator design phase provides higher natural components MTBFs, which translates in higher global facility MTBF. Strong component design ("overdesign") can be obtained choosing components far from their technological limits and employing significant operation margins, or derating.

Reparability, or more specifically short MTTRs, is required to guarantee high availability. Within the MYRRHA design, given the very short "grace period", true on-line reparability is hard to achieve on a failing element, the reparability concept is restrained to applications in conjunction to redundancy (like hot-swap capability).

Design choices

Since the MYRRHA accelerator is set to be a high power proton accelerator with strongly enhanced reliability, moreover to be operated in CW mode, and in agreement with several high power accelerator projects [1] [4] [61], the technical solution of a superconducting linac has been adopted [52]. The compatibility of this choice with the three above-mentioned reliability principles is clear: the architecture of a superconducting linac, consisting of a sequence of nearly identical and modular RF cavities, complies perfectly with the serial redundancy scheme; besides, a superconducting linac

can handle a beam current of 4 mA with performances of the superconducting RF cavity very far from present limits.

The linac consists of two clearly distinct sections (see Fig. 5.7):

- a medium and high energy section, highly modular, based on individual, independently controlled, superconducting cavities and warm quadrupole insertions. In this section the serial redundancy may be applied successfully to obtain a strong fault tolerance [62]. The function of a faulty cavity may typically be taken over by four adjacent cavities [63];
- a low energy section (or injector) [64], in which the modularity and fault tolerance principles are not applicable: in this section the beam optics is frozen by design and the accelerating structures are mainly based on multi-cell cavities. Here redundancy has to be applied in its parallel form, so the adoption of two complete injectors is foreseen. The transition energy between the two sections is fixed at 17 MeV. At this energy a fast dual input switching magnet will be installed for merging the injector lines.

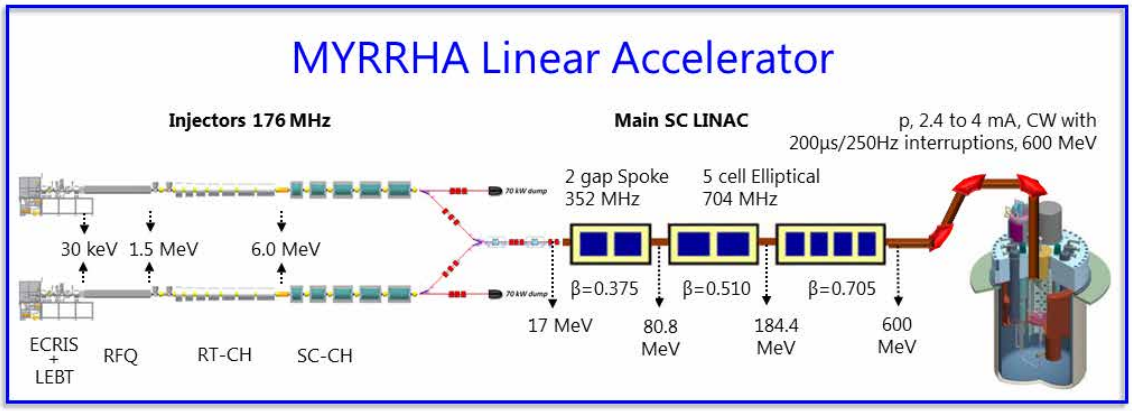

Figure 5.7: Schematic view of the MYRRHA Linear Accelerator.

5.5.1 The superconducting LINAC

The current 17-600 MeV MYRRHA main superconducting (SC) LINAC design is the optimized and consolidated version provided by the FP7 MAX programme [65]. Its architecture [66] is composed of an array of independently powered superconducting cavities with high energy acceptance and moderate energy gain per cavity. A design employing a low number of cells per cryomodule and very conservative accelerating gradients allows to increase as much as possible the tuning flexibility and provides sufficient margins for the implementation of the fault-tolerance scheme. Three distinct families of superconducting cavities are used to cover the full energy range:

- the first section from 17.0 MeV to 80.8 MeV employs 352.2 MHz Spoke 2-gap cavities (β_{opt}=0.37);
- a second section with 704.4 MHz elliptical 5-cells cavities and β_{opt}=0.51 accelerates the beam from 80.8 MeV to 184.2 MeV;
- the last section, up to 600.0 MeV, is composed by 704.4 MHz elliptical 5-cells cavities with β_{opt}=0.705.

Such architecture is summarized in Table 5.4, where the main RF characteristics of the MYRRHA accelerating cavities are also listed.

The design of the MYRRHA β_{opt}=0.37 spoke cavity and cryomodule [67] has been recently achieved within MAX programme and a phase of prototyping is scheduled. The design of the elliptical cavities has been performed through previous dedicated R&D programs, including prototyping and RF tests [68] [69].

The operating accelerating gradients of the MYRRHA cavities have been conservatively chosen, following the fault-tolerance principle discussed in precedence. The general rule chosen for design and operation of the MYRRHA superconducting cavities is to limit the RF fields at the inner surface of the SC cavities under 35MV/m peak electric field and 60mT peak magnetic field. The MYRRHA SC cavities operation point will be, then, a 30% below their design working points. Such derating increases the fault-tolerance and is used as a margin for fault compensation. The obtained nominal accelerating gradients are 6.4, 8.2 and 11.0 MV/m in the 3 different sections, with a required maximum field capability of 8.3, 10.7 and 14.3 MV/m, respectively.

The superconducting LINAC focusing and transport is assured by regular focusing lattices. A maximum of 6 meters cryostat length with room-temperature quadrupoles doublets in between is chosen by design. This scheme provides easy maintenance and fast replacement, and leaves the availability diagnostic ports at each lattice location. A nearly perfect optical lattice regularity requiring no specific beam matching between the cryostats is foreseen. Such elements makes the possibility to operate the beam with a full cryomodule missing realistic.

The quadrupole magnets are conceptually devised as follows. Low operating gradients are adopted to ensure reliable operation, while their length is optimized to minimize fringe field effects. In nominal operation, a maximum magnetic field on the pole tip below 0.3 T is conceived. This characteristics allow the adoption of warm magnets with still enough room for gradients increases, if required during commissioning. For space economy, additional coils should be included in the quadrupole magnet design to ensure the presence of dipole field component allowing the required steering capability for beam orbit correction. Beam steering and alignment will be performed employing about 60 beam position monitors (BPM), located at each lattice warm section.

Foreseen beam instrumentation includes beam profilers and bunch shape monitors, to be installed typically in the first lattices of each LINAC section such that a suitable beam matching could be performed. Beam current measurement is expected at few longitudinal stages while several (>100) beam loss monitors are expected along the LINAC. As previously discussed, the early detection of abnormal beam losses is highly required in high power beam applications and requires a (wise) triggering of the machine protection system.

The MYRRHA main linac is designed to be fault resistant, a characteristic which must be achieved naturally, from design, to reach its reliability goal. This is achieved by providing a modular structure with significant RF power and gradient margin throughout the three superconducting sections. A local compensation method is employed to as reference scheme for recovering a RF unit/s failure/s [62] [63]. In such transients, beam is unloaded and the whole interruption should not last more than 3 seconds. A RF fault is compensated acting on the RF gradient and phase of the nearest four neighbouring cavities, which are not yet employed for fault compensation. The main conclusion of the fault-recovery scenario analyses is that a fault recovery scheme is in principle feasible everywhere in the MYRRHA main linac to compensate for the loss of a single cavity or of even a full cryomodule [63]. The maximum allowed number of consecutive faulty cavities is two in the spoke and elliptical β=0.51 sections, while is increased to four in the elliptical β=0.705 LINAC section.

Within the MAX programme [70], the fault-tolerance capability of the up-to-date MYRRHA main linac design has been assessed so to foresee the acceptable RF failure modes and the induced hardware requirements, such as the amplifiers power, the power couplers coupling factors, and strategies, e.g. the LLRF tuning regulation and the machine reconfiguration procedures. In order to practically implement such compensation schemes, a first detailed recovery procedure has been defined and is available in [71]. The outstanding switching time of three seconds is still considered a critical issue, especially for the machine control system and the dedicated Low Level RF digital systems and cold tuning systems. For the operation of the MYRRHA LINAC, the coupling to a Virtual Accelerator based control system, capable of very fast implementation (<3 sec) of the fault tolerance procedures, is envisaged and currently studied [72]. The Virtual Accelerator model employs a beam dynamics code (like Tracewin [73] or TRACK [74]) to compute the model of the real accelerator in operation and interacts with it through the accelerator control system. In the event of element failure, the beam dynamics code would upload pre-calculated matched lattices. The set of pre-calculated configurations is kept in coherence with the actual machine online. A Virtual Accelerator based test control system has been envisaged as one study aspect of the RFQ@UCL programme [75] for the MYRRHA Injector.

Table 5.4: MYRRHA superconducting linac main parameters

Section	*1*	*2*	*3*	*units*
Energy range	17.0 - 80.8	80.8 - 184.2	184.2 - 600.0	MeV
Cavity technology	spoke	elliptical		
Frenquency	352.2	704.4	704.4	MHz
Cavity optimal β	0.375	0.510	0.705	
N. of cavity/cryomodule	2	2	4	
N. of cells/cavitiy	2	5	5	
Tot. n. of cavities	48	34	60	
Section lenght	73.0	63.9	100.8	m
E_{acc}^{nom} [a]	6.4	8.2	11.0	MV/m
E_{acc}^{design}	8.3	10.7	14.3	MV/m
E_{peak}/E_{acc}	4.3	3.3	2.5	
B_{peak}/E_{acc}	7.3	5.5	4.6	mT/(MV/m)
Q	$2.2{\cdot}10^6$	$8.2{\cdot}10^6$	$6.9{\cdot}10^6$	
R/Q	217	159	315	Ω
Synch. phase	-40 to 18	-36 to -15		°
Beam load per cavity (4 mA)	1.5 to 8	2 to 17	14 to 32	kW
Nom. quadrupole gradient	5.1 to 7.7	4.8 to 7.0	5.1 to 6.6	T/m
Beam aperture	56	80	90	mm

[a] normalized to $L_{acc} = N_{gap}\beta_{opt}\lambda/2$

5.5.2 The injectors

The injector part (0÷17 MeV) is based on some rather unconventional solutions. In this section the serial redundancy mechanism is not achievable, because of the frozen beam optics and fast evolution of the beam parameters along the line, precluding the modularity. In order to preserve the fault tolerance capability of the linac, a full parallel redundancy scheme has been implemented in the MYRRHA injector, implying the installation of two identical accelerating sections up to 17 MeV (one being operational, the other in hot-standby).

The principal architects of this section are SCK•CENwith CNRS/IN2P3 laboratories IPN Orsay (IPNO) and LPSC Grenoble for the beam source and low energy part, and the Institute for Applied Physics (IAP) in Frankfurt, Germany, for the front-end accelerator stage.

A 352.2 MHz version of the injector was developed in the framework of the FP6 EUROTRANS project, in which a common accelerator layout was envisaged for the ADS demonstrator (i.e. MYRRHA) and for the industrial transmuter prototype (called EFIT) [64]. In the framework of the FP7 the EUROTRANS project was followed by the so called MYRRHA Accelerator eXperiment (MAX) R&D program, started in 2011 and ended in 2014. The MAX program continued the R&D studies on the accelerator candidate for ADS purposes, delivering an updated and consolidated design of a real machine including prototyping and demonstration.

Focusing the requirements only on an ADS demonstrator, i.e. MYRRHA, it was decided to investigate the potential benefits of a 176.1 MHz injector [76], achieving an optimized reliability and economic efficiency but at the cost of a reduced maximum beam current capability. The expected benefits are: a lower input energy of the copper CH DTL, therefore a shorter RFQ; reduced power density in the copper structures; a lower input energy of the RFQ, thus a reduced electrostatic potential on the ion source; the possibility to consider a 4-rod RFQ instead of a 4-vane version, yielding relaxed tolerances, easier adjustments and significant savings. A pre-study of this 176.1 MHz scheme confirmed all these benefits [76] (in particular the input and output energies of the 4-rod RFQ at 30 keV and 1.5 MeV, respectively) and added the possibility of reducing the inter-electrode voltage in the 4-rod RFQ for a Kilpatrick factor of 1.2. For the MYRRHA injector a very compact and efficient KONUS beam dynamics design could then be found [77].

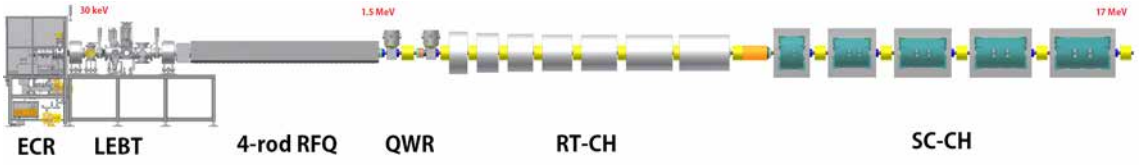

Figure 5.8: Schematic view of the MYRRHA Injector layout.

In order to increase the longitudinal acceptance of each injector cavity, new consolidated beam dynamics were based on shorter cavities with constant phase profile in the RT section and constant beta profile in the SC section [78]. The use of multiple diagnostic elements has been considered for fast failure detection. With monitoring the beam quality after each CH structure particle losses in the main linac could be minimized. At the end of the MAX program (2014), a further advancement in the design based on the error studies proposed an optimized matching section between the RFQ and the accelerator booster, with the employment of doublet focusing lattice [79]. This provided a robust beam dynamics design with low emittance growth rates and additional drift spaces, which improves diagnostic capability and eases integration issues.

At the end of such R&D and optimization process, the schematic layout of the 176.1 MHz injector design [80] [79] shown in Figure 5.8 and consisting of the following elements was adopted:

1. a Electron Cyclotron Resonance (ECR) type ion source, for optimal longevity, delivering a moderate 30 keV proton beam;

2. a magnetic type Low Energy Beam Transport (LEBT) line, for low energy beam characterization, manipulation, and appropriate matching into the next element;

3. a 4-rod Radio Frequency Quadrupole (RFQ), focusing, bunching and accelerating the beam up to 1.5 MeV;

4. two room temperature double gap Quarter Wave Resonators (QWR) rebunchers;

5. seven copper multi-cell Crossbar H-mode (CH) DTL structures, bringing the beam up to 5.9 MeV;

6. five superconducting CH-DTL structures for the acceleration till 17.3 MeV. The rationale of this solution is of course to extend the advantages of the superconducting RF to the lowest possible energy.

This scheme is now considered as the preferred one for the MYRRHA double injector, and it is the object of a dedicated R&D program through the RFQ@UCL program [75] (see Chapter 6) and the EU MARISA and MYRTE Horizon 2020 programmes.

Chapter 6

The MYRRHA low energy front-end design

6.1 The RFQ@UCL R&D programme

The experimental program RFQ@UCL is executed, in collaboration with the Cyclotron Resources Center (CRC), at Louvain-la-Neuve, Belgium, where the experimental test line is located. The program profits of strong bilateral collaboration agreements with the CNRS/IN2P3 laboratories IPN Orsay (IPNO) and LPSC Grenoble and the IAP Frankfurt laboratory. The RFQ@UCL program obviously interacts and relies with the European programs, like FP7 MAX and MYRTE H2020. The construction of the Injector@UCL, up to final 17 MeV energy and including beam diagnostics development, has been strongly supported by the MYRRHA accelerator 1st International Design Review, held in Bruxelles in November 2012. An overview of the foreseen experimental setup is shown in Figure 6.1.

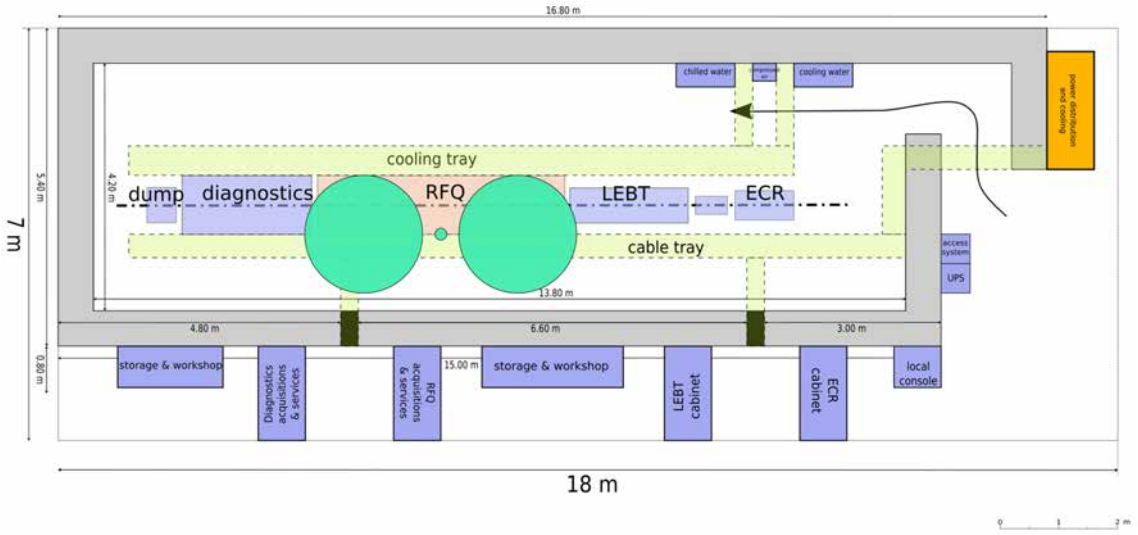

Figure 6.1: General experimental layout of the RFQ@UCL programme in Louvain-la-Neuve, Belgium.

While the EURATOM FP7 MAX project goal is to deliver an updated consolidated conceptual design of the superconducting linac, with strong provisions for enhanced reliability, the RFQ@UCL program is devoted to the injector engineering design and subsequent construction, followed by extensive testing and feedback to design. The principal motivation of RFQ@UCL is to experimentally address the MYRRHA injector design, gaining experience from a tangible prototype.

The initial experimental test stand is constituted by a commercial 30 keV ECR proton source followed by a Low Energy Beam Transport (LEBT) section, injecting a matched beam into the

4-rod RFQ. This test stand is meant both to experimentally investigate a number of beam-related critical issues and to validate technological choices in this accelerator part. These include: the CW operability of the 4-rod RFQ and the Space Charge Compensation (SCC) phenomenon in the LEBT, the adoption of interceptive and non-interceptive diagnostic devices for high intensity CW beams, the design and exploitation of a high power, modular, 176.1 MHz Solid State RF amplifier, the development of a robust and comprehensive control system, based on innate propensity to fault-tolerance and predictive intelligence.

6.2 The Ion Source

The proton source adopted for the MYRRHA low-energy front-end falls in the family of the DC Electron Cyclotron Resonance Ion Sources (ECRIS). This technology offers maturity and reliable delivery of high intensity ion beams, in the mADC range. For the MYRRHA low-energy front-end test stand, the ECRIS of the family Monogan 1000 has been procured by Pantechnik SA (France) [81].

In ECR ion sources, electron cyclotron resonance is employed to ionize a plasma. A volume containing a low pressure gas or vapour (usually pure or in compound) is exposed to RF microwaves at the frequency corresponding to the electron cyclotron resonance, defined by the magnetic field applied to a region inside the volume. The alternating electric field of the microwaves latches synchronously with the gyration period of the free electrons of the gas and increases their transverse kinetic energy. Subsequently, if their kinetic energy is larger than the ionization energy of the gas atoms, a plasma of ionized particles can be produced.

High intensity monocharged beams can be produced by ECR ion sources - commonly called microwave ion sources - with different magnetic configurations. The adopted RF frequency is intimately related to the angular frequency ($\omega = 2\pi f$) of the electron cyclotron motion for a chosen available magnetic field strength B [82] and is given by:

$$\omega = \frac{eB}{m}, \tag{6.1}$$

where e is the elementary charge and m is the mass of the electron (in SI units). For a microwave frequency $f = 2.45$ GHz and rest electron charge and mass, the resonance condition is met when $B = 0.0875T$, which is accessible in principle by normal conducting solenoid magnets or permanent magnets.

In developing a design for high intensity ECR ion sources, low emittance should be pursued, as key parameter for source beam quality [83]. The divergence of an ion beam extracted from an axially symmetric magnetic field is deduced from

$$x' = \frac{1}{2}\frac{qBr}{p}, \tag{6.2}$$

being q the ions charge, B is the magnetic field strength at the extraction aperture, r the radius of the ionization chamber aperture and p the ions momentum at extraction. If we assume a constant (i.e. *flat*) magnetic induction, from Eq. 6.2 the obtained ion beam divergence is

$$x' = \frac{1}{2}\frac{qm\omega r}{ep}. \tag{6.3}$$

Thus, the divergence (and therefore emittance) of the extracted beam is strongly dependent on the magnetic field in the extraction region. A lower magnetic field (corresponding to lower cyclotron frequency) returns smaller beam emittance at the extraction aperture of the ionization chamber. On top of that, the production of monocharged states (1+) ions requires less energetic electrons, therefore the RF frequency can be significantly smaller than the ones used for multiple charged states. In order to ensure optimum beam quality and employ low magnetic fields, the RF frequency design choice of the MYRRHA ECR ion source for production of high intensity proton beams is 2.45 GHz.

For the MYRRHA ECRIS, a specific flat plasma magnetic confinement configuration is provided by two Permanent Magnets (PMs). The magnetic structure is patented in Europe (EU/FR

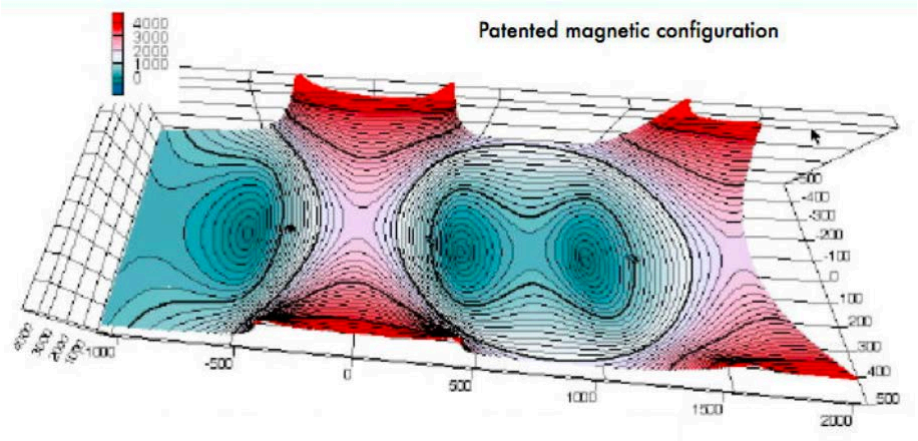

Figure 6.2: Magnetic representation of the Pantechnik Monogan field, based on EU/FR 9615572 and US 6194836 patent. Courtesy of Pantechnik SA, all rights reserved ®.

9615572) and USA (US 6194836) [84] by CNRS and CEA and offers a unique symmetry allowing radial and axial (3D) confinement without adoption of multipole magnets. The choice and arrangement of the PMs is such that a magnetic field **B** comprising an inherent multi-pole structure is generated. The vector sum of the fields created by each of these elements at each point is such that at least one continuous and closed line of minima inside a surface with constant modulus, closed in the source space, is defined. A representation of such concept is shown in Figure 6.2.

The magnetic circuit of the ion source is generated by two coaxial NeFeB permanent magnets rings (B_r=1.29 T per individual magnet). This system allows to reach a magnetic confinement of axial revolution symmetry with a field module for the last closed surface of 2000 Gauss, without adoption of powered electromagnets or multipolar assemblies. The circular permanent magnets surrounding the plasma chamber are spaced longitudinally so to allow direct access to the plasma region not only axially, but also radially. The RF coupling is therefore possible both axially or radially. The absence of electric power for the production of the plasma magnetic trap, where ions are created, enhances reliability and stability of this source.

Tapered axial 2.45 GHz RF injection up to 1.2 kW is adopted for the MYRRHA ECRIS. RF power is provided by a power variable magnetron based generator with automatic stubs for RF tuning. A multi-gap DC breaker, insulated up to 40 kV under air (no windows), is fitted between the RF stubs and the RF injection to allows for galvanic separation from the source body, which is positively polarised. The RF injection is tapered and its chamber is physically separated from the ionization chamber through a RF window.

The source body is placed at a positive potential (nominally 30 kV). It includes a single wall, externally water cooled, plasma chamber with a 4 to 7 mm diameter aperture for the beam extraction. Gas is provided to the plasma chamber though a mass flow controller, calibrated for H_2 gas injection, ranging from 0.1 to 2 sccm. The accuracy and stability of the gas injection is vital for beam stability, and must be ensured by the mass flow controller, which is specified within ±1% and ±0.1%, respectively.

Beam is produced in the plasma chamber and extracted (toward ground potential) by a multi-stage cascade of differently polarized electrodes, forming a pentode extraction system. The system is designed to withstand the extraction of >10 mA DC intensity (all species), up to 40 keV energy (nominally 30 keV), particle beam, with no active (water) cooling. It includes the following electrodes:

1. the *plasma electrode* of the ECRIS, at high voltage (nominally: +30 kV). This electrode presents a central circular aperture which can be adjusted from 4 mm to 7 mm. During commissioning, the plasma electrode hole has been redesigned: the borders of the central hole have been modified to create a 110° conical smoother reduction instead of a sharp edge, in order to better sustain the high plasma temperature;

2. the *puller electrode*, which offers the first potential cascade and is adjusted to optimize the

beam extraction from the plasma chamber. It is typically biased at 22 to 26 kV;

3. a *first ground electrode*;

4. a screen electrode (*electron repeller*), used to: *i)* reduce the leakage of electrons from the source plasma aperture and improve the plasma ionization efficiency, *ii)* repel the electrons available in the beam extraction chamber, enhancing the origin of a degree of space charge compensation in this region (see Section 6.7). A negative DC bias of 1 kV is sufficient to offer a full-screening potential well for this purpose;

5. a *second ground electrode*.

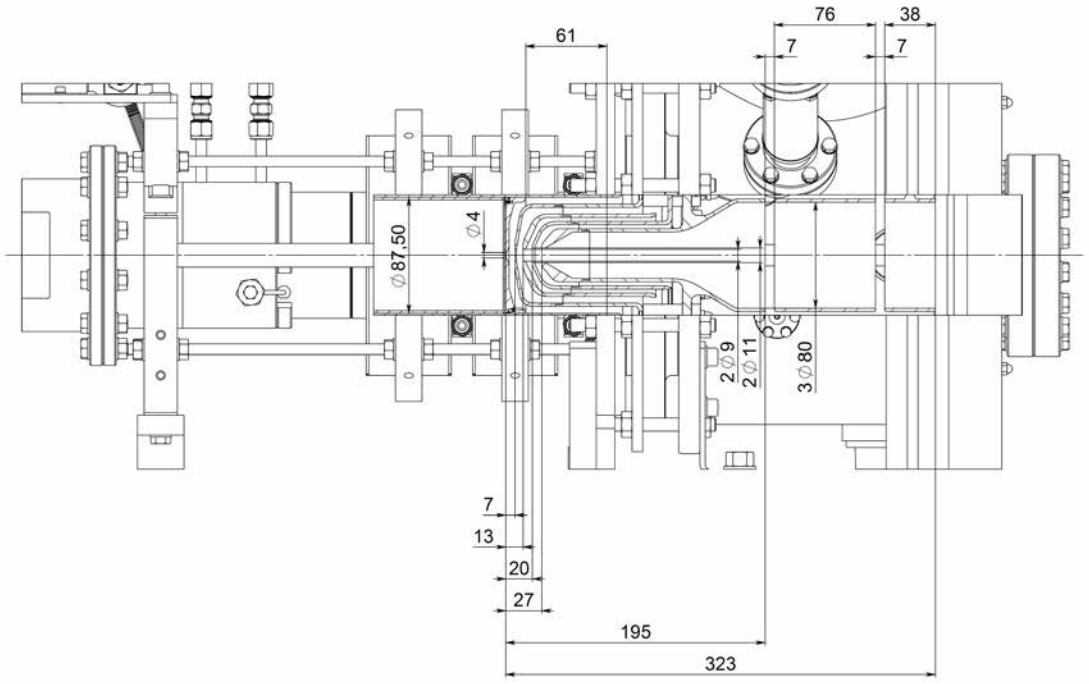

Figure 6.3: Cross section of the plasma chamber and pentode extraction of the Pantechnik Monogan 1000 Ion Source. Courtesy of Pantechnik SA, all rights reserved ®.

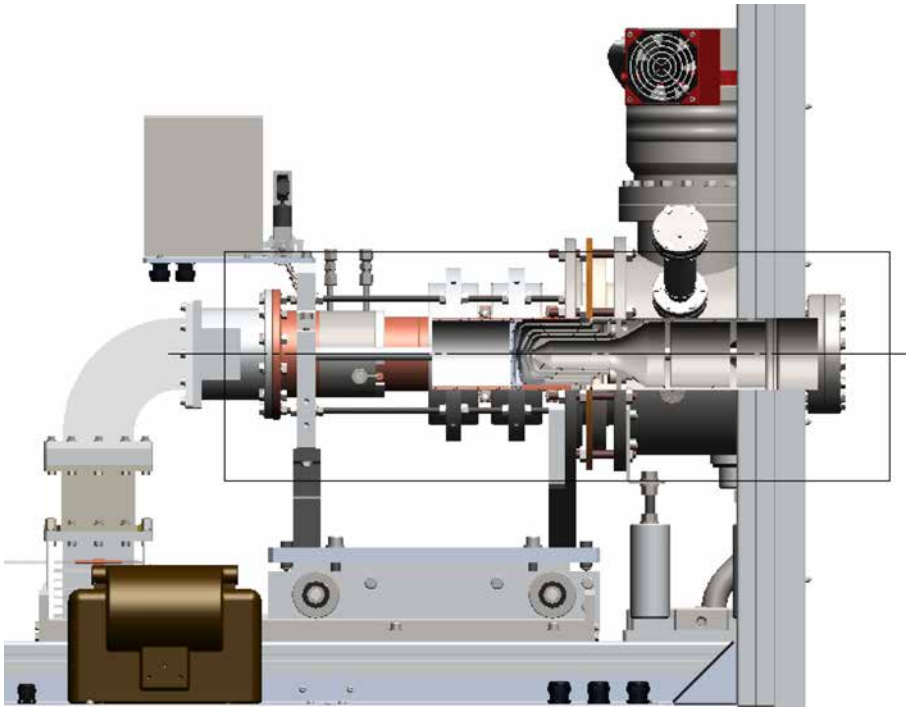

Figure 6.4: CAD section of the full Pantechnik Monogan 1000 Ion Source procured for the MYRRHA low energy front-end test stand. Courtesy of Pantechnik SA, all rights reserved ®.

The source extraction box is then equipped with a Einzel electrostatic focusing lens, which can be used to adjust the beam size in case of excessive beam divergence at this stage. The lens is formed by three ∅80 mm circular electrodes, distanced 7 mm. The first electrode is extended toward the source extraction in order to offer a ground potential external boundary and screen the source extraction system, which is structurally anchored and insulated in this region. It also adjusts the beam aperture to the Einzel lens. Both the first and third electodes of the Einzel lens are grounded. The central electrode can be positively or negatively polarised up to 25 kV, so to offer an deceleration-acceleration or acceleration-deceleration net beam focusing. Concerning the Einzel lens, two important choices have been pursued for the MYRRHA ECRIS:

- such electrostatic lens is foreseen by design, but should not be employed unless required (excessive beam divergence at source exit) for beam tuning: the Einzel lens provides an additional focusing effect very close to the source extraction at the expense of stronger space-charge conditions in this area (expected degree of compensation: 0%, Section 6.7), which are expected to turn into a noticeable emittance growth downstream the low-energy line;
- in case of employment, a positive potential is discarded, as the significant beam deceleration occurring at the center of the lens enhances the space charge blow-up.

In order to enhance reliability, specific design choices are done. The advantages of permanent magnets for plasma confinement and ion production have been already described. All the power supplies are characterized by low ripple output voltage and are placed at ground potential: the absence of electronics at high voltage improves the reliability and long term stability. The ionization efficiency of such ECR ion source is very high and, consequently, the gas load on the vacuum system is low. The gas injection is particularly accurate and stable. The automatic RF tuning responds quickly to minimize reflected power transients during plasma ignition. This kind of source not having filaments or cathodes, its lifetime is defined as the time between maintenance. Maintenance is required for replacement of "consumable" parts, such as only the gas reservoir in principle, but also the plasma electrode and the puller nose in practice. The internal parts of the source body, at high voltage, suffer arc discharge transients and can result to be mechanically or superficially damaged after a certain number of electric breakdowns. Cleaning of the plasma chamber (Cu made) is advised for removal of sputtered material.

This kind of source has been capable to deliver a 30 keV proton (H^+) beam up to 16 mA DC, with transverse beam emittances below 0.2π·mm·mrad RMS norm. A resume of the characteristics of this ion source are available in Table 6.1. The tests executed for characterization of the source are presented in Section 6.6.

Table 6.1: Characterics of the Ion Source adopted for MYRRHA low energy front-end test bench

Accelerating voltage	30 kV (40 kV capable)
Max. proton beam current	16 mA DC
RF	2.45 GHz, 1200 W
Transverse norm. emittance @ 5mA (H^+)	0.1π·mm·mrad RMS norm.
Plasma magnetic confinement	Permanent Magnets (PMs)
Autonomous control system	National Instruments CompactRIO

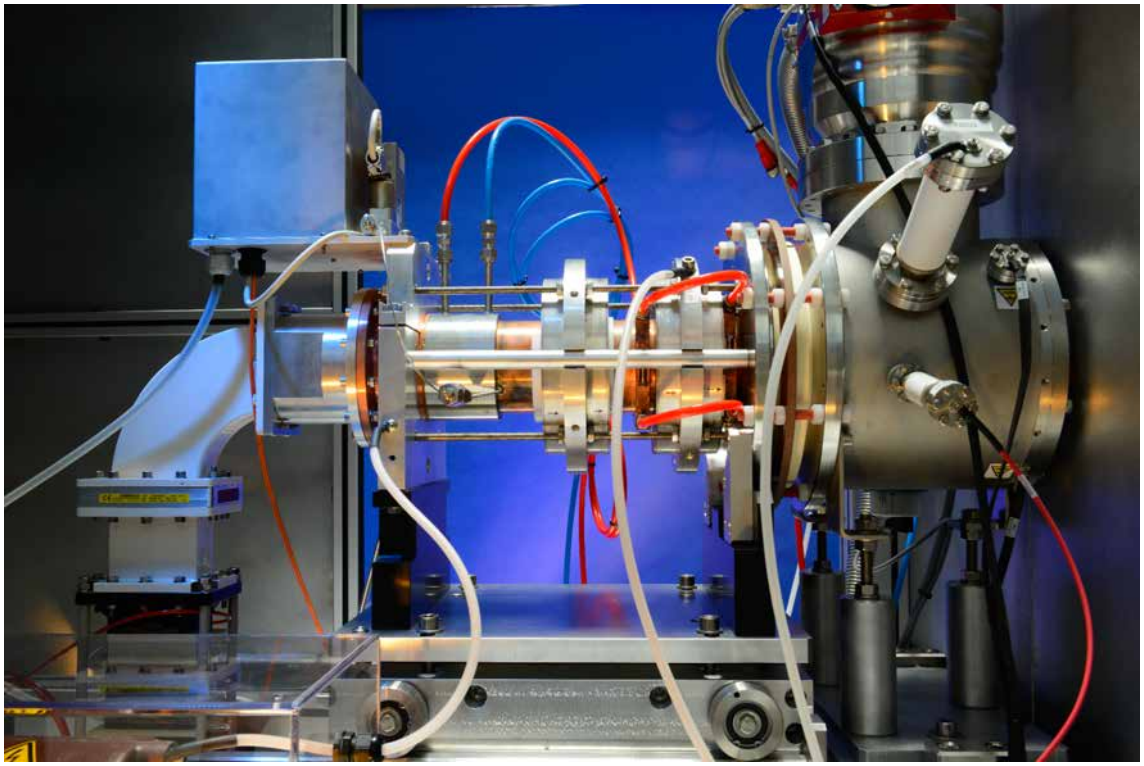

Figure 6.5: Picture of the Pantechnik Monogan 1000 Ion Source procured for the MYRRHA low energy front-end test stand. Courtesy of Pantechnik SA, all rights reserved ®.

6.3 The Low Energy Beam Transport (LEBT) line

The MYRRHA LEBT design and engineering is a collaboration bewteen SCK•CEN, LPSC Grenoble and IPNO. The conceptual design bases have been drawn by SCK•CENand IPNO, the latter supporting with beam dynamics simulations and error analysis, within the EU MAX R&D programme. The implementation, engineering, construction, testing and commissioning is executed by LPSC Grenoble with SCK•CENunder a bilateral agreement. The realization includes a number of external industrial procurements, requiring a dedicated engineering study in the case of the magnetic elements (SigmaPhi, France) or integration in the case of the control system development (Cosylab, Slovenia).

The goal of the LEBT transport line is to efficiently inject the proton beam provided by the Ion Source in the RFQ structure, providing at the RFQ entrance a centered beam with matched

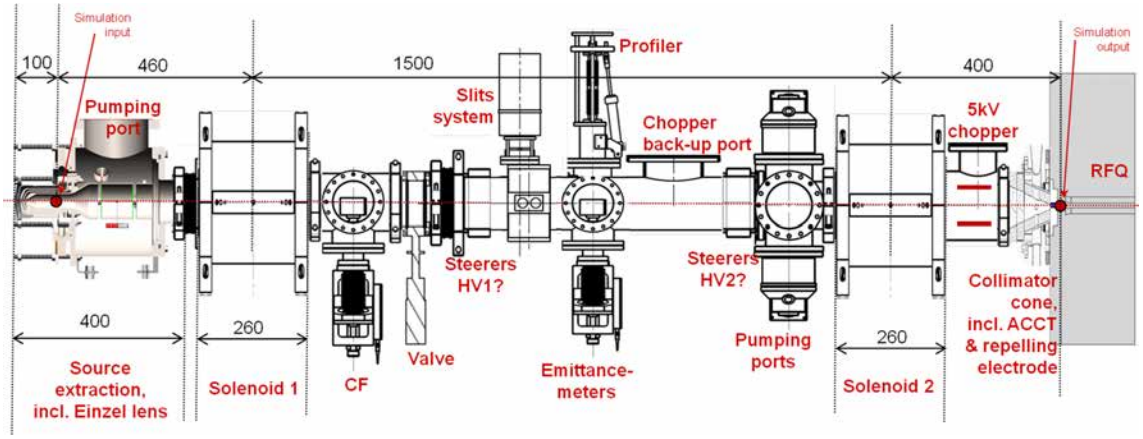

Figure 6.6: Conceptual sketch of the MYRRHA LEBT consolidated layout, from [39].

transverse emittances, lower or equal to the RFQ design value, that is 0.2π·mm·mrad RMS norm., with the following Twiss parameters:

- $\alpha = 0.88$;
- $\beta_{x,y} = 0.04$ mm/π·mrad

The MYRRHA LEBT layout is based on a short magnetic solution and is designed to maximize the proton beam quality injected into the RFQ by considering the Space Charge Compensation (SCC) effects of the beam. At the same time, this solution helps to fulfill the ADS reliability requirements, minimizing beam trip risks due to HV breakdowns and beam losses [85]. The choice of a classical short magnetic LEBT layout, inspired from similar injection lines, has been validated in October 2011. Since then, additional studies have been performed with realistic field maps for the focusing elements, leading to the preparation of the MAX Deliverable 1.2 in 2013 [39], which contains the conceptual design of the reference layout for the MYRRHA LEBT. The engineering, integration and construction phase, followed by commissioning and R&D, followed from 2013.

The overall length of the line, from the source plasma chamber extraction hole to the RFQ rods, is around 2800 mm long. The baseline height of the line is 1.5 m. The beam aperture is commonly >150 mm where transport elements are located, whilst less aperture is left in collimation zones (diaphragm, collimator slits). Such big aperture is adapted to the expected beam size after the first magnetic solenoid (see Section 6.7). For integration reasons, lower diameter restrictions are present in specific parts where the beam size is supposed small by design (i.e. after the second solenoid) or in collimation stages.

The beam transport from the source extraction system to the RFQ entrance is ensured by a couple of magnetic solenoids with integrated dipole steerers. This choice allows for a compact magnetic line where enough space is left for diagnostics. The overall distance between the two solenoid centers has been set to 1500 mm. The first magnetic solenoid is located as close as possible to the source extraction chamber in order to minimize the beam size at its entrance. The second magnetic solenoid should be located as close as possible to the RFQ entrance (maximum 400 mm) in order to focus the proton beam inside the RFQ within nominal specifications. This solenoid produces, in turn, a net beam species separation, as higher mass species (H_2^+, H_3^+) are focused with a longer focal length, therefore result mismatched both with the RFQ collimator aperture (lost on the collimator surface, see next) and the RFQ acceptance itself (lost, mainly longitudinally, along the RFQ, due to energy mismatch with the RF structure during acceleration).

The magnetic solution leaves enough room for insertion, between the magnets, of beam diagnostics allowing for interceptive beam current, profile and transverse emittance measurements (see Section 6.4). For this purpose, a Faraday cup is installed right after the first solenoid, and is used for ion source tuning and safety aspects. A collimation stage (diaphragm + slits) is fitted to cut the beam halo and perform a first cleaning of the beam species other then H^+. The collimation stage is useful also for reshaping the beam emittances or reduce the beam intensity delivered by

the Ion Source. A couple of horizontal and vertical emittancemeters are installed after the collimation stage in order to measure the transverse beam emittances at this longitudinal position. Some additional ports are located downstream for the installation of further beam diagnostic. One couple of ports is designed to host the beam chopper in a back-up position. This center line is enclosed by two vacuum gate valves and has dedicated ports for pumping and gas injection.

Right after the second magnetic solenoid and before the RFQ injection flange, a very compact (270 mm) RFQ interface section hosts a slow electrostatic beam chopper, a beam deflector adopted to modulate the beam delivery and create a precise and flexible beam time structure towards the future MYRRHA reactor for sub-criticality monitoring. The LEBT beam chopper could be used as Machine Protection System device to unload the accelerator and impede the beam delivery further the accelerator structure and toward the MYRRHA reactor in case of accelerator or reactor trip. The RFQ interface section is imperatively short to allow the positioning of the second solenoid the closer to the RFQ injection, which helps the beam focusing within the already mentioned nominal RFQ specifications. On top of that, the adoption of an electrostatic beam chopper rules out any space charge compensation in this section. So, the adoption of a short interface reduces the beam path travelled fully or partially uncompensated (see Section 6.7).

A collimator is placed before the RFQ injection to dump the chopped and deflected beam and perform a final cleaning of the polluting beam species. A non-destructive measurement of beam intensity is foreseen at this stage to monitor on-line the transport along the LEBT line and further alongside the RFQ. Lastly, before the RFQ rods, a negative electron repeller lens offers a screen to the electrons present in this zone, preventing their spurious injection in the RFQ field as well as confining them in the RFQ interface zone.

A complete picture of the MYRRHA ion source, LEBT and RFQ interface is shown in Fig. 6.7, 6.8, 6.9.

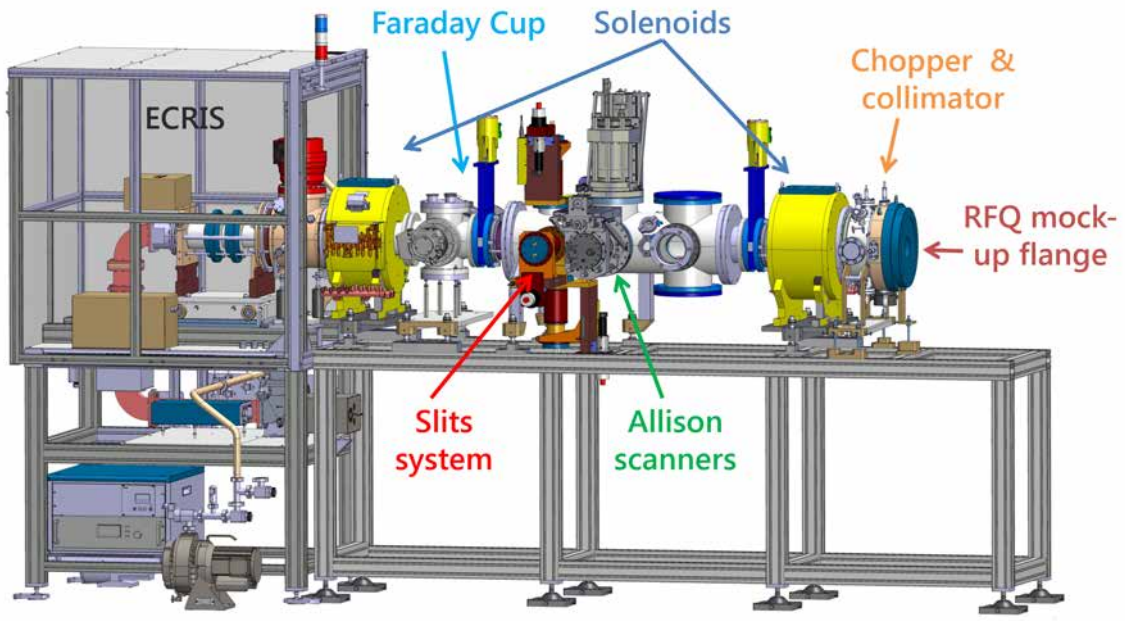

Figure 6.7: 3D CAD model of the MYRRHA low energy front-end, comprising the Ion Source, the LEBT line and the RFQ interface. Courtesy of LPSC Grenoble and SCK•CEN.

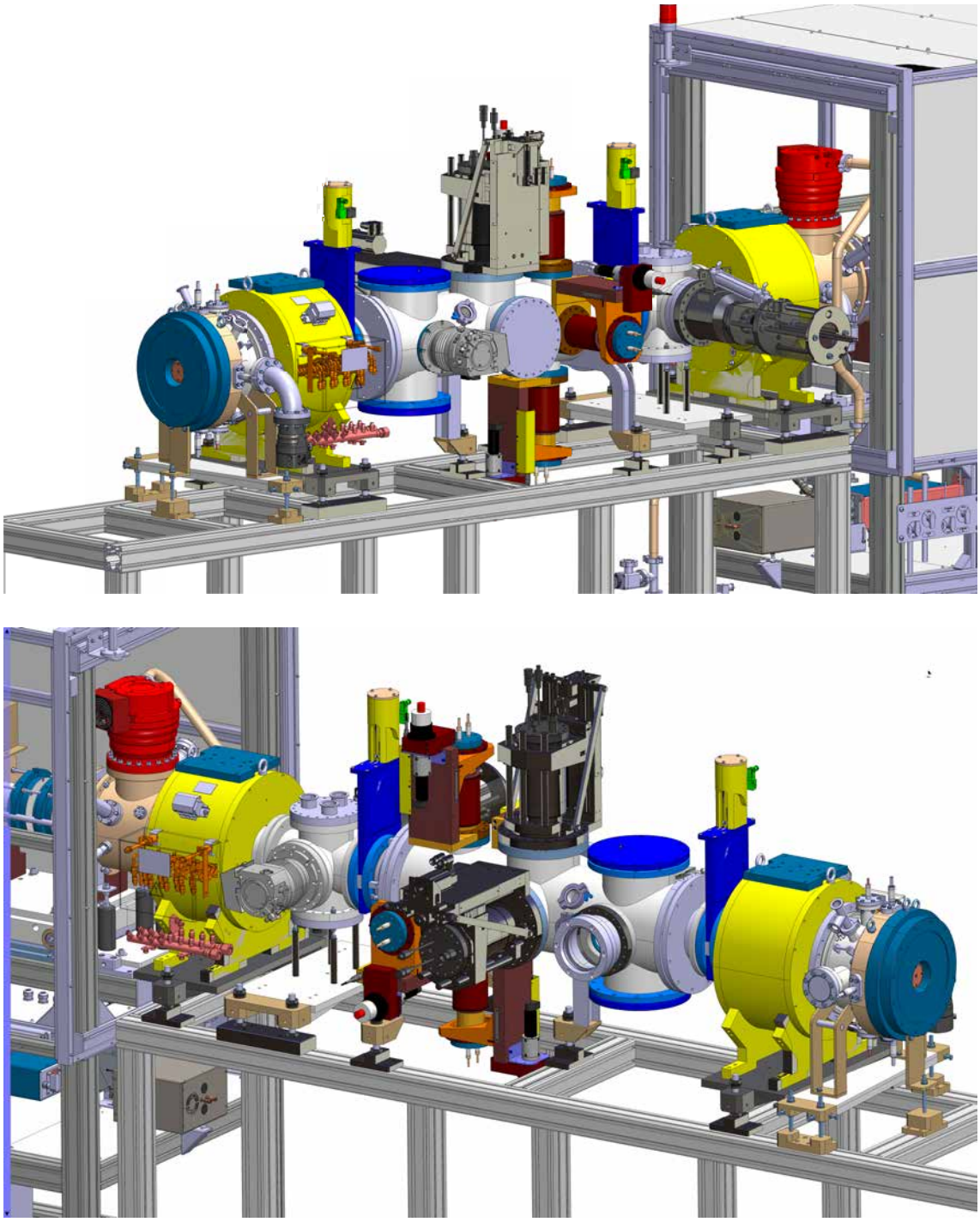

Figure 6.8: 3D CAD model of the MYRRHA low energy front-end: zoom on the LEBT line and the RFQ interface, left and right sides. Courtesy of LPSC Grenoble and SCK•CEN.

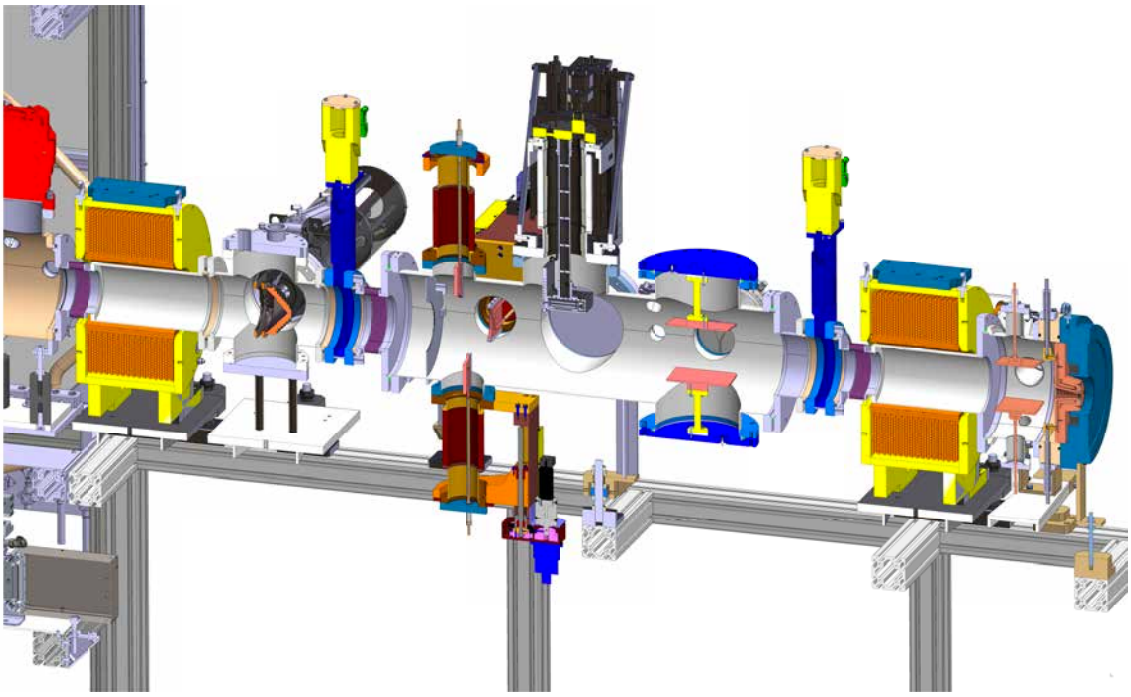

Figure 6.9: Cross section of the 3D CAD model of the MYRRHA LEBT line and the RFQ interface. Courtesy of LPSC Grenoble and SCK•CEN.

6.3.1 LEBT solenoid sets

A magnetic setup comprising two solenoid sets with embedded dipole steerers is present in the MYRRHA LEBT. The solenoid magnets main task is to assure focusing of the main proton DC beam while separating other species from the beam envelope. Solenoidal type magnetic field is suitable at low energy for beam focusing and is characterized by axial symmetry, so it acts both on horizontal and vertical transverse planes. Moreover, its adoption does not prevent the establishment of Space Charge Compensation regimes.

A first solenoid magnet is placed just after the ECR Ion Source extraction box to limit beam divergence at the exit of source. This element gives a global beam focusing while leaving further beam drift space for diagnostic insertion. A second solenoid is placed at the end of the LEBT line and is set to prepare the beam with right Twiss parameters for subsequent injection into the RFQ. Each solenoid magnet hosts independent horizontal and vertical coils for dipole correction. Their net effect is to steer the beam allowing compensation of possible beam and/or magnets misalignments and transversal adjustment. The physics of low energy beam transport constrains the space available in the LEBT, therefore the integration of the dipole steerers into the solenoid sets has been foreseen by design. The H/V steerers coils are composed by copper wires and wrapped coaxially on the inner side of a solenoid. The design of these steerers is constrained by the space left between the vacuum tube and the solenoid coil.

A magnetic model of the magnet set has been created in OPERA 3D [86]. The overall length of the solenoid is limited to 260 mm. The length of the solenoid coil is 216 mm. This is surrounded by a yoke consisting of two end shield discs made of steel similar to XC 10 (low carbon) and of thickness 22 mm and a tube of low carbon steel of wall thickness 20 mm. The inner solenoid diameter (including steerers' coils) is 158 mm, a good compromise to minimize geometrical aberrations potentially leading to emittance growth.

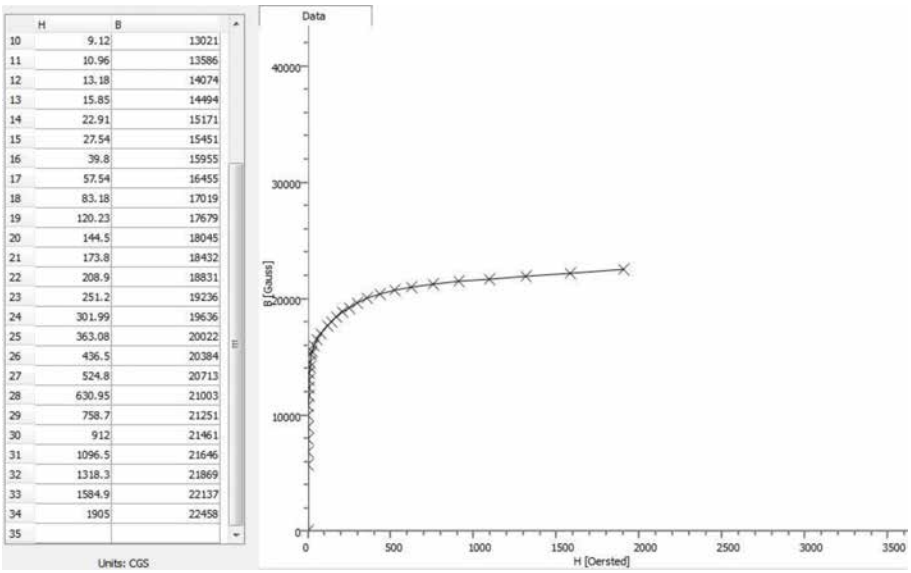

Figure 6.10: B-H curve of the XC10 steel adopted for the OPERA model of the MYRRHA LEBT solenoid set yoke.

The nominal field strength at the center of a solenoid is 0.250 T. The field integral is

$$\int_r B_z(r=0,z)dz = 0.061T{\cdot}m, \tag{6.4}$$

corresponding to a magnetic length over an integration length of 1600 mm

$$L_{magn} = \frac{\int_r B_z(r=0,z)dz}{B_{max}} = 0.241m \tag{6.5}$$

The cited overall dimensions and performances set the basic electromechanical requirements of the MYRRHA LEBT solenoid sets. In order to generate the nominal axial magnetic field B_0= 0.25 T at the center of the solenoid, the dimensions of the coil and the yoke and the B-H curve of the 1010 steel used in the model set the current intensity to 48900 A·turns, generated by 496 hollow OFHC copper conductor turns, dimensions 5.6 mm x 5.6 mm, with cooling hole ⌀ 3.6 mm. The maximum field in the steel yoke is up to 1.2 T, which is sufficiently low to avoid any saturation.

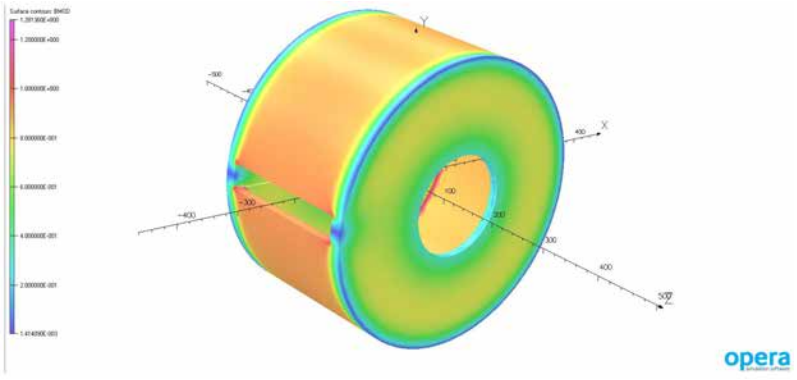

Figure 6.11: OPERA model of the MYRRHA LEBT solenoid set: modulus of the B field in the steel yoke.

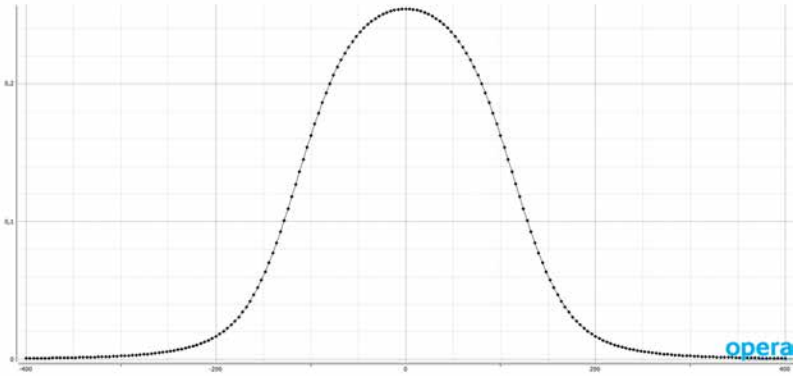

Figure 6.12: OPERA model of the MYRRHA LEBT solenoid set: modulus B field along the z axis, at r = 0 mm.

The good field region has a radius R = 50 mm. A strict requirement on the field extension outside the yoke (stray fields) is given by the presence of nearby turbo molecular pumps. The most sensitive turbo pump near the solenoids should not experience a magnetic field strength larger than 3.3 mT. The axis of this pump is at approximately 270 mm from the solenoid centre and it is radially displaced from the magnetic axis by typically 100 mm. So, particular care was taken in limiting stray magnetic fields, which led to a maximum of 2.55 mT at r = 0 mm, z = 300 mm and 1.65 mT at r = 100 mm, z = 300 mm.

The steerers must be capable of a minimum field integral of $> 3.1 \cdot 10^{-4}$ T·m. This relatively low value allows to have two layer of conductors per steerer (four layers for a XY steerer). The coils of a full XY steerer are therefore superimposed. The steerers coil are made of plain copper, 0.8 mm x 2 mm, and produce a nominal magnetic field of B= 2 mT with 200 A·turns for the horizontal steerer (inner layers) and 250 A·turns for the vertical steerer (outer layers). This two separate inner windings produce an additional transverse component for dipole corrections (H&V) up to 12.5 mrad.

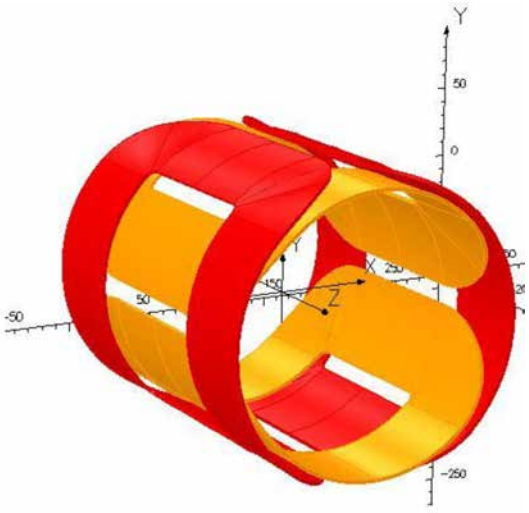

Figure 6.13: OPERA model of the MYRRHA LEBT solenoid set: the H and V steerers coils model.

A reference plate allowing accurate positioning of alignment tools is added upon the tube of the yoke. This plate is fitted with calibrated holes near the corners for the introduction of an geometric alignment target.

Solenoid magnets have been specified by SCK•CENand industrially procured from SigmaPhi (France). Table 6.2 resumes the main characteristics of the MYRRHA LEBT solenoid sets.

Table 6.2: Overview of the MYRRHA LEBT solenoid with integrated H/V steerers sets specifications.

Full length	=	260	±0.25	mm
Outer diameter	∼	450		mm
Central field B_z(r=0,z=0)	>	0.25		T
Inner diameter with steerer coils	=	158	±0.5	mm
End plate central hole diameter	=	157	±0.05	mm
Solenoidal field integral	>	0.06		T·m
H,V steerer dipole field integral	>	$3.1{\cdot}10^{-4}$		T·m
Stray field ||B|| at (r=0, z=300)	<	3.3		mT
Stray field ||B|| at (r=100, z=270)	<	3.3		mT

6.3.2 Collimator slits

In MYRRHA LEBT, four independent beam collimators or slits are present. Their function is to reshape the beam profile at the exit of the first solenoid magnet and to cut beam tails at large sigma ($> 6\sigma$). This process increase isolation of the proton beam core from other particle species and prevents particles to imping on undesired locations downstream the accelerator, depositing thermal power and provoking superficial sputtering. Besides, slits may also have the following functions:

- reduce transverse (horizontal and vertical) beam emittances (particles at larger displacements are cut-out) or reshape distorted emittances;
- reduce the beam intensity delivered by the ECR Ion Source to a percentage of the generated intensity, absorbing a portion of the beam in a destructive manner.

The collimation stage is preceded by a diaphragm (not actively cooled), which has a diameter of 120 mm and screens the mechanical interfaces of the slits. The four slits are transversally coupled and arranged onto two axis. Longitudinally, they look staggered, in order to avoid any chance of collision by means of a small but relevant longitudinal geometric offset (any chance of physical interception is prevented). This is due two different reasons. The first is that this solution makes each slit independent from the control system point of view. The second is related to the geometrical shape of the slits, that is rounded, in order to produce a circular aperture to the beam: looking through the longitudinal axis, some interception between the slits is necessary to produce small apertures. The selected longitudinal offset is 12 mm. The slits bodies are cooled by individual water channels welded on the back of their absorbing faces.

Slits positioning is operated to reach an exact position on the basis of an (external) position detector (absolute angular encoder) and in a repeatable and reliable manner. The requested position precision is in order of 0.1 mm. The selected motor type is stepper. This motorization allows precise positioning and enough holding torque, provided a small angular step and proper mechanical gear ratio. Slits movement is operated via an open-loop procedure, easily achievable with the stepper motorization. The motion controller sends out pulses to the power driver, which in turns supplies the motor in a precise and verifiable manner. An angular encoder installed on the shaft of the motor checks the response between the sent pulse and the actual movement. Each slits is equipped with garage (G) and limit (L) switches to prevent collisions between mechanical parts of their structure. In between the limit switches, a home (H) switch is installed.

In order to measure the portion of impinging and absorbed beam, each slit is relied to ground through a dedicated path and current flowing to ground is measured independently. Conditioning of the current signal into a 0-to-10 V signal is procured as analogue interface to the data acquisition system in appropriated dynamic range/s.

6.3.3 Vacuum

Continuous vacuum pumping is necessary to keep a good vacuum level in the whole LEBT line and assure low particle scattering or charge exchange and high electric insulation. The LEBT line

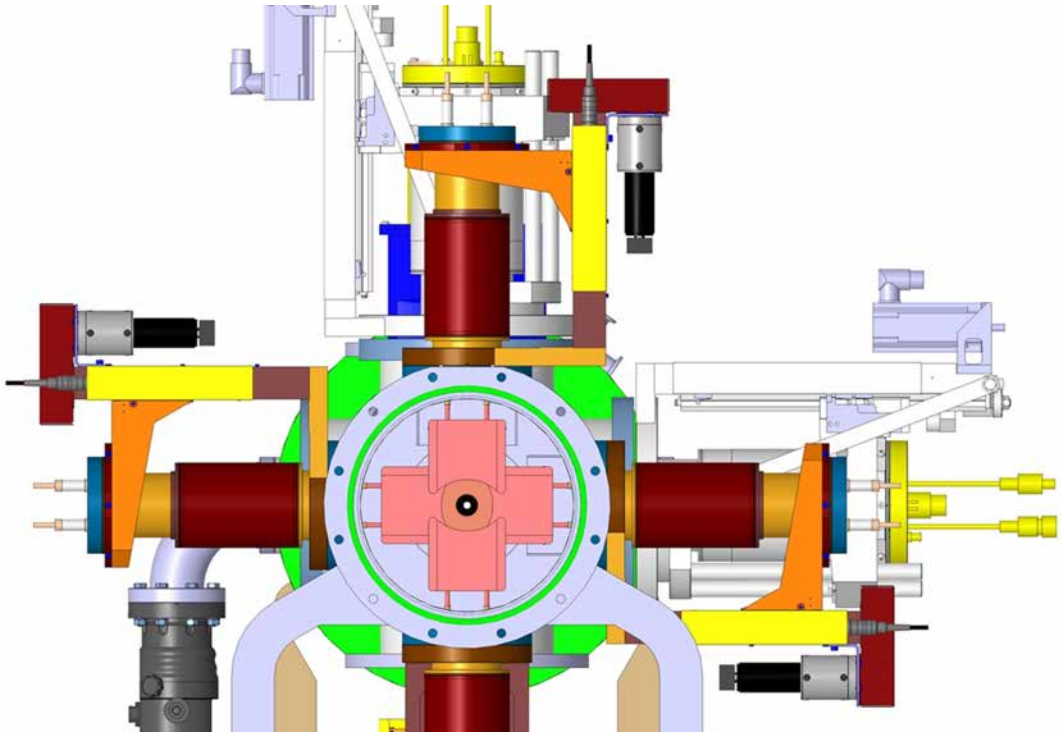

Figure 6.14: CAD model of the collimation stage designed for the MYRRHA LEBT. The diaphragm preceding the first slit is not shown. The ultimate beam aperture is defined by the RFQ collimator, visible on the back. Courtesy of LPSC Grenoble.

is constituted by three different vacuum environments, defined by interposition of two interception gate valves between three chambers.

Oil sealed rotary vane vacuum pumps are adopted as primary vacuum pumps. They work in viscous regime and are mainly used to evacuate the atmosphere present in the vacuum chambers at startup and provide an ultimate pressure of $\sim 5 \cdot 10^{-3}$ mbar. In the MYRRHA Ion source and LEBT line, a set of three rotary vane vacuum pumps is installed.

Turbomolecular vacuum pumps are adopted as secondary vacuum pumps. They work under the so-called particles momentum transfer principle and so they are installed in the proximities of the pumped volume to maximize the effective pumping speed. A set of four turbo pumps is installed onto each vacuum chamber volume to reduce gas pressure to design ultimate pressure of $\sim 1 \cdot 10^{-8}$ (unbaked system).

High gas load is expected from the Ion Source plasma chamber due to injection of pure H_2 for plasma feeding. A significant pressure level can be present in this region and is detrimental for the extraction system, because of the charge exchange process potentially acting on the extracted beam and the presence of high voltage electrodes. Therefore, a turbomolecular pump is installed on the Ion Source extraction box, providing a pumping speed 555 l/s for H_2. On the two main LEBT tanks, two 220 l/s (H_2) turbomolecular pumps are installed.

Few vacuum ports are provided for fitting a gas injection dosing valve, both on the cross after the first solenoid and the central vacuum chamber, in order to allow injection of precise quantities of gas mass flows into the system and produce desired pressure regimes during studies on space charge compensation phenomena (see Section 6.7). The obtained pressure levels and profiles derives from the balance of the gas load sources (degassing, outgassing, gas injection) and the available effective pumping speed:

$$p_{eq} = \frac{Q}{S_{eff}} \tag{6.6}$$

One 48 l/s pumping speed (H_2) turbomolecular pump is installed on the RFQ interface. The RFQ interface collimator plays, among the others, also an important role from the vacuum point

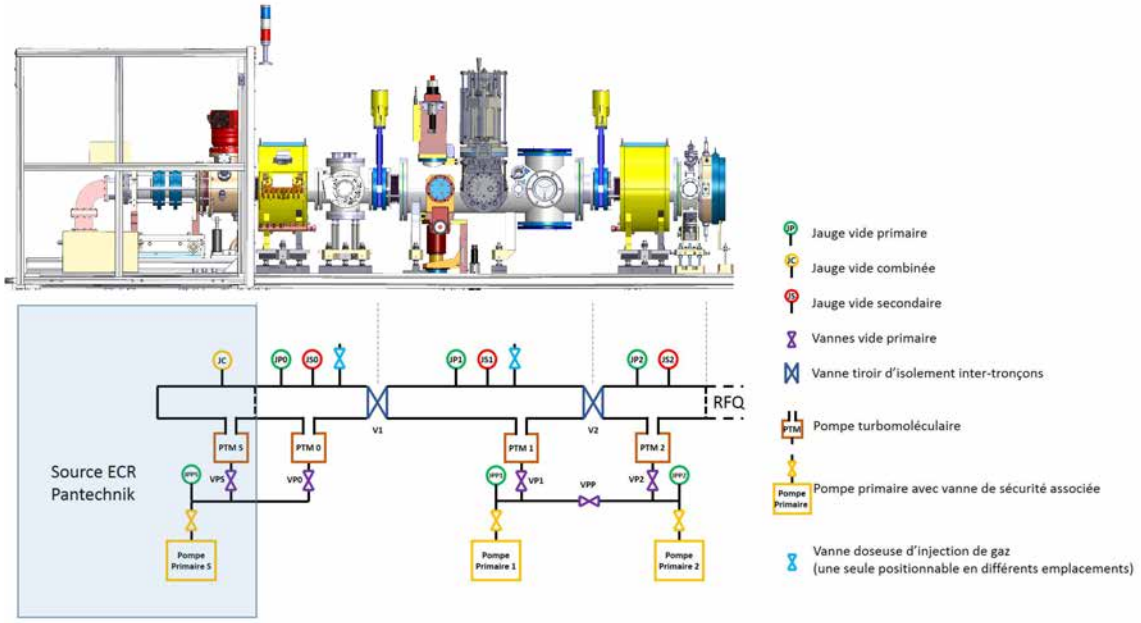

Figure 6.15: Scheme of the MYRRHA low energy front-end vacuum system. Courtesy of LPSC Grenoble.

of view, as it is determines an orifice allowing for differential pumping between the LEBT line and the RFQ vacua.

A series of vacuum gauges is necessary to monitor the vacuum pressure levels. Pirani gauges are adopted to measure primary vacuum levels employing a thermal conductivity principle. They are installed on the vacuum chambers as well as on the primary pumps inlet. Penning (cold cathode) are ionization based gauges and are adopted to measure secondary vacuum levels. They are installed on LEBT chambers.

6.3.4 Cooling

A dedicated cooling system is necessary to cool down hot elements present in the LEBT, like solenoids coils, collimating slits, Allison Scanner emittancemeters, Faraday cup, RFQ collimator, beam dump, vacuum turbomolecular pumps. The selected cooling fluid is water, available at moderate pressure (<10 bar) and previously deionized (prevents corrosion and assures low electric conductivity).

Given the rather low total cooling power and the passive typology of users, a room temperature water supply is adducted to users with constant pressure at their inlet. In the cooling system, no control logic is implemented at any stage to assure feedback control on temperature or on removed thermal power.

6.4 Beam diagnostics

6.4.1 Faraday cup

A Faraday Cup (FC) is a device adopted to measure the current (or intensity) of a beam of charged particles. In its simplest form it consists of a conducting metallic chamber or cup, which intercepts a particle beam. The cup is electrically relied through a lead to a grounded instrument, which measures the beam charge dumped over time (beam current). In the MYRRHA LEBT, a FC is placed at the exit of the first solenoid and is used during the tuning of the ion source in order to measure the beam intensity in a destructive manner (interceptive method). The cup has a 100 mm diameter aperture, necessary to fully intercept the incoming beam, which nominally has large size after the first solenoid. Given the longitudinal position of the cup, the measured intensity is the one corresponding all the particle species produced by the Ion Source (H^+,H_2^+, H_3^+). The FC

design is made by monolithic OFHC copper and is designed to evacuate a deposited centered beam power up to 1.2 kW (σ_x= 3 mm) by active water cooling.

In the MYRRHA accelerator, the FC will be used to intercept beam produced by the ECR Ion Source during periods of commissioning or settings. Moreover, the FC may acquire a safety role if it is used to unload the whole accelerator and prevents beam undergoing further acceleration into subsequent Injector structures (RFQ, CH-cavities). For these reasons, the FC is a normally inserted device, to be extracted whenever the machine allows further loading. FC movement is between two positions ("fully in", "fully out") and it is pneumatic, so no stoke adjustment is performed.

A bias voltage applied to a repeller ring preceding the cup (nominally: -200 V) prevents the escape of secondary, low energy charges (electrons) produced by secondary electron emission. This functionality is required to collect the whole net beam charge and therefore have a reliable current reading. The beam current measurement is performed conditioning the electrical current flowing in the conducting lead to ground into a voltage signal. This is developed across a calibrated resistor placed in the path to ground. Conditioning of the current signal to a 0-to-10 V signal is procured into appropriated dynamic range/s.

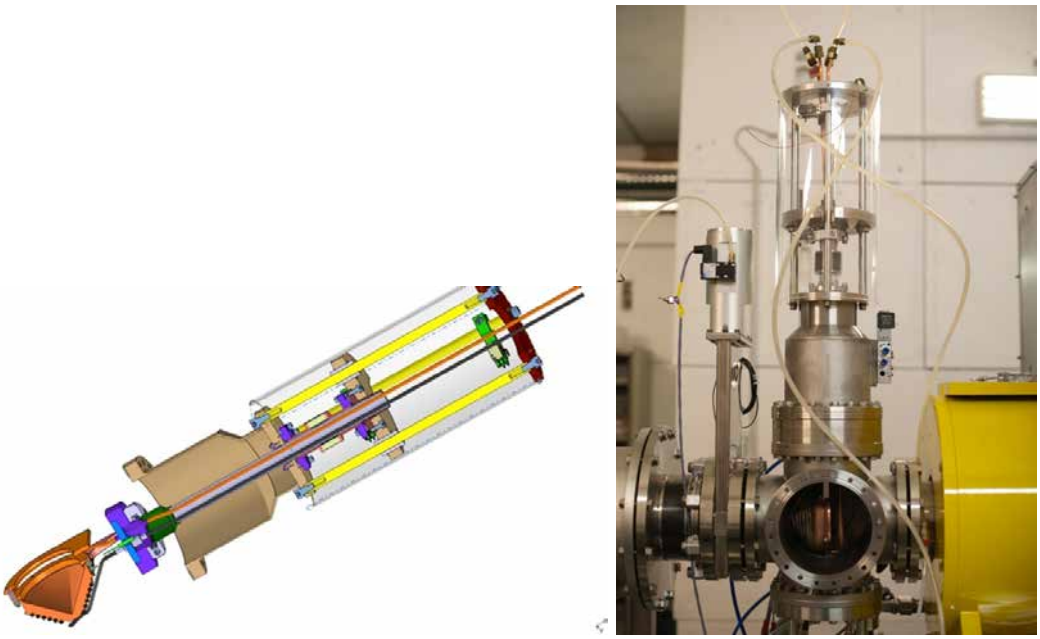

Figure 6.16: CAD cross section and picture of the MYRRHA LEBT Faraday Cup. Courtesy of LPSC Grenoble.

6.4.2 Emittancemeters

Two independent, respectively horizontal and vertical Allison scanner type emittancemeters are adopted to measure beam transverse emittances. The Allison Scanners have been procured from IPHC Strasbourg. In the MYRRHA LEBT, the Allison scanners are placed right after the collimation stage and, therefore, measure a collimated beam, which is partially (nominally: 50%) cleaned from the molecular pollutants H_2^+, H_3^+. The measurement implies a destructive manner, so, in the MYRRHA accelerator operational context, it will be performed during LEBT line tuning. During the LEBT commissioning, the Allison scanners acquire instead a fundamental role as they are employed to determine the beam quality. The adopted figure of merit is the 1σ RMS beam emittance, normalized. The longitudinal position of the Allison scanners is moved during the LEBT commissioning in order to transversally characterize the beam at different position and assess the quality of beam transport. Two important z positions are identified for their primary importance in the beam quality assessment:

- at the exit of the Ion Source, in order to characterize the beam and optimize the extraction settings. This stage is required as well for validating the LEBT beam input parameters (see Section 6.6);
- at the end of the LEBT, at the longitudinal position of the RFQ rods, in order to optimize the beam transport along the LEBT line and fulfil the required RFQ input parameters (ε_{norm}=0.2π·mm·mrad RMS norm., $\alpha = 0.88$, $\beta_{x,y} = 0.04$ mm/π·mrad).

The Allison scanner emittancemeter is equipped by a shielded head which is inserted transversally in the beam line (full stroke: 120 mm). During a scan, the beam is sorted by two collimator windows by step: two narrow (0.1 mm) tungsten slits scan the incoming beam, longitudinally distant determining the particles displacement (δx). The slits are shielded by an actively water cooled Cu thermal screen and are designed to sustain a 1.6 kW, Gaussian (σ_x=1.5 mm) DC beam. Between the slits, the beamlet crosses a pair of electric deflection plates driven by a voltage power supply through a double linear ramp (up to ±1.4 kV), which sorts the particles angle and determines the particles divergence ($\delta x'$). A maximum of 80 mm beam size, ±100 mrad divergence can be measured. After a data cleaning process, the collected particles charge at each δx-$\delta x'$ corresponds to the beam distribution density in a transversal phase space. The beam distribution is then plotted in the phase space xx' and its emittance and Twiss parameters are calculated.

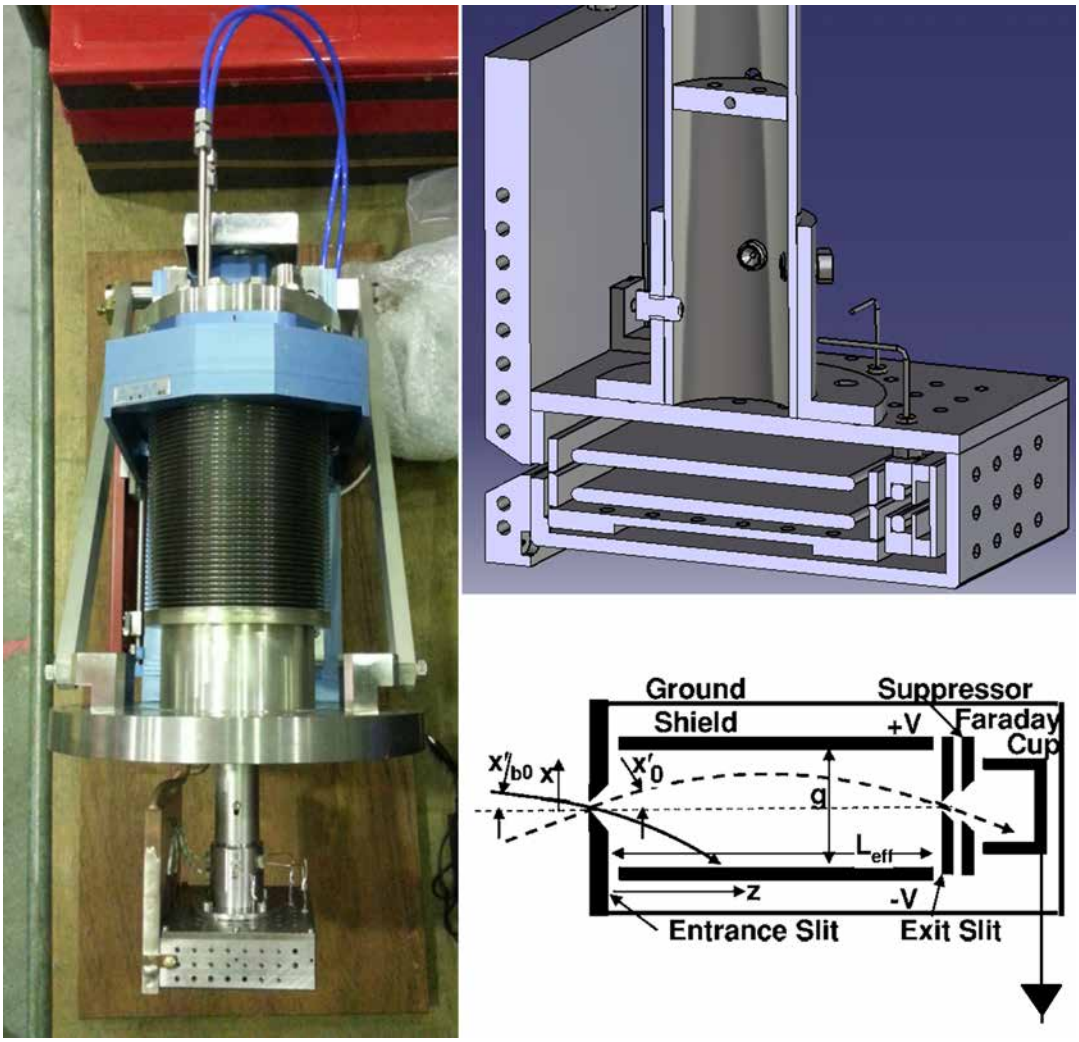

Figure 6.17: Allison Scanners emittancemeter adopted for the MYRRHA LEBT line. Left: picture before installation. Top right: a cross section from the CAD drawing. Bottom right: measurement principle of a Allison Scanner. Courtesy of IPHC Strasbourg.

6.5 The RFQ interface

6.5.1 Beam chopper

The beam chopper is an electrostatic deflector which allows production of specific beam time structures through precise and timed beam cuts. In an operational context, the MYRRHA LEBT chopper may play the fundamental role of modulating the beam current to the reactor by adjusting the chopper timing, in turn allowing to keep the linac focusing settings constant in spite of changing intensity. The chopper may be also considered as a safety system since it allows beam interception in case of Main Protection System signal, therefore beam unloading.

In the MYRRHA linear accelerator, proton beam is created in DC from the Ion Source and bunches are formed in the RFQ. It is then accelerated, in Continuous Wave (CW), through a series of RF cavities and delivered to the reactor. Beam delivery interruptions are foreseen for reactor subcriticality monitoring [44]. So 200 μs bursts at 250Hz have been planned (see Fig.6.18) in order to enable pulses with an interesting duty cycle to be redirected to a target other than the MYRRHA reactor, for instance to an ISOL@MYRRHA facility for physics experiments [87], via an extraction line. The required kicker magnet transfer function (rising ramp, flat-top, falling ramp) has a rising/falling time typically in order of 2% of the cycle, so 5 μs. This figure is a design basis. The kicker ramps would cause high intensity power beam losses while beam is steering direction from/to target to/from ISOL (CW beam). Therefore, these 5 μs up/down slopes are cut-out by an electrostatic beam chopper, operating on the low energy DC beam in the LEBT, with operation time-spatially synchronized to the kicker magnet. The timing system is in charge to provide equidistant timing structures to the LEBT chopper. By adjusting the chopped on/off duration (duty cycle), the power sent to ISOL/reactor targets is modulated.

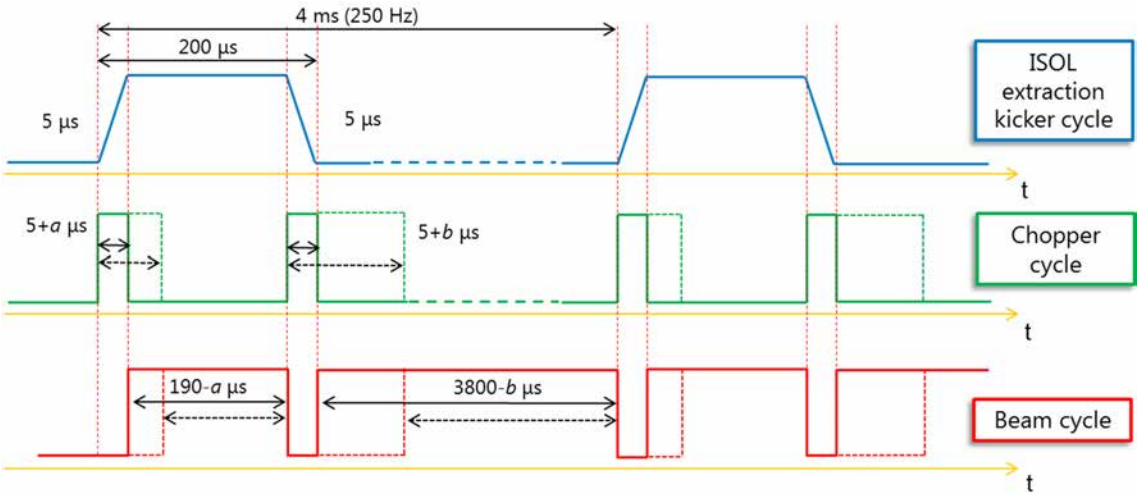

Figure 6.18: Required beam structure and chopper timing for sub-criticality monitoring of the MYRRHA reactor and potential beam extraction to an ISOL@MYRRHA facility.

From the chopper point of view, a very special duty cycle is foreseen. The a and b factors describe the modulation parameters in the duty cycle, as follows:

- a couple of 5 μs holes (spaced 190 μs, at 250 Hz) is required to unload the machine during the rising/falling flanks of the extraction kicker magnetic field;
- using an extraction kicker, 600 MeV, 190 μs at 250 Hz beam pulses become available for an ISOL facility. Intensity modulation of the beam pulses sent is to be foreseen: $0 < a < 185$ μs;
- for reactor subcritical monitoring 200 μs at 250 Hz beam interruptions are required. However, a possible intensity modulation of the beam delivery to the reactor, in particular during machine commissioning but also operationally (burn-up follow-up, beam resuming following a trip): $0 < b < 3795$ μs;

- if adopted as MPS device, the beam chopper could be required to fire as soon as a MPS protection signal triggers.

Besides the design motivation, the experimental investigations of the LEBT line will rely of the presence of the beam chopper. In order to maximize the injector performances, it is highly necessary to have a better understanding of SCC effects. The MYRRHA LEBT test stand is a valuable opportunity to develop and improve existing models against experimental results, establishing pulsed beam regimes for SCC studies onto the DC LEBT beam. The SCC rise time can be investigated following the intensity and emittance evolution of the low energy beam emerging totally uncompensated from a beam chop (see Section 6.7).

The beam chopper operates onto a DC low energy beam in the LEBT. In its nominal position, it is installed between the second solenoid set and the RFQ injection flange: this minimizes the impact onto beam characteristics due to Space Charge uncompensation. The high electric field produced during a chopper pulse steers and accelerates the electrons responsible for the SC compensation out of the beam area. The emerging beam is therefore totally uncompensated and the respective SCC degree is 0% in this region. While the absence of SCC is not detrimental for the chopped beam - which is however to be dumped onto the RFQ collimator [1] - it is for the nominally beam, after a beam chop.

The system is constituted by a couple of electrostatic copper plates, geometrically symmetric with respect to the xz plane. One plate is alternatively charged/discharged (from the electric point of view, the plate and its feed-through thus constitute an equivalent capacitance) up to a moderate potential (∼5-10 kV) while the other is relied to the ground potential. This process generates an alternative transverse electric field across the plates. The particle beam experiences a net transverse steering while passing through the field and, after a small drift, is dumped over a collimator placed just before the RFQ injection flange.

In order to compute the deflection offered by the electrostatic chopper for beam switching, we consider a straight parallel plates deflector as depicted in Fig.6.19. We here assume the LINACs xyz convention for the coordinates system.

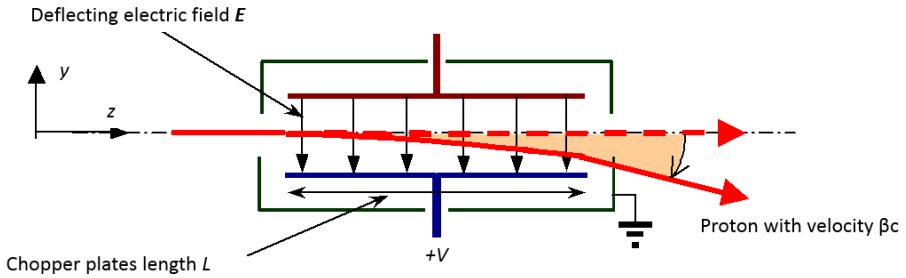

Figure 6.19: A simple symmetric electrostatic, straight parallel plates, deflector for charged particles.

The equation of motion due to chopper kick is described on the vertical plane by a balance between the force exerted by the vertical component of the electric field and the centripetal force required to steer a charged particle in the vertical plane:

$$eE_y(z) = \frac{mv^2}{\rho} \tag{6.7}$$

being e the unitary charge of an electron, E_y the vertical component of the electric field locally experienced by the beam, and ρ the bending radius obtained. The expression in Eq. 6.7 can be rewritten as

$$E_y(z)\rho = \frac{2E_{kin}}{e} \tag{6.8}$$

[1] the size of the dumped beam could, instead, increase, with some pros (diluted superficial power dissipated onto th RFQ collimator surface, distributed sputtering) and cons (a larger deflection angle is required to cut-out the deflected beam from the RFQ collimator acceptance)

which describes the *electric rigidity* $|E_0\rho|$ defining the central orbit in an electrostatic bend. This quantity is equivalent to the magnetic rigidity times the particle velocity $B\rho\beta c$ and is 60 kV for the 30 keV beam in the MYRRHA LEBT.

Traveling the electrostatic bend, a particle experience the bending angle given by

$$y' = \frac{z}{\rho} \tag{6.9}$$

Integrating Eq. 6.8 along the particle path and employing the definition available in Eq. 6.9 we finally get

$$\alpha = \frac{\int E_y(z)ds}{\frac{2E_{kin}}{e}} \tag{6.10}$$

that is the vertical equivalent kick accumulated integrating the vertical electric field experienced in the electrostatic bend of lenght L.

In order to calculate the total displacement at the RFQ collimator, Eq. 6.10 is integrated along the electrostatic lens

$$y = \int y'ds = \frac{\iint E_y(z)ds^2}{\frac{2E_{kin}}{e}}. \tag{6.11}$$

To get an analytical feeling of Eq. 6.11, we now assume a constant vertical electric field V/d of an hard edge deflecting lens of length L_{eq}. Solving Eq. 6.11 we get to the displacement of a particle across the lens

$$y = \frac{z^2}{\rho} = \frac{y'z}{2} \tag{6.12}$$

that corresponds to the equation of a parabola in the yz plane (the central orbit is therefore not circular).

We now have all the elements to build up the approximated (without momentum dispersion) transverse equations of motion for a symmetric electrostatic, straight parallel plates, deflector:

$$\begin{cases} x = x_0 \\ y = y_0 + y'z + \frac{z^2}{\rho} \end{cases} \tag{6.13}$$

From Eq.6.10 and 6.12, the total displacement produced by the electrostatic chopper, considering the drift space available before the RFQ collimator, is finally

$$y_T = \alpha\left(\frac{L_{eq}}{2} + L_{drift}\right) \tag{6.14}$$

In the norminal position, the MYRRHA LEBT chopper is situated in the RFQ interface (longitudinal overall dimension: fixed to 270 mm) and operates on a converging beam, having at its foreseen longitudinal location a diameter ϕ=50 mm (H^+, RMS beam size, Tracewin simulations, see Section 6.7). In order to minimize its longitudinal dimension, the chopper plates length is fixed to a maximum of 100 mm by design. An asymmetric polarization (only one plate to full potential) is adopted to reduce the power electronics and avoid timing synchronization. Due to space constraints, large lateral vacuum ports are avoided, so the chopper electrodes are inserted from the front face of the vacuum chamber, then clamped to stems emerging from a feedthrough flange.

Electric field simulations have been carried out in Poisson [88] to design the chopper plates and optimize its field quality, in order to get an acceptable good field region comparable with the H^+ RMS beam size. In its nominal position, the chopper is not designed to steer out the RFQ collimator accepted the other particle species, as H_2^+ and H_3^+, which are principally lost in the LEBT slits and the RFQ collimator due to mismatched size, and in minor part, in the RFQ itself. However, in order to minimize the losses on the chopper plates, the aperture of this insertion is designed big enough not to intercept any beam particle.

Figure 6.20 shows the transverse central plane electrostatic simulation of the MYRRHA LEBT chopper, at the nominal plate voltage of 7 kV, carried in Poisson. The DN250 vacuum chamber allows comfortable housing of copper plates while reducing field peaks next the electrodes edges. The peculiarity of the electrodes is their shape, which is curved. The curvature is set to increase the electric field in the region of interest and improve electric field quality. In fact, the curvature artificially compensates the effect of depletion in the field leaking out of the plates. The chosen radius of curvature of the bent electrodes is 310 mm. This parameter has been optimized as a compromise of an improved the field flatness versus a smaller good field region. The plates maximum distance is 108 mm and they are large 140 mm. The electrodes are 3 mm thick for fabrication ease and robustness. In order to avoid large peak field in the region close to their edges, all the sides are circularly rounded.

The highest $|\mathbf{E}|$ field values are obtained in the upper part of the chamber (closer to the larger grounded surface), that in principle is not interesting from the beam chopping point of view. The maximum $|\mathbf{E}|$ field is next to the electrodes edges (r = 1.5 mm) and is limited to $\sim$ 4000 V/cm, which is well below the dielectric strength for vacuum. A degraded vacuum is expected in this region, due limited pumping speed and high gas load (proton stimulated desorption during beam chops), free particles and charges presence (sputtered atoms and secondary electrons emitted the RFQ collimator). Given the moderate peak field, both the chamber diameter and the natural electrodes edges curvature are retained safe for operation.

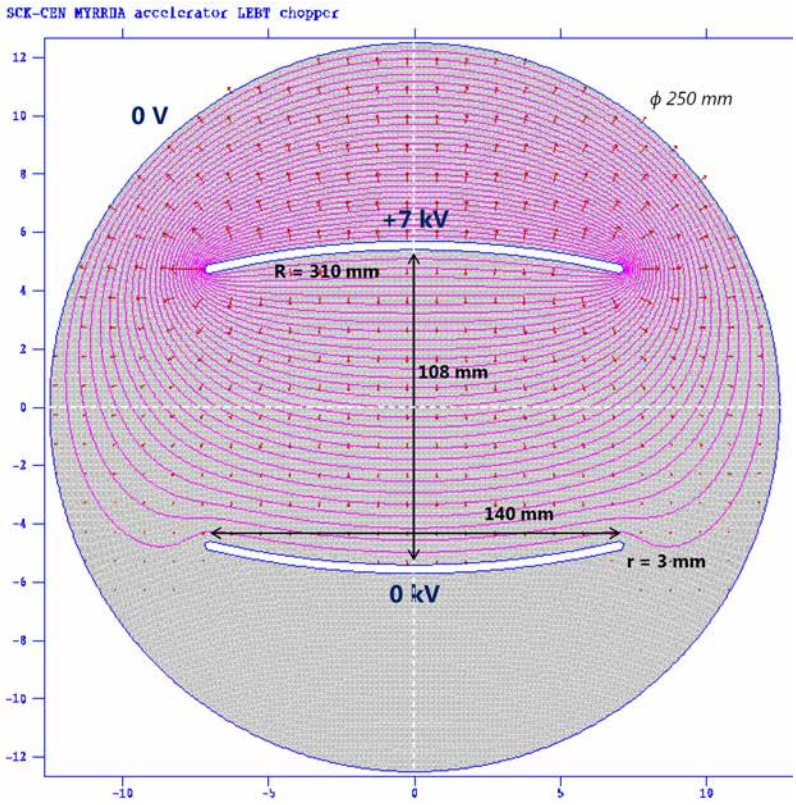

Figure 6.20: Poisson simulation of the electric field equipotential lines and direction/magnitude (arrows) on the transverse plane of the MYRRHA LEBT chopper, nominal position. Geometric units are in cm.

As only one electrode is polarized, the resulting electric field is not symmetric. Figure 6.21 shows the transverse field quality along the x axis. The asymmetric design of the plates gives birth to a non-negligible horizontal E_x field component, which has a diverging effect on the beam. This component is tolerable as it gives in return the advantage of horizontal beam power dilution on the RFQ collimator. The field flatness in the region of interest ([-2.5;0] to [+2.5;0] cm) is $\pm$ 0.5 V/cm, which corresponds to field homogeneity below 10^{-3}. The achieved field homogeneity is a result of a compromise between the field plateau width and its flatness, resulting in the mentioned

electrodes curvature of R = 310 mm.

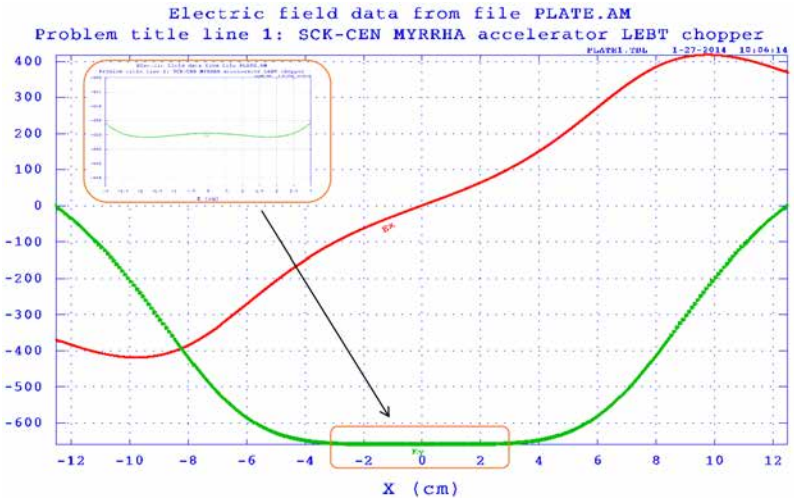

Figure 6.21: Horizontal E_x and vertical E_y electric field components, along the x axis in the transverse xy plane, of MYRRHA LEBT chopper, nominal position.

Figure 6.22 shows the transverse field quality along the y axis. On this line (and only on this, as discussed before), the horizontal component of the electric field E_x is zero. E_y increases along the vertical ordinate, which is in principal detrimental as it produces a spectrum of different angles of deflection for each beam slice on the vertical axis and, in practice, has a slight convergent effect on the beam itself. This effect is impossible to be geometrically cured with an asymmetrical design and is, in any case, considerable negligible with respect to the expected beam convergence after the second solenoid (75 mrad, see Section 6.7).

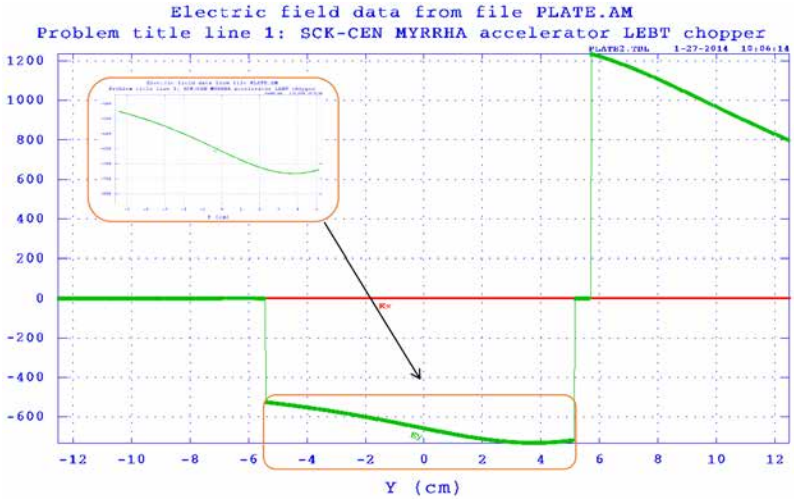

Figure 6.22: Horizontal E_x and vertical E_y electric field components, along the y axis in the transverse xy plane, of MYRRHA LEBT chopper, nominal position.

Figure 6.23 shows the electrostatic simulation of the beam chopper in the xz longitudinal plane. The simulation is a conservative approximation as it does not take into account the curvature of the chopper plates. A large aperture (DN150) is left to the beam in the second LEBT solenoid beam pipe, while the chopper plates are distanced 108 mm in the central plane. As the chopper plates aperture is comparable to the DN150/250 hybrid flange, lateral free gaps larger than 25 mm are left longitudinally for safe electric insulation and less capacitance to ground.

In Figure 6.24, the longitudinal field quality is represented along the z axis. Longitudinally, a quasi-equivalent decelerating, than accelerating E_z electric field is present. This returns as slight

momentum deviation which is irrelevant for the chopped beam. In this plane, the deflecting E_y field component is visible along the longitudinal ordinate. Its shape is not perfectly a Gaussian curve due to the different free air spaces and ground surfaces present on the two sides of the chopper insertion. Its integral is of great importance as it is responsible for the beam deflection: it equals 8612 V, corresponding to total punctual equivalent kick of 0.1435 mrad from Eq. 6.10. The chopper plates equivalent hard edges length is $\int E_y ds / E_y^{max} \cong 130$ mm.

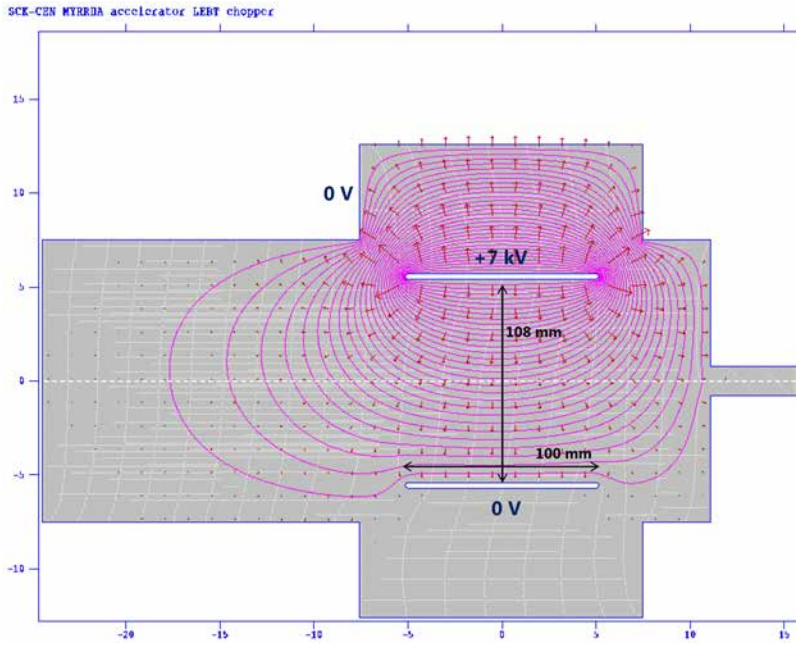

Figure 6.23: Poisson simulation of the electric field equipotential lines and direction/magnitude (arrows) on the longitudinal plane of the MYRRHA LEBT chopper, nominal position.

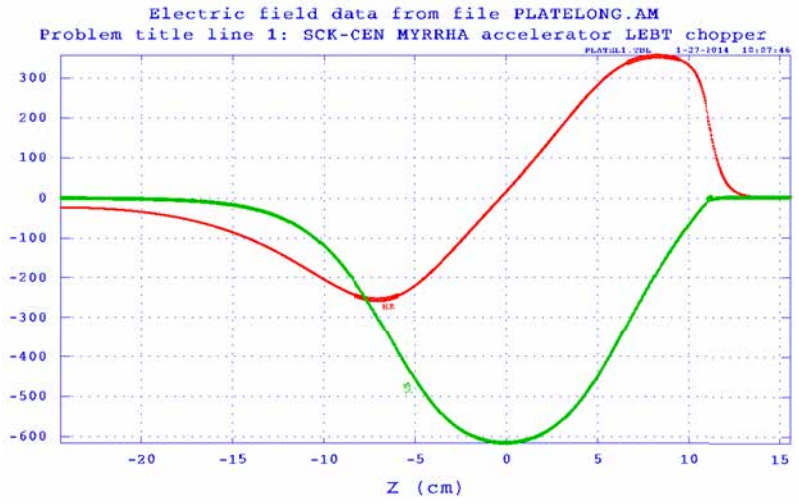

Figure 6.24: Longitudinal E_z and vertical E_y electric field components, along the z axis in the longitudinal yz plane, of MYRRHA LEBT chopper, nominal position.

The final RFQ interface geometry is an integration compromise between beam dynamics simulations, chopper design, RFQ collimator and Beam Current Transformer integration, and is visible in Figure 6.25.

The drift distance from the chopper plates is limited to 46.7 mm, due to mechanical integration requirements of the RFQ collimator water feedthroughs. This defines a short but still sufficient

drift space for the deflected H^+ beam. During a chopper pulse, the H^+ beam centroid is displaced (Eq. 6.14) of

$$y_T = \alpha \left(\frac{L^H_{elect} D}{2} + L_{drift} \right) = 0.1465 \left(\frac{130}{2} + 46.7 \right) \cong 16.5mm \tag{6.15}$$

sufficient not only to set the beam out the RFQ collimator acceptance (ϕ = 9 mm), but also to determine a beam impact in the planar face of the RFQ collimator (ϕ = 25 mm). As the full beam H^+ should be deflected, a further margin on the chopper available voltage (up to 10 kV) is left by design for adjusting the impinging beam spot during experimental commissioning. The exact point of impact will depend from the beam dynamics achieved with the optimized LEBT focusing elements settings, to be found during commissioning phase. At design level, the planar face is the preferred zone for full beam H^+ dump during chopper transients. This will allow to minimize not only the perturbations in the RFQ injection zone occurring due to an abrupt beam dump (secondary electron emission, collimator surface sputtering, proton stimulated desorption), but also to lessen the superficial power density to be evacuated (being the beam highly convergent, its power distribution increases along z, approaching the RFQ injection point). Being the exact point not *a priori* known, the whole collimator has been designed to withstand the full beam H^+ impact for harsh conditions (see Section 6.5.2).

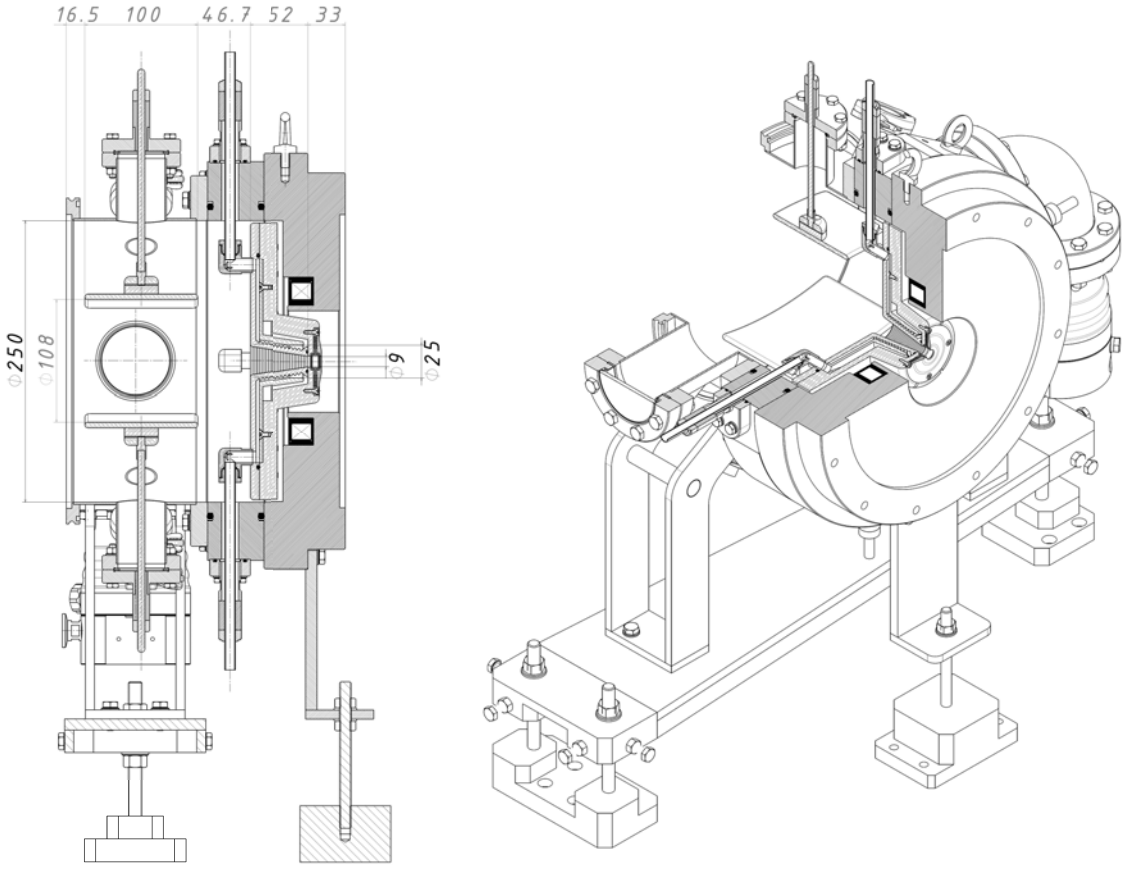

Figure 6.25: 3D CAD model of the MYRRHA LEBT RFQ interface and cross section. The longitudinal dimensions and the beam aperture are quoted, in mm.

Back-up position

The beam chopper is located, in its reference configuration, as close as possible to the RFQ (electrode center at ∼200 mm from the RFQ entrance) in order to minimize the effects of the space charge compensation transients (distance travelled while restoring SCC). However, a possible back-up solution is foreseen from design. Its position is situated before the second LEBT solenoid, ∼950

mm from the RFQ entrance. From the beam dynamics point of view, this position is disadvantaged with respect to the nominal one. The beam resuming from a chopper cut would be completely (or quasi-completely, if we assume that the chopped, deviated beam could still create a non-negligible electron density before being dumped) uncompensated, therefore the distance travelled before SCC restore would become significant (characteristic neutralization transient time: in order of 10 μs, see Section 6.7) and the effects on the emittance distortion and blow-up (space charge forces) could cause a mismatch with the RFQ acceptance.

From the chopper point of view, a different beam size ϕ = 80 mm (H^+, RMS beam size, Tracewin simulations, Section 6.7) is expected. While the electrodes geometry (physical gap, bending radius) should be redesigned in order to cope with an increased beam size, the available plate length and drift space is considerable larger, therefore a reduced field integral would be required. This would allow a significant relaxation in the electrode voltage polarisation, benefiting of an increased charging/de-charging speed and improved reliability. However, from the beam dynamics point of view, the focusing/defocusing and spiralling effects on the deflected beam due to the presence of a second magnetic solenoid, before the RFQ collimator, should be definitively studied.

Chopper driver

The chopper charging process is commanded by a High Voltage Solid State switch and sustained by a 10 kV, 50 mA voltage Power Supply (PS), limited to a power of 500 W.

In order to speed the process of charge-up, a buffer capacitor is placed in parallel. The presence of correct potential levels should be sensed by a pick-up capacitor installed nearby the copper plates: a comparison process (in magnitude and timing) can be operated at this stage.

The capacitance encountered during the chopper charging process is mainly related to three different elements: the switch, the feed-through and the energy to be stored in the electric field of the chopper plate. The capacitance due to the chopper geometric design is estimated from the energy stored in the electric field, simulated in Poisson (see Fig. 6.20). Such energy is per unit length - as the simulation is a 2D model - and can be approximated to the real, 3D, case, as follows. The energy stored in the electric field per unit length of the chopper transverse geometry is

$$\frac{E}{L} = \frac{1}{2}CV^2 = 7 \cdot 10^{-6} J/cm \tag{6.16}$$

therefore the equivalent capacitance is

$$C = \frac{2EL}{V^2} \sim 4pF \tag{6.17}$$

for a polarizing voltage of 7 kV and a length L = 0.1 m This figure, even taking into account the errors due to the 2D simulation, is well below the common capacitance exhibited by the power circuitry serving the chopper, therefore particular care is done principally in the choice of the switch and in the design of the feed-through.

The selected switch is a push-pull 2x15 KV, peak current 30 A. The push-pull principle has considerable advantages in comparison with conventional circuitry adopting a single switch with a working resistor. Two identical MOSFET switching paths form a so-called half bridge circuit. The switching paths are controlled in push-pull by a common pulser driver up to a design frequency in the order of kHz. This kind of switch exhibits a typical natural capacitance rated tents of pF. The selected feed-through is a stem power plug, rated up to 15 kV, 185 A. The capacitance of the feed-through is a-priori unknown, but probably of the same order of magnitude of the switch, if not greater. It should be characterized during the commissioning of such device.

For design purposes, the total electric equivalent capacitance of 100 pF is considered, keeping into account some engineering margin. The chopper driver design voltage is 10 kV, in order to give some degree of freedom in the available spectra of deflection angles.

In order to limit the rise and fall time, the time constant of the RC circuit serving the chopper plates should be low. Considering, for instance $\tau_C = RC$ = 50 ns, a rise/fall time of ~1% is

obtained with respect to the pulse length (5 μs). The required current and therefore power is:

$$I = \frac{V}{\tau/C} = 20A \longrightarrow P = VI = 200kW \tag{6.18}$$

which cannot be delivered a normal Power Supply. For this reason, a buffer capacitor is put in between, in parallel. Such buffer is quickly reacting to the charging process, delivering the required energy in the first instants of charging process. The energy required to charge the chopper capacitance is $\Delta E_c = \frac{1}{2} C_c V_c^2 = 5 \cdot 10^{-3}$ J. This is done at cost of a ΔV_b on the buffer capacitor:

$$Q_b \Delta V_b = \Delta E_c \longrightarrow \Delta V_b = \frac{C_b V_b}{\Delta E_c} \tag{6.19}$$

which should be, then, sustained by the Power supply. ΔV_b is, also, the maximum chopper deflecting voltage deviation occurring in the first instants of charging. The size of the buffer is principally selected to contain such acceptable deviation and by the availability of current deliverable by an off-the-shelf power supply. For a 200 nF buffer, we get $\Delta V_b = 2.5$ V. Such gap is closed the power supply (PS), the maximum current being 50 mA, so that a working resistor $R_{PS} > 2.5/0.05 = 60\Omega$ is chosen. The time constant $R_{PS} C_b = 1.2 \cdot 10^{-5}$ s is defined in the PS loop.

Finally, the electric circuit chosen for the MYRRHA LEBT chopper is depicted in Figure 6.26. For safety reasons, resistances of high values are placed in parallel of each capacitance, so that a depolarisation is always assured in case of long stops or failure.

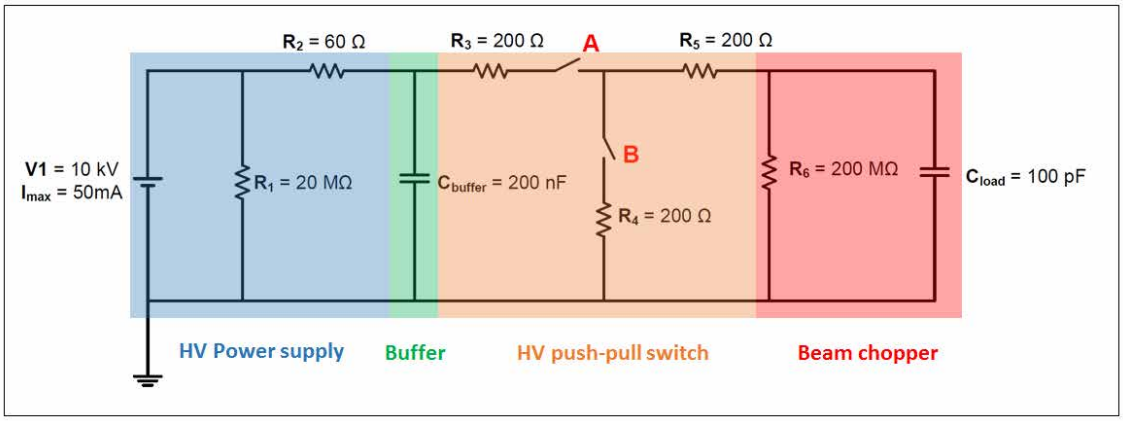

Figure 6.26: Electric equivalent of the MYRRHA LEBT chopper driver.

6.5.2 RFQ collimator

The RFQ collimator is a vital piece in the LEBT line as it defines the limit aperture before the RFQ injection. This piece of equipment has, on top of that, additional functions. Its limited aperture fixes the ultimate aperture left to the beam and thus allows interception of a large part of particle species other than protons, as H_2^+, H_3^+, previously separated by the magnetic LEBT focusing system. It should be noted that a significant part (up to 50%) of the polluting species can be already separated in the first LEBT magnetic stage by the collimating slits (see Section 6.7). Both from the chopper and H_2^+, H_3^+ collimation point of view, the position of the RFQ collimator (and its limit aperture) must be pushed at the very end of the LEBT line, for the following reasons:

- a larger drift space, requiring less deflecting electric field and, in turn, lower inter-electrodes potential and faster rise time, is then available for beam chopping;
- the polluting species collimation is done at end of the line while the H^+ has the correct beam Twiss parameters.

The main drawback is that, pushing the collimator forward the RFQ injection point, the H^+ beam power distribution increases, as the beam is highly convergent.

Figure 6.27 shows the transverse spot and the transverse phase spaces of the three different particle species (H^+, H_2^+, H_3^+) present at the RFQ entrance in the MYRRHA LEBT simulated in the multiparticle code TRACK. The H^+ RMS emittance matches the RFQ acceptance. In order to close the collimator aperture and limit the H_2^+, H_3^+ transmission in the RFQ, the H^+ should be in a waist, so its ellipse should be vertical as much as possible ($\alpha \approx 0$, β close in its minimum). This should be achieved adjusting the second LEBT solenoid field strength. At the same time, the difference in focal length of the second solenoid for the heavier masses allows to have a convergent but still completely unfocused H_2^+, H_3^+ beam at this location (see the red and green ellipses in Fig. 6.27). The presence of strong space charge is visible already in the H^+ ellipse, which suffers of distortion due to non-linear space charge forces. In case of intolerable H^+ beam emittance, or, furthermore, in order to the reduce the transmission of H_2^+, H_3^+ in the RFQ, the RFQ collimator ultimate aperture could be further reduced, at the cost of lower LEBT transmission efficiency and a higher ECRIS generated beam intensity.

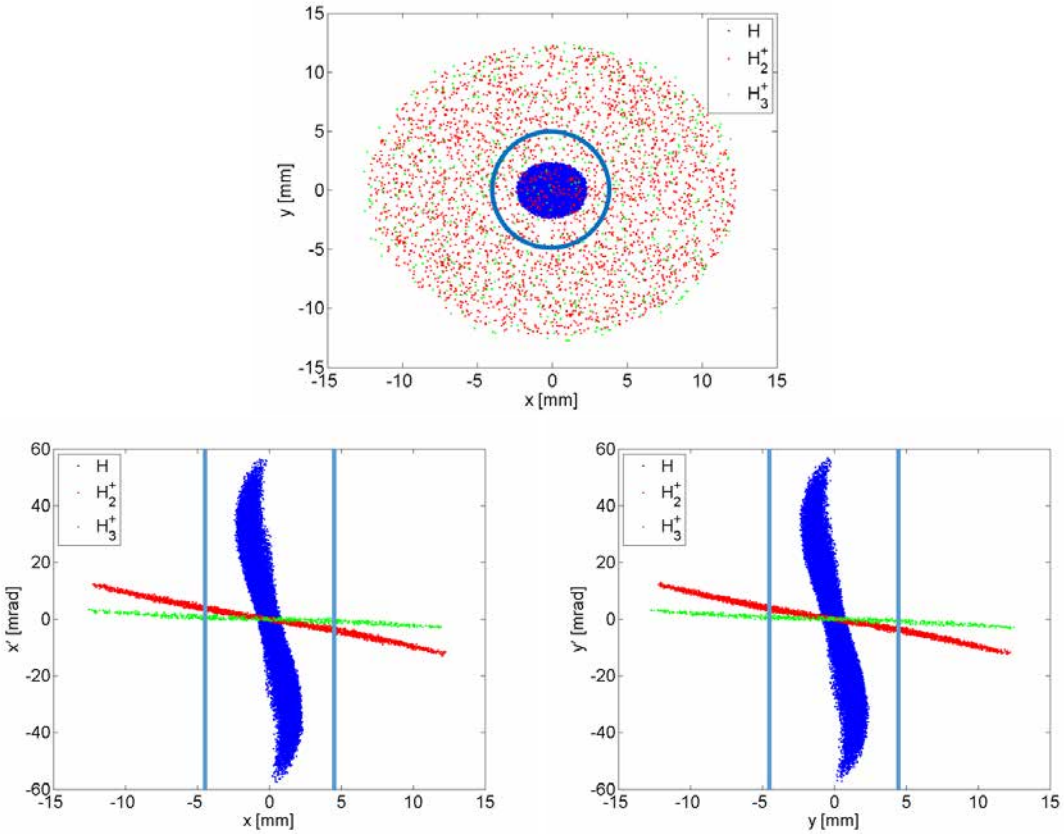

Figure 6.27: Multiparticle simulation in TRACK of the transverse spot, horizontal and vertical phase space at the RFQ entrance for the three particle species (H^+, H_2^+, H_3^+) present in the MYRRHA LEBT. The limit, circular aperture (9 mm) left by the RFQ collimator is depicted in blue. Courtesy of J.-P. Carneiro.

The RFQ collimator is in charge to absorb the deflected beam cut by the LEBT chopper. For this purpose, the deflected beam is directed out of the collimator acceptance. The total beam power (all species) density should be safely evacuated during the chopper transients. Considering a typical MYRRHA ECRIS ionization efficiency H^+ of 63%, a total beam power up to 900 W is expected. At 30 keV, the power deposition occurs in the first nanometers of matter, therefore it is considered perfectly superficial. Since no long conical reductions can be achieved on the collimator for longitudinal space constraints, this method cannot be employed for thermal power dilution. The RFQ collimator cooling performances are essential for both concentrated and distributed thermal power evacuation, so they have been thoroughly 3D simulated in a coupled Ansys/Fluent simulation.

The cooling flow required to extract, in steady state, a total beam power of 900 W, is given by

$$\dot{m} = \frac{P}{c_p \Delta T}. \tag{6.20}$$

Considering demilitarized water as the common coolant employed in the LEBT line, available at moderate pressure (6 bar), a modest cooling flow of 0.01 kg/s is required to obtain a ΔT of 20 K. Such flow can be in principle delivered by cooling channels of hydraulic diameter D_H=5 mm, with a safe mass flow velocity up to 0.5 m/s.

As during the commissioning phase the beam transmission along the LEBT line will be studied by adjustment of the focusing elements, the maximum power density onto the RFQ collimator face is not *a priori* known. A conservative approach consists in simulating a steady-steady highly focused, H^+, DC beam being dumped onto the RFQ collimator while a distributed thermal power, nominally due to the H_2^+, H_3^+ beams and corresponding to a maximum of 300 W in steady state, is evacuated. The H^+ beam distribution can be assimilated to the one of a two dimensional Gaussian function (see Fig. 6.28), as follows

$$q''(x,y) = \frac{1}{2\pi\sigma_x\sigma_y} e^{-\left(\frac{x^2}{2\sigma_x} + \frac{y^2}{2\sigma_y}\right)} \tag{6.21}$$

being $\sigma_{x,y}$ the 1σ RMS H^+ horizontal and vertical beam size. Considering a 20 mA, 30 keV H^+ beam, $P = 600W$, having a $\sigma = \sigma_x = \sigma_y = 1$ mm in the worst case scenario, its power distribution results

$$q''(x,y) = \frac{600}{2\pi\sigma^2} e^{\frac{x^2+y^2}{2\sigma^2}} \tag{6.22}$$

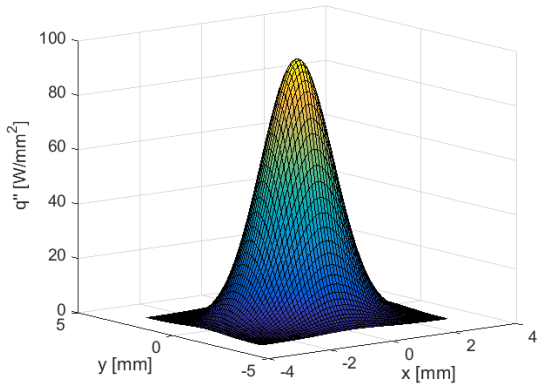

Figure 6.28: Gaussian power distribution deposited by a concentrated 600 W, RMS $\sigma = 1$ mm beam.

In order to simulate the equivalent beam spot, we take into account the peak power density, that is 96 W/mm^2. The corresponding beam spot has a surface $S_{eq} = \frac{P}{q''_{max}} = 2\pi$ mm^2 and an equivalent diameter equal to $2\sqrt{2}$ mm.

A preliminary FEM thermal-hydraulic simulation on a collimator mock-up shows that, for a cooled surface made of Cu OFHC and thick 5 mm, the required wall heat transfer coefficient should be in 10000 W/m^{2}K range, that corresponds to a rather efficient forced convention with demineralized water. The resulting maximum surface temperature is up to 400 °C (Fig. 6.29). A further decrease of the wall thickness is not an option, first for structural reasons (temperature gradient) and secondly for sputtering erosion (see next Section).

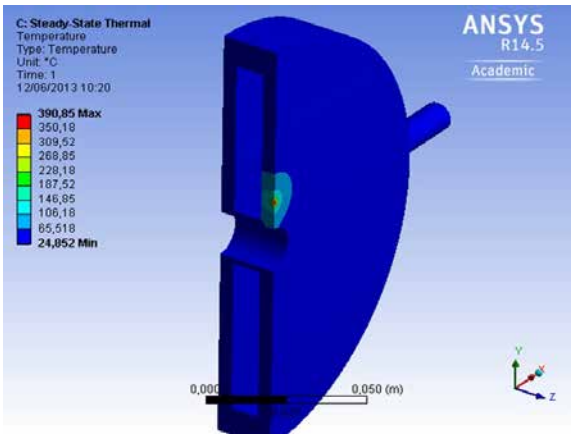

Figure 6.29: Coupled thermo-mechanical/fluid dynamics Ansys/Fluent simulation of a RFQ collimator mockup surface exposed to a peak power density of 96 W/mm^2 and cooled by demineralized water in forced convection.

Once the external geometric shape of the collimator fixed from beam dynamics, final FEM thermal-hydraulic simulation have been carried in order to maximize its cooling performance. Active water cooling (0.01 kg/s) is provided directly in the mass of the collimator, which is composed by three pieces. Coolant is brought by hollow, ID = 7.7 mm, electrically insulated feedthroughs commonly adopted for high power applications. The coolant flow is diverted by the intermediate cone and is uniformed along the axis. The flow is then forced centripetally toward the restriction left in correspondence of the RFQ limit aperture, where it acquires the maximum velocity of 2 m/s. The local heat transfer coefficient hits more than 20 000 W/(m^{2}K). As the restriction operates as a distributor, the flow leaves this area quasi-uniformly and reduces in velocity due to cross section enlargement. Nice concentric and uniform heat transfer coefficient zones are so created. In order to enhance the turbulence, in the final collimator design 2 mm steps are produced in the collimator inner wall in order to force a momentum change in the flow and some recirculation. The flow then reaches a plenum which reduces the disturbance created in correspondence of the outlet feedthroughs. The achieved pressure drop is contained to 0.1 bar.

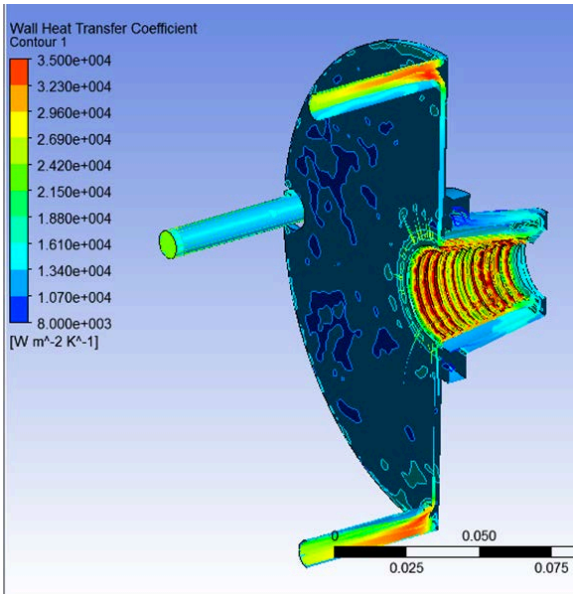

Figure 6.30: Fluid dynamics Fluent simulation of the fianl RFQ collimator cooled by 0.1 kg/s of demineralized water in forced convection.

The collimator is electrically isolated from the surrounding ground potential by shielded Macor® inserts. The water feedthroughs are as well insulated by alumina, so that the whole collimator piece can be grounded by a dedicated path. The portion of beam current impinging on it can be measured, as well as the collimator itself can be polarised by an external voltage power supply. This is an innovative design option which opens the way to interesting new experimental studies. For instance, during deflection, the chopper is bombarded by electrons produced by secondary electron emission stimulated by proton impingement on the collimator surface. This is detrimental from the chopper point of view as its electrodes tend to be depolarised: the negative charge deposition must be sustained by the chopper supply system. A positive polarisation of the collimator surface could therefore mitigate the spurious electron emission due to proton bombardment and limit the negative charge leaving the collimator surface. The presence of free electrons could be, on the other hand, useful for SCC. As the beam area is periodically depleted of compensating charges by the presence of a strong electric field produced by the chopper operation, the parasitic charge emission resulting during a beam chop could foster the accumulation of neutralizing particles in the area, after a chopper pulse, reducing the transient time required for restoring full SCC. For this purpose, the RFQ collimator could be grounded or slightly negatively polarized, acting like an electron repeller.

Sputtering

The RFQ collimator is expected to experience high surface sputtering during the repetitive beam dump operated by chopper pulses. Sputtering is the process whereby material particles are ejected from a solid target material due to bombardment by energetic projectile. The process occurs when the kinetic energy of the incoming projectile is much higher than conventional thermal energies, typically larger than 1 eV.

The physics behind sputtering is driven by momentum exchange occurring in collisions between the ions and atoms in the materials. When an incident ion, of sufficient momentum, bombards the target surface, a collision cascade can be set off. When such cascade recoils and reaches back the target surface, with an energy greater than the surface binding energy, a sputtered atom is ejected. The average number of atoms ejected from the target per incident ion is called the *sputtering yield* and depends on the ion incident angle and its energy, the masses of the ion and target atoms and the surface binding energy of atoms in the target:

$$Y_s = \frac{N_e}{N_p} \tag{6.23}$$

where N_e is the average number of sputtered atoms ejected by the impinging projectiles N_p.

In principle, if the number of projectile is reduced, sputtering can lead to mild consequences, such as vacuum degradation and surface pollution. During prolonged and high intensity ion bombardment onto a material surface, this process could evolve in significant surface erosion; moreover, it is harmful for the surrounding surfaces, which are hit and surface covered by a considerable amount of sputtered material.

In the MYRRHA LEBT, sputtering is expected and unavoidable in the following locations: in the Ion Source, in the collimation intermediate stage and in the RFQ interface. In the MYRRHA IS, sputtering occurs particularly in the plasma chamber, therefore specific cleaning is prescribed by routine maintenance. At the collimation stage, moderate beam (principally H_2^+, H_3^+) intensity is expected to be adsorbed and no critical equipment is installed in the upstream zone.

Sputtering is instead expected to be very harmful in the RFQ interface. The full, concentrated, H^+ beam is dumped repetitively onto the RFQ collimator. As we will calculate in the following, the erosion that may occur is significant; the quantity of sputtered matter, harmful for exposed surface meant to be insulators, is expected high.

The Montecarlo code TRIM-2013 (*Transport of Ions in Matter*) [89] of the family SRIM (*Stopping and Range of Ions in Matter*) has been employed to give estimations of the magnitude of the phenomenon and its possible impacts. The selected projectiles have been always 30keV H atoms. Results from TRIM have normally a 30 to 40% inaccuracy, so they should be considered for reference.

A set of simulations has been carried to assess the key parameter, the sputtering yield, on a set of technical material. Results are resumed in Table 6.3. Sputtering has a not negligible yield of few units per thousand projectiles for protons at 30 keV impinging perpendicularly on the different materials.

Table 6.3: Sputtering yield calculated in SRIM for H^+ (30 keV) impinging on normal direction for different technical surfaces.

	Y_s [atoms/projectile]
Cu63	$8.45 \cdot 10^{-3}$
Al27	$3.64 \cdot 10^{-3}$
W184	$4.65 \cdot 10^{-3}$

The quantity of sputtered matter due to continuous particle impingement can be therefore estimated. The number of atoms per unit volume is defined by

$$N_m = \frac{\rho}{A} N_A \tag{6.24}$$

where ρ is the material density, A its mass number and N_A the Avogadro number.

The typical number of incoming particles on the RFQ collimator is estimated taking into account a nominal LEBT chopper cycle, i.e. a couple of 5 μs chops at 250 Hz, yearly operated. Those particle are the sputtering projectiles and correspond to the number of proton per chopper pulse multiplied by its duty cycle. In such pulses, the full, H^+ beam current is dumped on the RFQ collimator, so that the integrated proton dose is

$$N_p = \frac{\int Q dt}{e} = \frac{0.02A \cdot (250 \cdot 2 \cdot 5 \cdot 10^{-6}) \cdot 60 \cdot 60 \cdot 24 \cdot 365s}{1.6 \cdot 10^{-19} C} \cong 9.86 \cdot 10^{21} [\text{protons}] \tag{6.25}$$

The number of sputtered atom is readily available from the sputtering yield Y_s definition:

$$N_e = N_p \cdot Y_s \tag{6.26}$$

Table 6.4 resumes the results of such calculation. Given a nominal high beam current, the amount of extracted matter i,s in all the material cases, tangible. The number of atoms, translated in volume, falls in the unity of mm^3 eroded. High contamination of the vacuum vessels/experimental equipment is expected in the RFQ interface. Adopting materials like Al and W for the RFQ collimator surface can give half of the yield, therefore the amount of sputtered matter can be roughly divided by two (density dependent). Given the expected tiny beam imprint spot, the material thickness removed per year from the collimator is significant.

Curative methods such as collimator surface replacement or rotating beam impact are two ways identified as possible curative measures. The first has been employed for the MYRRHA RFQ collimator design.

Table 6.4: Results from the sputtering calculation: n. of atoms, n. of mm^3 of matter, n. of μm eroded in correspondence of a $\sigma = 3$mm beam spot.

	N_e [atoms]	N_e [mm^3]	Δs [μm]
Cu63	$7.88 \cdot 10^{19}$	$9.35 \cdot 10^{-1}$	16.5
Al27	$5.95 \cdot 10^{19}$	$5.95 \cdot 10^{-1}$	10.5
W184	$4.29 \cdot 10^{19}$	$6.08 \cdot 10^{-1}$	12.5

In a second simulation set, the angular dependence of the phenomenon is assessed. The projectile angle with respect to the normal direction is swept from 0 to 90 degrees. Results are summarized by Fig. 6.31.

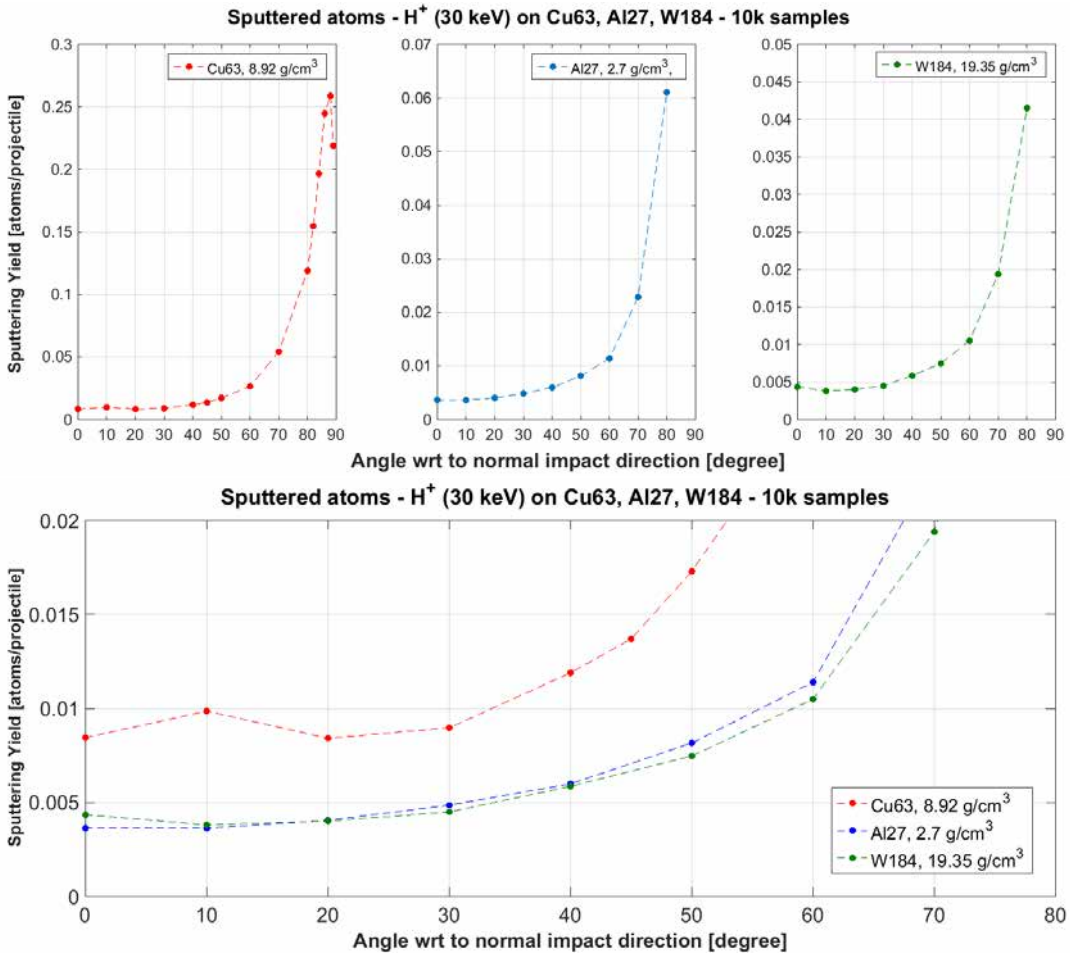

Figure 6.31: Typical sputtering yield for H^+ (30 keV) impinging at different angles with respect to normal direction on three technical surfaces.

For small angular deviations (small angle w.r.t. a normal impinging direction), the sputtering yield does not change significantly. The phenomenon is significantly boosted for larger impact angles, as expected, and slightly less for grazing directions (see the Cu only simulated case). In the case of the LEBT RFQ collimator, the chopped beam is expected impinging at ∼150 mrad, i.e. 8 degrees, therefore a nominal sputtering yield can be safely retained.

In a third simulation set, the extraction of atoms from a surface due to sputtering phenomenon is analysed (Fig. 6.32). This is a result of a 1M 30 keV H^+ samples, returning around 8000 sputtered Cu atoms (an indirect confirmation that the yield of 0.008 for copper is consistent).

The distance of the emission point from the projectile impact point, i.e. the range of the projectiles in matter (H, 30keV), is always less than a nanometer. A sputtered atom is extracted very close to the ion impinging point, so a point-like source approximation is correct. When leaving the surface, the sputtered atoms direction is mostly full-backward ($cos(x)$ principally between 0.9 and 0.6), with a transversal spread that follows a Lamberts cosine law (look at $cos(y)$ and $cos(z)$ plots). The quantity of sputtered atoms decreases as the directions of emission (w.r.t. to the normal direction) increases in tilt. The energy of the sputtered atom is nominally 10-100eV, with some peak at 1keV.

Concerning the emission geometry, a fundamental aspect should be kept in mind: the sputtered atoms, once emitted, are distributed over spherical surfaces, like radiation emitted in space. The more is the distance from the source, the less is the superficial density deposited (decreases with $1/r^2$).

As seen, sputtering in the RFQ interface is non-neglibile phenomenon, which can be slightly reduced employing different technical surfaces, like W184, but cannot be mitigated. The number

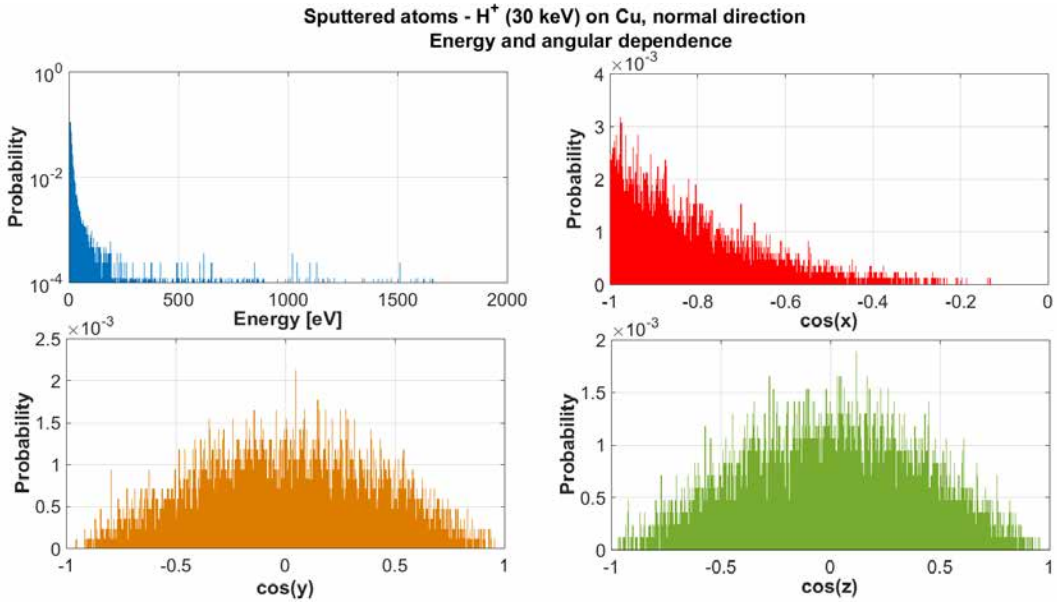

Figure 6.32: Spectra of the energy (E) and directions in space ($cos(x)$, $cos(y)$, $cos(z)$) of sputtered atoms emitted from Cu after impingement of H^+ (30 keV) projectiles in normal direction.

of projectiles expected during beam chopper operation is high. The design method adopted in the RFQ interface is shielding (masking, distance). Particular care has been therefore used for distancing the electric insulator of both the chopper electrodes feedthoughts. The RFQ collimator insulators have been instead fully shielded. The turbomolecular vacuum pump installed in this area has been 90 degrees rotated and further distanced from the beam line.

6.5.3 RFQ electron repeller

As often mentioned, the presence of electric field applied in the beam line remove the neutralising particles (electrons) from the beam area. Locally, the beam is therefore uncompensated and subjected by strong space charge forces. One of the most important areas of interest in high beam intensity LEBT lines is the injection area into the RFQ, which is very critical for two reasons:

- the still low energy beam is highly convergent and experiences the maximum space charge forces;
- the RFQ beam capture and transmission depend on the quality of the beam injected: a matched centered beam, with correct beam emittance and Twiss parameters, is required.

This area is often critical since the presence of the RFQ electric fields depletes the zone from free electrons, which in turn results in an unavailability of neutralizing particles. This effect can be mitigated by the presence of a sort of screen for electrons, an electron repeller. The role of the repeller is to confine the electrons available at the end of the LEBT line, creating a potential barrier from the RFQ field. As a drawback, locally, at the longitudinal position of this insertion, the beam is totally uncompensated. It is therefore of paramount importance that this electrode is situated at the very end of the line and its shape does not produce long stray electric fields.

In the MYRRHA LEBT, the electron repeller is integrated in the RFQ collimator. A circular electrode, of diameter D = 11 mm, is mounted in an alcove produced in the back collimator face. The selected material for the repeller ring is AISI 304L stainless steel. The polarization lead is soldered on the back of the ring. As the RFQ collimator is grounded through a dedicated current path, the electrode is insulated in a sandwich of Macor® insulators. The electrode is shielded both from impact of impinging beam and the RFQ field by two upstream and downstream restrictions of 9 mm and 10 mm in diameter.

Electrostatic simulations have been carried in Poisson to design the RFQ electron repeller and characterize its field quality. Given the axial symmetry, the cylindrical coordinates zr have been chosen. For circular symmetry, at $z = 0$, the Neumann boundary condition $dV/dz = 0$ has been imposed (**E** field lines perpendicular). As the potential of the beam itself cannot be neglected in this region, the electric field produced by an homogeneous circular beam, of radius $r = 2.5$ mm (H_+, RMS beam size, Tracewin simulations, see Section 6.7) has been assumed. The charge density (per unit of surface area, cm^2) in this region is calculated imposing a proton current of $I =$ 20 mA flowing at $v = \beta c$, $\beta \cong 0.008$, along a simulated length of $l = 12$ cm (RFQ injection zone):

$$\frac{Q}{S} = \frac{I(\frac{l}{\beta c})}{rl} \tag{6.27}$$

Figure 6.33 shows the results of the electrostatic simulation. The beam envelope, depicted by a blue boundary line, can be observed. The electrode offers a longitudinal circular surface long 6 mm, polarized by design at -500 V. The ring diameter is fixed by the limit beam aperture and therefore cannot be reduced to increase the electric field in the beam line. The largest part of the electric field is contained in the perfect coaxial capacitor offered by the grounded surfaces surrounding the electrode supports. The electric field in this region is the one analytically calculable for straight parallel surfaces and corresponds 5000 V/cm. The peak electric field is situated in the proximities of the electrode edges, circular (r = 0.5 mm). A maximum of 8000 V/cm is reached in this region. Due to space constraints, this value cannot be relaxed and is accepted for design. The largest surface possible (∼207 mm^2) is offered longitudinally by the inner side of the electrode ring, toward the beam line, in order to push the peak electric field at its geometrical center.

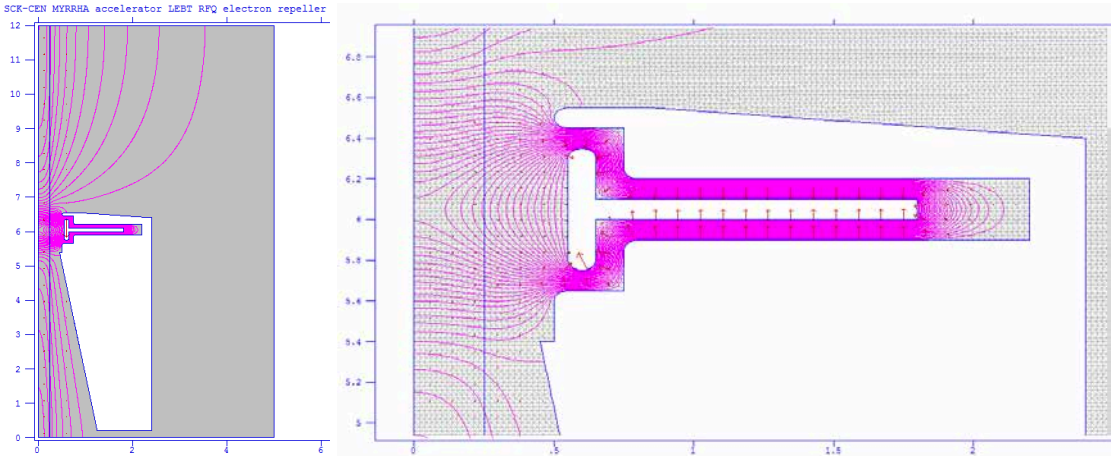

Figure 6.33: Poisson simulation of the electric field equipotential lines and direction/magnitude (arrows) on the longitudinal plane, in cylindrical coordinates, of the MYRRHA LEBT RFQ collimator electron repeller.

The radial and longitudinal electric fields are plotted in Figure 6.34 along the z axis. E_r is clearly zero, as expected for symmetry reasons. A screening longitudinal electric field is available on the two sides of the electrode, up to 500 V/cm. The equivalent potential barrier of -245 V is produced at the beam center line (see Fig. 6.35).

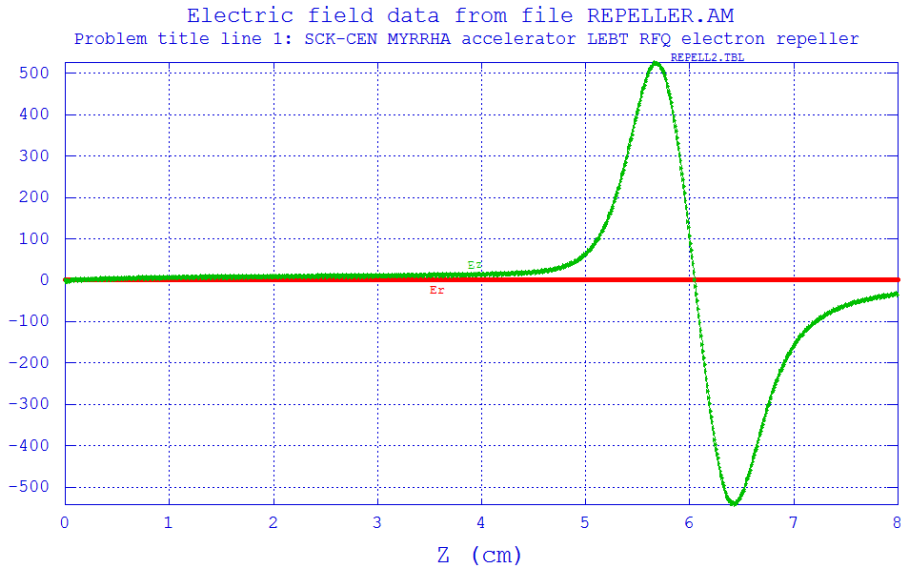

Figure 6.34: Longitudinal E_z (green) and radial E_r (red) electric field components, along the z axis in the longitudinal rz plane, of MYRRHA LEBT RFQ collimator electron repeller.

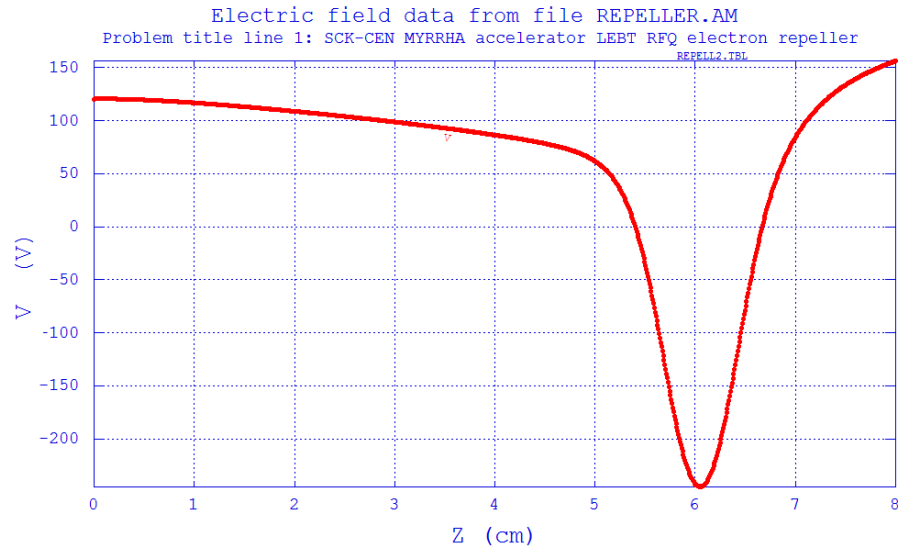

Figure 6.35: Potential available across the RFQ collimator. The electron repeller electrode is polarised at a nominal voltage of -500 V.

The electrostatic design is translated into mechanical design visible in Fig. 6.36. Although the repeller ring should be off the beam line-of-flight, it is very likely that some charged particle could hit directly the electrode. This (depolarising) positive charge should be sourced by the associated repeller power supply. In order to prevent continuous polarisation and consequent destructive sparking, its insulators are recessed and shielded by the electrode itself and collimator grounded surfaces.

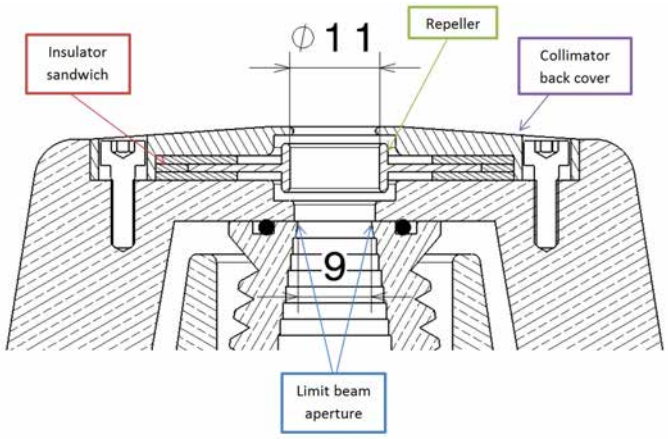

Figure 6.36: Cross section of the RFQ collimator equipped with RFQ electron repeller. The electrode, isolated from the ground by an insulator sandwich, is visible.

6.5.4 Current Transformer

A non-interceptive beam current monitor is installed at the end of the LEBT line. This beam diagnostic allows measurement of pulsed (by the beam chopper) beam currents and accurate monitoring of produced pulsed beam structure. In parallel, an on-line measurement of the RFQ transmission efficiency can be obtained. The selected technology falls on short ACCT current transformers. ACCTs allow precise waveform measurement of long pulses and macropulses, up to several ms, with minimal droop and noise.

The selected device is a 100 mm diameter, up to 1 MHz, magnetic shielded ACCT (Fig. 6.37), which has been integrated in the RFQ flank, under vacuum. The instrument was provided by Bergoz Instrumentation, France. The solution integrates perfectly with the tight space requirements of the RFQ interface and avoids the provision of an electric isolating gap, as the beam image current bypasses the device going around the instrument.

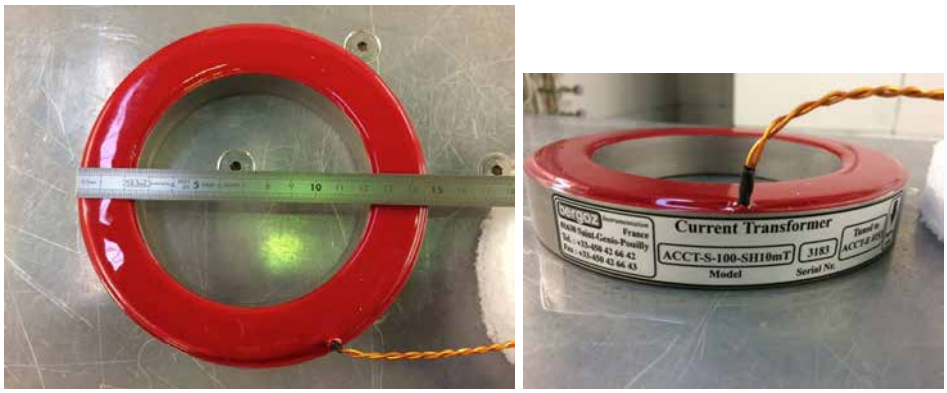

Figure 6.37: Picture of the MYRRHA LEBT AC Current Transformer procured by Bergoz Instrumentation, France.

In order to avoid saturation of its magnetic core, the ACCT is designed to be shielded from magnetic stray fields, such as the one occurring at the exit of the second LEBT solenoid, or induced by the RFQ field [90].

The ACCT comes with proprietary electronics delivering a low voltage (5 to 10V) analog signal, with a large bandwidth, typically ranging from few Hz to 1MHz (-3dB).

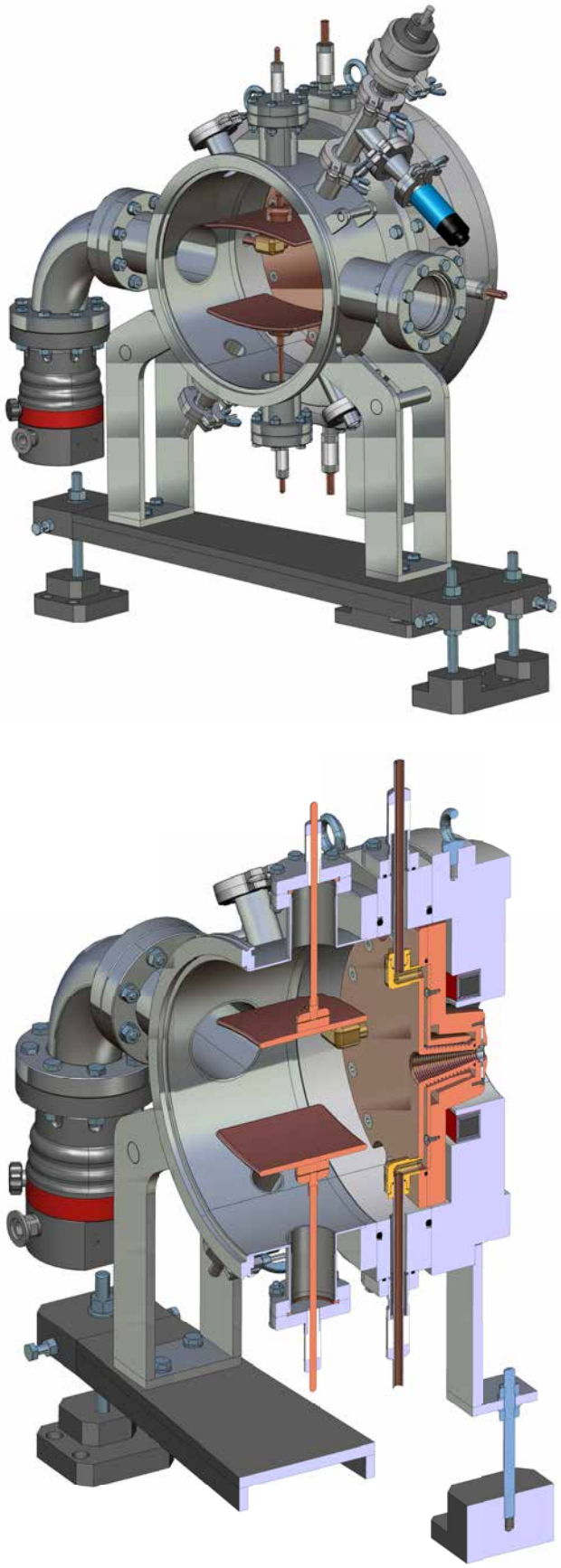

Figure 6.38: 3D CAD model of the MYRRHA LEBT RFQ interface, including the beam chopper, the RFQ collimator, the RFQ electron repeller and the ACCT. A RFQ mock-up flange, to be adopted during the LEBT commissioning phase, is represented on the back. Courtesy of SCK•CENand UCL/CRC.

6.6 Characterization of the Ion Source

The MYRRHA LEBT Ion Source has been characterized during the Factory and Site Acceptance Tests (FAT, SAT) and in the experimental set-ups available at UCL/CRC in Louvain-la-Neuve, Belgium (Fig. 6.42). In 2016, it was installed at LPSC, Grenoble, France, for the LEBT commissioning.

During FAT, the H^+ beam production was demonstrated in range of different intensities. The source has been capable to deliver a 30 keV H^+ beam up to 16 mA (DC), with a vertical beam emittance of $\sim 0.1\pi$·mm·mrad RMS norm. at 5 mA H^+ (Fig. 6.39).

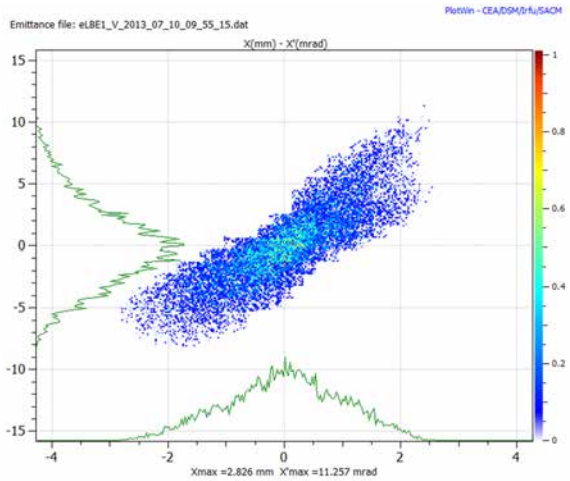

Figure 6.39: Vertical H^+ beam emittance measured during the MYRRHA Ion Source FATs after species separation (dipole bend). No polarisation is applied to the Einzel lens present in the extraction box.

The total beam production efficiency, calculated as the total current provided by the plasma chamber power supply divided by the sum of measured beam intensities (all species) collected at the Faraday Cup, has been estimated around 84% (comprising HV losses due to the bleeder resistance, engineering inevitable).

The particular ionization efficiency for each beam specie has been measured. The measurement is carried adopting the dipole as a spectrometer: each particle specie, having different beam rigidity, is steered into the downstream Faraday Cup, allowing the measurement of the particular ion intensity (see Fig. 6.40). Each intensity is then divided by the total measured beam intensity (all species).

A $\sim 63\%$ ionization efficiency was achieved for H^+, while $\sim 30\%$ for H_2^+ and a spurious $\sim 7\%$ for H_3^+.

A long test run (24 hours) has been carried to assess the beam stability. Results were encouraging, as a large ($> 90\%$) beam availability was measured for a beam current between 12 and 12.3 mA, with minor regulations: those concerned mainly the RF power and H_2 gas flow, which determine the particular beam intensity once the extraction settings (principally puller electrode polarisation) are optimized. Fast beam interruptions were only characterized by quick self-extinguishing breakdowns followed by brief recovery times in case of electrical discharges.

The beam size has been estimated in a interceptive manner in the extraction region of the source. This measurement is the closest practicable and available to the extraction hole. A water-cooled screen has been placed a first vacuum port available just after the Ion Source extraction box, so that a rough beam imprint was left by sputtering induced by beam impact. The longitudinal coordinate of the screen was z=0.465 mm.

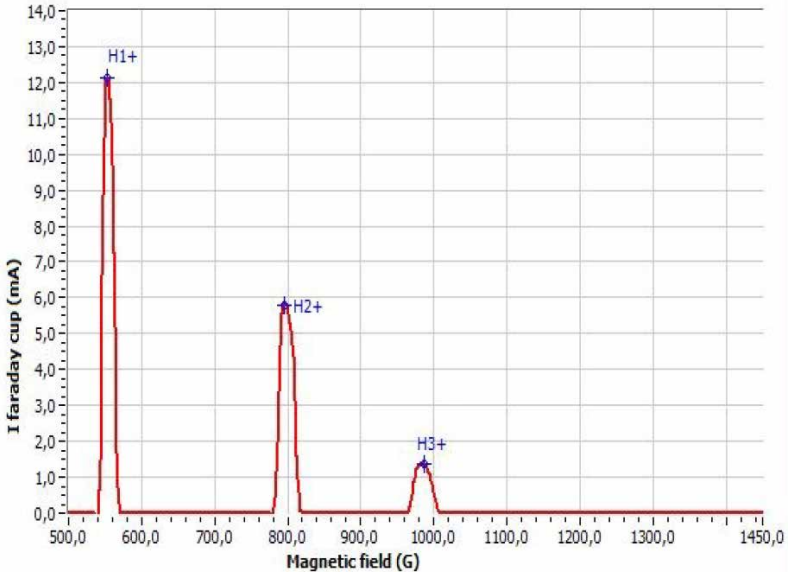

Figure 6.40: Ionization efficiency measured by scanning dipole method during the MYRRHA Ion Source FATs. The peaks corresponds to the three ion intensities recorded.

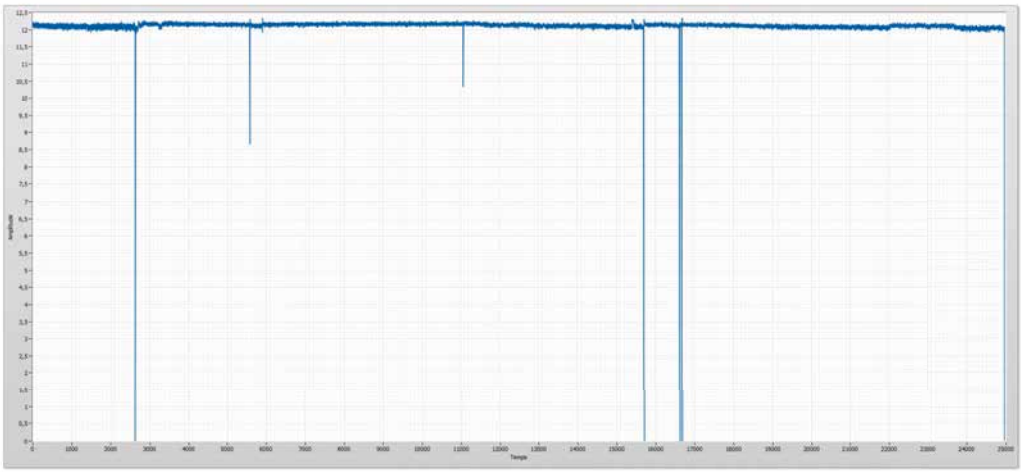

Figure 6.41: Snapshot of the recorded H^+ beam intensity during the MYRRHA Ion Source FATs. The vertical peaks correspond to instabilities in the beam intensity mainly caused by HV sparking.

A trace, visible in Fig. 6.43, of diameter equal to 29 mm was left the impact of the 11.5 mA total beam (H^+=60%, H_2^+=34%, H_3^+=4%) delivered by the Ion Source in absence of any external focusing (Einzel lens not polarised).

As seen in Sect. 2.3, the equation of expansion in a beam envelope dominated by space charge in a drift space is described by

$$\frac{dr_{env}}{dz} = \frac{dr_{env}}{dz} = \sqrt{2K}\sqrt{ln\left(\frac{r_{env}(z)}{r_0}\right)} = \sqrt{2K}\sqrt{ln(\chi)} \tag{6.28}$$

where $\chi = \frac{r_{env}(z)}{r_0}$. We apply the same calculation procedure done in precedence to estimate the totally uncompensated beam size expected at z=0.465 m.

For the initial beam size, we consider the nominal LEBT input parameter, i.e. a transverse emittance equal to 0.1π·mm·mrad RMS norm. at 0.1 m from the source extraction hole. The full (3σ) beam size diameter is d_0=10 mm. The variation of the beam envelope size with the distance

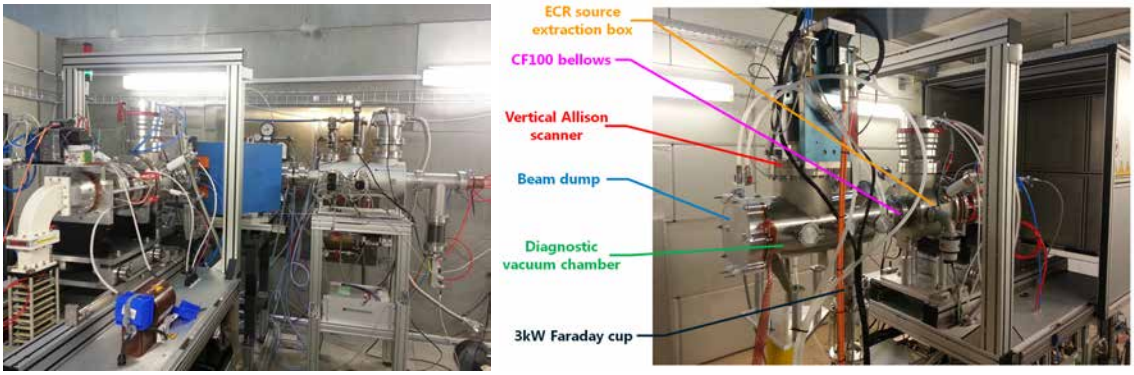

Figure 6.42: Experimental setup during the MYRRHA IS Factory Acceptance Tests (up) and Site Acceptance Tests (down), in Pantechnik SA, Bayeux, France and UCL/CRC, Louvain-la-Neuve, Belgium.

is

$$z = \frac{r_0(z = 0.1m)}{\sqrt{2K}} F(\chi) \tag{6.29}$$

where K is the generalized perseverance of the beam, that is

$$K = \frac{qI}{2\pi\epsilon_0 m_0 c^3 \beta^3 \gamma^3} = 1.433 \cdot 10^{-3} \tag{6.30}$$

in the case of the MYRRHA low energy proton beam.
We now have all the ingredients to find

$$F(\chi) = \frac{(0.465 - 0.1)\sqrt{2 \cdot 1.24 \cdot 10^{-3}}}{0.005} \cong 3.908 \tag{6.31}$$

The ratio $\chi = \frac{r_{env}(z)}{r_0}$ should be found from the integral $F(\chi) = \int_1^{\chi} \frac{dy}{\sqrt{ln(y)}}$, which is analytically not solvable. By numerical integration, employing a trapezoidal method (see Fig. 2.4), we get

$$\chi = \frac{r_{env}(z = 0.465)}{r_0} \cong 3.925 \tag{6.32}$$

$$r_{env}(z = 0.365) = 3.5 r_0 \rightarrow d_{env}(z = 0.365) = 39.25 \text{ mm} \tag{6.33}$$

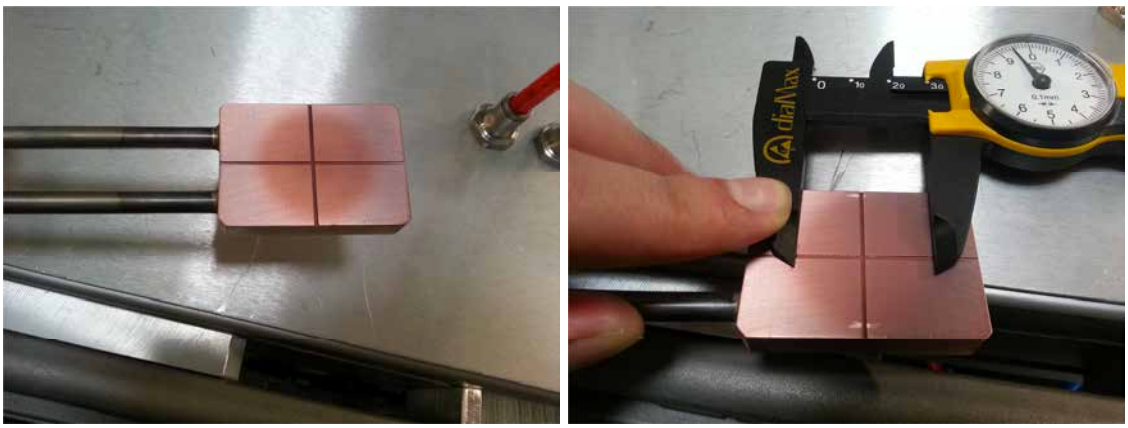

Figure 6.43: Beam imprint left by exposition of a planar, water cooled, target to a 11.5 mA beam delivered by the MYRRHA Ion Source for 1 hour. The diameter of the trace is ∼29 mm.

which is the expected size of the beam envelope for a totally uncompensated beam.

The same experiment was simulated in presence of space charge compensation in the multiparticle tracking code TRACK. An input beam as described in precedence, of respectively 7.0 mA, 4.0 mA and 0.5 mA of H^+, H_2^+, H_3^+, was tracked by 100K multiparticles along the mentioned drift. A scan of the degree of space charge neutralization ϕ between 50 % and 100% returned that a beam spot diameter varies between 32 and 26 mm, and that a ϕ=80% is required to observe a beam of spot of ∼29 mm at z=0.465 (Fig. 6.44, left). The transverse emittance at such longitudinal coordinate is 0.11π·mm·mrad RMS norm (Fig. 6.44, right).

This rough estimate indicates that the beam emergent from the ECRIS is indeed partially compensated: a 80% to 100% neutralization factor, employed as input parameter in LEBT beam dynamics for the source extraction zone, is coherent with what was measured.

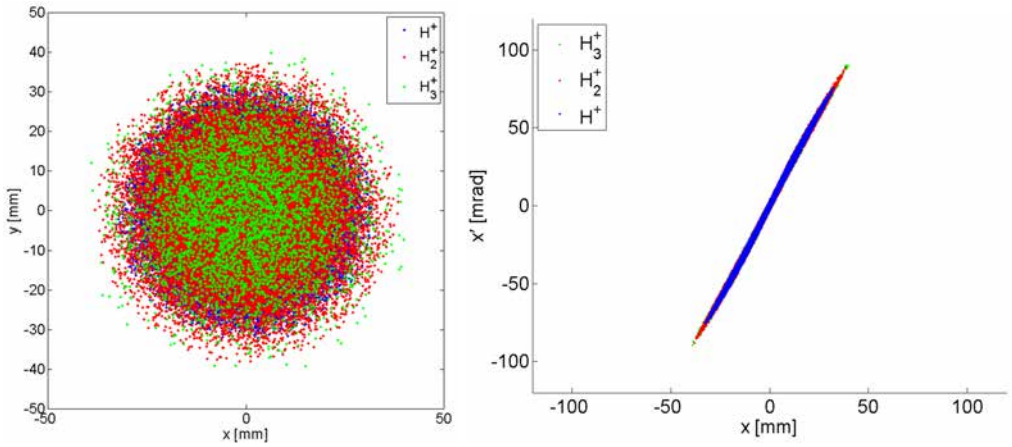

Figure 6.44: Simulation in TRACK of the beam spot and transverse $x - x'$ phase space at z=0.465 m for a partial (80%) space charge compensated beam leaving the MYRRHA Ion Source.

Preliminary investigations on the source extraction settings and the influence of the Einzel lens on the transverse beam emittances are currently performed. The goal is to optimize the extraction settings in view of the future LEBT line commissioning.

Figure 6.45 shows three vertical emittance measured sweeping the Einzel lens polarisation level from 0 to 25.5 kV. In the first phase space, we observe the highly divergent beam emerging from the Ion Source after a drift of 0.765 m. The three particle species are superimposed as no magnetic separation is available. Note that the zero in the x scale corresponds the half stroke of the Allison Scanner, not to the alignment reference coordinate. The total vertical beam size is approximately 40 mm, with a envelope divergence up to 80 mrad. The RMS emittance is ~ 21.9·mm·mrad. In the second phase space, a 22.3 kV polarization is adopted on the central electrode of the Einzel lens. The focusing effect of this lens is clearly appreciable in the reduction in both the beam size and divergence: the vertical RMS emittance is ~ 16.4·mm·mrad. A further step in the polarisation voltage is visible in the third phase space. While a more focalised beam is measured (RMS emittance equal to ~ 14.4·mm·mrad), a distortion in its shape appears evident. This could indicate the presence of a degree of non linear forces imputable to space charge forces. A strong impact of the Einzel lens on the space charge neutralization is highly expected in the extraction region of the Ion Source (first 400 mm). From the MYRRHA LEBT operational point of view, one recommendation is to employ such focal lens only if the beam size will appear incompatible with the optics of the first LEBT solenoid magnet. Therefore, particular care have been practised at design level to push the center of the first solenoid the closer to the IS extraction region. After a mechanical integration study (principally for assuring practical mounting and inspection), such distance have been optimized to ∼ 470 mm.

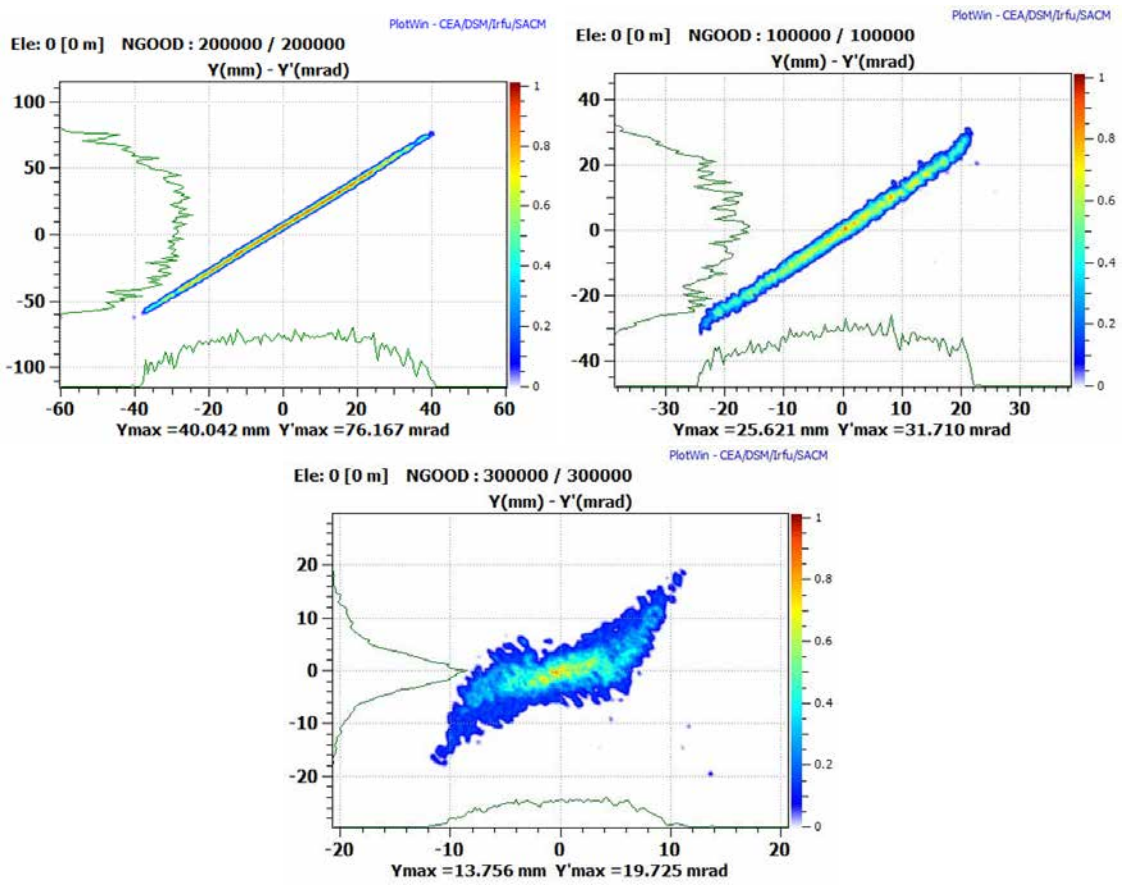

Figure 6.45: Vertical emittance measurements at exit of the MYRRHA Ion Source (z∼0.765 m) for different Einzel lens polarisation levels: 0 kV, 22.3 kV, 25.5 kV. Total beam intensity 9 mA (all species), V_{puller}=23 kV, $V_{repeller}$=1206 V, RF forward power = 212 W, gas flow = 0.4 sccm (pure H_2).

In a second experimental campaign, the source extraction parameters were slightly optimized, so that the vertical phase space at z∼0.900 m is the one shown in Figure 6.46. The RMS emittance is $\sim 0.24 \cdot \pi$mm·mrad norm., with β=10.16 mm/(π mrad) and α=-15. This corresponds to the input beam that will further characterized once the full LEBT will be commissioned.

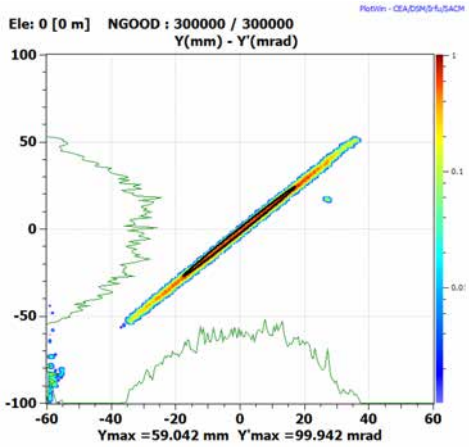

Figure 6.46: Vertical emittance measurement at exit of the MYRRHA Ion Source (z∼0.900 m). No polarisation on the Einzel lens. Total beam intensity is 13 mA (all species), V_{puller}=25.8 kV, RF forward power=263 W, gas flow=0.3 sccm (pure H_2), p_{source}=8.7·10^{-6} mbar.

6.7 LEBT beam transport and space charge compensation

The LEBT design is based on beam dynamics simulations carried out at IPNO with the CEA TraceWin code [73], using a 3D space-charge PIC routine for multiparticle simulations. The design goal is to ensure the beam transport providing a centered matched beam at the RFQ entrance with an acceptable transverse emittance (below 0.2 π·mm·mrad RMS norm. [79]).

As an input hypothesis, the transverse beam emittances $\epsilon_x = \epsilon_y = 0.1$ π·mm·mrad RMS norm. ($\beta_{x,y}$= 0.32 mm/(π·mrad), $\alpha_{x,y}$= -3.4) are assumed at z = 100 mm after the ECRIS plasma chamber extraction hole 6.47. These values are inspired from past experiences, especially from the SPIRAL-2 project [91] [92], and must be confirmed during the LEBT commissioning via emittance measurement and back-tracking up to the source extraction zone.

The beam intensity of 5mA CW is simulated as representative of the MYRRHA Accelerator design current (4 mA). The beam distribution has a Gaussian shape, truncated at 4σ.

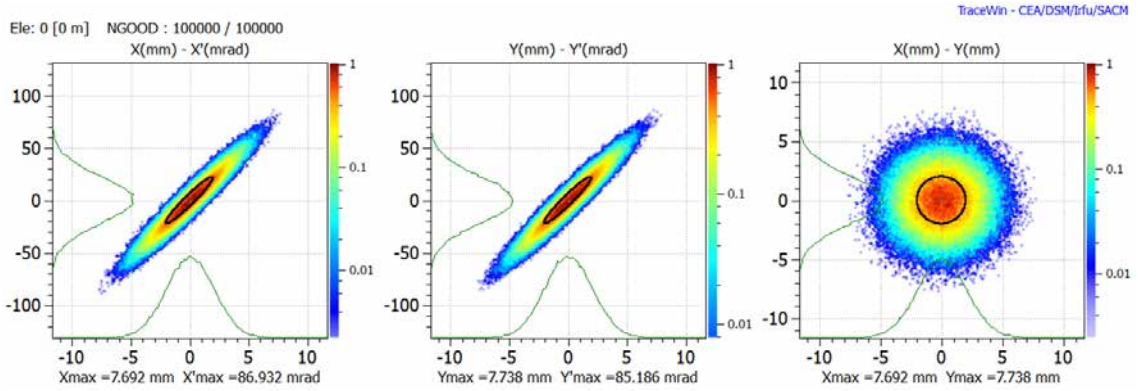

Figure 6.47: Input beam horizontal and vertical emittances and transverse distribution adopted as reference for the LEBT multiparticle simulations, corresponding to the beam properties available at z = 100mm, i.e. after ten centimetres of the MYRRHA ECRIS plasma chamber extraction hole.

Transport tuning is performed by adjusting the magnetic field of each solenoid and steerer. The fields are adjusted according to the magnetic engineering design. The goal of the tracking simulation is to obtain a centered matched beam the RFQ entrance, being focused with the right Twiss parameters especially by the second solenoid. In the MYRRHA operational context, such phase is validated during the LEBT commissioning, where the standalone line is tested. The found settings are then exploited during the accelerator operation, when the final configuration is found by optimising the RFQ transmission. The figure of merit is the ratio between the beam current measured after the RFQ (for instance by a beam current transformer during operation, or by a high power Faraday Cup in commissioning) over the one measured in the LEBT (by the ACCT in chopper pulsed mode, by the Faraday Cup in DC mode).

In nominal conditions, the required axis magnetic fields are respectively 0.17 T and 0.19 T for the first and second solenoid. Figure 6.48 shows the efficiency maps of the LEBT solenoids possible working points in a $|\mathbf{B}_1|$-$|\mathbf{B}_2|$ phase space. Two possible regions with maximized beam transmission along the low energy are identifiable. The lowest field regions is the preferred one for few reasons. Firstly, less current, i.e. less power, is required by the solenoid magnets and this increases their operational margin and reliability. Secondly, a lower field in the LEBT first solenoid is preferable in order to allow a net polluting species (H_2^+, H_3^+) separation already in the first collimation stage: due to the larger magnetic rigidity, their envelope is made incompatible with size left by the collimation aperture.

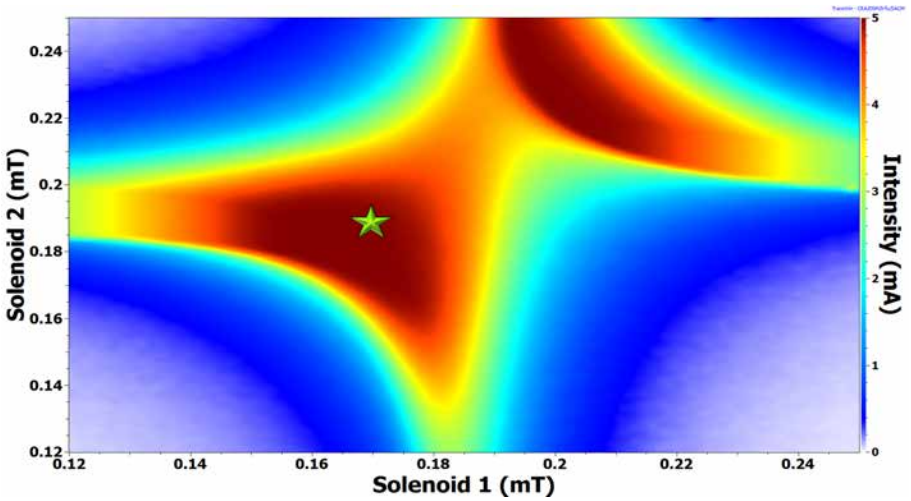

Figure 6.48: LEBT beam transmission efficiency for a 5mA H^+ beam generated by the MYRRHA IS, transported and matched by the LEBT into the RFQ in a LEBT solenoids fields $|B_1|$-$|B_2|$ phase space. The optimum solenoids working point is marked.

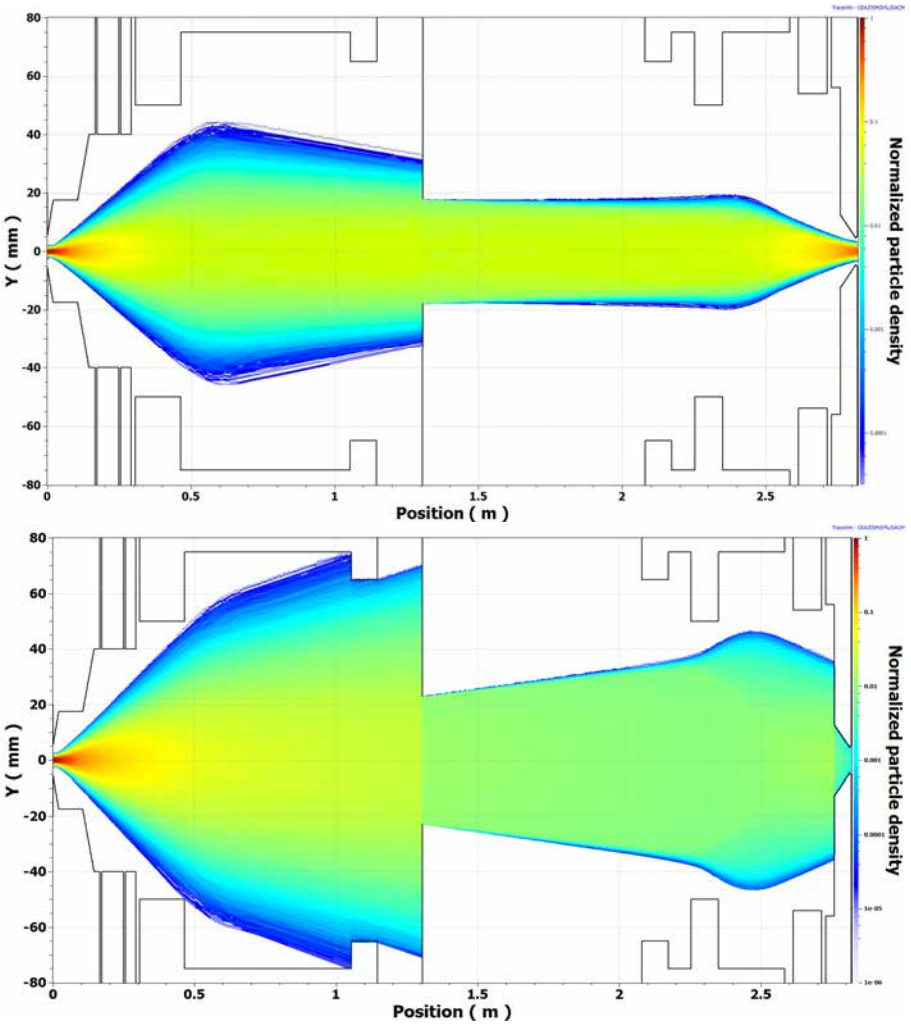

Figure 6.49: Multiparticle H^+ (up) and H_2^+ (down) tracking simulation and aperture model through the MYRRHA LEBT implemented in Tracewin.

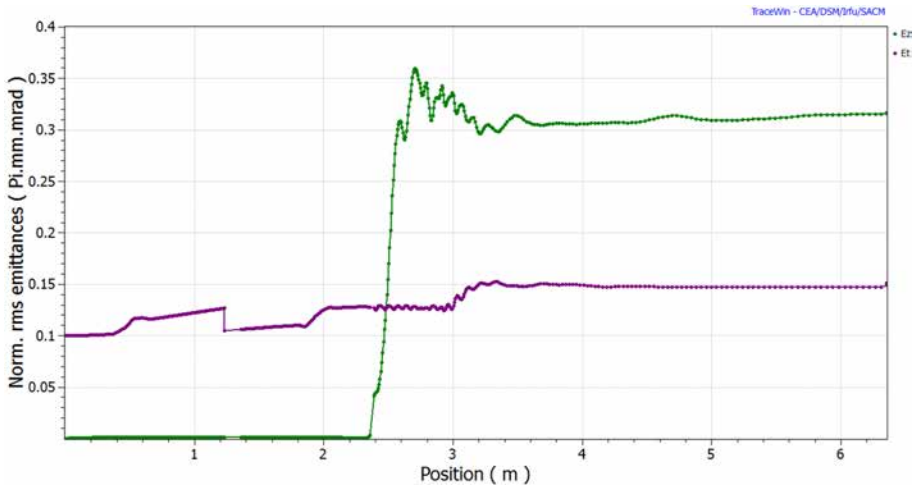

Figure 6.50: Transverse emittance evolution along the MYRRHA LEBT and the MAX RFQ, with a collimation stage in the middle and at the RFQ injection.

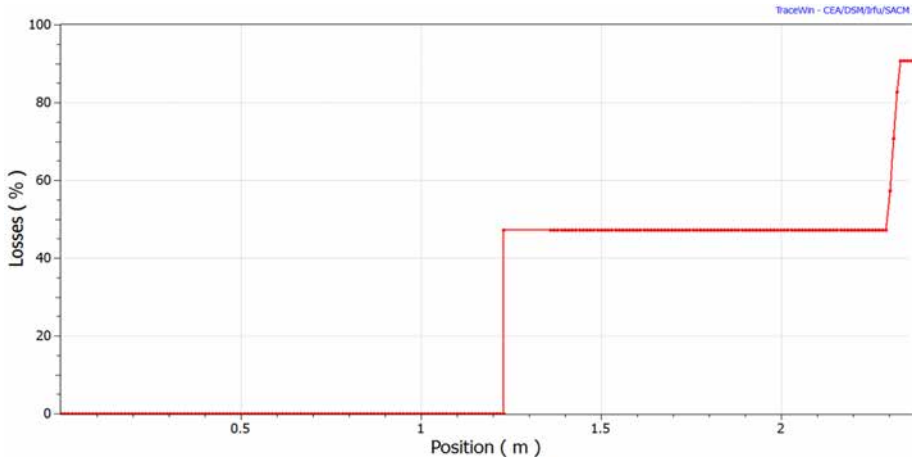

Figure 6.51: H_2^+ transmission along the MYRRHA LEBT. The cleaning efficiency of the middle and RFQ collimation stage is appreciable.

The beam transport along the LEBT is shown in Figure 6.49. The transverse beam emittance is < 0.18 π·mm·mrad RMS norm. at the RFQ entrance for a matched beam. With such input beam, the RFQ transmission reaches >98%, which is very close to the typical natural RFQ transmission for a perfectly matched beam ($\sim$ 99%).

The adoption of collimation slits, located in the middle of the LEBT, is useful for beam H^+ halo cleaning, also with such a nominal beam, to further minimize the losses in the RFQ. A wise employment in the LEBT is recommended as it could increase the RFQ transmission by an additional percentage point. As already mentioned, the slits also enable to intercept unwanted ions species, in particular H_2^+. In conditions of Fig. 6.49, ~98% of the H_2^+ are lost in the slits (aperture: 36 mm) and the collimation aperture (9 mm) at the LEBT end: the losses are approximately equally split at this two locations 6.51. The remaining 2%, i.e. about 45 μA, will be eventually and inevitably lost in the RFQ structure due to RF mismatch.

The beam chopper is located, in its reference position, the closest possible to the RFQ injection (electrodes center at $\sim$ 180 mm from the RFQ rods) to minimize the detrimental effects due to uncompensation occurring the SCC transients between the chops. The RFQ collimator is shaped to follow the H^+ converging envelope, while the H_2^+ beam is mainly cut out already at its planar face (see Fig. 6.53).

As calculated in Section 6.5.1, a deflection of >100 mrad is sufficient to take the H^+ beam of the RFQ collimator acceptance (Fig. 6.52). A deflection >150 mrad (for a beam size of 10 mm at

this z coordinate and with the nominal solenoid settings) is expected necessary to take the beam out the conical reduction and dump it already in the collimator planar face.

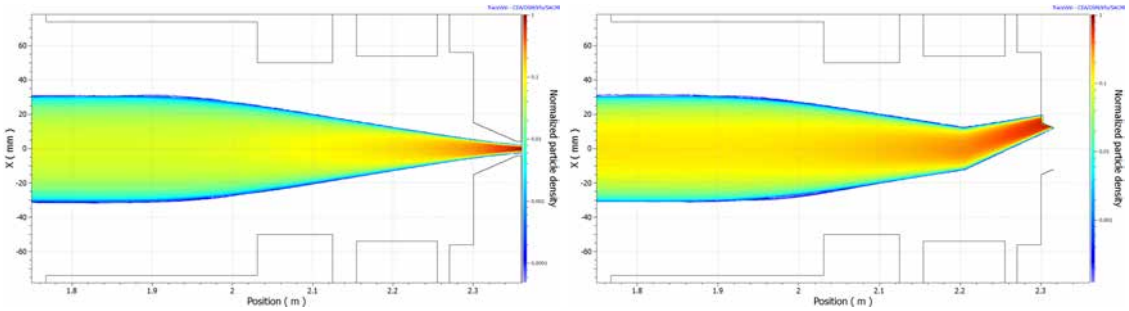

Figure 6.52: Multiparticle H^+ tracking simulation through the MYRRHA RFQ interface in Tracewin, in nominal conditions (left) and with a chopper deflection of 116 mrad (right). The apertures of the conical reduction are 30/9 mm.

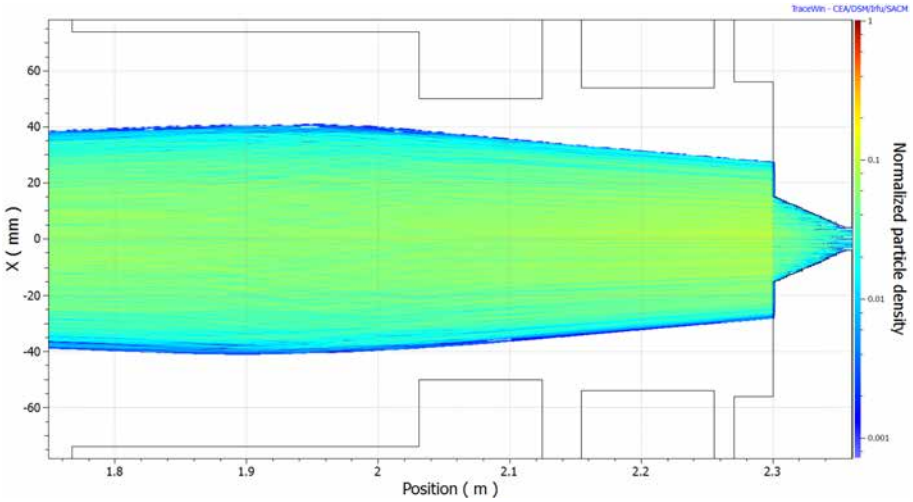

Figure 6.53: H_2^+ transmission in the RFQ interface.

The beam tuning has been additionally checked employing the Einzel lens with a positive (+20kV, decelerate/accelerate case) and negative (-20kV, accelerate/decelerate case) polarisation. The obtained additional focusing effect at the source extraction, before the first solenoid, is obtained at the cost of strong space-charge conditions in this area (uncompensated beam). A noticeable emittance growth before the first solenoid, especially in the +20kV case, was simulated. The obtained emittances at the RFQ output, if compared to the nominal case, are slightly higher (still within specifications) while and the RFQ transmission is similar. As already mentioned, this confirms that the employment of electrostatic lens returns little practical benefit. Its use is advised only if a higher than expected divergence is observed at the source exit, which is excluded by the preliminary measurement shown in Section 6.6.

Space charge effects are high for already for 5 mA 30 keV proton beam. The generalized perveance, as defined in Eq. 2.28, is $6.22 \cdot 10^{-4}$. The Space Charge Compensation level is therefore a crucial, and at the same time difficult, parameter to take into account. Design simulations have been carried out with rough estimates of the Space Charge Compensation (SCC) effect on the basis of the experimental and simulation work done at CEA Saclay [93] [94].

In steady-state simulations, the beam is assumed to be SC compensated as follows:

- in the main part of the LEBT, the beam is considered almost fully compensated thanks to the ionization of the residual gas by the protons and to the subsequent trapping of the electrons by the beam. The SCC level, ϕ, is assumed 90%;

- in the source extraction area, the low energy beam is partially space charge compensated, thanks to both the presence of a negative electrode (about -1kV) installed in the source extraction pentode after the puller electrode, acting as an electron repeller, and the relative high pressure due to gas load coming from the source plasma chamber. The assumed SCC level, ϕ, is 80%, and is coherent with what measured during the source characterization (Sect. 6.6). Such compensation level is adopted for the first ∼65 mm of the multiparticle simulation, i.e. from z=0.1 m to z=0.165 m. This is a strong assumption and therefore should be validated experimentally, by measuring the emittance the closest to the source extraction and benchmarking the simulation output thorough backtracking. The adoption Einzel lens obviously breaks the compensation, due to the high static electric fields, therefore in such case the beam is assumed uncompensated (ϕ=0%) from from z=0.1 m to z=0.350 m;
- in the RFQ interface area, close to the RFQ injection area, the beam is considered completely uncompensated (ϕ=0%) in the last 30 mm of the beam line, i.e. between the electron repeller to the RFQ rods, due to static electric field of the repeller. Such choice seems counterinteractive, as the SCC is abrupt broken where the RFQ injection takes place: it is instead highly beneficial during SCC restoring transients as a more populated neutralizing particle density is achieved during chopper transients [93].

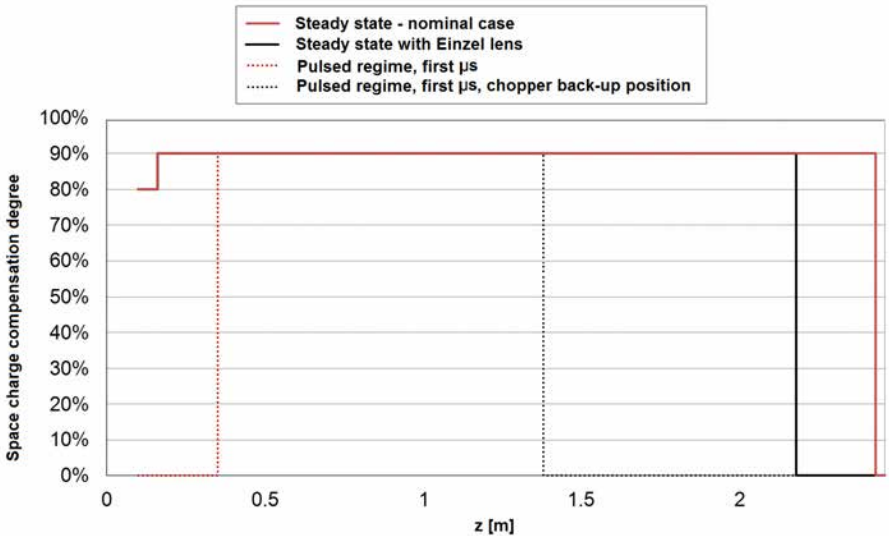

Figure 6.54: Space charge compensation degree considered along the MYRRHA LEBT in multiparticle beam transport design simulations.

In LEBT chopper pulsed regime, the process is more difficult to be accurately modelled. The SCC process is broken each time the beam is chopped, due to the high electric field exerted by the deflector, and in the first instants after restoring the beam experiences an uncompensated regime until the SCC reaches its steady-state. Such a process can have crucial consequences on the beam behaviour and emittance growth. In order to minimize the *amplitude* of the induced mismatching at each pulse beginning, the chopper is inserted as close as possible to the RFQ injection, such to minimize the distance to be traveled by the resuming beam at $\phi \approx$0%.

A multiparticle simulation of such conditions has been carried to asses the beam behaviour. The simulated emittance evolution, corresponding to a picture of the beam dynamics emerging in the first microseconds of a chopper pulsed regime, is visible in Figure 6.55. With respect to the nominal tuning obtained in the steady-state simulation (see Fig. 6.50), the beam is considered to be completely uncompensated (ϕ=0%) in the RFQ interface, i.e. in last 270 mm of the beam line. The SCC induced transient are clearly visible in the emittance growth resulting at the RFQ output, that is about 20% higher than in steady state. The beam is still capable to enter the RFQ injection but with a slight mismatch inducing a degradation in the RFQ transmission, which lowers

to about 95%. Such transient would mean a loss in beam intensity delivered to the MYRRHA reactor of about 0.2 mA.

The same study has been applied for the chopper in back-up position. Harsh transients are expected due to the increased distance to be covered in uncompensated regime. The simulations confirm such expectations: in the first microseconds of a chopper pulsed regime, the RFQ transmission reduces to less than 30%, due to largely mismatched conditions provided by the LEBT at its entrance. These conditions, if confirmed, are unacceptable and require a further beam cleaning, for instance with the adoption of a fast magnetic kicker in the Medium Energy Beam Transfer (MEBT) line.

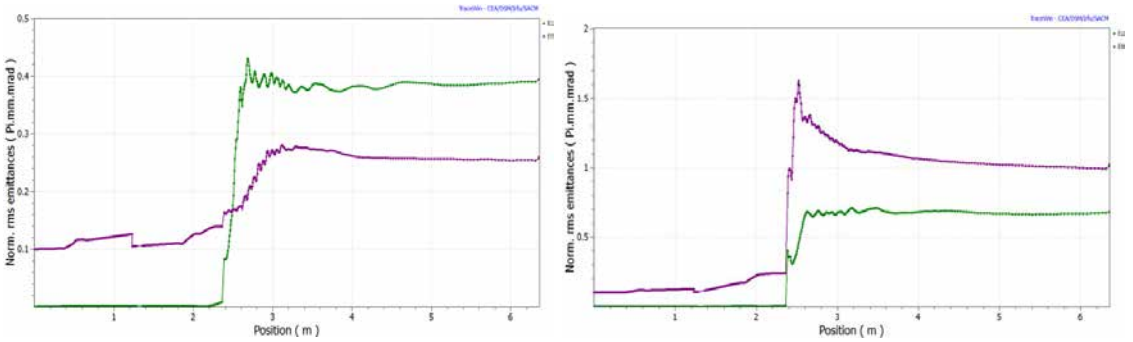

Figure 6.55: Snapshot of the transverse emittance evolution along the MYRRHA LEBT and the MAX RFQ during the first microseconds after a beam chopper pulse: chopper in nominal position (left) and in back-up position (right).

The emerging picture shows a negative impact of SCC uncompensation transients, which should be minimized in terms of duration. Longer times before restoring of a neutralized regime will imply more severe lasting of beam degraded conditions and so higher induced beam losses in the downstream section. In case the transients will appear incompatible in amplitude, the adoption of a fast chopper, as mentioned, will bring additional limitations in term beam delivery, as the possible span of beam time structures processable will reduce due to the difficulty of producing very short beam interruptions.

As introduced in Section 4.2, the characteristic space charge compensation transient time, τ, is the figure of merit of the SCC uncompensation transients, which here we rewrite in explicit manner

$$\tau = \frac{k_B T}{\sigma_{ioniz} p \beta c} \tag{6.34}$$

where k_B is the Boltzmann constant, T the temperature of the residual gas and σ_{ioniz} is the ionization cross section for 30 keV protons. The SCC transient time can typically range from a few tens to a few hundreds of microseconds and mainly depends on the main residual gas nature and its pressure conditions. As noticeable in Eq. 6.34, fixed a gas type, the higher is the pressure and the lower will result the SCC characteristic transient time.

On the other hand, in order to ensure a correct beam transmission (>80% at least) over the LEBT, the pressure level has to be contained to limit proton losses by electron capture, or charge exchange, $H^+ \rightarrow H$. A figure of merit is the transmission efficiency, calculated as the probability for a proton of overcoming a parasitically capturing perfect residual gas slab over the L=2.8 m of the LEBT line

$$T = e^{-(\sigma_{capt} n_{gas} L)} = e^{-\frac{\sigma_{capt} p L}{k_B T}} \tag{6.35}$$

where σ_{capt} is the capture cross section for 30 keV protons.

Figure 6.56 shows the estimated transmission probability T and the neutralization characteristic transient time τ for different vacuum pressure levels. The adopted ionization and capture cross sections are the ones for hydrogen, $\sigma_{ioniz} = 2 \cdot 10^{-20}\text{m}^2$ and $\sigma_{capt} = 1 \cdot 10^{-19}\text{m}^2$ [95]. In order to guarantee at least a transmission of $> 80\%$, the expected SCC transient time will not be shorter than typically 20 μs, which is non negligible if we compare with pulse length the MYRRHA

accelerator has to a ISOL facility (190 μs). A non-preferred option is to tolerate the induced beam losses and admit a 50% LEBT transmission, allowing to increase the pressure level up to 10^{-4} mbar and reducing the SCC transient time of an order of magnitude, while requiring the ECRIS to deliver a doubled beam current.

Figure 6.57 shows influence of different dominant residual gases on achievable neutralization characteristic transient times τ for different vacuum pressure levels. The adopted ionization and capture cross sections are the ones for hydrogen, nitrogen, argon and krypton [95]. Increasing the mass number, the availability of less energetic (on outer shells) electrons increases σ_{ioniz}, therefore, for an equal gas density, τ is less for heavier mass gases.

In order to maximize the LEBT performances, it is highly necessary to have a better understanding of those SCC effects, and in particular in transient regime. The MYRRHA LEBT test stand being built up in the RFQ@UCL program represents a valuable opportunity to develop and improve existing analytical models and simulation (such as SOLMAXP [93] and WARP [96] codes) against experimental results. A set of dedicated experiments is foreseen to assess the SCC level and transient time along the whole line. Chopper-synchronized beam instrumentation and control of the vacuum system will be required, in order to evaluate the influence of different injected gas types (N_2, Ar, Kr, etc.) and pressures on the SC compensation process.

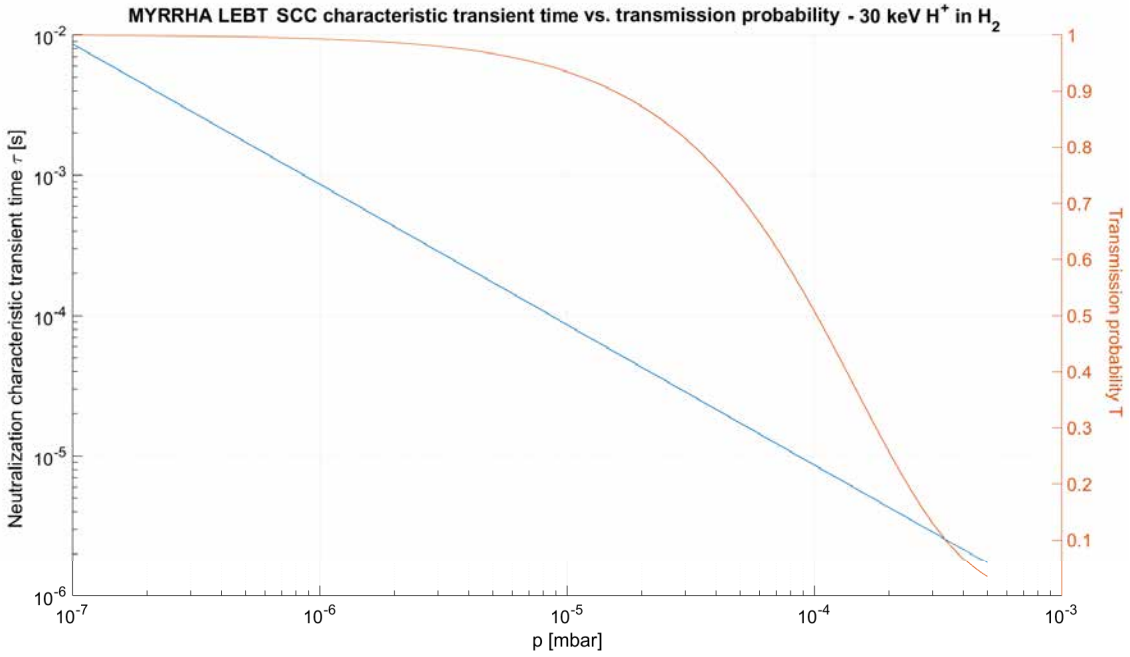

Figure 6.56: Calculated neutralization characteristic transient time and LEBT transmission probability for different pressure levels along the MYRRHA LEBT.

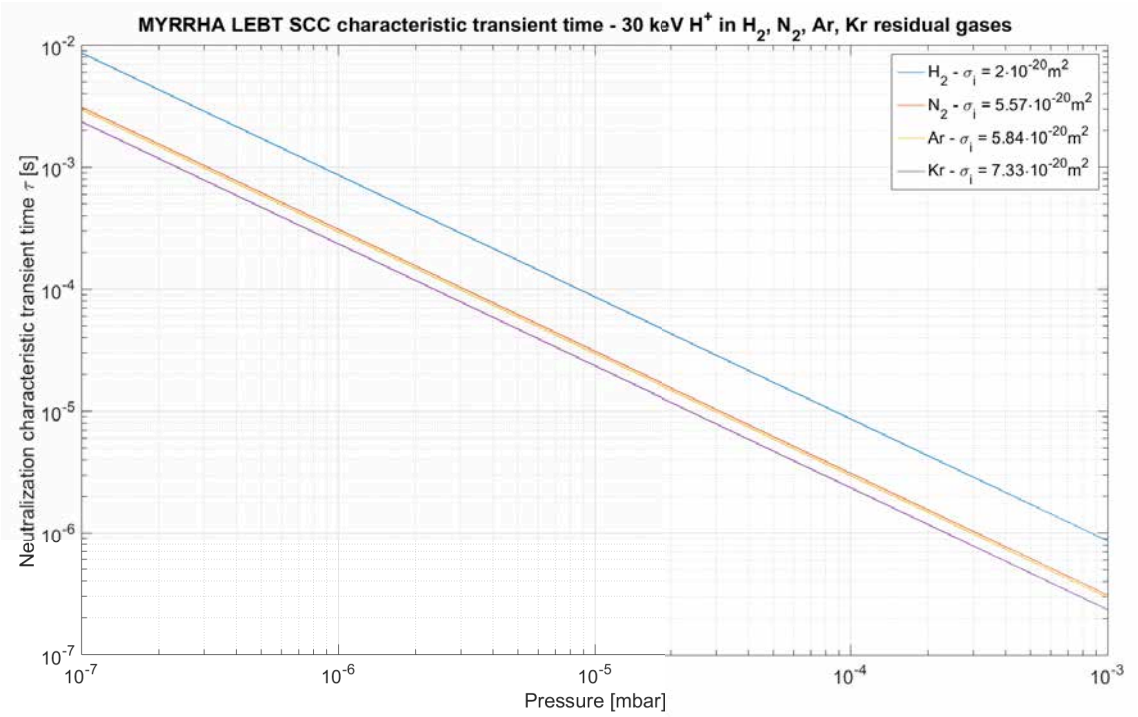

Figure 6.57: Calculated neutralization characteristic transient time for different levels of H_2, N_2, Ar, Kr dominant residual gases along the MYRRHA LEBT.

Part II

Electron cloud effects

Chapter 7

Electron cloud build-up

7.1 Introduction

In high energy particle accelerators, the secondary emission of electrons in conjunction with alternating electromagnetic fields can meet the conditions required to build-up an avalanche electron multiplication. The underlying mechanisms, the multipactor effect, is commonly observed in radio frequency (RF) engineering, and is usually associated with deleterious effects, such as voltage breakdown, heating, gas desorption. In particle accelerators, beam induced multipacting is driven by the electric field generated by the successive passage of charged particle bunches, which may rise a resonance motion of secondary electrons leading to the formation of a so-called Electron Cloud (EC).

Low energy electrons have shown to be a serious concern in high energy positively charged (e.g. proton, positron, ion) particle accelerators since 50 years [13], and electron cloud effects are among the major limitations of present high energy colliders, such CERN Large Hadron Collider (LHC) [14], Relativistic Heavy Ion Collider (RHIC) [15], KEKB [16] and DAΦNE [17] electron-positron colliders.

Figure 7.1 presents a qualitative scheme of the electron cloud build-up in positively charged circular accelerators. Beam particles can produce low energy negatively charged particles, so-called primary or *seed* electrons, via different mechanisms: e.g. residual gas ionization, photoemission on the beam chambers' walls by synchrotron radiation photons, slow beam particle losses on the beam pipe. Seed electrons may interact with the circulating beam bunch via Coulomb attraction and, after the bunch passage, can result to be accelerated to energies of several hundreds of eV before striking the beam pipe walls. At this stage, depending on the impinging electron parameters and the surface properties, both reflection and secondary electron emission can occur. The second leads to the production of *secondary* electrons, whose typical energy can run up to few tens of eV. Depending on their emission direction and velocity (energy), some of them could reach the pipe walls before a second beam bunch passage, and in this case, due to their low energy, absorption or reflection - but no secondary emission - may take place. Electrons surviving until a new bunch passage, instead, are in turn accelerated and projected on the wall, producing new secondary electrons. The recurrent multiplication of electrons due to short distanced bunch passages finally builds-up, forming an avalanche, which constitutes an electron cloud persisting the passage of the complete bunch train.

Electron cloud can have a charge density so high to influence the beam quality at each passage, inducing instabilities and losses. On the machine side, detrimental effects such as vacuum pressure rise and heat dissipation can become so harmful to trigger the protection schemes and cause a beam stop.

In this chapter, the processes leading to the formation of electron cloud will be analysed in each mechanism, presenting their key parameters. The implication on the beam and on the machine will be then presented.

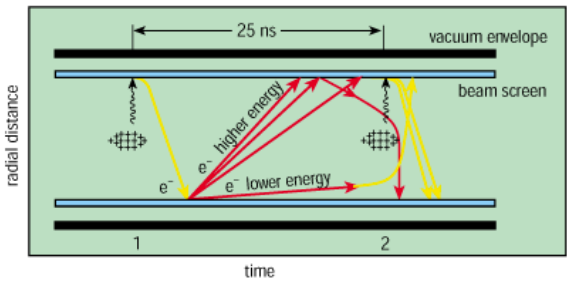

Figure 7.1: Qualitative scheme of the electron cloud formation process in the LHC, appeared on the CERN Courier in 1999 [97].

7.2 Primary electrons production mechanisms

Three primary electrons production mechanisms are of interest for proton bunched particle accelerators: residual gas ionization, photoemission by synchrotron radiation and beam losses.

7.2.1 Residual gas ionization

In order to guarantee the required beam lifetime and low radiation background, particle beams circulate within a volume - defined by beam chamber - where low gas density is ensured. The rate of nuclear scattering leading to beam losses is thereby minimised. In a vacuum system, the residual gas molecular density is defined by the ideal gas state equation:

$$pV = nk_BT \tag{7.1}$$

It relates the pressure p (in Pa $= 10^{-2}$ mbar) and volume V (m^3) of a rarefied gas to its number of molecules per unit volume and temperature through the Boltzmann constant ($1.38 \cdot 10^{-23}$ Pa m^3 K^{-1}). In the case of the LHC arcs (86% of the machine length), held at cryogenic temperature (5-20 K), in order to ensure a beam lifetime of 100 h the design gas density is $\leq 1 \cdot 10^{15}$ $\frac{\text{molecules}}{\text{m}^{-3}}$ for the dominating residual specie (H_2), and corresponds to a vacuum pressure of $\leq 1 \cdot 10^{-7}$ Pa.

Within the beam volume, the circulating beam high energy particles ionise the molecules of residual gas, producing free electron-ion pairs. The electron-ion production rate per unit volume depends on the partial pressure p_n of the single species present in the residual gas and their relative ionization microscopic cross section σ_n^{ion}, and is

$$\frac{dn_{ion}}{dtdAds} = \phi_b(x,y,s,t)\frac{\sum p_n(x,y,s,t)\sigma_n^{ion}}{k_BT} \tag{7.2}$$

where ϕ_b is the beam particle intensity per unit area, or beam flux.

The ionization cross section differs for the different gas species of the residual gas [98]. A compilation of ionization cross sections σ_n^{ion} for the gas species of interest in UHV is available from [99] and is reported in Table 7.1 for single charged particle proton beams at SPS injection energy and LHC design top energy.

Table 7.1: Ionization cross sections for different gas species for singly charged ultrarelativistic positive particles in 10^{-18} cm^2, or Mbarn, from Rieke and Prepejchal [98], calculated at SPS injection energy and LHC design energy. From [99].

	σ_n^{ion} [Mbarn]	
Gas	**26 GeV**	**7 TeV**
H_2	0.22	0.37
He	0.23	0.38
CH_4	1.2	2.1
CO	1.0	1.8
Ar	1.1	2.0
CO_2	1.6	2.8

Globally, the ionization cross section of relativistic proton beams interacting within a UHV system is in the order of few tents to few units of Mbarn (10^{-18} cm) and roughly doubles from 26 GeV to 7 TeV.

When the residual gas is dominated by a single specie and can be safely considered uniform in space and constant in time (at least in the time scale of some beam revolutions), Eq. 7.2 is reduced to

$$\frac{dn_{ion}}{dt} = \sigma^{ion} n_{gas} \phi_b \tag{7.3}$$

where σ^{ion} is the ionization cross section of the considered dominating single gas specie of density n_{gas}.

The amount of electrons produced by residual gas ionization is therefore primarily determined by the quality of vacuum and the beam intensity. The composition of the residual gas, which influences ionization cross section, can vary the electron-ion pair production rate of a order of magnitude. A weak dependence on the beam energy is observed through the ionization cross section as its variation is small over the beam energy of interest for modern proton accelerators.

It is worth to mention that, in some applications, ionization of electron/ion pairs can be produced, along beam scattering, by other sources. An example is the application of strong external electric fields, such electric fields present in particular machine insertions (RF cavities, etc.). This contribution can locally overcome the one produced by beam scattering.

7.2.2 Photoemission by synchrotron radiation

Synchrotron radiation is the emission of photons occurring when a charged particle undergoes a transverse acceleration. In a synchrotron, the most important source of synchrotron radiation is by the bending dipole magnets, or artificially by undulators or wigglers. Synchrotron radiation is characterized by specific quantities [100] [101]. The average power emitted per unit length by a beam of particles of current I_b undergoing a bending curvature of radius ρ is

$$P_0 = \frac{e\beta}{3\varepsilon_0 (m_0 c^2)^4} \frac{E_b^4}{2\pi\rho^2} I_b \tag{7.4}$$

where ε_0 is the vacuum permittivity, e the elementary charge, m_0 the rest mass of the beam particle. The emitted power has a strong dependence ($1/m_0^4$) on the rest mass, and increases rapidly with the beam energy (fourth power). It is quadratically inversely proportional to the bending radius. Considering a beam of ultrarelativistic protons, a practical form of the power emitted per unit length can be obtained from Eq. 7.4 as:

$$P_0 = 7.79 \cdot 10^{-12} \frac{E^4[\mathrm{GeV}^4]}{2\pi\rho^2[\mathrm{m}^2]} I_b[\mathrm{mA}] \frac{\mathrm{W}}{\mathrm{m}} \tag{7.5}$$

For example, in the case of LHC, synchrotron radiation power deposited on the arc dipoles accounts 0.2 W/m at design energy.

The emitted synchrotron radiation spectrum is characterised by its critical energy, ε_c, which corresponds to the energy at which the integrated synchrotron radiation power spectrum is divided by two:

$$\varepsilon_c = \frac{3}{2} \frac{hc}{2\pi} \frac{\gamma^3}{\rho} \tag{7.6}$$

Again, a practical form of Eq. 7.6 for protons is

$$\varepsilon_c = 3.85353 \cdot 10^{-7} \frac{E^3\ [\mathrm{GeV}^3]}{\rho\ [\mathrm{m}]} \mathrm{eV} \tag{7.7}$$

It is worth to note that the critical energy of synchrotron radiation emitted by the LHC proton beam at 7 TeV corresponds to 44 eV.

The total flux of photons produced per unit length in a bend is:

$$\dot{\Gamma} = \frac{5\sqrt{3}e}{12h\varepsilon_0 c}\frac{\gamma}{\rho}I \tag{7.8}$$

which reduces to the pratical form for protons of

$$\dot{\Gamma} = 7.017 \cdot 10^{13}\frac{E\ [\text{GeV}]}{\rho\ [\text{m}]}I\ [\text{mA}]\frac{\text{photons}}{\text{m}} \tag{7.9}$$

The flux of photons emitted by synchrotron radiation is characterized by a spacial and energy distribution. For a relativistic emitting particle, synchrotron radiation is forward emitted, with an angular aperture that goes with $1/\gamma_{rel}$. For ultrarelativistic protons at LHC top energy, photons are practically distributed in a mrad aperture cone (see Fig. 7.2, left). The photon energy spectrum strongly varies with beam energy. In Fig. 7.2 (right), one can appreciate the photon spectrum at LHC injection (450 GeV) and top (7 TeV) design energy. The LHC emits in the VUV range, and only above ∼2.5 TeV a significant fraction of photons has energies in the eV range.

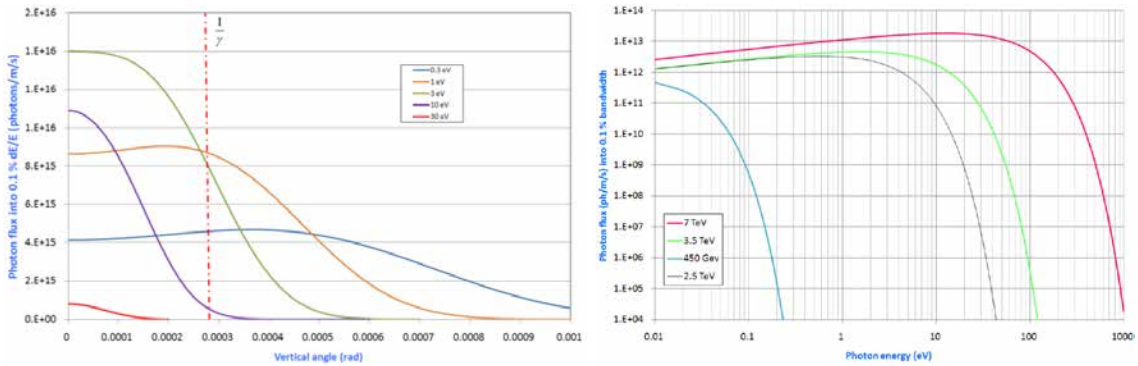

Figure 7.2: Left: the LHC synchrotron radiation photon flux spatial distribution in the vertical plane. Right: Synchrotron radiation energy spectra of an LHC dipole evaluated at injection energy (450 GeV), at energy where synchrotron radiation energy becomes relevant for electron cloud (2.5 TeV), Run 1 top energy (3.5 TeV) and design top energy (7 TeV). From [101].

Photoemission of electrons by synchrotron radiation impinging photons can occur when a non-negligible portion of the synchrotron radiation spectrum falls above the surface material work function. For instance, the work function of Cu is 4.2 eV [102]. For LHC beams, synchrotron radiation becomes a relevant primary electrons source as of 2.5 TeV (see Fig. 7.2). In this conditions, photons, when impinging on the beam chamber surface, will have enough energy to extract one electron from the material, undergoing photoelectric effect. The quantity characterizing photoemission is the photoelectric yield (Y) or quantum efficiency, which corresponds the number of electrons produced per incident photon by photoelectric effect as a function of the angle of incidence and photon energy. In general, $Y(E, \theta)$ increases with the photon energy; the same effect is observed increasing the incidence angle, as for grazing angle, given the small penetration depth, more photoelectrons are produced closer to the surface and therefore become able to escape.

In particle accelerators, the beam chambers are illuminated by synchrotron radiation at grazing incidence. In the case of LHC, each dipole emits synchrotron radiation over its magnetic length (14.3 m), which impinges the same element at the grazing incidence angle of 5.1 mrad, for only 2.9m (the remaining part carried to the next element or straight section) [101].

Due to grazing impinging incidence, however, specular photon reflection is highly expected at LHC photon energies and incident angles [103]. For smooth surfaces, for instance, reflectivity can run up to the unity [104]. In the LHC case, VUV photons are expected to scatter more readily than higher energy photons (soft x-rays). In reality, technical surfaces have a finite roughness and are not perfectly radiators. Thus, a percentage of the incident photons are absorbed, another mirror (forward) reflected, another diffused and a last one backscattered. An azimuthal (spatial) distribution - corresponding to the undergone process - will come as a result (see Fig. 7.3, left).

Lastly, reflected and/or diffused photons do not perfectly conserve their emission energy spectrum, which tends to be shifted toward lower energies (Fig. 7.3, right).

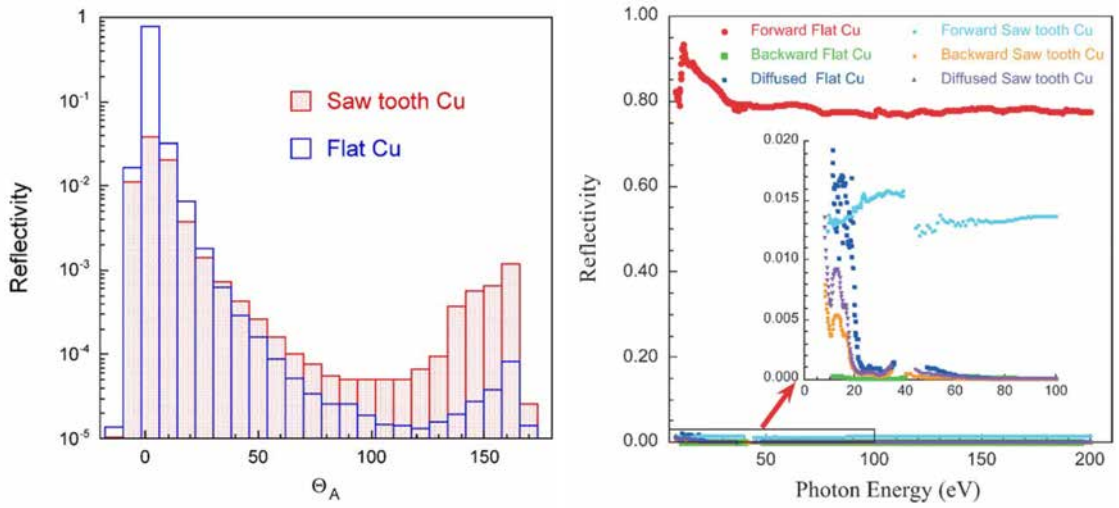

Figure 7.3: Laboratory reflectivity characterization. Left: measured azimuthal distribution of the reflectivity of Cu and sawtooth-ed Cu samples with a LHC-type photon spectrum distribution. Right: spectral composition of the reflectivity in three reflection regimes (forward, backward, diffused) of Cu and sawtooth-ed Cu samples, employing monochromatic incident light. From [103].

As such, photoemission is characterized by two figures of merit: the surface photon reflectivity, R, and the photoelectron yield per absorbed photon, Y^*, respectively defined as the fraction of photons scattered on the material surface over the total number of impinging photons, and the number of photoelectrons produced per absorbed photon. Both have been characterized in many theoretical and experimental campaigns during the design phase of LHC [105] [106] [107] [103].

Table 7.2 provides a compilation of such parameters as a result of the experimental campaign carried during the LHC design phase in [105]. The colaminated Cu showed the highest forward reflectivity and photoelectric yield. Increasing the surface roughness (air baking forming an oxide layer, electroplated deposition, and finally geometrical sawtoothing) offers a convenient method for decreasing both parameters, in particular the reflectivity.

		45 eV	
Surface	Status	R (%)	Y* (e/ph)
Cu co-lam.	as-received	80.9	0.114
	air baked	21.7	0.096
Cu elect.	as-received	5.0	0.084
Cu sawtooth	as-received	1.8	0.053
	150°C, 9h	1.3	0.053
	150°C, 24h	1.3	0.040

Table 7.2: Forward scattering photon reflectivity and photoelectron yield per absorbed photon with a LHC-type synchroton radiation spectrum (critical energy: 45 eV) for three Cu surfaces. From [105].

Once the impinging photon flux is known, the rate of production of photoelectrons per unit length and per beam particle can be estimated as

$$\frac{dn_{ph}}{ds} = Y^* \dot{\Gamma} \cong Y^* \frac{5}{2\sqrt{3}} \frac{\alpha \gamma_{rel}}{\rho} \tag{7.10}$$

where α is the fine structure constant [108].

As mentioned, the azimuthal distribution of the photoemitted electrons depends on the photon spectrum spatial characteristics (and in turn, to the beam parameters) and the shape and reflective properties of the beam chamber. With respect to electron cloud, such element have a great importance in the build-up and multipacting.

Photoelectrons emitted in the beam orbit plane are affected by the (perpendicular) dipole magnetic field, which constrains the electrons to rotate around the field line with a small cyclotron revolution radius. Such effect is beneficial as these electron cannot participate to the electron cloud formation as they do not gain energy in the beam field crossing the beam chamber.

On the other hand, depending on the surface roughness, a fraction of the impinging photons will be (mainly forward) reflected, illuminating different portions of the beam chamber and producing in turn photoelectrons with a non-zero azimuthal component perpendicular to the orbit plane and parallel to the magnetic field lines. Such electrons will spiral vertically across the beam chamber cross section, gain energy in the beam field and actively participate to the secondary electron production and multiplication, as it is the case in the field-free regions. For all these reasons, not only the photoelectric yield is of great importance, but also the photon reflectivity, which should be minimized if one wants to constrain the photoemission on the orbital plane. This condition was enhanced in the LHC beam screen design, which foresees a sawtooth surface (30 μm steps over a 500 μm period) reducing the specular photon reflectivity to less than $\sim 2\%$ [105].

7.2.3 Losses

Emission of electrons can be caused by the impact of protons or heavy ions on the solid wall of the beam chambers. This is the case of beam losses occurring in collimation areas or energetic ions (produced by residual gas ionization) in experimental chambers exposed to external solenoidal magnetic fields [109]. For ion energies above 100 KeV/amu, the electron emission yield is infact remarkable (>> 1) at nearly grazing angles [110]. At such energies, the impingement/escape of an ion into/from a solid surface results in an electron emission from within the solid: the production follows a threefold process following described.

Firstly, the impinging ion transfers energy to the electrons in the solid, at a rate determined by the electronic stopping power $\left(\frac{dE}{dx}\right)_e$, which is dominant at energies above 100 KeV/amu. The produced electrons scatter and cascade, multiplying and diffusing through the solid. The emission of electron from the ion impingement surface side is thought to be caused principally by soft collisions, which produce low energy electrons. A small fraction of them - mostly originating from an escape zone or the surface layer - can overcome the surface potential barrier and escape into the vacuum side. The diffusion length of such low energy electrons should depend principally on the target material, and not relevantly on the projectile mass and kinetic energy.

Following the described process, the relation providing the backward electron yield for thick targets (the mean number of electrons backward emitted per incident ion) has the form of

$$\delta_l = \Lambda_M \beta_S \left(\frac{dE}{dx}\right)_e cos^{-1}(\theta) \tag{7.11}$$

where Λ_M is a phenomenological constant for the material, θ the impingement angle with respect to the surface normal, and $\beta_S = 1 - \beta_\delta$ the amount of soft collisions, i.e. the fraction of projectile energy lost in low energy electrons in the matter. The relation in Eq. 7.11 should be corrected for heavier ions both for what concerns the yield and the angular dependence as follows

$$\delta_l = \delta_l(0) cos^{-f}(\theta) = C_B \Lambda_B^{Z=1} \left(\frac{dE}{dx}\right)_e cos^{-f}(\theta) \tag{7.12}$$

where $C_B = 1$ for protons and $\Lambda_B^{Z=1}$ is the ratio of the same emission for protons at normal incidence over their electronic stopping power $\delta_l^{Z=1}(0)/(dE/dx)_e$.

In Figure 7.4, the measured electron yield per impinging ion is shown, for three kind of high energy ion beams, as a function of their impingement angle. In the case of protons, the yield spans over three orders of magnitude. Data well fits the relation proposed in Eq. 7.11 for angles between 0°and 89.5°. With respect to Eq. 7.11, the measured data is extrapolated to 1 GeV protons, which was of interest for the collimation regions of the Spallation Neutron Source [111].

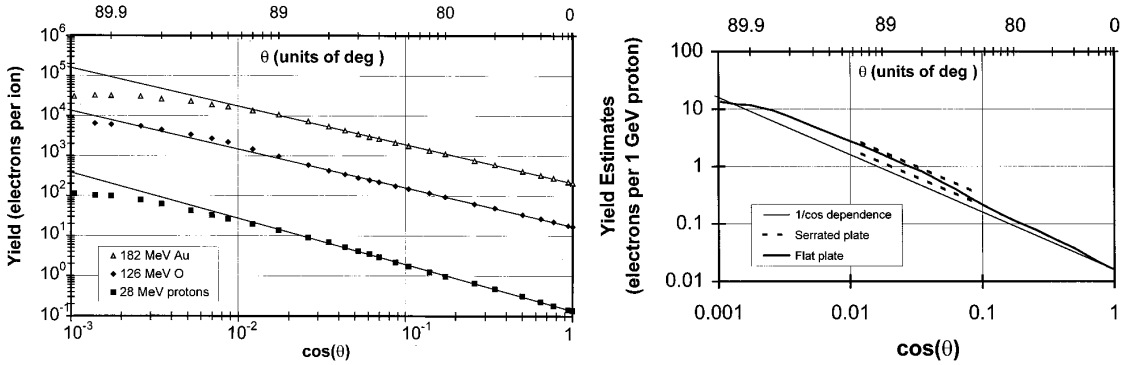

Figure 7.4: Electron yield measured for 26 MeV H, 126 MeV Au, and 182 MeV O beams incident on flat or serrated stainless steel surfaces as a function of the impingement angle θ. From [110].

7.3 Secondary electron emission

The secondary emission of electrons for laboratory prepared or technical surfaces has been extensively studied in the last decades, in order to provide the required input data to the electron cloud build-up estimations in circular particle accelerators. One of the biggest efforts to characterize the driving mechanisms and key parameters of secondary electron emission was during the Large Hadron Collider technical design phase, across the 2000's [112] [113] [114].

Following the incidence a of a primary electron, the surface secondary electron emission process can be summarized in three steps [115]: penetration or reflection of the primary electron, transmission of the secondary electrons through the material, escape from the impingement surface into the vacuum barrier (see Fig. 7.5).

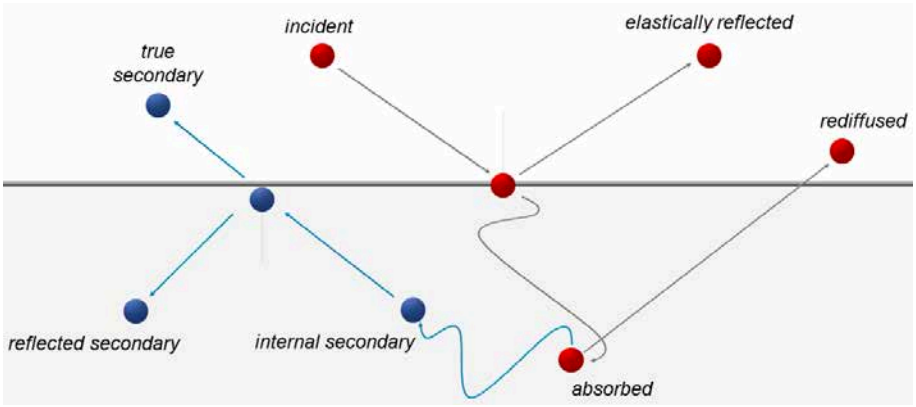

Figure 7.5: Schematic depiction of the possible processes occurring when an electron interacts on a solid surface.

The first two processes are intrinsically related to the electron ability to travel within the solid. From the universal mean free path visible in Fig. 7.6, one can observe that electrons of energy in the range of interest of the electron cloud build-up (10 eV to 1 keV) can travel in the solid up to few atomic layers, e.g. 10 Å. A primary electron - with reasonable kinetic energy - therefore travels very short distances in the solid before interacting and generating secondary electrons. This first determines the sensitivity of a material to emit electrons by secondary emission.

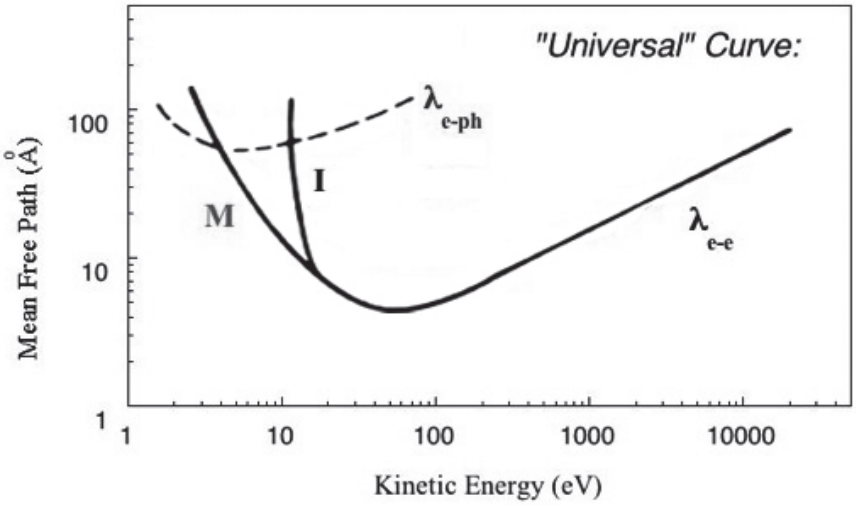

Figure 7.6: The universal mean free path curve describing the energy dependence (mediated over a range of materials) of the escape depth of electrons in metallic (M) and insulator (I) solid, for electron-electron (λ_{e-e}) and electron-phonon (λ_{e-ph}) scattering.

The subsequent production and transmission of secondary electron depends on the electronic properties of the material, which in turn affect the secondary electron yield. Electrons travelling in metals lose energy by interaction with the conduction electrons, lattice vibrations (phonons) and defects. So, while transmitting, secondary electrons lose their energy very efficiently, producing a cascade of internal secondary electrons. As soon as these electrons reach the solid surface, only a small fraction has the energy required to overcome the surface potential and escape back into vacuum. In insulators, due to the wide band gap, low energy electrons cannot produce efficiently secondary electrons via electron-electron interaction. One can observe from Fig. 7.5 that, below 10 eV, the electron-phonon scattering is dominating. Such effect results in a lower surface sensitivity to emit secondary electrons, and a higher yield, as the electron reaching the surface barrier are more energetic.

It should be observed that grain boundaries, defects, impurities greatly affect the mean free path, modifying the dominant interaction (electron-electron, electron-phonon) process. In addition, the electron escape (third) step is essential to determine the secondary emission yield. The kinetic energy required to an internal secondary electron to escape into vacuum should be at least larger than the surface work function W. In some conditions, due to their angle, internal reflection may occur even to electrons whose energy is slightly above W, determining a limit angle θ_{lim}. The outermost layer of the surface can determine the actual surface work function, and so add an additional dependence on the secondary electron emission. For instance, metals work function can vary on the crystal surface orientation and reconstruction. Metals with different surface roughness exhibit different W. Submonolayer quantities of gas adsorbed on metals can significantly vary their work function. The sensitivity of the surface conditions and their degree of contamination (by insulators for instance) can thus vary greatly W and so, in particular, enhance the secondary emission of the so-called *technical surfaces*.

The secondary emission of a surface is described by the Secondary Emission Yield curve, defined as the ratio of the emitted secondary current arising from the impingement of a primary electron current on a solid surface; it is a function of the energy of the impinging electrons:

$$\delta(E) = \frac{I_{emitt}}{I_{imp}(E)} \tag{7.13}$$

A typical example of SEY curve is presented in Fig. 7.7.

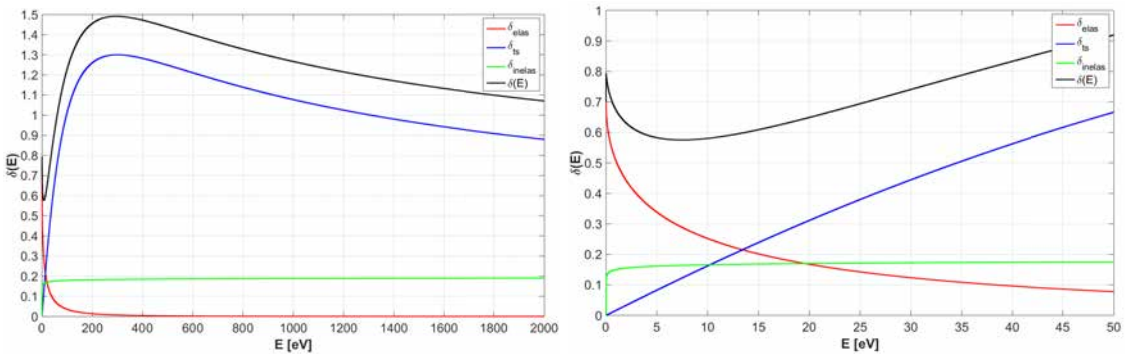

Figure 7.7: The Secondary Emission Yield (SEY) curve in the energy range of interest for electron cloud. The contribution of the elastic (low energy) and inelastic (high energy) electrons with respect to the true secondaries is better visible on the zoomed plot on the right.

The curve is the result of three main contributions:

$$\delta(E) = \delta_{elas}(E) + \delta_{sec}(E) + \delta_{inelas}(E) \tag{7.14}$$

The low energy component is dominated by the elastically reflected electrons, which is prevalent for the first tenths of eV. The electrons corresponding to this region of SEY interact elastically with the surface and so are specular backscattered with the same energy of impact. This component is well fitted by the following relation [113]

$$\delta_{elas}(E) = R_0 \left(\frac{\sqrt{E} - \sqrt{E + E_0}}{\sqrt{E} + \sqrt{E + E_0}} \right)^2 \tag{7.15}$$

which is similar to the solution of a quantum-mechanical problem considering a plane-wave electron wave function incident on a negative step potential of depth E_0, equal to 150 V for fully scrubbed Cu held at 10 K (LHC case). R_0 is the reflectivity factor for electrons impinging at zero energy and is considered to vary between 0.5 and 1. Considering elastically reflected electrons, from Fig. 7.7 one observes that the SEY curve is relatively high in such energy region, and this suggests that low energy electrons may have a much longer survival time inside vacuum chambers, which in turn could significantly enhance the electron cloud build-up process. The role of low energy electrons has been firstly introduced in [113], and their impact on the electron cloud build-up and associated heat load has been shown to be rather significant [116]. —There is a great debate on such energy region [115], which is difficult to be experimentally addressed in laboratory due to extreme sensitivity to small electromagnetic fields, space charge effects and limited control in the primary electron beam energy resolution. Latest measurements [116] carried on technical surface show evidence on significant SEY in such region, which is linked to the surface contamination rather than experimental artefacts.

The true secondaries component, appearing significant above the elastically reflected region (e.g. >20 eV), has the form [117] of

$$\delta_{sec}(E) = \delta_{max} \frac{s \frac{E}{E_{max}}}{s - 1 + \left(\frac{E}{E_{max}} \right)^s} \tag{7.16}$$

where s≈1.35 is a parametrization coefficient obtained from several measured datasets for Cu [113]. E_{max} is the energy to which corresponds the maximum yield of true secondaries, and where the global SEY curve reaches the maximum value of

$$\delta(E_{max}) \simeq \delta_{sec}(E_{max}) = \delta_{max} \tag{7.17}$$

δ_{max} is the main parameter describing the secondary emission properties of a surface, and is strongly dependent on the surface material, its roughness and the history; as it plays a key role in the electron cloud build-up, it is always used as the reference parameter resuming the accelerator chamber wall conditions.

True secondary electrons are emitted with a cosine angular distribution with respect to the surface normal. They have a energy spectrum well fitted by a lognormal distribution [118] [119], as follows

$$\frac{dn_{sec}}{dE} = \frac{1}{\sqrt{2\pi}E\sigma_{sec}} e^{-\frac{[ln(E)-\mu_{sec}]^2}{2\sigma_{sec}^2}} \tag{7.18}$$

where, in the case of the LHC beam screen, the fitting parameters used are $\sigma_{sec} = 1.0828$ and $\mu_{sec} = 1.6636$. The energy distribution of the true secondaries in the LHC case are plotted in Fig. 7.8.

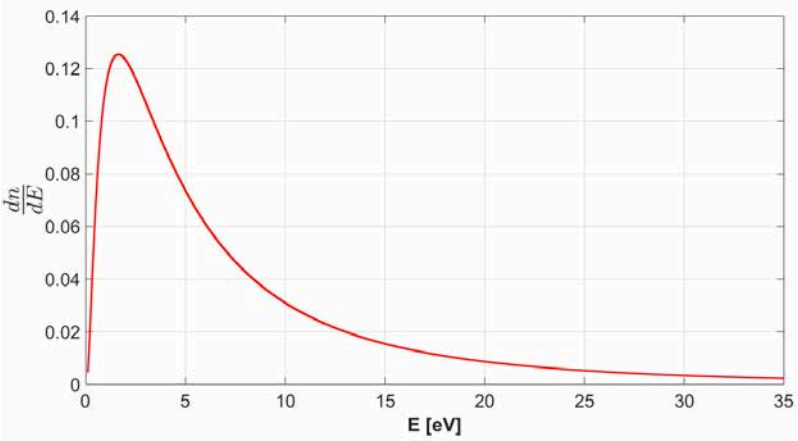

Figure 7.8: Normalized energy distribution of true secondary electrons in the low energies range.

Some of the incident electrons, penetrating into the solid wall, will scatter from one or more atoms inside the material and be inelastically reflected back out of the surface. From experimental data, the rediffused electron component can be written in the phenomenological form of [117]

$$\delta_{inelas}(E) = A\left(1 - e^{-\left(\frac{E}{E_r}\right)^r}\right) \tag{7.19}$$

where A=0.2, E_r=0.041 and r=0.104 for Cu [117].

The effect of the angle of incidence of the primary electrons is also of great importance for the electron cloud generation. An increase of SEY is expected when the angle of incidence shifts from the normal, because the primary electrons tend to dissipate their energy closer to the surface. In order to take into account this effect, the parameters E_{max} and δ_{max} can be rescaled as a function of the angle of incidence θ (with respect to the surface normal) as follows [117] [118] [120]:

$$E_{max}(\theta) = E_{max}(\theta = 0)[1 + 0.7(1 - cos\theta)] \tag{7.20}$$

$$\delta_{max}(\theta) = \delta_{max}(\theta = 0)e^{\frac{1}{2}(1-cos\theta)}. \tag{7.21}$$

The importance of the electron emission angular dependence is manifest in the case of accelerators arcs, where electrons tend to spiral along the dipole magnetic field lines.

7.4 Energy gain

Electrons produced by the mechanisms presented in Sect. 7.3 are commonly non-relativistic ($\|\mathbf{v_e}\| \ll c$): their limited kinetic energy goes up to few keV. When a bunch of positively charged beam particles, moving in the longitudinal direction s of a beam pipe, passes by, electrons are pulled toward the opposite charge by Coulomb attraction. The electric field responsible for the electrons energy gain is produced by the relativistic beam bunch distribution, and is Lorentz contracted of an angle proportional to $1/\gamma$ on the normal to the beam circulation direction. The first

result is that, with ultrarelativistic beams, electrons receive principally a transverse kick in the beam field, and their longitudinal motion can be neglected.

The charge distribution associated to a perfectly rigid beam (good approximation on the time scale of the electron cloud build-up) can be factorized as the convolution of a transverse charge distribution λ over the linear charge density at the section s in the instant t:

$$\rho(x, y, s, t) = \lambda(s - ct)\rho_\perp(x, y) \tag{7.22}$$

The transverse charge distribution associated to a slice of proton bunch is well approximated by a 2D Gaussian beam distribution, like

$$\rho_\perp(x, y) = \frac{N_b e}{2\pi\sigma_x\sigma_y} e^{-\left(\frac{x^2}{\sigma_x^2}+\frac{y^2}{\sigma_y^2}\right)} \tag{7.23}$$

which should satisfy the normalization integral over the transverse section S of the beam pipe

$$\int_S \rho_\perp(x, y)dxdy = 1. \tag{7.24}$$

The electric field generated by the charge distribution of Eq. 7.22 has itself the form of

$$\mathbf{E}(x, y, s, t) = \lambda(s - ct)\mathbf{E}_\perp(x, y). \tag{7.25}$$

Employing the first and third Maxwell's equations, the transverse electric field $\mathbf{E}_\perp$ is computed adopting the perfect electric boundary condition $\mathbf{n} \times \mathbf{E}_\perp = 0$ at the beam pipe's surface:

$$\begin{cases} \nabla \cdot \mathbf{E} = \frac{\rho}{\epsilon_0} \\ \nabla \times \mathbf{E} = -\frac{\partial \mathbf{B}}{\partial t} \end{cases} \rightarrow \begin{cases} \frac{\partial E_{\perp x}}{\partial x} + \frac{\partial E_{\perp y}}{\partial y} = \frac{\rho_\perp}{\epsilon_0} \\ \frac{\partial E_{\perp y}}{\partial x} - \frac{\partial E_{\perp x}}{\partial y} = 0 \end{cases} \tag{7.26}$$

For the Gaussian beam distribution introduced in Eq. 7.23, the associated scalar potential $\phi(x, y)$, satisfying the Gauss law $\nabla^2\phi = \frac{\rho}{\epsilon_0}$, is analytically available and has been derived in [121]. It can be written as

$$\phi(x, y) = \frac{N_b e}{4\pi\epsilon_0} \int_0^\infty \frac{e^{-\left(\frac{x^2}{\sigma_x^2+q}+\frac{y^2}{\sigma_y^2+q}\right)}}{\sqrt{(\sigma_x^2 + q)(\sigma_y^2 + q)}} dq \tag{7.27}$$

The associated electric field has been evaluated by Bassetti-Erskine (BE) by means of the complex error function [122] and provides a 2D analytical formulation of the transverse electric field $\mathbf{E}_\perp(x, y)$ in Cartesian coordinates.

Fig. 7.9 shows an example of the result of the application of the BE formula in the case of the LHC beam at 450 GeV/c inside an arc beam screen.

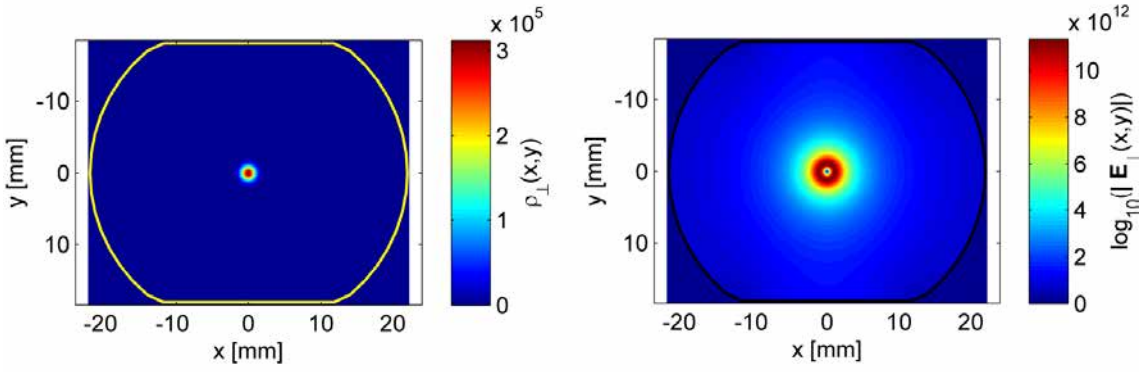

Figure 7.9: The transverse charge distribution $\rho(x, y)$ and relative electric field modulus $\|\mathbf{E}(x, y)\|$ calculated by pyECLOUD for the simulation of a Gaussian LHC proton bunch slice at 450 GeV/c inside an arc beam screen. From [123].

While the electron density is building-up due to beam induced multipacting, an increase of the negative space charge field associated with the electrons takes place. The effect of the electron density space charge must be taken into account when calculating the effective electric field seen by an electron. The electron space charge acts in opposition of positive charge field produced by the beam bunch passage. As we will discuss in Sect. 7.5, due to the compensation of the two fields, the electron cloud density and related impinging flux usually reaches an equilibrium after few bunch passages.

The electrostatic potential $\phi(x, y)$ associated to the electron density is the solution of the Poisson equation

$$\nabla^2 \phi(x, y) = -\frac{\rho}{\epsilon_0} \tag{7.28}$$

with the homogeneous boundary condition of perfect conductivity on the beam pipe, i.e. $\phi(x_p, y_p) = 0$. As the electron density varies during the build-up and strongly depends on the conditions of the considered section (geometry, surface properties, presence of magnetic fields, etc.), it cannot have, *a priori*, an analytical form. The electric field associated to the electron density is therefore often calculated adopting a Particle-In-Cell (PIC) algorithm, dividing the the beam chamber section in a squared grid of equally spaced points. The charge of the electron density is discretely distributed on the grid points, and the differential equation Eq. 7.28 is solved by Finite Difference (FD) method, applying the zero potential condition of the grid points identifying the chamber boundaries.

The electric field $\mathbf{E}(x, y) = -\nabla\phi(x, y)$ is finally calculated on the grid points and interpolated on the charges positions.

We have finally all the ingredients to estimate the energy gain of: *i)* the primary electrons created by residual gas ionization (in the central part of the pipe) or synchrotron radiation photoemission (next to the pipe's wall), *ii)* the secondary electrons created by impingement of the electrons via secondary emission, *iii)* the electrons already present in the beam pipe. This is computed by integrating the equation of motion in presence of the computed effective electric field and the external magnetic field (if present) provided by dipole or quadrupole magnets:

$$\frac{d\mathbf{v}}{dt} = -\frac{q}{m}\mathbf{E}(t) + v \times \mathbf{B}(t). \tag{7.29}$$

The precise tracking of the direction, velocity/momentum and final impact's position and angle is the key behind the electron build-up prediction, and requires refined numerical modelling. Many codes, such as pyECLOUD [123] [124], POSINST [125], CLOUDLAND [126] etc. have reached a mature level development and are employed for this purpose.

In the following, we offer a simplified but effective analytical method to estimate the energy gain of an electron during the passage of a proton bunch, developed in [127] and [115].

Consider the approximation of a relativistic Gaussian proton bunch of total number of charges N_b with a uniformly charged circular distribution cylinder, characterized by a rectangular and constant linear density

$$\lambda_b = \frac{N_b}{\sqrt{2\pi}\sigma_s} \tag{7.30}$$

where σ_s is the RMS bunch length. Assuming a perfectly conducting beam pipe, the electric field produced during the passage of a bunch, of RMS size σ_r, is purely radial, and has the form of

$$\mathbf{E}(r, s-ct) = \begin{cases} \frac{\lambda_b}{2\pi\epsilon_0\sigma_r^2} r \Pi\left(\frac{s-ct}{\sqrt{2\pi}\sigma_s}\right) & \text{for } r \le \sigma_r \\ \frac{\lambda_b}{2\pi\epsilon_0}\frac{1}{r}\Pi\left(\frac{s-ct}{\sqrt{2\pi}\sigma_s}\right) & \text{for } r > \sigma_r \end{cases} \tag{7.31}$$

In order to compute the energy gain, two different types of electron motion can be identified within the passage of the bunch, as a function of the initial electron position:

- in the "kick approximation", a test electron charge initially lies outside the beam core and is considered quasi-stationary throughout the bunch passage. This is the case of photoelectrons created by synchrotron radiation photoemission, and more specifically when the bunch and

its generated photons travel synchronously at c (true for non-reflected photons), or the case of secondary emitted electrons;

- in the "autonomous approximation", the test electron charge initially lies close or within the beam core and is strongly trapped in the bunch distribution. This is representative of the electrons created by residual gas ionization.

We assume here and in the following that the electron test charge has no initial momentum. A schematic view of the interaction of electrons with the proton bunch in these two regimes is available in Fig. 7.10.

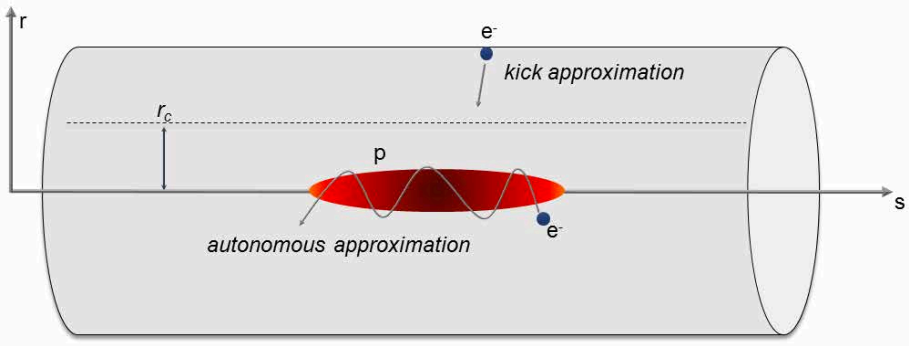

Figure 7.10: The considered "kick" and "autonomous" electron-bunch interaction regimes in a circular beam pipe.

The energy gained by an electron in the "kick approximation" regime is obtained by Eq. 7.31 and is

$$\Delta E_{kick} = 2m_e c^2 \left(\frac{N_b r_e}{r}\right)^2 \tag{7.32}$$

where r_e is the classical radius of an electron. Photoelectrons are generally created within the bunch passage. For an electron created at a time Δt, in a position Δs after the bunch head, the momentum gain can be rescaled by a factor $(\Delta t_s - \Delta t)/\Delta t_s = (\sigma_s - \Delta s)/\sigma_s$, where Δt_s or σ_s are the bunch lengths in time or length units.

In the "autonomous approximation" regime, electrons close to the beam core are trapped in the beam field and perform harmonic oscillations at a frequency of

$$\omega_e = \sqrt{\frac{2\pi r_e N_b}{\sigma_r^2 \sigma_s}} c. \tag{7.33}$$

The approximation ignores the time dependence of the longitudinal bunch profile, which is true if the frequency of the electron oscillations is large with respect to evolution time scale of the real longitudinal charge distribution function. The energy gained by an electron in such regime with the above assumptions is

$$\Delta E_{auto} = \frac{1}{2} m_e \omega_e^2 \sigma_r^2 = \frac{1}{2} m_e c^2 \frac{r_e N_b}{\sigma_s}. \tag{7.34}$$

One should note that, when the assumptions made for the "autonomous approximation" regime do not hold, i.e. the variation of the longitudinal bunch charge distribution is slow if compared to the oscillation period, than the process is quasi-adiabatic and little or no energy can be gained by an electron via this process.

In order to choose of approximation, the oscillation period of the autonomous approximation can be used as discriminant. If the oscillation period of Eq. 7.33 is long compared to the bunch length, than one should employ the kick approximation; in the opposite case, one should consider applying the autonomous one. Intuitively, one expects longer oscillation periods at large radii, due to the $1/r^2$ relation in the bunch electric field (see Eq. 7.31). A transition radius can be

therefore established. Taking into account that the maximum energy obtainable in the autonomous approximation is the one acquired performing a quarter oscillation, the critical radius r_c, separating the two regimes, corresponds to the radial distance for which the time of a bunch passage equals a quarter of the electron oscillation period, i.e.

$$r_c \cong 2\sqrt{N_b r_e \sigma_s \sqrt{\frac{2}{\pi}}}. \tag{7.35}$$

According to the assumptions made, the introduced definition clearly stands only if $r_e > \sigma_r$.

The above relationships have been applied to the LHC case ($\sigma_r = 0.2$mm, $\sigma_s = 77$mm) at top energy, at its nominal ($N_b = 1.15 \cdot 10^{11}$ppb) and ultimate ($N_b^* = 1.6 \cdot 10^{11}$ppb) design bunch intensity. The average value of energy gain in the two approximations are listed in the Table 7.3 below. The value corresponding to the energy gain of an electron laying next to the the beam pipe ($r = r_p$) is also calculated.

	r_c	$\overline{\Delta E_{auto}}$	$\overline{\Delta E_{kick}}$	$\Delta_{kick}(r = r_p)$
Nominal	8.5 mm	376 eV	350 eV	189 eV
Ultimate	10.5 mm	931 eV	632 eV	439 eV

Table 7.3: Analytic results for the energy gain of electrons in the LHC nominal and ultimate case in the autonomous and kick approximation regime [127].

A more realistic model [127] can be developed considering a non-uniform longitudinal and transverse bunch distribution, and taking into account the actual motion of electrons during the bunch passage. The equation of motion, governed by the electron Hamiltonian equation taking into account both the transverse and longitudinal bunch charge distribution, has been integrated numerically and the energy gain plotted against the initial electron's radial position. For the LHC nominal parameters, the result is presented in Fig. 7.11.

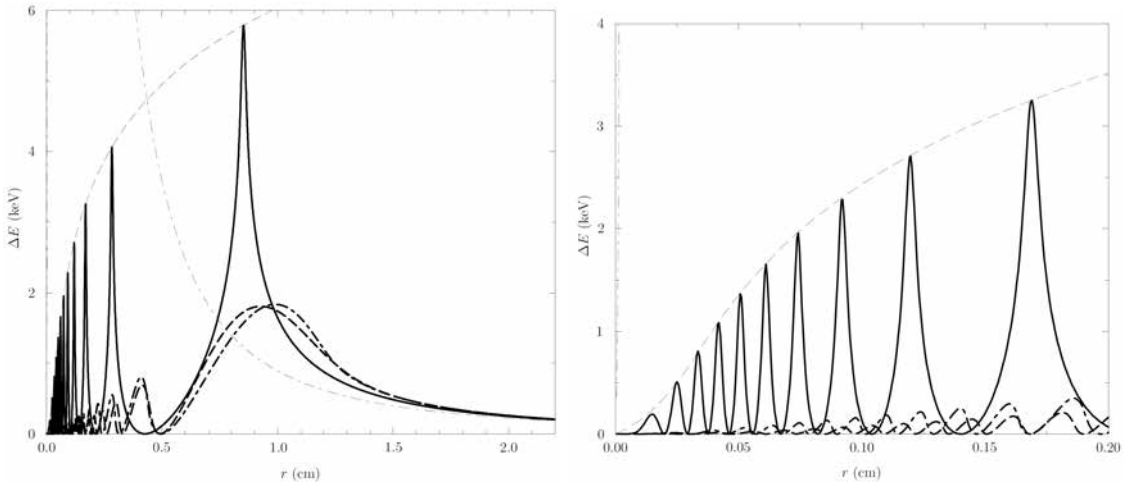

Figure 7.11: Left: Energy gain as a function of the initial electron's radial position, in the LHC nominal case, with three (rectangular, Gaussian, parabolic) longitudinal bunch distributions (solid, dashed, dot-dashed lines). Right: zoom at low radii. The envelope dashed lines correspond to the analytical forms in the autonomous and kick approximation found in Eq. 7.32 and 7.34. From [127].

Fig. 7.11 shows that a dependence in the energy gain with the actual longitudinal bunch profile is present. The analytic estimates well reproduce the energy gain at large radii, in the kick approximation; for low radii, only the maximum peaks in energy are well reproduced in the case of a parabolic longitudinal distribution. The peaks in energy with respect to the radial position of the electrons are significantly reduced for smooth (parabolic, Gaussian) distributions, sign that the longitudinal bunch distribution has a great relevance in the electron oscillation regime. This

result is somewhat important if one wants to investigate the build-up of electron cloud and needs to enter such energy gain as an input in the wall material SEY curve (e.g. see Fig. 7.7). The total energy acquired by electrons is instead well reproduced with all three longitudinal distributions. This is an useful result if one is interested in the energy deposited by the electron cloud.

7.5 Build-up and beam induced multipacting

The primary mechanism behind the electron cloud build-up is beam induced multipacting, driven by the successive passage of the beam bunches. Beam induced multipacting was observed for the first time in the ISR proton-proton storage ring [128] at CERN.

The first condition required for beam induced multipacting is the resonance motion of the electrons with the accelerating beam field [129]. In particular, a multiplication of secondary electrons takes place if the electrons, produced and accelerated during the passage of a bunch, cross and strike the beam pipe, of radius r_p, in synchronism with the successive bunch passage. If we consider electrons with no initial energy, generated close to the beam pipe wall (e.g. $r = r_p$, similarly to the case of photoelectrons) and in absence of external magnetic field, their velocity is readily obtained by Eq. 7.32 and is

$$\Delta v_e = \sqrt{\frac{2\Delta W}{m_e}} = 2cr_e\frac{N_b}{r_p} \tag{7.36}$$

In a round beam pipe, the wall-to-wall transit time condition, required to obtain multipacting, is met if the pipe electrons crossing time is less than or equal to the beam bunch spacing time Δt_b:

$$\frac{2r_p}{\Delta v_e} \leq \Delta t_b \tag{7.37}$$

The multipacting condition finally becomes:

$$N_b r_e \Delta t_b c = r_p^2 \tag{7.38}$$

which can be also manipulated so to define a threshold beam intensity,

$$N_b = \frac{r_p^2}{r_e \Delta t_b c}. \tag{7.39}$$

A further and necessary condition concerns the secondary emission properties of the surface, i.e the SEY. In particular, multiplication occurs if the electrons, accelerated in the beam field, imping the beam pipe wall with an energy sufficiently large to produce more than one electron. The required condition translates in $\delta(E) > 1$ and is visually shown in Fig. 7.12, for an arbitrary surface with SEY energy dependence similar to Cu. Given a determined wall material and its conditions, there is a region $E_1 < E < E_2$ for which $\delta(E_1 < E < E_2)$ is larger than 1. For technical materials, such energy range can run from few tents of eV up to few keV, mainly depending on the δ_{max} parameter.

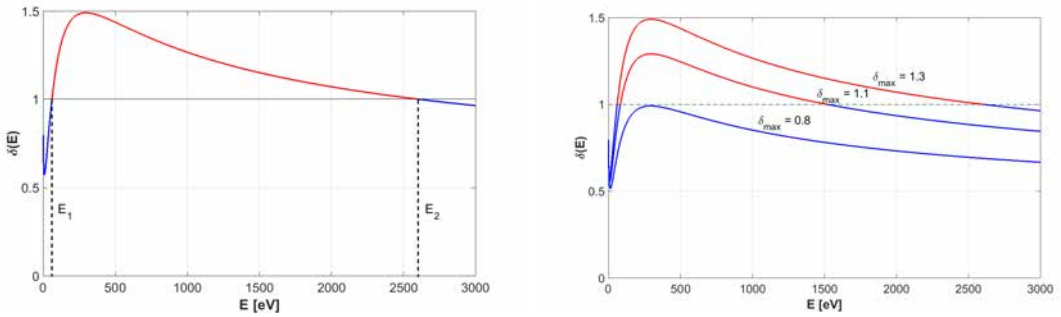

Figure 7.12: Left: SEY curve of scrubbed Cu ($\delta_{max} = 1.3$) and definition of E_1 and E_2. The regions where the material acts as a net electron absorber (blue) or emitter (red) are shown. Right: Evolution of $\delta(E_1 < E < E_2) > 1$ for different δ_{max}.

When the electron flux does match both the above conditions, at every bunch passage not only new primary electrons will be created, accelerated and become capable of produce secondary electrons, but also all the produced secondaries will be as well accelerated, leading to an exponential growth of the electron density.

The condition in Eq. 7.38 should - however - be treated as an upper limit, as it neglects the dynamics of secondary electrons before a new bunch passage. The synchronism condition of Eq. 7.37 can be infact invalidated by the presence low velocity drifting of secondary electrons, which is concomitant to their survival thanks to the high reflectivity at low energy. Secondary electrons not satisfying the wall-to-wall transit time condition are not usually completely lost before a new bunch passage. Some are instead capable to survive in the beam pipe long enough to be captured and accelerated by a next bunch, producing new generations of secondaries. For the same reason, on the other hand, for bunch spacings longer than suggested by Eq. 7.38, multiple interactions with several passing bunches could be performed so to get enough energy to strike the wall with $\delta(E) > 1$.

Resuming, the key parameters behind beam induced multipacting are: the bunch charge distribution (electric field), the bunch spacing and the beam chamber dimensions (transit time conditions) and surface's material properties. While, in general, higher bunch charges and shorter spacings tend to facilitate the multipacting, it is finally the combination of these three parameters to determine how low is the SEY threshold above which multipacting occurs.

Basing on these preconditions, we here present an analytical build-up model of the electron cloud.

Consider a train of equally spaced bunches passing at a certain section S of the accelerator, initially free of electrons. Let us denote with n_0 the number of primary electrons generated, via one or more mechanisms described in Sect. 7.2, per each bunch passage (independent of i), and with n_i the number of electrons present in the section in the instant t_i before the passage of the i-th bunch. We can simply define a $\delta_{\text{eff},i}$ as the effective "gain" (positive if the material wall acts as an emitter, or negative if acts as an absorber) in electrons population achieved at each bunch passage, such as that

$$n_{i+1} = \delta_{\text{eff},i} n_i + n_0. \tag{7.40}$$

Here the quantity $\delta_{\text{eff},i} n_i$ represents the number of electrons generated by the electron cloud striking on the wall. Such quantity is related to the emission properties of the wall $\delta(E)$ and the instantaneous energy spectrum of the impinging electron flux, $\Phi(E,t) = \frac{dn}{dE}$, as follows

$$n_{i+1} = n_i + \int_0^{\infty} \int_{t_i}^{t_{i+1}} \Phi(E,t)[\delta(E) - 1] dt dE + n_0 \tag{7.41}$$

Introducing the normalized integrated energy spectrum for each i-th bunch passage,

$$\phi_i(E) = \frac{1}{n_i} \int_{t_i}^{t_{i+1}} \Phi(E,t) dt \tag{7.42}$$

Eq. 7.41 is reduced to

$$n_{i+1} = n_i \left(1 + \int_0^{\infty} \phi_i(E)[\delta(E) - 1] dE\right) + n_0 \tag{7.43}$$

Comparing Eq. 7.43 to Eq. 7.40, we obtain the analytical definition of $\delta_{\text{eff},i}$, that is

$$\delta_{\text{eff},i} = 1 + \int_0^{\infty} \phi_i(E)[\delta(E) - 1] dE. \tag{7.44}$$

Eq. 7.44 describes the conditions behind the electron cloud build-up. If the impinging electron flux $\phi_i(E)$ lies principally in a energy range where $\delta(E) > 1$, then the integral result is positive, the chamber wall acts as a net emitter and $\delta_{\text{eff},i}$ is larger than one, which means that the electron population, as described by Eq. 7.40, will grow up. On the other hand, when the impinging electron flux $\phi_i(E)$ lies in a energy range where $\delta(E) < 1$, then the integral result is negative, the chamber wall acts as a net absorber and $\delta_{\text{eff},i}$ is smaller than one, which means that the electron population described by Eq. 7.40 will only reach an upper limit.

As long as the electrons dynamics is dominated by the beam, i.e. the evolving electron density is reasonably low so that their mutual interaction is negligible (space charge), the normalized integrated energy spectrum does not depend on the bunch index

$$\phi_i(E) = \phi(E), \tag{7.45}$$

hence, the same applies to the $\delta_{\text{eff},i}$

$$\delta_{\text{eff},i} = \delta_{\text{eff}}. \tag{7.46}$$

In such conditions, by recursive application of Eq. 7.40, we find that n_i is the series

$$n_i = n_0 \sum_{k=1}^{i} \delta_{\text{eff}}^k \tag{7.47}$$

which is the partial sum of a geometric series. Its convergence is easily found:

$$n_i = n_0 \frac{1 - \delta_{\text{eff}}^i}{1 - \delta_{\text{eff}}}. \tag{7.48}$$

The result presented in Eq. 7.48 reveals two possible regimes of build-up:

- if $\delta_{\text{eff}} < 1$, for sufficiently large i, n_i tends to a constant value of

$$n_i \cong \frac{n_0}{1 - \delta_{\text{eff}}} \tag{7.49}$$

  which marks an equilibrium condition, at regime, between the primary seed electron production and electron loss due to net wall absorption. This regime is called *seed accumulation regime*;

- if $\delta_{\text{eff}} > 1$, an exponential growth of electrons takes places during the bunch passages, and for sufficiently large i,

$$n_i \cong n_0 \frac{\delta_{\text{eff}}^i}{\delta_{\text{eff}} - 1} \tag{7.50}$$

  which corresponds to the avalanche multiplication of electrons driven by the secondary wall emission and is the *multipacting regime*. Although in this regime the electron density rapidly increases, an upper limit is reached as soon as the interaction between electrons is no longer negligible. The space charge of the electron density becomes so high to compensate the driving bunch electric field, so that the impinging electron flux $\phi_i(E)$ is similar to the characteristic spectrum of secondary electrons, peaked at low energies (see for instance Fig. 7.8).

The conditions $\delta_{\text{eff}} = 1$ marks the inception of multipacting and determines whether an accelerator section will suffer of electron cloud or not. As mentioned before, and now visible also in the δ_{eff} definition (Eq. 7.44), the parameters influencing the establishment of beam induced multipacting are the bunch charge distribution (electric field), the bunch spacing and the beam chamber dimensions (transit time conditions) and surface's material properties. The beam chamber dimension is often a design choice linked to the required beam aperture, magnet design, etc. and is not, in practice, a design parameter when it comes to avoid multipacting. The bunch spacing is principally related to the chosen RF harmonic and is, preferentially, as short as possible so to maximize the machine exploitation. The bunch charge distribution, which intimately relates to the bunch intensity N_b, and the surface properties $\delta(E)$, are *de facto* the key parameters determining whether the electron density will build-up in a seed accumulation or multipacting regime.

The values of N_b or δ_{max} for which $\delta_{\text{eff}} = 1$ are the so-called the *multipacting threshold*, and separate the conditions for which the two regimes are established.

In Fig. 7.13 we show the simulated maximum electron density in a LHC arc beam chamber and the δ_{eff} in the first instants of the build-up (before space charge equilibrium) as a function of the surface property δ_{max}. The value of δ_{max} for which $\delta_{\text{eff}} = 1$ is the multipacting threshold.

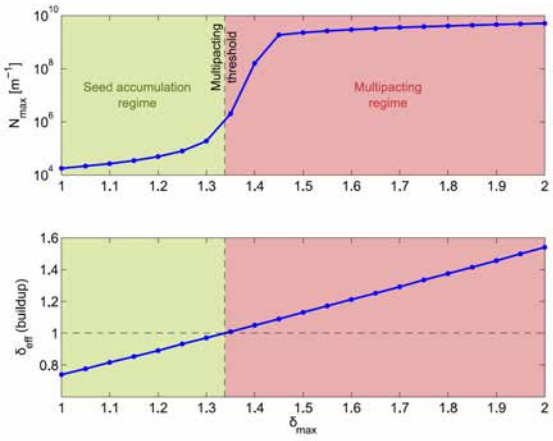

Figure 7.13: Maximum electron density (top)and δ_{eff} (bottom) as a function of δ_{max} parameter in the SEY for the case of the LHC beam screen, but in absence of magnetic field. From [123].

The multipacting threshold can be qualitatively recognized on a number of other quantities by parameter variation. For instance, an increase of several orders of magnitude in the electron density in the beam pipe is observed across the multipacting threshold (e.g. Fig. 7.13, top). The impinging electron flux and the energy deposition of the wall, behave similarly across this threshold. The electron density at the beam position is instead depleted when crossing the multipacting threshold, because of the space charge potential confining the secondary electrons next to the beam pipe walls.

Below multipacting threshold, the electron cloud density - in seed accumulation regime - is so low to be practically harmless, unless of a very strong seeding mechanism. As typically one wants to push the bunch intensity N_b as much as possible to maximize the machine performance, keeping the δ_{max} parameter below the threshold is the essential recipe to fight against beam induced multipacting. This aspect will be thoroughly described in Chapter 8.

7.6 Effect of external magnetic fields

The electron cloud build-up is strongly influenced by the presence of external electromagnetic fields. The presence of externally applied electric fields will be discussed in the Chapter 8.3 in the case of the clearing electrodes. Strong magnetic fields are extensively present all around a synchrotron accelerator, like in the bending dipoles and focusing quadrupoles, and heavily influence the electron cloud build-up and its features.

A non-relativistic electron moving in a uniform magnetic field is subjected to Lorentz force. In the case of electron cloud, electrons are thus forced to move along helicoidal paths around the field lines. The cyclotron gyration is characterized by a period T_c, radius r_c and pitch p of the helix respectively described by:

$$T_c = \frac{2\pi m_e}{eB} \tag{7.51}$$

$$r_c = \frac{m v_\perp}{eB} \tag{7.52}$$

$$p = v_\parallel T_c = \frac{2\pi v_\parallel}{eB} \tag{7.53}$$

being $v_\perp \hat{i} + v_\parallel \hat{j} = \mathbf{v_e}$ respectively the components of the velocity vectors in the perpendicular and parallel directions with respect to the field lines.

Inserting typical values for the magnetic field employed to steer and focus high energy proton beams (range: 0.1 to 8 T) in Eq. 7.51, one finds that the typical electron cyclotron period spans from one to three orders of magnitude below the time constants of a bunch passage, e.g. the bunch spacing and lengths, studied in the case of electron cloud (for instance, in the LHC nominal case, respectively 25 ns and 1 ns). As discussed in Sect. 7.4, the typical total kinetic energy of electrons

participating to electron cloud build-up spans from low energies (e.g. 0-20 eV), for emitted true secondaries, to some keV (e.g. 2-3 keV) for electrons accelerated in the beam field. The typical cyclotron radii can be estimated by applying, with the same magnetic fields of before, Eq. 7.52 inserting kinetic energies associated to the motion in the normal plane with respect to the field lines (i.e. $\frac{1}{2}mv_{\perp}^2$) in the mentioned range. One so finds that the cyclotron radius does never exceed the millimetre range.

These two aspects have multiple consequences on the electron cloud build-up, here discussed.

Although an electron trapped in the field lines could perform many cyclotron gyrations during the bunch passages, in reality its revolution has a small effect in his displacement and practically all electrons are constrained to move around the field lines and drift toward the beam pipe walls at $v_{\parallel}$.

Electrons trapped along different field lines, will receive different kicks from the bunch field during the bunch passages. Depending on the beam field (bunch intensity) and the wall material secondary emission properties (in this instance, particularly the value of E_{max}), the electron will multiply efficiently only in spatial regions where the electron energy gain is favourable. The typical electron distribution in a dipole field region will be therefore characterized by a pattern, which corresponds to one central to two sided stripes (see Fig. 7.14, left).

In quadrupole field regions, the electrons will tend to multipact along the pole-to-pole field lines in a cross section. The consequent electron distribution patter has a *x-like* shape (e.g. Fig. 7.14, right). In quadrupoles, the multipacting thresholds will be usually lower than in other field regions. Due to the magnetic field gradient, electrons can be possibly trapped during periods without bunch presence. In this situation, electrons do not interact with the walls and are very prone to survive during bunch passages. The higher residual electron density can be source of a more severe build-up and therefore cause the lowest multipacting thresholds if compared to field-free or dipole regions.

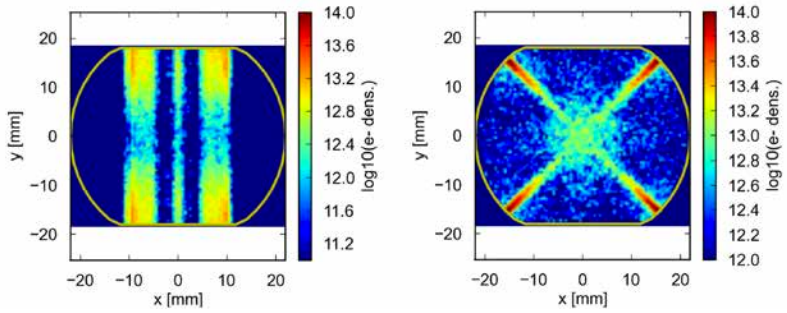

Figure 7.14: Electron density, during the electron cloud build-up, simulated in a dipole (left) and quadrupole (right) magnetic region of the LHC. From [123].

7.7 Electron cloud implications

As soon as the electron cloud forms due to beam induced multipacting, its presence in the beam chambers can limit a circular accelerator performance through different effects, that can be divided in effects on the beam and on the machine. Such effects, in turn, produce typical *signatures*, which can be usefully employed to identify the presence of electron cloud inside particular machine regions or sections.

7.7.1 Implications on the beam

As soon as the electron density ρ_e becomes comparable to the bunch charge distribution, the electron cloud starts interacting with the particle beam. The beam effects can be divided in three branches: coherent tune shift, transverse beam instabilities and incoherent beam effects.

The electron distribution generates an electric field acting on the positive charged beam as a supplementary focusing force. The result is a **coherent tune shift** - or positive detuning - of a

quantity proportional to

$$\Delta Q_{x,y} \propto \frac{r_e}{2\gamma}\beta\rho_e\sigma_s \tag{7.54}$$

being r_e the classical electron radius, γ the beam Lorentz factor, β the local betatron function.

Since the electron density build-up occurs along the bunch train, the electron cloud presence becomes effective only from a certain bunch number of the train, and so, it preferentially affects the bunches at the tail of the train. Therefore, the bunch-by-bunch tune shift increases along the bunch train and is a characteristic of the presence of electron cloud (see e.g. Fig. 7.15).

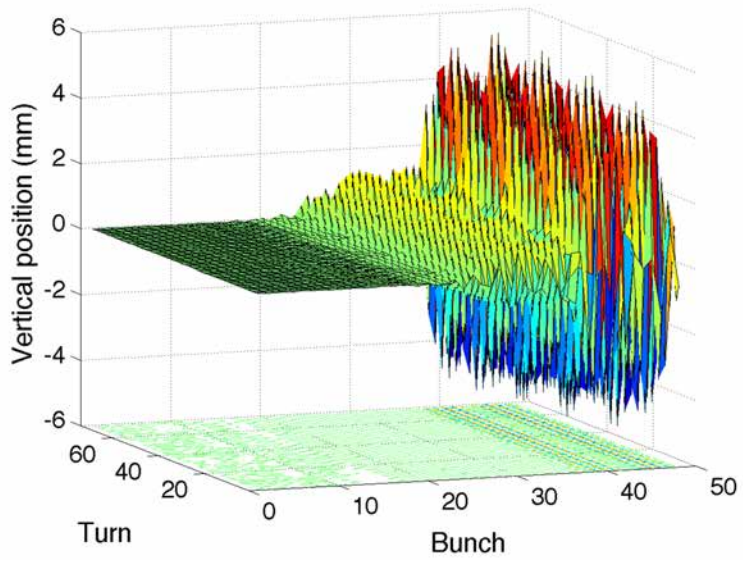

Figure 7.15: Transverse oscillation measured with the transverse feedback pick-ups at the first injection of 48 bunches of 25 ns beam into the LHC in 2011. Beam was dumped twice due to a violent instability in the vertical plane, causing losses above the interlock threshold. From [130].

The stable synchrotron phase is also affected by the electron cloud. As a bunch loses energy when interacting the electron cloud, the RF working point moves in the longitudinal phase space. Since the energy lost by a bunch depends on the density of the electron cloud it interacts with, a bunch-by-bunch shift in the stable phase is observed along the train (see e.g. Fig. 7.16).

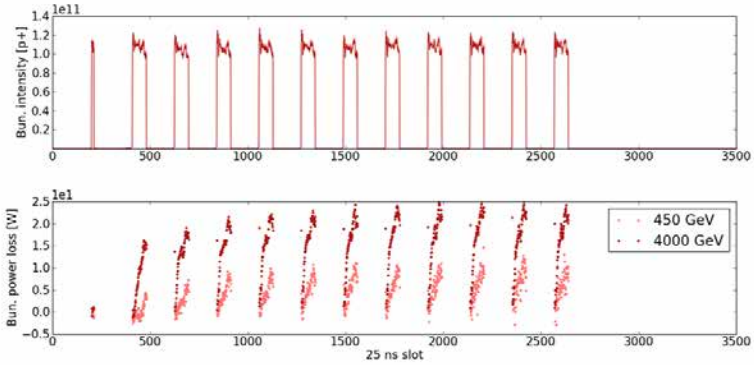

Figure 7.16: Bunch-by-bunch energy loss and phase shift of 11 trains of 72 bunches (25ns spacing) in the LHC. The larger values at 4 TeV are due to the contribution of the synchrotron radiation photoelectrons to the electron cloud build-up. From [130].

The force exerted by the electron cloud on a particle beam can drive transverse exponentially

growing oscillations of the bunch particles around the nominal trajectory, causing **transverse instabilities**. When the beam goes through an electron cloud, the electrons are in turn focused toward the bunch local centroid, performing a fraction, one or more non-linear oscillations according to their initial amplitudes (*electron pinch*). The electron density changes along the bunch longitudinal direction: this process results into an increasing electron density seen by particles along the passing bunch. The main contribution is due to the electrons close to the beam, next to its centroid.

The pinched electrons induce non-linear fields that can couple the motion of the head and tail of the bunch. As long as the bunch is perfectly centered on the pipe axis, the pinch also happens symmetrically and no coherent kick is generated along the bunch. If the head of the bunch is slightly displaced by an amount Δy_{head}, an asymmetric pinch will take place, resulting into a net kick felt by the bunch tail $\Delta y'_{\text{tail}}$. After several turns (and so passages through the electron cloud), the perturbation in the head motion transfers to the bunch tail and its amplitude may grow and lead to unstable coherent motion of the whole bunch.

Depending on the electron density, the instability could appear as a beam break-up with a rise time shorter than the synchrotron period ($\tau \ll T_s$), as a transverse mode coupling instability with a rise time comparable to the synchrotron period ($\tau \approx T_s$), or as a conventional head-tail instability, which typically has a slower growth rate ($\tau \gg T_s$).

Both the intra-bunch motion and the single bunch electron cloud instability lead to transverse emittance blow-up and particle losses, which may result in a disruption of the beam preservation. Due to an important high frequency content, a conventional transverse feedback system is usually ineffective to control the electron cloud driven instabilities. The introduction of Landau damping, through high chromaticity settings or by using octupoles magnets, can mitigate the effects at the cost of loss of transverse emittance preservation and reduced beam lifetime.

The presence of electron cloud can correlate also the motion of the bunches with each other and be responsible of bunch-to-bunch coupling. If one bunch is displaced with respect to the center of symmetry of the cloud, then an asymmetry is induced on the electron distribution. This asymmetry could last long enough to kick the following bunches. Hence even small betatron oscillations of one bunch can couple to the motion of other bunches via the electron cloud, resulting in a coupled bunch instability. This mechanism is facilitated in the horizontal plane in dipoles, through the presence of concentrated electron distribution zones (the stripes). The process is however more complicated than the single bunch electron cloud instability, because it involves electron motion between bunches (with secondary emission).

Even when the transverse instabilities can be avoided - thanks to low electron density or by using Landau damping - the interaction of the beam with electron cloud is source of non-linear fields inducing **incoherent beam effects**, such as a tune spread which may lead to resonance crossing excitation, slow emittance growth and particle losses (see e.g. Fig. 7.17 and Fig. 7.18). Such effects are detrimental for storage rings, where the beam is meant to be stored for long time (several hours) with preserved beam quality. Emittance grow leads to loss of luminosity at the Interaction Points in beam colliders, whereas beam losses may have implications on the machine safety and operation, such as undesired magnet quenches in superconducting colliders and beam operation disruption due to protective dumps.

Although analytical models of the beam-electron cloud interaction provide useful scaling laws, numerical simulations are indispensable for prediction and understanding of the electron cloud induced instabilities.

Simulation of coupled bunch-electron cloud instabilities needs a self-consistent solution of the electron cloud problem and a broad time scale to cover. The process can be extremely time consuming when it comes to simulate a large number of turns of multi-trains beams. Current instability codes model the interaction of an electron cloud with a single bunch on successive turns. The two branches are simulated separately: the electron cloud build-up is first modelled via a multi-bunch system and simulated usually along a single train passage, a single beam turn or just few turns. The electron cloud interaction and beam instability is then modelled via a single bunch system, where electron cloud kicks are simulated over multiple turns. The electron cloud is assumed to be generated by preceding bunches. Build-up simulation codes are used to obtain its transverse distribution. The electrons are then concentrated at one or several locations along the ring with an initial transverse distribution. Information on how many electrons interact with a bunch, like

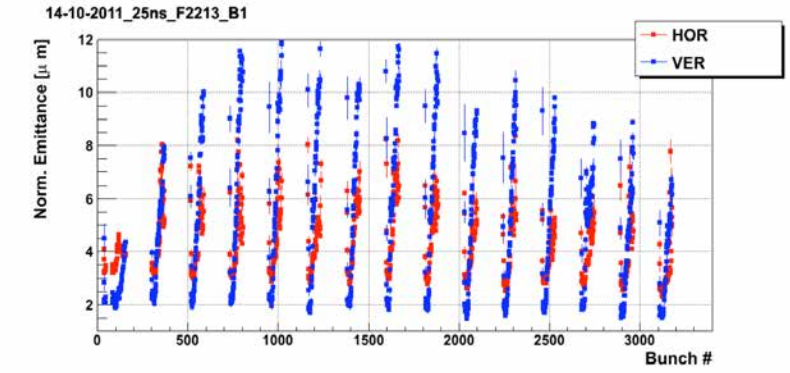

Figure 7.17: Horizontal and vertical bunch-by-bunch emittance measurement on Beam 1 during a LHC 25 ns scrubbing fill. From [123].

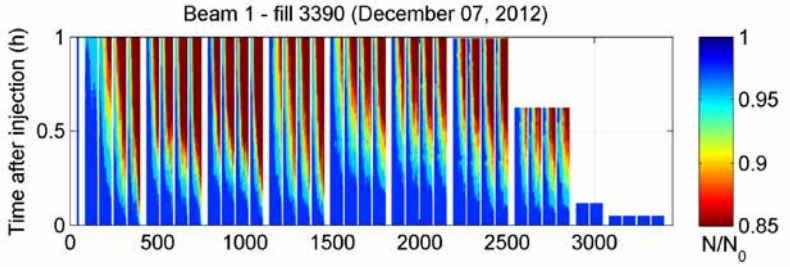

Figure 7.18: Evolution of the bunch-by-bunch intensity of Beam 1, normalized to the injected value, in the first hours of the 2012 LHC 25 ns Scrubbing Run. From [123].

the central density, is essential. In the instability section, the bunch is subdivided in slices and interacts with the cloud in sequence: the beam particles are transported to the next interaction point along the ring by using of convenient transportation maps. At every bunch passage through the cloud the mutual force between beam and electrons is computed using the same module as for the electron build-up and kicks are applied to both bunch and electron distributions. After a bunch passage, the electron distribution is then refreshed to its initial state and the effect of the electron cloud on the beam instability becomes visible only after many turns.

7.7.2 Implications on the machine

Other than on the beam, electron cloud may have implications in particle accelerators resulting in heavy design issues or limitations in performance and operation.

One of the outstanding effects of electron cloud in a beam chamber is **vacuum degradation**. The electron flux impinging on the beam chamber is source of a release of gas. As soon as the energy acquired by the electrons is above the binding energy of physically adsorbed (physisorbed) and/or chemisorbed molecules (range: 0.1 to 1 eV), their bombardment stimulates gas desorption and fragmentation from the vacuum chamber wall. In absence of an adequate pumping speed, the gas released by Electron Stimulated Desorption (ESD) may contribute significantly to the residual gas density, which practically translates in dynamic pressure rises induced by the beam/electron cloud passage. Considering a single gas specie, the residual gas density increase produced by the impingement of the electrons present in the chamber at the arrival of a bunch at space charge equilibrium (electron density: constant), accelerated in the beam field, is

$$\frac{dn}{dt} = \frac{n_e}{\tau_{\text{spacing}}} \int_0^\infty \eta_e(E)\phi(E)dE \tag{7.55}$$

where $\frac{dn}{dt}$ is the desorption rate per unit time and unit length and η_e the electron stimulated desorption yield.

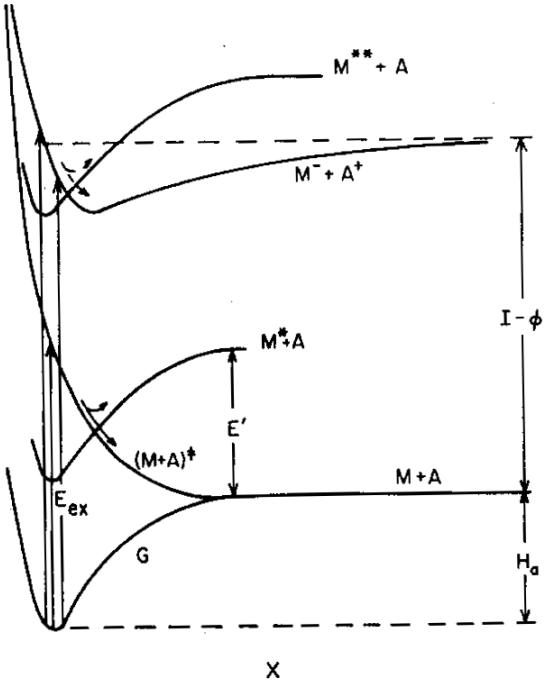

Figure 7.19: The ESD mechanism proposed by MGR model. From [132].

The dominant mechanism behind ESD is electron transition at the beam chamber surface layer.

In order to point out this aspect, let us for instance consider a classical collision between an electron of mass m_e and energy E_e and an atom of mass M. The maximum possible energy transfer is

$$\frac{\Delta E}{E_e} \approx \frac{2m_e}{M}. \tag{7.56}$$

Eq. 7.56 points out that only a small fraction of the impinging electron energy can be transferred to a molecule by direct momentum transfer. An electronic excitation is required to describe the dissociation of atoms or molecules from the surface. The most known model of desorption of the adsorbates during the electronic bombardment of a surface is provided by Menzel, Gomer and Redhead (MGR) [131] [132]. The model is essentially composed of two steps. First, under the electron bombardment, the surfaces undergoes a Franck-Condon electronic transition from the ground state to a repulsive state, on a time scale which is much lower than nuclear motion. During the electronic excitation and transition, the adsorbed specie undergoes nuclear motion on the repulsively excited surface's state potential, moving to the most favourable vibrational level, which corresponds to the minimal change in position. The second step involves quenching of the excitation. The adsorbate is brought back to the ground state and the electronic energy is converted into substrate excitation. In this step, the adsorbate can so be either recaptured, or, if enough kinetic energy was transferred and the total energy of the adsorbed particle is higher than the surface binding energy, be desorbed.

The ground-state desorption yield is determined by the cross section for the initial electronic excitation, times the probability that sufficient kinetic energy will be gained on the excited state curve before a quenching transition takes place. Fig. 7.19 shows the ESD mechanism proposed by the MGR model. Once the Franck-Condon transition has took place, the adsorbed particle can experience one of the antibonding states (the repulsive and the excited states) and so desorb as a neutral molecule, or the ionic state, where it is emitted as an ion.

It is experimental evidence, however, that ESD preferentially leads to desorption of neutral particles, rather than ion species. This preferential desorption branching is explained by an electron tunneling process, which can take place whilst the ion specie is desorbing from the surface, in case of an ionic primary excitation. If no electron tunneling occurs, then the ionized particle can desorb;

otherwise, the excited particle is quenched and so be either recaptured (resulting in no desorption) or desorbed as a neutral.

The gross quantity characterizing ESD is the desorption yield η_e, i.e. the number of molecules desorbed per impinging electron.

In general, photon, electron, and ion desorption yields are at the bases of dynamic vacuum problems and are the quantities required to design vacuum system of particle accelerators subject to beam induced dynamic phenomena. The desorption yield depends on the nature and energy of the impinging particle, the material of the vacuum chamber, the nature of the desorbed gas, the integrated quantity of particles (fluence) that have already impinged on the surface, i.e. the dose D in particles per unit surface.

Looking at the universal curve for inelastic mean free path as a function of electron kinetic energy (see, for reference, Fig. 7.6), the penetration depth of electrons of energy typical for electron cloud (e.g. 5 to 2000 eV) is in the order of or lower than 1 nm. ESD thus strongly depends on the chemical composition of the oxide layer (typical thickness is 1-10 nm) of the surface and the presence of the sorbed species. Large spreading in the quantity of desorbed molecules per impinging electron are expected, as such, depending on nature of the material and surface treatment. The cleanliness of the surface, i.e. the presence of contaminants, may have crucial influence on desorption yield. Electron bombardment cleans the surface by desorption of the contaminants, so a decrease in the desorption yield is expected as a function of the integrated electron dose D.

The electron desorption yield, can be expressed as a function of the initial desorption yield, η_0, and the initial and accumulated electron dose, D_0 and D, by

$$\eta_e = \eta_0 \left(\frac{D}{D_0} \right)^{-a} . \tag{7.57}$$

Table 7.4 provides a compilation of desorption yield parameters for unbaked and baked copper perpendicularly irradiated by 300 eV electrons, measured during laboratory characterization of the LHC OFHC beam screen surface. In Fig. 7.20, one can appreciate the strong reduction of electron desorption yield (up to 4 orders of magnitude), for different gas species, as a function of the increasing electron dose.

Electron desorption yields of metallic surfaces are very similar. As a comparison to the copper baked case, the initial yields of NEG coatings are further reduced after activation by 1 and 2 orders of magnitude for H_2 and CH_4, CO, respectively. For the specific case of hydrogen, its electron desorption yield can be explained by a diffusion model ($a \approx 0.5$). Electrons stimulate the dissociation of oxides, hydroxides and carbides. The dissociated atoms migrate towards the surface where they combines to give neutral molecules. This model is however correct only if the C and H atom densities decay exponentially from the surface.

The desorption yield depends on impinging electron energy. It roughly increases of a factor 10 from 10 eV to 300 eV. For energies above 300 eV, the desorption yield increases almost linearly with the energy of the impinging electrons. The following relation is proposed for OFHC copper,

		H_2	CH_4	H_2O	CO	CO_2
Unbaked	η_0	2×10^{-1}	3×10^{-2}	1×10^{-1}	4×10^{-2}	5×10^{-2}
	D_0 [$\times10^{14}$]	3	1	6	2	4
	a	0.5	0.6	0.7	0.5	0.5
Baked	η_0	4×10^{-3}	2×10^{-4}	–	1×10^{-3}	7×10^{-4}
	D_0 [$\times10^{16}$]	5	5	–	5	5
	a	0.6	1.3	–	0.6	0.9

Table 7.4: Electron desorption yield parameters for unbaked and baked copper perpendicularly irradiated by 300 eV electrons. From [133] and references therein.

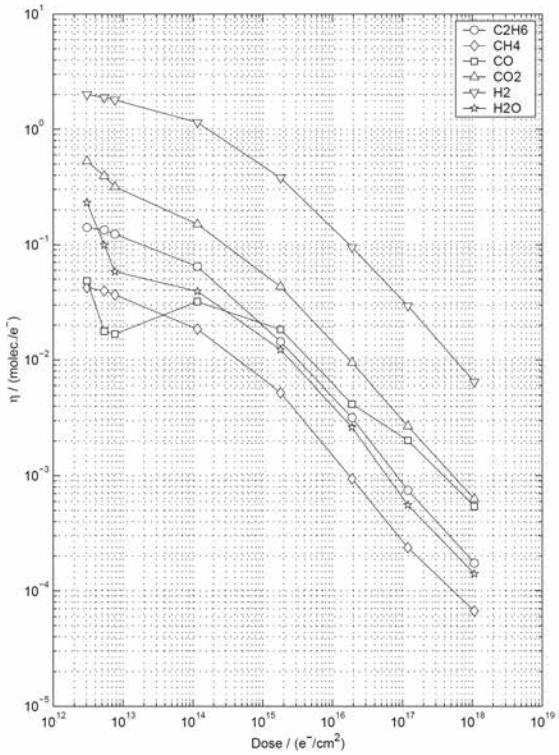

Figure 7.20: Electron desorption yield, for different gas species, as a function of the electron dose for an unbaked OFHC copper sample bombarded with 300 eV electrons. From [134].

cleaned following CERN recipe (stored in plastic bag for weeks, after 24 h of pumping, not baked):

$$\eta = \eta(E_0) \left(\frac{E - E_0}{E_0 - E_c} \right)^{-\gamma} \tag{7.58}$$

being $E_c \approx 10$ eV the cut-off electron energy for which $\eta(E_c) = 0$.

The desorbed quantity of the main species of the residual gas in UHV, such as H_2, CO and CO_2 can be as large as one or more monolayes. For instance, after an accumulated dose of 10^{18} e^-/cm^2, 1 to 10 monolayers of H_2, CO and CO_2 have been desorbed, with the dominant specie being H_2.

The electron desorption yield does not depend significantly on substrate temperature. For instance, the desorption yield depends, in a factor of 10, on standard bake-out temperatures. At an integrated dose of $5 \cdot 10^{16}$ e^-/cm^2, the desorption yield of the baked Cu is about one order of magnitude lower than unbaked Cu. The presence of physisorbed and condensed gas may, however, result in a dramatic increase of the desorption yields. Desorption yields of condensed gas are indeed higher than the primary yields of chemisorbed gas (several orders of magnitude), due to the much lower binding energy of the former (van der Walls forces). At 4.2 K, the electron desorption yield of physisorbed/condensed molecules is linear up to a monolayer, then levels-off. Values up to 500 H_2/e^- are reported with 300 eV electrons [135].

Pressure rises induced by electron stimulated desorption have several deleterious effects on the machine. A reduction in the beam lifetime due to increase in nuclear scattering is experienced. In turn, this becomes a source of higher equipment irradiation and worsening of background in experimental areas, due to higher stray ionizing radiation. An uncontrolled increase of beam losses and radiation is particularly dangerous for superconducting devices, which could suffer of quenches. Dynamic pressure rise increases the probability of electric breakdown in high voltage devices, such as beam kickers and electrostatic septa, decreasing their availability. The increased radioactive activation of the equipment translates in higher doses to personnel during machine interventions. Operational limitations due to dynamic vacuum induced by electron cloud are often experienced

with higher rates of protection beam dumps due to vacuum or magnets safety interlocks.

In addition to ESD, the bombardment of electrons on the beam vacuum chamber's wall induces the loss and deposition of energy of the impinging electron flux. Although electron cloud usually produces high electron fluxes (e.g. above 10^9 electron/m in a LHC dipole at design energy), the amount of power deposited by electron is usually limited - in the order of magnitude of units of W/m - due to the broad low energy component of the secondary electrons. In analogy to the Eq. 7.55, the power deposited on the walls by electron cloud per unit length can be described by

$$P = \frac{n_e}{\tau_{\text{spacing}}} \int_0^\infty \phi(E) E dE. \tag{7.59}$$

Even though the amount of power deposited by electron cloud is usually insignificant in room temperature accelerator sections, in cryogenic sections - like the LHC arcs - the electron cloud **heat load** is a relevant contribution to the beam induced budget burdening on the cryogenic system. The main figure quantifying the load caused by heat inleaks onto a cryogenic system is the Coefficient of Performance (COP), defined - for a refrigerator - by the ratio of the heat load Q submitted at low temperature over the work at room temperature required to remove it,

$$\text{COP} = \frac{Q}{W}. \tag{7.60}$$

The minimum COP is the one of the reversed Carnot cycle, and depends only on the temperature of the hot and cold sources, respectively T_h and T_c:

$$\text{COP}_{\text{Carnot}} = \frac{T_c}{T_h - T_c}. \tag{7.61}$$

In reality, the relative COP of an actual refrigerator is lower of the Carnot ideal cycle, by an amount called relative efficiency (second thermodynamic's law),

$$\eta = \frac{\text{COP}}{\text{COP}_{\text{Carnot}}}. \tag{7.62}$$

The relative efficiency rises exponentially at low temperatures. The inverse of the COP is called the specific power and represents the input power to be supplied per unit of power of refrigeration. As low as LHe temperatures, the installed specific power of an LHC cryoplant is about 250 W/W at 4.5K, and rises to 940 W/W at 1.9K. The interest of maximizing the capability to extract the load at the maximum energy efficiency possible (i.e. producing the lowest total refrigeration power) is the reason of the conception of beam screens in cryogenic superconducting high energy particle accelerators, providing the interception of beam induced heat loads before they reach the cold mass at lowest temperature of the system. The LHC beam screen functions and design principles will be thoroughly described in Sect. 8.1.

As introduced by Eq. 7.59, the heat load dissipated by electron cloud is intimately related to the electron cloud build-up characteristics, namely the impinging electron flux and its energy spectrum. Those quantities are highly dependent on the beam parameters and beam chamber size and surface properties (see Sect. 7.5) and are proportional to the electron density reached at multipacting equilibrium. Once the electron cloud is established and its characteristic are figured, the integrated electron flux is linearly proportional to stored beam intensity, i.e. the number of trains of bunches.

Attempts to build scaling laws capable to predict such quantities have been made (see for instance in [136]). Detailed build-up simulations are usually required to provide quantitatively reliable predictions for technical design. Useful information and indirect extrapolation can be obtained by small scale experiments in real accelerator conditions, like for instance the COLDEX experiment [137]. Fig. 7.21 shows the measured electron cloud power dissipated onto a ID67 OFHC Cu beam screen in the LHC-type cryogenic vacuum set-up of the COLDEX experiment installed in the Super Proton Synchrotron, in presence of 4x72 bunches circulating at injection energy (26 GeV) [138]. The heat load is plotted against the proton intensity per bunch. One can identify the abrupt increase in the measured power once the multipacting threshold is reached (across $7 \cdot 10^{10}$ and $8 \cdot 10^{10}$ ppb, for an estimated $\delta_{max} = 1.3$).

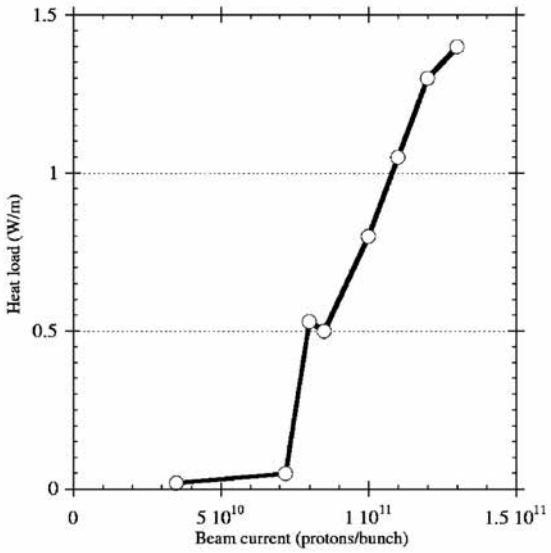

Figure 7.21: Electron cloud dissipated power per unit lenght as a function of the beam bunch intensity, with four trains of 72 bunches, measured with the COLDEX experiment with a ID67 OFHC Cu beam screen. From [138].

The impact of electron cloud dissipated heat load in cryogenic systems is twofold. The build-up of electron cloud is accompanied by a reaction from the cooling system control system, required to compensate the temperature rise due to the rapid increase of heat deposition. The transient can be, is some cases, so violent to lose the cryogenic maintain conditions and cause a trigger of the protection dump. When the transient is mitigated - for instance, slowing down the beam injection rate - the induced heat load can reach the installed cooling capacity of the cryogenic plant, which represent a hard limit and will slow down the intensity ramp-up of the machine and limit its operational performance [139].

The presence of an unforeseen electron flux can impact on the performance of **beam diagnostic** and induce malfunctions on devices like RF pick-ups and Beam Position Monitors (BPMs). Exemplar is perturbation recorded [140] [141] on the transverse feedback system (or *damper*) employed in the SPS to damp injection oscillations and to stabilize the beam against transverse coupled bunch instabilities with high intensity beams. The signal of vertical position induced by a single beam batch saw a baseline drift starting half through the 2 μs batch, at threshold bunch intensity of $4 \cdot 10^{10}$ ppb. This drift was later explained by the deposition of charge of electrons hitting the pick-up electrode. Applying a longitudinal solenoid magnetic field mitigated the phenomenon up to a new threshold bunch intensity of $7 \cdot 10^{10}$ ppb, however clearly pointing out its origins, i.e. caused by electron build-up.

Chapter 8

Electron cloud mitigation in cryogenic vacuum systems

8.1 The Large Hadron Collider (LHC) beam vacuum

The Large Hadron Collider (LHC) is the world's largest and most powerful particle collider. Built at the European Organization for Nuclear Research (CERN) from 1998 to 2008, its purpose is to give answers to the most basic inquiries of the dynamics and structure of matter, space and time, investigating the predictions of different theories of particle and high-energy physics and pushing the limits of human knowledge toward a deeper understanding of fundamental nature of the universe, beyond the Standard Model [12]. The announcement given by CERN on July 4th 2012 about the discovery of a new boson at ≈125 GeV, the long-awaited Higgs particle [142] [143], is the only one of first fundamental discovery delivered by LHC.

The LHC lies in a 27 km underground tunnel, on average 100 m deep, across the France-Swiss border near Geneva, Switzerland. The LHC synchrotron is designed to accelerate and collide two counter-rotating particle beams of protons at up to an energy of 7 TeV, or lead nuclei up to 574 TeV per nucleus. The product of the collisions is analysed by four major experiments located at the LHC's intersection points (ATLAS, CMS, LHCb and ALICE) and by few smaller detectors for dedicated research (e.g. TOTEM, LHCf).

The LHC is designed as a collider with separate magnet fields and vacuum chambers, with common sections basically only at the insertion regions, where the experimental detectors are located. The two beams share an approximately 130 m long common beam pipe along the interaction regions (IRs). In order to fit the 7 TeV rings into the existing Large Electron Positron (LEP) collider tunnel, the design concept is based on magnetic bending superconducting magnets of 8.3 T dipole field. The LHC employs twin bore magnets consisting of two sets of NbTi superconductor coils, operating in a bath of superfluid helium at 1.9 K, and beam pipes within the same mechanical structure and cryostat.

The layout of the machine is shown in Fig. 8.1. The LHC is divided in eight octants, having eight arcs and straight sections. Out of the 54 km total length, 48 km of UHV beam vacuum is at cryogenic temperature, while 6 km is at room temperature, in the Long Straight Sections (LSS). About 48 km of insulation vacuum serves instead the helium distribution lines and the magnet cryostats.

Each LHC straight section is approximately 528 m long and serves as experimental or utility insertion. The two high luminosity experiments are located at LSS1 (ATLAS) and LSS5 (CMS), while the two low luminosity experiments are situated in the LSS2 (ALICE) and LSS8 (LHCb), which also contain the beam injection transfer lines. The two beams cross and collide at the Interaction Points (IPs). Beams are focused at the interaction point by superconducting low-beta triplets, or Inner Triplets (ITs). LSS3 and LSS7 contain the collimation system. LSS4 contains the radiofrequency cavities station and LSS6 the beam ejection system to the dumps.

The room temperature UHV beam vacuum of the LHC LSS [144] is made of 7 m long, 2 mm thick OFHC copper chambers. The inner diameter is 80 mm and each chamber is fitted

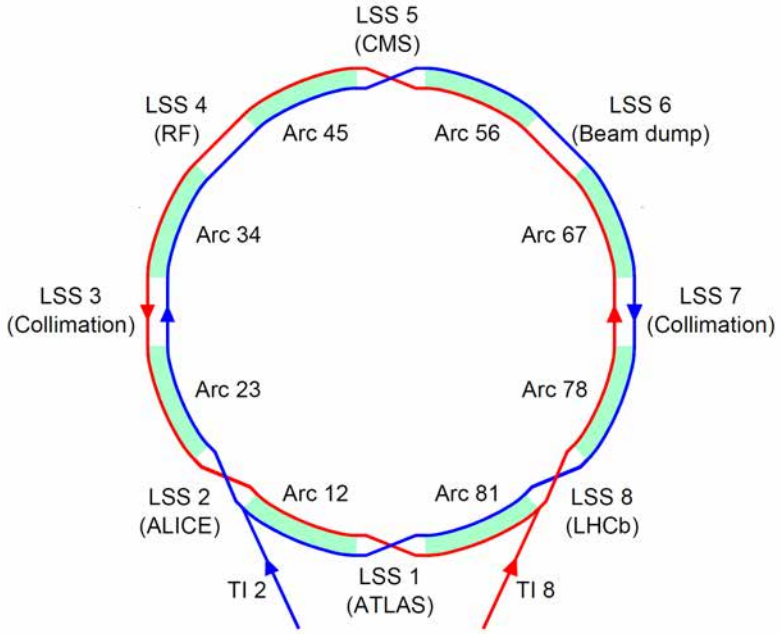

Figure 8.1: Schematic layout of the LHC: Beam 1 (blue) circulates clockwise and is injected by the SPS in TI2 at Point 2, while Beam 2 (red) counter-clockwise and is injected by the SPS in TI8 at Point 8.

with standard DN100 ConFlat® flanges. A TiZrV non-evaporable getter (NEG) coating is used as baseline distributed pumping scheme on the entire LSS vacuum sectors to ensure the required residual gas density and low background to the experiments during beam operation. The chambers are connected by means of stainless steel bellows equipped with RF copper screens to reduce the longitudinal impedance. Half of them are fitted with pumping and diagnostic ports. Sector valves isolate the sectors at cryogenic temperature from the RT sectors. Such insertions are equipped with bellows and fitted with an ion pump and a set of gauges, generally a Pirani and a cold-cathode inverted-magnetron gauge. Pumping ports, installed in the centre of the vacuum sector, are used for initial pump-down from atmospheric pressure and for vacuum pumping during the bake-out and NEG activation. The final vacuum pumping of the RT vacuum system relies on the activated NEG coatings, capable to the chemisorb the H_2, CO, CO_2, H_2O (N_2 and O_2 in the case of leaks) gas species present in UHV system. Negligible pumping is provided for methane (CH_4) due to the high dissociation energy for this molecule at metal surface and a low sticking probability at room temperature. The NEG coatings are also not able to pump noble gases. For that reason, a limited number of sputter ion pumps are installed on each sector. The maximum distance between ion pumps is fixed to 28 m in order to avoid ion-induced pressure instabilities.

Concerning the electron cloud build-up, the choice of NEG coatings, activated at 200 °C, ensures a reduction of the initial SEY from 2.0 (Cu) to below 1.1 [145] in the room temperature LHC vacuum system. Saturation with H_2, CO, CO_2, H_2O at low pressure increases the SEY of about 0.1. This outcome was validated by the results of a NEG coated sector installed in the SPS accelerator ring in presence of LHC type beams [145]. The combined choice of NEG coatings for low outgassing, vacuum pumping and low SEY allows to safely prevent electron cloud build-up in the LSS, with the exception of the stainless steel interfaces. Signatures of the electron cloud were recorded [146] in fast pressure increases due stimulated desorption at stainless steel modules with copper RF shields, connecting the room temperature to cryogenic sections, already with 150 ns spaced beams. Suppression was achieved by installation of solenoids providing a $\sim$ 50 Gauss longitudinal magnetic field around the cold-to-warm transitions.

The arcs of the LHC lattice are made of 23 regular cells (FODO lattice). The arc cells are 106.9 m long and are made of two 53.45 m long half cells: each contains four main magnets, i.e. one 3.1 m long quadrupole magnet and three 14.3 m long dipole magnets. The section of the LHC arc dipole is shown in Fig. 8.2. Two separate bores identify the beam vacuum for the two

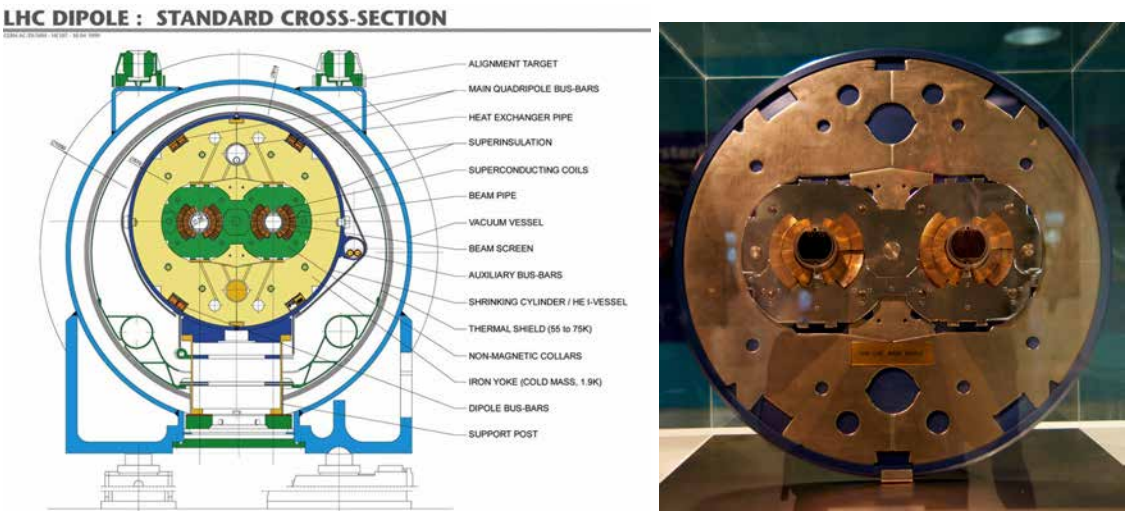

Figure 8.2: Left: LHC main dipole magnet cross section within the cryostat. Courtesy of CERN, 1999. Right: picture of a cross section of the cold mass; the superconducting coils, the cold bore and beams screens are visible.

counter-rotating beams. The superconducting coils operating at 1.9 K with superfluid He II. The cold bore, which is direct contact with the helium bath, is at the same temperature.

At 1.9 K, the vacuum envelope becomes a very efficient cryopump (see Annex A), with practically infinite capacity for all condensable gas species with the sole exception of He. The concept of having a beam vacuum at cryogenic temperature has the drawback that the cryogenic system has to remove even very small amounts of beam induced power, which, for conventional room temperature accelerators, would be insignificant. The removal of 1 W deposited at 1.9 K requires nearly 1 kW of electric power (see Sect. 7.7.2). Avoiding or intercepting any source of heat in-leak to the cold beam pipe was subject of extensive studies during the LHC design, which brought to the conception of a stainless steel beam screen [147]. The beams screen is a perforated liner inserted in the cold bore and held with low thermal conductivity supports. Its temperature is controlled between 5 and 20 K with a gaseous helium circuit and a set of heaters. Its function is to absorb and remove the beam induced heat load due to the distinct beam and vacuum related heat sources, while ensuring proper vacuum conditions capable to contain the beam degradation within acceptable levels. In the LHC, the possible span of heat sources can be divided in four branches [148]:

- **synchrotron radiation**: due to the centripetal acceleration in the bending magnets the beams emits a synchrotron radiation flux of about 10^{17} photons/(m·s) at 7 TeV, with a critical energy of the photon spectrum of 44 eV, equivalent to a distributed linear power of 0.2 W/m. The total LHC synchrotron radiation load amounts to 7.6 kW;

- **longitudinal beam coupling impedance**: image currents, produced along the pipe walls by the beam circulation, induce ohmic losses, due to the resistive nature of the pipe material. The power dissipated amounts 0.05 W/m per beam. The losses are proportional to the squared proton beam bunch charge and to the square root of the electrical resistivity of the material. In order to increase the surface conductivity (and therefore to reduce impedance related effects) the beam screen is colaminated with high purity copper, providing a RRR of 100;

- **electron multipacting**: the successive passage of the 1 ns short bunches of $1.1 \cdot 10^{11}$ ppb, separated by 25 ns, produce an electron cloud build-up leading to multipacting in the LHC cold beam vacuum. The LHC is the first hadron collider where the primary electrons come from the residual gas ionisation and, above all, from the photoelectric effect of the synchrotron radiation striking on the beam screen surface. While the photoelectric yield and reflectivity were minimized by a sawtooth geometry (see Sect. 7.2.2), the SEY is a key parameter of

the multipacting process in the LHC arcs. In the as-received state, the copper surface of the LHC beam screen exhibits typically a δ_{max} of 1.9, with $E(\delta_{max}) \approx 250$ eV. Basing on these parameters, plus numerous other inputs, simulations predicted an average arc heat load larger than 4 W/m with half of the nominal bunch population ($0.5 \cdot 10^{11}$ ppb). The cited heat load was not acceptable by the cryogenic system. The mitigation strategy of the electron cloud build-up in the LHC cold vacuum is beam conditioning (discussed later in this Chapter), with the purpose of reducing the heat load to an acceptable value. Studies have shown that beam scrubbing gives access to a δ_{max} reliably below 1.3, down to 1.2 with large electron dose. Provided these conditions, the average design heat load in the arcs with nominal bunch current reduces to about 0.2 W/m;

- **beam loss by nuclear scattering**: for the first time in an accelerator, beam losses due to nuclear scattering of the high-energy protons on the residual gas represent a non-negligible design heat load. Nuclear scattering generates an unavoidable continuous flux of high-energy particles uniformly distributed around the arcs, which is lost from the circulating beams and can only be partially collimated. A small fraction of scattered protons is also not absorbed by the collimation system in the beam cleaning insertions. The lost particles escape from the aperture of the machine and penetrate through the cold bore, where they deposit energy through a shower of secondary particles. The continuous heat input to the cryogenic system, especially the most onerous at 1.9K, is proportional to the gas density. Hence, a definition of the upper limit of the gas density in the beam pipe is required. The beam lifetime τ, due to nuclear scattering is given by

$$\tau = \frac{1}{c\sigma_i n} \tag{8.1}$$

where the c is the speed of light, n the residual gas density, and σ_i cross section for 7 TeV protons on H_2 atoms, $\sigma_i(H_2) \approx 0.37 \cdot 10^{-18}$ cm^2. The power load per unit length is proportional to the beam current I and the beam energy E and is expressed in terms of the beam-gas lifetime as

$$P = \frac{IE}{c\tau} \approx 0.93 \frac{E[\text{TeV}]I[\text{A}]}{\tau[\text{h}]} \tag{8.2}$$

The machine design includes provisions for a nuclear scattering heat load of ∼0.1 W/m for the two beams. Consistent with this requirement, a beam lifetime of ∼100 hours has been chosen. The above parameters allow to define the design H_2 density, that is $\leq 1 \cdot 10^{15}$ molecules/m^3, equivalent to a pressure of $\leq 1 \cdot 10^{-9}$ mbar at 10 K. Correspondingly, the density required for heavier gases is lower, and is resumed in Table 8.1.

Gas	$\sigma_i/\sigma_i^{H_2}$	N (m^{-3}) for τ = 100 h
H_2	1	1 10^{15}
He	1.26	7.8 10^{14}
CH_4	5.4	1.8 10^{14}
H_2O	5.4	1.8 10^{14}
CO	7.8	1.2 10^{14}
CO_2	12.2	8.0 10^{13}

Table 8.1: Proton cross sections relative to H_2 and design maximum gas densities at LHC design energy for different gas species. From [148].

Fig. 8.3 gives a resume of the heat loads dissipated by beam-induced losses in the LHC cryogenic vacuum as a function of the proton beam energy. Among the mentioned heat sources, synchrotron radiation, image currents and photoelectrons heat load is intercepted at a thermodynamically more efficient temperature of 5 to 20 K by the designed LHC beam screen. The heat load due to scattered high-energy protons cannot be intercepted by the beam screen and is included in the cryogenic budget of the 1.9 K cooling subsystem. It is because of this effect, which has a practical

importance for the first time in the LHC, that a defined lifetime limit is set on the maximum average gas density in the LHC arcs (of $1 \cdot 10^{15}$ molecules/m^3), which should be provided also in presence of beam-induced dynamic effects on the beam vacuum.

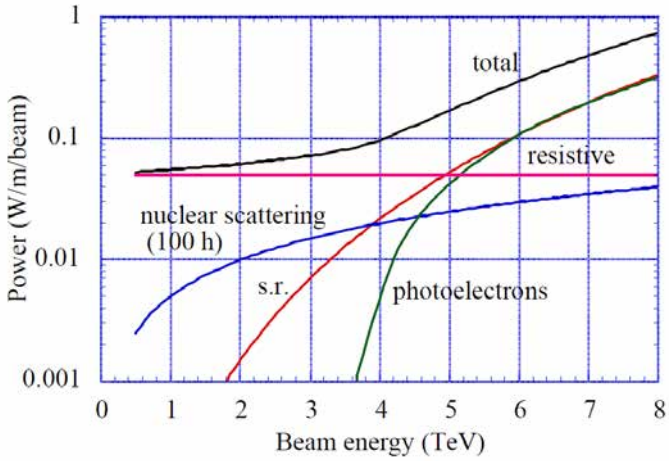

Figure 8.3: Heat loads dissipated by beam-induced losses in the LHC cryogenic vacuum as a function of the LHC beam energy. From [148].

The LHC beam screen is a highly technological product combining several functions: it is designed to intercept the thermal loads induced by the circulating beam while providing maximum beam clearance and electric conductivity, low thermal bridging to the 1.9 K cold mass, low magnetic permeability, and leaving enough space to accommodate cooling and mechanical features which should also guarantee sufficient structural rigidity to withstand a magnetic quench forces. Control of the gas densities, required by design, is ensured by perforation of the beam screen, allowing cryopumping of gas on the cold surfaces of the cold bore held at 1.9 K. This design choice ensures low vapour pressure for all gases, of which H_2 and He are the most critical species.

During LHC operation, the proton beams stimulate molecular desorption by photon, electron and ion bombardment. Consequently, the desorbed gas load must be pumped to ensure a beam lifetime of 100 h.

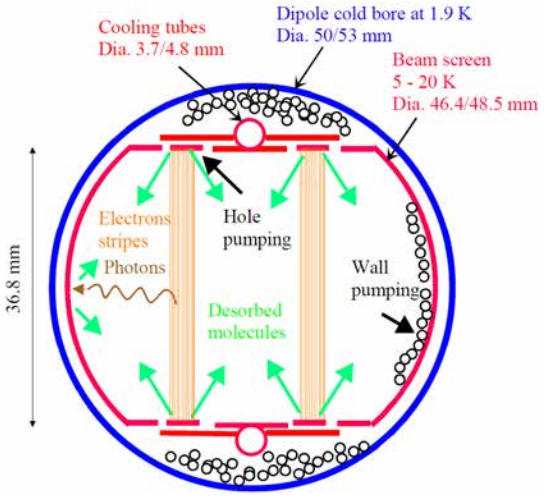

Figure 8.4: Cross section of the schematic cryogenic LHC vacuum principle. From [149].

Figure 8.4 shows the cross-section of the schematic cryogenic LHC vacuum principle [149]. The positions of the source of gases are sketched. Chemisorbed molecules are desorbed from the beam screen surface by photons, electrons or ion induced desorption. These molecules are either

physisorbed onto the beam screen surface or pumped through the slots where they are condensed onto the cold bore at 1.9 K. Hydrogen, which has the higher vapour pressure with excpetion of helium, cannot be physisorbed in large quantities on the beam screen surface (up to a few monolayers, that corresponds to $3 \cdot 10^{15}$ molecules/cm^2). Its main source of removal is through the pumping slots, cryocondensed on the cold bore. Other heavier molecules, like CO, CO_2, CH_4, H_2O, which have lower vapour pressure, are physisorbed/cryocondensed onto the beam screen or can be removed through the pumping slots. Scattered photons and electrons can recycle the molecules adsorbed on the beam screen surface into the gas phase via stimulated desorption. When the amount of desorbed molecules is balanced by the amount of removed molecules, an equilibrium pressure and surface coverage is reached. The equilibrium density n_{eq} is given by

$$n_{eq} = \frac{\eta \dot{\Gamma}}{C} \tag{8.3}$$

where the gas load, product of the photon, electron and ion fluxes, $\dot{\Gamma}$, times the respective primary desorption yields (here globally η), is counterbalanced by the cold bore presence through the pumping speed of the BS slots, C. From Eq. 8.3, one observes that the quality of the technical surface (source of the gas load) and the BS trasparency (permanent removal) must fulfil certain design requirements in order to reach a satisfactory equilibrium density.

The equilibrium surface coverage on the beam screen, θ_{eq}, is a function of the monolayer capacity θ_m and is driven by the BS pumping speed, σS, over the slots conductance (pumping speed), C, multiplied by the gas source given by the primary desorption yield, η, over the recycling desorption yield η_0' (a gas release), at one monolayer:

$$\theta_{eq} = \left(\frac{\sigma S}{C} \frac{\eta}{\eta_0'} \right) \theta_m \tag{8.4}$$

The equilibrium surface coverage is below a monolayer on Cu for low sticking probability and large recycling desorption yields.

Fig. 8.5 shows an example of the LHC cryogenic beam vacuum pumping principle. The hydrogen dynamic pressure inside a LHC type beam screen irradiated with synchrotron radiation is experimentally simulated with one third of the LHC design current [150]. Without the pumping slots, the pressure increases due to the recycling desorption of the physisorbed hydrogen caused by the scattered photons, reaching a level which - in the case of this measurement - is only limited by external pumping speed provided at the extremities. At that level, the rate of primary desorption and external pumping are equal. The perforation of the beam screen allows pumping the recycled hydrogen directly towards the cold bore, providing a much lower and stable equilibrium pressure.

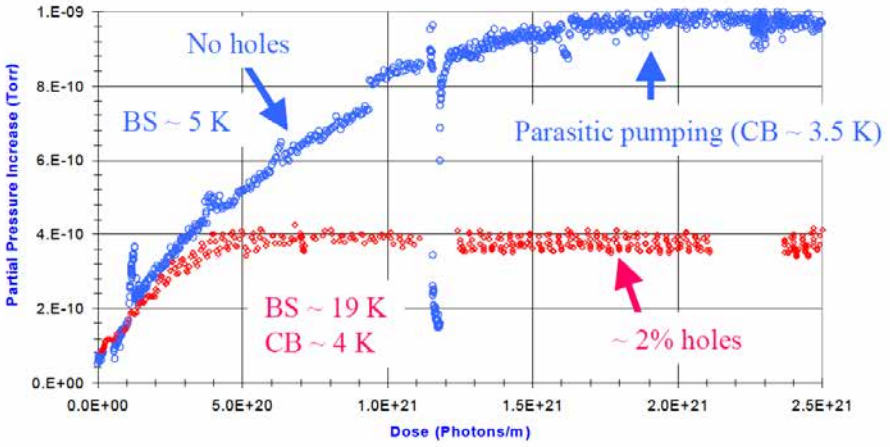

Figure 8.5: H_2 photodesorption in a LHC type cryogenic vacuum system employing a beam screen with and without holes. From [150].

8.1.1 Electron cloud mitigation in the LHC cryogenic vacuum

All materials used in accelerator technology do not exhibit a significantly low SEY as-received. In the case of the LHC cryogenic vacuum, the SEY of colaminated Cu was found higher than what needed to avoid any of the electron cloud related effects [151]. In the LHC room temperature vacuum, we have described that electron cloud build-up was preventively cured by the adoption of NEG coating, which combined a mix of different roles. The same approach could not be retained in the LHC cryogenic vacuum, as it is, by definition, difficulty bake-able. Pioneering work done at CERN observed that when a surface is exposed to a prolonged electron irradiation, its SEY decreases [152]. This was called SEY conditioning, or scrubbing effect. Fig. 8.6 shows the evolution of the beam induced scrubbing in a real machine environment [141], where the decrease of the SEY of a copper sample exposed to the bombardment of the electrons from the electron cloud developed in the SPS by LHC-type beams was observed as a function of the time of exposure. The observation of beam induced conditioning was extremely remarkable: the electron cloud has a negative feedback and seems, like that, asymptotically self-mitigating, thanks to its electron bombardment that is actually a result of the electron cloud formation. The process of SEY conditioning was studied during the LHC design phase and has become the baseline design strategy to cope with detrimental effects of electron cloud effects [112].

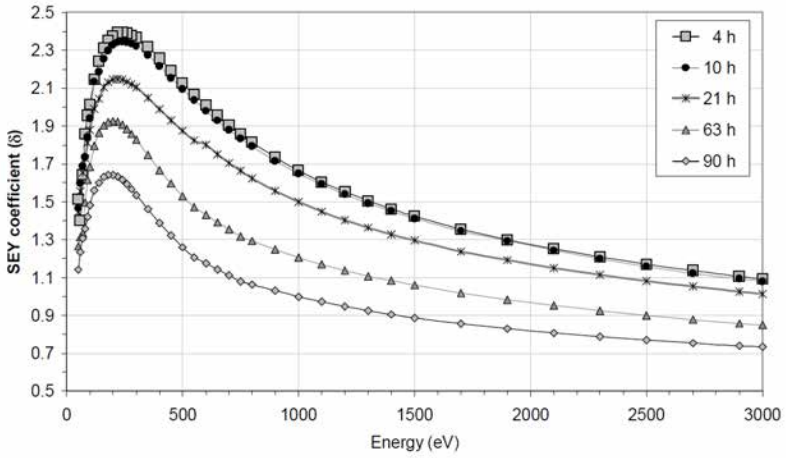

Figure 8.6: Decrease of the SEY of a copper sample exposed to the bombardment of the electrons from the electron cloud developed in the SPS by LHC-type beams, as a function of the time of exposure. From [141].

In Fig. 8.7 the laboratory results [153] at the base of such mitigation solution is shown. The reduction of the initially high SEY ($\delta_{max} = 1.9 \div 2.1$) of a Cu colaminated sample of LHC beam screen to a much lower value ($\delta_{max} \approx 1.1$) is observed as a function of the dose of impinging electrons at different energy levels and normal incidence. For energies above 200 eV, a dose in the order 10^{-3} C/mm^2 is sufficient to lower δ_{max} below ~ 1.3. Much higher doses, above 10^{-2} C/mm^2, are necessary to reach the level of $\delta_{max} \approx 1.1$, which is considered the fully-scrubbed condition of Cu. The dependence on the adopted impinging electrons energy is remarkable: not only the conditioning process is slower with low energy electrons, but also the final state exhibits higher δ_{max}. Resuming for the LHC case, a dose of 10^{-3} to 10^{-2} C/mm^2 is required to fulfil the LHC design of $\delta_{max} < 1.3$. At the same time, we note that the gas desorption due to electron stimulated desorption will have reduced of 10^3 times (see Fig. 7.20), meaning that the surface has undergone a vacuum cleaning through ESD.

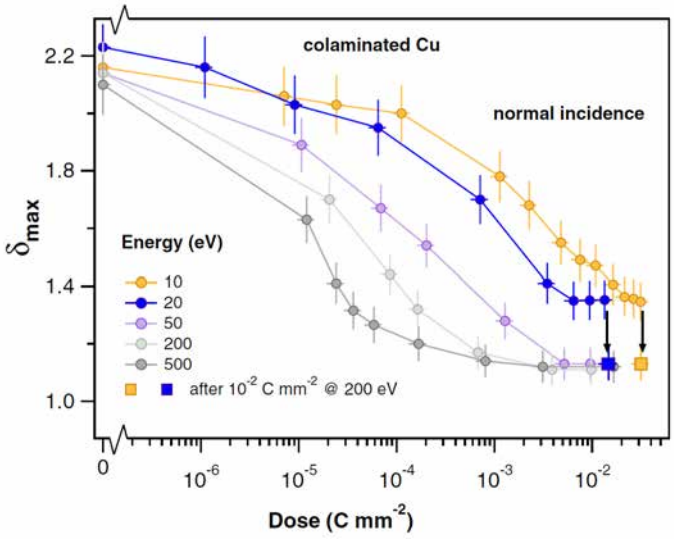

Figure 8.7: Decrease of δ_{max} on a Cu colaminated sample of LHC beam screen as a function of the dose of impinging electrons at different energy levels and normal incidence. From [153].

At the time of the LHC design, the phenomenon of conditioning was obtained reproducibly on many samples, in different experimental setups, but the exact mechanism leading to this effect was not properly understood [112]. Detailed comprehension of the surface variations induced by electron irradiation on technical surfaces were obtained only after the LHC construction period [153].

The conditioning process can be described in a twofold mechanism: initially a surface cleaning through ESD, in particular of H_2, takes place and is the dominant process. The surface cleaning causes a strong reduction of the SEY and of ESD yields, due to removal of surface contaminants. When the electron dose exceeds 10^{-4} C/mm^2, the effect of scrubbing coincides with the formation of a graphitic surface film: the electron induced carbon layer growth becomes the dominant process and graphitisation is the leading phenomenon. The SEY is further reduced to values which are even below those of an atomically clean metal surface. The occurrence of material transformation at the atomic level induced by electron irradiation was measured by combined SEY and X-ray photoelectron spectroscopy (XPS) with core level deconvolution [153]. In the case of as received surface samples, the measured C1s spectrum can be decomposed into a main peak, to be attributed to sp^3 hybridized C atoms in C–C and C–H bonds, and two weak components ascribed to single or double C–O bonds. Under electron beam irradiation, a modification of C1s core level is observed. Electrons decompose the weakly bound species and converts the sp^3 hybridized C atoms into a network having predominantly sp^2 bonds, as shown by the appearance of the graphitic component in the C1s spectrum. Electron irradiation at higher energies (e.g. above 200 eV) are capable to modify the chemical state of almost all the contaminating C atoms, producing a graphitic-like layer coating the copper surface exhibiting low SEY. Hence, the decrease in SEY is found dependent on the kinetic energy of the primary electrons.

Combined to electron bombardment, it has been observed that photon irradiation can be capable to produce a sort of scrubbing effect, as shown in Fig. 8.8, where a reduction in the measured photoelectron yield (PY) per adsorbed photon is observed after intense WL SR exposure, roughly equivalent to one day of LHC run at full operation [150]. The correlation of SEY to PY reduction and vice versa is far from trivial: although SEY and PY scrubbing seem to interplay, the only solid conclusion is that a PY reduction is beneficial at least on the same level than the one of SEY, as at least mitigates the primary cause of electron emission.

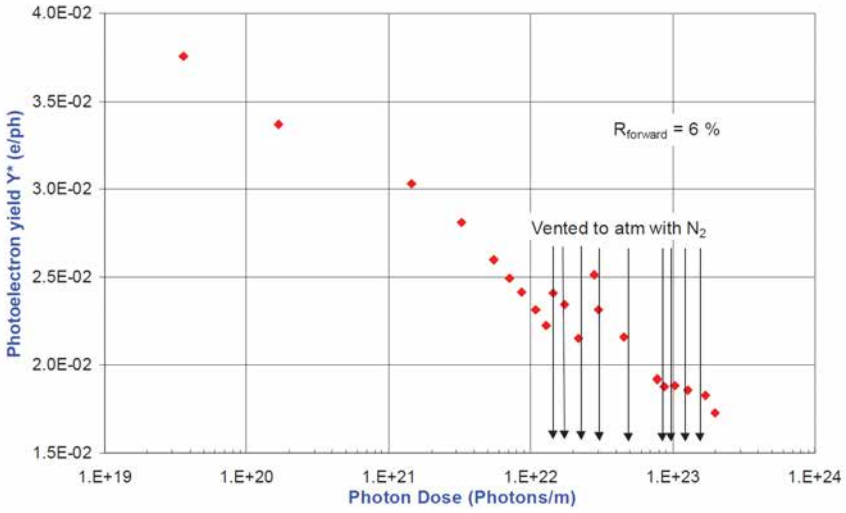

Figure 8.8: Measured reduction of the photoelectron yield per adsorbed photon of a copper colaminated sleeve with a LHC-type sawtooth structure, during irradiation with synchrotron White Light radiation from EPA (critical energy: 194 eV) at 11 mrad incidence. From [150].

8.2 The High Luminosity upgrade of the Large Hadron Collider: HL-LHC

The Large Hadron Collider was successfully commissioned in 2010 for proton−proton collisions at 7 TeV centre-of-mass energy and delivered 8 TeV centre-of-mass proton collisions from April 2012 to the end of 2013, before its Long Shutdown (LS) 1. After consolidation in the 2013-2014 period, the world record of 13 TeV centre-of-mass proton collisions was set in April 2015. The LHC is most powerful accelerator collider currently (2016) available in the world. Its role is at the forefront of the high energy particle physics. The full exploitation of the LHC potentialities is the highest priority of the European Strategy for Particle Physics and is strongly supported by the CERN Council. In order to extend its discovery potential, a major upgrade of the LHC, called the High Luminosity HL-LHC upgrade, is planned for the 2020s, in order to increase its luminosity (and thus the collision rate) above the design value.

The instantaneous luminosity L is the figure of merit of a particle collider and is expressed as

$$L = \gamma \frac{N n_b^2 f_{\text{rev}}}{4\pi\beta^* \varepsilon_n} R, \quad R = \frac{1}{\sqrt{1 + \frac{\theta_c \sigma_z}{2\sigma}}} \tag{8.5}$$

being,

- γ the beam relativist Lorenz factor: $\gamma = 7460.52$ for proton beams at 7 TeV;
- N the number of bunches per beam colliding at the IP. The nominal LHC value for 25 ns bunch spacing is 2808, the HL-LHC baseline assumes 2736 bunches for collisions in IR1 and IR5;
- n_b is the bunch intensity or population. The LHC nominal at 25 ns is $1.15 \cdot 10^{11}$ ppb, translating in 0.58 A of beam current with $N = 2808$ bunches;
- f_{rev} is the revolution frequency: 11.2 kHz;
- β^* is the beam betatron function (focal length) at the collision point: the nominal design value is 0.55 m;
- ε_n is the transverse normalized emittance: the nominal design value is 3.75 μm;

- R is the luminosity geometrical reduction factor arising from the crossing angle, not including the Hourglass effect: 0.85 at a β^* of 0.55 m, down to 0.5 at 0.25 m;
- θ_c is the full crossing angle between colliding beam: 285 μrad as nominal design;
- σ and σ_z are the transverse and longitudinal RMS sizes, nominally 16.7 μm and 7.55 cm, respectively.

Inserting the listed nominal LHC parameters, a luminosity of $1 \cdot 10^{34}$ cm^{-2}s^{-1} is obtained by Eq. 8.5, with an average pile-up (number of events in the same bunch crossing) of $\mu = 27$.

The HL-LHC design goal is to increase by a factor of five the instantaneous luminosity and by a factor of ten - than originally foreseen - the integrated luminosity during the machine lifetime. The novel machine configuration, the High Luminosity LHC, will rely on a number of key innovative technologies representing exceptional technological challenges. These include among others: cutting-edge 11 to 12 T superconducting magnets; very compact superconducting *crab* cavities for beam rotation with ultra-precise phase control; new technology for beam collimation; high-power superconducting links with almost zero energy dissipation.

As LHC represents a highly technological, complex, integrated and optimized machine, such an upgrade requires to be prepared well in time - about ten years - to prototype, test and realize new equipment. HL-LHC joints the efforts and R&D of a large international community and sees contributions from various partners, in particular from leading US and Japanese laboratories, in the design and execution phases. The US LHC Accelerator R&D Program (LARP) has developed some of the key technologies for the HL-LHC, such as the large-aperture niobium-tin (Nb_3Sn) quadrupoles and the crab cavities. The HiLumi LHC Design Study, which was supported in part by funding from the Seventh Framework programme (FP7) of the European Commission (EC), delivered in 2015 the first HL-LHC Technical Design Report. The project and its budget for construction have been approved by the CERN Council in September 2015. In 2016, the governance model is being tailored to support the construction phase, officially started at the end of the Design Study.

8.2.1 From LHC to HL-LHC

The last LHC baseline programme, defined as of June 2015, is shown schematically in Fig. 8.9 for the upcoming ten years. Thanks to a successful Long Shutdown 1 (LS1) in 2013–2014, the LHC is expected entering into the nominal energy regime of 14 TeV centre-of-mass energy by LS2, and reach and pass the design luminosity of 10^{34} cm^{-2}s^{-1} by 2016. Considering this peak value, the capability of delivering a total integrated luminosity of about 40 fb^{-1} per year is foreseen. In the period 2015–2022, further increase in the peak luminosity is conceivable employing the margins in the LHC design. In principle, a factor two in the nominal design performance is considered as potential exploitable. The second Long Shutdown (LS2) in 2019–2020 will consolidate luminosity and reliability as well as see the upgrade of the LHC injectors. The High Luminosity LHC project is in fact in close collaboration with the CERN project for the LHC Injector complex Upgrade (LIU), the companion ATLAS and CMS upgrade projects of 2019–2020 and 2024–2026 and the upgrade foreseen in 2019–2020 for both LHCb and Alice.

After Run 3, foreseen for the period 2021–2023, the statistical gain in running the accelerator without a significant luminosity increase beyond its design value will become marginal. The running time necessary to halve the statistical error in measurements after 2020 will be more than ten years. In order to maintain scientific progress and exploit the machine full capacities, the LHC will need to have a decisive increase of its luminosity after 2020. The luminosity upgrade, motivated by physics results and operation experience, is the rationale behind the HL-LHC upgrade. The main objective of the High Luminosity LHC design study is to determine a set of beam parameters and the hardware configuration that will enable the LHC to reach the following quantitative targets:

- a peak luminosity of $5 \cdot 10^{34}$ cm^{-2}s^{-1} with levelling;
- an integrated luminosity of 250 fb^{-1} per year with the goal of 3000 fb^{-1} in about a dozen years after the upgrade. This integrated luminosity is about ten times the expected luminosity reach of the first twelve years of the LHC lifetime.

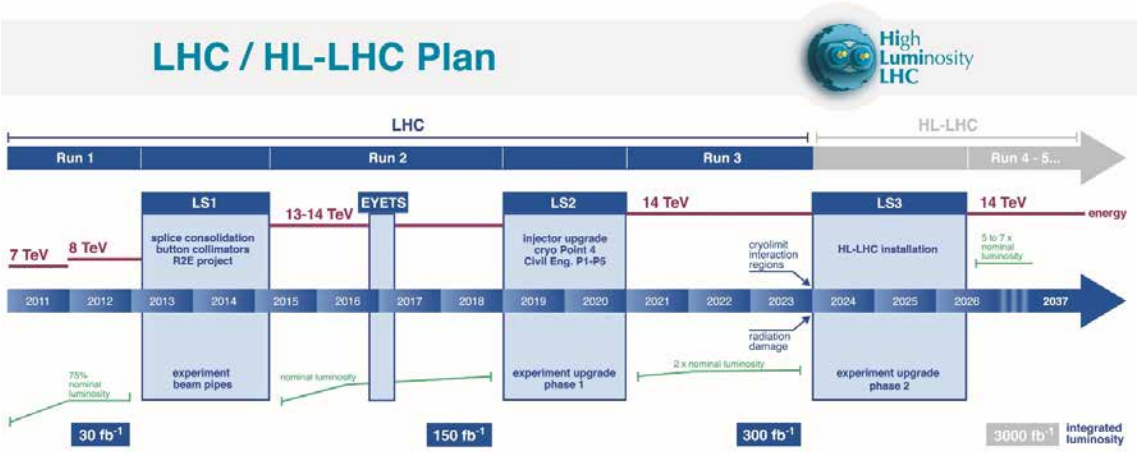

Figure 8.9: LHC baseline plan for the next decade and beyond showing the energy of the collisions (upper red line) and luminosity (lower green lines).

For comparison, all of the hadron colliders in the world before the LHC have produced a combined total integrated luminosity of about 10 fb^{-1}. The LHC delivered nearly 30 fb^{-1} by the end of 2012 and should reach 300 fb^{-1} in its first 13–15 years of operation.

Being the new equipment designed with a 50% margins (with respect to the forecast instantaneous heat deposition and the integrated radiation dose), the concept of ultimate performance has been defined, wherein all margins are used for a performance increase. The ultimate parameters should push the machine peak levelled luminosity to about $7 \div 7.5 \cdot 10^{34}$ cm^{-2}s^{-1}, increasing the total pile-up in the detectors up to around 200. This luminosity level should enable the collection of up to 300–350 fb^{-1}/year, provided the experiments can sustain the pile-up level. In terms of total integrated luminosity, the ultimate performance corresponds to a value of about 4000 fb^{-1}.

The installation of the main hardware for the HL-LHC is targeted for LS3, scheduled for 2024–2026. The hardware commissioning is foreseen at the machine restart by 2026, in order to ensure high efficiency operation until 2035–2040.

8.2.2 Present limitations and hardware upgrade

The new machine configuration requires replacement or improvement of specific systems, because of their vulnerability to breakdown and accelerated ageing, or due to bottleneck for operation in a higher radiation environment.

The LHC **Inner triplet magnets**, providing the last beam focusing at the LHC experiments, are designed for a dose of about 30 MGy, corresponding to about 300 fb^{-1}. Some components of the inner triplet quadrupoles and their corrector magnets, by LS3, will be entering into the region of possible radiation damage. Quadrupoles are expected to withstand a maximum of 400 fb^{-1} to 700 fb^{-1}, whereas the corrector magnets of nested type could fail already at 300 fb^{-1}. Actual damage must be anticipated because the most likely failure mode is through sudden electric breakdown, entailing serious and long repairs. Hence, the replacement of the triplet magnets must be envisaged before damage occurs. Replacement of a low-beta triplet string is a long intervention, requiring a one to two year shutdown, and must be coupled with a major detector upgrades (which also are required at around 300 fb^{-1}).

To increase intervention flexibility and machine availability, upgrade in the **cryogenic** plant and establishment of full separation between superconducting RF and magnet cooling is foreseen. In the long term, the cooling of the inner triplets and matching section magnets must be separated from the arc magnets, in order to avoid the warm-up of an entire arc in the case of triplet region intervention.

The LHC **collimation system** was designed for a first operational phase. The present system was optimized for robustness and will need an upgrade that takes into account the need for the

lower impedance required for the planned increase of beam intensity. A new configuration will also be required to protect the new triplets in IR1 and IR5.

Special attention is in the **dispersion suppressor** (DS) regions, where a leakage of off-momentum particles into the first and second main superconducting dipoles has already been identified as a possible LHC performance limitation. The most promising concept is to substitute an LHC main dipole with dipoles of equal bending strength (120 T·m) obtained by a higher field (11 T) and shorter length (11 m) than those of the LHC dipoles (8.3 T and 14.2 m), the space gained being employed for the installation of additional DS collimators.

Radiation to electronics (R2E) is an important issue for the LHC operation. Effort should be put in substituting radiation sensitive electronic boards of the power converter system with radiation-hard cards. In the high luminosity regions, displacement of the power converters and associated electrical feedboxes (the DFBs) far from the LHC tunnel is considered essential. While a removal to the surface was initially considered, this equipment is now foreseen to be finally installed in a new underground area, following an integration optimization. **Superconducting links** - made from High Temperature Superconductors (like YBCO or Bi-2223) or MgB_2 superconductors - are studied to place power converters in distant locations and allow remote powering of cold circuits.

8.2.3 HL-LHC parameter list

We present in Table 8.2 the machine parameter sets foreseen for the High Luminosity upgrade of LHC. The nominal LHC machine parameters are also listed for reference. The 25 ns bunch spacing is the baseline operation mode; however, an alternative filling scheme, comprising, every eight bunches, four empty, (so-called 8b4e), is considered in case the electron cloud or other unforeseen effects undermine 25 ns performance. The 8b4e scheme replaces the previous alternative of 50 ns space bunching that is detrimental from the point of view of pile up. A slightly different parameter set at 25 ns (the batch compression and beam merging scheme, so-called BCMS) with very small transverse beam emittance is also shown and might be interesting for HL-LHC operation in case high beam intensities will result in unforeseen emittance blow-up.

The upgrade should provide the potential for good performance over a wide range of parameters: it goes by experience that both the machine and experiments will find the best practical set of parameters in actual operation. In any case, the key areas targeted for luminosity performance upgrade are the following:

- The total **beam current** may be a hard limit in the LHC since many systems are affected: RF power system and RF cavities, collimation, cryogenics, kickers, vacuum, beam diagnostics, Quench Protection System (QPS) etc. Radiation effects aside, all existing systems have been designed in principle for $I_{beam} = 0.86$ A, i.e. the ultimate LHC beam current. The ability to go to ultimate limit is still to be experimentally demonstrated and the HL-LHC will need to go 30% beyond with 25 ns bunch spacing.

- The **beam brightness**, the ratio of the bunch intensity over its transverse emittance, is a beam characteristic that must be maximized at the beginning of beam generation and then preserved throughout the entire injector chain and in LHC itself. The LIU project has the primary objective of increasing the number of protons per bunch by a factor of two above the nominal design value in the LHC injector chain, while keeping emittance at the present low value.

- The classical route for a luminosity upgrade is to reduce the **beam betatron function at the interaction point** β^*, by means of stronger and larger aperture low-β triplet quadrupoles. This reduces the transverse size of the luminous region resulting in the gain in peak luminosity. However, a reduction in β^* values implies not only larger beam sizes in the triplet magnet, but also, respecting the requirement for a constant normalized beam separation over the common part of the insertion, an increase in crossing angle. The increased crossing angle in turn requires increased aperture in the triplet magnets, a larger aperture D1 dipole (first separation dipole) and further modifications to the matching section. Stronger chromatic aberrations coming from the larger betatron functions inside the triplet magnets may furthermore exceed the strength of the existing correction circuits. The peak β function

Parameter	Nominal LHC (design report)	HL-LHC 25 ns (standard)	HL-LHC 25 ns (BCMS)	HL-LHC 8b+4e
Beam energy in collision [TeV]	7	7	7	7
N_b	1.15×10^{11}	2.2×10^{11}	2.2×10^{11}	2.3×10^{11}
n_b	2808	2748	2604	1968
Number of collisions in IP1 and IP5	2808	2736	2592	1960
N_{tot}	3.2×10^{14}	6×10^{14}	5.7×10^{14}	4.5×10^{14}
Beam current [A]	0.58	1.09	1.03	0.82
Crossing angle [μrad]	285	590	590	554[10]
Beam separation [σ]	9.4	12.5	12.5	12.5[10]
β^* [m]	0.55	0.15	0.15	0.15
ε_n [μm]	3.75	2.50	2.50	2.2
ε_L [eVs]	2.50	2.50	2.50	2.50
r.m.s. energy spread	1.13×10^{-4}	1.13×10^{-4}	1.13×10^{-4}	1.13×10^{-4}
r.m.s. bunch length	7.55×10^{-2}	7.55×10^{-2}	7.55×10^{-2}	7.55×10^{-2}
IBS horizontal [h]	80–106	18.5	18.5	13.1
IBS longitudinal [h]	61–60	20.4	20.4	17.6
Piwinski parameter	0.65	3.14	3.14	3.14
Geometric loss factor R_0 without crab cavity	0.836	0.305	0.305	0.304
Geometric loss factor R_1 with crab cavity	(0.981)	0.829	0.829	0.828
Beam–beam/IP without crab cavity	3.1×10^{-3}	3.3×10^{-3}	3.3×10^{-3}	3.9×10^{-3}
Beam–beam/IP with crab cavity	3.8×10^{-3}	1.1×10^{-2}	1.1×10^{-2}	1.3×10^{-2}
Peak luminosity without crab cavity [$cm^{-2}\,s^{-2}$]	1.00×10^{34}	7.18×10^{34}	6.80×10^{34}	6.38×10^{34}
Virtual luminosity with crab cavity, $L_{peak} \times R_1/R_0$ [$cm^{-2}\,s^{-2}$]	(1.18×10^{34})	19.54×10^{34}	18.52×10^{34}	17.40×10^{34}
Events/crossing without levelling and without crab cavity	27	198	198	246
Levelled luminosity [$cm^{-2}\,s^{-2}$]	-	5.00×10^{34} [5]	5.00×10^{34}	3.63×10^{34}
Events/crossing (with levelling and without crab cavities for HL-LHC)	27	138	146	140
Peak line density of pile-up event [event/mm] (maximum over stable beams)	0.21	1.25	1.31	1.28
Levelling time [h] (assuming no emittance growth)	-	8.3	7.6	9.5
Number of collisions in IP2/IP8	2808	2452/2524[7]	2288/2396	1163/1868
N_b at SPS extraction	1.20×10^{11}	2.30×10^{11}	2.30×10^{11}	2.40×10^{11}
n_b/injection	288	288	288	224
N_{tot}/injection	3.46×10^{13}	6.62×10^{13}	6.62×10^{13}	5.30×10^{13}
ε_n at SPS extraction [μm]	3.40	2.00	<2.00[8]	1.70

Table 8.2: High Luminosity LHC parameters list for proton-proton collisions.

is also limited by the possibility to match the optics to the regular beta functions of the arcs. A previous study has shown that in the nominal LHC the practical limit for β^* is 30 cm to 40 cm versus a nominal value of 55 cm. However, a novel scheme called Achromatic Telescopic Squeeze (ATS) uses the adjacent arcs as enhanced matching sections. The increase of the beta functions in these arcs can boost, at constant strength, the efficiency of the arc correction circuits. In this way a β^* value of 15 cm can be envisaged and flat optics with a β^* as low as 5 cm in the plane perpendicular to the crossing plane could be realized. For such a β^* reduction the triplet quadrupoles need to double their aperture and require a peak field 50% above the present LHC. This implies the use of new, advanced, superconducting technology based on Nb_3Sn.

- The drawback of very small β^* is the larger crossing angle θ_c at the Interaction Point. This causes a severe reduction of the **geometrical luminosity reduction factor** R. In Fig. 8.10 the reduction factor is plotted against β^* values. A countermeasure for compensating the geometric reduction factor is the use of special superconducting RF cavities, so-called crab cavities, capable of generating transverse electric fields that apply a torque and rotate each bunch longitudinally by $\theta_c/2$, such that every bunch effectively collide head-on, overlapping

perfectly at the collision points. Crab cavities allow access to the full performance of the small β^* values offered by the ATS scheme and the larger triplet quadrupole magnets, restoring the reduction value R to that of the present LHC despite the much larger θ_c.

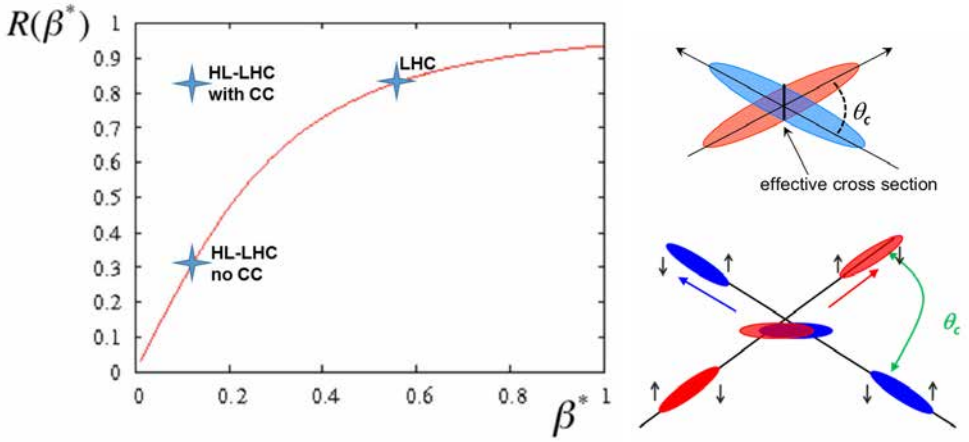

Figure 8.10: Geometrical luminosity reduction factor R vs. β^*. Left: constant normalized beam separation for the nominal LHC, for HL-LHC without crab cavities and for HL-LHC with crab cavities cases. Right: depiction of bunch crossing overlap reduction effect (top), and the crab cavity beam manipulation (bottom).

8.3 Electron cloud in the HL-LHC

During the Large Hadron Collider Run 1 (2009-2013), considerable heat load (∼200W) due to electron cloud was observed on the Inner Triplets (IT) beam screens during operation with 25 ns bunch spaced beams of nominal intensity. After successful completion of the Long Shutdown 1, the Large Hadron Collider resumed operation in 2015 with circulation of 25 ns spaced beams, accelerated for the first time to 6.5 TeV. Strong electron cloud effects were observed in all the machine, with the main performance limitation sitting in the response to the beam induced heat load transients at injection and reach of the available cooling capacity of the cryogenic system (estimated: 135 W/half-cell in arc 2-3, 160 W/half-cell in the others) [154]. Mitigation was achieved by modulation of the intensity ramp-up, optimization of the filling schemes and beam conditioning in dedicated scrubbing runs and throughout the physics runtime.

Observations in the Standalone and Inner Triplet areas confirmed the importance of electron cloud multipacting at IT1/5 and IT 2/8, exhibiting a specific (global) heat load of ≈3.1 W/m/aperture (≈110 W) and of ≈2.2 W/m/aperture (≈100 W), over a current expected global operational limit of 120 W [154]. In view of the intensity ramp-up toward 2748 bunches - in trains of 288 - of 2016, the expected rise in heat load transients will be counterbalanced by new feed-forward logic in the beam screen control loop [154] and optimization of the global capacity of the cryogenic plants.

The first extrapolations of these observations to the High Luminosity upgrade (HL-LHC) beam parameters and IT layout predicted in 2014 a sensible increase of heat load due to electron cloud build-up [155]. The increase of heat load was expected to be accompanied by increase of background to the LHC experiments due to vacuum pressure increase: both effects were considered intolerable.

The most recent extrapolations [156] with a HL-LHC nominal bunch intensity of $2.2{\cdot}10^{11}$ ppb predict no significant increase in the heat due to electron cloud in the HL-LHC arcs and quadrupoles for fully scrubbed Cu (SEY≤1.3) (see Fig. 8.11). The exact behaviour depends on the detailed features of the SEY dependence on electron energy, which the model can predict with difficulty. The access to a low SEY regime, close to the operational Cu limit of SEY≈1.2, seems essential, while the effect of deconditioning is yet far from being controllable. Experience from Run 1 and the beginning of Run 2 show that beam scrubbing can allow to approach SEY≈1.3 in the arcs: going further will be the challenge already of the LHC, before the HL-LHC. On top of that, the

increased HL-LHC bunch intensity will reduce the cooling margin available for the electron cloud, as the increasing contribution of the image currents ($\sim k_b N_b^2$) and synchrotron radiation ($\sim k_b N_b$) heat load will be inevitable. Provided a sufficiently low SEY is reached, there is confidence that an increased HL-LHC bunch intensity will be considered acceptable for heat load. The evaluation of the effects of an increase bunch intensity on the beam stability is currently (2016) in study. Back-up solutions are in place: the adoption of 200 MHz main RF will produce longer bunches and have a positive impact on the electron cloud threshold, which will move forward; the fallback scenario of employing filling patterns - with 25 ns spacing - interleaving batches of 8 bunches with gaps of 4 slots, shows a significantly increased multipacting threshold compared the standard 25 ns scheme. This backup scheme, which would slightly impact on the maximum circulating intensity, is yet considered a source of safe operation with 25 ns beam, providing still 50% more bunches than with 50 ns spacing.

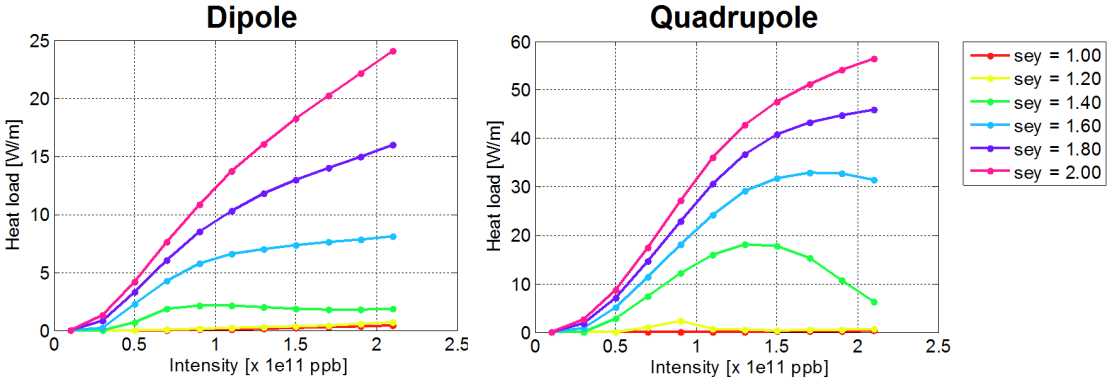

Figure 8.11: Bunch intensity dependence for the LHC arc main dipole (left) and quadrupole (right) magnets. The model assumes constant E_{max} and uniform SEY over the beam screen surface. From [156].

The recent extrapolations confirm, instead, an intolerable increase of heat load in IT 1/5 and IT-D1 2/8 of a factor 5÷7 for 1.2≤SEY≤1.3 (see Fig. 8.12). Not only the increase in the heat load is considerable, but this extrapolations show that, even with a fully scrubbed Cu surface, an acceptable heat load will never be reached with beam induced scrubbing. Modifications in the cryogenic installation like, the increase of the valves K_v parameter (replacement of the valve seats or their entire bodies) or the cooling of the triplet with parallel circuits, could allow an increase in the cooling capacity of a factor 2, but are hardware invasive and should be pursed as *extrema ratio*. Even if the heat load is mastered, the increase of electron flux bombarding the BS of the Inner Triplets, close to the interaction region, will be accompanied by an increase of the vacuum density in the LHC experiments, in turn raising the background in the experiment to levels not satisfactory. On top of that, an increase in the maximum tolerable temperature excursion of the beam screen during the electron cloud transients, to e.g. 30-35 K, would turn in undesirable dynamic pressure rises, due to loss of condensation of gas species like CO or CH_4, and will translate again in an increase of background to the LHC experiments. Limitations in the maximum luminosity and total beam intensity in collision operational mode and potential beam stability issues are expected.

The emerging picture shows that measures for mitigation of the electron cloud build-up in the HL-LHC Inner Triplets are mandatory. A possible operational compromise has been found in the region of SEY=1.05÷1.15 (see Fig. 8.12), where the energy dissipated by electron cloud will be compatible with a cooling budget of ∼200 W. Previous studies have shown that carbon coating provides reliably low as-received SEY, typically below 1.1 at room temperature, and is suitable in un-bakeable vacuum systems [157] [158]. Successful, long-term, mitigation of the electron cloud build-up with a-C coatings has been demonstrated in some SPS room temperature (RT) vacuum chambers with LHC type beams [158]. The current HL-LHC baseline ("12.6 Beam screen requirements", HL-LHC PDR [159]) is therefore to mitigate the beam induced electron cloud by lowering the IT beam screen surface's Secondary Electron Yield (SEY). The baseline mitigation measure is amorphous carbon (a-C) thin film coating for the new HL-LHC triplets in IR1/5. In 2015, it was further decided to study the coating *in-situ* of the ITs at IR2/8. The HL-LHC baseline must be

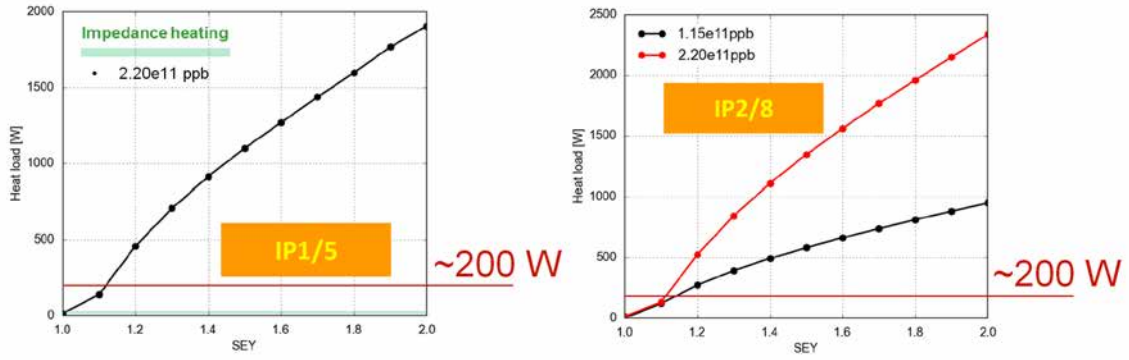

Figure 8.12: Expected total heat load dissipated by electron cloud on the HL-LHC upgraded Inner Triplets beam screen at IP1/5 (left) and at IP2/8 (right) as a function of the surface SEY. The cooling capacity of $\sim$ 200 W is marked in red. From [156].

validated at cryogenic temperature: for that reason, the COLD bore EXperiment (COLDEX) has been re-commissioned in 2014 [20], with the objective of validating the performance of amorphous carbon (a-C) coating at cryogenic temperature in the Super Proton Synchrotron, in presence of LHC type beams.

Alternative scenarii have been identified as back-up options to the baseline HL-LHC mitigation strategy.

Electron density control and suppression techniques employing clearing electrodes were developed and successfully applied in the Intersecting Storage Rings at CERN already in the 70's [160]. More recently, the DAΦNE lepton collider was equipped with clearing electrode to suppress the electron cloud [161]. Strip-line electrodes have been inserted in all dipole and wiggler vacuum chambers of the positron ring and have been connected to external DC voltage generators in order to absorb the photo-electron. The objective was to overcome the limitations in the maximum storable positron current due to the electron cloud driven instabilities. Experimental measurements have shown the their effectiveness with respect to a former average electron cloud density in the order of $1 \cdot 10^{11}$ e^-/m^3. A low DC voltage (in the order of 1kV) applied to the electrodes allowed the collection of electrons right after their emission, eradicating the possibilities to have electron multipacting.

Several design issues have been identified for the installation of clearing electrodes in the cryogenic vacuum systems like the one of LHC. First, their integration in a limited space cryogenic environment is extremely difficult. Secondly, their interaction with the beam environment, subordinated to their effectiveness, cannot be avoided. The impact on the additional impedance must be controlled by wise design. The confinement of the electrons due to high magnetic fields in the dipoles defines specific vertical regions, or stripes. The electric field of electrodes, that would have to be placed in the vertical plane, should be sufficiently wide to cover the entire region where the (symmetric) electron stripes are located. The position of the stripes and their separation, besides, are not predefined and depend on the bunch population. Lastly, the inevitable interface toward room temperature requires a non-trivial integration work in the already existing interconnection layout.

A potential alternative surface treatment for electron cloud eradication is currently offered by the Laser Engineered Structured Surfaces (LESS) [162] [163] [164] and is under study at CERN [165]. It has been recently (April 2016) decided the LESS is of interest for HL-LHC and a prototype installation and test should be pursued by LS2.

The LESS surface treatment is produced by a high power, short pulse length, laser of 400 nm wavelength. At high irradiance, short (ns) laser pulses deposite energy on the material surface, which is conducted into the bulk and in part converted into directed kinetic energy by thermal expansion of the heated layer. The surface treatment result is hence dominated by expansion and ablation. The surface response to much faster and ultra short (ps to fs) pulses is instead dominated by heat conduction, as hydrodynamic motion during the pulse duration is negligible. Like that, the thermal expansion of the heated layer is negligible. A beam of the cited characteristics can be

rastered on the material surface, so that the average laser energy fluence is just above the ablation threshold. The resulting effect is the production of repetitive structures (pyramids, grooves, etc.). In Fig. 8.13 we observe the surface finish of a LESS treatment with pyramidal structures, called Type A. The treatment does not require inert protective atmosphere and can performed in air at room temperature. The final surface finish is black and only partially oxidized. The treatment robustness and the capability of polishing by solvent are currently unknown, which is a vital information for compatibility in UHV systems. Its manipulation is currently considered detrimental for the surface finish and polluting.

The produced pattern becomes suitable for secondary electron emission mitigation, as the secondary electrons emitted by such textured surface have less probability of escape. The best performance is obtained by LESS structures type C, visible on Fig. 8.14, where the measured at room temperature SEY is shown in Fig. 8.15. The maximum electron yield reaches the extremely low value of 0.8 over a large energy spectrum. We observe an energy dependence which qualitatively differs from the typical one of metallic surfaces (described in Sect. 7.3).This aspect is probably related to the fact that LESS low emission properties are linked more to a geometrical effects, rather a material electronic configuration.

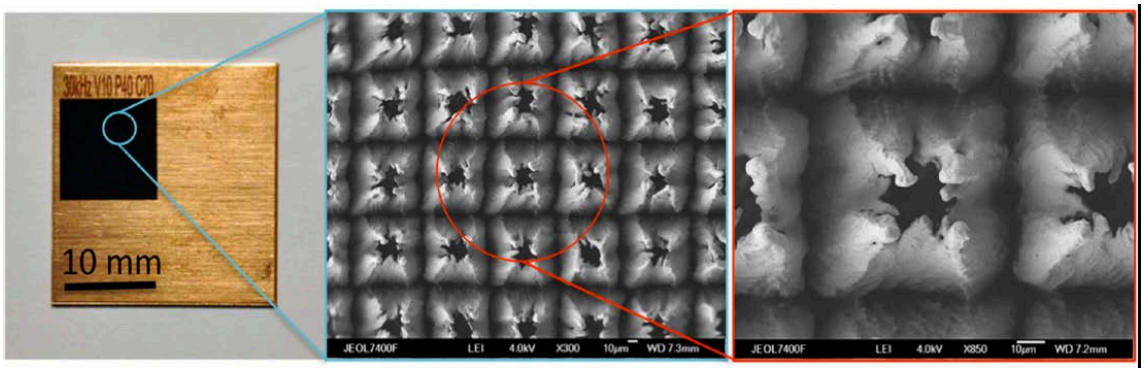

Figure 8.13: Laser Engineered Structured Surfaces, type A. Courtesy of A. Abdolvand, University of Dundee.

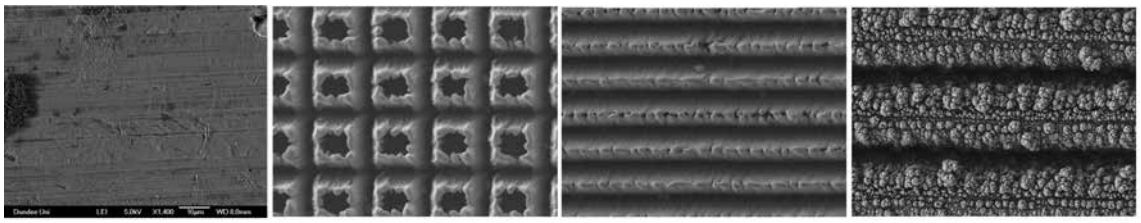

Figure 8.14: From left to right: copper surface before laser processing; LESS type A structures, LESS type B structures, LESS type C structures. Courtesy of A. Abdolvand, University of Dundee.

Preliminary considerations for the application of such laser treatment to the HL-LHC are ongoing. The established results see a reliably low SEY obtained over a large span of laser parameters. The increase of roughness has shown an increase of roughly 5% RF impedance at 7.8 GHz, measured at room temperature in laboratory. The increase could become more relevant at cryogenic temperature, therefore a test at LHe temperature and at frequency of interest for LHC (400 MHz) is required. The practicability of treating a Cu colaminated BS (80 μm) has to be demonstrated and its impact on the Residual Resistivity Ratio sized. First measurements indicate a reduction of a factor 2 in the resistivity at 4.2 K. A thorough UHV vacuum characterization is required, considering the pump-down, outgassing, UHV cleaning with solvents and detergents and bake-out capability. The production of dust has to be characterized and minimized. In view of a potential need for HL-LHC triplets for in-situ treatment, the technology required for deported treatment, such as in long tubes, must be developed; for that, the adoption of industrially available technology for the optics and the laser is seen feasible. The next steps foresee a validation in real accelera-

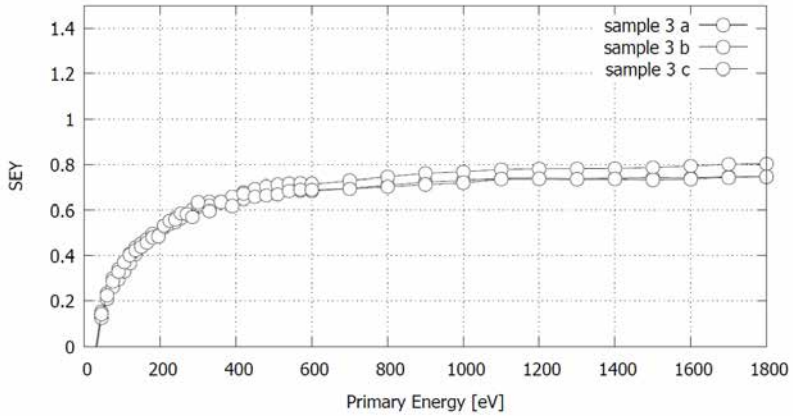

Figure 8.15: Secondary Electron Yield of a Cu sample treated with Laser Engineered Structured Surfaces, type C, measured at room temperature. From [165].

tor environment: a test installation in SPS dipole magnet chamber with electron cloud monitor (strip detector) has been successfully achieved in 2016. Future tests at cryogenic temperature are foreseen in the COLD bore EXperiment by the 2017-2018 period.

Chapter 9

The COLD bore EXperiment (COLDEX)

9.1 Motivation and amorphous carbon coating

The COLD bore EXperiment (COLDEX) is an experimental test vacuum sector that mimics the cold bore and beam screen cryogenic vacuum system adopted in the LHC cryomagnets. Originally designed to measure synchrotron radiation induced gas desorption [150], COLDEX was installed in Super Proton Synchrotron (SPS) in 2001 to evaluate the impact of electron cloud effects onto cryogenic vacuum systems [137]. The experimental campaign carried during the LHC design phase allowed to validate the current LHC cryogenic vacuum system principle with LHC type proton beams.

The COLDEX experiment has been re-commissioned in 2014 [20] with the objective of validating the performance of amorphous carbon (a-C) coating at cryogenic temperature in the SPS, in presence of LHC type beams. Typical measurements obtainable by the COLDEX setup during beam runtime are the dynamic pressure rise, gas composition, dissipated heat load and electron activity observed as a function of the beam parameters and the cold bore and beam screen surface conditions (temperature and gas coverage). The existing COLDEX Cu ID67 beam screen, employed in period 2003-2004, was dismounted and carbon coated in 2014, while an overhaul and upgrade of the vacuum, cryogenic and control systems have been carried out [20].

During the COLDEX re-commissioning, the inner walls of the COLDEX BS were coated with a 400 nm thick a-C film using DC magnetron sputtering in cylindrical configuration. A graphite rod (ashes content below 400 ppm) was used as target. A magnetic flux of 180 Gauss was applied by a solenoid during the coating process. Krypton was adopted as discharge gas at a pressure of $5{\cdot}10^{-2}$ mbar. The power density was kept at 100 W/m and the discharge voltage at $\sim$ 700 V.

The surface SEY was measured on witness samples after two months of air exposure, wrapped in aluminium foil. Details of the laboratory SEY measurement system can be found in [157]. The measurement results (Fig. 9.1) show that the obtained δ_{max} after coating was reliably below 1.1 at room temperature. The corresponding E_{max} is situated in the 280$\div$300 eV window. The surface SEY at cryogenic temperature (4.2 K) is expected to be similar [166], unless a relevant change in the structure of the coating leads, for instance, to loss of electric conductivity [167]. In general, the excitations leading to secondary electron emission are in the order of few eV. A change in temperature would bring to a change in the electron distribution in the density of states in a typical range of thermal energy, kT, i.e. tens of meV, does not influencing the properties of the SEY.

9.2 Experimental layout

The COLD bore EXperiment (COLDEX) is installed on a vacuum by-pass sector (431) derived from the sector 430 of the SPS Long Straight Section (LSS) 4, specifically in the half-cell 417 (see Fig. 9.2), has been recovered in 2014. The previous SPS experimental program based on the

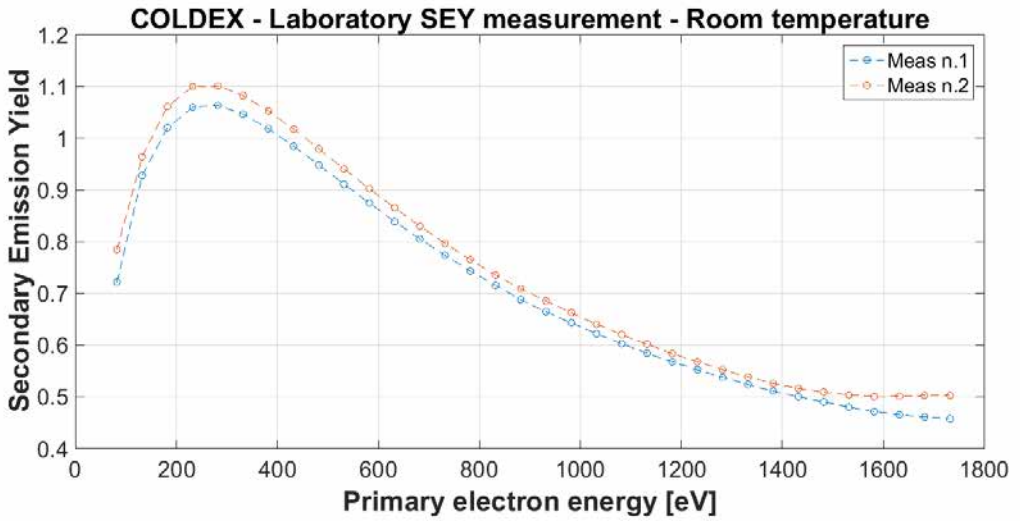

Figure 9.1: Laboratory measurements of SEY on one witness sample obtained during COLDEX BS a-C coating.

validation of a LHC-type cryogenic vacuum system subjected to electron cloud was successfully run and completed between 2001 and 2004 with a copper beam screen [168].

The SPS LSS4 by-pass (sectors 430 and 431) is assembled on a transversally (x-axis, beam convention) movable stage. Beam can pass either through the COLDEX experiment (sector 431) during dedicated experimental runs or through the standard ID 156mm SPS beam pipe (sector 430) during SPS normal operation (see Fig. 9.2). The vacuum by-pass (see Fig. 9.3) is realised by two opposite Y-chambers built in 2001 from CERN-ISR Intersection Point chambers. A similar, single, by-pass chamber is adopted in the SPS LSS1 for insertion of the single-turn SPS beam dump TBSM11672.

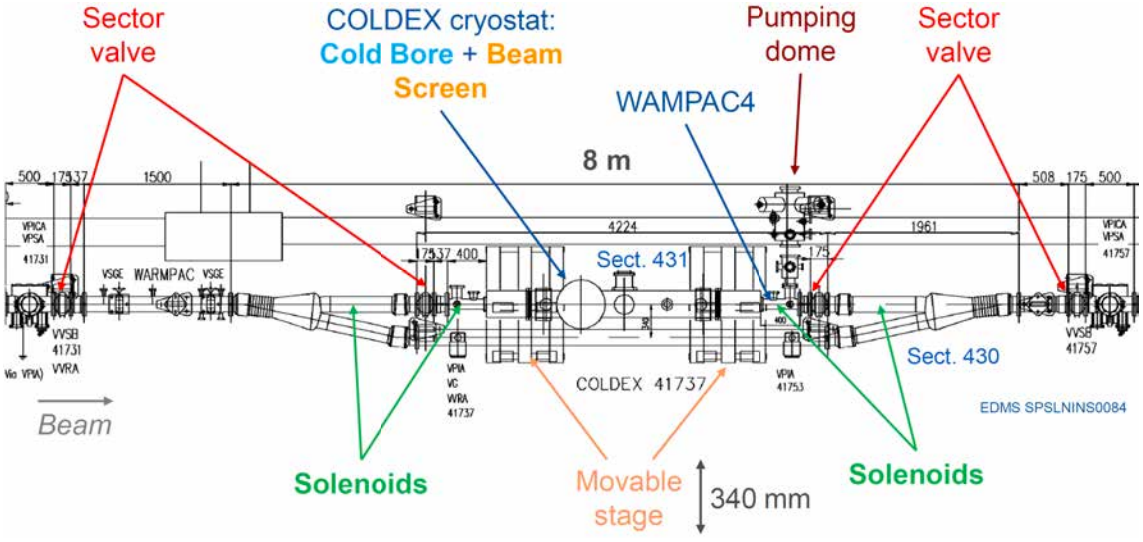

Figure 9.2: Layout of sectors 431/430 elaborated from the SPS LSS4 layout drawing of period 41410-42210 (SPSLNINS0084).

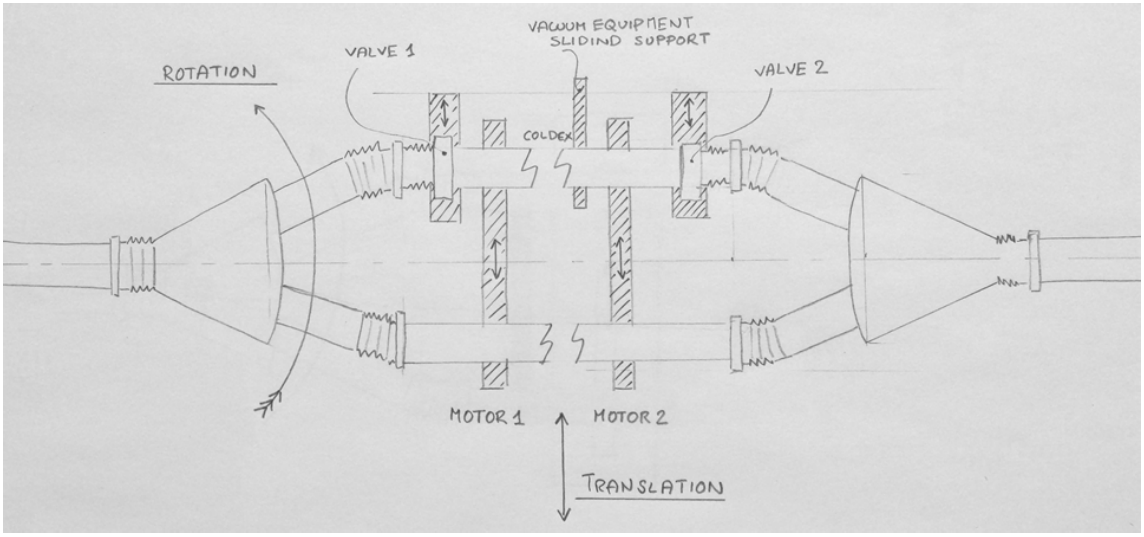

Figure 9.3: Schematic view of the LSS4 by-pass movement system. Courtesy of P. Chiggiato.

The displacement system is composed by two screw axes anchored to two Al plates, in turn installed on standard yellow SPS busbar supports. The axes support the COLDEX cryostat on a hinge (left) and slide (right) mechanism. Sector 430 is anchored to sector 431 by two supports installed on the COLDEX cryostat which define, rigidly, a parallel longitudinal displacement of 340 mm. During the by-pass movement, the two motorized axes translate the COLDEX cryostat and the SPS beam pipe, while the rotation is allowed by three bellows on each side (one belonging to the Y-chamber, two belonging to sectors 430 and 431). Additional three passive sliding axes (two needed to support each sector 431 valves, one for the pumping dome) follow the transverse movement during COLDEX displacement. The experiment insertion and extraction is operated during period of no beam and requires access to the SPS accelerator tunnel after a short period of radiation cool-down (typically the whole operation is executed in less than 60 minutes).

SPS sector 430 (see Fig. 9.2) is identified by the all-metal pneumatic sector valves VVSB_41731 and VVSB_41757. Sector 431 can be further vacuum isolated from sector 430 by two sector valves (VVSB_41737, VVSB_41753), that are opened only when the COLDEX cryostat is inserted in the SPS ring and the experiment is in operation. When the experiment is isolated, the setup is used to study the vacuum performance of a a-C coatings in a LHC-type system (see Section 9.5).

For the HL-LHC experimental program, the COLDEX cryostat and BS design were left unchanged from the 2001-2004 SPS layout. The existing Cu BS was dismounted, internally coated with a thin film layer (400 nm) of amorphous carbon and then reinstalled during the CERN Long Shutdown 1 (LS1, 2013-2014).

The COLDEX cryostat houses a 2232 mm long OFHC copper beam screen (BS) inserted in a 316LN stainless steel cold bore vessel (CB). Figure 9.4 shows a longitudinal cross section of the cryostat. Beam vacuum is identified by the BS. The BS is mounted coaxial to the CB and is a circular, ID67/OD70 mm, extruded pipe (Figure 9.5 and 9.6), perforated by two rows of 7.5x2 mm elongated holes, or LHC-type slots. The pumping slots are regularly arranged and form a total number of 264, which returns a transparency of 1% to the CB. The holes length (and therefore their longitudinal positioning) is repetitive and not pseudo-random as in the LHC BS design. The impact of such choice on the beam impedance is discussed in [138] and was considered negligible. In addition, the COLDEX transparency to the CB is lower than the LHC case, which is 4%.

Similarly to the LHC arc beam screen, an electron shield is mounted behind the slots. Opportunely bent copper plates are screwed on the BS back side and serve as slots "baffles", i.e. they shield the pumping slots and intercept any straight path to the CB. The role of the baffles is to protect the cold bore from electron cloud. The clearance of the electron shield from the BS back side is 4 mm, i.e. twice the LHC design. Former circular, 4.75 mm, pumping holes (used before 2003) are also covered by such Cu plates.

The BS hosts two central, vertical vacuum ports, respectively of ID 35 and 18 mm. Both ports are shielded via 316LN stainless steel grids, forming a 2x2 mm reticule with a wire diameter of

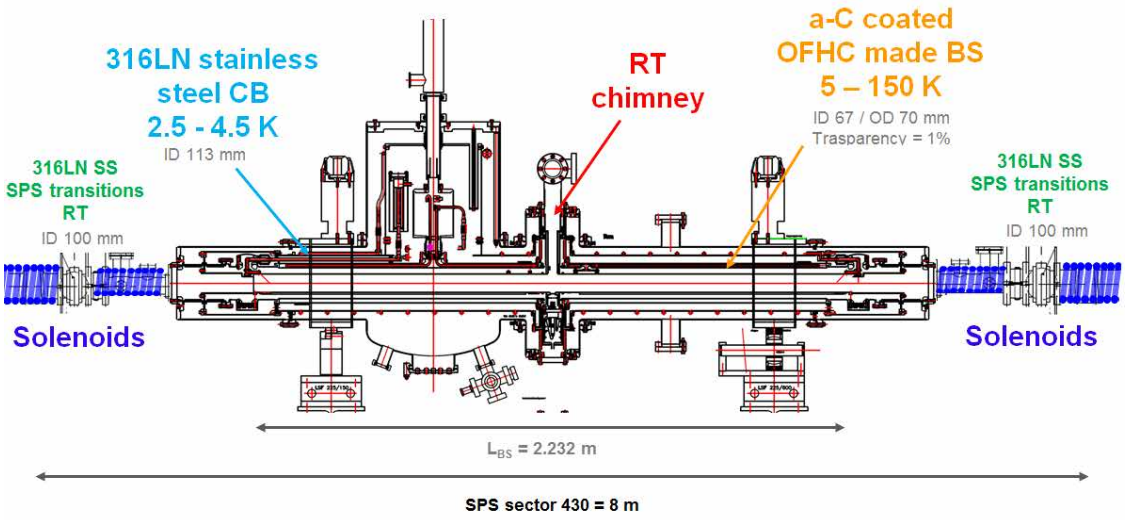

Figure 9.4: Vertical cross section of the COLDEX cryostat and vacuum principle.

0.5 mm. The grid transparency is 0.5625 cm^2/cm^2, or 56.25%. The upper vacuum port derived at the centre of the BS faces a room temperature chimney (also visible in Fig. 9.8), installed on the central vertical axis of the cryostat. A clearance gap of 1 mm is left between the chimney and the BS in order to minimise the heat transfer. Such choice helps also minimizing the parasitic pumping (conductance) to the cold bore. The ratio of the vacuum conductance of the chimney shielded port over the gap aperture is 0.78. Opposite to the chimney, an extractor gauge is installed on the cold system, facing the second, circular, BS vacuum port. The extractor gauge is surrounded by a copper shield which is thermally connected to the cryostat cryogenic thermal shield. The extractor gauge has not been recommissioned in 2014.

The BS is actively cooled by GHe by means of two, electron beam welded, opposite cooling channels, which assure good transverse temperature homogeneity and limited longitudinal ΔT (which depends on the available cooling mass flow rate). The BS can be thermally controlled in a large range of temperature, virtually between 4.5 K and 300 K with GHe. Cooling with LHe is possible but not endurable. The selected experimental conditions and in the particular the CB temperature, narrow the temperature window, which is determined by the available GHe cooling flow, and in turn, by the dissipated static or/and dynamic heat load that can be extracted from the cryogenic refrigeration capacity. As a result, during the experimental studies for cryogenic vacuum characterization of the a-C coating, the full temperature range can be employed while the CB - not actively cooled - temperature floats due to radiative heat exchange. During beam time, when the BS/CB nominal cryogenic temperature conditions are met, the BS can be safely operated up to 130 K, while having an acceptable heat leak into the CB LHe bath. Such BS temperature conditions match with both the present LHC and future HL-LHC baseline specification, which are 5-20 K and 40-60 K, respectively.

The BS is equipped with two, LHC type, 0.1 mm thin cold-to-warm transitions (CWTs) at its extremities, made of copper coated (2 μm) 316LN stainless steel. RF continuity is assured with Cu RF fingers. The CWTs surfaces were not a-C coated during recommissioning. The total length of a CWT is 280 mm. At approximately 2/3 of its length, a thermal anchoring to the CB thermal shield is performed. Such feature minimises the heat inleaks to the BS from room temperature and differentiates the temperature gradients established before and after the anchoring. The final adaptations to the upstream and downstream, room temperature, ID 100 mm, 316LN stainless steel chambers are tapered, for impedance minimization, with conical Cu inserts of 45°aperture.

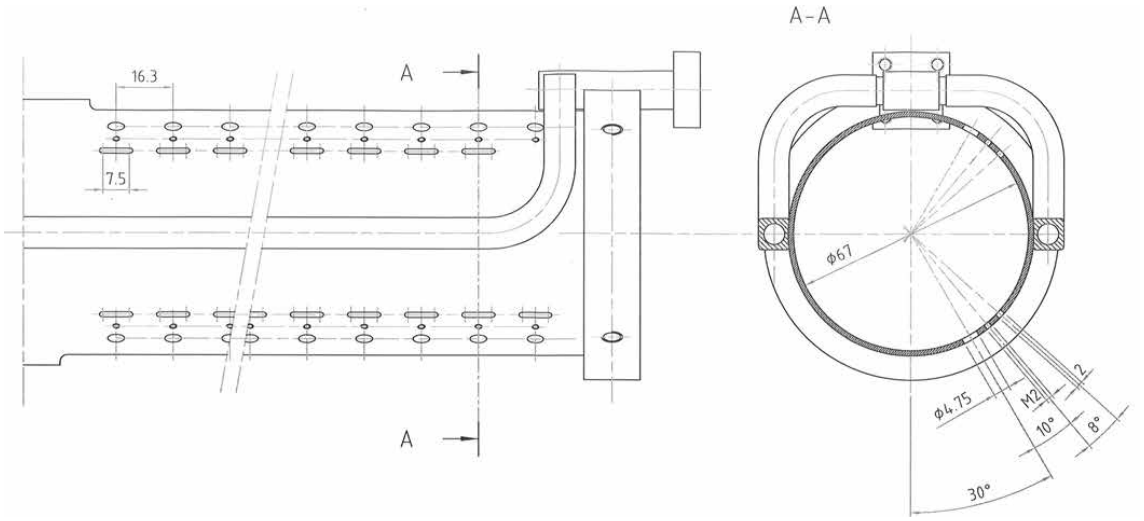

Figure 9.5: 2014 COLDEX a-C coated beam screen layout drawing following 2003 modification.

Figure 9.6: Picture of 2014 COLDEX a-C coated beam screen during re-installation. Courtesy of G. Bregliozzi.

Besides the BS, the arrangement of the cryostat internal structure is depicted in the schematics available in Figure 9.7 and is further described.

The Cold Bore is a 17 liter, 316LN stainless steel, vessel defining an inner, circular, surface of diameter (ID) 113 mm. Some apertures are left at its centre and extremities for the chimney/extractor gauge and the BS cooling supply flanges, respectively. Such vessel is representative of the Cold Mass of a LHC cryomagnet and in particular of its cold bore. The CB provides the design vacuum cryopumping surface. The CB vessel can be filled with liquid He at 4.5 K (1.3 bara) and then eventually be cooled below 3 K by lowering the He bath pressure - following the He saturation curve on a p-T phase diagram - pumping the He gaseous phase. The Cold Bore is

surrounded by a 316LN stainless steel thermal shield, actively cooled employing the return GHe from the BS. Due to the long He circuit, the temperature profile can be significantly non-uniform. The average thermal shield temperature is defined principally by the GHe enthalpy available at the BS outlet, but also by the CB conditions (warm, cold). Reference figures are 30 K when the BS is held at 10 K and 70 K when the BS is held at 50 K (CB filled with LHe). This has an implication only on the cryogenic efficiency of the experiment, not on its experimental conditions.

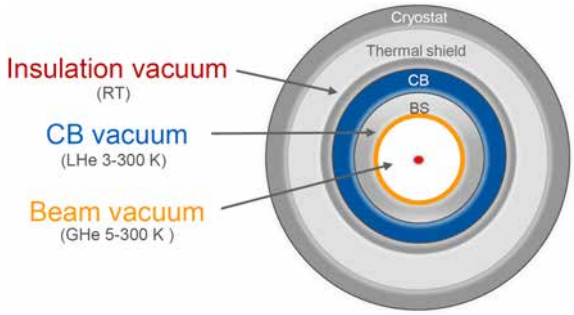

Figure 9.7: Schematic view of the COLDEX vertical, transverse cryostat cross section.

The COLDEX cryostat is connected to the SPS machine by two, ID100, 316LN stainless steel vacuum transition chambers at room temperature, via the sector 431 valves VVSB_41737 and VVSB_41753. Solenoid coils (VIESA_41738 and VIESA_41752, connected in series) are wrapped on such chambers. Additional solenoids coils (VIESA_41732 and VIESA_41755, connected in series) are wrapped also on the by-pass Y chambers (sector 430, COLDEX leg), i.e. upstream and downstream COLDEX. A longitudinal magnetic field up to 2 mT is obtainable. This field is sufficiently large to clear out secondary electrons potentially produced by multipacting in these parts, thus partially isolating COLDEX from electron cloud side effects (gas transmission, spurious heat load).

On the downstream ID100 transition, a completely bakeable gas injection system is fitted. This system is used to perform studies of gas transmission along the BS and pre-condensation of gas species onto the cold surface of the BS. In 2016, the system was upgraded. It consists of two main parts: one 316LN stainless steel 3.2 litre gas reservoir equipped with two capacitance pressure gauges (ranges: 1100-1 mbar, 1-10^{-4} mbar) and connected to the beam vacuum system via a series of one all-metal remote controlled pneumatic gate valve and one remotely controllable variable fine leak valve; a fully bakeable gas battery of 4 tanks (5 l), deported from the beam line. An unprecedented span of fully remotely operated gas injections with 4 gases (e.g. H_2, CO, N_2 and CO_2 have been initially charged) is available and is employed to characterize the a-C coating cryogenic vacuum performance, both without and with beams.

A dedicated pumping dome (or "warm site") is connected on the same downstream ID100 transition, through a remotely controllable sector valve. This vessel hosts squared (25x25 mm) apertures of known conductance (273.8 l/s for H_2). Between the orifices, two getter pumping units (n. 2 sublimators, n. 1 sputter ion pump) are installed. Those units have not been refurbished in 2014. A LEP-type, remote controllable, turbomolecular pumping group is installed at the dome extremity. The estimated pumping speed of this group is 230 l/s for N_2.

In order to give direct indication of electrons activity in the BS, two electrodes are employed. The chimney circular, 18 mm, copper electrode (chimney electrode, see Fig. 9.8) is inserted through the RT chimney and faces the BS aperture to the chimney port. It is shielded against beam image current by the BS chimney port grid. The surface facing the BS is 143.1 mm^2; however, when the electrode is sufficiently polarized, the collection surface may extend to the whole chimney port (keeping into account the grid transparency). The BS electrode (Fig. 9.9) is instead obtained by electrically insulating one of the 178.5 mm long copper baffles facing the BS slots, by means of a Kapton foil. The effective electron collection surface is the one offered by the BS apertures (circular and elongated pumping slots), and is estimated 394.5 mm^2. The electrodes are electrically linked to the surface electronics via triaxial cables.

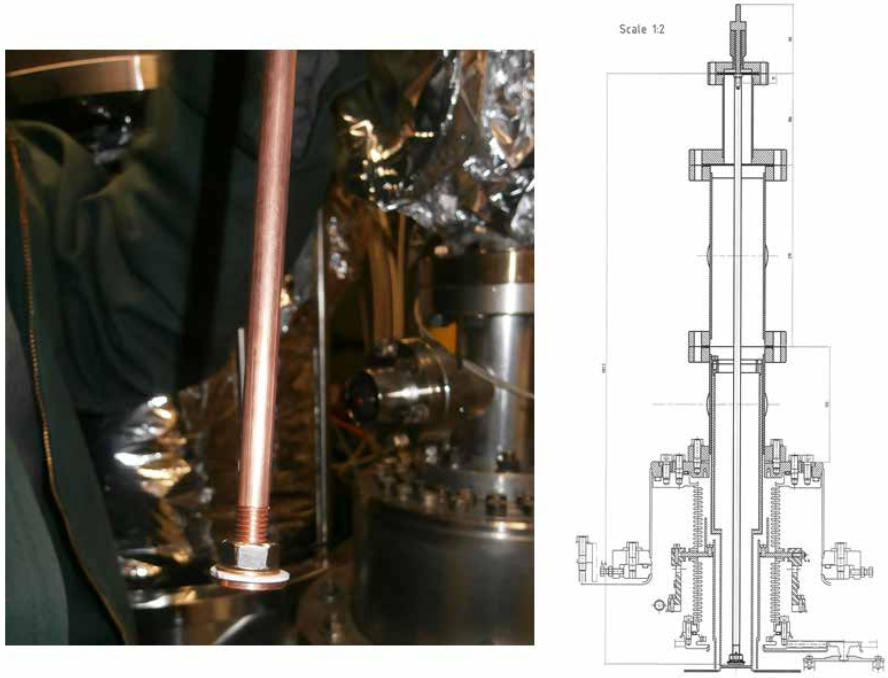

Figure 9.8: Left: Picture of the COLDEX chimney electrode and its bakeable support. Right: drawing of the room temperature chimney, with the chimney electrode inserted.

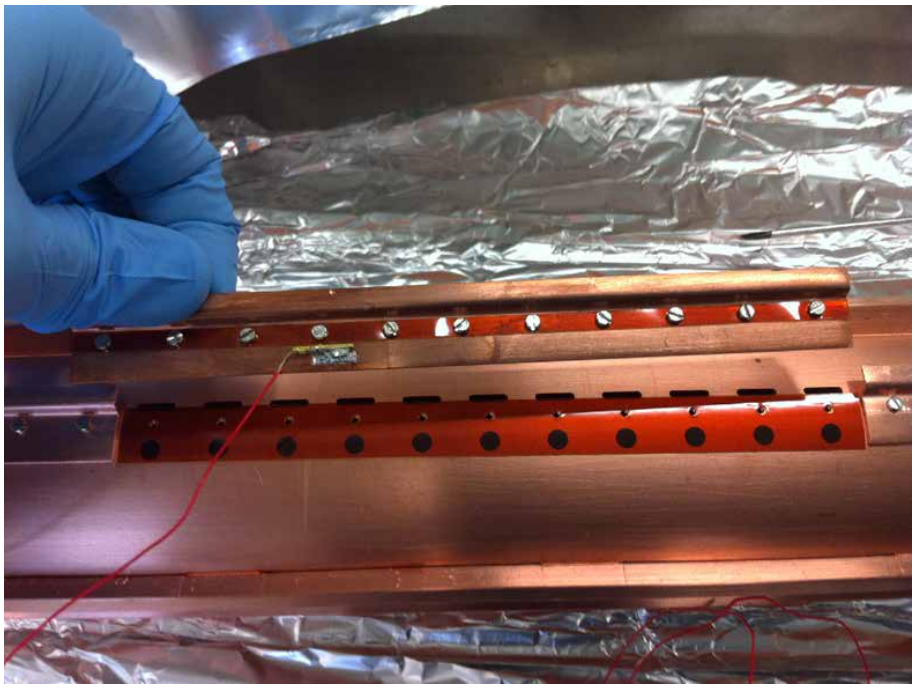

Figure 9.9: Picture of one of the insulated BS baffle, serving as BS electrode.

A TiZrV non-evaporable getter (NEG) coated WAMPAC [169] calorimeter (WAMPAC4, ID 67 mm), previously ex-situ activated and already electron cloud conditioned in the past, was left installed downstream to COLDEX inside (coaxially) the downstream sector 431 transition.

A picture of sectors 430 and 431 and a simplified schematic layout of the COLDEX experiment after 2014 recommissioning and updated to 2016 are shown in Figures 9.10 and 9.11.

Figure 9.10: Picture of SPS vacuum sectors 430 and 431 installed in TS45 of SPS/LSS4.

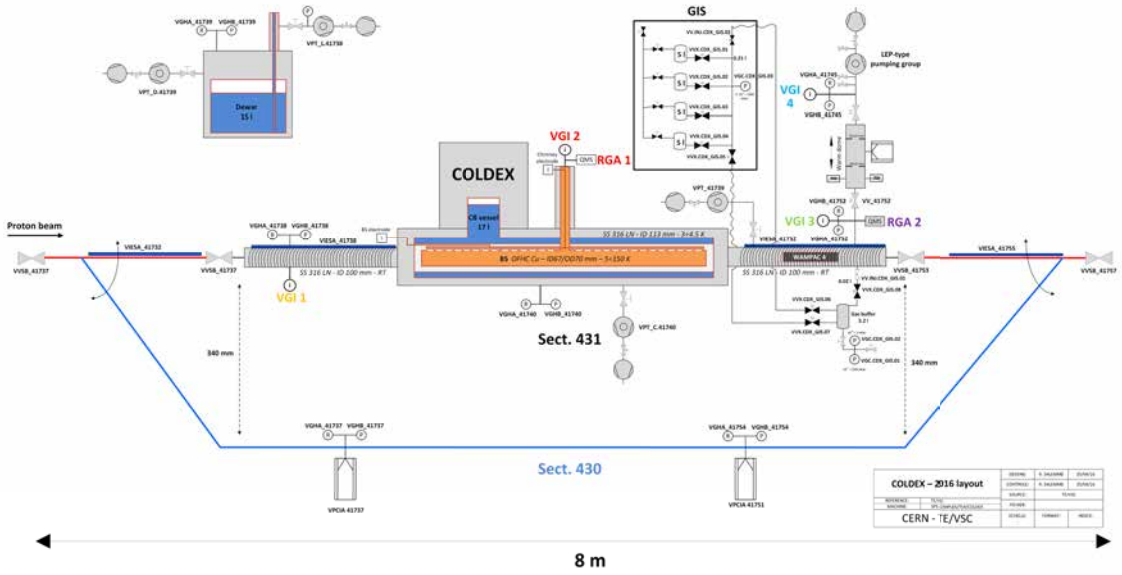

Figure 9.11: Schematic view of SPS/LSS4 vacuum sectors 430 and 431 vacuum devices and instrumentation following 2014 COLDEX recommissioning and further 2016 upgrade (new GIS).

9.3 COLDEX measurements

The experimental setup is conceived to study the beam induced multipacting in a LHC type cryogenic vacuum system as a function of the BS temperature (depending on it, of the presence of adsorbed gas species on its surface) and the circulating beam parameters (bunch intensity, spacing, total circulating intensity, at injection and flat-top energy).

During a run, total pressure is measured along the vacuum system, i.e. in the RT upstream and downstream sections and in the cryogenic BS vacuum envelope. Total pressure will be herein expressed always in N_2 equivalent and at room temperature (293 K), which is the standard in UHV. Vacuum total pressure is measured at sector 431 extremities, i.e. on the ID 100 mm 316LN stainless steel transition chambers mounted upstream and downstream the COLDEX cryostat, via

calibrated Bayard-Alpert (VGI1, VGI3) hot cathode, Penning (VGHB_41738, VGHB_41752) cold cathode ionization gauges and Pirani (VGHA_41738, VGHA_41752) thermal conductivity gauges. At the top of the room temperature chimney, a Bayard-Alpert (VGI2) gauge is installed. This gauge gives a direct indication of the gas pressure in the BS. Such configuration is unique in cryogenic devices and is key for measuring electron stimulated desorption during electron cloud bombardment. The dynamic pressure rise due to electron cloud can be monitored with respect to the different circulating beams, while the conditioning obtained by beam scrubbing is observed.

The gas composition is followed-up constantly in both cryogenic and warm parts by residual gas analysers. In case of gas desorption, the primary and recycling desorption yields of the system can be estimated. Two calibrated Quadrupole Mass Spectrometers (RGA1, RGA2) are mounted on the BS chimney top and on the downstream sector 431, RT, ID 100 chamber and operated in SEM mode to perform analyses of the residual gas species in the cryogenic and room temperature parts, respectively. Due to radiation incompatibility, their RF boxes are permanently deported far from the beam line (6 m cables) and installed on the overhead platform available in the LSS4 alcove. Both RGA have been calibrated for H_2, CO and N_2 gases, so indication of such gas species partial pressure is available.

The heat load dissipated by electron cloud onto the BS surface can be measured and estimated, in multiple manners. The heat load per unit meter dissipated on the BS and evacuated by GHe is thermodynamically measured as following:

$$Q_{cryo} = \frac{\dot{m}\left[h(T_{out}) - h(T_{in})\right]}{L_{BS}} \tag{9.1}$$

where $\dot{m}$ is the mass flow rate (g/s), h the gas enthalpy of the fluid at the BS outlet (T_{out}) and inlet (T_{in}) respectively, and L_{BS}=2.232 m the length of the BS. In 2014, the typical static heat load measured on the BS was Q_0=1.1 W/m after facility cool-down. Dynamic heat load can be dissipated due electron cloud and is therefore monitored during experimental runs, provided a steady-state in reached on the BS cooling conditions. The last assumption is strong and definition of a clear Q_0 can be tricky or sometimes impossible due to cryogenic instabilities. The contribution of power losses due to coupling impedance heating have been studied in the past [138] and have been estimated negligible.

Electron activity is a direct indication of beam induced multipacting and is measured through the chimney and BS electrodes. Each can be polarized typically up to ±1 kV, so to cover a large part of the energy spectrum typical of the electron cloud. Two methods are used: adjustable, constant DC bias voltage is adopted to produce an electric field of adjustable magnitude and monitor the BS electron activity; quick DC bias voltage sweeps are adopted to observe the electrons energy spectrum. The electric current resulting from electron bombardment and charge deposition is measured through electrometers, shunted to ground. In 2014, after the BS re-installation and cool-down, the BS electrode was not employable, as it was found shorted to ground. Known the active surface and the collection efficiency of the electrodes, an average electron flux (in A/m, or e^-/mm^2) can be deducted. This measurement can be used to cross-check the heat load measured by cryogenics, assuming an average electron energy impinging on the BS:

$$Q_{elect} = \frac{Ie}{S_{electrode}} \pi D_{BS} \langle E_e \rangle \tag{9.2}$$

where I is the current measured by the electrode during multipacting, e the electron elementary charge, $S_{electrode}$ the electrode effective collection surface (keeping into account the collection efficiency and transparency, if any), D_{BS} the inner BS diameter and $\langle E_e \rangle$ the average impinging electron energy, which is measured through voltage/energy sweep and also calculated mediating the electrons energy spectrum from simulations (see Section 10.2).

Through benchmarking with available electron cloud build-up codes, the SEY of the surface can be deduced from the measured or estimated dissipated heat load. The effect of beam scrubbing is such observed.

The effects of adsorbed gas on the BS surface at cryogenic temperature is reproduced in dedicate runs by gas injections. A desired and precise gas quantity Q_{inj} can be injected from the RT gas

reservoir of well known volume (V=3.2 l), temperature T (thermocouple) and pressure $p_{reservoir}$ (capacitance gauge), such that

$$Q_{inj} = \Delta p_{reservoir} V \rightarrow n = \frac{Q_{inj}}{S_{BS} K_B T} \tag{9.3}$$

where $n = \left[\frac{\text{molecules}}{\text{cm}^2}\right]$ is the target gas coverage, K_B the Boltzmann constant ($1.38 \cdot 10^{-22}$ mbar·l/K) and S_{BS} is the considered BS surface. The gas injection is usually operated days before the beam run and is done with the BS in cryogenic conditions (the CB being still "warm") and vacuum isolated system. Since the injection is done non uniformly (from one only injection point, i.e. the COLDEX right RT transition), the gas would stick non uniformly and preferentially at the BS (right) extremity. For this reason, a gas uniformisation along the BS is operated through warm-up up to a temperature corresponding to a complete loss of adsorption (gas dependent). The system is kept vacuum isolated in order to conserve the injected gas inventory. A slow cool-down ramp (<1K/min) is then operated on the BS to minimize ΔT along its length and uniformly distribute the gas coverage over the surface.

9.4 Beam measurements

Beam parameters are monitored through the standard SPS diagnostic devices. The circulating beam intensity is measured by the Beam Current Transformer SPS.BCTDC.31832, operated for high intensity beams and with a sampling time of 10 ms. The evolution of the injected bunches on the beam intensity and the beam storage and lifetime are followed-up. From the BCT, the integrated beam dose (in Ah) can be accounted as follows:

$$D = \int I(t)dt = \int \frac{I(t)\ [\text{p/s}]\ e}{\tau_{\text{rev}} \cdot 3600} \tag{9.4}$$

being τ_{rev} the revolution period of the SPS beam, i.e. 23.11 μs at 26 GeV/c and 23.05 μs at 450 GeV/c. The Fast Beam Current Transformer SPS.BCTFR.51895 is adopted to monitor the bunch-by-bunch intensity and is a valid instrument to check the longitudinal beam quality (uncaptured or debunched beam, or wrongly injected *satellite* bunches) or electron cloud driven instabilities (beam intensity loss at the trailing bunches). The longitudinal plane can be monitored - in particular bunch shape and oscillations - via the SPS RF pick-ups in so called Mountain Range data displays.

In some cases, the 1σ beam emittance is measured with the rotational wire scanners SPS.BWS.41677 or SPS.BWS.51995 both in the horizontal and vertical plan. With low intensities, the bunch-by-bunch emittance can be measured so to characterize the signatures of electron cloud on the trailing bunches quality.

In conjunction to beam measurements, beam losses are followed-up in whole machine and, in expert mode i.e. at 10 ms integration time, in the whole LSS4. The closer SPS ring BLM to COLDEX is the SPS.BLM.417, which is distant 21.2 m from the COLDEX cryostat.

9.5 Vacuum characterization of a-C coating at cryogenic temperature

During periods without beam, the COLDEX setup is used to study the cryogenic vacuum characteristics of a-C coating in the 5 to 150 K temperature range. For the purpose of better understanding the experimental results during beam conditions - in particular, the vacuum observables - which will be discussed in Chapter 11, we briefly resume in this Section the results of the preliminary vacuum characterization of a-C coatings at cryogenic temperature performed in COLDEX carried in the 2014-2016 period [170].

The COLDEX setup provides a quasi-closed geometry where the physical adsorption of gas species onto the a-C coated (400 nm) BS surface can be studied. The tubular BS geometry is characterized by a L/R = 66.6. BS temperatures ranging from 5 to 150 K are obtained in steady state. For cryogenic vacuum studies, the CB temperature is usually kept well above the

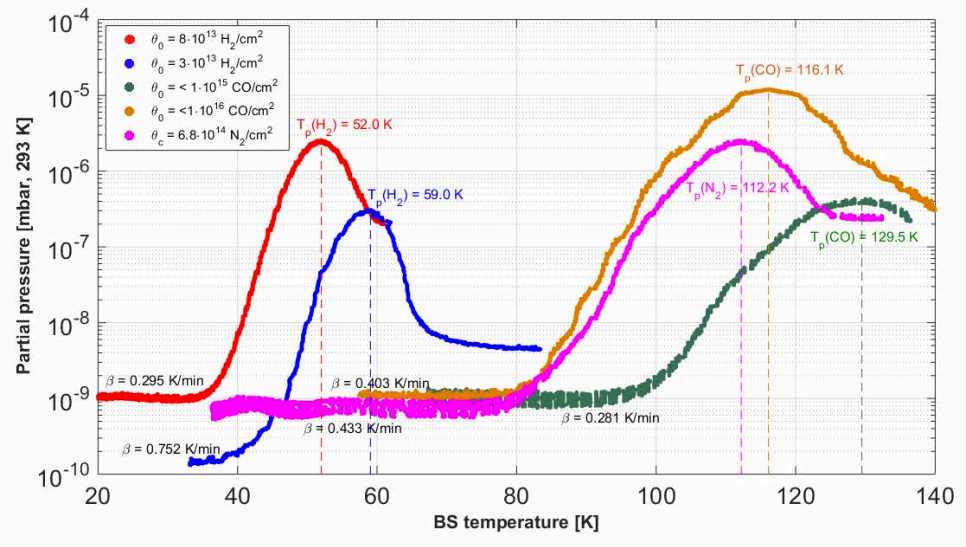

Figure 9.12: Thermal Desorption Spectroscopy of H_2, N_2 and CO measured on a-C coating as a function of the initial coverage θ_0 and β.

corresponding temperature of physisorption and condensation for most of the gases (e.g. >150 K) on stainless steel, so that adsorption is practically only possible for H_2O.

The adsorption of a gas specie is studied either by accumulation on a-C from desorption of room temperature parts, or by injection of the specie at room temperature from a single, downstream, point via the COLDEX Gas Injection System (GIS). The gas molecules stick preferentially at the BS extremities. In order to obtain an homogeneous surface status, their coverage is redistributed uniformly along the a-C surface by complete thermal desorption via induced warm-up, followed by a slow (<1 K/min) cool-down. Successful redistribution must be checked: this is done by observing a pressure uniformity along the system (VGI1, VGI2, VGI3).

Effective physical adsorption was observed on a-C for temperatures well above than of Cu or SS. In particular, for a coverage $\theta_0 < 1 \cdot 10^{15}$ molecules/cm^2, H_2 is adsorbed (physisorption) on a-C coating below 35 K and released when warming-up in the 40 to 65 K temperature range; CO and N_2 are adsorbed (physisorption) on a-C coating below 70 K and released when warming-up in the 75 to 140 K temperature range.

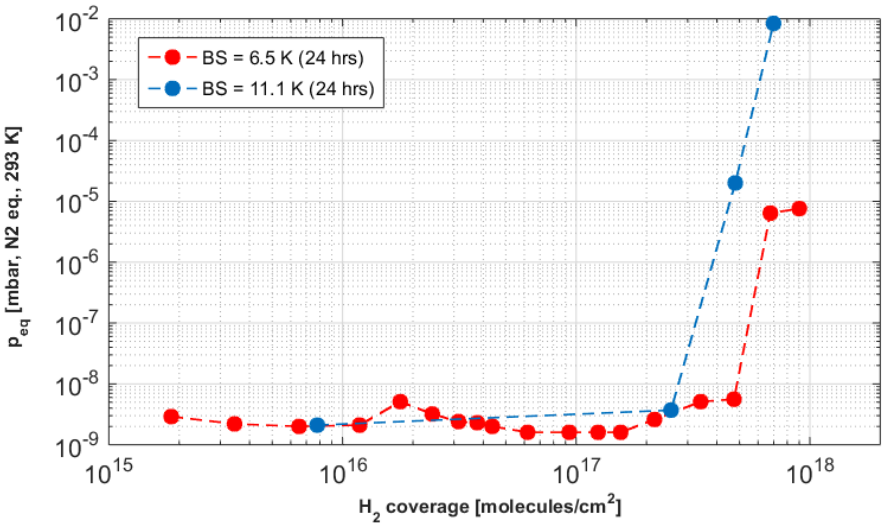

Figure 9.13: Adsorption isotherms of H_2 on a-C coating at 6.5 K and 11.1 K.

Desorption, i.e. loss of physisorption, can be monitored in slow ($\leq$0.5 K/min) induced warm-up obtaining a Thermal Desorption Spectroscopy (TDS) at constant heating rate β [171]. The effect of re-adsorption during the process is assumed negligible. Fig. 9.12 shows a compilation of TDS for H_2, N_2 and CO measured on a-C coating as a function of the initial coverage θ_0 and β. The maximum desorption rate, identified by $T_p = T(p_{max})$, is dependent on the initial coverage θ_0; in particular, T_p decreases with increasing coverage. Assuming a first order desorption model [171] (i.e. a desorption process which takes place in one only step), differences in β spanning over one order of magnitude do not reflect the shift in the peaks. The a-C is capable of twofold process molecule adsorption (i.e. two processes are required for thermal desorption: first recombination, then desorption) and desorbs thermally following a second order model [171]. The symmetry of the desorption peaks is a further confirmation [171].

The adsorption capacity of a-C for H_2 (i.e. the quantity of molecules that can be adsorbed before reaching saturation) has been measured in COLDEX by subsequent gas injections and uniformizations. The adsorption isotherms built-up for a-C coating are shown in Fig. 9.13. Signs of surface saturation were recorded with a coverage of $> 4 \cdot 10^{17}$ H_2/cm^2 and $> 2 \cdot 10^{17}$ H_2/cm^2 respectively at 6.5 K and 11.1 K, i.e. a capacity two orders of magnitude higher than the monolayer capacity of metallic surfaces like Cu or SS was measured. The result points to a porous surface morphology of a-C, capable to accommodate many molecules in numerous adsorption sites.

Chapter 10

Electron cloud modeling and build-up simulations for COLDEX

10.1 Introduction: the pyECLOUD code

pyECLOUD [172] [124] is the reference code at CERN for the simulation of the electron cloud build-up in particle accelerators. Principally written in Python in the period 2011-2014, it inherits most of the physical models already developed and employed in the ECLOUD code, developed and maintained at CERN since 1997 and used for build-up and instability simulations of the SPS and LHC accelerators [151] [173] [174] [175].

pyECLOUD is a 2D macroparticle (MP) code: the electron density is grouped in macroparticles to reduce the computational burden arising from the tracking of $\gg 10^6$ e^- per iteration. The size of the MP is dynamically managed during the simulation steps. The code is capable of simulating the electron cloud build-up in arbitrary shaped (convex) chambers, but recently efforts have been put to remove this limitation. The code is conceived for ultra-relativistic charged beams and is explicitly designed to deal with irregular beam structures, e.g. different bunch intensities and bunch lengths along the train, arbitrary spacings and profiles. Externally applied magnetic fields are charged by field maps. It must be noted that the code assumes a rigid beam, i.e. the effects of electron cloud (instabilities, vacuum pressure rises etc.) are small in the time considered by the simulation, which is usually limited to few full train passages. Thanks to the implementation of new optimized algorithms, pyECLOUD exhibits a significantly improved performance in terms of accuracy, speed, reliability and flexibility with respect to ECLOUD. For a detailed description of the code structure and physics we refer to [123]; in the following, we present the main features of the code, which will be employed in this Chapter.

Fig. 10.1 represents the flow diagram employed in the pyECLOUD main loop to simulate the dynamics of the electron density, i.e. the MPs, during the build-up process.

At each time step, seed electrons are generated due to residual gas ionization and/or to synchrotron radiation induced photoemission from the chamber walls (see Sect. 7.2). Their quantity is evaluated consistently with the considered passing beam slice; their position and momenta is determined by available theoretical or empirical models.

The electric field acting on each MP is then evaluated. The beam electric field (see Sect. 7.4) is usually precomputed on a suitable rectangular grid, loaded from file and obtained at each MP location by a linear (4 points) interpolation; the space charge contribution due to the electron density (see Sect. 7.4) is calculated by a Particle in Cell (PIC) algorithm: the finite difference method is employed to solve the Poisson equation with perfectly conducting boundary conditions on the beam chamber.

As soon as the total electric field at each MP location is known, MP positions and momenta are updated by integrating the equation of motion; at this stage the presence of an externally applied dipolar magnetic field is taken into account.

At each time step, a certain number of MPs hits the wall. For these MPs, a proper model of the secondary emission process, similar to what described in Sect. 7.3, is applied to generate charge,

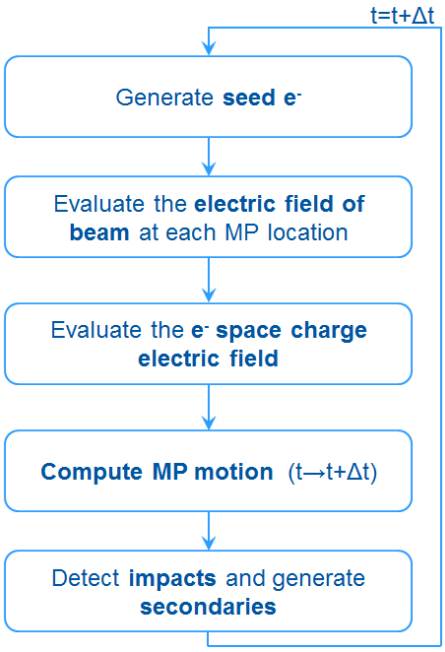

Figure 10.1: Flowchart of the steps carried in a pyECLOUD simulation main loop. From [124].

energy and angle of the emitted electrons. According to the size of the emitted charge, a dynamic rescaling of the impinging MP may be performed or simply new MPs are emitted.

One of the features of the electron cloud build-up process is that, due to multipacting, the electron density varies rapidly and can spread over several orders of magnitude during the passage of the bunch train. The choice of a unique MP size, *a priori* suitable for the entire simulation and capable to correctly follow the phenomenon while keeping the computational burden acceptable, is limited to some specific cases. pyECLOUD employs a MP size management which dynamically adapts to a target reference N_{ref} to control the number of electrons per MP. The size of the generated MP is a close as possible to the reference size: the size of MPs generated by seeding is exactly N_{ref}, whereas when an MP hits the wall, secondary emission is accounted either rescaling its size according to the wall SEY, or new MPs are generated. A cleaning procedure deletes MPs with a charge lower than a threshold (usually $10^{-4}N_{ref}$). N_{ref} is controlled so that the number of MPs does not exceed a predefined threshold (e.g. 10^5): regeneration is applied to the set of MPs by rescaling their number while preserving their 5-D phase space distribution (x, y, v_x, v_y, v_z).

10.2 Build-up simulations

The COLDEX experiment case has been simulated in the electron cloud build-up code pyECLOUD v4.09. As input geometry, the BS elliptical geometry, of $x_{aper} = 0.0335$ m and $y_{aper} = 0.0335$ m, has been simulated. Given to the injection and flat-top SPS beam energies, the presence of synchrotron radiation has been neglected (see Section 10.2.2 for a throughout analysis). Only the electron seeding due to residual gas ionization was therefore took into account. The underlying SEY angular and energy dependence model proposed by [117] and [113] and described in Sect. 7.3 was adopted.

Tables 10.1, 10.2, 10.3, 10.4 resume the input parameters adopted. As seen in Sect. 9.1, the expected a-C coating SEY is 1.1 at cryogenic temperature. A $E_{max}(\delta_{max}) = 300$ eV has been initially chosen. The secondary emission angular and energy spectrum proposed in [118] and described in Sect. 7.3 were adopted, with a reflectivity factor $R_0 = 0.7$. Nevertheless, it is re-known that the presence of adsorbed gas species can modify the surface response to electron bombardment, i.e. its SEY. Such effect has been already observed with the COLDEX experiment, on Cu, during 2001-2004 [176] and is reproduced and thoroughly studied in many laboratory measurements (for instance [177]). For this reason, a simulation set always consists in a parameter scan of SEY.

The selected range is from SEY=1.0 to SEY=2.0. This method allows not only to identify the multipacting threshold, but also to verify the results with respect to Cu (expected SEY=1.3, after a scrubbing dose of 10^{-3}C/mm^2 from as-received conditions [112]), or observe the sensibility of the experiment to surface modification (scrubbing, presence of adsorbed gas, flushing). A second parameter scan is operated on the circulating bunch intensity, which is usually varied from $0.7{\cdot}10^{11}$ to $1.9{\cdot}10^{11}$ protons per bunch (ppb). For reference, in 2014 the nominal 25 ns LHC type beam bunch intensity was $1.2{\cdot}10^{11}$ ppb.

Simulations are carried always with 4 batches of 72 bunches, spaced 25 ns, circulating at SPS injection energy (26 GeV), or, after acceleration (not simulated), at SPS flat-top energy (450 GeV). A normalized transverse beam emittance of $2.5{\cdot}10^{-6}$ m, both on the horizontal and vertical plane, is supposed: such values are compatible with what experimentally measured. The simulation considers the time frame corresponding to 320 times a bunch distance, i.e. 8.0 μs, which is approximately the 30% of a SPS complete beam turn (23.1 μs). This artifice allows to fully observe the whole electron cloud transient, while discarding the large time frame before a complete revolution without beam presence at COLDEX.

The applied timestep has been varied from 25 ps, down to 12.5 ps. The expected benefits of such increase in time resolution are supposed in a better follow-up of the electron density increase during multipacting, at the cost of significant higher computational burden (from 7h to 12 hours CPU time, >8 GB of memory allocation). For the heat load calculation, what matters is the equilibrium impinging electron density reached when the beam field is compensated by the electrons space charge. Such equilibrium is reached very quickly ($<$ 1 μs simulation time) above multipacting threshold. So, a consistency and reproducibility of the results was observed with both 25 and 12.5 ps timesteps. The upper limit in the electron macroparticle size - which dynamically varies during the simulation - has been fixed to a maximum of $2.5{\cdot}10^{5}$.

Table 10.1: Beam input parameters for the PyECLOUD simulation of the COLDEX case.

Parameter	Value	Unit	Comment
Energy	$2.6{\cdot}10^{10}$ $4.5{\cdot}10^{11}$	eV	SPS injection energy SPS flat top energy
Norm. transverse, x plane, emittance	$2.5{\cdot}10^{-6}$	m	for LHC type beams
Norm.transverse, y plane, emittance	$2.5{\cdot}10^{-6}$	m	for LHC type beams
Momentum spread	0.0		
Beam field	'compteBE'		Bassetti-Erskine formula + image terms from the elliptical chamber
N. of points beam field map (x)	830		
N. of points beam field map (y)	830		
N. of image terms	1		
Bunch spacing	$25{\cdot}10^{-9}$	s	
Bunch intensity	from $1.2{\cdot}10^{11}$ to $1.9{\cdot}10^{11}$	ppb	
Bunch length (1σ)	$2.2{\cdot}10^{-1}$ $1.2{\cdot}10^{-1}$	m	at SPS injection energy at SPS flat top energy
First bunch delay	$2.5{\cdot}10^{-9}$	s	
Filling pattern	4*(72*[1]+8*[0])		4 batches of 72 bunches

Table 10.2: Secondary emission model input parameters for the PyECLOUD simulation of the COLDEX case.

Parameter	Value	Unit	Comment
$E_{max}(\delta_{max})$	300	eV	
δ_{max}	from 1.0 to 2.0		
Weight of reflected electrons component (R_0)	0.7		[118]
Max energy for true sec. electrons	35	eV	
δ of lognormal distribution	1.0828		[118]
μ of lognormal distribution	1.6636		[118]
Min. energy of scrubbing electrons	20		used for scrubbing current estimation

Table 10.3: Machine input parameters for the PyECLOUD simulation of the COLDEX case.

Parameter	Value	Unit	Comment
Chamber profile	'ellip'		
Hor. semiaxes of the transverse chamber section	0.0335	m	circular BS ID67
Ver. semiaxes of the transverse chamber section	0.0335	m	circular BS ID67
Hor. betatron function	43.5	m	SPS Q20 optics
Ver. betatron function	83.5	m	SPS Q20 optics
Primary generation of electrons due to residual gas ionization	1		
Vacuum chamber pressure	$2{\cdot}10^{-8}$ $2{\cdot}10^{-9}$	mbar	at 300 K at 10 K

Table 10.4: Simulation settings for the PyECLOUD simulation of the COLDEX case.

Parameter	Value	Unit	Comment
Simulation time step	$2.5{\cdot}10^{-11}$	s	
Limit beam linear density for primary electrons generation	100	p/m	
N. of max MP sizes	$2.5{\cdot}10^{5}$		
MP regeneration high threshold	$2.0{\cdot}10^{5}$		
MP regeneration low threshold	$5.0{\cdot}10^{3}$		
Target MP size after regeneraton	$2.0{\cdot}10^{4}$		
MP split factor	1.5		
Initial MP size	5	e^-/m	
Space charge time step	$0.5{\cdot}10^{-9}$	s	
Grid size space charge	$0.2{\cdot}10^{-3}$	s	

10.2.1 LHC type beams at SPS injection energy

The first simulation set considers the nominal COLDEX case, when LHC-type beam at 26 GeV is let circulate through the COLDEX experiment, with the BS held at T=10 K. The considered residual gas pressure is the one typically observed at the COLDEX BS middle (VGI2) at cryogenic temperature, $2{\cdot}10^{-9}$ mbar. The corresponding gas density is approximately equivalent to $2 \cdot 10^{15}$ molecules/m^3. The considered ionization cross section (for 26 GeV relativistic protons) is referred to the dominant residual gas, which is H_2 in a ordinary cryogenic vacuum system, and is σ_i=0.2 Mbarn.

Fig. 10.2 illustrates the simulated heat load of this case, versus the surface SEY and for different bunch intensities.

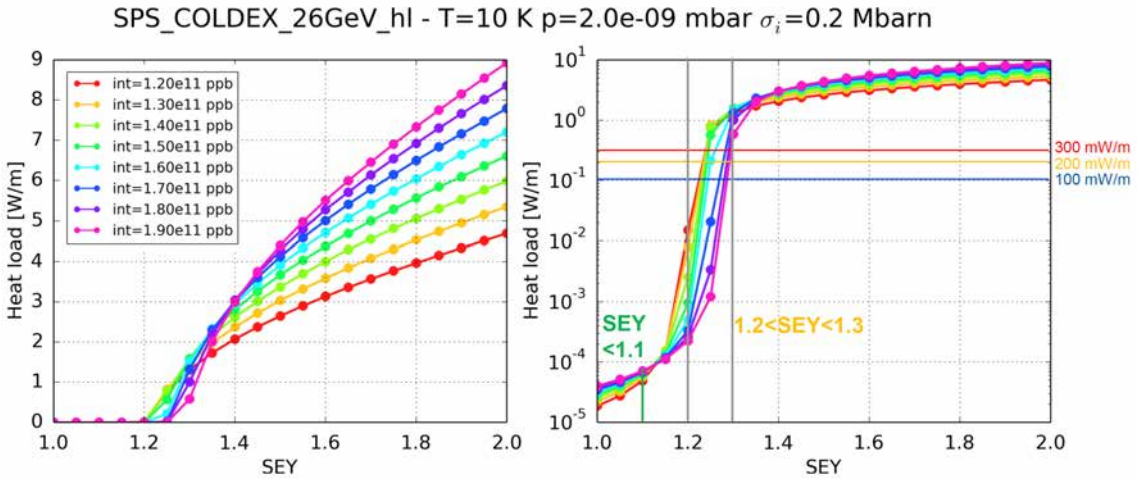

Figure 10.2: PyECLOUD simulation of heat load in the COLDEX nominal case, 26 GeV, T=10 K, σ_i=0.2 Mbarn, versus SEY for different bunch intensities.

In COLDEX, the multipacting threshold is situated in the 1.15<SEY<1.3 window. For SEY<1.1, the heat load is always below 1 mW/m, while between SEY=1.2 and SEY=1.3, the heat load spans from tents of mW/m to 1 W/m, importantly depending on the bunch intensity. Sufficiently below and above multipacting threshold, the heat load evolves linearly increasing with the surface SEY. This is a consequence of the impinging electron density reached at equilibrium, which is only dominated by the regime seeding electron production in the first case, and by the regime surface multipacting in the second case. In such situations, the heat load is proportional to bunch intensity, i.e. increases with larger bunch population.

Already in linear scale, but better in logarithmic scale, we observe that the threshold advances toward lower SEY when decreasing the bunch intensity, which seems counter-intuitively. The situation is better shown in the plot of Fig. 10.3, where the heat load is plotted against the bunch intensity for different surface SEY.

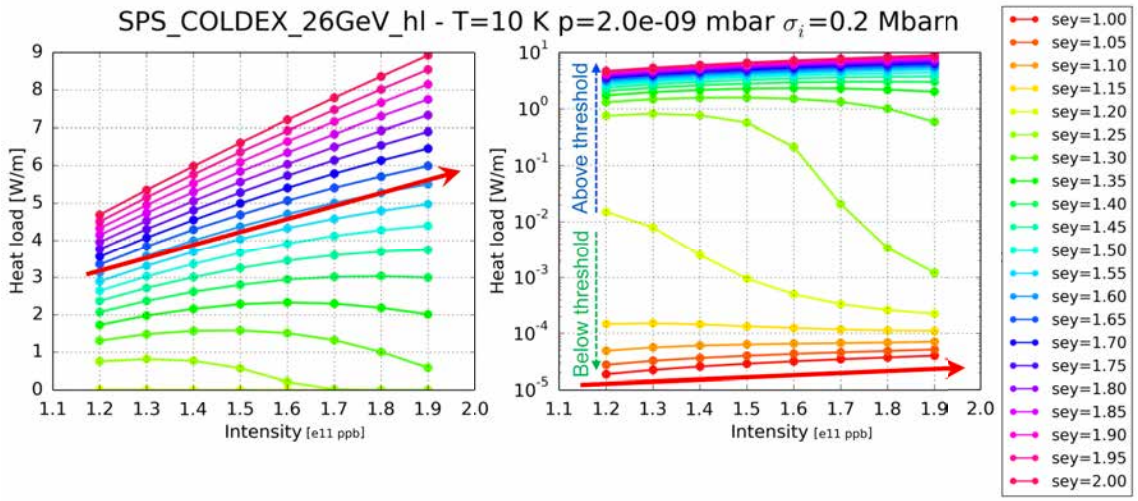

Figure 10.3: PyECLOUD simulation of heat load in the COLDEX nominal case, 26 GeV, T=10 K, σ_i=0.2 Mbarn, versus bunch intensity for different surface SEY.

Well below (logarithmic scale) or above (linear scale) threshold, for larger bunch intensities, the heat load (impinging electrons rate) increases. Across the multipacting threshold (SEY = 1.15

$\div$ 1.30), the heat load decreases for higher bunch intensities (as a consequence of the reduced impinging electron density). For instance, for SEY = 1.3 the heat load spans from 0.8 W/m to 1.6 W/m (see linear scale). The effect is quite remarkable also for SEY = 1.20 and SEY = 1.25 (see logarithmic scale). This a direct consequence of the energy spectra of the impinging electron, which are shown in Fig. 10.4 and 10.5.

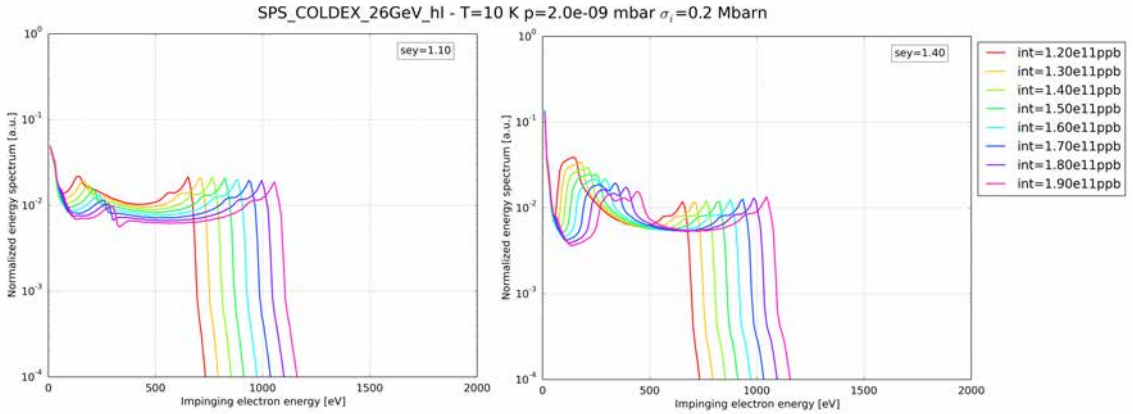

Figure 10.4: Normalized impinging electrons energy spectra (over 320 passages) in the case of SEY=1.1 (left) and SEY=1.4 (right), for different bunch intensities. PyECLOUD simulation, 26 GeV, T=10 K, σ_i=0.2 Mbarn.

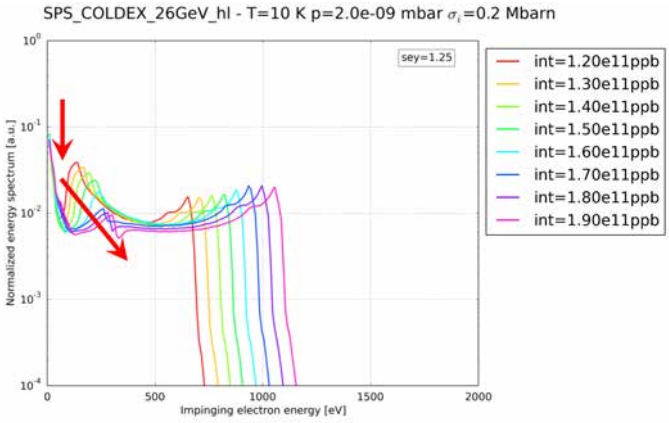

Figure 10.5: Normalized impinging electrons energy spectra (over 320 passages) in the case of SEY=1.25, for different bunch intensities. PyECLOUD simulation, 26 GeV, T=10 K, σ_i=0.2 Mbarn.

In all cases, we observe that increasing the bunch intensity, the energy spectrum broadens toward larger energy. This is a direct consequence of the beam electric field, which increases for larger bunch intensities. The electrons receive a stronger kick from the beam, thus their energy spectrum tends to shift toward larger energies. Increasing the bunch intensity, the electron density at low energies (secondary electrons) is invariant. Such electrons are produced by surface secondary emission and, due to their low energy, do not interact with the beam field during a bunch passage (they float close to the emission surface, even in absence of magnetic field). In the intermediate energy range (100 to 200 eV energy range below threshold, 100 to 500 eV above threshold), i.e. the range where multipacting is taking principally place, we observe a broadening and shift toward higher energies. Finally, we observe a shift in the peak energy of the spectrum due to the increased average kick received by the electrons in the beam field region.

Below threshold (SEY=1.1, Fig. 10.4, left), we observe the presence of secondary electrons in the low (0-20eV) energies, which is not yet predominant above the other energies, where the electron population is rather well distributed (except for the limited zone where $\delta(E)$ >1). Above

threshold (SEY=1.4, Fig. 10.4, right), the effects of multipacting are visible. The low (0-20 eV) energies are more populated (by the secondary electrons). The 200-500 eV region is wider and as well more populated: this is an effect of the larger $\delta(E)$ >1 energy range for SEY = 1.4.

The situation is completely different for SEY=1.25 (Fig. 10.5). Across the multipacting threshold, i.e. for SEYs in the range 1.15 ÷ 1.30, the energy range for which $\delta(E)$ >1 is small. Increasing the bunch intensity, the electrons energy spectrum moves to higher energies, so the zone around 200-500 eV becomes depleted. Fewer electrons hit the wall with energies capable to produce efficient multipacting: the true secondaries energy region (0-20 eV) is less and less populated as the bunch intensity increases. The effect of such phenomenon is visible also on the impinging electron density, plotted in Fig. 10.6 (linear scale).

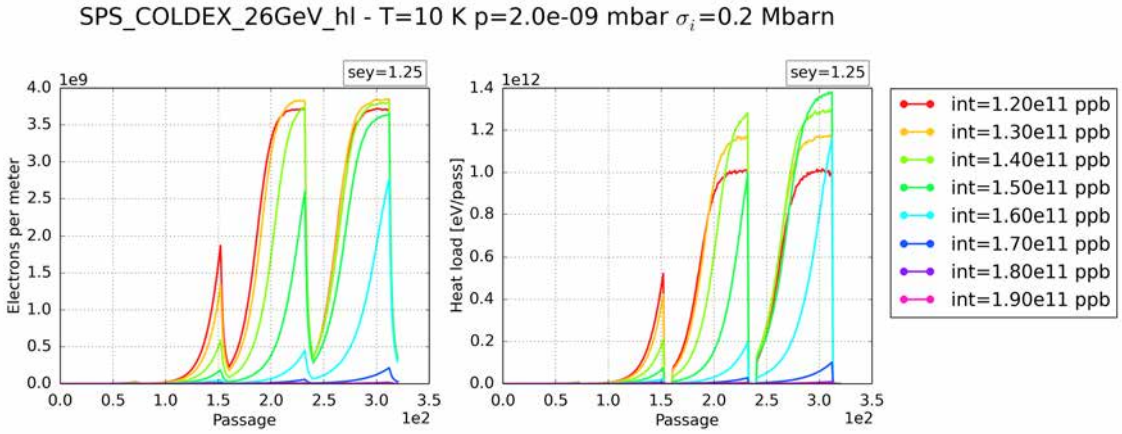

Figure 10.6: Electron density per passage (left) and sum of the kinetic energies of the impinging electrons (right) in the intermediate case of SEY = 1.25. PyECLOUD simulation, 26 GeV, T=10 K, σ_i=0.2 Mbarn.

For SEY=1.25, the electron density per passage (1 passage = 25 ns) increases up to equilibrium already after the third batch with $1.2{\cdot}10^{11}$ ppb. As of $1.4{\cdot}10^{11}$ ppb, we observe a slower electron build-up, i.e. a not so efficient multipacting. The situation worsen, from now on, if the bunch intensity increases more. A similar effect is clearly visible also on the cumulated kinetic energy of the impinging electrons, which is the direct responsible for the dissipated heat load. The exact dynamics in the reduction of the electron density per passage is not reproduced by the cumulated kinetic energy of the impinging ones, due to concurrent change in their spectrum.

Finally, the impinging electron fluxes are shown in Fig. 10.7 and 10.8.

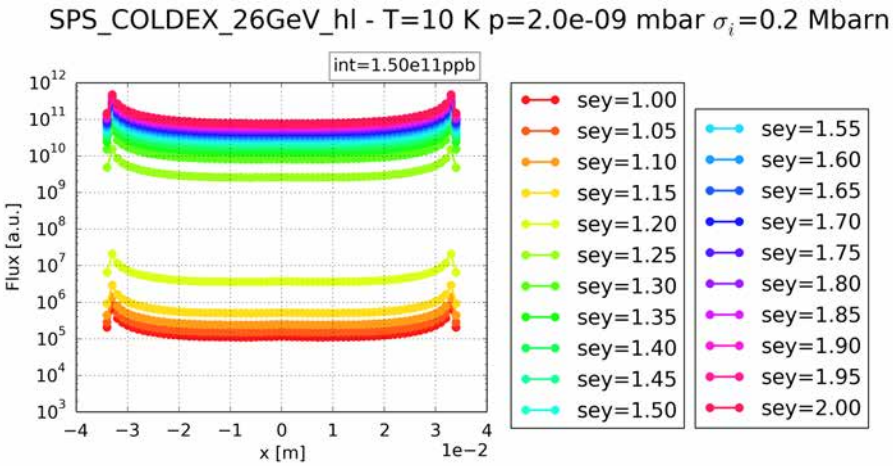

Figure 10.7: Impinging electron flux per vertical slice for $1.5{\cdot}10^{11}$ ppb and different surface SEY. PyECLOUD simulation, 26 GeV, T=10 K, σ_i=0.2 Mbarn.

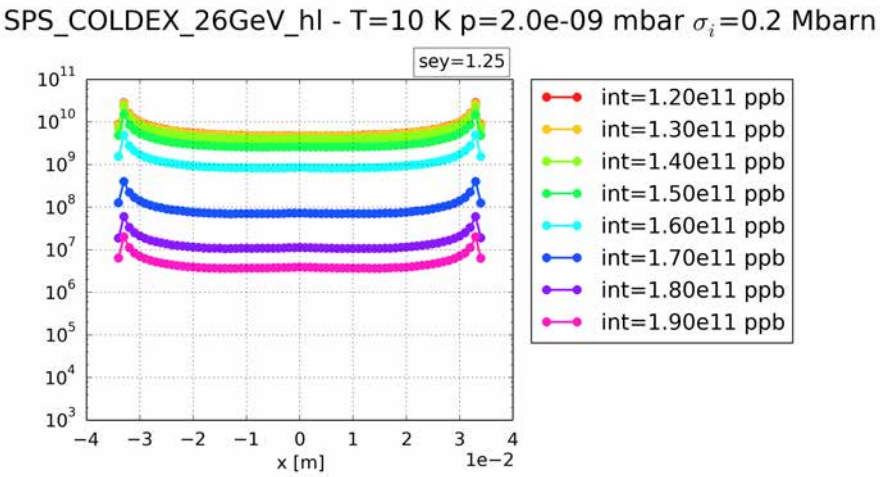

Figure 10.8: Impinging electron flux per vertical slice for SEY=1.25 and different bunch intensities. PyECLOUD simulation, 26 GeV, T=10 K, σ_i=0.2 Mbarn.

In Fig. 10.7 we observe the cumulated electron flux per slice (1 slice = 0.5 mm) of circular beam screen. Because of the absence of magnetic field (which confines the electrons along vertical "strips" in the case of a LHC cryodipole, due to cyclotron revolution), the circular geometry and the limited difference in the horizontal and vertical beam size, the imping electron flux is equally partitioned in the chamber, i.e. the electron cloud density is quasi homogeneous. The peak at the geometry extremities is an inevitable artefact of the selected slicing method. Given a bunch intensity of $1.5{\cdot}10^{11}$ ppb, the multipacting regime is clearly visible as of SEY>1.30 and a difference of 5 orders of magnitude is detectable in the electron flux.

The situation is remarkably different across threshold. Fig. 10.8 shows the cumulated electron flux per slice for SEY=1.25, varying the bunch intensity. After a maximum, the impinging electron flux gets degraded when increasing the bunch intensity, as a direct consequence of the energy spectrum shift previously discussed.

10.2.2 LHC type beams at SPS flat-top energy

The second simulation set considers the alternative COLDEX case, when LHC-type beam, injected and stored in SPS, is accelerated and let circulate at 450 GeV through the COLDEX experiment, with the BS held at T=10 K. The considered residual gas pressure and therefore its density are unchanged. The ionization cross section for 450 GeV relativistic protons in H_2 is very similar to the 26 GeV case, so we will employ the same value of the previous case and profit of one less parameter variation. The effect of the residual gas type and therefore the ionization cross section will be thoroughly reviewed in Sect. 10.2.4.

The electron seeding mechanism at top energy (450 GeV), responsible for the production of primary electrons, remains residual gas ionization. In fact, the synchrotron radiation photoelectric emission by 4x72 bunches of $1.5{\cdot}10^{11}$ ppb (i.e. a beam current of I = 264 mA) can still be considered negligible at 450 GeV.

The photon flux obtainable in a SPS bending dipole at flat-top energy is:

$$\dot{\Gamma} = \frac{5\sqrt{3}e}{12h\varepsilon_0 c}\frac{\gamma}{\rho}I = 7.017\cdot 10^{13}\frac{E\ [\mathrm{GeV}]}{\rho\ [\mathrm{m}]}I\ [\mathrm{mA}] = 1\cdot 10^{16}\frac{\mathrm{photons}}{\mathrm{ms}} \tag{10.1}$$

(ρ = 743 m is the SPS MBA and MBB dipole bending radius), i.e. one order of magnitude less than a LHC arc dipole (10^{17} photons/(ms)). The emitted synchrotron radiation spectrum is characterised by its critical energy, ϵ_c, which corresponds to the energy at which the synchrotron radiation power spectrum is divided by two, and for the SPS accelerator at flat-top energy is:

$$\epsilon = \frac{3}{2}\frac{hc}{2\pi}\frac{\gamma^3}{\rho} = 3.85353\cdot 10^{-7}\frac{E^3\ [\mathrm{GeV}^3]}{\rho\ [\mathrm{m}]} = 31.5\mathrm{meV} \tag{10.2}$$

i.e. four orders of magnitude less than a LHC arc dipole (43.9 eV). The spectrum in energy for the LHC is shown in Fig. 7.2.

One can observe that, at 450 GeV, the energy of photons, emitted by synchrotron energy both by SPS or LHC, falls mainly in the tens of meV range. A slight energy shift toward visible red light (eV range), due edge radiation emission [178], is present in SPS at the edges of the bending magnets in correspondence of their magnetic field discontinuity. In this locations, the critical energy can raise up to 2 eV. Such phenomenon is for instance employed by the SPS beam synchrotron light monitor (BSRT). Following the LEP period, the photon flux on the SPS dipole chambers is however still reduced by tungsten synchrotron radiation masks located at the extremities of the dipole chambers [179].

The minimum photon energy required to produce a photoelectron from an irradiated surface depends strongly on the material work function (W), which typically ranges between 3 and 5 eV for technical surfaces. Therefore, the extremely low quantity of photoelectron in the right energy window guarantees in SPS a negligible photoelectric yield at flat-top proton energy [173]. The relatively "synchrotron radiation free" position of the COLDEX experiment (field free region of a SPS Long Straight Section) helps confirming the lack of primary contribution of synchrotron radiation to electron cloud in COLDEX.

The effects of the acceleration are instead considerable on the beam characteristics. In the longitudinal beam plane, during acceleration, the SPS longitudinal bunch length decreases considerably. Basing on the definition of invariant longitudinal emittance ε_l, in eV·s units,

$$\varepsilon_l = 4\pi\sigma_t\sigma_{\frac{\Delta E}{E_0}}E_0 \tag{10.3}$$

where $4\sigma_t$ is four times the RMS bunch length (CERN convention for bunch length), $\sigma_{\frac{\Delta E}{E_0}}$ the relative energy spread and E_0 the beam energy, the adiabatic evolution of the bunch length can be expressed by [180]:

$$\sigma_t = \sqrt{\frac{\varepsilon_l}{4\pi}}\left(\frac{2\pi|\eta|}{\omega_0^2\beta_0^2 heV|cos\varphi_s|}\right)^{\frac{1}{4}}. \tag{10.4}$$

Given a longitudinal emittance, the bunch length thus scales with the accelerating voltage, as

$$\sigma_t \propto (|\eta|V)^{\frac{1}{4}}. \tag{10.5}$$

During the SPS ramp, a special program is charged to cope with the single and coupled bunch instabilities. Controlled longitudinal emittance blow-up, performed during the ramp injecting band limited noise on the phase loop of the 200 MHz RF system, helps stabilizing the beam at high energy [181]. During this phase, the RF voltage is increased to enlarge the bucket size and limit the particle losses (see Fig. 10.9). Ramping LHC beams of high intensity is very challenging, because it requires a longitudinal blow-up so large to potentially reach the limits in the available RF power. Alongside, the effective RF voltage seen by the beam is reduced due to beam loading.

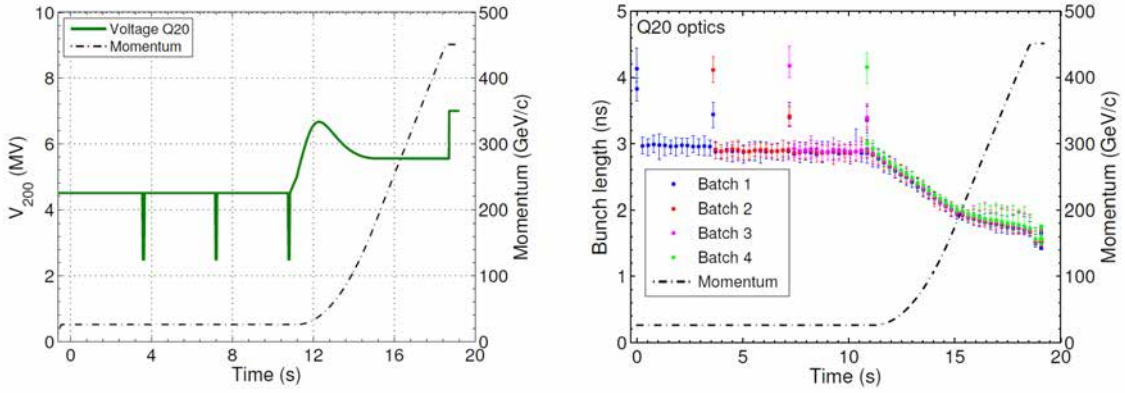

Figure 10.9: SPS 200 MHz cavities RF voltage cycle (left) and average bunch length evolution (right) during a SPS cycle with a LHC type beam, 4x72 bunches spaced 25 ns, of $1.3{\cdot}10^{11}$ ppb [182].

In 2015, almost the maximum available RF voltage of $V_{200\ \mathrm{MHz}}$=7.5 MV is used for beam manipulations during the ramp for the nominal 25 ns beams. At the flat top, the RF voltage is again increased for reducing the bunch length before beam transfer from the SPS 200 MHz bucket to the LHC 400 MHz bucket.

Thus, the SPS longitudinal bunch length shrinks from 26 GeV to 450 GeV as resumed in Table 10.5.

Table 10.5: SPS bunch lengths at injection (26 GeV) and flat-top (450 GeV) energy.

	$1\sigma_t$ [m]	$4\sigma_t$ [s]
26 GeV	0.22 m	3 ns
450 GeV	0.12 m	1.6 ns

The effect of bunch shortening reflects in its peak intensity, that is higher at 450 GeV. Such effect is responsible for an higher peak electric field seen by the secondary electrons and has a significant impact on the build-up of the electron density. A shorter bunch also implies a larger time for the electron density to damp between two bunches, however the effect on the global electron cloud build-up is still too limited due to small bunch spacing (25 ns).

On the transverse plane, the increase in beam momentum reduces its transverse emittance and hence the physical size of the beam (*adiabatic damping*). If we consider the invariant normalised transverse beam emittance,

$$\varepsilon_t^{norm} = \beta\gamma\varepsilon_t = \text{const} \tag{10.6}$$

for ultra-relativistic beams, the transverse emittance (and therefore the physical size) of the beam is inversely proportional to its momentum.

A physical shrink in the beam size produces an increase of the transverse charge distribution, that is:

$$\rho_\perp(x,y) = \frac{1}{2\pi\sigma_x\sigma_y} e^{-\left(\frac{x^2}{2\sigma_x^2}+\frac{y^2}{2\sigma_y^2}\right)}. \tag{10.7}$$

The beam electric field, responsible for accelerating electrons in the electron cloud build-up, is thus strongly enhanced at 450 GeV due to an increase of the transverse charge distribution:

$$\nabla \cdot E = \frac{\rho}{\varepsilon_0} \tag{10.8}$$

$$\frac{\partial E_{\perp x}}{\partial x} + \frac{\partial E_{\perp y}}{\partial y} = \frac{\rho_\perp}{\varepsilon_0} \quad \text{(2D case)}. \tag{10.9}$$

Figure 10.10 shows the normalized energy spectra (over 320 passages) for SEY=1.4 and different bunch intensities at SPS injection (left) and flat-top (right) energy, with COLDEX nominal parameters.

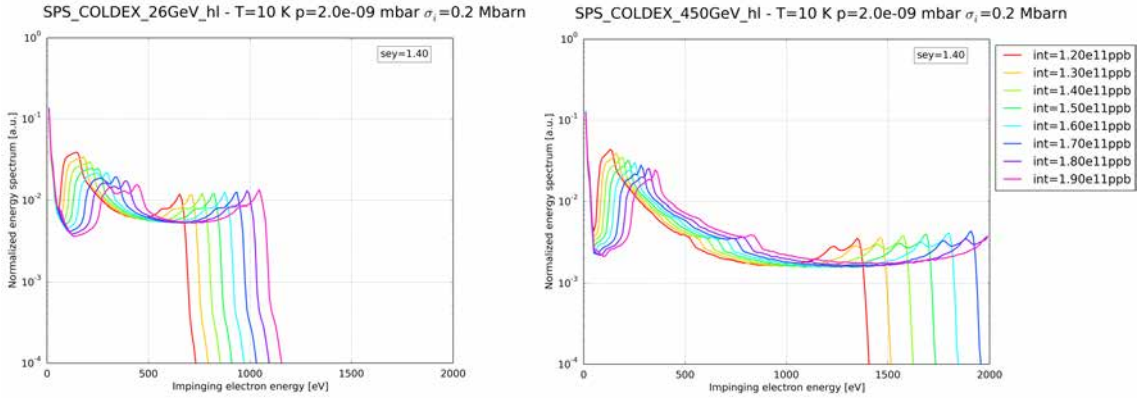

Figure 10.10: Normalized impinging electrons energy spectra (over 320 passages) in the case of SEY=1.4, for different bunch intensities. PyECLOUD simulation, 26 GeV (left) and 450 GeV (right), T=10 K, σ_i=0.2 Mbarn.

For SEY=1.40 (i.e. above threshold in both cases), we see a global shift toward larger energies into the energy spectrum of the impinging electrons.

While the seeding rate remains constant thanks to the almost unvaried ionization cross section, the secondary emission, linked to the impinging electrons energy spectrum, can vary considerably, and so the resulting heat load (eV/passage, or W/m). In Figure 10.11, we show the electron densities per passage and the resultant of the kinetic energies dissipated by the impinging electrons per passage, for a bunch intensity of $1.5{\cdot}10^{11}$ ppb, at SPS flat-top energy (below), in comparison to previous case (top).

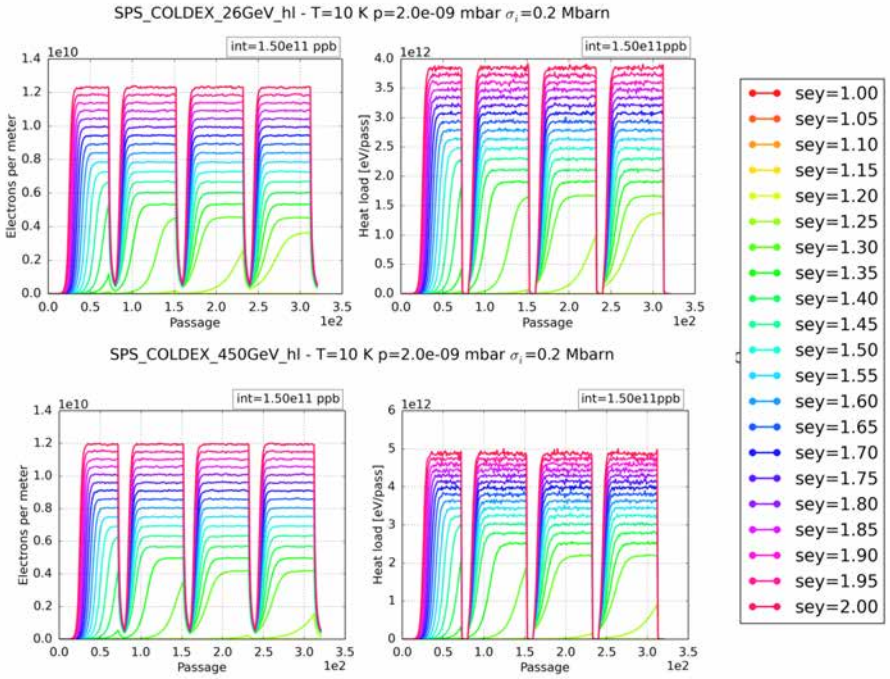

Figure 10.11: Electron density per passage (left) and sum of the kinetic energies of the impinging electrons (right) vs SEY for $1.5{\cdot}10^{11}$ ppb. PyECLOUD simulation, 26 GeV (top) and 450 GeV (bottom), T=10 K, σ_i=0.2 Mbarn.

The equilibrium electron density per unit length (left), in case of multipacting (SEY>1.30) is very similar. The significant shift in the energy is instead observable on the dissipated energy, which is slightly higher. In both plots, we observe a different electron cloud build-up dynamics for SEY across threshold (e.g. SEY = 1.25), which is more efficient in the 26 GeV case.

Figure 10.12 finally shows the simulated heat load of this case, at top versus the surface SEY and for different bunch intensities, below versus the bunch intensity for different the surface SEY.

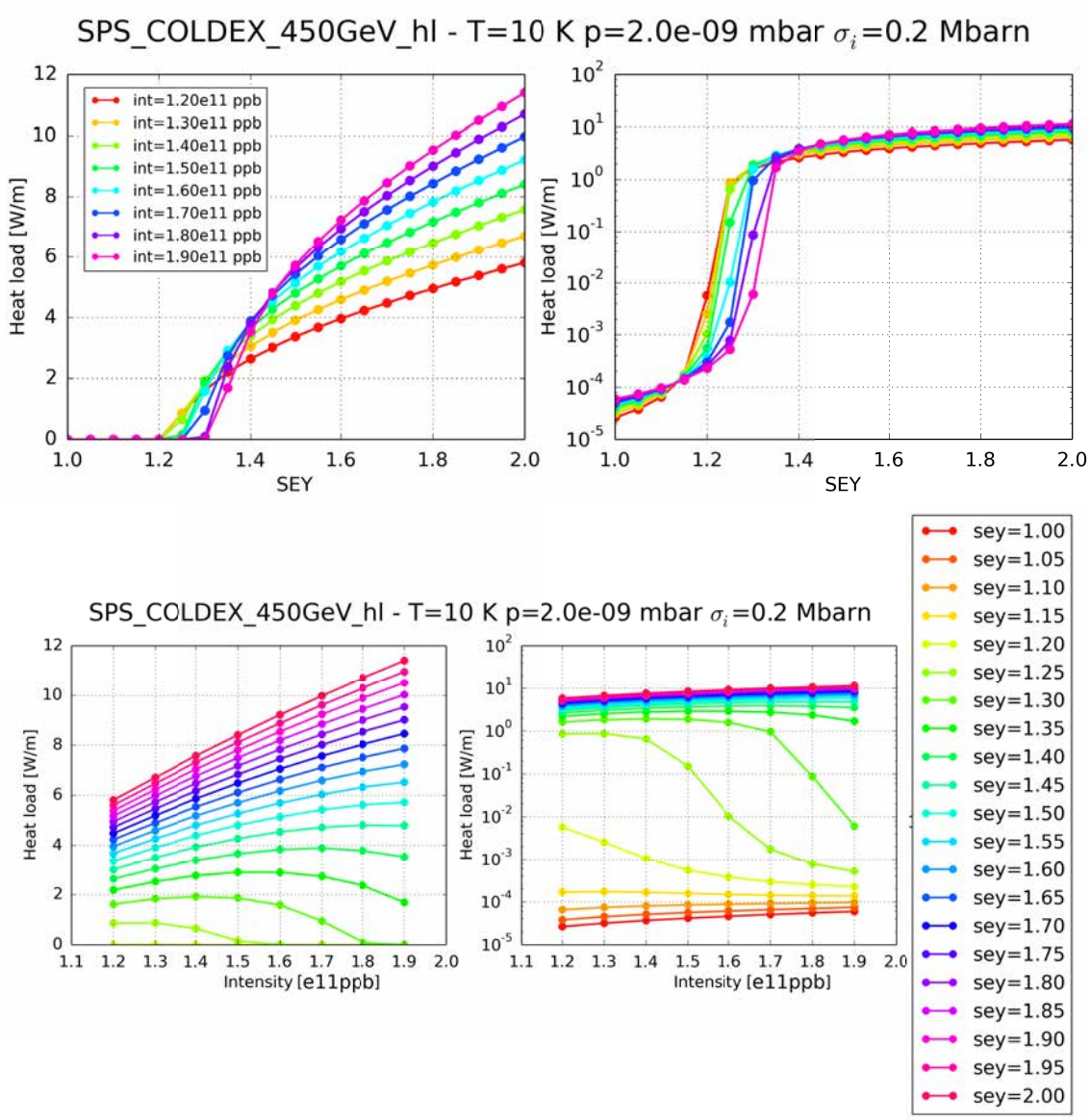

Figure 10.12: PyECLOUD simulation of heat load in the COLDEX alternative case, 450 GeV, T=10 K, σ_i=0.2 Mbarn. Top: versus surface SEY for different bunch intensity; bottom: versus bunch intensity for different surface SEY.

At 450 GeV, the impact on the heat load is a combined effect of the bunch shortening, i.e. the variation on the e-cloud build-up dynamics, and the emittance shrink, which produces an increased transverse charge distribution and in turn a higher beam electric field. The variation of the impinging electrons energy spectrum impacts heavily on the secondary emission and in particular on its efficiency when entering the SEY curve. In parallel, the secondary electrons deposited energy is increased by the increased beam electric field.

From Fig.10.12, the multipacting threshold in COLDEX at 450 GeV is slightly larger, but still globally situated in the 1.15<SEY<1.35 window. Below threshold (logarithmic scale), we observe little change in the dissipated power, due the same seeding rate. The heat load is slightly increased with respect to the 26 GeV case for high intensities, thanks to the stronger kick received by the electrons. However, such increase in the impinging electron energy delays the inception

of a proper multipacting regime when increasing the SEY. For instance, for the considered input parameters, efficient multipacting is observed only for SEY>1.3 for $1.9{\cdot}10^{11}$ ppb. Above threshold, a quantitative estimation of the heat load has to be given on a case by case basis. Considered a single bunch intensity and in well defined multipacting regimes, the heat load increases by a factor 1.2-1.3 with respect to the 26 GeV case, principally due to the higher electrons dissipated energy.

10.2.3 Warm case

The COLDEX case has been also simulated in warm (room temperature) conditions. The room temperature T=300 K was chosen, in combination to a typical vacuum of pressure of p=$2{\cdot}10^{-8}$ mbar, being COLDEX an unbaked system kept, in this case, under turbomolecular pumping. Such increase in temperature (30 times) and pressure (10 times) is reflected in the residual gas density by the relation:

$$n_{gas} = \frac{p}{k_B \cdot T} \tag{10.10}$$

i.e. an increase of 3 times in the gas density is produced.

Figure 10.13 shows the simulated heat load on the COLDEX BS for the nominal (T=10 K) and warm (T=300 K) cases.

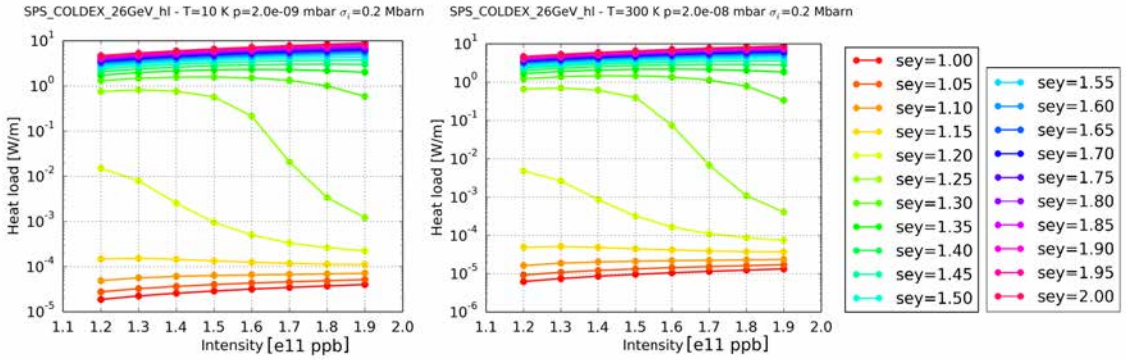

Figure 10.13: PyECLOUD simulation of heat load in the COLDEX nominal (left) and warm (right) case, 26 GeV, σ_i=0.2 Mbarn, versus surface SEY for different bunch intensity. Left: T=10 K, right: T=300 K.

In seed accumulation regime, we observe that a change of 3 times in the residual gas density leads to an equally proportional change in the heat load. In such regime, the production of electrons is principally due to ionization of the residual gas, which is dominant over the secondary emission. The electron-ion pairs production is directly proportional to the residual gas density, as follows:

$$\frac{dn_{ion}}{dtdAds} = \sigma_{ion} n_{gas} \varphi_p(x, y, s, t) \tag{10.11}$$

The same increase applies for the equilibrium electron density and impinging electron flux in this regime. Across threshold (e.g. SEY=1.20 or SEY=1.25), the increase in the heat load is tangible. Above threshold, the situation is, however, unchanged between T=10K and T=300K. This is expected, as above threshold, the dominant effect is secondary electron emission and so the increase in the residual gas pressure is transparent to the electron density and the impinging electron flux.

This result is perfectly applicable to other temperature and pressure ranges. So, one does not need to perform a scan over pressure and temperature to observe the sensibility of electron cloud build-up to this parameters: values, below threshold, can be simply rescaled according to the considered n_{gas}, while above threshold, during electron cloud build-up, the equipment is practically insensible to its variation.

10.2.4 Residual gas type influence

The last case considers the influence of the residual gas in COLDEX on the electron cloud build-up. As seen in Sect. 7.2, for a selected particle beam energy, the ionization cross section extends over a order of magnitude. For 26 GeV, we can roughly divide the gas types into two categories: lighter gases, such as H_2 and He, exhibit a ionization cross section of roughly 0.2 Mbarn, while for heavier gases, σ_i ranges from 1 to 2 Mbarn. We observe a net general increase of a factor 2 when increasing the energy of two orders of magnitude.

For the COLDEX case, we are interested in the 26 GeV energy, typically used for scrubbing in SPS, and the residual gas species of H_2, CO, N_2 and CO_2, which are the typical gases found in cryogenic environments at different temperatures. For H_2, which is the common residual gas at cryogenic temperatures, we selected σ_i=0.2 Mbarn, while for the other gases, a σ_i=2.0M barn was adopted.

Figure 10.13 shows the simulated heat load on the COLDEX BS in nominal conditions with σ_i=0.2 Mbarn and σ_i=2.0 Mbarn.

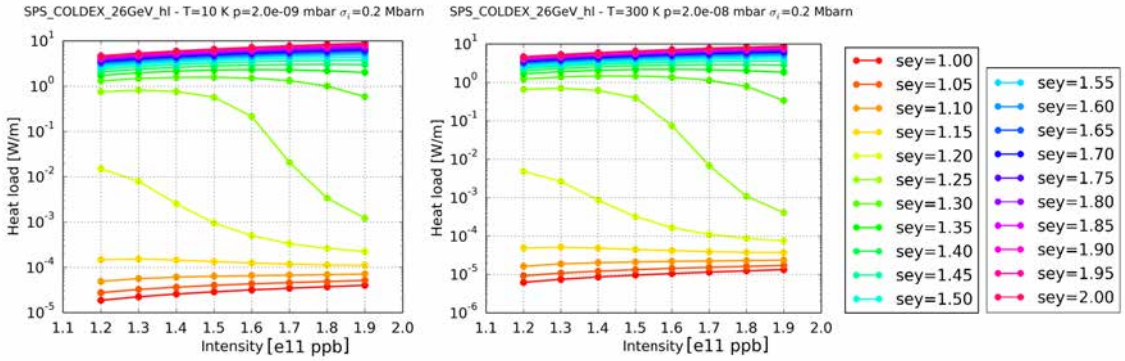

Figure 10.14: PyECLOUD simulation of heat load in COLDEX for σ_i=0.2 Mbarn (left) and σ_i=2.0 Mbarn (right) cases, 26 GeV, versus surface SEY for different bunch intensity.

In seed accumulation regime, a change of 10 times in the ionization cross section leads to an equally proportional variation in the heat load. As in this regime the production of electrons and so the regime electron density are principally due to ionization of the residual gas, this result is coherent and expected. If we apply again Eq. 10.11, we observe such direct proportion. The same increase applies for the equilibrium electron density and impinging electron flux in this regime.

Across threshold (e.g. SEY=1.20 or SEY=1.25), the increase in the heat load is tangible. In this region, where the heat load is measurable, one should therefore beware of this input parameter, as the simulation results can be quite easily misleading. Above threshold, the simulated heat load is unchanged. This is again expected, as above threshold, the dominant effect is secondary electron emission and so the increase in the ionization probability of the residual gas pressure is transparent to the electron density and the impinging electron flux.

As indicated in previous Section, the discussed results are perfectly applicable to a whole range of cross sections. So, below threshold, one does only need to simply rescale the obtained the values according to the considered σ_i, while above threshold, during electron cloud build-up, the equipment is practically insensible to its variation. As in cryogenic environments, the residual gas is often dominated by H_2, the little variation in his ionization cross with the beam energy going over two order of magnitude safely ensures reliable simulation results within the range σ_i=0.2-0.4 Mbarn, i.e. within a factor two.

10.3 Build-up simulations with a-C coatings

10.3.1 Updated model of SEY

In order to further refine the electron cloud build-up estimations offered by pyECLOUD predictions, an updated and novel model of secondary electron emission for a-C coatings was developed as input

to build-up simulations.

Basing on the phenomenological modeling of the SEY energy dependence described in [117] and [113], a set of secondary emission parameters for a-C coatings was derived by the measured (at room temperature) SEY curves available from samples obtained during the COLDEX beam screen a-C coating process (see Sect. 9.1).

Due to unavailability of data for electrons below the energy of 80 eV, the determination of the reflected component, parametrized by the term R_0 (see Sect. 7.3), is unknown. The expected electron reflectivity is $R_0 = 1.0$. Therefore, we included the complete set of possible SEY curves in the range $R_0 = [0.7{:}1.0]$.

Fig. 10.15 shows the result of the Non-Linear Least Squares analysis made on the COLDEX a-C experimental sample dataset #1, applying a bisquared robust method and a trust-region algorithm. In the window $R_0 = [0.7{:}1.0]$ and for $E_0 = 150$ eV, is found $\delta_{max} = 1.059 \pm 0.002$, $E_{max}(\delta_{max}) = 271.5 \pm 0.9$ eV, $s = 1.773 \pm 0.001$. The experimental data is contained in a prediction bound of 95th percentile. The influence of electron reflectivity on the fitted curves is shown on the right of Fig. 10.15.

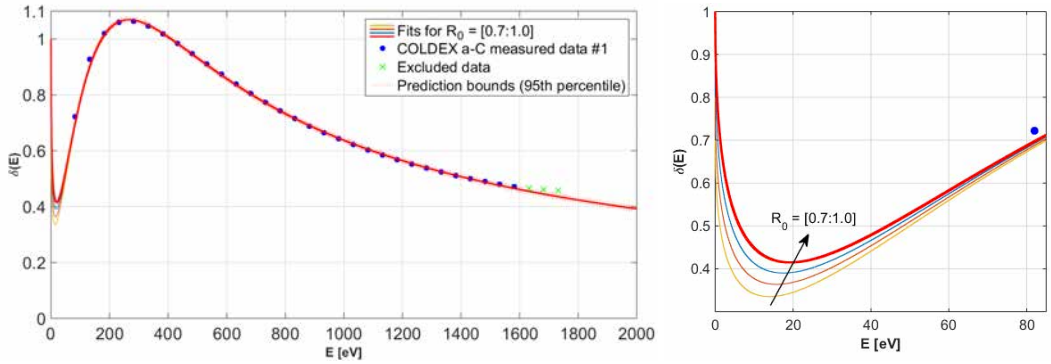

Figure 10.15: COLDEX a-C coating SEY model fitted following the phenomenological modeling formalism proposed in [117] and [113].

The results for each fit are resumed in Table 10.6.

R_0	δ_{max}	$E(\delta_{max})$ [eV]	s	E_0 [eV]
0.7	1.061	270.6	1.773	150
0.8	1.060	271.2	1.773	150
0.9	1.058	271.8	1.773	150
1.0	1.057	272.4	1.774	150

Table 10.6: COLDEX a-C coating SEY model: parameters fitted for $R_0 = [0.7{:}1.0]$.

We observe a rather good agreement of the fitting curves to the experimental data, with a set of parameters which is quasi-invariant with R_0. Looking at Eq. 7.15, little influence of the elastically reflected component was expected on the secondary electron emission for energies above 200 eV, where the true secondaries component is peaked. The phenomenological model, which was originally conceived for metallic technical surfaces such as Cu, stainless steel or Ti [117], seems applicable also to a-C coatings, confirming a secondary emission energy dependence intrinsic of the material surface, rather than based on its morphological features. The proposed fitting parameters represent a good approximation for the true secondaries component of the SEY for a-C; the elastically reflected component requires additional experimental data.

10.3.2 Simulation results

The developed model was entered in a pyECLOUD simulation set considering the nominal COLDEX parameters and LHC type beams, similarly to the studies performed in Sections 10.2.1 and 10.2.2.

The nominal case boundary parameters are chosen: T=10 K, $\sim 2 \cdot 10^{-9}$ mbar, σ_i=0.2 Mbarn. In order to illustrate the dependence of the electron cloud build-up on the SEY, we sweep δ_{max} at constant $E_{max}(\delta_{max})$, similarly to what accepted for metallic surfaces. Although the effect of electron conditioning has been addressed concerning the surface contamination [183], the concept of "scrubbing" has never been yet extensively studied (principally because the purpose of a-C coating is to mitigate electron cloud *ab-initio*, i.e. as received), so a better relationship is not yet available. On the other hand, it is re-known that the hydrogen content may modify the a-C SEY. In Fig. 10.7, on the left, a compilation [183] of SEY curves for various carbon thin films is shown with respect to the coating technique employed: it is shown, on the right, that the amount of H_2 in the plasma discharge (impure gas, outgassing during the coating process) correlates with an increase of the SEY resulting at the end of the coating process. In particular, an enrichment of H_2 content increases the energy loss of primary electrons: the larger energy dissipation implies that more secondary electrons are produced within the escape depth and so capable to be secondly emitted [183]. For the purpose of our simulation set, we observe that different coating techniques and H_2 impurities qualitatively produce a shift of δ_{max}, with $E_{max}(\delta_{max})$ very slightly decreasing with increasing H_2 content.

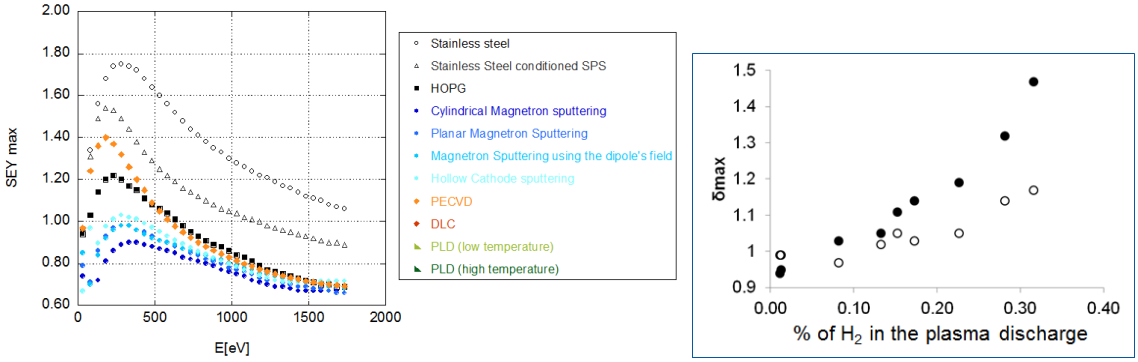

Table 10.7: Right: SEY curve for different carbon thin film coating techniques tested at CERN. Left: influence of the H_2 content in the plasma discharge on δ_{max}. From [183].

In Fig. 10.16, we observe the result of the pyECLOUD simulation set with an upgraded a-C SEY model, showing the dependency of the heat load for different SEY, increasing the bunch intensity, for the COLDEX nominal parameters. For SEY = 1.05, the expected deposited heat load due to electron cloud is well below 1 mW/m for every bunch intensity. Above, the multipacting threshold is severely dependent on the bunch intensity. In particular, for a selected SEY, an increase in the bunch intensity does not correspond to a monotonic increase of heat load. Looking at the SEY energy dependence of a-C e.g. in Fig. 10.17, the window $E_1 < E < E_2$ for which $\delta(E_1 < E < E_2) > 1$ is narrower than Cu, essentially because of a higher s parameter than Cu. Due to a lower SEY curve portion for which $\int \phi(E)[\delta(E) - 1]dE > 1$ (being $\phi(E)$ the normalized impinging electron flux), the multipacting efficiency is constrained to a narrower range of impinging electron energies. The situation is enhanced by the fact that the sensibility of impinging electron energy over the bunch intensity (and so its electric field) is maximized in the COLDEX case thanks to the absence of magnetic field and relatively small aperture.

Above SEY=1.75, where the a-C SEY is $\delta(E) > 1$ up to $E \approx 1000$ eV, an increase of bunch intensity matches quasi-linearly with an increase of heat load: this because the heat load (or electron energy flux) is in practice dependent only on the energy gain and not anymore to $\delta(E)$, sufficiently above 1.

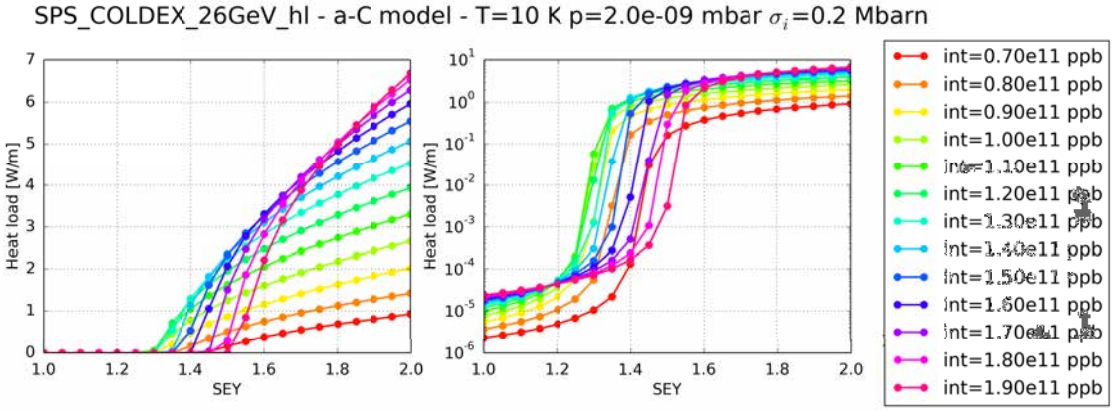

Figure 10.16: PyECLOUD simulation of heat load in the COLDEX nominal case with an upgrade a-C SEY model, 26 GeV, T=10 K, σ_i=0.2 Mbarn, versus SEY for different bunch intensities.

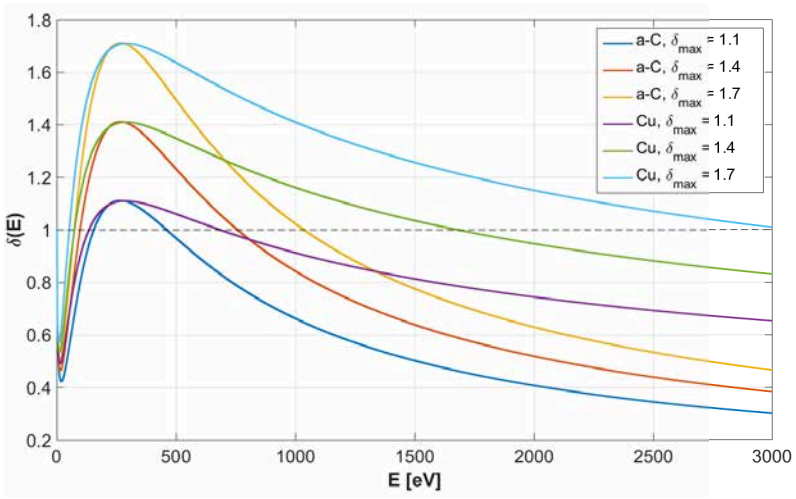

Figure 10.17: SEY model for a-C versus Cu for δ_{max} =1.1, 1.4, 1.7.

Already in linear scale, but better in logarithmic scale, we observe the same of dependence in the plot of Fig. 10.18, where the heat load is plotted against the bunch intensity for different surface SEY. Below threshold, the heat load increase monotonically with the bunch intensity for every SEY, which is a consequence of the increased energy gained by the primary electrons and a negligible secondary emission. Quite remarkably, a sudden increase in electron density, and so heat load, followed by a net decrease is observed with intensities above $0.7 \cdot 10^{11}$ ppb for SEY larger than 1.15. The multipacting efficiency, with respect to the bunch intensity, is narrower for lower SEY; a decrease of heat load is obtained if the bunch intensity (and so the energy gain) does not match anymore the secondary emission energy dependence of the SEY in study. The energy spectra of the impinging electrons, shown in Fig. 10.19 for the two cases of SEY=1.1 (left) and SEY=1.4 (right), are a further confirmation of this effect.

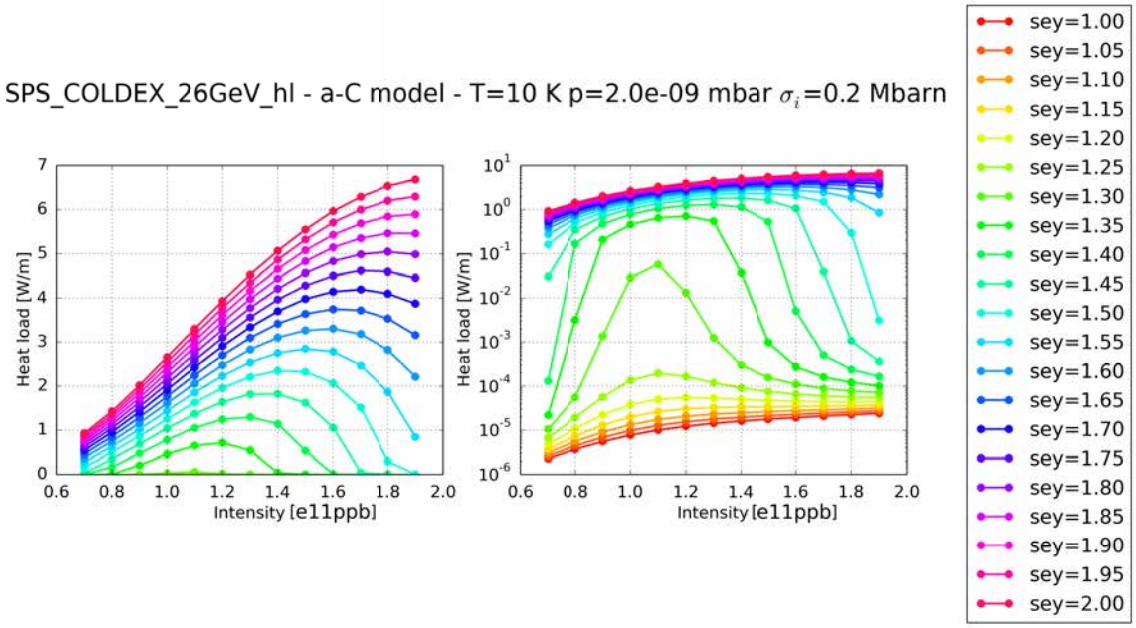

Figure 10.18: PyECLOUD simulation of heat load in the COLDEX nominal case with an upgrade a-C SEY model, 26 GeV, T=10 K, σ_i=0.2 Mbarn, versus bunch intensity for different surface SEY.

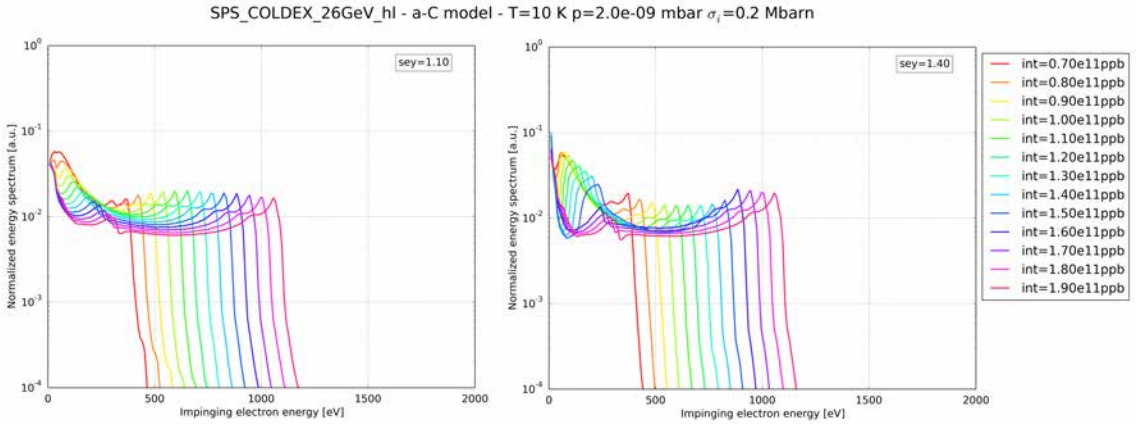

Figure 10.19: Normalized impinging electrons energy spectra (over 320 passages) in the case of SEY=1.1 (left) and SEY=1.4 (right), for different bunch intensities. PyECLOUD simulation, a-C SEY model, 26 GeV, T=10 K, σ_i=0.2 Mbarn.

Basing on these considerations, a multipacting threshold cannot be fixed a priori, and is severely dependent on the bunch intensity, for SEY > 1.25. For SEY above 1.5, the heat load is above 0.1 W/m (i.e. measurable) for any bunch intensity.

The same study has been carried for the COLDEX alternative case considering the beam energy ramped to 450 GeV and the upgraded a-C SEY model. Fig. 10.20 shows the dependency of the heat load for different SEY, increasing the bunch intensity; in Fig. 10.21 the heat load is plotted against the bunch intensity for different surface SEY. The energy spectra of the impinging electron are shown in Fig. 10.22 for the two cases of SEY=1.1 (left) and SEY=1.4 (right).

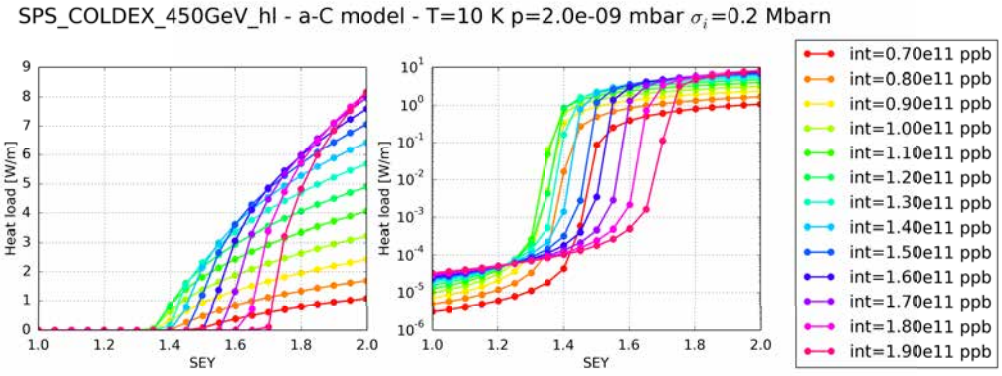

Figure 10.20: PyECLOUD simulation of heat load in the COLDEX alternative case with an upgrade a-C SEY model, 450 GeV, T=10 K, σ_i=0.2 Mbarn, versus SEY for different bunch intensities.

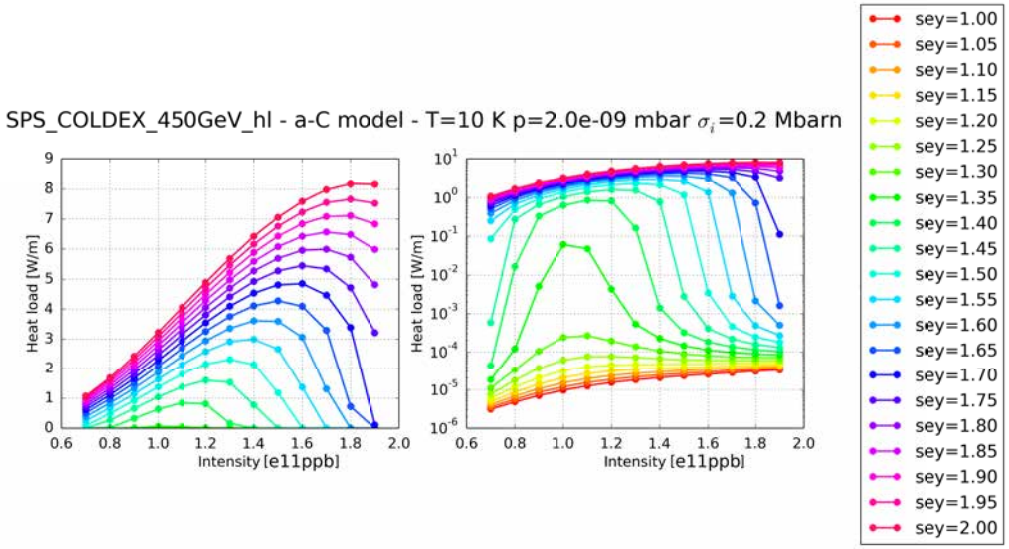

Figure 10.21: PyECLOUD simulation of heat load in the COLDEX alternative case with an upgrade a-C SEY model, 450 GeV, T=10 K, σ_i=0.2 Mbarn, versus bunch intensity for different surface SEY.

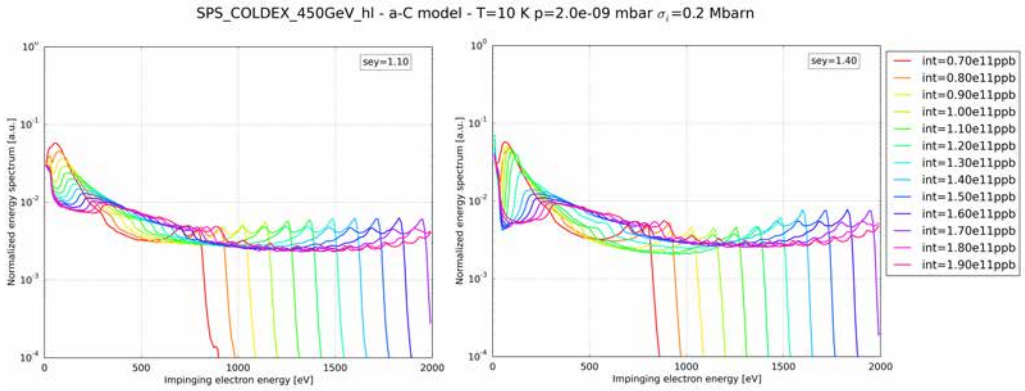

Figure 10.22: Normalized impinging electrons energy spectra (over 320 passages) in the case of SEY=1.1 (left) and SEY=1.4 (right), for different bunch intensities. PyECLOUD simulation, a-C SEY model, 450 GeV, T=10 K, σ_i=0.2 Mbarn.

The effects observed for the nominal case are confirmed also at 450 GeV: in particular, the higher bunch electric field pushes further the multipacting threshold, toward values above SEY=1.4, and the dependence on the bunch intensity is more even more severe.

10.3.3 Effect of electron reflectivity

The proposed a-C model is influenced, at low energies, by the uncertainties on the electron reflectivity R_0, which could not be accessed by the setup employed for the SEY experimental measurement. From Fig. 10.15, we have also shown that the influence of R_0 is negligible for energies above 200 eV.

As previously discussed (Sect. 7.3), the problem of the low energy electrons is of actual importance [116], because the much longer survival time can potentially boost the electron cloud build-up process. In this regard, a simulation set has been carried to study the influence of the electron reflectivity R_0 in the range [0.6:1.0] on the electron cloud build-up of COLDEX with an upgraded a-C SEY model, in the specific case of interest of SEY = 1.1. Fig. 10.23 shows the dependency of the heat load for an increasing bunch intensity and different R_0, with a beam energy of 26 GeV (left) and 450 GeV (right).

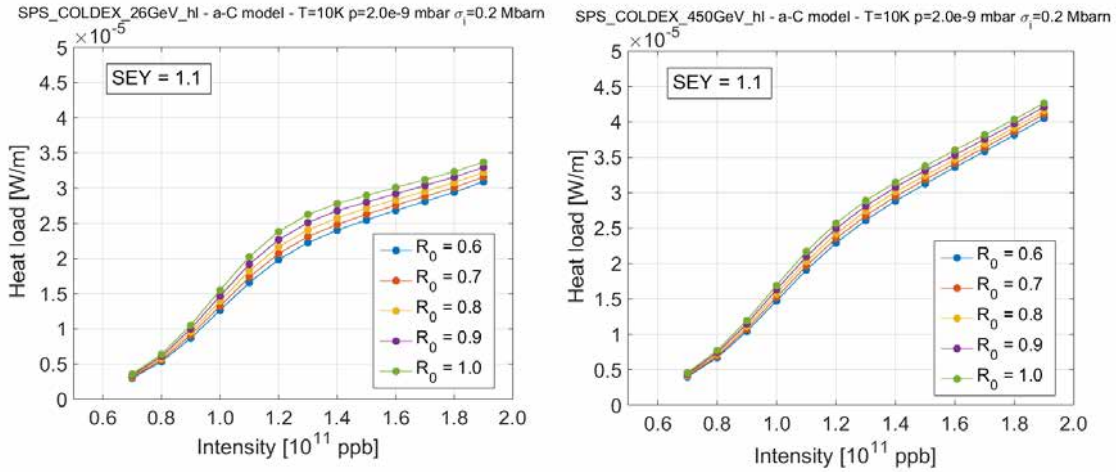

Figure 10.23: Effect of the electron reflectivity R_0 on the simulated of heat load in the COLDEX nominal (26 GeV, left) and alternative (450 GeV, right) cases with an upgrade a-C SEY model, for different bunch intensity at constant $\delta_{max} = 1.1$. T=10K, σ_i=0.2Mbarn.

A weak dependency - below a factor 2 - of R_0 on the heat load (or impinging electron energy flux) is observed in the range $R_0 = [0.6{:}1.0]$ for every bunch intensity; the influence on the heat load can only be appreciated with larger bunch intensities (and this because of a larger production rate of primary electrons). Heat load is reduced by lowering R_0: this was expected, as a reduction of R_0 significantly reduces the secondary emission (or, inversely, enhances the "absorber" behaviour) of the surface in the energy range spanning few tens of eV.

Chapter 11

Experimental results with a-C coating in COLDEX

11.1 Introduction

The main goal of the experimental beam runs with COLDEX is the performance qualification of a-C coatings with LHC type beams while operating the beam screen in two temperature windows: the 5 to 20 K range, currently adopted for LHC and suitable for the HL-LHC matching sections, and the 40 to 60 K range under study for HL-LHC Inner Triplets.

The experimental setup is conceived to study the beam induced multipacting in a LHC type cryogenic vacuum system as a function of the CB and BS temperature (depending on it, the presence of adsorbed gas species on their surface) and the circulating beam parameters (bunch intensity, spacing, total circulating intensity, at injection and flat-top energy). During a run, total pressure is measured along the vacuum system, i.e. in the RT upstream and downstream sections and in the cryogenic BS through the room temperature chimney. The dynamic pressure rise due to electron cloud is monitored with respect to the different circulating beams, and the conditioning obtained by beam dose is observed. The gas composition is followed-up constantly in both cryogenic and warm parts by residual gas analysers. In case of gas desorption, the primary and recycling desorption yields of the system can be estimated. The heat load dissipated by electron cloud onto the BS surface is measured via cryogenic calorimetry. The electrons activity (flux) is measured in the cryogenic environment of the BS with the electrode inserted through the chimney (chimney electrode) and with one of the BS slot shielding baffles (BS electrode). The benchmarking of heat loads and electron fluxes with available electron cloud build-up codes allows the deduction of the SEY of the surface. The effects of adsorbed gas on the BS surface at cryogenic temperature is reproduced in dedicate runs by controlled pre-adsorptions via gas injections.

During a COLDEX run, the SPS LSS4 by-pass is moved so that the SPS vacuum sector 430 is replaced by the sector 431. As described in Section 9.2, this thus includes:

- symmetrically - upstream and downstream - two ID156 by-pass chambers (1963 mm long), two standard SPS sector valves, two ID 100 transition chambers, 400 mm long. This parts are at room temperature and are made of 316LN stainless steel. Concerning electron cloud, the surfaces have been conditioned throughout the previous beam runs of 2001-2004, but the long exposition to air during the experiment recommissioning have practically reset their SEY to an estimated unconditioned initial value of SEY$\approx$1.9;
- two - upstream and downstream - tapers from ID100 to ID67 and two Cold-to-Warm transitions. This parts are made of untreated OFHC copper, their initial SEY is estimated $\approx$2.2;
- the COLDEX CB and BS system thoroughly described in Sect. 9.2.

Once the experiment is inserted, beam is circulated in the SPS machine ring in periods of dedicated scrubbing (Scrubbing Runs) or dedicated mode only for COLDEX. The typical beams are of LHC-type: high intensity, 25 ns spaced bunches in trains of 72, usually ramped-up from one

to finally four batches at the beginning of the run. The beam, coming from the Proton Synchrotron at 26 GeV/c, is usually left at the flat bottom momentum on a dedicated scrubbing cycle of 18 basic periods, i.e. 21.6 s. For the purpose of LHC qualification, acceleration tests to 450 GeV/c are done. The available bunch intensity, important parameter for the electron cloud build-up, can be chosen over a large span, i.e. from $0.7{\cdot}10^{11}$ proton per bunch (ppb) to $2.0{\cdot}10^{11}$ ppb, at constant beam brightness provided by the Proton Synchrotron Booster. After resume of the SPS machine after the Long Shutdown 1, the bunch intensity was adjusted in steps, this following-up the machine conditions (scrubbing) and the beam quality (losses, observation of instabilities). The higher bunch intensities resulted difficult to handle because of the poor lifetime, high losses at injection and impedance heating of specific machine parts (especially the injection kicker MKP) and were deployed only after extensive machine scrubbing for a limited time period.

Alternative filling schemes have been developed to improve the effectiveness of scrubbing periods: hybrid spaced beams, such as the (20+5) ns *doublet* beams [184], were tested and successfully employed in the SPS to increase the frequency of the beam electric field presence and decrease the electron cloud decay time between subsequent bunch passages. Those beams are fruit of a novel production scheme, where long bunches (10 ns full bunch length) in 25 ns spaced trains are injected from the Proton Synchrotron on the unstable phase of the 200 MHz SPS RF system: ramping up the RF voltage shortly after injection from 1 MV to 3 MV allows to capture the long bunches in two neighbouring buckets, resulting in the generation of 5 ns spaced doublets out of each incoming PS bunch.

During the SPS Scrubbing Runs of 2014, additional filling schemes have been deployed in the SPS as test bench for the LHC. Low emittance beams from the injectors, produced with the Batch Compression Merging and Splittings (BCMS) production scheme [184], were developed to provide the LHC experiments with the highest possible luminosity with 25 ns beams; micro-batches composed by 8 bunches followed by 4 empty buckets (8b+4e, [184]) were tested as a measure to mitigate the electron cloud build-up in the LHC during 25 ns operation.

The SPS duty cycle, during SPS Scrubbing Runs and the COLDEX dedicate runs, was variable and depended on the machine conditions and the vacuum and/or impedance heating recovery needs, or more simply because of the presence of additional users. Common duty cycles spanned from 50% to 85%.

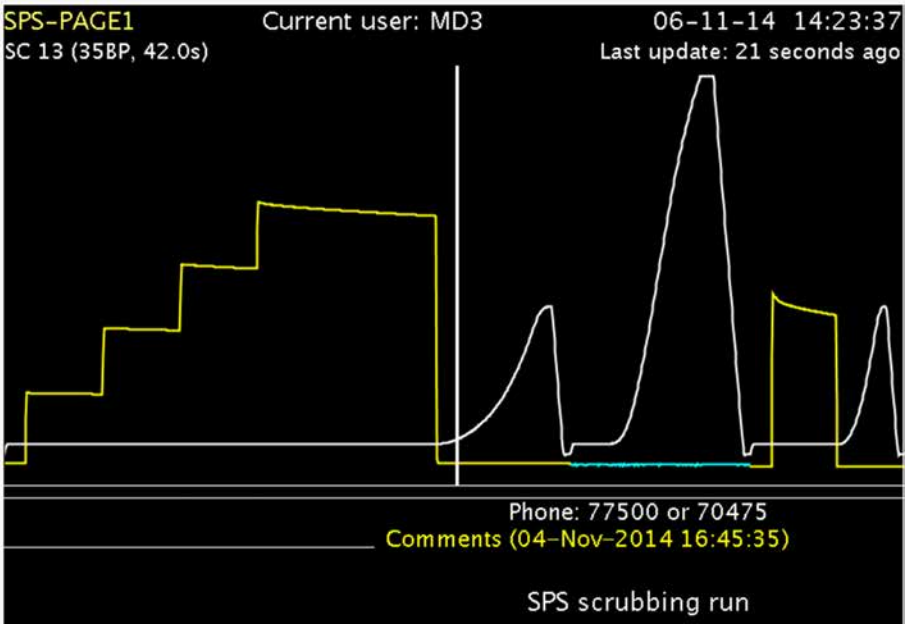

Figure 11.1: SPS Page 1 displaying the machine beam intensity and magnetic cycles during a SPS Scrubbing Run. The scrubbing cycle is here MD3: four batches are being injected at a rate of 72 bunches ($1.7{\cdot}10^{11}$ ppb) per injection every 2 basic periods (3.6 s) and left circulate at 26 GeV/c for 7.2 s. Beams is dumped right before the acceleration ramp.

11.2 Results during Run 1

The COLDEX first experimental run with a-C coating took place during the first SPS Scrubbing Run after LS1, in November 2014. In a 7 days period, the accumulated beam dose exceeded 3.5 Ah. Two BS temperatures windows have been chosen: first 50 K, then 5 to 10 K. The CB was constantly kept at 4.5 K.

One to four batches of 72 bunches, 25 ns bunch spaced, up to $1.3{\cdot}10^{11}$ ppb, circulated into COLDEX, mainly at 26 GeV/c, but also with energy ramp to 450 GeV/c. Hybrid (5+20 ns) bunch spaced doublet beams circulated as well, up to 4 batches and with a maximum intensity of $1.4{\cdot}10^{11}$ proton per doublet (ppd), equally split.

Figure 11.2 offers a global resume of the Run, showing the beam intensity integrated per cycle (top), the pressure evolution during the run along the COLDEX sector (center) as well as the RGA1 ion current relative to H_2 specie and the temperature range kept on the BS (bottom).

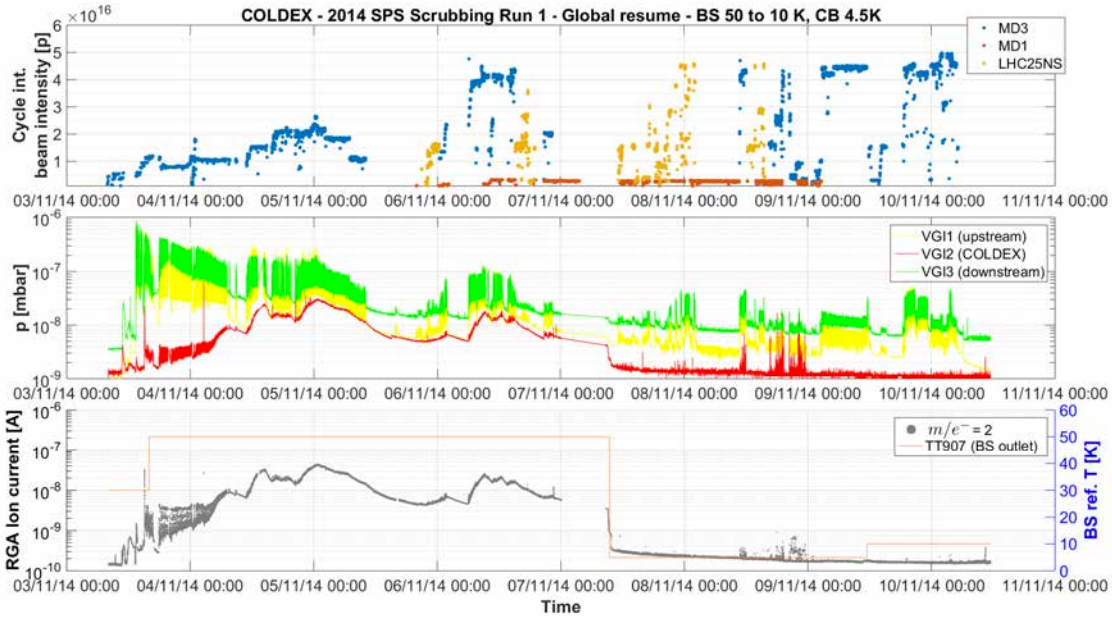

Figure 11.2: COLDEX Run 1 during the SPS Scrubbing Run 1 of 2014. Top: cycle integrated beam intensity; center: vacuum pressure along the sector 431; bottom: RGA ion current relative to H_2 and reference BS temperature.

Significant pressure rises (up to $\sim 5{\cdot}10^{-7}$ mbar, see VGI1 and VGI3 on green and yellow curves) correlated to the beam circulation were observed upstream and downstream the COLDEX BS due to electron cloud stimulated desorption of mainly H_2 and CO. These parts are made of bare 316LN stainless steel, DN100, room temperature pipes, vented to air during COLDEX re-commissioning. Their initial δ_{max} is expected 1.9. A global conditioning of those surfaces is visible throughout the scrubbing run. In particular, after a beam dose only 0.3 Ah (first $\sim$ 12hours), four batches of 72 bunches at $0.7{\cdot}10^{11}$ ppb could be injected. From there on, following the machine conditioning, the bunch intensity was progressively increased, up to $1.3{\cdot}10^{11}$ ppb by the end of the run.

In COLDEX (see VGI2 on red curve, see zoom in Fig. 11.3), the BS temperature was initially adjusted to $\sim$30 K. No pressure rises linked to electron stimulated desorption were observed. A Δp up to $\sim 6 \cdot 10^{-7}$ mbar was observed with respect to the RT extremities, indicating a gas transmission of pressure ratio equal to 300. The gas load was not detectable in the BS centre, as the BS a-C surface provided an extremely high effective pumping speed for all gas species, roughly of 33000 l/s for H_2 at 30 K (sticking probability $\sigma \approx 0.5$ for bare surface).

The BS temperature was then adjusted to 50 K. The temperature increase induced desorption of the adsorbed gas, provoking the pressure bump visible at around 15:00. The gas was flushed to the CB at 4.5K. During beam circulation, a dynamic slow pressure rise, up to$\sim 3.5{\cdot}10^{-8}$ mbar, was

observed in the COLDEX BS at 50 K. The pressure rise was dominated by H_2, as observed through residual gas analysis, and linked to the large desorption rate from the RT beam pipes of the SPS LSS during electron bombardment. At 50 K, the BS was capable to adsorb only CO_2 and H_2O by cryocondensation and N_2 and CO by physisorption (see Sect. 9.5), therefore the only, limited, source of pumping for the other relevant gas (H_2) was the CB. The CB, at 4.5 K, was capable of condensing all gas species (except He, which is only adsorbed up to 10^{14} He/cm^2), with a pumping speed fixed by the 1% transparency to the BS, until the saturated vapour pressure of each specie is reached: with exception of He, the highest saturate vapour pressure at 4.5K is the one of H_2, about $1 \cdot 10^{-5}$ mbar measured at room temperature. The transmission of gas toward the BS was initially well visible in the dynamic pressure rises observed due to H_2 transmission (see the peaks on the RGA for $m/e^- = 2$ from the 19:12 to 07:12), which then became covered in the increasing background residual gas pressure, due to monolayer build-up on the CB. After one day and half of beam run (5/11, midnight), the accumulation of the gas load due to stimulated desorption from the extremities covered the CB with about 80% of a monolayer; as such, it dominated by its H_2 vapour pressure, which was $4 \cdot 10^{-8}$ mbar at 4.5 K (see Appendix A.5).

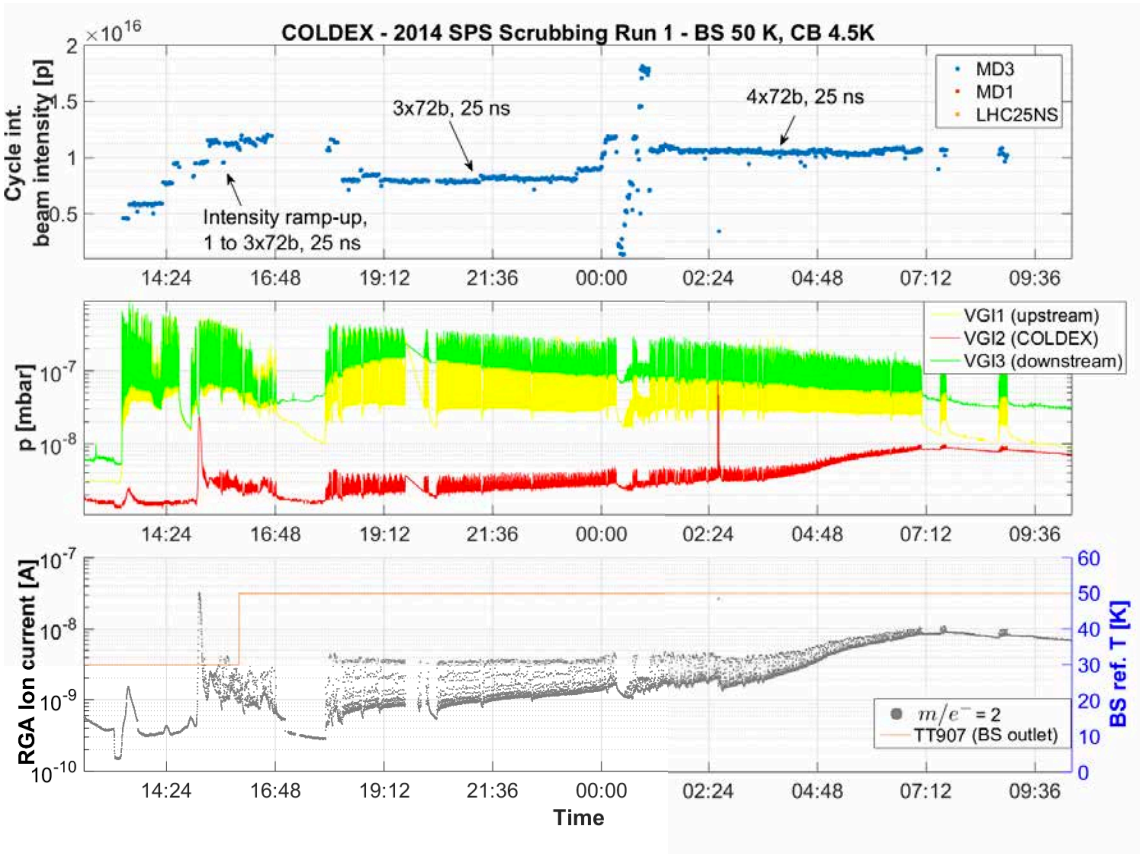

Figure 11.3: COLDEX Run 1: zoom at the first 20 hours, while the BS was held at 50 K.

The run kept on for two days (from 05/11 to 06/11) with limited beam circulating intensity and availability, due to impedance heating of the SPS injection kicker MKP, which had to be controlled. In periods without beam, the pressure inside COLDEX was observed lowering, thanks to the external pumping offered by the ion pumps installed in the sectors adjacent to COLDEX.

On 07/11, at midday, the BS was cooled down from 50 K to 5 K (see zoom in Fig. 11.4). A net pressure decrease was observed in the BS ($\sim 4 \cdot 10^{-9}$ mbar) and partially at the extremities ($\sim 2 \cdot 10^{-9}$ mbar). At 5-10 K, the BS was capable of physisorbing the residual H_2 (see Sect. 9.5) and fully cryocondense N_2 and CO with a negligible saturated vapour pressure. Throughout the run, during beam circulation, no pressure rise was observed at 5-10 K in the COLDEX BS in stable beam conditions (spikes were detected during beam losses: those are often artefacts produced

by charge deposition on the cables), nor vacuum degradation imputable to electron stimulated desorption. Pressure rises up to $\sim 2 \cdot 10^{-8}$ mbar were instead measured at the extremities. In this period, beam acceleration was tested to the flat-top momentum of 450 GeV/c (cycle tag: LHC25NS). Beam circulation in storage mode is limited at this energy in the SPS, due to the high current required by the mains and the poor beam lifetime.

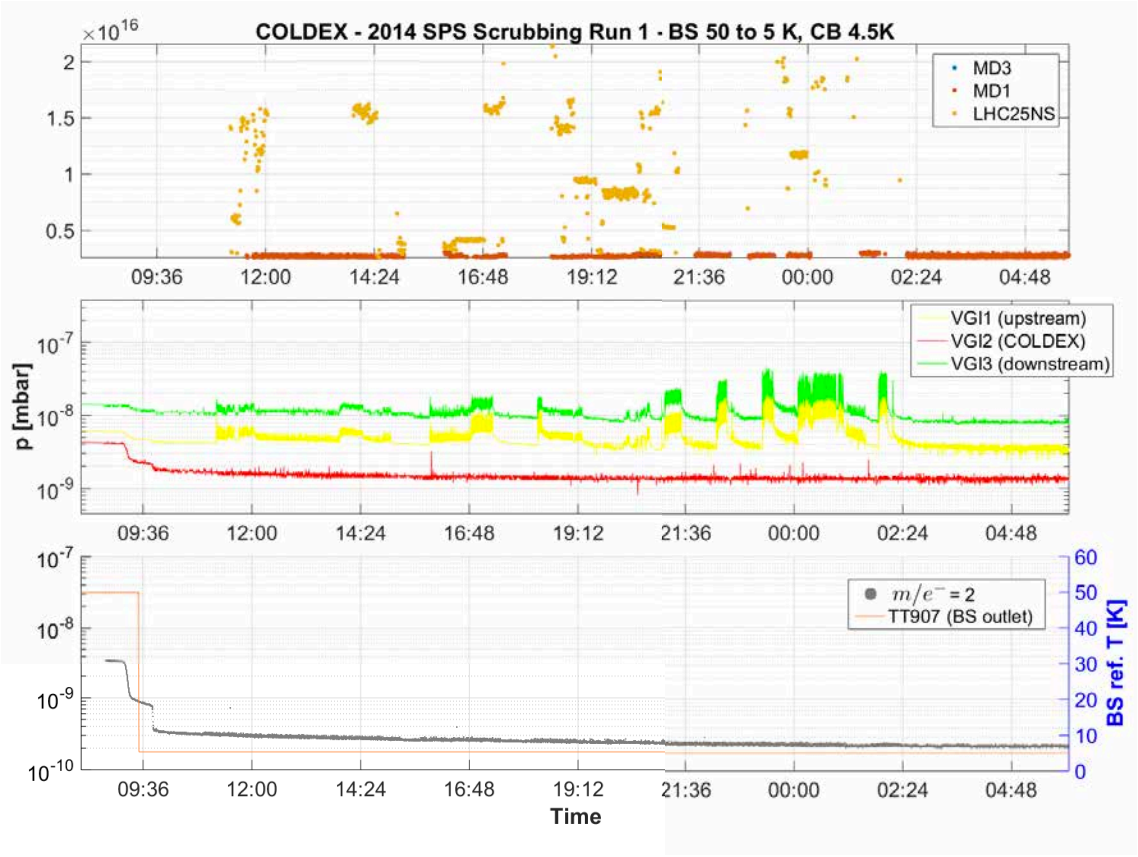

Figure 11.4: COLDEX Run 1: zoom at the first 20 hours after cool-down of the BS to 5 K.

Extensive use of doublet 5+20 ns beams was deployed in the machine for further scrubbing (MD1, then MD3 cycle tags). No dynamic pressure rise was observed in COLDEX in these beam periods, at 10 K. With respect to comparable 25 ns bunch and circulating beam intensities, no increase in the electron stimulated desorption rate was observable in the RT COLDEX sections. This behaviour is consistent with what was observed in the other SPS field-free regions.

Due to cryogenics control loops being under commissioning, no measurement of the dynamic dissipated heat load was possible on the a-C coated BS, being a static heat load never clearly been established. The electron activity has been instead followed with the chimney electrode, with a lower detection limit of $6.5 \cdot 10^{-9}$ A, corresponding to the noise level induced by the measuring sourcemeter. The electron flux detection limit was therefore of $2.8 \cdot 10^{8}$ $e^{-}/(mm^2 s)$. Different bias voltages have been applied, spanning from -1 kV to +1 kV. Throughout the experimental run, no signal correlated to electron cloud activity was detected. Peaks of $\sim 2 \cdot 10^{-8}$ A signal were instead observed during periods of high beam losses (unstable or longitudinally debunched beam). Those signals (measured at 10 Hz) were correlated to the increase of electric noise on the vacuum ionization gauges (VGI) (1 Hz) and partially correlated to the closer SPS Beam Loss Monitor signal available (almost 30 m downstream), which is stored every 15 seconds, e.g. in Fig. 11.5.

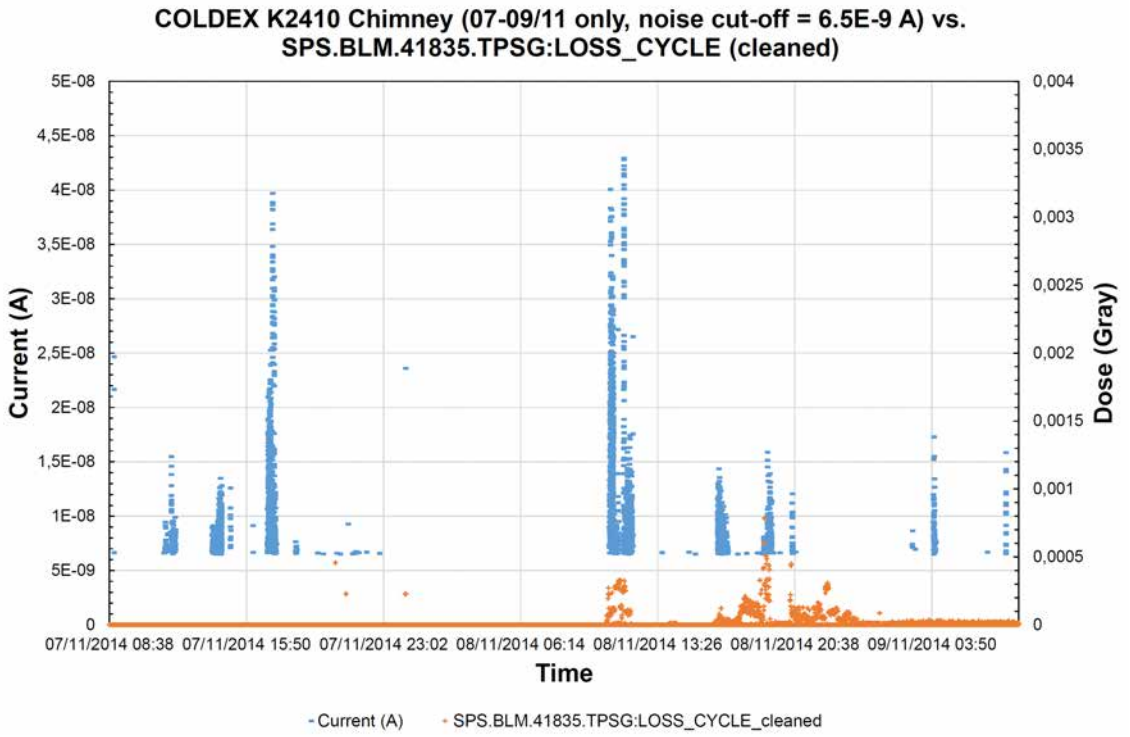

Figure 11.5: COLDEX Run 1: zoom at the electron activity measured by the chimney electrode with a bias voltage of +1 kV and the SPS BLM 41835 located at the MSE41835 over a period of 48 hours. The electrode signal is cut-off below the noise level of $6.5 \cdot 10^{-9}$ A.

11.3 Results during Run 2

The second COLDEX experimental run with a-C coating took place during the second SPS Scrubbing Run in December 2014. In a 4 days period, the accumulated beam intensity was up to 1.7 Ah. In this run the BS temperature was permanently kept at 10 K, while the CB was initially at 4.5 K, and afterwards, at 3 K. One to five batches of 72 bunches, 25 ns bunch spaced, were circulated into COLDEX, with a top bunch intensity of $1.9{\cdot}10^{11}$ ppb, mainly at 26 GeV/c (cycle tag: MD3), but also ramped to 450 GeV/c (LHC25NS). Hybrid (5+20 ns) bunch spaced doublet beams were circulated (LHCMD4), and, in addition, different intermediate injection schemes (8b+4e, BCMS) were adopted at the end of the run (on 10/12, LHC25NS). Figure 11.6 shows the beam intensity integrated per cycle (top), the pressure evolution during the run along the COLDEX sector and CB reference temperature (center) as well as the RGA1 ion current relative to H_2 specie and the BS temperature (bottom).

The vacuum observations of the second part of the Run 1 were confirmed. Significant pressure rises were observed at COLDEX extremities with highly intense beams ($\sim 2 \cdot 10^{-7}$ mbar with up to 4 batches, $4.6{\cdot}10^{13}$ p, $1.6{\cdot}10^{11}$ ppb, dump at 17 s), while a steady pressure trend ($\sim 1 \cdot 10^{-9}$ mbar) was measured in the COLDEX BS held at 10 K. No stimulated desorption correlated to electron cloud was observed. The CB cool-down to 3K had no effect on the BS pressure trend.

The doublet beams, spaced 5+20 ns, had an equivalent behaviour to standard 25 ns beams, of comparable intensity, as a confirmation to Run 1 observations.

During the initial intensity ramp-up, signs of a dynamic heat load, dissipated on the BS, were recorded during beam circulation. Although the definition of a stable static heat load was difficult and carried *a priori* on a period of 30 minutes before the first beam circulation, the evolution of the measured total heat load during the beam presence and ramp-up, as shown in Fig. 11.7 on the left, showed the presence of a dynamic heat load, linked to the beam presence. In order to optimize the scrubbing effect while preserving the machine availability, the intensity ramp-up was carried increasing the number of batches from 2 to 4, while reducing the bunch intensity. The observed

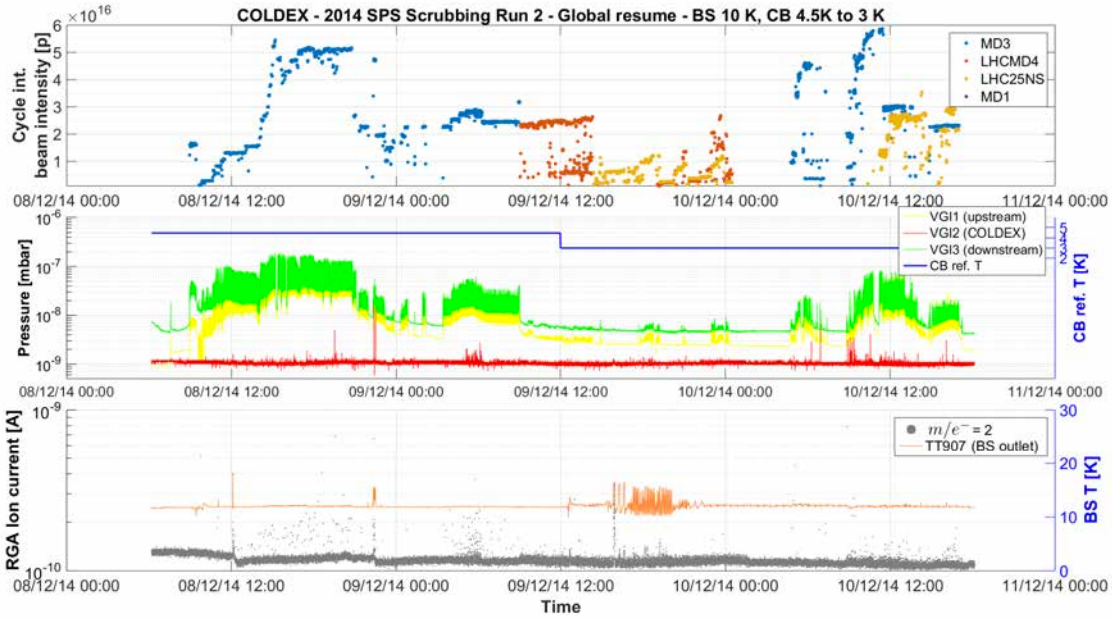

Figure 11.6: COLDEX Run 2 during the SPS Scrubbing Run 2 of 2014. Top: cycle integrated beam intensity; center: vacuum pressure along the sector 431 and CB reference temperature; bottom: RGA ion current relative to H_2 and reference BS temperature.

dynamic heat load, shown in Fig. 11.7 and plotted in Fig. 11.8, was less than 0.3±0.1 W/m for 4x72 bunches of $1.9{\cdot}10^{11}$ ppb at 26 GeV/c.

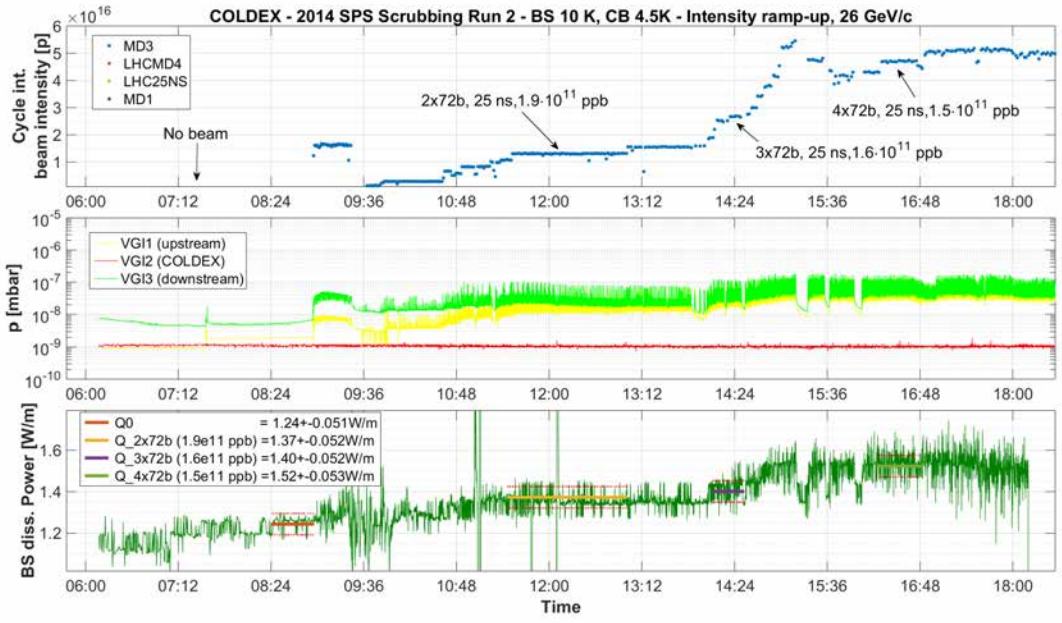

Figure 11.7: COLDEX Run 2: total dissipated heat load measured on the BS during the initial intensity ramp-up.

The electron activity, followed with the chimney electrode, had a lower detection limit of $1.7{\cdot}10^{8}$ $e^{-}/(mm^2 s)$, corresponding to the noise level of $4{\cdot}10^{-9}$ A with a bias voltage of +1 kV. Throughout the experimental run, no signal correlated to electron cloud activity was detected. Peaks of $\sim 1.5 \cdot 10^{-8}$ A signal was instead observed during periods of high beam losses, specifically when the

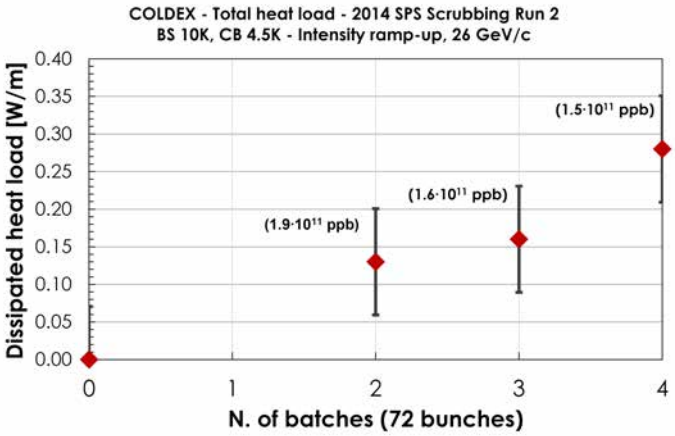

Figure 11.8: COLDEX Run 2: measured dynamic heat load as a function of the number of circulating batches, for different bunch intensities.

mismatched bunch length, caused by failure of PS 40 MHz RF cavities, produced longitudinal blow-up of the bunches transferred to the SPS.

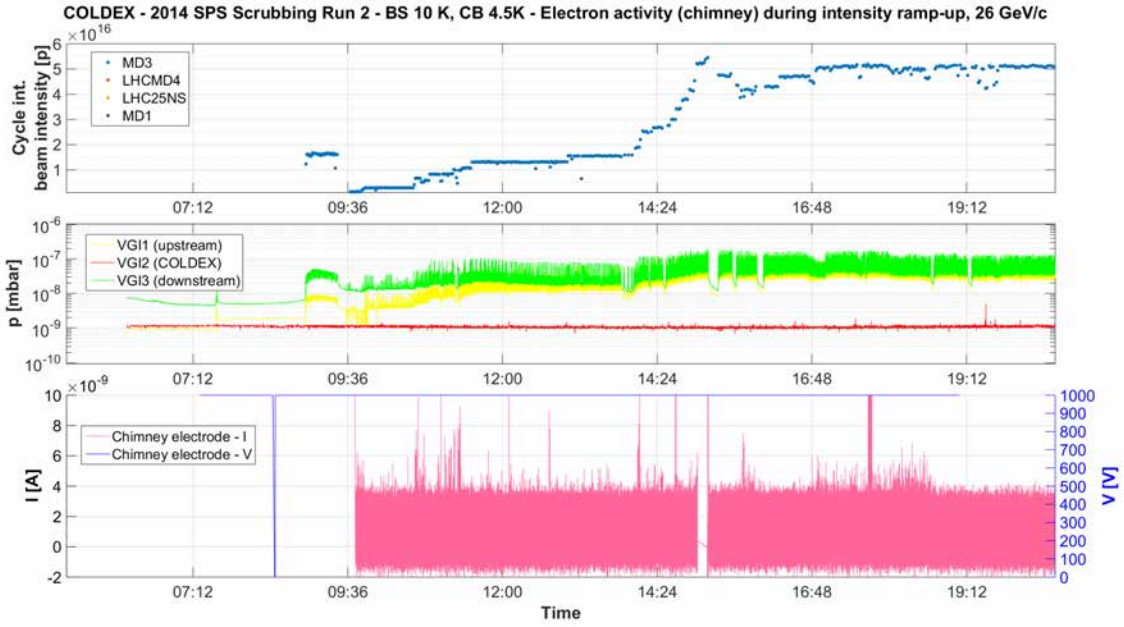

Figure 11.9: COLDEX Run 2: electron activity during the initial intensity ramp-up, in the time frame similar to Fig. 11.7, left.

11.4 Results during Run 3

The COLDEX Run 3 was the first experimental beam run of 2015, which took place in June in a 3.5 days period. The accumulated beam dose exceeded 2.5 Ah. Two BS temperatures have been chosen: first ∼10 K, then ∼60 K, while the CB was kept at ∼4.5 K and ∼3K, respectively. Figure 11.10 shows the beam intensity integrated per cycle (top), the pressure evolution during the run along the COLDEX sector (center) as well as the BS inlet and outlet temperatures and He gas flow (bottom), which allowed to estimate the dissipated heat load in specific cases discussed later.

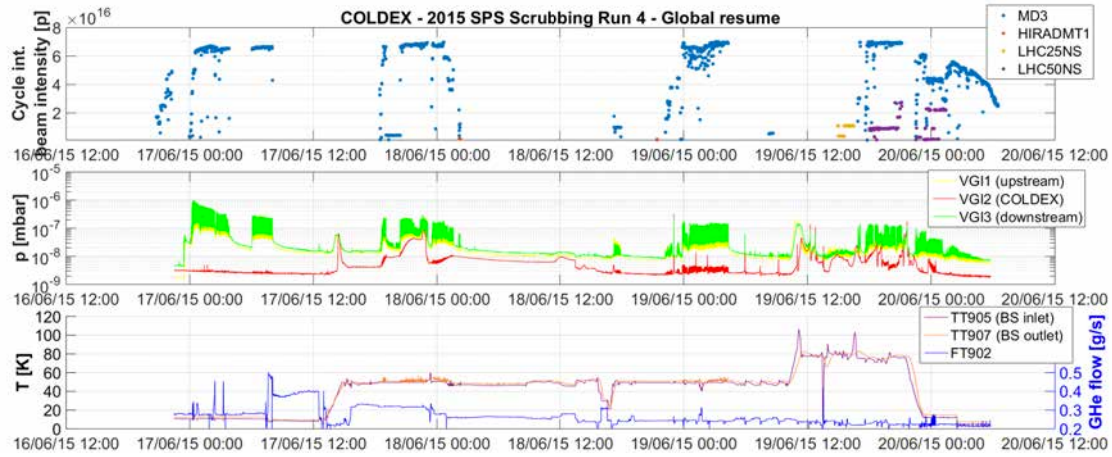

Figure 11.10: COLDEX Run 3 during the SPS Scrubbing Run 4 of 2015. Top: cycle integrated beam intensity; center: vacuum pressure along the sector 431; bottom: BS inlet, outlet temperatures and He gas flow.

One to four batches of 72 bunches, 25 ns spaced, up to $2.0{\cdot}10^{11}$ ppb, circulated into COLDEX, principally at 26 GeV/c. At 10 K (see Fig. 11.11), pressure rises up to $\sim 1 \cdot 10^{-6}$ mbar, correlated to the beam circulation, were observed upstream and downstream of COLDEX due to electron stimulated desorption in RT parts (principally: H_2 and CO gas species), while a steady pressure trend ($\sim 3 \cdot 10^{-9}$ mbar) was observed at the BS centre. A global re-conditioning of the RT surfaces was visible thanks to beam scrubbing, reducing the dynamic pressure rise by a factor 3 in 0.7 Ah.

During beam off (at 12:00, Fig. 11.12), the sector valves were closed and the BS temperature raised to 60 K, inducing desorption of the accumulated gas, which was principally H_2. The flushing of about $2.3 \cdot 10^{-3}$ mbarl of H_2 covered the CB surface, held at 4.2 K, with a tenth of monolayer.

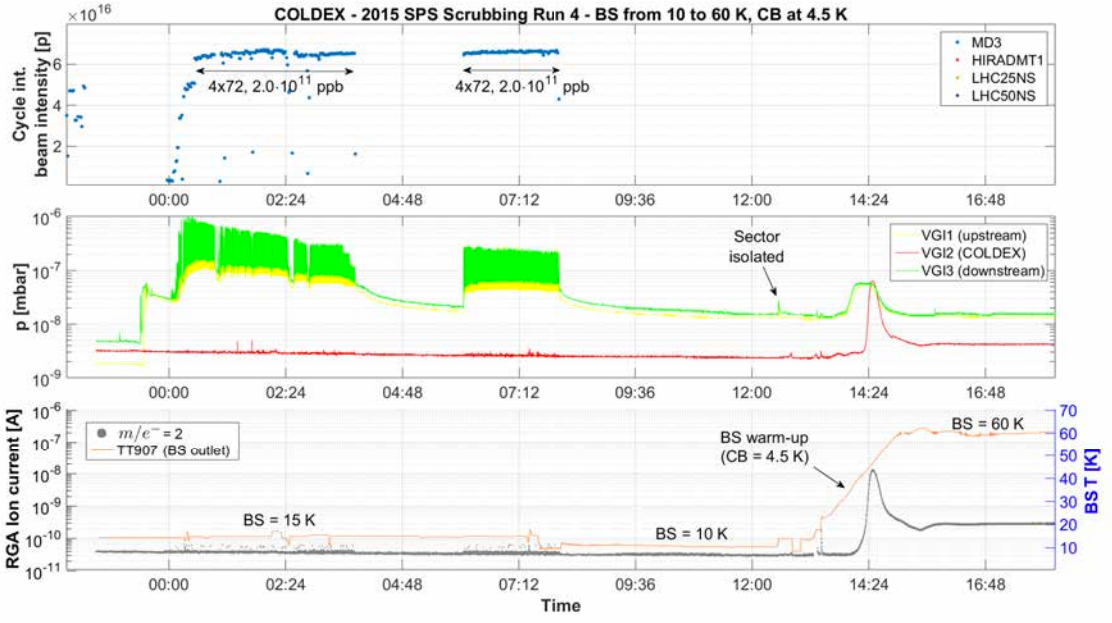

Figure 11.11: COLDEX Run 3: zoom at the first 10 hours, when the BS was held at 10-15K.

Beam was resumed in these conditions (see Fig. 11.12), and transmission of the desorbed H_2 from the RT parts toward the BS was observed building-up in a dynamic slow pressure rise up to $\sim 6.5 \cdot 10^{-6}$ mbar (in H_2 equivalent, at RT), similarly to what observed in Run 1 (Sect. 11.2). At 60 K, the BS was capable to physisorb only a very limited quantity of H_2 (as discussed in Sect.

9.5) and the only source of pumping was the CB held at 4.2 K. At the end of the transient, the CB was covered with about 8 tenth of a monolayer and, as such, dominated by its vapour pressure ($\sim 7.7 \cdot 10^{-9}$ mbar at 4.2 K). A rapid variation of the CB LHe bath pressure from 950 mbar to 700 mbar lowered the CB temperature to 3.8 K, thereby significantly reduced its H_2 vapour pressure (see Fig. 11.13), and re-established a Δp of two orders of magnitude between RT parts and the BS centre. The background pressure inside COLDEX lowered to $\sim 6 \cdot 10^{-9}$ mbar (RT) and transmission peaks of ratio ~25 were again visible during beam induced desorption of the RT parts.

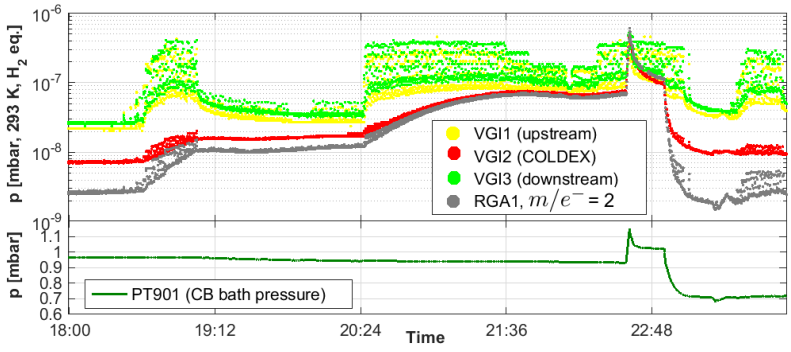

Figure 11.12: COLDEX Run 3: zoom after the BS warm-up to 60K, showing the monolayer build-up the CB caused by transmission of the gas desorbed at the RT extremities due to electron cloud.

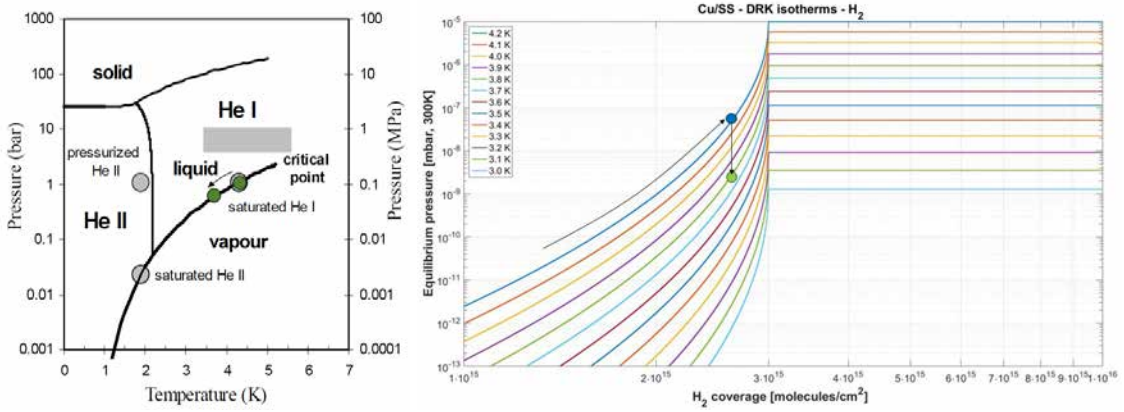

Figure 11.13: Effect of the monolayer build-up and temperature reduction in the CB observed in Run 3. Left: phase diagram of He; the described thermodynamic transformation is shown on the transition curve of the saturated He I. Right: adsorption isotherms of H_2 on Cu/stainless steel, DRK (Dubinin-Radusckevisch-Kanager) model [185]; the monolayer build-up at 4.2 K and reduction of equilibrium pressure arising from a CB temperature reduction to 3.8 K are sketched.

The run continued with the CB at 3 K. At this temperature, a negligible saturated vapour pressure due to H_2 is obtained. The solenoids installed at the RT extremities (as described in Sect. 9.2) were employed to mitigate the electron multipacting in these regions. In Fig. 11.13, the reduction in the gas transmission of a factor about 2 was observed with the application of a solenoidal magnetic field (2 mT). The mitigation of multipacting in these regions reduces the local impinging electron flux, so the electron desorbed gas load coming from the RT transitions. This observation became a clear indication that pressure rises measured in COLDEX with a BS at >50 K are due to gas load coming from the extremities. Although a CB at 3 K ensures no pressure build-up thanks to its adsorption capacity, only a limited pumping speed is provided by the 1% transparency of the BS: this reduces its effective pumping speed to approximatively 200 l/s for H_2. As such, the incoming gas load induced by electron cloud in the RT extremities is visible also in COLDEX if the only source of pumping is the CB.

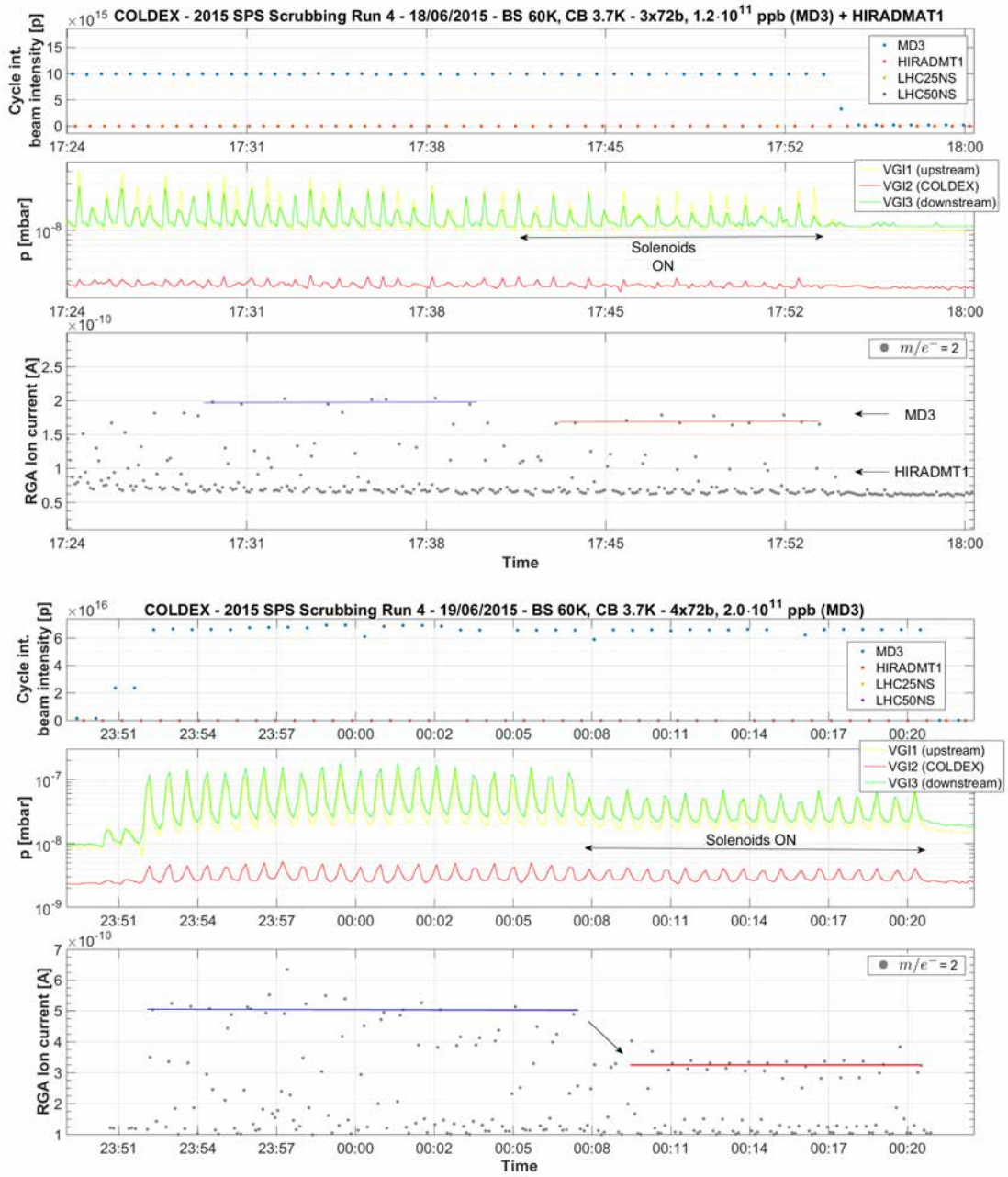

Figure 11.14: COLDEX Run 3: impact of the installed solenoids at the RT extremities. Top: 3x72 bunches, $1.2{\cdot}10^{11}$ ppb. Bottom: 4x72 bunches, $2.0{\cdot}10^{11}$ ppb.

Throughout the whole run, due to unstable cryogenic conditions - especially with the CB at 3 K - caused by poor insulation vacuum, observations of dynamic heat load were limited to beam/no beam transients. No dynamic heat load was observed - above the measurement detection sensitivity (∼100 mW/m) - during beam circulation with respect to the static heat load. As shown in Fig. 11.15, the circulation of 4x72 bunches of $1.7{\cdot}10^{11}$ ppb do not correspond to an increase of measured dissipated heat load on the BS, i.e. no dynamic heat load is identified within the detection limits.

At the same time, the electron activity, monitored by the chimney electrode with a noise level corresponding to a flux of $2.1 \cdot 10^8$ e$^-$/(mm^{2}s), did not show signals correlated to electron cloud. Small signs of electron current, potentially arising from gas ionization, were instead recorded during periods of high pressure, as the Fig. 11.16 shows. The ion-electron current caused by residual gas

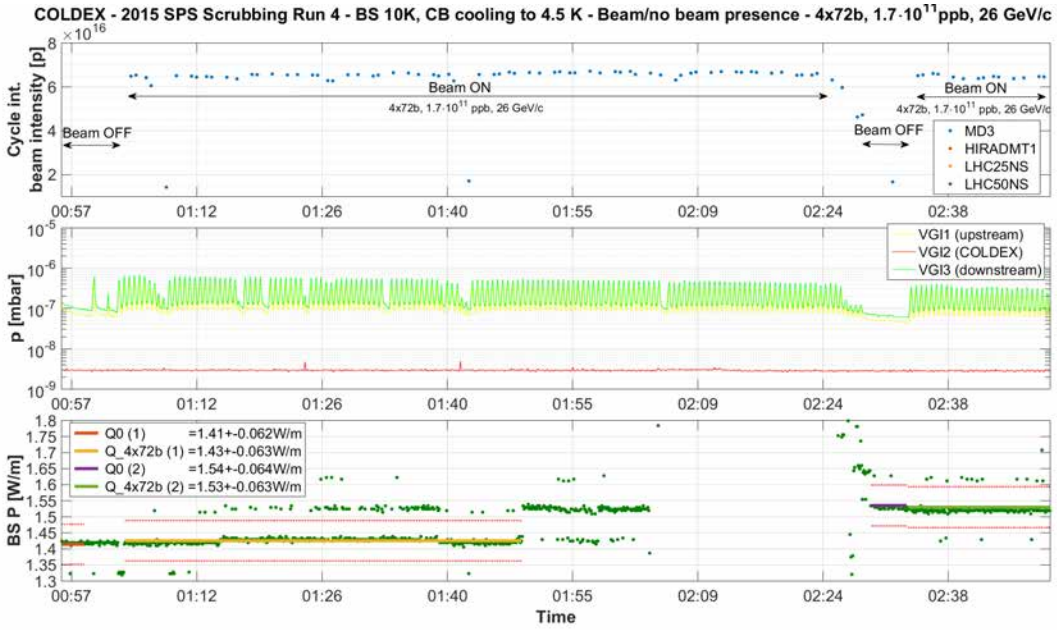

Figure 11.15: COLDEX Run 3: observation of the dissipated dynamic heat load in beam/no beam transients.

primary ionization per unit length is

$$I_p = \sigma_i(H_2, p) n_{\text{gas}} I_{\text{beam}} \tag{11.1}$$

being $\sigma_i(H_2, p) = 0.22$ Mbarn for 26 GeV protons (see Table 7.1) and $I_{\text{beam}} \approx 0.4$ A for 4x72 bunches of $2.0{\cdot}10^{11}$ ppb circulating in SPS. The highest residual gas density, to which corresponded the highest ionization current, was the one due to H_2 peaked during the CB bath pressure cycling, at 22:37 equal to (see also Fig. 11.12):

$$n_{H_2}(60\text{ K}) = \frac{p_{H_2} 60\text{ K}}{k_B T} = 3.28 \cdot 10^{16} \text{m}^{-3} \tag{11.2}$$

The electron-ion current produced by primary beam ionization (we here neglect the effect of any other secondary ionization) was at that moment and per unit length:

$$I_p = 2.88 \cdot 10^{-7} \text{A/m} \tag{11.3}$$

In absence of magnetic field, the ionized species are spread over the entire BS circumference. The presence of the chimney aperture with a biased electrode can be estimated, in first approximation, by a geometrical collection efficiency accounting a factor $2arcsin(0.035/0.067)/(2\pi) = 0.175$ over the BS circumference. The expected electron current (the positive current or the effect of secondary emitted electron being neglected thanks to the positive bias voltage applied to the electrode, which was +100 V) was therefore:

$$I_p^{\text{chimney}} \approx 1.76 \cdot 10^{-9} \text{A} \tag{11.4}$$

This result is comparable with the measured $\Delta I_{\text{electrode}} = 3 \cdot 10^{-9}$A (see Fig. 11.16). The supposition of electron current arising from gas ionization is corroborated by the fact that, once the vacuum pressure was lowered to $< 1 \cdot 10^{-8}$, the signal disappeared in the noise.

Clear current signal over noise was measured during periods of high beam losses, as shown in Fig. 11.17. In this time frame, the generator of one of the four RF cavities at 800 MHz tripped due to an electric malfunction; a signal, which was probably due to charges lost on the electrode or the cable, was especially correlated to the injection of the fourth and last batch of 72 bunches.

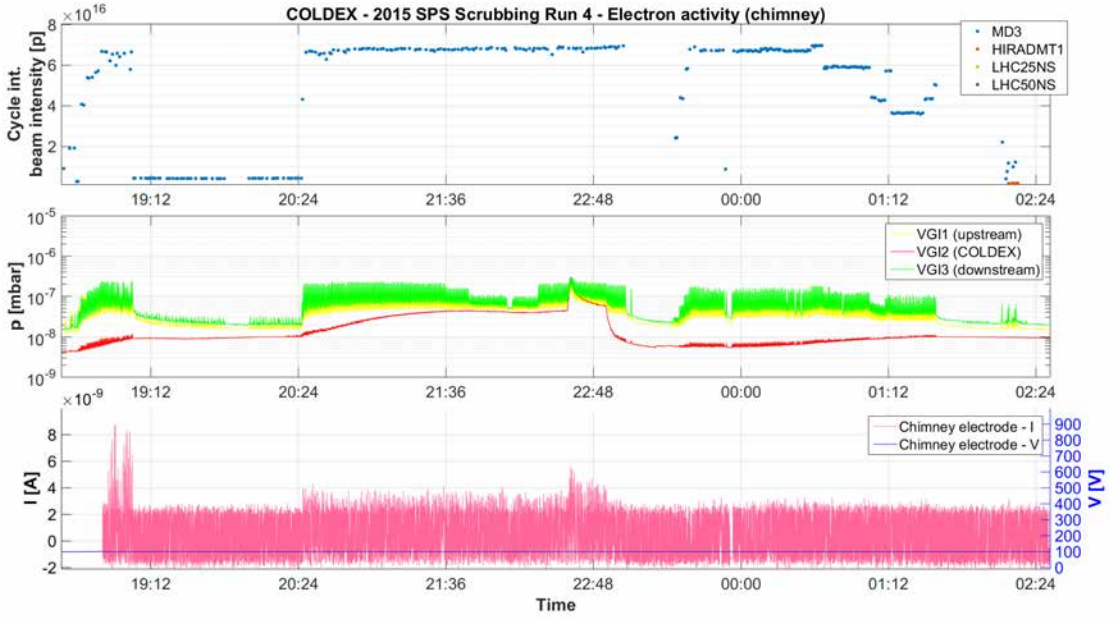

Figure 11.16: COLDEX Run 3: measured electron activity during the pressure build-up due to monolayer accumulation of the CB.

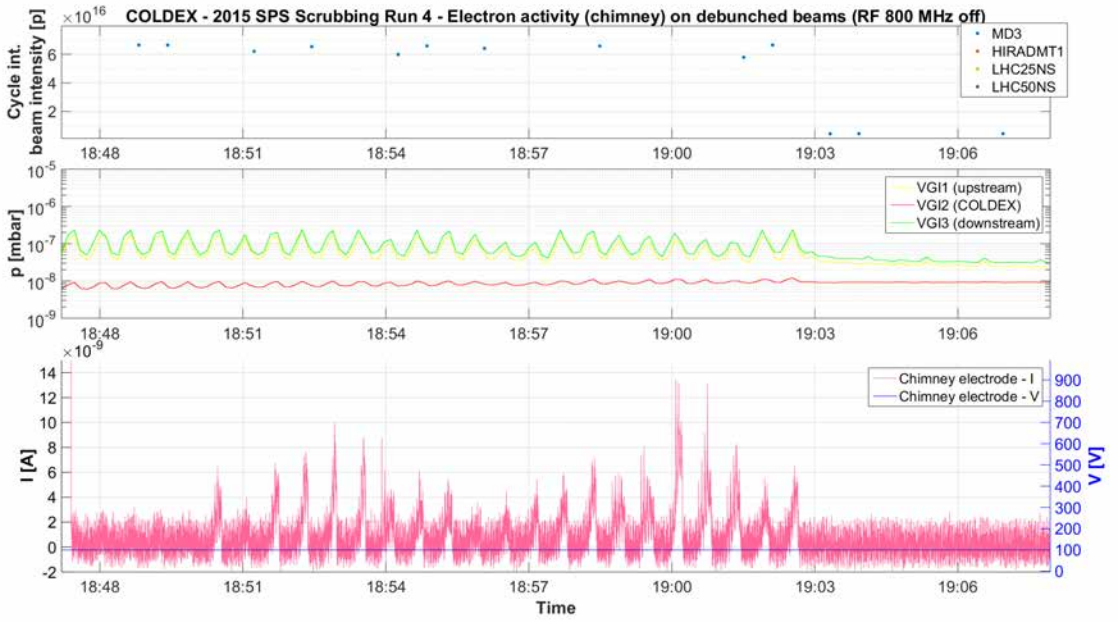

Figure 11.17: COLDEX Run 3: electron current measured by the chimney electrode during a period of pronounced beam losses. The peaks are especially correlated to the injection of the fourth and last batch of 72 bunches.

11.5 Results of dedicated experiments

11.5.1 MD1: H_2 coverage

The first dedicated 24 hours experiment with gas pre-adsorption took place in September 2015 with the BS surface prepared 10 days in advance with a coverage of $\sim 3.2 \cdot 10^{16}$ H_2/cm^2. The BS

temperature was scanned from 14 K, to 21 K and finally 28 K (see Fig. 11.18), while the CB was held at 3 K, i.e. a saturated vapour pressure of $\sim 10 \cdot 10^{-10}$ mbar was ensured.

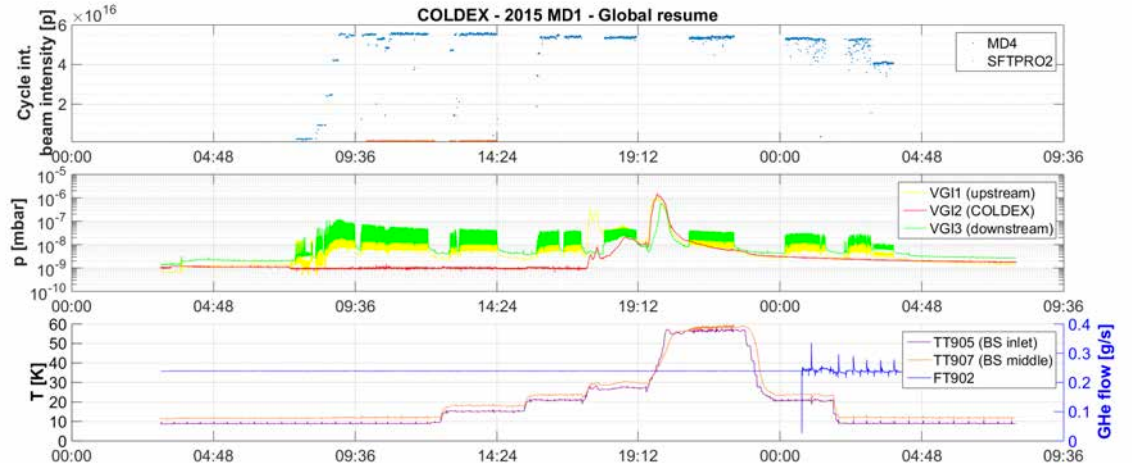

Figure 11.18: COLDEX MD1 with a coverage of $\sim 3.2 \cdot 10^{16}$ H_2/cm^2, 2015. Top: cycle integrated beam intensity; center: vacuum pressure along the sector 431; bottom: BS inlet, outlet temperatures and He gas flow.

No total or partial pressure rise due to stimulated desorption was observed in COLDEX (see Fig. 11.18) in any beam condition with such H_2 coverage. No H_2 recycling and/or flushing to CB was thus observable. Loss of the previously physisorbed H_2 was later thermally induced by heating the BS above 31 K.

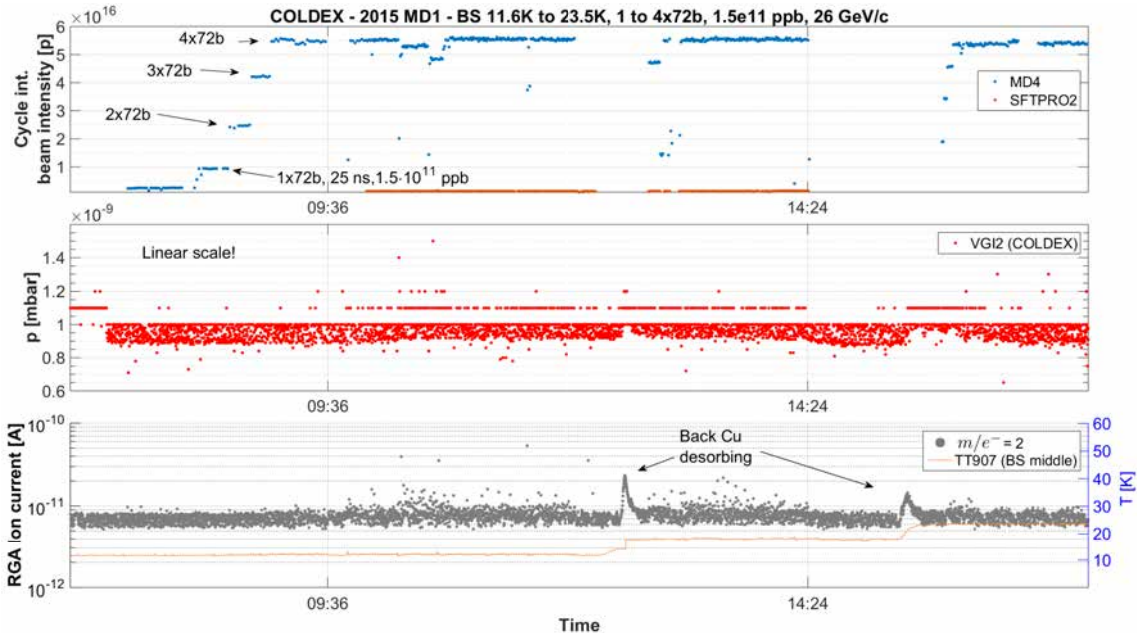

Figure 11.19: COLDEX MD1: evolution of the total and partial H_2 pressure during the intensity ramp-up and BS warm-up.

During the intensity ramp-up from $N_B = 1$ to 4 batches of 72 bunches ($1.5{\cdot}10^{11}$ ppb), at 26 GeV/c, a linear dynamic heat load, associated to the beam circulation, was instead observed. The observed relation was

$$Q[\mathrm{W/m}] \approx 4.87 \cdot 10^{-2} N_B \pm 7.8 \cdot 10^{-2} \tag{11.5}$$

that corresponds to $\sim 0.2 \pm 0.08$ W/m for four batches.

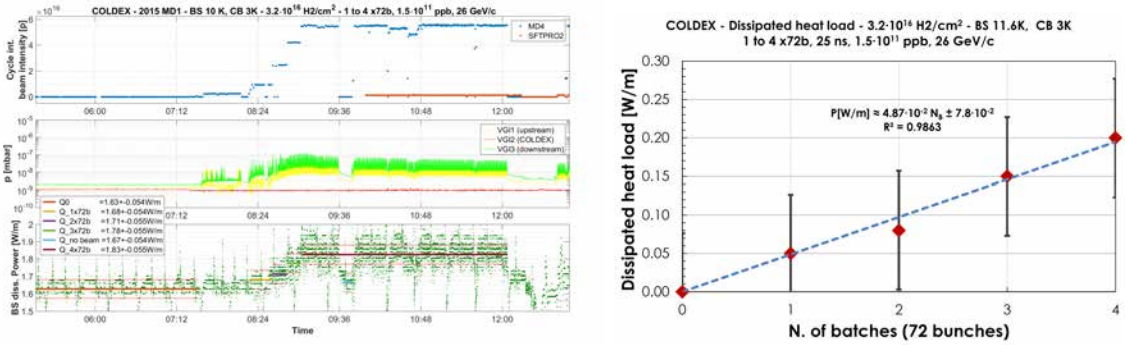

Figure 11.20: COLDEX MD1: dissipated heat load measured during the intensity ramp-up and final long term circulation of 4x72 bunches of $1.5{\cdot}10^{11}$ ppb.

At the same time, the electron activity was monitored and no electron flux was observed above a detection limit of $8.7 \cdot 10^7$ e$^-$/(mm^{2}s) during the intensity ramp-up (see Fig. 11.21). Considering a mean electron impinging energy of e.g. $\langle E_e \rangle = 100$ eV, the heat load observations seem inconsistent with electron cloud. The calculated (by Eq. 9.2) heat load for an electron flux at least equal to the detection limit is

$$Q_{electrode}[\mathrm{W/m}] = 8.7 \cdot 10^{13} \frac{\mathrm{e^-}}{\mathrm{m^2 s}} \cdot 1.6 \cdot 10^{-17} \frac{\mathrm{J}}{\mathrm{e^-}} \cdot \pi \cdot 0.067\mathrm{m} \approx 2.9 \cdot 10^{-4} \mathrm{W/m} \tag{11.6}$$

and do not correspond to the measured one by three orders of magnitude. An electron current was instead measured during periods of pronounced beam losses. Fig. 11.22 shows an example of electron current measured during mis-injection of the fourth and last batch.

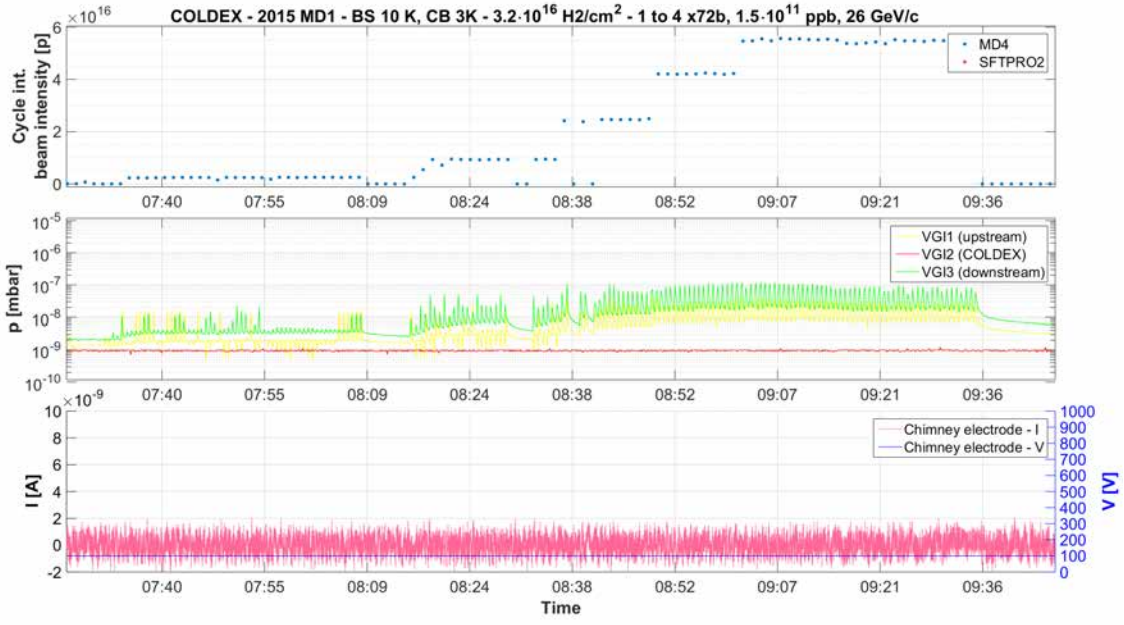

Figure 11.21: COLDEX MD1: electron activity measured by the chimney electrode during the initial intensity ramp-up.

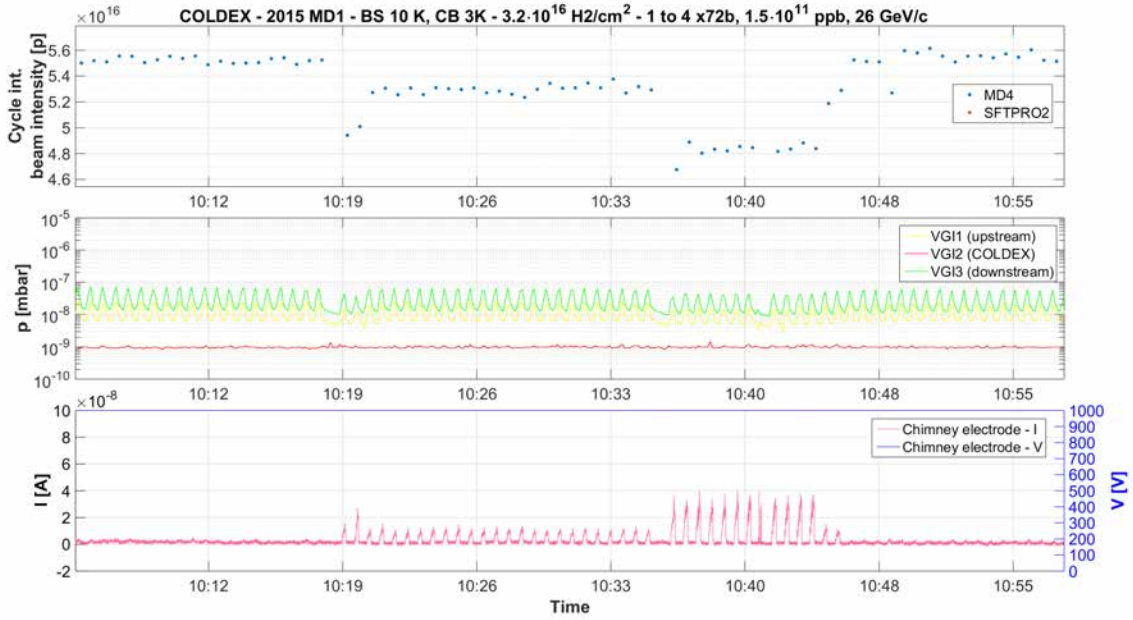

Figure 11.22: COLDEX MD1: electron current measured by the chimney electrode during a period of pronounced beam losses.

11.5.2 MD2: CO coverage

A second dedicated 24 hours experimental run was performed in November 2015 with a BS surface prepared 14 days in advance with a coverage of $\sim 2.1 \cdot 10^{16}$ CO/cm^2.

The run was negatively influenced by two separate elements. Longitudinally uncaptured beam, accounting to ∼1% on the 200 MHz component measured by the SPS Mountain Range and shown in Fig. 11.23, was caused during PS to SPS bucket transfer, especially of the first batch. The uncaptured beam produced non negligible losses all around the ring and beam induced electronic noise on the COLDEX instrumentation. Unstable cryogenic conditions (Fig. 11.24), caused by poor insulation vacuum of the COLDEX cryostat - lately ascribed to multiple vacuum leaks - impacted the stability of the CB LHe bath, which in turn caused instability of the GHe flow cooling the BS. Due to these influences, a static dissipate heat load was never established on the BS, so no dynamic heat load was measurable.

Figure 11.23: COLDEX MD2: 1% of the beam is uncaptured at the first batch injection and leads/lags in the longitudinal phase space, as measured by the SPS Mountain Range 200 MHz RF pick-up.

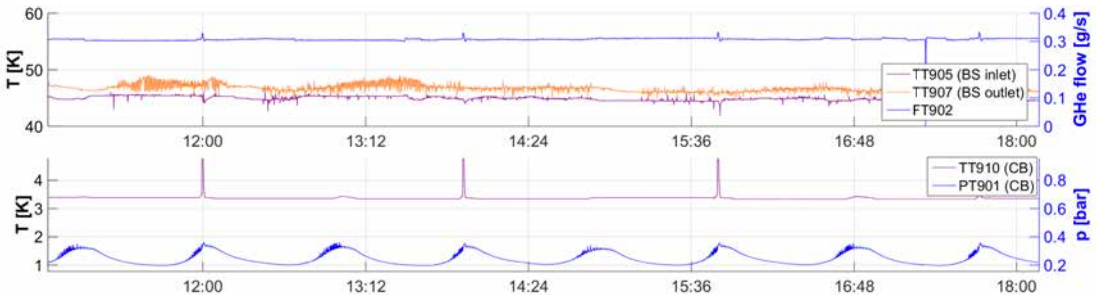

Figure 11.24: COLDEX MD2: Cold Bore bath pressure and temperature instability.

At the beginning of the run, the BS temperature was held at 56 K, while the CB was permanently at 3.4 K. In this conditions (see Fig. 11.25), transmission of H_2 was observed from the RT parts toward the BS centre with pressure rise ratio of 10, with 4x72 bunches of $1.4{\cdot}10^{11}$ ppb, coherently with what expected. No partial pressure rise linked to electron stimulated desorption of CO was observed, nor CO recycling and/or flushing in any beam condition.

The BS temperature was then lowered, by steps, to 12 K with beam off. Beam was resumed (see Fig. 11.25, at 20:00), and slightly lower pressure rises were still detected at the BS centre, with a transmission ratio now increased to 16. Analysing the partial pressures for all gases, no specie was prevalently transmitted, instead, the RGA ion current was suffering of beam induced background distortion. An indication of the background current produced by the Secondary Electron Multiplier (SEM) of the RGA is in fact available on the channel $m/e^- = 5$. Applying a 2 mT solenoid field over the RT extremities did not decrease the pressure rise in COLDEX, hence decrease a potential gas transmission. Reduction of the bunch intensity to $0.8{\cdot}10^{11}$ ppb was expected to have a great impact on the electron cloud build-up, as so was observed at the RT extremities, where lower pressure rises were measured, roughly of a factor 3. The bunch intensity reduction had little/no effect on the pressure rises detected in COLDEX instead. Based on these clues and considered the detected high beam losses, a preliminary conclusion is the instrumentation was influenced by beam induced electronic noise.

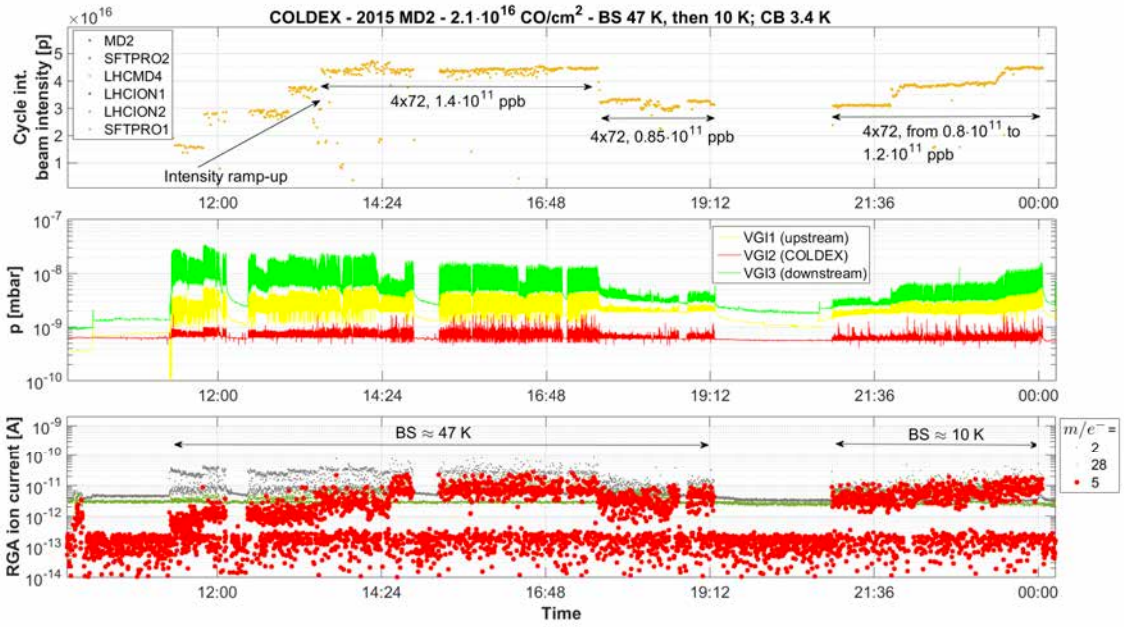

Figure 11.25: COLDEX MD2 with a coverage of $\sim 2.1{\cdot}10^{16}$ CO/cm^2, 2015. By 19:12, the BS temperature was lowered to 12K. Top: cycle integrated beam intensity; center: vacuum pressure along the sector 431; bottom: RGA1 (COLDEX) ion currents representative of the H_2 ($m/e^- = 2$) and CO/N_2 ($m/e^- = 28$) gas species, with respect to the baseline background current, detected on the channel $m/e^- = 5$.

The electron activity was surveyed throughout the whole run with a bias voltage of +100 V. No electron flux was observed above a detection limit of $8.7 \cdot 10^7$ $e^-/(mm^2 s)$ with all beam conditions (see Fig. 11.20)

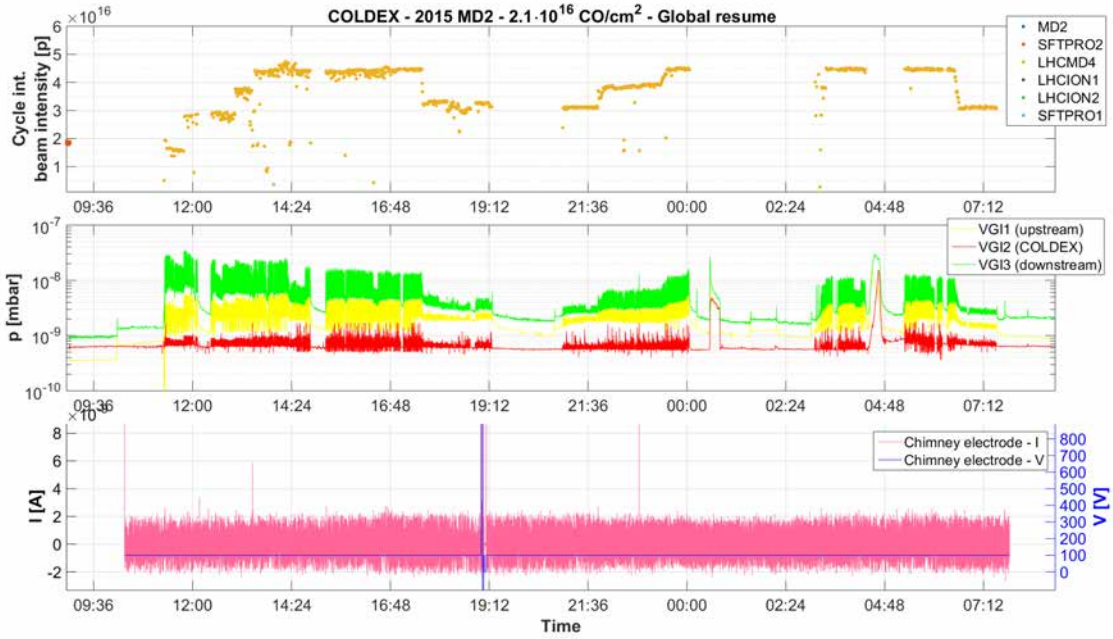

Figure 11.26: COLDEX MD2: electron activity measured by the chimney electrode during the whole run.

11.6 Discussion

The COLDEX experiment, re-commissioned in 2014, is further validating the HL-LHC electron cloud mitigation baseline in the Super Proton Synchrotron (SPS) in presence of LHC type beams, with the purpose of validating the performance of adopting a-C coatings at cryogenic temperature in a real machine environment. Typical measurements during beam runtime of 2014-2015 were the dynamic pressure rise, gas composition, dissipated heat load and electron activity observed as a function of the beam parameters and the cold bore and beam screen surface conditions (temperature and gas coverage).

Fig. 11.27 shows a resume of the integrated beam intensity, or beam doses, accumulated during the 2014-2015 beam runtime. The first two long beam runs in 2014 took place during the SPS Scrubbing Runs after the CERN Long Shutdown 1 and allowed to accumulated more than 5 Ah. The total beam intensity quickly reached 4x72 bunches, with a top bunch intensity of $1.9 \cdot 10^{11}$ ppb during the Run 2. Three additional runs were carried in 2015, pushing the total accumulated beam time to 9.88 Ah. The first was the fourth SPS Scrubbing Run of 2015, when the record $2.0 \cdot 10^{11}$ ppb bunch intensity was deployed, principally to study the configuration of the SPS as injector for HL-LHC (LIU project). The other two runs were dedicated for COLDEX and included pre-adsorption of a gas specie, H_2 and CO respectively. During periods without beam, the setup was instead used to study the cryogenic vacuum characteristics of a-C coating in the 5 to 150 K temperature range, briefly described in Sect. 9.5 and often recalled in this Chapter.

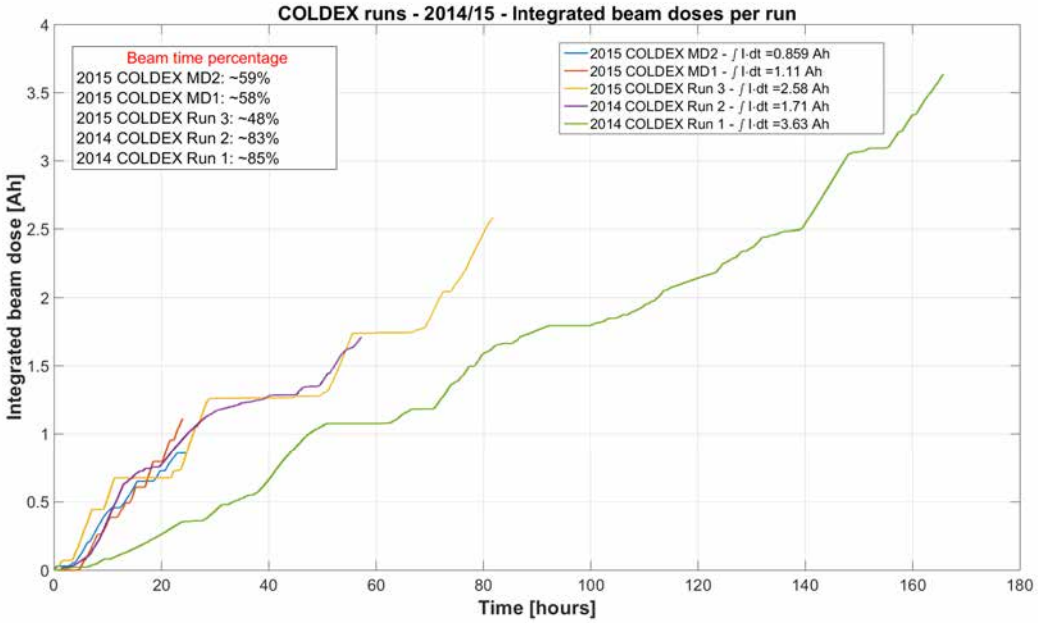

Figure 11.27: Cumulated beam intensity per COLDEX run. The total beam dose is ∼9.89 Ah and is equivalent to 9 hours of HL-LHC nominal beam operation.

Within the beam time accumulated, the vacuum observations on a-C coating at 50 K and 5-10 K with LHC type beams and doublet hybrid spacing (5+20 ns) beams did not reveal effects of vacuum degradation imputable to electron cloud. Throughout the runs, significant pressure rises (up to $1 \cdot 10^{-6}$ mbar) were observed outside the cold system due to electron stimulated desorption. Beam conditioning, or scrubbing, was rapidly observed in Run 1 (the first run after the 1.5 years SPS machine shutdown and COLDEX experiment re-commissioning, when the surfaces SEY was practically reset) lowering the pressure increase of a factor 5 in just 0.3 Ah. After a venting to air at the beginning of 2015, a quick re-conditioning was visible in Run 3. No electron cloud complete mitigation was achieved in the room temperature extremities, neither outside the allocated beam time, which is in line with what is observed in the whole SPS machine with LHC type beams.

In COLDEX, dynamic pressure rises convoluting in a slow residual gas background pressure increase were observed mainly due to H_2 gas accumulation, with a BS at 50-60 K and the CB held above 4 K. The peak of the dynamic slow pressure build-up was reached when an equilibrium between the CB vapour pressure - linked to its molecular coverage (fraction of monolayer) and temperature - and the external pumping speed was reached. No cleaning effect or recycling was observed further. The slow dynamic pressure build-up could be fully ascribed to accumulation on the CB of the gas (principally H_2) transmitted by the RT extremities: a reduction of the CB vapour pressure, by lowering its temperature, re-established the initial Δp.

With a CB held at 3 K, negligible saturated vapour pressure for all gas (with except of He) was ensured. The CB providing a virtually infinite pumping capacity, no dynamic slow pressure build-up was observed due to gas accumulation at this temperature. However, dynamic pressure rises linked to gas transmission were still visible at COLDEX centre during beam circulation and electron bombardment at RT extremities, due to the finite CB pumping speed, which is limited by the BS transparency (1%). The adoption of electron cloud suppression measures at the RT extremities could prove that the pressure rises observed in COLDEX with a BS$>$ 50 K are due to gas transmission. A reduction in the gas transmission of a factor about 2 was observed with the application of a solenoidal magnetic field (2 mT) over ∼2 m upstream and downstream COLDEX. Although suppression of multipacting in the close vicinities of the COLDEX cryostat provides a reduction of the gas load, the effect of electron stimulated desorption all along the ∼200 m Long Straight Section combined to a large conductance offered by the standard beam pipe (ID 156 mm) could not be overcome.

With the BS at 10 K, no pressure rise was observed during beam circulation in COLDEX. At 10

K, the COLDEX system is fact quasi-closed. The transmitted gas load, in any, is accumulated on the BS a-C surface. After exposure to beam, a warm-up to 60 K allowed to thermally desorb the gas accumulated, providing a second proof of transmission for the dynamic pressure rises observed above 50 K.

Basing on these results, we can deduce the maximum electron stimulated molecular desorption yield corresponding to the observation of pressure and electron flux. For the pressure increase, we assume - as an upper bound - the minimum detectable pressure increase observed at 10 K. With the Bayard-Alpert gauge (VGI2) installed at the centre of COLDEX, the minimum detectable total pressure increase was $1 \cdot 10^{-10}$ mbar when a background pressure in the order of 10^{-9} mbar was established (e.g. in Run 2, Run 3 or Run 4). The electron flux $\dot{\Gamma}$ can be either taken from the electron activity observed on the chimney electrode, or deduced from the heat load measurements considering a mean electron energy. In this analysis, the beam screen is assumed uniformly irradiated by the electrons.

In a cryogenic beam vacuum systems, the desorption of molecules can be divided in two kinds, which depend on the level of energy binding the molecule to the surface. Chemisorbed molecules are strongly bounded and their desorption is described by the primary desorption yield, η. The primary desorption is the source of gas into a vacuum chamber. Physically adsorbed (physisorbed) molecules are weakly bound molecules and their desorption is described by the recycling desorption yield, η'. The recycling yield characterises the ability of a physisorbed molecule on a cold surface to be desorbed (recycled) into the gas phase. The recycling yield is an increasing function of the gas coverage, so, in the absence of a perforated beam screen the pressure increases continuously. In a LHC type cryogenic vacuum system, like COLDEX, an equilibrium pressure value is reached when the flux of recycled gas is balanced by the flux of physisorbed gas onto the beam screen. The level is defined by the flux of gas stimulated by primary desorption over the pumping speed of the slots. Therefore, the primary desorption yield is derived as

$$\eta = \frac{GC\Delta p}{\dot{\Gamma}} \tag{11.7}$$

where G is a constant converting mbar·l to molecules ($2.4 \cdot 10^{19}$ molecules/(mbar·l) at 300 K) and C is the conductance of BS slots (or the CB effective pumping speed).

The result of the application of Eq. 11.7 to the observations of e.g. Run 3, for a minimum detectable pressure increase of $1 \cdot 10^{-10}$ mbar and an electron flux arising from the measurement of $8.7 \cdot 10^{7}$ $e^-/(mm^2 s)$ (chimney detection limit) or 200 mW/m (dynamic heat load measured) is shown in Table 11.1. It returns an upper limit of primary desorption yield η for H_2 detectable for the a-C coated BS held at 10 K in COLDEX.

Table 11.1: Upper limit of primary desorption yield η for H_2 detectable for the a-C coated BS held at 10 K in COLDEX.

Method	$\dot{\Gamma}$ [$e^-/(ms)$]	$\eta_{H_2}^{max}$ [H_2/e^-]
Chimney	$4.42 \cdot 10^{13}$	$1.2 \cdot 10^{-1}$
Cryo	$1.25 \cdot 10^{16}$	$1.8 \cdot 10^{-4}$

The combined effect of primary and recycling desorption and total pumping (offered by the BS either by physisorption on its surface, or via the pumping slots toward the CB) is resumed by the sum of the primary and recycling desorption yield over the sticking coefficient, and is expressed by Eq. 11.8, where S is the ideal pumping speed of the beam screen and σ is the sticking coefficient:

$$\frac{\eta + \eta'}{\sigma} = \frac{GS\Delta p}{\dot{\Gamma}} \tag{11.8}$$

With the parameters described above, for a measured $\sigma \cong 0.5$ (low coverage), the upper limit of the sum of the primary and recycling desorption yield over the sticking coefficient $\frac{\eta+\eta'}{\sigma}$ for H_2 detectable for the a-C coated BS held at 10 K in COLDEX is shown in Table 11.2.

Table 11.2: Upper limit of the sum of the primary and recycling desorption yield over the sticking coefficient $\frac{\eta+\eta'}{\sigma}$ for H_2 detectable for the a-C coated BS held at 10 K in COLDEX.

Method	$\dot{\Gamma}$ [e^-/(ms)]	$\left[\frac{\eta+\eta'}{\sigma}\right]^{max}_{H_2}$ [H_2/e^-]
Chimney	$4.42 \cdot 10^{13}$	6.1
Cryo	$1.25 \cdot 10^{16}$	$8.9 \cdot 10^{-3}$

We observe that, for both the primary desorption yield and the sum of the primary and recycling yield over the sticking coefficient, the detection limit differs of 3 orders of magnitude, which is an artefact of the electron flux considered. It is in fact clear that for an higher electron flux at parity of pressure rise, the yields become lower: this is why the upper limits for each yield, if calculated on the heat load observations, are much lower than those with the chimney electron activity. We consider the upper detection limits offered by the chimney method more reliable and in line with all the combined vacuum, cryogenic and electron observations. For this reason, within the beam time obtained and the described experiment conditions, we consider the real measure of the primary desorption yield and the sum of the primary and recycling yield over the sticking coefficient below detection limit, which is in line with the few laboratory measurements available at room temperature at least for the primary desorption yield [183]. It is equally true that, if electron cloud is strongly mitigated, or better suppressed, by a-C coating, then the minimization or control of the electron desorption yields becomes, in part, less relevant.

The survey of heat load was limited to specific cases due to unstable cryogenic conditions, especially with a CB LHe bath pumped at 3 K. Within the limited data, two observations were made.

In some cases (e.g. Run 3), the dynamic heat load was below detection limit, which corresponds to the measurement precision of $\sim$ 100mW/m, i.e. no difference was observable with and without beam circulation. Fig. 11.28 shows a calibration of the employed measurement method where its accuracy and precision are appreciable. Thanks to the extremely high specific heat of GHe, roughly corresponding 5.2 kJ/(kg·K) between 10 K and 60 K and the good thermal conductivity of the OHFC Cu made BS, the time constant expected in such measured is roughly 1 min.

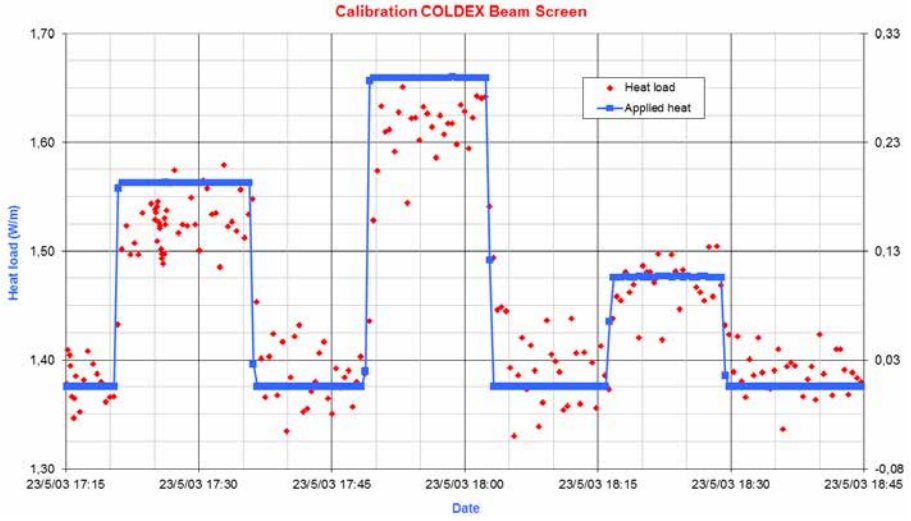

Figure 11.28: BS heat load measurement calibration with an heating wire by Joule effect. Courtesy of V. Baglin, 2003.

In other cases (e.g. Run 2 or Run 4), the observed dissipated dynamic heat loads along the a-C coated beam screen were measurable, and smaller than 0.3 W/m for 4x72 bunches of $1.5{\cdot}10^{11}$ ppb, spaced 25 ns. The dynamic heat load observed in Run 4 was linear with the number of batches N_B,

with a constant of $4.87 \cdot 10^{-2} N_B$. Due to limited data and because not observed systematically, an effect of beam conditioning on the dissipated heat load was not observable. In all the cases a heat load was measured, no electron activity, which was expected above $1{\cdot}10^{10}$ $e^-/(mm^2 s)$, was measured by the chimney electrode, with a sensibility of about $1 \cdot 10^8$ $e^-/(mm^2 s)$. For comparison with past results [168] with a scrubbed Cu BS (SEY≈1.3), held at 12 K with no pre-adsorbed molecular coverage, the circulation of 4x72 bunches of $1.1{\cdot}10^1 1$ ppb induced an electron cloud flux of $4.5{\cdot}10^{11}$ $e^-/(mm^2 s)$ (Fig. 11.29), corresponding to a power of 1.6 W/m, which was readily observed as cryogenic load (see Fig. 11.30).

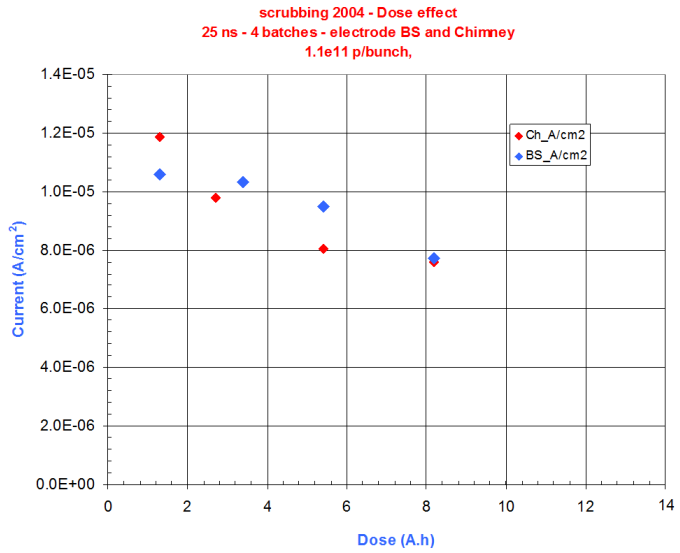

Figure 11.29: COLDEX Scrubbing Run with a scrubbed OFHC BS, 2004. Measurement of the electron activity due to electron cloud on both the chimney and BS electrodes, with 4x72 bunches of $1.1{\cdot}10^1 1$ ppb, spaced 25 ns. Courtesy of V. Baglin, from [186].

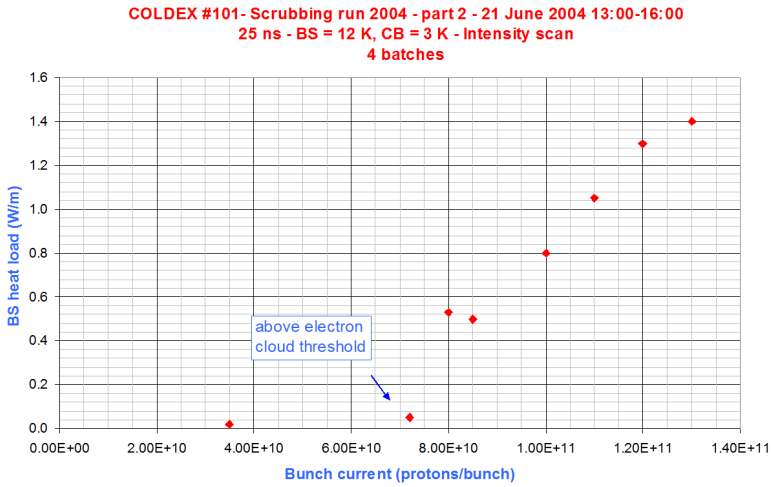

Figure 11.30: COLDEX Scrubbing Run with a scrubbed OFHC BS, 2004. Measurement of the dynamic heat load due to electron cloud with 4x72 bunches of increasing bunch intensity, spaced 25 ns. Courtesy of V. Baglin, from [186] and [138].

Basing on these observations, a reduction of the BS dissipated heat load of at least 85% was obtained in COLDEX thanks to a-C coating. The observation of a residual heat load of approximatively 0.2±0.1 W/m (with 4x72 bunches of $1.5{\cdot}10^1 1$ ppb, spaced 25 ns) is inconsistent with the

other measurements of pressure increase and electron activity. Such heat load is not expected by simulation, which predicts an heat load below 1 mW/m for SEY=1.1 with the mentioned beam parameters (see Fig. 11.31).

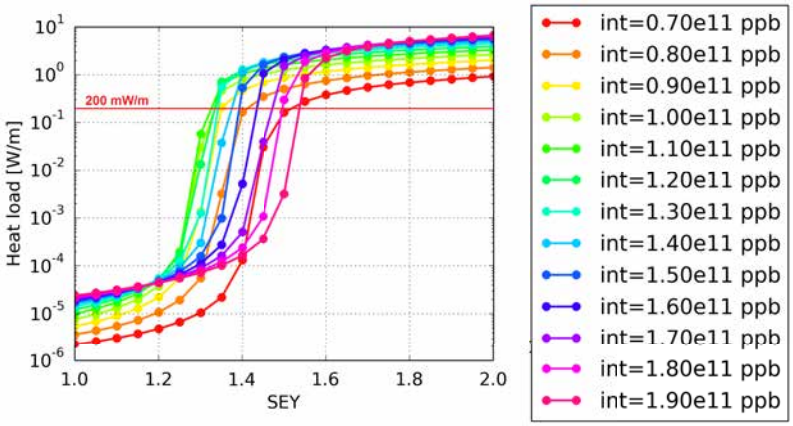

Figure 11.31: PyECLOUD simulation of heat load in the COLDEX nominal case with a a-C SEY model, 26 GeV, T=10 K, σ_i=0.2 Mbarn, versus SEY for different bunch intensities. The level corrisponding to heat load of 200 mW/m is marked.

The absence of consistency between the observed heat load and the other electron cloud signatures (pressure rise, electron activity) tends to show that the observed dynamic heat load is not related to electron cloud. Besides, it was neither observed systematically. While the exact cause(s) is still under analysis, we examine here the numerous possible sources.

The influence of a potentially drifting static heat load baseline was checked by observing the heat load before and after the beam circulation: reasonable agreement, within the measurement error, was found in all the observations.

Impedance heating was studied in deep for the COLDEX geometry with an OFHC Cu BS and LHC-type beam parameters in [187] and [138]. The analysis showed that the impact of the geometry features (pumping slots, Cold-to-Warm transitions) and the ohmic losses is expected negligible (in the order of μW/m) with respect to the heat load measurable with a cryogenic method. The impact of the thin film a-C coating deposited in 2014 is expected to bring a negligible increase on the total resistive wall impedance. Considering the case of 26 GeV/c proton beams spectrum circulating in the SPS, the skin depth in a thick layer of a-C is estimated as

$$\delta_{a-C} = \sqrt{\frac{2\rho_{a-C}(20\text{ K})}{2\pi f \mu_0}} \approx 1.38\text{ mm} \tag{11.9}$$

being $\rho_{a-C} \cong 2.5 \cdot 10^{-3}$ Ωm is the a-C resistivity assumed at 20 K, $f = 1/\sigma_l \approx 333$ MHz the characteristic frequency of 26 GeV/c proton bunches circulating in SPS ($4\sigma_l$=3 ns), μ_0 the vacuum permeability. The skin depth is much larger than the applied layer thickness (400 nm), thus making the layer transparent to beam bunches. Recently, more refined studies on the impact of a-C thin films coating has been carried at CERN for the case of the HL-LHC Inner Triplets in IR1 and IR5 [188]. The analysis studied the impact of coating on the new triplet beam screen for the HL-LHC beam parameters: an increase of a factor 2-3 was observed on the imaginary part of both the longitudinal and transverse effective impedance due to a-C coating of the beam screen, while the effect on the real part was negligible, i.e. no effect on the beam induced heating is expected. The imaginary part increase is expected to be in the background of the total LHC impedance budget.

Beam losses represent the most indicted source, but quantitative estimation could not be made due to the lack of radiation monitors next to the experiment. Beam losses at SPS flat bottom (26 GeV) are usually observed in a short beam lifetime, due to a combination of multiple causes: electron cloud effects, tune resonances, longitudinal instabilities causing incoherent emittance growth, aperture restrictions. The COLDEX BS does not provide one of the tightest aper-

tures in the SPS ring with LHC beams ($x_{aper} = y_{aper}$=33.5 mm i.e. $46.8\sigma_x$, being a $1\sigma_x$=0.71 mm at COLDEX.41737). A macroscopic effect of restriction on the circulating beam intensity was excluded in Run 1, where the insertion of the experiment (sector 431) did not show signs of degraded beam lifetime with respect to the normal SPS pipe (Sector 430). On top of that, no systematic correlation with the beam lifetime is yet found with respect to the observation of a measured heat load. Fig. 11.32 shows the beam circulating intensity cycle during the heat load observations carried during Run 3 (left) and 4 (right). While a more degraded beam lifetime is visually appreciable during Run 3 than in Run 4, no correlation - with an expected higher beam loss background - is found, as a heat load was effectively measured only in Run 4. Finally, the application of passive dosimeters through the beam run and the measurement of the radiation activation after the run along the COLDEX sector could indicate that the equipment was indeed subjected to particle showers due to beam losses (in particular during the Run 5), but no quantitative conclusions can be drawn.

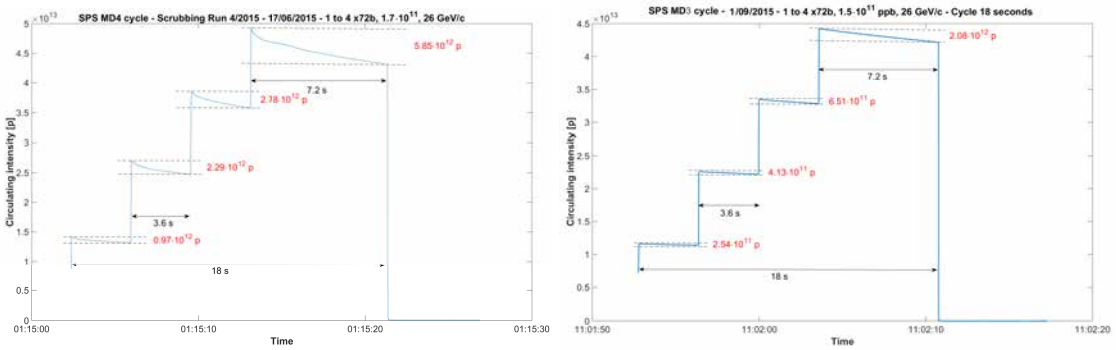

Figure 11.32: Beam life time during Run 3 (left, when no dynamic heat load was detectable, see Fig. 11.15) and Run 4 (right, when a dynamic heat load was observed, see Fig. 11.20).

Uncaptured beam, which is observed systematically with LHC-type beams transferred from the pre-injectors (PSB, PS) to the SPS since 2002 [189], have been accounting 1% to 4% during the COLDEX runs. The uncaptured beam is spread outside the separatrix in the longitudinal phase space and coasts in the ring in absence of an enhanced energy loss mechanism. Possible slow sources of energy loss are residual gas nuclear scattering (especially due the high pressure caused by desorption due to electron cloud) and resistive impedance losses. While losing energy, the uncaptured beam spirals toward the centre of the machine and is principally lost in the tightest machine aperture (both the betatronic and dispersion component must be kept into account). Fig. 11.33, left, shows the impact of the uncaptured beam during a ramp from 26 GeV/c to 450 GeV/c with 2x72 bunches of nominal LHC intensity: roughly 4% of beam circulating intensity is lost at the beginning of the ramp due to induced loss of orbit stability of the coasting unbunched beam. On the right of Fig. 11.33, we appreciate instead the continuous losses distribution around the SPS ring while 4x72 bunches of $2.0 \cdot 10^{11}$ ppb are circulating at 26 GeV/c during a scrubbing run (COLDEX Run 3): losses can be observed all around the ring, with peaks in the half-cells at high dispersion (COLDEX is installed in a dispersion-free region of Long Straight Section 4, specifically in the half-cell 417).

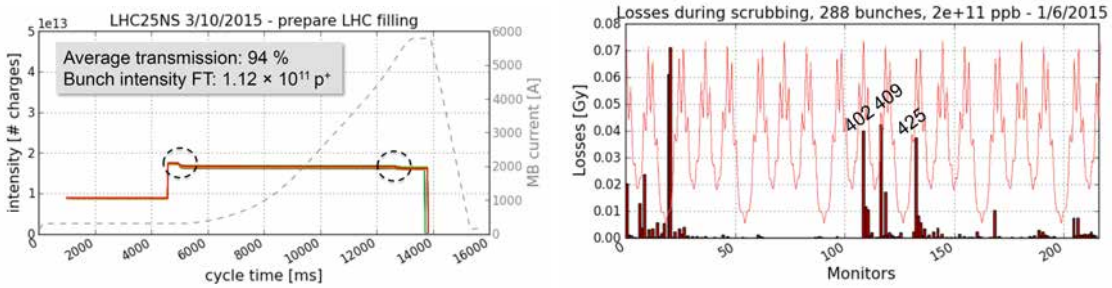

Figure 11.33: Left: LHC type beams ramped to 450 GeV during LHC filling (fill 4452): the losses due to uncaptured beam are visible at the beginning of the acceleration ramp. Right: loss maps of the SPS ring during Run 3, when 4x72 bunches of $2 \cdot 10^{11}$ ppb were circulating: the losses are located in the arcs (especially of Sextant 1 and 4), in high dispersion areas, with a Q20 optics. Courtesy of V. Kain, from [190].

Although the presence of losses in the ring was acknowledged during the COLDEX runs, a quantitative estimation of the energy possibly deposited on the COLDEX BS is yet difficult. While attempts of combined tracking and energy distribution simulations are being made to give an order of magnitude to this mechanism, the installation of beam loss monitors close to the experiment and far from it (for comparison) is being considered for the near future.

It is renown that the thick layers of CO and H_2O modify the SEY of metallic surfaces [152]. An net increase on all the electron cloud signatures (dynamic pressure rise, heat load, electron activity) was observed in COLDEX in 2002 with roughly 30 monolayers of H_2O condensed on the OHFC BS surface [176]. An heat load of 6 W/m was measured with 2x72 bunches of with $1.1 \cdot 10^{11}$ ppb, 95 % duty cycle. The expected δ_{max} was 1.9 [152]. Thick layers (60 monolayers) of CO induced similar effects [176]. The influence of pre-adsorbed gas species on a-C is one of the experimental purposes of the COLDEX recommissioning. The physisorption of H_2 and CO was reproduced in dedicated beam time in 2015, Run 4 and Run 5 respectively. The coverage of $3.2 \cdot 10^{16}$ H_2/cm^2 or $\sim 2.1 \cdot 10^{16}$ CO/cm^2, respectively, on a-C did not show a strong influence on all electron cloud signatures in COLDEX. Such coverages were chosen on purpose as they are well above the monolayer capacity of common metallic surfaces and representative of several months of HL-LHC operation. The influence of spuriously adsorbed species (like H_2O) is interesting, as in Run 2 and Run 4 (when a heat load was measured - but not an electron activity) the cryostat was cooled down 6 to 8 days in advance. Some accumulation of H_2O thermally desorbed by the room temperature extremities (unbaked) may have took place. Their influence was not yet reproduced and will be object of the future COLDEX experimental plan.

Measurement of the electron activity was obtained with the chimney electrode in all the Runs, whereas the BS baffle electrode was not employable, due to a contact short circuit, solved only later, in 2016. Measurement of the electron current deposited on the chimney electron is a reliable indication of the electron activity occurring in the COLDEX BS [168]. Electron activity was surveyed all along the described runs with a set of bias voltage going from -1 kV to + 1 kV and with a minimum detection limit of $2 \cdot 10^{-9}$ A, corresponding to a flux about $1 \cdot 10^8$ $e^-/(mm^2 s)$, at +100 V. No signal correlated to electron cloud was observable above the detection limit with a bias voltage spanning from -1 kV to +1 kV. Clear electron signal, correlated to beam circulation, was recorded during periods of charge deposition caused by beam losses. The signal was partially correlated to the closest available Beam Loss Monitor, e.g. in Run 1. In Run 3, the combination of high pressure and high circulating beam intensity (4x72 bunches of $2.0 \cdot 10^1 1$ ppb, i.e. $\sim$0.4 A) gave interesting signs which could be correlated to ion-electron current due to residual gas ionization.

In Fig. 11.34 we show the results of the simulated (a-C model) and expected chimney electrode current plotted as a function of the SEY for some bunch intensities of interest.

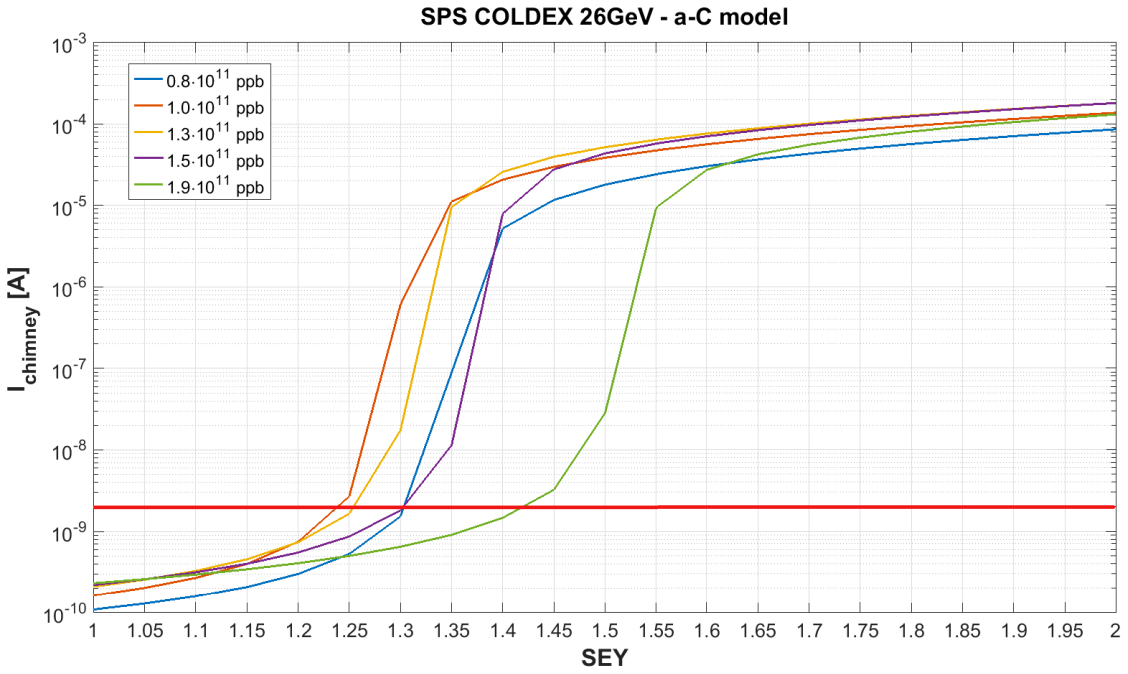

Figure 11.34: PyECLOUD simulation of expected electron current collected on the chimney electrode in the COLDEX nominal case with a a-C SEY model, 26 GeV, T=10 K, σ_i=0.2 Mbarn, versus SEY for some bunch intensities. The detection limit of $2 \cdot 10^{-9}$ A, corresponding to a flux of $1 \cdot 10^{8}$ $e^-/(mm^2 s)$, is marked in red.

We observe a trend similar for the heat load, discussed thoroughly in Sect. 10.3.2, where here the influence of the electron impinging energy is hidden and the total flux is plotted with all the electron energies, which corresponds to the measurement obtained with a chimney electrode sufficiently voltage biased. For SEY<1.2, the expected chimney electron current is below the available detection limit, which is coherent with the experimental observations. A lower sensibility is however obtained with respect to the heat load measurement: an electron flux not less than $3 \cdot 10^{12}$ $e^-/(cm^2 s)$ with a mean energy of 100 eV is required to observe a heat load of about 100 mW/m. With that flux, the chimney would measure at least $7 \cdot 10^{-7}$ A, that is coherent with was observed in the past with an OFHC BS (see Fig. 11.29).

Part III

Summary, conclusions and future perspectives

Chapter 12

Summary, conclusions and future perspectives

In the first part of this Thesis the problem of space charge in high intensity and low energy beams was analysed showing its effects in the beam transport and presenting the Space Charge Compensation technique.

We have shown that for non-relativistic particles (like low energy ion beams) the electric force of the space charge dominates and has a net defocusing effect. The space charge forces for different beam distributions has been evaluated analytically, with in particular the one for Gaussian beam distributions: we have shown that for such kind of beam distributions the defocusing effect is non-linear, from which arises the difficulty of control by external focusing. In order to describe the space charge expansion in a drift, we have defined the concept of generalized perveance, K.

The concept of RMS emittance, that is a statistical definition of emittance based on RMS quantities, has been introduced to describe the dynamics of non-laminar particle beams, where the phase space area differs from that of an ellipse. We have then derived the RMS envelope equation in presence of space charge and applied it to an elliptical continuous beam typical for long bunches or DC beams in low energy beam transport lines. The K-V envelope equations have been described for uniformly dense elliptic beam distributions and, then, generalized, thanks to the work of Lapostolle and Sacherer, to all density distributions with elliptical symmetry.

The increasing interest of the international scientific community in the availability of high power (MW range) accelerators poses the problem of transport of intense beams, particularly at very low energy (keV). After summarizing the major challenges to extract and transport high intense beam while still at low energy, with the objective of minimizing the emittance growth and halo formation, we introduced the concept of Space Charge Compensation (SCC) or neutralization. Minimization of the space charge field can be obtained by the accumulation of negative charge creating a negative potential counteracting the beam potential, with the net effect of reducing the space charge defocusing force. To show the impact of space charge neutralization, we have first introduced the concepts of SCC degree and transient characteristic time, essential figures to define the quality of the compensation in steady and transient states, and then derived the modified RMS envelope equation with space charge in presence of SCC.

The problem of space charge and the application of compensation techniques has been analysed in the applied case of the MYRRHA accelerator for ADS applications. After introducing the pros and cons of an Accelerator Driven System as opposed to critical reactors, we have shown how ADS may play an important role in the future energy production scheme including GEN-IV nuclear reactors, as it is a potential and promising candidate for transmutation purposes. The introduction of Partitioning & Transmutation in the nuclear waste reprocessing cycle has the potential to solve the one of the major weakness of fuel cycle in nuclear fission energy production schemes. We enunciated the accelerator requirements for ADS, which are quite peculiar and challenging. Not only we have shown that the required beam power falls in the multi-MW range, but being the energy about 1 GeV necessary to maximize the efficiency of the spallation reaction, the requested beam intensities reach several mA, to be delivered in a challenging Continuous Wave mode. The above requirements set the ADS driver accelerators in the High Power Proton Accelerators domain,

which an unprecedented quest to the highest reliability degree. Accelerators for ADS are required to deliver (and we underline by design, not as a result of an optimized operation!) their mission within a tight acceptable spectrum of undesired beam interruptions, such are the beam trips. The underlying motivation is both structural (thermo-mechanical fatigue of the reactor internals) and operational (reactor SCRAM): while on the former there is a long debate on the constraints and how to relax them, the latter is without doubt a show stopper. We have shown that the accelerator choices for ADS are essentially two: the isochronous, separated sector, cyclotron, and the superconducting LINAC, with the latter winner in terms of modularity, hence fault tolerance, and scalability. The layout of the MYRRHA high power proton accelerator, a superconducting LINAC characterized by a general philosophy of fault tolerance, has been discussed, focusing on the design choices which make the reliability goal reasonably approachable.

The design of the MYRRHA low energy front-end, object of the RFQ@UCL programme, has been extensively discussed from the Ion Source up to the RFQ. The MYRRHA Ion Source, a 2.45 GHz ECR proton source featuring a patented magnetic confinement with Permanent Magnets and enhanced reliability, has been described. The source, characterized in Factory and Site Acceptance Tests (FAT, SAT), has been capable to deliver a 30 keV H^+ beam up to 16 mA (DC), with a vertical beam emittance of $\sim$ 0.1π·mm·mrad RMS norm. at 5 mA H^+. A $\sim$ 63% ionization efficiency was achieved for H^+, while $\sim$ 30% for H_2^+ and a spurious $\sim$ 7% for H_3^+. The combined result of the experimental measurement of the beam size at the source exit and the simulated transport in presence of space charge compensation allowed to establish that a degree of space charge neutralization of roughly ϕ=80% was realistic. We offered a very much detailed overview of the design behind the MYRRHA Low Energy Beam Transport (LEBT) line, which has the role of efficiently transport and match the proton beam produced by the Ion source to the 4-rods 176.1 MHz RFQ, providing at the RFQ entrance a centered beam with matched transverse emittances, lower or equal to the RFQ design value, that is 0.2π·mm·mrad RMS norm. The layout of the MYRRHA LEBT is based on a short magnetic solution and is designed to maximize the proton beam quality (transverse emittance) by considering the Space Charge Compensation (SCC) effects of the beam. Permanent focus on this aspect was held throughout the presentation of the engineering design of each component of the line. Amongst all the LEBT sections, the RFQ interface was the most challenging, because the integration of a beam chopper, RFQ collimator, DC current transformer and electrode repeller had to face the requirements dictated by the beam dynamics, demanding the minimum impact on the Space Charge Compensation. The interface has been designed to fit in 270 mm - as close as possible to the RFQ injection flange - in order to minimize the detrimental effects of uncompensation due to SCC transients. Start-to-end design LEBT beam dynamics simulations have been carried, with initial estimates of the Space Charge Compensation (SCC) highly requiring experimental validation in the LEBT commissioning phase. The result of the beam tuning allowed to get a transverse beam emittance < 0.18 π·mm·mrad RMS norm. at the RFQ entrance for a matched beam. With such input beam, the RFQ transmission reaches >98%, which is very close to the typical natural RFQ transmission for a perfectly matched beam ($\sim$ 99%). A set of multiparticle simulation have been especially devoted to the LEBT chopper pulsed regime, where the negative impact of SCC uncompensation transients have been characterized and a trade-off between a short characteristic space charge compensation transient time and high transmission had to be found.

The future perspectives see the MYRRHA LEBT test stand being built-up in the RFQ@UCL program and currently (2016) in commissioning at LPSC in Grenoble up to the beam chopper. The goal of the test stand is characterize the space charge neutralization as a function of different parameters and find agreement with the simulation. This represents a valuable opportunity to develop and improve existing analytical models and simulations against experimental results. A set of dedicated experiments is foreseen to measure the SCC level and transient time along the whole line.

The design of accelerators for ADS applications has reached a mature level for practical implementation. Technological solutions are well identified and fall in the large community of Superconducting RF linear accelerators. The current challenge is all around the reliability issue, feature essential for ADS. With the support of the European Commission, a series of R&D program (FP5 PDS-XADS, FP6 EUROTRANS, FP7 MAX, Horizon2020 MYRTE) is pursuing both the design and the demonstration of the different technologies (injector, main LINAC elements). The pro-

totyping activities foreseen in the MYRRHA Research and Transmutation Endeavour (MYRTE) Work Package 2 aim at the completion of the construction of the fully equipped Low Energy front-end, followed by its experimental exploitation with beam. This will allow to obtain a thorough characterization of the 1.5 MeV beam out of the RFQ and to match it with the subsequent accelerating structures (CH-type multi-gap cavities).

The global MYRRHA project is now in the delicate phase of pre-licensing and Consortium building-up. It has been decided (2016) that the realization of MYRRHA accelerator will be phased: in a first stage, the energy of the LINAC will be limited to 100 MeV. The commissioning of a 100 MeV LINAC combines the aim of investigating the adequacy of the proposed fault tolerance schemes, relaxing the decision-taking process with regard to the full ADS, while profiting - at the same time - of a powerful facility for targetry experiments for nuclear and life science. This choice is pushing toward a simplified injector design, fully at room temperature, followed by a standard Medium Energy Beam Transport line (already fitted for a second injector) and a superconducting section consisting of 48 single spoke cavities arranged in 24 cryomodules (with warm focusing/diagnostics insertions). The array would be installed in a dedicated and extendible building in Mol, Belgium, at the SCK•CEN premises.

In the second part of the Thesis we have addressed the problem of electron cloud formation and build-up in high intensity and high energy colliders, with the final purpose of studying its mitigation in the specific case of the HL-LHC upgrade.

Three primary electrons production mechanisms are of interest in proton particle accelerators characterized by large bunch intensity and small spacing: residual gas ionization, photoemission due to synchrotron radiation and beam losses. While the first is always present and is enough to trigger the electron multipacting and electron cloud formation in the Super Proton Synchrotron and the Large Hadron Collider even at injection energy (26 GeV and 450 GeV, respectively), the photoemission requires higher beam energies, roughly 2.5 TeV for proton beams, and exhibits peculiar characteristics with respect to the surface photoelectric yield (PY) and photon reflectivity (PR), which have discussed in the applied case of the LHC. We have introduced an up-to-date secondary electron emission model, where the secondary electron emission of a surface is described by the Secondary Emission Yield curve. We have shown its energy and angular dependence and the spectrum of the true secondary emitted electrons. To analyse the main mechanisms behind the beam induced multipacting leading to the formation of an electron cloud, we have treated the electron energy gain in the beam field in the most analytical and accessible way possible. The limits of these approaches are overcome by complicated and sensitive build-up simulations. The conditions required to reach beam induced multipacting have been analytically shown, enlightening the key parameters behind an electron cloud formation, which can essentially be resumed in: the bunch charge distribution and intensity (electric field), the bunch spacing and the beam chamber dimensions (transit time conditions) and surface's material properties. While, in general, higher bunch charges and shorter spacings tend to facilitate the multipacting, it is finally the combination of these three parameters to determine how low is the SEY threshold above which multipacting occurs. The combined effects of externally applied magnetic field was presented, underlying, once more, the weakness of analytical models in favour of the necessity of accurate simulations. The negative implications of the electron cloud build-up have been analysed presenting the beam coherent tune shift, transverse instabilities and incoherent beam effects arising from the interaction of the beam with the electron cloud. The implications on the machine such as the detrimental effects of vacuum degradation, dissipated heat load and distorted beam diagnostic performance are discussed, with a particular theoretical excursus on the Electron Stimulated Desorption phenomenon.

Later, we have presented and discussed the LHC beam vacuum system, with focus on the beam induced loads and dynamic vacuum. We have described the mitigation strategy adopted in the design of the LHC, based on beam conditioning or scrubbing. Then, the goals of the High Luminosity upgrade of the Large Hadron Collider have been presented. HL-LHC foresee an increase of the instantaneous luminosity by a factor five, leading to an increase, by a factor of ten than originally foreseen, of the integrated luminosity. Amongst the present LHC limitations and HL-LHC hardware upgrades, we have shown how the extrapolations of the LHC Run 1 observations to the High Luminosity upgrade (HL-LHC) beam parameters and IT layout predict an intolerable

increase of heat load due to electron cloud build-up. In order to mitigate the electron cloud build-up and, in turn, limit the heat load to an amount compatible with the present IT cryogenics cooling capacity, postulated to 200 W, the current HL-LHC baseline is to mitigate the beam induced electron cloud by lowering the IT beam screen surface's Secondary Electron Yield (SEY) with amorphous carbon (a-C) thin film coating for the new HL-LHC triplets in IR1/5. In 2015, it was further decided to study the coating in-situ of the ITs at IR2/8. Such HL-LHC baseline is validated at cryogenic temperature by the COLDEX experiment, re-commissioned in 2014 with the objective of qualifying the performance of a-C coating at cryogenic temperature in the Super Proton Synchrotron, in presence of LHC type beams.

The COLDEX experiment provides a unique setup where the beam induced multipacting in a LHC type cryogenic vacuum system can be studied in a real machine environment, offered by the Super Proton Synchrotron, as a function of the BS temperature (depending on it, of the presence of adsorbed gas species on its surface) and the circulating beam parameters (bunch intensity, spacing, total circulating intensity, at injection and top energy). We have described the experimental layout and the measurements allowing to have a direct indication of the electron cloud build-up, such as the dynamic pressure rise, gas composition, dissipated heat load and electron activity in the COLDEX geometry with a-C coated beam screen. Before moving to the simulation and experimental results, we have shown the results of the preliminary vacuum characterization - without beams - of a-C coating at cryogenic temperature currently, as necessary basis for the understanding of the vacuum related results. Effective physical adsorption was observed on a-C for temperatures well above than of Cu or SS. In particular, for a coverage $\theta_0 < 1{\cdot}10^{15}$ molecules/cm^2, H_2 is adsorbed (physisorption) on a-C coating below 35 K and released when warming-up in the 40 to 65 K temperature range; CO and N_2 are adsorbed (physisorption) on a-C coating below 70 K and released when warming-up in the 75 to 140 K temperature range. Thermal desorption, i.e. loss of physisorption, is dependent on the initial coverage. The adsorption capacity of a-C for H_2 is $> 2 \cdot 10^{17}$ H_2/cm^2 below 10 K. Although more studies are required to fully characterize the a-C coating adsorption features, a first conclusion is that the proposed HL-LHC Inner Triplet BS temperature range baseline (currently 40 to 60 K) may be affected by vacuum transients, principally due to H_2 thermal desorption. A shift in the temperature range may be individuate a new window in the 55 to 70 K range; in any case, prediction and control of the HL-LHC beam screen coverage must be ensured.

The electron cloud modeling offered by the pyECLOUD code, used at CERN, has been introduced for build-up simulations of the COLDEX experiment case. We have shown how simulation is an useful tool to study the influence of the different parameters on the electron cloud. The electron cloud build-up is in fact extremely sensitive to the beam and surface emission features and a full characterization by complete build-up simulation sets has been carried in absence of comprehensive scaling laws. By that, we equally confirm the strong influence of the input parameters and the underlying representation of the various mechanisms on the simulation outcomes, which therefore should be compared to the experimental observations with care. We have shown the influence of the SEY, bunch intensity, beam energy, beam screen temperature and primary ionization on the electron cloud build-up in COLDEX expected by simulation. At the end of the Chapter, a novel and updated model of SEY specific for a-C coatings, developed on phenomenological modeling on real measurement datasets, is presented. This new input was inserted in a new simulation set where its influence, combined with the sensitivity to SEY, bunch intensity, beam energy and electron reflectivity, was studied. The results show that, considering the COLDEX nominal case with an a-C coated BS, the multipacting threshold cannot be fixed *a priori* and is severely dependent on the bunch intensity, for SEY > 1.25. For SEY $= 1.05$, the expected deposited heat load due to electron cloud is well below 1 mW/m for every bunch intensity. For SEY above 1.5, the heat load is above 10^{-1} W/m (i.e. measurable) for any bunch intensity. The absence of a reliable estimation of the electron reflectivity for a-C coatings was studied in a dedicated simulation set: for SEY=1.1, a weak dependency - below a factor 2 - of R_0 was observed in the range $R_0 = [0.7{:}1.0]$ for every bunch intensity.

We have presented the experimental results of five beam runs in which the performance of a-C coating was qualified at cryogenic temperature with LHC type beams. The total accumulated beam intensity was more than 9.5 Ah. The vacuum observations on a-C coating at 50 K and 5-10 K with LHC type beams and doublet hybrid spacing (5+20 ns) beams did not reveal effects of vacuum degradation imputable to electron cloud. Throughout the runs, significant pressure

rises (up to $1 \cdot 10^{-6}$ mbar) were observed outside the cold system due to electron stimulated desorption. Quick beam conditioning, or scrubbing, was observed, but no electron cloud complete mitigation was achieved in the room temperature extremities, neither outside the allocated beam time, which is in line with what is observed in the whole SPS machine with LHC type beams. In COLDEX, dynamic pressure rises convoluting in a slow residual gas background pressure increase were observed mainly due to H_2 gas accumulation, with a BS at 50-60 K and the CB held above 4 K. This effect was prevented by ensuring a low H_2 vapour pressure having the CB held at 3 K. In this condition, no dynamic slow pressure build-up was observed due to gas accumulation: however, dynamic pressure rises linked to gas transmission were still visible at COLDEX centre with the BS at 50 K during beam circulation and electron bombardment at RT extremities, and this due to the finite CB pumping speed, which is limited by the BS transparency (1%). With the BS at 10 K, no pressure rise was observed with any LHC type beam circulating in COLDEX: at this BS temperature, the cold system was made quasi-closed and, as such, independent of electron stimulated desorption effects at its extremities. Based on this exceptional result, we have provided the upper limit of primary and secondary electron stimulated molecular desorption yield corresponding to the observation of pressure and electron flux, the latter being evaluated from the heat load and electron activity measurements. Within the beam time obtained and the described experimental conditions, we consider the real measure of the primary desorption yield and the sum of the primary and recycling yield over the sticking coefficient below detection limit for the a-C coating in COLDEX, which is in line with the few laboratory measurements available at room temperature.

The survey of heat load was limited to specific cases due to unstable cryogenic conditions, especially with a CB LHe bath pumped at 3 K. A reduction of the BS dissipated heat load of at least 85% was obtained in COLDEX thanks to a-C coating, which is an impressive achievement with respect to what observed with a OHFC copper beam screen. The not-systematic observation of a residual heat load, approximatively 0.2±0.1 W/m with 4x72 bunches of $1.5 \cdot 10^{11}$ ppb, spaced 25 ns, is inconsistent with the other measurements of pressure increase and electron activity and is not expected by simulation. We have reviewed the possible sources of the observed dynamic heat load other than the electron cloud, identifying the beam losses as the most indicted source, although a quantitative estimation is yet difficult.

Measurement of the electron activity was obtained with the chimney electrode in all the runs. The measured electron activity, with a minimum detection limit of about $1 \cdot 10^8$ $e^-/(mm^2 s)$, did not show signals correlated to electron cloud with a bias voltage spanning from -1 kV to +1 kV. For SEY<1.2, the expected chimney electron current is below the available detection limit, which resulted coherent with the experimental observations. A lower sensibility is obtained with respect to the heat load measurement: an electron flux not less than $3 \cdot 10^{10}$ $e^-/(mm^2 s)$ with a mean energy of 100 eV is required to observe a heat load of about 100 mW/m, while a flux $1 \cdot 10^8$ $e^-/(mm^2 s)$ was measurable with the chimney electrode.

The coverage of $3.2 \cdot 10^{16}$ H_2/cm^2 or $\sim 2.1 \cdot 10^{16}$ CO/cm^2 on a-C did not show an influence on the electron cloud build-up in COLDEX. Such coverages were chosen on purpose as they are well above the monolayer capacity of common metallic surfaces and representative of several months of HL-LHC operation.

Future COLDEX runs with a-C coating have been already scheduled for 2016. More beam time is in fact required to get confirmations of the observed trends and, in particular, gain more statistic on the heat load measurement. Thanks to the repair of three cryostat insulation vacuum leaks (up to 10^{-2} mbarl/s) during the SPS Year End Technical Stop 2015-2016, a stable static heat load of 1.1 ± 0.1 W/m seems accessible. The BS electrode, as well repaired, will offer a new electron flux measurement behind the BS slots, which will be compared to the measurements of electron activity of the chimney electrode. A brand new Gas Injection System was also installed: an unprecedented span of fully remotely operated gas injections with 4 gases (e.g. H_2, CO, N_2 and CO_2 have been initially charged) is now available and will be employed as much as possible to further characterize the a-C coating cryogenic vacuum performance, both without and with beams. The experimental programme of COLDEX foresees numerous possible beam test. In particular, a run dedicated to the heat load measurement as a function of the total circulating beam intensity (number of batches) and of the bunch intensity (with 4x72 bunches) is mandatory. We plan to study the impact of temperature oscillations arising the desorption/adsorption of gas species like

H_2 and CO in a real operational context with LHC type beams. The impact of gases coverage, in particular those influencing the surface secondary emission, is planned in dedicated runs where the a-C coated BS surface will be prepared with gas pre-adsorption. Due to the instabilities and negative beam quality of Run 5, the run with CO will be probably repeated to acquire high quality data; the coverage with N_2, CO_2, CH_4 and H_2O is of interest. It is not excluded also to run in warm (room temperature) conditions.

The future perspectives for COLDEX see firstly constant upgrade and improvement of the experimental setup. The installation of dedicated Beam Loss Monitors is under consideration, in order to characterize the stray radiation field caused by beam losses in the COLDEX area; furthermore, as proposed by the HL-LHC Technical Coordination Committee, a survey of Unidentified Falling Objects (UFO), a disease of several colliders arising from the unexpected interaction of the beam with bodies left in the beam pipe, such as dust or metallic parts, would be possible with an a-C coated BS. New calorimeters for heat load measurement at room temperature (e.g. two WAMPAC 5 calorimeters with a copper and a-C coated liner, respectively) would enable to have a second indication of the heat load besides the BS calorimetry. Following the completion of the experimental qualification of a-C coatings at cryogenic temperature, the alternative technique offered by the Laser Engineered Surface Structures for SEY mitigation is in preparation for a potentially first test at cryogenic temperature in COLDEX by 2017-2018. This technology is extremely promising, as it gives the first reliable access to surface SEY below the unity, thus approaching to the full eradication of electron cloud multipacting. But little is yet known a cryogenic temperature.

Appendices

Appendix A

Vacuum at cryogenic temperatures

The adsorption of molecules onto the surfaces of a vacuum vessel held at cryogenic temperature provides an exceptional source of vacuum pumping. The Large Hadron Collider (LHC), currently under operation at CERN, is one of the worlds largest scientific instrument which was designed and contributed to the development of vacuum technology at cryogenic temperature. This appendix describes the foundations of cryogenic pumping science, necessary for the understanding of the working principles of cryogenic vacuum systems described in Part II. The dissertation of most of the concepts presented is inspired by dedicated and renowned monographies available in literature [191, 149, 192, 193].

A.1 Basic quantities

The thermodynamic properties of N_{moles} moles of a rarefied gas contained in a closed volume are described by the ideal gas equation of state

$$pV = N_{\text{moles}} RT \tag{A.1}$$

which relates the gas pressure p, temperature T and volume V through the ideal gas constant R (8.314 J·K^{-1} · mol^{-1} in SI units). From statistical physics, the equation of state Eq. A.1 is rewritten in terms of the total number of molecules N in the gas as:

$$pV = N k_B T \tag{A.2}$$

where k_B is the Boltzmann constant ($1.38 \cdot 10^{23}$ J·K^{-1} in SI units, or $1.38 \cdot 10^{22}$ mbar·l·K^{-1} in practical units). The unit for pressure is Pascal (1 Pa = 1 N·m^{-2}) or, most widespread in vacuum tecnique, millibar (1 mbar = 100 Pa). Ultra High Vacuum (UHV) is defined in the range of pressure $10^{-7} \div 10^{-10}$ Pa, or $10^{-9} \div 10^{-12}$ mbar. Quantities of gas may be expressed as number of molecules, number of moles or, by Eq. A.2, by pressure-volume units at a given temperature. The latter unit is mostly used in vacuum science. The quantities of gas expressed in pressure-volume units are converted to the number of molecules dividing them by $k_B T$ (1 Pa·m^3 = $2.41 \cdot 10^{20}$ molecules, 1 mbar·l = $2.41 \cdot 10^{19}$ molecules, both at 293 K): when converting, it is mandatory to state the referenced temperature.

Considering n the molecular density (molecules per unit volume), Eq. A.2 reduces to

$$p = n k_B T \tag{A.3}$$

where pressure and gas density are related by the product $k_B T$ in coherent units. In UHV, the gas density is the quantity of interest rather than the pressure. In cryogenic vacuum technique, pressure must be expressed specifying the system temperature.

The mean speed of gas molecules $\langle v \rangle$ is calculated by the Maxwell-Boltzmann distribution [194]:

$$\langle v \rangle = \sqrt{\frac{8 k_B T}{\pi \cdot m}} = \sqrt{\frac{8RT}{\pi \cdot M}} \tag{A.4}$$

where m is the mass of the molecule and M is the molar mass, both expressed in SI unit (kg). Assuming that the density of molecules all over the volume is uniform, the frequency with which molecules collide with the walls of the system is directly proportional to the mean molecular velocity, so the molecular impingent rate ϕ onto a surface of unit area (molecules/m^2) is calculated:

$$\phi = \frac{1}{4} n \langle v \rangle = \frac{1}{4} n \sqrt{\frac{8 k_B T}{\pi \cdot m}}. \tag{A.5}$$

In any physically limited volume containing a gas, molecules collide between each other and with the walls. When the gas density is so low that molecular collisions are improbable, the molecule transport changes drastically. The molecular trasport regime is described by the dimensionless Knudsen number K_n, that is the ratio of the average distance between two consecutive points of molecular collision $\bar{\lambda}$, i.e. the molecular mean free path, over a characteristic dimension D of a vacuum system, e.g. the diameter of a cylindrical beam pipe:

$$K_n = \frac{\bar{\lambda}}{D} \tag{A.6}$$

The Knudsen number is below 0.01 for a continuous viscous flow, where the gas dynamics is dominated by the intermolecular collisions. For $K_n > 0.5$, the transport is a free molecular flow and the gas dynamics is dominated by molecule-walls collisions: the molecules do not interact preferentially each other. In UHV, pumps and instruments act on the single molecules, rather than of a "fluid".

In stationary conditions (i.e. in absence of pumping, or a net flow) the molecular densities n_1 and n_2 and pressures p_1 and p_2 of two volumes connected by an orifice but held at different temperatures T_1 and T_2 (see Fig. A.1) are correlated by Knudsen relationship [195]:

$$\frac{n_1}{n_2} = \sqrt{\frac{T_2}{T_1}}; \quad \frac{p_1}{p_2} = \sqrt{\frac{T_1}{T_2}} \tag{A.7}$$

which is calculated by the applying the conservation of the rate with which molecules traverse the orifice separating the volumes.

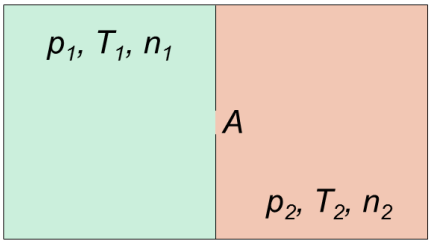

Figure A.1: Schematic depiction of two volumes, characterized by different thermodynamic properties, communicating through an orifice.

The "thermal transpiration" correction is essential in cryogenic vacuum systems, where different parts have different temperatures, and pressure is often measured and reported at room temperature. It is interesting to note that the pressure of a vacuum vessel held at LHe temperature is 8 times lower than what is measured at room temperature. It is far from intuitive that the molecular density is instead 8 times larger: this can be easily realized considering that the mean velocity scales like $\sqrt{T}$.

In the LHC vacuum system, the design density of 10^{15} H_2 molecules/m^3 is specified in the cryogenic arcs. At an average temperature of 15 K, this gives a room temperature gauge reading (commonly expressed as a N_2 equivalent) of $\sim 5 \cdot 10^{-9}$ mbar.

In the free molecular regime and isothermal conditions, the net gas flow Q between two points of a vacuum system is proportional to the pressure difference $\Delta p_{12} = p_1 - p_2$ at the same points:

$$Q = C(p_1 - p_2) \tag{A.8}$$

where C is the gas conductance of the vacuum system between the two points. In free molecular regime, the conductance does not depend on pressure, and if a function only of the mean molecular speed (i.e. of the considered gas specie and its temperature) and the system geometry. If the gas flow units are expressed in terms of pressure-volume (e.g. mbar·l/s or Pa·m^3/s), the conductance is quoted in volume per unit time (i.e. l/s or m^3/s).

The conductance of an orifice of surface area A between two vessels is obtained by calculating the difference between the impingement rates for the two volumes in isothermal conditions and is given by

$$C = \frac{1}{4} A \langle v \rangle \propto A \sqrt{\frac{T}{m}} \tag{A.9}$$

The conductance is inversely proportional to the square root of the molecular mass; for equal pressure drop, the gas flow of H_2 is the highest. The specific conductance C', per unit surface area, is shown for different gas species at room temperature in Table A.1.

Gas	H_2	He	CH_4	H_2O	N_2	Ar
C' at 293 K (l s^{-1} cm^{-2})	44	31.1	15.5	14.7	11.75	9.85

Table A.1: Orifice conductance C' per unit surface (in practical units) for UHV common gas species at room temperature.

In a geometrically articulated vacuum system, different sections traversed by the same gas flow are installed in series: in this case the inverse of the total conductance C is given by the sum of the inverse of the single conductances C_i:

$$\frac{1}{C} = \sum_1^N \frac{1}{C_i} \tag{A.10}$$

Section sharing equal pressures at the extremities are installed in parallel: the total conductance C is the sum of the single conductances C_i:

$$C = \sum_1^N C_i \tag{A.11}$$

In a vacuum system, a pump removes gas molecules from the gas phase. A vacuum pump is characterized by its pumping speed S, which is defined as the ratio between the pumped gas flow Q_P (pump throughput) and the pump inlet pressure p:

$$S = \frac{Q_P}{p} \tag{A.12}$$

The pump throughput can be written as the gas flow through the cross-section of the pump inlet (surface area A_P) multiplied by the capture probability σ_C, i.e. the probability for a molecule to enter the pump and being permanently removed:

$$Q_P = \phi A_P \sigma_C = \frac{1}{4} A_P n \langle v \rangle \sigma_C \tag{A.13}$$

which is equivalent, by using Eq. A.3 and Eq. A.9, to

$$Q_P = A_P C' \frac{p}{k_B T} \sigma_C \tag{A.14}$$

The pumping speed can thus be expresses as

$$S = A_P C' \sigma = A_P C' \sigma_C \tag{A.15}$$

which means that the maximum theoretical pumping speed of any pump is obtained for a capture factor equal to 1 and it is equal to the conductance of the pump inlet cross-section. For a

given pump, the pumping speed depending on C' and so on the inverse of the square root of the molecular mass, the maximum theoretical pumping speed is the one for H_2.

The effective pumping speed S_{eff} is the one acting directly in the vacuum vessel of interest. The effective pumping speed is lower than the nominal pumping speed because of gas flow restrictions interposed between the pump and the vessel (again a conductance, see Fig. A.2). The effective pumping speed is calculated equating the net gas flow incoming from the vessel to the one removed by the pump:

$$Q = C(p_1 - p_2) = Sp_2 = S_{\text{eff}}p_1 \tag{A.16}$$

that means

$$\frac{1}{S_{\text{eff}}} = \frac{1}{S} + \frac{1}{C} \tag{A.17}$$

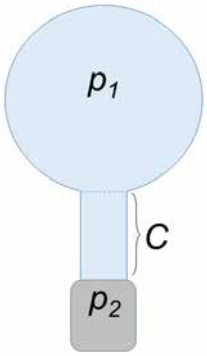

Figure A.2: Schematic depiction of a gas flow restriction offered by the conductance C situated between a pump of pumping speed S and a vacuum vessel.

Finally, from Eq. A.16 the equilibrium pressure of a vacuum system is found as

$$p_{eq} = \frac{Q}{S_{\text{eff}}} + p_0. \tag{A.18}$$

whew p_0 is the ultimate pressure (or background) of the pumping system (see e.g. A.6). In general S varies in a range of three orders of magnitude ($\approx 1 \div 1000$ l/s), while Q can extend over more than 10 orders of magnitude ($\approx 10^{-5} \div 10^{-15}$ mbar·l/(s·cm^2)). The right choice of materials and treatments is therefore compulsory in the design of vacuum systems for particle accelerators.

A.2 Monolayer

The concept of monolayer is used in UHV science to define a single, closely packed layer of molecules laying on a surface. Assuming for metallic surfaces typically $3 \cdot 10^{19}$ adsorption sites per m^2, a monolayer corresponds to $3 \cdot 10^{15}$ molecules/cm^2. The amount of gas present in a UHV system is usually much less than a monolayer. Considering an evacuated closed sphere covered with one monolayer, the gas quantity present in the system is

$$N = 4\pi R^2 \theta_m \tag{A.19}$$

If this gas layer is desorbed and gets fully in the gas phase, the resulting volume gas density becomes

$$n = \frac{N}{V} = \frac{3\theta_m}{R} \tag{A.20}$$

which would corresponds to a pressure of $4 \cdot 10^{-3}$ mbar in a closed sphere of 1 m^3.

The shortest conceivable time to form a single layer of adsorbed molecules, i.e. when all molecules impinging on a surface adhere with it, is called the monolayer formation time, and is an approximation of the useful operating time of a surface pump

$$t_{\theta_m} = \frac{10^{19}}{\phi} \approx 93 \cdot 10^6 \frac{\sqrt{mT}}{p} [\text{s}] \tag{A.21}$$

For a vacuum vessel exposed to N_2 at room temperature at a pressure of $1 \cdot 10^{-6}$ Torr, t_{θ_m} equals to 1 s: that is the definition of gas exposure, which is often measured in Langmuir (1L = 10^{-6}Torr·s).

Cryogenic pumps may therefore be adopted only in UHV systems, and require an alternative pumping method (e.g. turbomolecular pumps) pre-evacuating the vacuum vessel from atmospheric pressure.

A.3 Cryopumping regimes

Cryopumping is obtained when molecules of a gas are adsorbed on a cold surface so that the resulting sojourn time is long enough for the considered application. Several mechanisms of cryopumping are defined, and described below.

Physical adsorption, or **physisorption**, is the regime of the sub-monolayer mocoverage and is based on the attraction between the gas molecules and the substrates. In this regime, the van der Waals force acts between the adsorbed molecule and the material surface. The interaction forces with the substrate are much stronger than those between similar molecules. As a result, providing the adsorbed quantity is lower than one monolayer, the sojourn time can be long and gas molecules are pumped at a pressure (often referred as vapour pressure) much lower than the corresponding saturated vapour pressure. The binding energies for physical adsorption of H_2 typically varies from 20 to 65 meV for smooth to porous materials. One hour sojourn time is obtained at 5 K and 20 K, respectively. Since the binding energy for physisorption is larger than the heat of vaporization (e.g. 10 meV for H_2), submonolayer quantities of all gas can be physisorbed in sub-saturated conditions at their own boiling temperature. Pumps relying on physisorption are called cryosorption pumps.

In the **cryocondensation** regime, the mutual attraction of similar molecules at low temperature is obtained on a surface where coverage is above one monolayer. The van der Waals force now acts between the molecules themselves. A key property for each gas specie is the saturated vapour pressure p_{sat}, i.e. the pressure of the gas phase in equilibrium with the condensate at a given temperature, when a saturation equilibrium between gas adsorption and desorption is reached [196]. The lowest pressure attainable by cryocondensation pumps is limited by the saturated vapour pressure. The quantity of gas that may be cryocondensed is very large and only limited by the thermal conductivity of the condensate. The activation energy of desorption of each ga s specie equals their own energy of vaporization. It ranges from 10 to 175 meV for H_2 and CO_2, respectively. Pumps relying on condensation are called cryocondensation pumps.

The use a condensable gas to trap a non-condensable gas with a high vapour pressure is called **cryotrapping**. In this mechanism, the molecules of a low boiling temperature gas are trapped in the condensation layer of another gas. This is possible because the interaction energy between dissimilar molecules may be much higher than that between similar molecules. The trapped molecules are incorporated in the condensable carrier so that the equilibrium pressure is significantly lower than in pure physisorption. Typical examples of cryopumps working on this principle foresee Ar trapped in CO_2 at 77 K, or H_2 in N_2 at 20 K.

A.4 Cryogenic pumping

In cryogenic pumps, the pumping speed is the product of the "sticking probability" σ times the aperture conductance of the cold surface. The sticking coefficient for cryosorption and cryocondensation is the ratio of the average number of molecules which stick when impinging on a cold surface divided by the total number of impinging molecules. It is important to underline that the sticking coefficient ignores the effects of the vapour pressure. Its value is a function of the gas species,

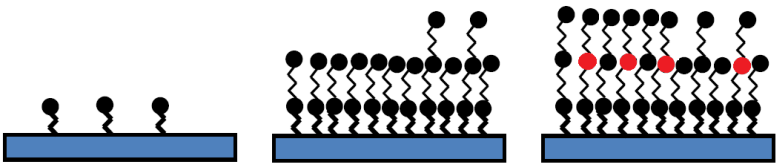

Figure A.3: Pictorial depiction of submonolayer physical adsorption, or physisorption (left), where the cryopuming mechanism is molecule-substrate interaction, cryocondensation (center), where the leading mechanism is intermolecular interaction, and cryotrapping (right), when a condensable gas carrier traps non-condensable molecules of another gas that would have a much higher vapour pressure.

the surface nature, the surface coverage, the temperature of the gas and the surface temperature. In general, the sticking probability increases with the surface coverage, which - at first sight - seems very counter-intuitive. It reaches the theoretical value of unity for a cryocondensed gas in saturation equilibrium.

A practical explanation is shown in Fig. A.4. On the left, the sticking coefficient of H_2 at 300 K incident onto a surface at 3.1 K is shown as a function of surface coverage, from submonolayer quantities up to few hundreds of monolayers [197]. For thick surface coverages, the sticking coefficient approaches unity, because the pumping mechanism has become cryocondensation. Once at these conditions, the variation of the hydrogen condensation coefficient onto a surface at 4 K for different incident temperatures (i.e. energies) [198] is shown in Fig. A.4, right.

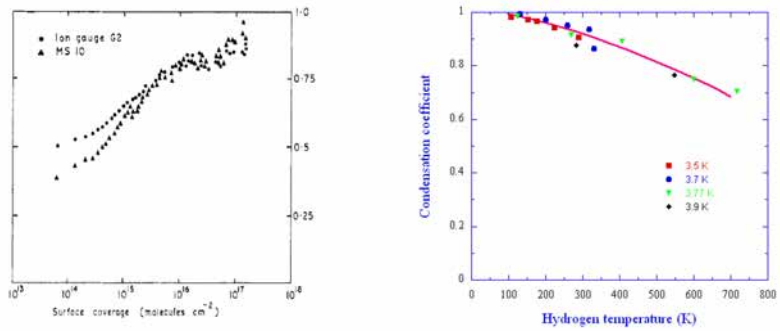

Figure A.4: Left: Sticking coefficient of H_2 as a function of the surface coverage. The H_2 is at 300 K incident onto a surface at 3.1 K. From [197]. Right: H_2 condensation coefficient onto a surface at 4 K as a function of the gas temperature. From [198].

If the temperature of the condensate at the surface is so high that its vapour pressure becomes comparable with the pressure of the incident gas p, then the effective pumping speed S reduces to zero when $p = p_{\text{sat}}$. In practice, the pumping speed decreases when the saturated vapour pressure of the adsorbed gas layer becomes comparable to the system pressure. Once reached p_{sat}, a saturation equilibrium between gas adsorption and desorption is reached and the saturated vapour pressure dominates.

Hence, for cryogenic surface pumps, the pumping speed is expressed as

$$S = \frac{1}{4}\sigma \left(1 - \frac{p}{p_{\text{sat}}}\right) A_P \langle v \rangle \tag{A.22}$$

A practical formula of pumping speed in $\text{l}\cdot\text{s}^{-1}\text{cm}^{-2}$ is given by

$$S \approx 3.64\sigma\sqrt{\frac{T}{M}} \tag{A.23}$$

where T is the temperature of the surface (which implies that the gas is fully accommodated to the surface temperature) and M the molecular weight of the incident gas. The highest pumping speed for H_2 and CO adsorbed on a cryopumping surface held at 4.2 K is 5.3 $\text{l}\cdot\text{s}^{-1}\text{cm}^{-2}$ and 1.41 $\text{l}\cdot\text{s}^{-1}\text{cm}^{-2}$, respectively.

A.5 Adsorption isotherms

The adsorption isotherm is the measurement - at constant temperature - of the equilibrium pressure (vapour pressure) recorded in a closed geometry as a function of the surface molecular coverage. It is a function of the molecular specie, surface temperature and nature, and the gas mixture.

Several semi-empirical models have been developed to describe adsorption isotherms. At low surface coverage, when there are no lateral interactions between the adsorbed gas molecules, the vapour pressure follows Henry's law, i.e. the surface coverage θ varies linearly with pressure p,

$$\theta = c \cdot p \tag{A.24}$$

which means the system pressure is inversely proportional to the coverage.

A more refined and widely accepted model describing adsorption isotherms on metallic, glass and porous substrates in sub-monolayer range is offered by Dubinin, Raduskevic and Kanager in the DRK isotherms [185]. The model is valid at low pressure and offers a good prediction of the isotherm as a function of temperature. The DRK equation relates the surface coverage θ, the monolayer surface capacity θ_m, the temperature T, the saturated vapour pressure p_{sat} and the pressure p via a constant D,

$$ln(\theta) = ln(\theta_m) - D\epsilon^2 = ln(\theta_m) - \left[k_B T ln\left(\frac{p_{\text{sat}}}{p}\right)\right]^2 \tag{A.25}$$

A plot in the DRK coordinates $ln(\theta)$ vs. ϵ^2 of a measured isotherm yields a straight line from which the constant D and the monolayer capacity are derived. Fig. A.5 shows the DRK isotherms for H_2 adsorbed on metallic surfaces like copper or stainless steel between 3.0 K and 4.2 K ($1/\sqrt{D} = 5.26$ meV, $k_B = 8.63 \cdot 10^{-2}$ meV/K, $\theta_m = 3 \cdot 10^{15}$ molecules/cm^2).

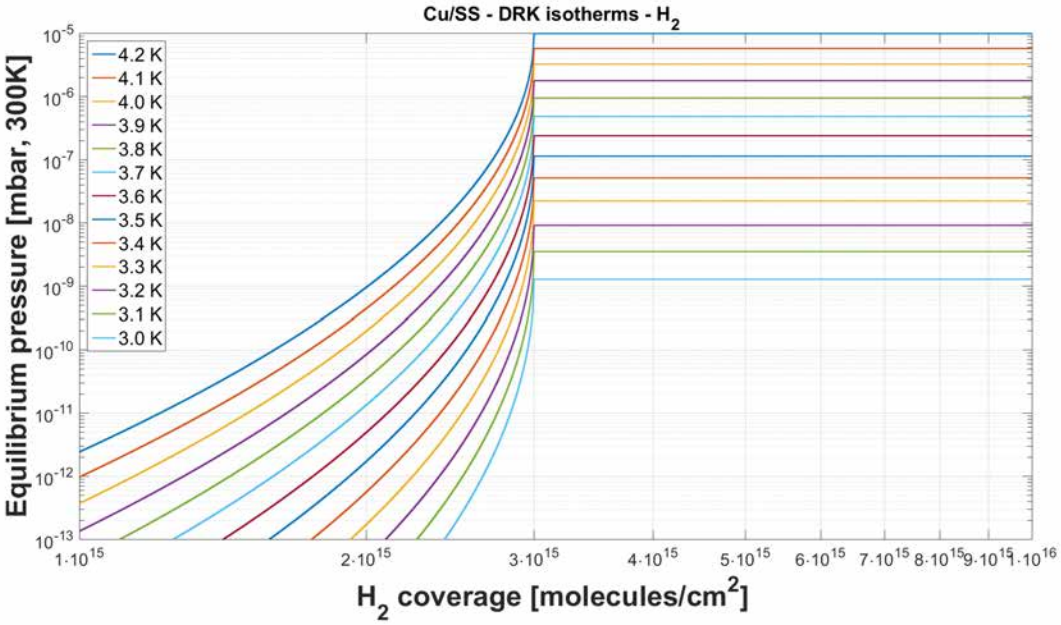

Figure A.5: DRK isotherms between 3.0 K and 4.2 K for H_2 adsorbed on metallic surfaces like copper or stainless steel.

The adsorption isotherms of stainless steel measured at LHe temperature [199] are plotted in Fig. A.5. The vapour pressure increases when increasing the adsorption of gas up to a few monolayers ($\sim 10^{15}$ molecules/cm^2). As soon as the surface has been filled, the vapour pressure saturates and the pressure level corresponds to the saturated vapour pressure (Clausius-Clapeyron), which is only a function of the temperature.

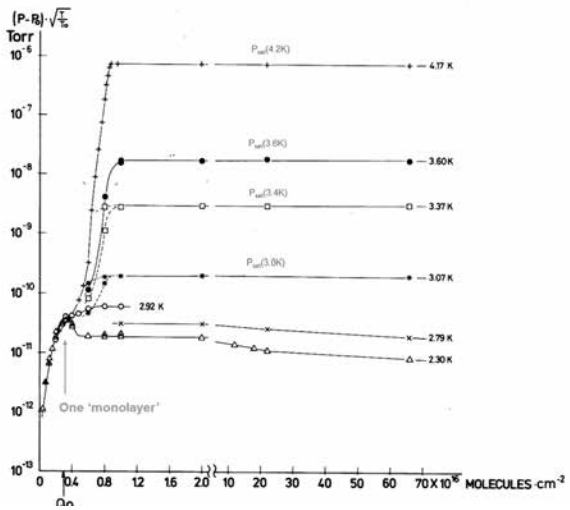

Figure A.6: Adsorption isotherms of H_2 on stainless steel measured at LHe temperatures. From [199].

A.6 Saturated vapour pressure

The saturated vapour pressure of the gases is the pressure of the gas over its condensate at a given temperature. It is reached when many monolayers of gas have been condensed. The saturated vapour pressure follows the Clausius-Clapeyron equation, which is in its simplest form:

$$log(p_{\mathrm{sat}}) = A - \frac{B}{T} \tag{A.26}$$

As a practical example, $A = -41.6$ Torr and $B = 3.85$ Torr·K for H_2 between 1 and 300 K [200].

In Fig. A.6, the saturated vapour pressures - corrected for the thermal transpiration and so when measured at room temperature - of the gases most common for UHV are shown as a function of temperature. Among all the gas species, only Ne, H_2 and He have p_{sat} higher than 10^{-11} mbar at 20 K. The p_{sat} of H_2 at LHe temperature is in the 10^{-7} mbar range, while is 10^{-11} mbar at 1.9 K. i.e. varies 4 orders of magnitude over a ΔT of only 2.3 K.

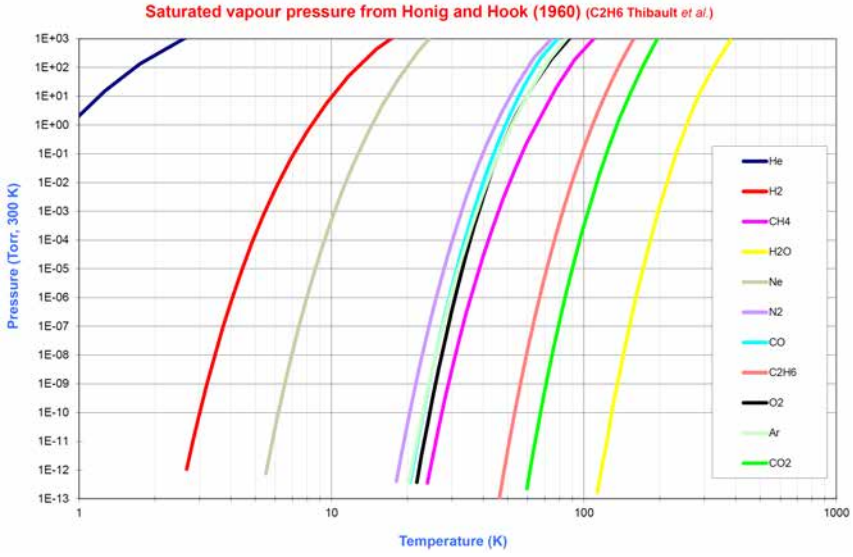

Figure A.7: Saturated vapour pressure of the most common gases present in UHV as a function of temperature, from [201] and references therein. Courtesy of V. Baglin, 1998.

A.7 Thermal Desorption Spectroscopy

The thermal desorption process is characterized by the sojourn time τ, or mean surface lifetime, given by

$$\tau = \tau_0 e^{\frac{E_d}{k_B T}} \tag{A.27}$$

where E_d is the activation energy of desorption (or binding energy), and τ_0 is the Frenkel period, inverse of the frequency of vibration of the molecule ν_0, expected $\sim 10^{-13}$ s at room temperature.

The probability of escape is

$$\nu = \nu_0 e^{-\frac{E_d}{k_B T}}. \tag{A.28}$$

We observe that the higher is the temperature, the shorter is the sojourn time. This relation is routinely exploited for bake-out of a vacuum system, when mainly H_2O is desorbed from the surface held above 100°C. Molecules with even low binding energy, like physisorbed molecules, have instead significant sojourn time at cryogenic temperature.

When gas molecules are thermally desorbed from a surface at a given activation energy of desorption E_d, the rate of desorption is given by the Arrhenius equation

$$-\frac{d\theta}{dt} = v_n \theta^n e^{-\frac{E_d}{k_B T}} \tag{A.29}$$

where θ is the surface coverage (molecules/cm^2), n is the reaction order (1 for simply adsorbed molecules, 2 for a two-steps desorption kinetics) and v_n is the characteristic rate constant. In the first-order desorption model, which applies to molecules non-dissociatively adsorbed to a surface, the desorption rate depends linearly on the surface coverage θ.

The activation energy for desorption, E_d, can be measured by recording the pressure while the sample temperature T is increased heating at constant rate β, i.e. $T = T_0 + \beta t$. During the warm-up, the desorbed molecules are evacuated from the system. In order to avoid the effect of re-adsorption during the process, either the desorption sweep is made short compared to the characteristic pumping time or, inversely, very high pumping speed is provided. Under the cited assumptions and in presence of non-associative desorption, E_d is derived imposing the first derivative of the Arrhenius equation to zero (maximum desorption rate):

$$\frac{d\theta}{dt}\left(v_n \theta^n e^{-\frac{E_d}{k_B T}}\right) = 0 \tag{A.30}$$

For a first-order reaction, it results

$$\frac{E_d}{k_B T_p^2} = \frac{v_1}{\beta} e^{-\frac{E_d}{k_B T_p}} \tag{A.31}$$

where T_p is the maximum desorption rate temperature. The characteristic rate constant v_1 is expected to be corresponding to the inverse of the Frenkel frequency of vibration of the molecule ν_0, in the order of 10^{13} Hz at room temperature. E_d is derived by solving the implicit Eq. A.31, e.g. by trial and improvement method, considering an initial guess sized to the studied adsorption mechanism (e.g. meV for physisorbed molecules, eV for chemisorbed). In a first-order reaction, for a given heating rate, T_p is independent of the initial coverage and the desorption peak is asymmetric. A reduction in the heating rate, i.e. a slower warm-up, shifts the temperature corresponding to the maximum desorption rate towards lower values, and the desorption peak width is increased in time. If Fig. A.8, the weak influence of the heating rate $log(\beta)$ over the maximum desorption rate temperature T_p for an arbitrary activation energy for desorption is shown.

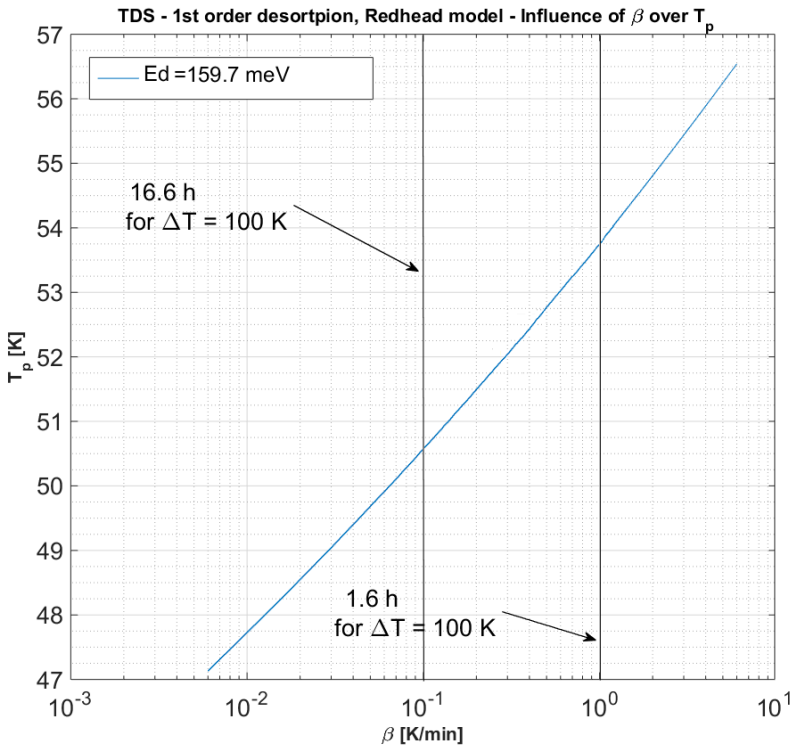

Figure A.8: Influence of the heating rate β over the maximum desorption rate temperature T_p for an arbitrary activation energy for desorption E_d=159.7 meV.

Solving Eq. A.30 this time for a second-order reaction, it results

$$\frac{E_d}{k_B T_p^2} = \begin{cases} \frac{2\theta_p v_2}{\beta} e^{-\frac{E_d}{k_B T_p}} \\ \frac{\theta_0 v_2}{\beta} e^{-\frac{E_d}{k_B T_p}} \end{cases} \tag{A.32}$$

where θ_0 is the initial surface coverage and θ_p=$\theta(T = T_p)$. It can be shown that $\theta_0/\theta_p \approx 2$ [171]. Rewriting the second of Eq. A.32, a second order reaction leads a straight line in the $ln(\theta_0 T_p^2)$ vs. $1/T_p$ phase space,

$$ln(\theta_0 T_p^2) = \frac{E_d}{k_B}\frac{1}{T_p} + ln\left(\beta \frac{E_d}{v_2 k_B}\right) \tag{A.33}$$

where the activation energy for desorption is calculated from the slope $\frac{E_d}{k_B}$. The characteristic rate constant v_2 (in cm^2/s), sometimes called pre-exponential factor, is derived by substitution in Eq. A.32,

$$v_2 = \frac{\frac{E_d}{k_B T_p^2}\frac{\beta}{\theta_0}}{e^{-\frac{E_d}{k_B T_p}}}. \tag{A.34}$$

In a second-order reaction, for a given heating rate, the maximum desorption rate temperature (T_p) is dependent of the initial coverage and the desorption peak is symmetric.

Bibliography

[1] D. Rej, "High-power LINAC for the Spallation Neutron Source," in *Pulsed Power Plasma Science, IEEE Conference Record*, 2001.

[2] Y. Yamazaki, K. Hasegawa, M. Ikegami, Y. Irie, T. Kato, H. Kobayashi, S. Machida, Y. Mori, F. Noda, H. Suzuki, *et al.*, "Accelerator technical design report for J-PARC," *J-PARC-03-01*, 2003.

[3] C. Wilson, "ISIS, the UK spallation neutron source: a guided tour," *Neutron News*, vol. 1, no. 1, pp. 14–19, 1990.

[4] M. Lindroos, C. Oyon, and S. Peggs, "The ESS superconducting linear accelerator," in *Proceedings of 14th International Conference on RF Superconductivity (SRF2009)*, 2009.

[5] J. Wei, H. Chen, Y. Chen, Y. Chen, Y. Chi, C. Deng, H. Dong, L. Dong, S. Fang, J. Feng, *et al.*, "China Spallation Neutron Source: design, R&D, and outlook," *Nuclear Instruments and Methods in Physics Research Section A: Accelerators, Spectrometers, Detectors and Associated Equipment*, vol. 600, no. 1, pp. 10–13, 2009.

[6] M. Vretenar, "Conceptual design of the SPL, a high-power superconducting H- LINAC at CERN," *CERN-2000-012*, 2000.

[7] M. Lewitowicz, "The SPIRAL 2 project," in *Proceedings of Symposium on Nuclear Physics VI (TOURS 2006)*, vol. 891, pp. 91–98, 2006.

[8] P. Spiller and G. Franchetti, "The FAIR accelerator project at GSI," *Nuclear Instruments and Methods in Physics Research Section A: Accelerators, Spectrometers, Detectors and Associated Equipment*, vol. 561, no. 2, pp. 305–309, 2006.

[9] H. A. Abderrahim, "MYRRHA: an innovative and unique research facility," in *Proceedings of 10th International Topical Meeting on Nuclear Applications of Accelerators (AccApp'11)*, 2011.

[10] J.-Y. Tang, Z. Li, *et al.*, "Conceptual Physics Design on the C-ADS Accelerators," *IHEP-CADS-Report/2012-01E*, 2012.

[11] M. Martone, V. Teplyakov, M. Rennich, A. Moeslang, H. Katsuta, T. Shannon, H. Maekawa, and R. Jameson, "IFMIF (International Fusion Materials Irradiation Facility): A High Intensity Deuteron Beam Application," 1998.

[12] L. R. Evans, *The Large Hadron Collider: a marvel of technology*. EPFL Press, 2009.

[13] F. Zimmermann, "Electron-cloud effects in past and future machines-walk through 50 years of electron-cloud studies," in *Proceedings of 5th Workshop on Electron-Cloud Effects (ECLOUD'12)*, 2012.

[14] O. Dominguez, K. Li, G. Arduini, E. Métral, G. Rumolo, F. Zimmermann, and H. M. Cuna, "First electron-cloud studies at the Large Hadron Collider," *Physical Review Special Topics-Accelerators and Beams*, vol. 16, no. 1, p. 011003, 2013.

[15] W. Fischer, M. Blaskiewicz, J. Brennan, H. Huang, H.-C. Hseuh, V. Ptitsyn, T. Roser, P. Thieberger, D. Trbojevic, J. Wei, *et al.*, "Electron cloud observations and cures in the Relativistic Heavy Ion Collider," *Physical Review Special Topics-Accelerators and Beams*, vol. 11, no. 4, p. 041002, 2008.

[16] H. Fukuma, "Electron cloud observations and predictions at KEKB, PEP-II and SuperB Factories," in *Proceedings of 5th Workshop on Electron-Cloud Effects (ECLOUD'12)*, 2012.

[17] M. Zobov, D. Alesini, A. Drago, A. Gallo, S. Guiducci, C. Milardi, A. Stella, S. De Santis, T. Demma, and P. Raimondi, "Operating experience with electron cloud clearing electrodes at DAFNE," in *Proceedings of 5th Workshop on Electron-Cloud Effects (ECLOUD'12)*, 2012.

[18] L. Rossi, "LHC upgrade plans: options and strategy," in *Proceedings of 2nd International Particle Accelerator Conference (IPAC 2011)*, 2011.

[19] Y. Ohnishi, T. Abe, T. Adachi, K. Akai, Y. Arimoto, K. Ebihara, K. Egawa, J. Flanagan, H. Fukuma, Y. Funakoshi, *et al.*, "Accelerator design at SuperKEKB," *Progress of Theoretical and Experimental Physics*, vol. 2013, no. 3, 2013.

[20] R. Salemme *et al.*, "Recommissioning of the COLDEX experiment at CERN," in *Proceedings of 6th International Particle Accelerator Conference (IPAC 2015)*, 2015.

[21] M. Reiser, *Theory and design of charged particle beams*. John Wiley & Sons, 2008.

[22] T. P. Wangler, *RF Linear accelerators*. John Wiley & Sons, 2008.

[23] S. Humphries, *Charged particle beams*. Courier Corporation, 2013.

[24] M. Ferrario, "Accelerator physics: basic principles on beam focusing and transport," in *Proceedings of the International School of Physics Enrico Fermi "Laser-Plasma Acceleration"*, 2011.

[25] K. Schindl, "Space charge," in *Proceedings of the Joint US-CERN-Japan-Russia School on Particle Accelerators*, 1998.

[26] I. M. Kapchinskiy and V. V. Vladimirskiy, "Limitations of proton beam current in a strong focusing linear accelerator associated with beam space charge," in *Proceedings of 2nd International Conference on High Energy Accelerators*, 1959.

[27] P. Lapostolle, "Possible emittance increase through filamentation due to space charge in continuous beams," *IEEE Trans. Nuc. Sci. NS-18, No. 3, 1101*, 1971.

[28] F. Sacherer, "RMS envelope equations with space charge," *IEEE Trans. Nuc. Sci. NS-18, No. 3, 1105*, 1971.

[29] A. Ben Ismail, *Etude des effets transitoires de la Compensation de Charge d'Espace sur la dynamique dun faisceau intense*. PhD thesis, Université Paris XI, 2005.

[30] Y. Baconnier, A. Poncet, and P. Tavares, "Neutralization of accelerator beams by ionization of the residual gas," in *Proceedings of CAS-CERN Accelerator School: General Accelerator Physics, CERN-1985-019-V-1*, 1992.

[31] I. A. Soloshenko, "Space charge compensation of technological ion beams," *Plasma Science, IEEE Transactions on*, vol. 27, no. 4, pp. 1097–1100, 1999.

[32] R. Ferdinand, J. Sherman, R. R. Stevens Jr, and T. Zaugg, "Space-charge neutralization measurement of a 75 keV, 130 mA hydrogen ion beam," in *Proceedings of 17th Particle Accelerator Conference (PAC'97)*, 1997.

[33] R. Gobin, P.-Y. Beauvais, R. Ferdinand, P.-A. Leroy, L. Celona, G. Ciavola, and S. Gammino, "Improvement of beam emittance of the CEA high intensity proton source SILHI," *Review of scientific instruments*, vol. 70, no. 6, pp. 2652–2654, 1999.

[34] X. Fleury, *Modelization and simulation of proton beam space charge compensation.* PhD thesis, 2000.

[35] J. Sherman, E. Pitcher, R. Stevens, and P. Allison, "H- beam neutralization measurements in a solenoidal beam transport system," in *Proceedings of Production and neutralization of negative ions and beams*, 1992.

[36] J.-L. Vay and C. Deutsch, "Intense ion beam propagation in a reactor sized chamber," *Nuclear Instruments and Methods in Physics Research Section A: Accelerators, Spectrometers, Detectors and Associated Equipment*, vol. 464, no. 1, pp. 293–298, 2001.

[37] A. BenIsmail, R. Duperrier, D. Uriot, and N. Pichoff, "Space charge compensation studies of hydrogen ion beams in a drift section," *Physical Review Special Topics-Accelerators and Beams*, vol. 10, no. 7, p. 070101, 2007.

[38] R. Keller, R. Thomae, M. Stockli, and R. Welton, "Design, operational experiences and beam results obtained with the SNS H- ion source and LEBT at Berkeley Lab," in *Proceedings of Ninth International Symposium on Production and neutralization of negative ions and beams*, 2002.

[39] J.-L. Biarrotte, D. Uriot, D. Klein, H. Podlech, D. Mader, R. Tiede, C. Zhang, and D. Vandeplassche, "Design fine-tuning & beam simulation codes benchmarking," *MYRRHA Accelerator Experiment (MAX) Delivrable n. 1.2*, 2013.

[40] M. Cumo, *Impianti nucleari.* Casa Editrice Università La Sapienza, 2008.

[41] C. Rubbia, C. Roche, J. A. Rubio, F. Carminati, Y. Kadi, P. Mandrillon, J. P. C. Revol, S. Buono, R. Klapisch, and N. Fiétier, "Conceptual design of a fast neutron operated high power energy amplifier," Tech. Rep. CERN-AT-95-44-ET, CERN, Geneva, Sep 1995.

[42] H. A. Abderrahim, J. Galambos, Y. Gohar, S. Henderson, G. Lawrence, T. McManamy, A. Mueller, S. Nagaitsev, J. Nolen, and E. Pitcher, "Accelerator and target technology for accelerator driven transmutation and energy production," *DOE White Paper on ADS*, 2010.

[43] NEA Nuclear Science Committee, "Accelerator-driven Systems (ADS) and fast reactor (FR) in advanced nuclear cycles: A comparative study," 2002.

[44] A. Billebaud, P. Baeten, H. A. Abderrahim, G. Ban, M. Baylac, G. Bergmans, D. Bondoux, J. Bouvier, S. Chabod, and J. M. De Conto, "The GUINEVERE project for accelerator driven system physics," in *Proceedings of International Conference "GLOBAL 2009" The Nuclear Fuel Cycle: Sustainable Options and Industrial Perspectives"*, 2009.

[45] M. Plum, "Status of the SNS power ramp up," in *Proceedings of 1st International Particle Accelerator Conference (IPAC 2010)*, 2010.

[46] A. Apollonio, R. Schmidt, M. Jonker, D. Wollmann, M. Zerlauth, S. Wagner, and B. Todd, "HL-LHC: integrated luminosity and availability," in *Proceedings of 4th International Particle Accelerator Conference (IPAC 2013*, 2013.

[47] G. Rimpault, P. Darde, F. Mellier, R. Dagan, M. Schikorr, A. Weisenburger, D. Maes, V. Sobolev, B. Arien, D. Lamberts, *et al.*, "The issue of accelerator beam trips for efficient ADS operation," *Nuclear Technology*, vol. 184, no. 2, pp. 249–260, 2013.

[48] A. Woaye-Hune in *CDT project meeting*, Bruxelles, Belgium, October 2009.

[49] H. Takei, K. Nishihara, K. Tsujimoto, and H. Oigawa, "Estimation of acceptable beam-trip frequencies of accelerators for accelerator-driven systems and comparison with existing performance data," *Journal of nuclear science and technology*, vol. 49, no. 4, pp. 384–397, 2012.

[50] B. Giraud, L. Cinotti, and B. Farrar, "Preliminary engineering requirements on accelerators for ADS," in *Proceedings of 2nd Workshop on Utilisation and reliability of high power proton accelerators*, 2001.

[51] J. Biarrotte, A. Mueller, H. Klein, P. Pierini, and D. Vandeplassche, "Accelerator reference design for the MYRRHA European ADS demonstrator," in *Proceedings of 25th Linear Accelerator Conference (LINAC10)*, 2010.

[52] D. Vandeplassche, J.-L. Biarrotte, H. Klein, and H. Podlech, "The MYRRHA linear accelerator," in *Proceedings of 2nd International Particle Accelerator Conference (IPAC 2011)*, 2011.

[53] D. Vandeplassche and L. M. Romao, "Accelerator driven systems," in *Proceedings of 3rd International Particle Accelerator Conference (IPAC 2012)*, 2012.

[54] J. Galambos, T. Koseshi, and M. Seidel, "Commissioning strategies, operations and performance, beam loss management, activation, machine protection," in *Proceedings of 42nd ICFA Advanced Beam Dynamics Workshop on High-Intensity, High-Brightness Hadron Beams*, 2008.

[55] S.-H. Kim, "SNS lessons learned from design, integration, and operation," in *4th Open Collaboration Meeting on Superconducting Linacs for High Power Proton Beams (SLHiPP-4)*, 2014.

[56] M. Seidel, S. Adam, A. Adelmann, C. Baumgarten, Y. Bi, R. Doelling, H. Fitze, A. Fuchs, M. Humbel, J. Grillenberger, *et al.*, "Production of a 1.3 MW proton beam at PSI," in *Proceedings of 1st International Particle Accelerator Conference (IPAC 2010)*, 2010.

[57] G. Kim, D. May, P. McIntyre, and A. Sattarov, "A superconducting isochronous cyclotron stack as a driver for a thorium-cycle power reactor," in *Proceedings of 19th Particle Accelerator Conference (PAC 2001)*, 2001.

[58] S. Sheehy, C. Johnstone, R. Barlow, and A. Adelmann, "The potential for a high power FFAG proton driver for ads," in *Proceedings of Eleventh International Topical Meeting on Nuclear Applications of Accelerators (AccApp'13)*, 2013.

[59] "MYRRHA project website." http://myrrha.sckcen.be.

[60] L. Burgazzi and P. Pierini, "Reliability studies of a high-power proton accelerator for accelerator-driven system applications for nuclear waste transmutation," *Reliability Engineering & System Safety*, vol. 92, no. 4, pp. 449–463, 2007.

[61] J. Cornell, "Final report of the EURISOL Design Study," *European Commission (EU) Contract nr. 515768*, 2009.

[62] J.-L. Biarrotte and D. Uriot, "Dynamic compensation of an RF cavity failure in a superconducting linac," *Physical Review Special Topics - Accelerators and Beams*, vol. 11, no. 7, 2008.

[63] J.-P. Carneiro, L. Medeiros Romao, R. Salemme, D. Vandeplassche, J.-L. Biarotte, F. Bouly, and D. Uriot, "Approach of a failure analysis for the MYRRHA linac," in *Proceedings of 2nd International Workshop on Technology and Components of Accelerator-Driven Systems (TCADS-2)*, 2013.

[64] H. Podlech, M. Amberg, H. Klein, D. Mäder, U. Ratzinger, A. Schempp, R. Tiede, M. Vossberg, and C. Zhang, "General layout of the 17 MeV injector for MYRRHA," in *Proceedings of 2nd International Particle Accelerator Conference (IPAC 2011)*, 2011.

[65] "MYRRHA Accelerator eXperiment (MAX) R&D program website." http://ipnwww.in2p3.fr/MAX/.

[66] J. Biarrotte, D. Uriot, F. Bouly, J. Carneiro, and D. Vandeplassche, "Design of the MYRRHA 17-600 MeV superconducting linac," in *Proceedings of 16th International Conference on RF Superconductivity (SRF2013)*, 2013.

[67] M. El Yakoubi, H. Saugnac, E. Rampenoux, J. L. Biarrotte, F. Bouly, R. Paparella, and P. Pierini, "Superconducting RF cavitiesactivities for the MAX project," in *Proceedings of 2nd International Workshop on Technology and Components of Accelerator-Driven Systems (TCADS-2)*, 2013.

[68] A. Bosotti, C. Pagani, P. Pierini, J. Charrier, B. Visentin, G. Ciovati, and P. Kneisel, "RF tests of the β=0.5 five cell TRASCO cavities," in *Proceedings of 9th European Particle Accelerator Conference (EPAC'04)*, 2004.

[69] B. Visentin, J. Charrier, D. Roudier, F. Simoens, E. Jacques, A. Aspart, Y. Gasser, J. Poupeau, P. Sahuquet, D. Braud, *et al.*, "Experimental results on 700 MHz multicell superconducting cavity for proton linac," in *Proceedings of 20th Particle Accelerator Conference (PAC 2003)*, 2003.

[70] F. Bouly, J. Biarrotte, and D. Uriot, "Fault tolerance and consequences in the MYRRHA superconducting linac," in *Proceedings of 27th Linear Accelerator Conference (LINAC14)*, 2014.

[71] J. L. Biarrotte, D. Uriot, L. Medeiros Romao, and D. Vandeplassche, "Beam operation aspects for the MYRRHA linear accelerator," in *Proceedings of 2nd International Workshop on Technology and Components of Accelerator-Driven Systems (TCADS-2)*, 2013.

[72] D. Vandeplassche, L. Medeiros-Romao, R. Salemme, J. Biarrotte, I. Orsay, F. Bouly, L. Grenoble, and J. Carneiro, "Toward a virtual accelerator control system for the MYRRHA linac," in *Proceedings of 5th International Particle Accelerator Conference (IPAC 2014)*, 2014.

[73] D. Uriot and N. Pichoff, "TraceWin documentation," 2011.

[74] V. Aseev, P. Ostroumov, E. Lessner, B. Mustapha, *et al.*, "TRACK: The new beam dynamics code," in *Proceedings of 21st Particle Accelerator Conference (PAC 2005)*, 2005.

[75] R. Salemme, D. Vandeplassche, L. M. Romão, J.-P. Carneiro, J.-L. Biarrotte, M. Baylac, D. Uriot, and H. Podlech, "The R&D@ UCL program in support of the MYRRHA Linear Accelerator," in *Proceedings of 2nd International Workshop on Technology and Components of Accelerator-Driven Systems (TCADS-2)*, 2013.

[76] C. Zhang, H. Klein, D. Mäder, H. Podlech, U. Ratzinger, A. Schempp, and R. Tiede, "From EUROTRANS to MAX: new strategies and approaches for the injector development," in *Proceedings of 2nd International Particle Accelerator Conference (IPAC 2011)*, 2011.

[77] C. Zhang, H. Klein, D. Mäder, H. Podlech, U. Ratzinger, A. Schempp, R. Tiede, and M. Vossberg, "Front-end linac design and beam dynamics simulations for MYRRHA," in *Proceedings of 26th Linear Accelerator Conference (LINAC12)*, 2012.

[78] D. Mäder, D. Koser, H. Podlech, and A. Schempp, "Consolidated design of the 17 MeV injector for MYRRHA," in *Proceedings of 16th International Conference on RF Superconductivity (SRF2013)*, 2013.

[79] D. Mäder, M. Basten, D. Koser, H. Lenz, N. Petry, H. Podlech, A. Schempp, M. Schwarz, M. Vossberg, and C. Zhang, "R&D of the 17 MeV MYRRHA injector," in *Proceedings of 27th Linear Accelerator Conference (LINAC14)*, 2014.

[80] R. Salemme, L. M. Romão, D. Vandeplassche, D. Uriot, J.-L. Biarrotte, M. Baylac, D. Bondoux, F. Bouly, J. De Conto, and E. Froidefond, "Design progress of the MYRRHA Low Energy Beam Line," in *Proceedings of 27th Linear Accelerator Conference (LINAC14)*, 2014.

[81] "PANTECHNIK webpage." http://www.pantechnik.com.

[82] R. Geller, *Electron cyclotron resonance ion sources and ECR plasmas*. CRC Press, 1996.

[83] T. Taylor and J. S. Wills, "A high-current low-emittance DC ECR proton source," *Nuclear Instruments and Methods in Physics Research Section A: Accelerators, Spectrometers, Detectors and Associated Equipment*, vol. 309, no. 1, pp. 37–42, 1991.

[84] J.-Y. Pacquet and R. Leroy, "Magnetic system, particularly for ECR sources, for producing closed surfaces of equimodule B of form dimensions," 2001. US Patent 6194836.

[85] N. Chauvin, O. Delferrière, R. Duperrier, R. Gobin, P. Nghiem, and D. Uriot, "Transport of intense ion beams and space charge compensation issues in low energy beam lines," *Review of Scientific Instruments*, vol. 83, no. 2, 2012.

[86] "OPERA-3D Reference Manual," *Vector Fields Limited, England*, 2004.

[87] "ISOL@MYRRHA webpage." http://isolmyrrha.sckcen.be.

[88] J. H. Billen and L. M. Young, "Poisson Superfish on PC compatibles," in *Proceedings of 15th Particle Accelerator Conference (PAC'93)*, 1993.

[89] J. F. Ziegler, "TRIM-90: The Transport of Ions in Matter," in *International Business Machines-Research*, 1990.

[90] H. Bayle, O. Delferrière, R. Gobin, F. Harrault, J. Marroncle, F. Senée, C. Simon, and O. Tuske, "Effective shielding to measure beam current from an ion source," *Review of Scientific Instruments*, vol. 85, no. 2, 2014.

[91] J.-L. Biarrotte, P. Bertrand, and D. Uriot, "Beam dynamics studies for the SPIRAL-2 project," in *Proceedings of 10th European Particle Accelerator Conference (EPAC'06)*, 2006.

[92] R. Gobin, P. Beauvais, G. Charruau, O. Delferrière, D. De Menezes, R. Ferdinand, Y. Gauthier, Y. Harrault, P. Leherissier, and J. Paquet, "Development of a permanent magnet ECR source to produce a 5mA deuteron beam at CEA saclay," in *Proceedings of 20th Linear Accelerator Conference (LINAC 2004)*, 2004.

[93] N. Chauvin, O. Delferrière, R. Duperrier, R. Gobin, P. Nghiem, and D. Uriot, "Source and injector design for intense light ion beams including space charge neutralisation," in *Proceedings of 25th Linear Accelerator Conference (LINAC10)*, 2010.

[94] D. Uriot and O. Tuske, "Commissioning of the SPIRAL2 deuteron injector," in *Proceedings of 4th International Particle Accelerator Conference (IPAC 2013)*, 2013.

[95] M. E. Rudd, R. DuBois, L. Toburen, C. Ratcliffe, and T. Goffe, "Cross sections for ionization of gases by 5–4000 keV protons and for electron capture by 5–150 keV protons," *Physical Review A*, vol. 28, no. 6, p. 3244, 1983.

[96] J.-L. Vay, D. Grote, R. Cohen, and A. Friedman, "Novel methods in the particle-in-cell accelerator code-framework WARP," *Computational Science & Discovery*, vol. 5, no. 1, p. 014019, 2012.

[97] "CERN Courier, Jun 28, 1999." http://cerncourier.com/cws/article/cern/28045/.

[98] F. F. Rieke and W. Prepejchal, "Ionization cross sections of gaseous atoms and molecules for high-energy electrons and positrons," *Physical Review A*, vol. 6, no. 4, 1972.

[99] O. Gröbner, "Dynamic outgassing," in *Proceedings of CAS-CERN Accelerator School: Vacuum Technology, CERN-1999-005*, 1999.

[100] A. Hofmann, "Characteristics of synchrotron radiation," in *Proceedings of CAS-CERN Accelerator School: Synchrotron Radiation and Free Electron Lasers, CERN 98-04*, 1998.

[101] V. Baglin, G. Bregliozzi, G. Lanza, and J. M. Jimenez, "Synchrotron radiation in the LHC vacuum system," in *Proceedings of 2nd International Particle Accelerator Conference (IPAC 2011)*, 2011.

[102] G. L. Weissler, "Handbuch der physik, vol. 21," 1956.

[103] N. Mahne, V. Baglin, I. Collins, A. Giglia, L. Pasquali, M. Pedio, S. Nannarone, and R. Cimino, "Photon reflectivity distributions from the LHC beam screen and their implications on the arc beam vacuum system," *Applied surface science*, vol. 235, no. 1, pp. 221–226, 2004.

[104] "Center for X-Ray Optics database, Lawrence Berkeley National Laboratory." http://henke.lbl.gov/optical_constants/.

[105] V. Baglin, I. Collins, and O. Gröbner, "Photoelectron yield and photon reflectivity from candidate LHC vacuum chamber materials with implications to the vacuum chamber design," in *Proceedings of 6th European Particle Accelerator Conference (EPAC'98)*, 1998.

[106] V. Anashin, O. Malyshev, N. Fedorov, V. Nazmov, B. Goldenberg, I. Collins, and O. Gröbner, "Reflection of photons and azimuthal distribution of photoelectrons in a cylindrical beam pipe," *Nuclear Instruments and Methods in Physics Research Section A: Accelerators, Spectrometers, Detectors and Associated Equipment*, vol. 448, no. 1, pp. 76–80, 2000.

[107] R. Cimino, I. Collins, and V. Baglin, "VUV photoemission studies of candidate Large Hadron Collider vacuum chamber materials," *Physical Review Special Topics-Accelerators and Beams*, vol. 2, no. 6, p. 063201, 1999.

[108] H. Wiedemann, *Synchrotron radiation*. Springer, 2003.

[109] O. B. Malyshev, "The ion impact energy on the LHC vacuum chamber walls," in *Proceedings of 7th European Particle Accelerator Conference (EPAC 2000)*, 2000.

[110] P. Thieberger, A. Hanson, D. Steski, V. Zajic, S. Zhang, and H. Ludewig, "Secondary-electron yields and their dependence on the angle of incidence on stainless-steel surfaces for three energetic ion beams," *Physical Review A*, vol. 61, no. 4, 2000.

[111] L. Wang, D. Raparia, J. Wei, and S. Zhang, "Mechanism of electron cloud clearing in the accumulator ring of the Spallation Neutron Source," *Physical Review Special Topics-Accelerators and Beams*, vol. 7, no. 3, p. 034401, 2004.

[112] V. Baglin, G. Vorlaufer, N. Hilleret, I. Collins, and B. Henrist, "A summary of main experimental results concerning the secondary electron emission of copper," in *CERN-LHC-Project-Report-472*, 2001.

[113] R. Cimino, I. Collins, M. Furman, M. Pivi, F. Ruggiero, G. Rumolo, and F. Zimmermann, "Can low-energy electrons affect high-energy physics accelerators?," *Physical review letters*, vol. 93, no. 1, 2004.

[114] R. Cimino and I. Collins, "Vacuum chamber surface electronic properties influencing electron cloud phenomena," *Applied surface science*, vol. 235, no. 1, 2004.

[115] R. Cimino and T. Demma, "Electron cloud in accelerators," *International Journal of Modern Physics A*, vol. 29, no. 17, 2014.

[116] R. Cimino, L. A. Gonzalez, R. Larciprete, A. Di Gaspare, G. Iadarola, and G. Rumolo, "Detailed investigation of the low energy secondary electron yield of technical Cu and its relevance for the LHC," *Physical Review Special Topics-Accelerators and Beams*, vol. 18, no. 5, 2015.

[117] M. Furman and M. Pivi, "Probabilistic model for the simulation of secondary electron emission," *Physical Review Special Topics-Accelerators and Beams*, vol. 5, no. 12, 2002.

[118] B. Henrist, G. Vorlaufer, C. Scheuerlein, N. Hilleret, M. Taborelli, and M. Jiménez, "Secondary electron emission data for the simulation of electron cloud," in *Proceedings of Mini Workshop on Electron Cloud Simulations for Proton and Positron Beams, CERN-2002-001*, 2002.

[119] J. Scholtz, D. Dijkkamp, and R. Schmitz, "Secondary electron emission properties," *Philips journal of research*, vol. 50, no. 3, pp. 375–389, 1996.

[120] R. Kirby and F. King, "Secondary electron emission yields from PEP-II accelerator materials," *Nuclear Instruments and Methods in Physics Research Section A: Accelerators, Spectrometers, Detectors and Associated Equipment*, vol. 469, no. 1, pp. 1–12, 2001.

[121] S. Kheifetes, "Three dimensional potential for gaussian bunch," *DESY Petra Note*, vol. 119, 1976, based on the original work by Houssain.

[122] M. Bassetti and G. Erskine, "Closed expression for the electrical field of a two-dimensional gaussian charge," tech. rep., CERN-ISRTH/80-06, 1980.

[123] G. Iadarola, *Electron cloud studies for CERN particle accelerators and simulation code development*. PhD thesis, CERN-THESIS-2014-047, 2014.

[124] G. Iadarola and G. Rumolo, "PyECLOUD and build-up simulations at CERN," in *Proceedings of 5th Workshop on Electron-Cloud Effects (ECLOUD'12)*, 2013.

[125] M. A. Furman and G. R. Lambertson, "The electron-cloud instability in the arcs of the PEP-II positron ring," *LBNL41123*, 1998.

[126] L. Wang, H. Fukuma, K. Ohmi, S. Kurokawa, K. Oide, and F. Zimmermann, "Numerical study of the photoelectron cloud in KEKB Low Energy Ring with a three-dimensional particle in cell method," *Physical Review Special Topics-Accelerators and Beams*, vol. 5, no. 12, 2002.

[127] J. S. Berg, "Energy gain in an electron cloud during the passage of a bunch," *LHC-Project-Note-97*, 1997.

[128] O. Gröbner, "Beam induced multipacting," in *Proceedings of the 10th International Conference on High-Energy Accelerators, Protvino, Russia*, Institute of High Energy Physics, 1977.

[129] O. Gröbner, "Beam induced multipacting," in *Proceedings of 17th Particle Accelerator Conference (PAC'97)*, 1997.

[130] G. Rumolo, H. Bartosik, and L. Kevin, "Collective Effects in Beam Dynamics course," *US Particle Accelerator School*, 2015.

[131] D. Menzel, "Thirty years of MGR: How it came about, and what came of it," *Nuclear Instruments and Methods in Physics Research Section B: Beam Interactions with Materials and Atoms*, vol. 101, no. 1, pp. 1–10, 1995.

[132] D. Menzel and R. Gomer, "Desorption from metal surfaces by low-energy electrons," *The Journal of Chemical Physics*, vol. 41, no. 11, pp. 3311–3328, 1964.

[133] V. Baglin and J. Jimenez, "Ultra-high vacuum," in *Landolt-Brnstein - Group I Elementary Particles, Nuclei and Atoms - Accelerators and Colliders*, pp. 278–290, 2013.

[134] F. Billard, N. Hilleret, and G. Vorlaufer, "Some results on the electron induced desorption yield of OFHC copper," *CERN Vacuum Technical Note 00-32*, 2000.

[135] H. Tratnik, N. Hilleret, and H. Störi, "The desorption of condensed noble gases and gas mixtures from cryogenic surfaces," *Vacuum*, vol. 81, no. 6, pp. 731–737, 2007.

[136] U. Iriso and S. Peggs, "Maps for electron clouds," *Physical Review Special Topics-Accelerators and Beams*, vol. 8, no. 2, 2005.

[137] V. Baglin, I. Collins, and B. Jenninger, "Performance of a cryogenic vacuum system (COLDEX) with an LHC type beam," *Vacuum*, vol. 73, no. 2, pp. 201–206, 2004.

[138] D. Alesini, B. Spataro, M. Migliorati, A. Mostacci, L. Palumbo, V. Baglin, B. Jenninger, and F. Ruggiero, "Coupling impedances studies and power loss measurements of the COLDEX upgraded vacuum chamber," *Nuclear Instruments and Methods in Physics Research Section A: Accelerators, Spectrometers, Detectors and Associated Equipment*, vol. 581, no. 3, pp. 885–889, 2007.

[139] L. Tavian, "Performance limitations of the LHC cryogenics: 2012 review and 2015 outlook," in *Proceedings of LHC beam operation Workshop, Evian*, 2012.

[140] W. Höfle, "Observation of the electron cloud effect on pick-up signals in the SPS," in *Proceedings of 10th Workshop on LEP-SPS Performance (Chamonix X)*, 2000.

[141] J. Jimenez, N. Hilleret, L. Jensen, F. Zimmermann, B. Henrist, G. Arduini, K. Weiss, G. Ferioli, and P. Collier, "Electron cloud with LHC-type beams in the SPS: a review of three years of measurements," in *Proceedings of Mini Workshop on Electron Cloud Simulations for Proton and Positron Beams, CERN-2002-001*, 2002.

[142] ATLAS collaboration *et al.*, "Observation of a new particle in the search for the Standard Model Higgs boson with the ATLAS detector at the LHC," *Physics Letters B*, vol. 716, no. 1, pp. 1–29, 2012.

[143] CMS collaboration *et al.*, "Observation of a new boson at a mass of 125 GeV with the CMS experiment at the LHC," *Physics Letters B*, vol. 716, no. 1, pp. 30–61, 2012.

[144] G. Bregliozzi, J. Hansen, V. Baglin, J. Jiménez, S. Blanchard, and K. Weiss, "Achievement and evaluation of the beam vacuum performance of the LHC long straight sections," in *Proceedings of 11th European Particle Accelerator Conference (EPAC'08)*, 2008.

[145] A. Rossi, "SEY and electron cloud build-up with NEG materials," in *Proceedings of 31st ICFA Advanced Beam Dynamics Workshop on Electron-Cloud Effects (ECLOUD'04)*, 2004.

[146] G. Bregliozzi, V. Baglin, P. Chiggiato, P. Cruikshank, J. Jimenez, G. Lan, *et al.*, "Observations of electron cloud effects with the LHC vacuum system," in *Proceedings of 2nd International Particle Accelerator Conference (IPAC 2011)*, 2011.

[147] B. Angerth, F. Bertinelli, J. Brunet, R. Calder, F. Caspers, O. Gröbner, *et al.*, "The LHC beam screen, specification and design," in *Proceedings of 4th European Particle Accelerator Conference (EPAC'94)*, 1994.

[148] O. Gröbner, "The LHC vacuum system," in *Proceedings of 17th Particle Accelerator Conference (PAC'97)*, 1997.

[149] V. Baglin, "Cold/sticky systems," in *Proceedings of CAS - CERN Accelerator School: Vacuum in Accelerators, CERN-2007-003*, 2007.

[150] V. Baglin, I. Collins, C. Grünhagel, O. Gröbner, and B. Jenninger, "First results from COLDEX applicable to the LHC cryogenic vacuum system," in *Proceedings of 7th European Particle Accelerator Conference (EPAC'00)*, 2000.

[151] F. Zimmermann, "A simulation study of electron-cloud instability and beam-induced multipacting in the LHC," *SLAC-PUB-7664*, 1997.

[152] N. Hilleret, V. Baglin, J. Bojko, C. Scheuerlein, O. Gröbner, M. Taborelli, and B. Henrist, "The secondary electron yield of technical materials and its variation with surface treatments," in *Proceedings of 7h European Particle Accelerator Conference (EPAC 2000)*, 2000.

[153] R. Cimino, M. Commisso, D. Grosso, T. Demma, V. Baglin, R. Flammini, and R. Larciprete, "Nature of the decrease of the secondary-electron yield by electron bombardment and its energy dependence," *Physical review letters*, vol. 109, no. 6, p. 064801, 2012.

[154] G. Ferlin, "Cryogenics," in *LHC Performance Workshop (Chamonix 2016)*, 2016.

[155] G. Iadarola and G. Rumolo, "Electron cloud effects and expected limitations in the HL-LHC era," in *3rd Joint Hi-Lumi LHC-LARP Annual Meeting*, 2013.

[156] G. Arduini, "Performance Limitations in HL-LHC after LIU Upgrade," in *LHC Performance Workshop (Chamonix 2016)*, 2016.

[157] P. C. Pinto, S. Calatroni, H. Neupert, D. Letant-Delrieux, P. Edwards, P. Chiggiato, M. Taborelli, W. Vollenberg, C. Yin-Vallgren, J. Colaux, *et al.*, "Carbon coatings with low secondary electron yield," *Vacuum*, vol. 98, pp. 29–36, 2013.

[158] C. Y. Vallgren, G. Arduini, J. Bauche, S. Calatroni, P. Chiggiato, K. Cornelis, P. C. Pinto, B. Henrist, E. Métral, H. Neupert, *et al.*, "Amorphous carbon coatings for the mitigation of electron cloud in the CERN Super Proton Synchrotron," *Physical Review Special Topics-Accelerators and Beams*, vol. 14, no. 7, 2011.

[159] V. Baglin, P. Chiggiato, P. Cruikshank, M. Gallilee, C. Garion, and R. Kersevan, "High-Luminosity Large Hadron Collider (HL-LHC): Preliminary Design Report - Chapter 12: Vacuum System," 2015.

[160] B. Angerth, E. Fischer, and O. Gröbner, "The clearing fields of the ISR," in *Proceedings of 8th International Conference on High Energy Accelerators*, p. 238, 1971.

[161] D. Alesini, A. Drago, A. Gallo, S. Guiducci, C. Milardi, and M. Zobov, "Experimental Measurements of e-Cloud Mitigation using Clearing Electrodes in the DAΦNE Collider," in *Proceedings of 3rd International Particle Accelerator Conference (IPAC 2012)*, 2012.

[162] G. Tang, A. C. Hourd, and A. Abdolvand, "Nanosecond pulsed laser blackening of copper," *Applied Physics Letters*, vol. 101, no. 23, 2012.

[163] R. Valizadeh, O. B. Malyshev, S. Wang, S. A. Zolotovskaya, W. A. Gillespie, and A. Abdolvand, "Low secondary electron yield engineered surface for electron cloud mitigation," *Applied Physics Letters*, vol. 105, no. 23, 2014.

[164] G. Tang and A. Abdolvand, "Laser-assisted highly organized structuring of copper," *Optical Materials Express*, vol. 1, no. 8, pp. 1425–1432, 2011.

[165] S. Calatroni, "LESS (Laser Engineered Surface Structures): perspectives for application at CERN," in *International Workshop on Functional Surface Coating and Treatment for UHV/XHV Applications*, 2015.

[166] C. Y. Vallgren, S. Calatroni, P. C. Pinto, A. Kuzucan, H. Neupert, and M. Taborelli, "Characterization of carbon coatings with low secondary electron yield," in *Proceedings of 2nd International Particle Accelerator Conference (IPAC 2011)*, 2011.

[167] M. Taborelli. Private communication, 2015.

[168] V. Baglin and B. Jenninger, "Pressure and heat load in a LHC type cryogenic vacuum system subjected to electron cloud," in *Proceedings of 31st ICFA Advanced Beam Dynamics Workshop on Electron-Cloud Effects (ECLOUD'04)*, 2004.

[169] V. Baglin and B. Jenninger, "CERN SPS electron cloud heat load measurements and simulations," *Physical Review Special Topics-Accelerators and Beams*, vol. 6, no. 6, 2003.

[170] R. Salemme, V. Baglin, G. Bregliozzi, and P. Chiggiato, "Vacuum performance of amorphous carbon coating at cryogenic temperature with presence of proton beams," in *Proceedings of 7th International Particle Accelerator Conference (IPAC'16)*, 2016.

[171] P. Redhead, "Thermal desorption of gases," *Vacuum*, vol. 12, no. 4, pp. 203–211, 1962.

[172] G. Iadarola and G. Rumolo, "Electron cloud simulations with PyECLOUD," in *Proceedings of 23rd International Conference on Atomic Physics (ICAP 2012)*, 2012.

[173] F. Zimmermann, "Electron cloud simulations for SPS and LHC," in *Proceedings of 10th Workshop on LEP-SPS Performance (Chamonix X)*, 2000.

[174] G. Rumolo and F. Zimmermann, "Practical user guide for ECLOUD," *CERN-SL-Note-2002-016*, 2002.

[175] G. Rumolo, F. Ruggiero, and F. Zimmermann, "Simulation of the electron-cloud build up and its consequences on heat load, beam stability, and diagnostics," *Physical Review Special Topics-Accelerators and Beams*, vol. 4, no. 1, 2001.

[176] V. Baglin and B. Jenninger, "Gas condensates onto a LHC type cryogenic vacuum system subjected to electron cloud," in *Proceedings of 9th European Particle Accelerator Conference (EPAC'04)*, 2004.

[177] A. Kuzucan, H. Neupert, M. Taborelli, and H. Störi, "Secondary electron yield on cryogenic surfaces as a function of physisorbed gases," *Journal of Vacuum Science & Technology A*, vol. 30, no. 5, 2012.

[178] R. Coisson, R. Bossart, J. Bosser, L. Burnod, E. d'Amico, A. Hofmann, and J. Mann, "Observation of visible synchrotron radiation emitted by a high-energy proton beam at the edge of a magnetic field," *Nuclear Instruments and Methods*, vol. 164, no. 2, pp. 375–380, 1979.

[179] G. Arduini, N. Hilleret, F. Ruggiero, K. Cornelis, J. Jiménez, F. Caspers, O. S. Brüning, P. Collier, L. Vos, R. Garoby, *et al.*, "Electron cloud effects in the CERN SPS and LHC," in *Proceedings of 7th European Particle Accelerator Conference (EPAC 2000)*, 2000.

[180] S.-Y. Lee, *Accelerator physics*, vol. 491. World scientific Singapore, 1999.

[181] G. Papotti, T. Bohl, T. Linnecar, J. Tückmantel, and E. Shaposhnikova, "Study of controlled longitudinal emittance blow-up for high intensity LHC beams in the CERN SPS," in *Proceedings of 11th European Particle Accelerator Conference (EPAC 2008)*, 2000.

[182] H. Bartosik, *Beam dynamics and optics studies for the LHC injectors upgrade*. PhD thesis, 2013.

[183] M. Taborelli, "Carbon thin films for accelerator applications," in *International Workshop on Functional Surface Coating and Treatment for UHV/XHV Applications*, 2015.

[184] Y. Papaphilippou, H. Bartosik, G. Rumolo, and D. Manglunki, "Operational Beams for the LHC," *CERN Yellow Reports*, vol. 2, p. 80, 2016.

[185] J. P. Hobson, "Physical adsorption isotherms extending from ultrahigh vacuum to vapor pressure," *The Journal of Physical Chemistry*, vol. 73, no. 8, pp. 2720–2727, 1969.

[186] V. Baglin, "Latest results from COLDEX," in *47th Accelerator Performance Committee (APC), CERN*, 2005.

[187] B. Spataro, D. Alesini, M. Migliorati, A. Mostacci, L. Palumbo, V. Baglin, B. Jenninger, and F. Ruggiero, "Impedances of the cold bore experiment, COLDEX, installed in the SPS machine," *Nuclear Instruments and Methods in Physics Research Section A: Accelerators, Spectrometers, Detectors and Associated Equipment*, vol. 564, no. 1, pp. 38–43, 2006.

[188] "CERN Impedance Working Group," 2015.

[189] E. Shaposhnikova, T. Bohl, T. Linnecar, and J. Tückmantel, "Capture Loss of the LHC Beam in the CERN SPS," in *Proceedings of 9th European Particle Accelerator Conference (EPAC'04)*, 2004.

[190] V. Kain *et al.*, "Proton beam operation in SPS," *Joint LIU/HL-LHC day, October*, 2015.

[191] P. Chiggiato, "Vacuum Technology for Superconducting Devices," in *Proceedings of CAS - CERN Accelerator School: Course on Superconductivity for Accelerators, CERN-2014-005*, 2014.

[192] O. Gröbner, "Vacuum and cryopumping," in *Proceedings of CAS - CERN Accelerator School: Superconductivity and Cryogenics for Accelerators and Detectors, CERN-2004-008*, 2004.

[193] C. Benvenuti, "Molecular surface pumping: cryopumping," in *Proceedings of CAS - CERN Accelerator School: Vacuum Technology, CERN-1999-005*, 1999.

[194] J. Jeans, *An introduction to the kinetic theory of gases*. Cambridge University Press, Cambridge, 1967.

[195] S. Dushman, J. M. Lafferty, S. C. Brown, *et al.*, "Scientific foundations of vacuum technique," *American Journal of Physics*, vol. 30, no. 8, pp. 612–612, 1962.

[196] R. Haefer, "Cryopumping. Theory and practice," *Monographies on Cryogenics, Oxford: Clarendon Press, 1989*, vol. 1, 1989.

[197] J. Chubb, L. Gowland, and I. Pollard, "Condensation pumping of hydrogen and deuterium on to liquid-helium-cooled surfaces," *Journal of Physics D: Applied Physics*, vol. 1, no. 3, p. 361, 1968.

[198] J. Chubb and I. Pollard, "Experimental studies of hydrogen condensation on to liquid helium cooled surfaces," *Vacuum*, vol. 15, no. 10, pp. 491–496, 1965.

[199] C. Benvenuti, R. Calder, and G. Passardi, "The influence of thermal radiation on the vapour pressure of condensed hydrogen (and isotopes) between 2 and 4.5 K," *J. Vac. Sci. Technol.*, vol. 13, pp. 1172–1182, 1976.

[200] R. E. Honig and H. O. Hook, "Vapor pressure data for some common gases," *RCA review*, vol. 21, no. 3, pp. 360–368, 1960.

[201] P. Redhead, J. Hobson, and E. Kornelsen, *The Physical Basis of Ultrahigh Vacuum*. AVS Classics in Vacuum Science and Technology, American Inst. of Physics, 1997.

List of Figures

2.1 Repulsing Coulomb force exerted by two charges at rest and magnetic attractive force derived by Ampere's law for moving charges. . . . 17
2.2 Focusing/defocusing force F_x vs. x of a quadrupole magnet (left), and of two space-charge dominated beams: uniform (center) and Gaussian (right) density distributions. From [25]. . . . 20
2.3 Examples of generalized perveance K values at different energies in various LINAC designs. Courtesy of N. Chauvin. . . . 21
2.4 $F(\chi) = \int_1^{\chi} \frac{dy}{\sqrt{ln(y)}}$ between χ=1 and χ=4.5 . . . 22

3.1 Examples of (x-x') phase spaces for two beam divergence relationships of zero geometric emittance: $n = 1$ (left), $n = 3$ (right). . . . 24

4.1 Pictorial depiction of ionization, production and trapping of neutralizing particles leading to Space Charge Compensation. From [29]. . . . 28
4.2 Scheme of an uniform cylindrical beam propagating through a beam pipe. . . . 29
4.3 Space charge potential in the MYRRHA LEBT in presence of a degree of SCC ranging from 0 to 90%. . . . 29
4.4 Measured SILHI 75mA, 95 keV DC beam emittance without (left) and with ^{84}Kr injection [33]. . . . 30
4.5 Evolution of measured SILHI 75mA, 95 keV DC beam emittance with different gas species injection and at different pressure [33]. . . . 31
4.6 Spallation Neutron Source (SNS) electrostatic H^- LEBT. . . . 32
4.7 Multiparticle tracking simulation of the MYRRHA magnetic LEBT line from the ECR Ion Source to the first RFQ cells & corresponding RMS envelopes [39]. . . . 33

5.1 Schematic overview of the cascade and the products of a nuclear spallation reaction. 36
5.2 Spallation neutron yield per different incident proton energies and targets. . . . 37
5.3 Composition of a typical PWR spent nuclear fuel after an average in-pile burn-up and in-pool radiation waiting-time decay . . . 38
5.4 Nuclear waste problem: the impact of Partitioning & Transmutation . . . 39
5.5 Simulation of fuel cladding (left) and reactor primary coolant (right) temperature evolution in the XT-ADS reactor caused by beam interruptions of different length [48]. . . . 41
5.6 Beam trip frequency spectrum: recorded by SNS operation (2008), design basis for the Japanese ADS (JAEA), accepted for the MYRRHA accelerator project. From [53]. . . . 42
5.7 Schematic view of the MYRRHA Linear Accelerator. . . . 46
5.8 Schematic view of the MYRRHA Injector layout. . . . 49

6.1 General experimental layout of the RFQ@UCL programme in Louvain-la-Neuve, Belgium. . . . 51
6.2 Magnetic representation of the Pantechnik Monogan field, based on EU/FR 9615572 and US 6194836 patent. Courtesy of Pantechnik SA, all rights reserved ®. . . . 53

6.3 Cross section of the plasma chamber and pentode extraction of the Pantechnik Monogan 1000 Ion Source. Courtesy of Pantechnik SA, all rights reserved ®. . . . 54
6.4 CAD section of the full Pantechnik Monogan 1000 Ion Source procured for the MYRRHA low energy front-end test stand. Courtesy of Pantechnik SA, all rights reserved ®. . . . 55
6.5 Picture of the Pantechnik Monogan 1000 Ion Source procured for the MYRRHA low energy front-end test stand. Courtesy of Pantechnik SA, all rights reserved ®. 56
6.6 Conceptual sketch of the MYRRHA LEBT consolidated layout, from [39]. 57
6.7 3D CAD model of the MYRRHA low energy front-end, comprising the Ion Source, the LEBT line and the RFQ interface. Courtesy of LPSC Grenoble and SCK•CEN. 58
6.8 3D CAD model of the MYRRHA low energy front-end: zoom on the LEBT line and the RFQ interface, left and right sides. Courtesy of LPSC Grenoble and SCK•CEN. 59
6.9 Cross section of the 3D CAD model of the MYRRHA LEBT line and the RFQ interface. Courtesy of LPSC Grenoble and SCK•CEN. . . . 60
6.10 B-H curve of the XC10 steel adopted for the OPERA model of the MYRRHA LEBT solenoid set yoke. . . . 61
6.11 OPERA model of the MYRRHA LEBT solenoid set: modulus of the B field in the steel yoke. . . . 61
6.12 OPERA model of the MYRRHA LEBT solenoid set: modulus B field along the z axis, at r = 0 mm. . . . 62
6.13 OPERA model of the MYRRHA LEBT solenoid set: the H and V steerers coils model. . . . 62
6.14 CAD model of the collimation stage designed for the MYRRHA LEBT. The diaphragm preceding the first slit is not shown. The ultimate beam aperture is defined by the RFQ collimator, visible on the back. Courtesy of LPSC Grenoble. . . . 64
6.15 Scheme of the MYRRHA low energy front-end vacuum system. Courtesy of LPSC Grenoble. . . . 65
6.16 CAD cross section and picture of the MYRRHA LEBT Faraday Cup. Courtesy of LPSC Grenoble. . . . 66
6.17 Allison Scanners emittancemeter adopted for the MYRRHA LEBT line. Left: picture before installation. Top right: a cross section from the CAD drawing. Bottom right: measurement principle of a Allison Scanner. Courtesy of IPHC Strasbourg. . 67
6.18 Required beam structure and chopper timing for sub-criticality monitoring of the MYRRHA reactor and potential beam extraction to an ISOL@MYRRHA facility. . 68
6.19 A simple symmetric electrostatic, straight parallel plates, deflector for charged particles. . . . 69
6.20 Poisson simulation of the electric field equipotential lines and direction/magnitude (arrows) on the transverse plane of the MYRRHA LEBT chopper, nominal position. Geometric units are in cm. . . . 71
6.21 Horizontal E_x and vertical E_y electric field components, along the x axis in the transverse xy plane, of MYRRHA LEBT chopper, nominal position. . . . 72
6.22 Horizontal E_x and vertical E_y electric field components, along the y axis in the transverse xy plane, of MYRRHA LEBT chopper, nominal position. . . . 72
6.23 Poisson simulation of the electric field equipotential lines and direction/magnitude (arrows) on the longitudinal plane of the MYRRHA LEBT chopper, nominal position. 73
6.24 Longitudinal E_z and vertical E_y electric field components, along the z axis in the longitudinal yz plane, of MYRRHA LEBT chopper, nominal position. . . . 73
6.25 3D CAD model of the MYRRHA LEBT RFQ interface and cross section. The longitudinal dimensions and the beam aperture are quoted, in mm. . . . 74
6.26 Electric equivalent of the MYRRHA LEBT chopper driver. . . . 76
6.27 Multiparticle simulation in TRACK of the transverse spot, horizontal and vertical phase space at the RFQ entrance for the three particle species (H^+, H_2^+, H_3^+) present in the MYRRHA LEBT. The limit, circular aperture (9 mm) left by the RFQ collimator is depicted in blue. Courtesy of J.-P. Carneiro. . . . 77
6.28 Gaussian power distribution deposited by a concentrated 600 W, RMS $\sigma = 1$ mm beam. . . . 78

6.29 Coupled thermo-mechanical/fluid dynamics Ansys/Fluent simulation of a RFQ collimator mockup surface exposed to a peak power density of 96 W/mm^2 and cooled by demineralized water in forced convection. . . . 79
6.30 Fluid dynamics Fluent simulation of the fianl RFQ collimator cooled by 0.1 kg/s of demineralized water in forced convection. . . . 79
6.31 Typical sputtering yield for H^+ (30 keV) impinging at different angles with respect to normal direction on three technical surfaces. . . . 82
6.32 Spectra of the energy (E) and directions in space ($cos(x)$, $cos(y)$, $cos(z)$) of sputtered atoms emitted from Cu after impingement of H^+ (30 keV) projectiles in normal direction. . . . 83
6.33 Poisson simulation of the electric field equipotential lines and direction/magnitude (arrows) on the longitudinal plane, in cylindrical coordinates, of the MYRRHA LEBT RFQ collimator electron repeller. . . . 84
6.34 Longitudinal E_z (green) and radial E_r (red) electric field components, along the z axis in the longitudinal rz plane, of MYRRHA LEBT RFQ collimator electron repeller. . . . 85
6.35 Potential available across the RFQ collimator. The electron repeller electrode is polarised at a nominal voltage of -500 V. . . . 85
6.36 Cross section of the RFQ collimator equipped with RFQ electron repeller. The electrode, isolated from the ground by an insulator sandwich, is visible. . . . 86
6.37 Picture of the MYRRHA LEBT AC Current Transformer procured by Bergoz Instrumentation, France. . . . 86
6.38 3D CAD model of the MYRRHA LEBT RFQ interface, including the beam chopper, the RFQ collimator, the RFQ electron repeller and the ACCT. A RFQ mock-up flange, to be adopted during the LEBT commissioning phase, is represented on the back. Courtesy of SCK•CENand UCL/CRC. . . . 87
6.39 Vertical H^+ beam emittance measured during the MYRRHA Ion Source FATs after species separation (dipole bend). No polarisation is applied to the Einzel lens present in the extraction box. . . . 88
6.40 Ionization efficiency measured by scanning dipole method during the MYRRHA Ion Source FATs. The peaks corresponds to the three ion intensities recorded. . . . 89
6.41 Snapshot of the recorded H^+ beam intensity during the MYRRHA Ion Source FATs. The vertical peaks correspond to instabilities in the beam intensity mainly caused by HV sparking. . . . 89
6.42 Experimental setup during the MYRRHA IS Factory Acceptance Tests (up) and Site Acceptance Tests (down), in Pantechnik SA, Bayeux, France and UCL/CRC, Louvain-la-Neuve, Belgium. . . . 90
6.43 Beam imprint left by exposition of a planar, water cooled, target to a 11.5 mA beam delivered by the MYRRHA Ion Source for 1 hour. The diameter of the trace is ∼29 mm. . . . 90
6.44 Simulation in TRACK of the beam spot and transverse $x-x'$ phase space at z=0.465 m for a partial (80%) space charge compensated beam leaving the MYRRHA Ion Source. . . . 91
6.45 Vertical emittance measurements at exit of the MYRRHA Ion Source (z∼0.765 m) for different Einzel lens polarisation levels: 0 kV, 22.3 kV, 25.5 kV. Total beam intensity 9 mA (all species), V_{puller}=23 kV, $V_{repeller}$=1206 V, RF forward power = 212 W, gas flow = 0.4 sccm (pure H_2). . . . 92
6.46 Vertical emittance measurement at exit of the MYRRHA Ion Source (z∼0.900 m). No polarisation on the Einzel lens. Total beam intensity is 13 mA (all species), V_{puller}=25.8 kV, RF forward power=263 W, gas flow=0.3 sccm (pure H_2), p_{source}=8.7·10^{-6} mbar. . . . 92
6.47 Input beam horizontal and vertical emittances and transverse distribution adopted as reference for the LEBT multiparticle simulations, corresponding to the beam properties available at z = 100mm, i.e. after ten centimetres of the MYRRHA ECRIS plasma chamber extraction hole. . . . 93

6.48 LEBT beam transmission efficiency for a 5mA H^+ beam generated by the MYRRHA IS, transported and matched by the LEBT into the RFQ in a LEBT solenoids fields $|B_1|$-$|B_2|$ phase space. The optimum solenoids working point is marked. 94
6.49 Multiparticle H^+ (up) and H_2^+ (down) tracking simulation and aperture model through the MYRRHA LEBT implemented in Tracewin. 94
6.50 Transverse emittance evolution along the MYRRHA LEBT and the MAX RFQ, with a collimation stage in the middle and at the RFQ injection. 95
6.51 H_2^+ transmission along the MYRRHA LEBT. The cleaning efficiency of the middle and RFQ collimation stage is appreciable. 95
6.52 Multiparticle H^+ tracking simulation through the MYRRHA RFQ interface in Tracewin, in nominal conditions (left) and with a chopper deflection of 116 mrad (right). The apertures of the conical reduction are 30/9 mm. 96
6.53 H_2^+ transmission in the RFQ interface. 96
6.54 Space charge compensation degree considered along the MYRRHA LEBT in multi-particle beam transport design simulations. 97
6.55 Snapshot of the transverse emittance evolution along the MYRRHA LEBT and the MAX RFQ during the first microseconds after a beam chopper pulse: chopper in nominal position (left) and in back-up position (right). 98
6.56 Calculated neutralization characteristic transient time and LEBT transmission probability for different pressure levels along the MYRRHA LEBT. 99
6.57 Calculated neutralization characteristic transient time for different levels of H_2, N_2, Ar, Kr dominant residual gases along the MYRRHA LEBT. 100

7.1 Qualitative scheme of the electron cloud formation process in the LHC, appeared on the CERN Courier in 1999 [97]. 104
7.2 Left: the LHC synchrotron radiation photon flux spatial distribution in the vertical plane. Right: Synchrotron radiation energy spectra of an LHC dipole evaluated at injection energy (450 GeV), at energy where synchrotron radiation energy becomes relevant for electron cloud (2.5 TeV), Run 1 top energy (3.5 TeV) and design top energy (7 TeV). From [101]. 106
7.3 Laboratory reflectivity characterization. Left: measured azimuthal distribution of the reflectivity of Cu and sawtooth-ed Cu samples with a LHC-type photon spectrum distribution. Right: spectral composition of the reflectivity in three reflection regimes (forward, backward, diffused) of Cu and sawtooth-ed Cu samples, employing monochromatic incident light. From [103]. 107
7.4 Electron yield measured for 26 MeV H, 126 MeV Au, and 182 MeV O beams incident on flat or serrated stainless steel surfaces as a function of the impingement angle θ. From [110]. 109
7.5 Schematic depiction of the possible processes occurring when an electron interacts on a solid surface. 109
7.6 The universal mean free path curve describing the energy dependence (mediated over a range of materials) of the escape depth of electrons in metallic (M) and insulator (I) solid, for electron-electron (λ_{e-e}) and electron-phonon (λ_{e-ph}) scattering. . . . 110
7.7 The Secondary Emission Yield (SEY) curve in the energy range of interest for electron cloud. The contribution of the elastic (low energy) and inelastic (high energy) electrons with respect to the true secondaries is better visible on the zoomed plot on the right. 111
7.8 Normalized energy distribution of true secondary electrons in the low energies range. 112
7.9 The transverse charge distribution $\rho(x, y)$ and relative electric field modulus $\|\mathbf{E}(x, y)\|$ calculated by pyECLOUD for the simulation of a Gaussian LHC proton bunch slice at 450 GeV/c inside an arc beam screen. From [123]. 113
7.10 The considered "kick" and "autonomous" electron-bunch interaction regimes in a circular beam pipe. 115

7.11 Left: Energy gain as a function of the initial electron's radial position, in the LHC nominal case, with three (rectangular, Gaussian, parabolic) longitudinal bunch distributions (solid, dashed, dot-dashed lines). Right: zoom at low radii. The envelope dashed lines correspond to the analytical forms in the autonomous and kick approximation found in Eq. 7.32 and 7.34. From [127]. 116
7.12 Left: SEY curve of scrubbed Cu ($\delta_{max} = 1.3$) and definition of E_1 and E_2. The regions where the material acts as a net electron absorber (blue) or emitter (red) are shown. Right: Evolution of $\delta(E_1 < E < E_2) > 1$ for different δ_{max}. 117
7.13 Maximum electron density (top)and δ_{eff} (bottom) as a function of δ_{max} parameter in the SEY for the case of the LHC beam screen, but in absence of magnetic field. From [123]. 120
7.14 Electron density, during the electron cloud build-up, simulated in a dipole (left) and quadrupole (right) magnetic region of the LHC. From [123]. 121
7.15 Transverse oscillation measured with the transverse feedback pick-ups at the first injection of 48 bunches of 25 ns beam into the LHC in 2011. Beam was dumped twice due to a violent instability in the vertical plane, causing losses above the interlock threshold. From [130]. 122
7.16 Bunch-by-bunch energy loss and phase shift of 11 trains of 72 bunches (25ns spacing) in the LHC. The larger values at 4 TeV are due to the contribution of the synchrotron radiation photoelectrons to the electron cloud build-up. From [130]. 122
7.17 Horizontal and vertical bunch-by-bunch emittance measurement on Beam 1 during a LHC 25 ns scrubbing fill. From [123]. 124
7.18 Evolution of the bunch-by-bunch intensity of Beam 1, normalized to the injected value, in the first hours of the 2012 LHC 25 ns Scrubbing Run. From [123]. 124
7.19 The ESD mechanism proposed by MGR model. From [132]. 125
7.20 Electron desorption yield, for different gas species, as a function of the electron dose for an unbaked OFHC copper sample bombarded with 300 eV electrons. From [134]. 127
7.21 Electron cloud dissipated power per unit lenght as a function of the beam bunch intensity, with four trains of 72 bunches, measured with the COLDEX experiment with a ID67 OFHC Cu beam screen. From [138]. 129

8.1 Schematic layout of the LHC: Beam 1 (blue) circulates clockwise and is injected by the SPS in TI2 at Point 2, while Beam 2 (red) counter-clockwise and is injected by the SPS in TI8 at Point 8. 132
8.2 Left: LHC main dipole magnet cross section within the cryostat. Courtesy of CERN, 1999. Right: picture of a cross section of the cold mass; the superconducting coils, the cold bore and beams screens are visible. 133
8.3 Heat loads dissipated by beam-induced losses in the LHC cryogenic vacuum as a function of the LHC beam energy. From [148]. 135
8.4 Cross section of the schematic cryogenic LHC vacuum principle. From [149]. 135
8.5 H_2 photodesorption in a LHC type cryogenic vacuum system employing a beam screen with and without holes. From [150]. 136
8.6 Decrease of the SEY of a copper sample exposed to the bombardment of the electrons from the electron cloud developed in the SPS by LHC-type beams, as a function of the time of exposure. From [141]. 137
8.7 Decrease of δ_{max} on a Cu colaminated sample of LHC beam screen as a function of the dose of impinging electrons at different energy levels and normal incidence. From [153]. 138
8.8 Measured reduction of the photoelectron yield per adsorbed photon of a copper colaminated sleeve with a LHC-type sawtooth structure, during irradiation with synchrotron White Light radiation from EPA (critical energy: 194 eV) at 11 mrad incidence. From [150]. 139
8.9 LHC baseline plan for the next decade and beyond showing the energy of the collisions (upper red line) and luminosity (lower green lines). 141

8.10 Geometrical luminosity reduction factor R vs. β^*. Left: constant normalized beam separation for the nominal LHC, for HL-LHC without crab cavities and for HL-LHC with crab cavities cases. Right: depiction of bunch crossing overlap reduction effect (top), and the crab cavity beam manipulation (bottom). 144
8.11 Bunch intensity dependence for the LHC arc main dipole (left) and quadrupole (right) magnets. The model assumes constant E_{max} and uniform SEY over the beam screen surface. From [156]. 145
8.12 Expected total heat load dissipated by electron cloud on the HL-LHC upgraded Inner Triplets beam screen at IP1/5 (left) and at IP2/8 (right) as a function of the surface SEY. The cooling capacity of $\sim$ 200 W is marked in red. From [156]. . . . 146
8.13 Laser Engineered Structured Surfaces, type A. Courtesy of A. Abdolvand, University of Dundee. 147
8.14 From left to right: copper surface before laser processing; LESS type A structures, LESS type B structures, LESS type C structures. Courtesy of A. Abdolvand, University of Dundee. 147
8.15 Secondary Electron Yield of a Cu sample treated with Laser Engineered Structured Surfaces, type C, measured at room temperature. From [165]. 148

9.1 Laboratory measurements of SEY on one witness sample obtained during COLDEX BS a-C coating. 150
9.2 Layout of sectors 431/430 elaborated from the SPS LSS4 layout drawing of period 41410-42210 (SPSLNINS0084). 150
9.3 Schematic view of the LSS4 by-pass movement system. Courtesy of P. Chiggiato. . 151
9.4 Vertical cross section of the COLDEX cryostat and vacuum principle. 152
9.5 2014 COLDEX a-C coated beam screen layout drawing following 2003 modification. 153
9.6 Picture of 2014 COLDEX a-C coated beam screen during re-installation. Courtesy of G. Bregliozzi. 153
9.7 Schematic view of the COLDEX vertical, transverse cryostat cross section. 154
9.8 Left: Picture of the COLDEX chimney electrode and its bakeable support. Right: drawing of the room temperature chimney, with the chimney electrode inserted. . 155
9.9 Picture of one of the insulated BS baffle, serving as BS electrode. 155
9.10 Picture of SPS vacuum sectors 430 and 431 installed in TS45 of SPS/LSS4. 156
9.11 Schematic view of SPS/LSS4 vacuum sectors 430 and 431 vacuum devices and instrumentation following 2014 COLDEX recommissioning and further 2016 upgrade (new GIS). 156
9.12 Thermal Desorption Spectroscopy of H_2, N_2 and CO measured on a-C coating as a function of the initial coverage θ_0 and β. 159
9.13 Adsorption isotherms of H_2 on a-C coating at 6.5 K and 11.1 K. 159

10.1 Flowchart of the steps carried in a pyECLOUD simulation main loop. From [124]. 162
10.2 PyECLOUD simulation of heat load in the COLDEX nominal case, 26 GeV, T=10 K, σ_i=0.2 Mbarn, versus SEY for different bunch intensities. 165
10.3 PyECLOUD simulation of heat load in the COLDEX nominal case, 26 GeV, T=10 K, σ_i=0.2 Mbarn, versus bunch intensity for different surface SEY. 165
10.4 Normalized impinging electrons energy spectra (over 320 passages) in the case of SEY=1.1 (left) and SEY=1.4 (right), for different bunch intensities. PyECLOUD simulation, 26 GeV, T=10 K, σ_i=0.2 Mbarn. 166
10.5 Normalized impinging electrons energy spectra (over 320 passages) in the case of SEY=1.25, for different bunch intensities. PyECLOUD simulation, 26 GeV, T=10 K, σ_i=0.2 Mbarn. 166
10.6 Electron density per passage (left) and sum of the kinetic energies of the impinging electrons (right) in the intermediate case of SEY = 1.25. PyECLOUD simulation, 26 GeV, T=10 K, σ_i=0.2 Mbarn. 167
10.7 Impinging electron flux per vertical slice for $1.5{\cdot}10^{11}$ ppb and different surface SEY. PyECLOUD simulation, 26 GeV, T=10 K, σ_i=0.2 Mbarn. 167

10.8 Impinging electron flux per vertical slice for SEY=1.25 and different bunch intensities. PyECLOUD simulation, 26 GeV, T=10 K, σ_i=0.2 Mbarn. 168
10.9 SPS 200 MHz cavities RF voltage cycle (left) and average bunch length evolution (right) during a SPS cycle with a LHC type beam, 4x72 bunches spaced 25 ns, of $1.3{\cdot}10^{11}$ ppb [182]. 169
10.10Normalized impinging electrons energy spectra (over 320 passages) in the case of SEY=1.4, for different bunch intensities. PyECLOUD simulation, 26 GeV (left) and 450 GeV (right), T=10 K, σ_i=0.2 Mbarn. 171
10.11Electron density per passage (left) and sum of the kinetic energies of the impinging electrons (right) vs SEY for $1.5{\cdot}10^{11}$ ppb. PyECLOUD simulation, 26 GeV (top) and 450 GeV (bottom), T=10 K, σ_i=0.2 Mbarn. 171
10.12PyECLOUD simulation of heat load in the COLDEX alternative case, 450 GeV, T=10 K, σ_i=0.2 Mbarn. Top: versus surface SEY for different bunch intensity; bottom: versus bunch intensity for different surface SEY. 172
10.13PyECLOUD simulation of heat load in the COLDEX nominal (left) and warm (right) case, 26 GeV, σ_i=0.2 Mbarn, versus surface SEY for different bunch intensity. Left: T=10 K, right: T=300 K. 173
10.14PyECLOUD simulation of heat load in COLDEX for σ_i=0.2 Mbarn (left) and σ_i=2.0 Mbarn (right) cases, 26 GeV, versus surface SEY for different bunch intensity. . . . 174
10.15COLDEX a-C coating SEY model fitted following the phenomenological modeling formalism proposed in [117] and [113]. 175
10.16PyECLOUD simulation of heat load in the COLDEX nominal case with an upgrade a-C SEY model, 26 GeV, T=10 K, σ_i=0.2 Mbarn, versus SEY for different bunch intensities. 177
10.17SEY model for a-C versus Cu for δ_{max} =1.1, 1.4, 1.7. 177
10.18PyECLOUD simulation of heat load in the COLDEX nominal case with an upgrade a-C SEY model, 26 GeV, T=10 K, σ_i=0.2 Mbarn, versus bunch intensity for different surface SEY. 178
10.19Normalized impinging electrons energy spectra (over 320 passages) in the case of SEY=1.1 (left) and SEY=1.4 (right), for different bunch intensities. PyECLOUD simulation, a-C SEY model, 26 GeV, T=10 K, σ_i=0.2 Mbarn. 178
10.20PyECLOUD simulation of heat load in the COLDEX alternative case with an upgrade a-C SEY model, 450 GeV, T=10 K, σ_i=0.2 Mbarn, versus SEY for different bunch intensities. 179
10.21PyECLOUD simulation of heat load in the COLDEX alternative case with an upgrade a-C SEY model, 450 GeV, T=10 K, σ_i=0.2 Mbarn, versus bunch intensity for different surface SEY. 179
10.22Normalized impinging electrons energy spectra (over 320 passages) in the case of SEY=1.1 (left) and SEY=1.4 (right), for different bunch intensities. PyECLOUD simulation, a-C SEY model, 450 GeV, T=10 K, σ_i=0.2 Mbarn. 179
10.23Effect of the electron reflectivity R_0 on the simulated of heat load in the COLDEX nominal (26 GeV, left) and alternative (450 GeV, right) cases with an upgrade a-C SEY model, for different bunch intensity at constant δ_{max} = 1.1. T=10K, σ_i=0.2Mbarn. 180

11.1 SPS Page 1 displaying the machine beam intensity and magnetic cycles during a SPS Scrubbing Run. The scrubbing cycle is here MD3: four batches are being injected at a rate of 72 bunches ($1.7{\cdot}10^{11}$ ppb) per injection every 2 basic periods (3.6 s) and left circulate at 26 GeV/c for 7.2 s. Beams is dumped right before the acceleration ramp. 182
11.2 COLDEX Run 1 during the SPS Scrubbing Run 1 of 2014. Top: cycle integrated beam intensity; center: vacuum pressure along the sector 431; bottom: RGA ion current relative to H_2 and reference BS temperature. 183
11.3 COLDEX Run 1: zoom at the first 20 hours, while the BS was held at 50 K. . . . 184
11.4 COLDEX Run 1: zoom at the first 20 hours after cool-down of the BS to 5 K. . . 185

11.5 COLDEX Run 1: zoom at the electron activity measured by the chimney electrode with a bias voltage of +1 kV and the SPS BLM 41835 located at the MSE41835 over a period of 48 hours. The electrode signal is cut-off below the noise level of $6.5 \cdot 10^{-9}$ A. 186
11.6 COLDEX Run 2 during the SPS Scrubbing Run 2 of 2014. Top: cycle integrated beam intensity; center: vacuum pressure along the sector 431 and CB reference temperature; bottom: RGA ion current relative to H_2 and reference BS temperature. 187
11.7 COLDEX Run 2: total dissipated heat load measured on the BS during the initial intensity ramp-up. 187
11.8 COLDEX Run 2: measured dynamic heat load as a function of the number of circulating batches, for different bunch intensities. 188
11.9 COLDEX Run 2: electron activity during the initial intensity ramp-up, in the time frame similar to Fig. 11.7, left. 188
11.10 COLDEX Run 3 during the SPS Scrubbing Run 4 of 2015. Top: cycle integrated beam intensity; center: vacuum pressure along the sector 431; bottom: BS inlet, outlet temperatures and He gas flow. 189
11.11 COLDEX Run 3: zoom at the first 10 hours, when the BS was held at 10-15K. . . 189
11.12 COLDEX Run 3: zoom after the BS warm-up to 60K, showing the monolayer build-up the CB caused by transmission of the gas desorbed at the RT extremities due to electron cloud. 190
11.13 Effect of the monolayer build-up and temperature reduction in the CB observed in Run 3. Left: phase diagram of He; the described thermodynamic transformation is shown on the transition curve of the saturated He I. Right: adsorption isotherms of H_2 on Cu/stainless steel, DRK (Dubinin-Radusckevisch-Kanager) model [185]; the monolayer build-up at 4.2 K and reduction of equilibrium pressure arising from a CB temperature reduction to 3.8 K are sketched. 190
11.14 COLDEX Run 3: impact of the installed solenoids at the RT extremities. Top: 3x72 bunches, $1.2 \cdot 10^{11}$ ppb. Bottom: 4x72 bunches, $2.0 \cdot 10^{11}$ ppb. 191
11.15 COLDEX Run 3: observation of the dissipated dynamic heat load in beam/no beam transients. 192
11.16 COLDEX Run 3: measured electron activity during the pressure build-up due to monolayer accumulation of the CB. 193
11.17 COLDEX Run 3: electron current measured by the chimney electrode during a period of pronounced beam losses. The peaks are especially correlated to the injection of the fourth and last batch of 72 bunches. 193
11.18 COLDEX MD1 with a coverage of $\sim 3.2 \cdot 10^{16}$ H_2/cm^2, 2015. Top: cycle integrated beam intensity; center: vacuum pressure along the sector 431; bottom: BS inlet, outlet temperatures and He gas flow. 194
11.19 COLDEX MD1: evolution of the total and partial H_2 pressure during the intensity ramp-up and BS warm-up. 194
11.20 COLDEX MD1: dissipated heat load measured during the intensity ramp-up and final long term circulation of 4x72 bunches of $1.5 \cdot 10^{11}$ ppb. 195
11.21 COLDEX MD1: electron activity measured by the chimney electrode during the initial intensity ramp-up. 195
11.22 COLDEX MD1: electron current measured by the chimney electrode during a period of pronounced beam losses. 196
11.23 COLDEX MD2: 1% of the beam is uncaptured at the first batch injection and leads/lags in the longitudinal phase space, as measured by the SPS Mountain Range 200 MHz RF pick-up. 196
11.24 COLDEX MD2: Cold Bore bath pressure and temperature instability. 197
11.25 COLDEX MD2 with a coverage of $\sim 2.1 \cdot 10^{16}$ CO/cm^2, 2015. By 19:12, the BS temperature was lowered to 12K. Top: cycle integrated beam intensity; center: vacuum pressure along the sector 431; bottom: RGA1 (COLDEX) ion currents representative of the H_2 ($m/e^- = 2$) and CO/N_2 ($m/e^- = 28$) gas species, with respect to the baseline background current, detected on the channel $m/e^- = 5$. . . 197

11.26COLDEX MD2: electron activity measured by the chimney electrode during the whole run. . . . 198
11.27Cumulated beam intensity per COLDEX run. The total beam dose is ∼9.89 Ah and is equivalent to 9 hours of HL-LHC nominal beam operation. . . . 199
11.28BS heat load measurement calibration with an heating wire by Joule effect. Courtesy of V. Baglin, 2003. . . . 201
11.29COLDEX Scrubbing Run with a scrubbed OFHC BS, 2004. Measurement of the electron activity due to electron cloud on both the chimney and BS electrodes, with 4x72 bunches of $1.1{\cdot}10^{1}1$ ppb, spaced 25 ns. Courtesy of V. Baglin, from [186]. . . 202
11.30COLDEX Scrubbing Run with a scrubbed OFHC BS, 2004. Measurement of the dynamic heat load due to electron cloud with 4x72 bunches of increasing bunch intensity, spaced 25 ns. Courtesy of V. Baglin, from [186] and [138]. . . . 202
11.31PyECLOUD simulation of heat load in the COLDEX nominal case with a a-C SEY model, 26 GeV, T=10 K, σ_i=0.2 Mbarn, versus SEY for different bunch intensities. The level corrisponding to heat load of 200 mW/m is marked. . . . 203
11.32Beam life time during Run 3 (left, when no dynamic heat load was detectable, see Fig. 11.15) and Run 4 (right, when a dynamic heat load was observed, see Fig. 11.20). 204
11.33Left: LHC type beams ramped to 450 GeV during LHC filling (fill 4452): the losses due to uncaptured beam are visible at the beginning of the acceleration ramp. Right: loss maps of the SPS ring during Run 3, when 4x72 bunches of $2 \cdot 10^{11}$ ppb were circulating: the losses are located in the arcs (especially of Sextant 1 and 4), in high dispersion areas, with a Q20 optics. Courtesy of V. Kain, from [190]. . . . 205
11.34PyECLOUD simulation of expected electron current collected on the chimney electrode in the COLDEX nominal case with a a-C SEY model, 26 GeV, T=10 K, σ_i=0.2 Mbarn, versus SEY for some bunch intensities. The detection limit of $2 \cdot 10^{-9}$ A, corresponding to a flux of $1 \cdot 10^{8}$ $e^-/(mm^2 s)$, is marked in red. . . . 206

A.1 Schematic depiction of two volumes, characterized by different thermodynamic properties, communicating through an orifice. . . . 218
A.2 Schematic depiction of a gas flow restriction offered by the conductance C situated between a pump of pumping speed S and a vacuum vessel. . . . 220
A.3 Pictorial depiction of submonolayer physical adsorption, or physisorption (left), where the cryopuming mechanism is molecule-substrate interaction, cryocondensation (center), where the leading mechanism is intermolecular interaction, and cryotrapping (right), when a condensable gas carrier traps non-condensable molecules of another gas that would have a much higher vapour pressure. . . . 222
A.4 Left: Sticking coefficient of H_2 as a function of the surface coverage. The H_2 is at 300 K incident onto a surface at 3.1 K. From [197]. Right: H_2 condensation coefficient onto a surface at 4 K as a function of the gas temperature. From [198]. 222
A.5 DRK isotherms between 3.0 K and 4.2 K for H_2 adsorbed on metallic surfaces like copper or stainless steel. . . . 223
A.6 Adsorption isotherms of H_2 on stainless steel measured at LHe temperatures. From [199]. . . . 224
A.7 Saturated vapour pressure of the most common gases present in UHV as a function of temperature, from [201] and references therein. Courtesy of V. Baglin, 1998. . . . 224
A.8 Influence of the heating rate β over the maximum desorption rate temperature T_p for an arbitrary activation energy for desorption E_d=159.7 meV. . . . 226

List of Tables

5.1 Comparison of accelerator-driven sub-critical and critical reactor systems: issues particularly relevant to MA and transuranic (TRU) are underlined [43]. 39
5.2 Accelerator beam requirements for different ADS stages. 40
5.3 MYRRHA beam characteristics 44
5.4 MYRRHA superconducting linac main parameters 48

6.1 Characterics of the Ion Source adopted for MYRRHA low energy front-end test bench 56
6.2 Overview of the MYRRHA LEBT solenoid with integrated H/V steerers sets specifications. 63
6.3 Sputtering yield calculated in SRIM for H^+ (30 keV) impinging on normal direction for different technical surfaces. 81
6.4 Results from the sputtering calculation: n. of atoms, n. of mm^3 of matter, n. of μm eroded in correspondence of a $\sigma = 3$mm beam spot. 81

7.1 Ionization cross sections for different gas species for singly charged ultrarelativistic positive particles in 10^{-18} cm^2, or Mbarn, from Rieke and Prepejchal [98], calculated at SPS injection energy and LHC design energy. From [99]. 104
7.2 Forward scattering photon reflectivity and photoelectron yield per absorbed photon with a LHC-type synchroton radiation spectrum (critical energy: 45 eV) for three Cu surfaces. From [105]. 107
7.3 Analytic results for the energy gain of electrons in the LHC nominal and ultimate case in the autonomous and kick approximation regime [127]. 116
7.4 Electron desorption yield parameters for unbaked and baked copper perpendicularly irradiated by 300 eV electrons. From [133] and references therein. 126

8.1 Proton cross sections relative to H_2 and design maximum gas densities at LHC design energy for different gas species. From [148]. 134
8.2 High Luminosity LHC parameters list for proton-proton collisions. 143

10.1 Beam input parameters for the PyECLOUD simulation of the COLDEX case. . . . 163
10.2 Secondary emission model input parameters for the PyECLOUD simulation of the COLDEX case. 164
10.3 Machine input parameters for the PyECLOUD simulation of the COLDEX case. . 164
10.4 Simulation settings for the PyECLOUD simulation of the COLDEX case. 164
10.5 SPS bunch lengths at injection (26 GeV) and flat-top (450 GeV) energy. 170
10.6 COLDEX a-C coating SEY model: parameters fitted for $R_0 = [0.7{:}1.0]$. 175
10.7 Right: SEY curve for different carbon thin film coating techniques tested at CERN. Left: influence of the H_2 content in the plasma discharge on δ_{max}. From [183]. . . 176

11.1 Upper limit of primary desorption yield η for H_2 detectable for the a-C coated BS held at 10 K in COLDEX. 200
11.2 Upper limit of the sum of the primary and recycling desorption yield over the sticking coefficient $\frac{\eta+\eta'}{\sigma}$ for H_2 detectable for the a-C coated BS held at 10 K in COLDEX. 201

A.1 Orifice conductance C' per unit surface (in practical units) for UHV common gas species at room temperature. 219